④

AD-A216 925

MSD-TR-89-21
VOLUME I

FOURTEENTH BIENNIAL GUIDANCE TEST SYMPOSIUM

PREPARED BY
CENTRAL INERTIAL GUIDANCE TEST FACILITY
GUIDANCE TEST DIVISION

DTIC
ELECTE
S JAN 18 1990 D
B

6585TH TEST GROUP
HOLLOMAN AFB, NEW MEXICO 88330-5000

3, 4, & 5 OCTOBER 1989

90 01 17 139

Publication of this report does not constitute approval or disapproval of the ideas or findings. It is published in the interest of exchanging scientific and technical information.

DISTRIBUTION STATEMENT: Approved for public release; distribution is unlimited.

The Public Affairs Office has reviewed this report, and it is releasable to the National Technical Information Service where it will be available to the general public, including foreign nationals.

REPORT DOCUMENTATION PAGE

Form Approved
OMB No. 0704-0188

1a. REPORT SECURITY CLASSIFICATION UNCLASSIFIED		1b. RESTRICTIVE MARKINGS NONE			
2a. SECURITY CLASSIFICATION AUTHORITY N/A		3. DISTRIBUTION/AVAILABILITY OF REPORT Approved for Public Release:			
2b. DECLASSIFICATION/DOWNGRADING SCHEDULE N/A		DISTRIBUTION UNLIMITED			
4. PERFORMING ORGANIZATION REPORT NUMBER(S) MSD-TR-89-21 (Volume I)		5. MONITORING ORGANIZATION REPORT NUMBER(S) MSD-TR-89-21 (Volume I)			
6a. NAME OF PERFORMING ORGANIZATION 6585th Test Group	6b. OFFICE SYMBOL (If applicable) 6585TG/PRX	7a. NAME OF MONITORING ORGANIZATION 3246th Test Wing			
6c. ADDRESS (City, State, and ZIP Code) Holloman AFB NM 88330-5000		7b. ADDRESS (City, State, and ZIP Code) Eglin AFB FL 32542-5000			
8a. NAME OF FUNDING/SPONSORING ORGANIZATION 6585th Test Group (MSD/AFSC)	8b. OFFICE SYMBOL (If applicable) 6585TG/GD	9. PROCUREMENT INSTRUMENT IDENTIFICATION NUMBER N/A			
8c. ADDRESS (City, State, and ZIP Code) Holloman AFB NM 88330-5000		10. SOURCE OF FUNDING NUMBERS			
		PROGRAM ELEMENT NO. 65708F	PROJECT NO. JON: 9993NGTS	TASK NO	WORK UNIT ACCESSION NO.

11. TITLE (Include Security Classification)

FOURTEENTH BIENNIAL GUIDANCE TEST SYMPOSIUM (VOLUME I)

12. PERSONAL AUTHOR(S)
The author's names are indicated on each individual paper.

13a. TYPE OF REPORT SYMPOSIUM PAPERS	13b. TIME COVERED FROM 3OCT89 TO 5OCT89	14. DATE OF REPORT (Year, Month, Day) 1989 OCTOBER 30	15. PAGE COUNT 502

16. SUPPLEMENTARY NOTATION

17.	COSATI CODES		18. SUBJECT TERMS (Continue on reverse if necessary and identify by block number)
FIELD	GROUP	SUB-GROUP	

19. ABSTRACT (Continue on reverse if necessary and identify by block number)

These proceedings contain papers which were presented at the Fourteenth Biennial Guidance Test Symposium. This symposium, hosted by the Central Inertial Guidance Test Facility, Holloman Air Force Base, New Mexico on 3-5 October 1989, was directed toward the exchange of information, stimulation of new ideas, and discussion of current techniques associated with the development and evaluation of inertial guidance and navigation systems.

The papers presented included such topics as new test and calibration techniques for accelerometers and ring laser gyros, advances in flight reference systems, new test equipment, and new software developments. Keywords: Inertial Measurement Units, Inertial Guidance, Strapdown Systems, Global Positioning Systems Guided Missiles, Aircraft Flight (tu)

20. DISTRIBUTION/AVAILABILITY OF ABSTRACT ☒ UNCLASSIFIED/UNLIMITED ☐ SAME AS RPT. ☐ DTIC USERS	21. ABSTRACT SECURITY CLASSIFICATION UNCLASSIFIED		
22a. NAME OF RESPONSIBLE INDIVIDUAL KENNETH R. HOLLAND, Symposium Manager	22b. TELEPHONE (Include Area Code) (505) 679-2125	22c. OFFICE SYMBOL 6585TG/GD	

DD Form 1473, JUN 86   Previous editions are obsolete.   SECURITY CLASSIFICATION OF THIS PAGE

FOURTEEN BIENNIAL
GUIDANCE TEST SYMPOSIUM
VOLUME I

ABSTRACT

These proceedings contain papers which were presented at the Fourteenth Biennial Guidance Test Symposium. This symposium, hosted by the Central Inertial Guidance Test Facility, Holloman Air Force Base, New Mexico, on 3-5 October 1989, was directed toward the exchange of information, stimulation of new ideas, and discussion of current techniques associated with the development and evaluation of inertial guidance and navigation systems. .

The papers presented included such topics as new test and calibration techniques for accelerometers and ring laser gyros, advances in flight reference systems, new test equipment, and new software developments.

This volume contains papers which are unclassified and have no distribution restriction.

Accession For	
NTIS GRA&I	☑
DTIC TAB	☐
Unannounced	☐
Justification	
By	
Distribution/	
Availability Codes	

Dist	Avail and/or Special
A-1	

FOURTEENTH BIENNIAL
GUIDANCE TEST SYMPOSIUM
VOLUME I

FOREWORD

The Fourteenth Biennial Guidance Test Symposium was held at Holloman Air Force Base, New Mexico, on 3-5 October 1989. This symposium was hosted by the Central Inertial Guidance Test Facility (CIGTF). The symposium's purpose was to provide a forum for approximately 400 people from industry, educational institutions, foreign governments, the Department of Defense, and other Government agencies. The forum provided an exchange of technical information and stimulation of new ideas associated with development, testing, and evaluation of inertial components, missile guidance, aircraft navigation, and global positioning systems.

Many excellent papers were received for presentation at this meeting, but due to the time allotted to this symposium, only a portion of those papers submitted could be included in the Program.

The Paper Selection Committee included Mr Gerald Anderson, AGMC/MAEE; Mr Jerry B. Bickenbach, Automated Sciences Group; Major Mike Chalifoux, USAF, 6510 TESTS/PM; Mr Richard E. Clark, TASC; Mr Gene DeNezza, TASC; Mr Sam George, OC-ALC/MMIRN; Mr Gaylord Green, Stanford University; Colonel O. Gogosha, USAF, BSD/EN; Mr Jim Hand, Charles Stark Draper Laboratory; Mr Richard Holdeman, TRW; Dr. Gib F. Kelley, DynCorp; LtCol Lewantowicz, USAF, AFIT/ENG; Colonel Roger McClain, USAF, BSD/CV; Major George Nemeyer, USAF, 4950 TESTW/FFS; Mr Jeff Robinette, ASD/AEAE; Mr Thomas E. Sanders, NADC; Mr Leonard Sugerman, PSL-NMSU; and Major J. Mathis, SSD/CWNUI GPS/JPO.

In addition to those mentioned above and the contributing authors, a large number of people contributed to the success of this symposium. I wish to express my appreciation to each of them for their efforts. Special thanks go to our Symposium Manager, Mr Kenneth R. Holland, and to the Assistant Symposium Manager, Ms Dora Walker.

Publication of this report does not constitute approval or disapproval of the ideas or findings. It is published in the interest of exchanging scientific and technical information

KENNETH R. WERNLE, Lt Col, USAF
Director, Guidance Test Division

PROCEEDINGS OF THE FOURTEENTH BIENNIAL GUIDANCE TEST SYMPOSIUM

CONDUCTED AT

HOLLOMAN AIR FORCE BASE, NEW MEXICO

HOSTED BY

6585th TEST GROUP
CENTRAL INERTIAL GUIDANCE TEST FACILITY
3-5 October 1989

FOURTEENTH BIENNIAL
GUIDANCE TEST SYMPOSIUM
VOLUME I

TABLE OF CONTENTS

FOURTEENTH BIENNIAL
GUIDANCE TEST SYMPOSIUM
VOLUME I

TABLE OF CONTENTS (Continued)

FOURTEENTH BIENNIAL
GUIDANCE TEST SYMPOSIUM
VOLUME I

TABLE OF CONTENTS (Continued)

FOURTEENTH BIENNIAL
GUIDANCE TEST SYMPOSIUM
VOLUME I

TABLE OF CONTENTS (Continued)

The Flight Test Program of the 10 $^{-11}$ Degree / Hour Gyroscope

by

**G. B. Green, C. W. F. Everitt, B. W. Parkinson
and the Stanford University Gyroscope Team**

Stanford University

October 1989

Presented to:

**Fourteenth Biennial Guidance Test Symposium
Department of the Air Force
Headquarters 6585th Test Group (AFSC)
Holloman Air Force Base, New Mexico 88330-5000**

The Flight Test Program of the 10^{-11} Degree / Hour Gyroscope
by
G. B. Green, C. W. F. Everitt, B. W. Parkinson and the Stanford Gyroscope Team

ABSTRACT

Physicists and engineers at Stanford University have created a wide range of exotic technologies to build and conduct a flight test of the lowest drift gyroscope ever built. These gyroscopes provide an absolute (without calibration of the gyroscope) reference system stable to 10^{-11} degrees / hour total drift—a million times better than the typically good calibrated inertial navigation system grade gyroscope. The flight test program of these gyroscopes will probe the very foundations of inertial space.

INTRODUCTION

The very formidable task of building and testing a gyroscope accurate absolutely (without calibration) to 10^{-11} degrees / hour starts with a group of very dedicated and creative people. Once you have assembled this group, the next step is to find a unique design capable of meeting the performance requirements, be very careful in manufacturing process, and plan an exotic test experiment to verify this absolute accuracy and then allow adequate time in the schedule to complete the project. The group at Stanford University has met this criteria.

The unique gyroscope design and fabrication is now complete after twenty-five years of effort. Error terms are controlled by the manufacturing process and the environmental control. The ground prototype environmental control system is complete for laboratory testing. The flight test environmental control system still is to be built. A startracker has been added to the stable member to measure the total integrated drift over a period of time and also a three axis accelerometer has been added consistent with the gyro accuracy. The laboratory test program of these devices is ongoing before commencing with the final environmental control system fabrication followed by the flight test program. The total integrated absolute Newtonian drift error expected of these instruments after a one year uninterrupted test is expected to be .0003 arc seconds.

THE GYROSCOPE

The gyroscope rotors are made from jewel-like spheres of solid fused quartz, roughly the size of ping-pong balls (1.5-inch diameter), each coated with a very thin (15 nanometer), very uniform, chemically pure, mechanically robust, electrically stable layer of the metal niobium. The rotor spheres achieve "near zero" extremes of homogeneity, mechanical sphericity, and electrical sphericity.

Homogeneity is achieved through the choice of material. Quartz is stable, has good inher-

ent uniformity and shrinks uniformly on cooling; being transparent it can also be optically selected to near-perfection. Density variations in these quartz spheres will be minute, parts in ten million, thousands of times less than in typical metal spheres. Equally severe constraints apply to the uniformity of the niobium coatings. To yield a uniform coating, the rotor is moved to 32 orientations corresponding to the faces and vertices of a regular icosahedron with an equal amount of niobium deposited for each orientation. Typical density homogeneity of the quartz rotor to better than $2 \times 10^{-6} \ \Delta \rho / \rho$ is achieved.

Mechanically, the 1.5-inch diameter rotors are within 40 atomic layers (0.8 millionth-inch) of a perfect sphere, rounder than anything within many light-years distance from us. If the Earth were smoothed to a proportionate sphericity, then the corresponding radial span, from towering mountain top to deep ocean trench, would be 20 feet. Only neutron stars are rounder.

Electrical sphericity, more subtly, requires that a quantity known as the electric dipole moment, fixed by the rotor's surface properties, be vanishingly small. Its value, scaled against the maximum allowable charge on the rotor, must be held to parts in ten million.

Attaining this triad of manufacturing extremes has demanded the invention of new methods for lapping, polishing and coating the spheres, and of new instruments for selecting the material and measuring the rotor's diameter, sphericity and surface properties. (References 1-3)

Each rotor spins inside a stator quartz housing, made in two halves to form a spherical cavity with clearances to the rotor of barely one thousandth of an inch. The matched housing halves are fabricated from the fused-quartz blanks into their final shape by ultrasonic machining, diamond grinding, lapping, and polishing. The stator surface is required to be spherical within 250 nanometers peak-to-valley. To achieve this requirement, approximate hemispheres are formed in the two halves by ultrasonic machining and hand lapping, the halves are precisely joined with tapered fused-quartz pins, and the assembled pair is tumble lapped. Tumble lapping is a process in which a weighted lapping element and slurry of grinding compound and water are located in the spherical cavity formed by the assembled housing, then the housing is randomly rotated about the lapping element.

To build a gyro absolutely accurate, early in the program four fundamental issues had to be resolved:

1) *Suspension:* How could the gyro rotors be suspended in mid-air (or mid-vacuum) without disturbance?

2) *Spin-up:* How could the rotors be set spinning and be kept spinning isolation for many years without disturbance?

3) *Readout:* Most baffling, how could the spin direction of a perfect unmarked sphere be observed and read out without disturbance?

4) *Environmental Control:* How could

the environment be controlled sufficiently so that no torques effect the rotating member?

In part, the answers lay in a separation of functions—electrical suspension, gas spin-up, and magnetic readout. In part, they lay in exploiting phenomena of superconductivity. And in part, they lay in precision control of gravity, magnetic and thermal environments.

Levitation is electrical with voltages applied to three pairs of saucer-shaped electrodes inside the spherical cavities, and the rotor stays centered to a few millionths of an inch while spinning at 10,000 rpm. To lift the rotor in a one g field takes 1,000 volts and resultant suspension torques. Mass-unbalance disturbance torques (where the mass unbalance is measured by the difference between the rotor center of support and center of mass) and the other disturbance torques coming from the suspension electrode voltages need to be further reduced. However if the gyroscopes are place in a controlled orbiting satellite, only micro-g levitation is required and only a fraction of a volt is needed for suspension.

Spin-up is by a scheme much like an old-fashioned water-wheel. A stream of helium gas is pumped past the ball at nearly the speed of sound, through a channel of sophisticated design cut in the inner surface of the stator housing. Full rotor speed is reached in half an hour. Again if this is accomplished in an orbiting satellite, evacuation to space is easy and the gas can be diminished to a pressure lower even than that of the space around the satellite, and the rotor coasts freely in vacuum. Figure 1 is the schematic of this process. The

subtleties lie in preventing electrical arcing during the spin-up cycle from the suspension system and in reaching final pressure—a pressure so low (10^{-11} torr or 1/100,000,000,000,000,000 of an atmosphere) that in 1,000 years the gyroscope will barely lose 1% of its starting speed. (Reference 4)
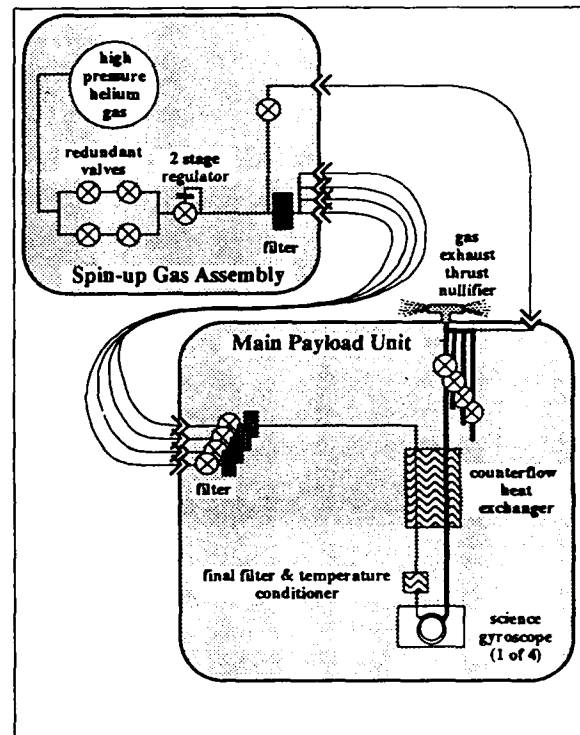
Figure 1 - Gyro Spinup Schematic

For a readout, the problem is to measure—to 1 milliarc-second—the direction of spin of a perfect unmarked sphere, and do so without disturbing it?

The answer comes through superconductivity, a phenomenon first seen in metals at low

temperatures by the Dutch physicist H. Kamerlingh Onnes in 1911, and now known in some ceramic materials at higher temperatures.

Superconductivity provides a spin pointer—one that is neither optical nor mechanical as in conventional gyroscopes but magnetic. It requires a sensitive noninterfering instrument, the SQUID (Superconducting QUantum Interference Device), to read the pointer. It also provides a region of very low and stable magnetic field for the gyroscope to minimize any magnetic error sources.

One property of superconductors is that when cooled below a specific "transition temperature" they completely lose their electrical resistance. Hence their name; they become not just "great" conductors, but for steady currents, perfect ones; currents have been shown to persist for many years absolutely unchanged.

Another phenomenon, equally surprising, is that when a superconductor—niobium, for example—spins, it generates a magnetic field effect known, after physicist Fritz London, as the London moment. Picture the niobium coating on the quartz gyro rotor as a crystalline lattice of positively charged atoms containing a sea of infinitely slippery electrons or to be more exact, electron-pairs. As the rotor starts turning, the niobium atoms move with it, but not the electron-pairs—not at first anyway.

Each circling positive charge, like a small electric current, generates a magnetic field parallel to the rotation axis. The total field

thus produced would be very large, were it not that the paired electrons themselves respond to it. Nearly all are forced to keep up with the lattice, generating a cancelling field of their own except in a shallow surface layer about 100 atoms thick. In this layer they lag slightly behind the charged lattice leaving a small difference field—the London moment—proportional to spin speed and exactly aligned with the spin axis. Here is our pointer for the readout.

To measure the spin direction, the rotor is encircled with a thin superconducting loop connected to a SQUID. As the gyro rotor tilts relative to the case (stator), the London moment tilts with it, changing minutely the magnetic field through the loop. So sensitive is the SQUID that a field change of 5×10^{-14} gauss (1/10,000,000,000,000 of the Earth's magnetic field), corresponding to a gyro tilt of 1 milliarc-second, is detectable within a few days of data collection.

The suspension, spin-up and readout stator housing features are produced by sputter deposition. These include the six suspension electrodes, the support lands around the electrodes, the spin-up land, and the gyro readout loop. The first three coatings are all thin copper films with a titanium bonding layer. The electrddes are about 3.5 mm thick and the lands are 13 mm thick. The readout loop is produced by depositing a 400 nm thick niobium layer overcoated with a 20 nm gold layer to assist in bonding wires and then by patterning the loop using either photolithographic or laser milling techniques. All of these coatings

have successfully undergone multiple thermal cycles between room temperature and 4°K. (Reference 5)

The exquisite sensitivity of the SQUID plus other constraints require that the gyroscope be operated in a magnetic field that is both very low and very stable. The field trapped in the rotor when it goes superconducting has to be practically zero; effects from the Earth's field varying from a spacecraft roll has to be attenuated by a factor of 10,000,000,000,000 before reaching the gyroscope.

One property of superconductors is that a closed superconducting shell cannot be penetrated by external magnetic fields. Long lead bags are used for shielding—the "balloons"— are applied first to pump magnetic fields out of the space containing the scientific instrument and then to keep them out. Four folded bags, known as lead balloons, are successively inserted each into the one before, cooled to superconducting temperatures and expanded. Each expansion lowers the field. Already large bags, containing operating gyroscopes, have been made with the lowest stable magnetic fields ever produced.
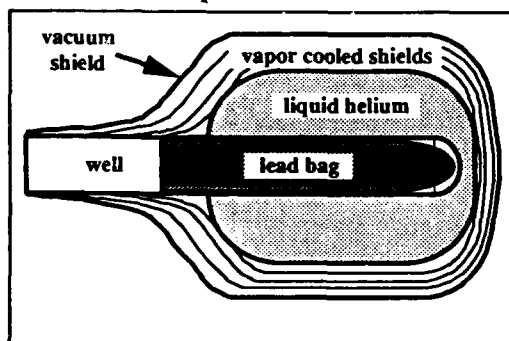
Figure 2 - Magnetic Shield

Attenuating the magnetic fluctuations by 10^{-12} for the SQUID readout takes, in addition to the lead bag, an outer shield of special iron alloy, local superconducting shields around each gyroscope, and finally the self-shielding action of the superconducting rotor within its own readout loop.

THE PLATFORM

A review shows that in order to conduct a test of an absolutely accurate 10^{-11} degree / hour gyroscope (without calibration) that the following platform design must be implemented:

1) The gyroscope should be tested in an orbiting platform so that the g forces can be minimized as well as the suspension torques.

2) The gyroscope must be cooled to at least superconducting temperatures for the readout and magnetic shielding.

The Platform core is a block of fused quartz, 21 inches long, bonded to a quartz telescope and containing within it four gyroscopes plus a drag-free proof mass. This gyro-telescope structure is kept at vacuum within a nine foot-long cigar-shaped chamber ("the probe"), which is inserted into a large dewar vessel filled initially with 400 gallons of superfluid helium The dewar maintains the instruments at a temperature of 1.8°K above absolute zero.

The drag free proof mass housed in the quartz block is a 1.5 inch quartz sphere in a slightly larger spherical cavity than that

of the gyroscope. The proof mass, being shielded from external accelerations, tends to
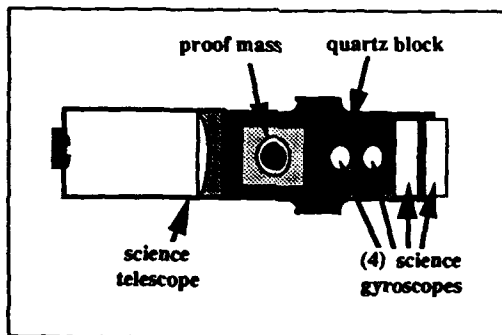
Figure 3 - Gyro, Proof Mass, and Quartz Block Assembly

follow an ideal gravitational orbit; and by sensing its position and applying thrust forces to make the spacecraft chase after it, the satellite can be made drag-free. The Helium gas boiling off from the dewar is expelled thru thrusters to maintain the proof mass at the center of the cavity. Because the mean acceleration on the gyroscopes is thus reduced to 10^{-12} g's by controlling to the proof mass, the gyroscope performance improves by a factor of 1,000. The drag free concept was developed at Stanford and demonstrated in 1972 by flight on the U.S. Navy's Triad Transit navigation satellite.

The flight telescope is used as sensor for the spacecraft attitude control system and for the measurement of the total gyro drift. The telescope provides the signal to maintain the satellite's roll axis pointing in the direction of the guide star to milliarc-seconds. Any small deviation in pointing is compared with the gyroscope readout signal to determine the spin-axis direction of the gyroscopes relative

to the reference. The telescope is also fabricated from fused quartz and is operated at a nominal 1.8°K. It has a physical length of 14 inches and a focal length of 150 inches. Readout is via light pipes into two photomultiplier chopper-detector assemblies. It's precision is 0.1 milliarc-second over a linear range of 70 milliarc-seconds. The total acquisition range is 2 arc-minutes. The readout of star direction is rigidly attached to the gyro readouts through the quartz block.
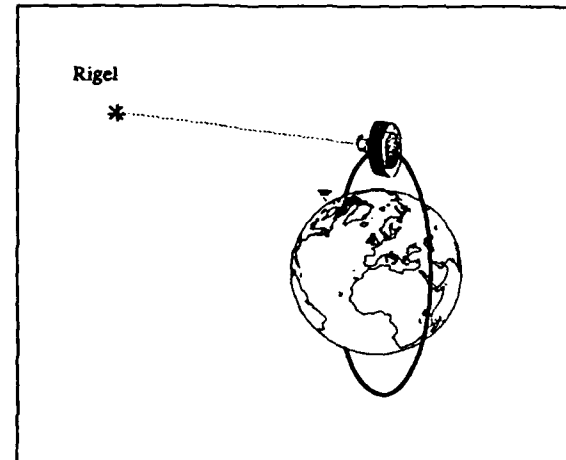
Figure 4 - Star Pitch / Yaw Reference

The gyro readout is referenced to the fixed stars since the readout loop is mechanically coupled to the telescope pointed at the guide star Rigel (the readout loop plane is aligned parallel to the telescope axis) and to a star blipper looking approximately normal to the telescope axis. The spacecraft together with the readout loop rolls about the line-of-sight to the star Rigel with a roll period of 10 minutes. The SQUID output is modulated at the 1.67 mHz roll frequency. The amplitude of the 1.67 mHz output is proportional to the angle be-

tween the gyro spin axis and the roll axis, and its phase is related to the position of the stars in the field of the star blipper. Misalignment between the roll axis and the line of-sight to Rigel can be subtracted from the SQUID output using the two-axis telescope readout signals, finally yielding an overall gyro readout.

The opening of the dewar is a necktube where the vacuum probe for the quartz block housing containing the gyroscopes is emplaced. The design of the vacuum probe and necktube represent a formidable physics and engineering challenge. First the assembly must survive launch loads. In addition it must meet the following abbreviated list of requirements: (1) Maintain stable quartz block temperatures of 1.8 °K, (2) Remove spin-up gas rapidly to prevent electrical breakdown, (3) Create an operating vacuum of better than 10-11 torr (gyro spin-down time constant is 4000 years), (4) Reduce the magnetic field to 10-14 gauss, (5) Minimize the heat leaks into the payload so the superfluid helium lasts 1 to 2 years, (6) Allow "rapid" assembly and disassembly, and (7) support all the interconnecting electrical cabling for the instruments of the stable quartz block assembly, readouts, heaters, thermometers, and other instrumentation (approximately 400 wires).

The evolved design supports the Quartz-Block load with a cantilevered aluminum cylinder. This is within the vacuum shell, both of which are attached at the base of the neck tube assembly. The neck-tube is wound of alumina fibers and bonded with epoxy.

This composite material has particularly high thermal resistance combined with high strength over the entire temperature range.
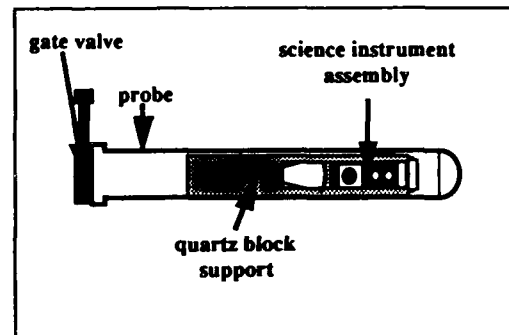
Figure 5 - Probe Assembly

In order to spin up the gyroscopes a system supplying each gyroscope with low temperature (5° - 7°K) helium gas through an in line class 100 articulate filter. Exhaust lines then vent most of the spin up gas to an external thrust nullifier located on the spacecraft. Five heat-exchanger stations allow the warm gyro spin-up gas to be efficiently cooled by the exhaust gas. Leakage gas is pumped out of the neck tube. A large gate valve on the front of the probe is open during spin up to vent to space a residual gas leaking into the probe. After spin-up the probe gate valve is closed and an innovative "bake out" scheme is used to attain the operating vacuum. To mount and demount the probe, a quick disconnect mechanism called an axial-lock is used. Gold-coated windows and radiation baffles further restrict the amount of stray heat that is admitted to the payload.

The helium dewar maintains the space telescope/quartz block assembly at a low tempera-

ture of less than 2 ˚K for 16 1/2 months. The helium boil off gas is used as a propellant by the spacecraft force and torque system to maintain the 10-11 g 's on the science gyroscopes. The dewar is a toroidal, 1580 Liter SFHe tank made from 6061-T6 aluminum. Its neck-tube section is also constructed of alumina-epoxy. In addition to the main tank a special guard-tank with 63 liters of normal helium is used to simplify launch pad operations by intercepting heat before it reaches the main superfluid helium. This avoids the necessity of complex helium transfer or pumping operations while c ; the launch pad. Insulation is provided by four vapor-cooled shields, multilayer insulation and 12 Passive Orbital Disconnect Struts (PODS) which offer high resistance heat paths in space, but stiff and strong capacities when placed under launch loads. The piping allows the normal filling, venting and burst relief through a system of remotely actuated valves.
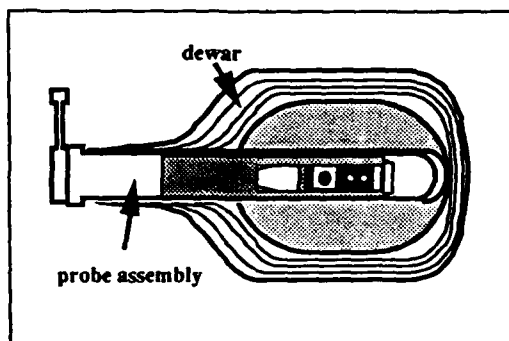
Figure 6 - Dewar

In the event of solar flares when the atmosphere boils up and exceeds the thrust capacity of the drag free system, a capability exists to

increase the helium flow rate for short periods of time. A heater is placed on a porous plug in the dewar, and when turned on the super critical liquid helium will seek the heat of the heater. The helium immediately turns into gas, thus increasing a helium mass flow. The porous plus is also used to maintain the helium at the necessary superfluid state. By changing the pressure across the porous plug the constant temperature can be maintained. The net result is the force and torque system, also controls the temperature of the experiment through the control loop.

To insure the torque system is not over loaded, and drag free control as adequate authority, the satellite is balanced on the ground to 1 millimeter and adjusted again while on orbit to maintain the center mass coincident with the rotation axis of the gyroscopes. The precision trim requires a mass trim system on board the spacecraft. The force and torque system consists of 18 unidirectional helium thrusters and magnetic torquers that interact with the earth's magnetic field. A torque distribution algorithm apportions instantaneous requirements among the available thrusters according to a set of priorities. The overall helium mass flow rate fluctuates because of the variations of heat flow into the dewar caused by roll orbital seasonal and other variations. The average mass flow from the dewer is 4.6 milligrams per second, literally equal to ones breath.

Pointing is controlled by generating suitable commands for the force and torque systems. The guide star Rigel is used for control. It is valid when the star is visible from the satellite and the line of sight is not unduly refracted by

the atmosphere. Otherwise, the science gyro-scopes are used for control when Rigel is invalid. To initialize the spacecraft to Rigel, a strap down rate integrating gyroscope is used.

The roll angle of the quartz block is measured by a roll attitude reference mounted on the spacecraft. The initial uncertainty of the refer-ence system with the respect of the quartz block is better than 1°. Changes over the one year experiment are controlled to better than 10 arc seconds per year, giving an ability to calculate the system to 10 arc seconds.

The spacecraft will be launched onboard a Delta II Launch Vehicle from Vandenberg Air Force Base, California.
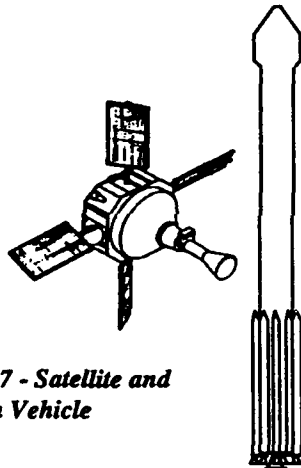
Figure 7 - Satellite and Launch Vehicle

The orbit parameters are extremely precise with the eccentricity not to exceed .00165 at any time and the inertial plane of the satellite aligned to the star Rigel within .027 °. To accomplish this a GPS Receiver provides the high precision required. The GPS will deter-mine the position of the satellite to 5 meters

and velocity to better than 0.1 meters per second. It also allows timing synchronization to better than 20 nanoseconds for all of the science data.
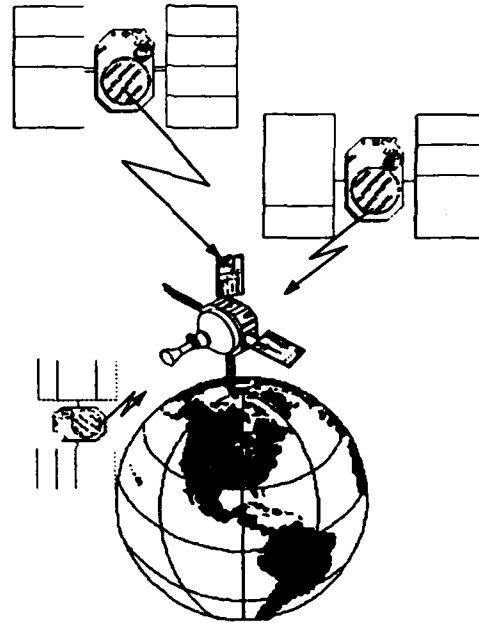
Figure 8 - GPS Orbital Update

THE ERROR BUDGET

By controlling the gravity forces to 10^{-11}, all mass and balance and compliance terms are reduced to near zero. By controlling the mag-netic field to 10^{-14} gauss, magnetic terms approach zero. By controlling the dewar temperature very accurately and adding micro temperature controllers where required, and keeping all heat from the passively rotating gyroscope, these thermal terms approach zero.

With precision manufacturing, many bearing terms approach zero. All bias terms are roll averaged to zero by a .1 revolution per minute of the experiment. The gyroscope is analyzed accurate to 10^{-11} degree per hour in inertial space. Because the gyroscope can not be tested to the necessary accuracy on the ground before the flight test, in-flight calibrations are used to ensure the accuracies are attained.

Unbalance effects. The effects of linear accelerations on the mass-unbalance of the gyroscopes shall be measured by applying "large milli g", known translational accelerations along various axes of the satellite before and after the main science experiment. The accelerations will be applied in two different modes, in body fixed coordinates and in inertial coordinates.

Gyroscope Suspension test. The performance of the gyroscope rotor suspension system shall be verified by applying known translational accelerations along various axes of the satellite. The applied acceleration levels will be compared with the estimated levels determined by the suspension system.

A known translational acceleration level at the science gyroscopes's may be set up by establishing angular dither. The amplitude of the dither is controlled by the gyro. The center of rotation shall be the Proof Mass, as the result of drag-free operation. With known angular dither and known radii of rotation., the linear accelerations at the gyroscopes are known. An acceleration level of $10^{-6}g$ is set up at 0.2 m

from the PM by sinusoidally dithering at a rate of 1 rad/sec and an amplitude of 10 arcsec. The dither frequently must be sufficiently lower than the bandwidth of the drag free control system so that the radius of rotation indeed approaches the known center of the PM. Care must be taken not to subject the gyroscopes to an excessive acceleration regime during calibration.

Gyro (SQUID) calibration. The precise calibration of the SQUID outputs is an essential issue. The calibration shall be based on known basic physical processes, such as the aberration and the bending of starlight. The movement of the satellite tracking the precisely known apparent motions of the guide star serves as the input against which the SQUID outputs are calibrated. The telescope signals provide the pointing errors, which are used as a correction term in the calibration.

The aberration and bending of starlight have characteristic, distinct, known spectral signatures. As the earth orbits the sun, there is a ±20.408 arcsec variation in the apparent position of the guide star. As the satellite orbits the earth, there is a ±5.5 arcsec variation in the apparent position of the guide star. The directions, amplitudes and dynamics of the variations are well known. JPL ephemerides gives annual aberration to 0.07 milliarcsec, or 3 parts in 10^6. Orbital aberration is known from tracking data to about the same precision. The deflection of light has an amplitude of 14.4 milliarcsec. (Reference 7)

Parallax is ±7 marsec 90 deg out of phase with

annual aberration.

Roll reference calibration. The well defined inertial direction of the aberration of starlight processes permits the calibration of the Roll reference system will be used because of its relatively fast dynamics.

THE FORGOTTEN ERROR TERMS

Stanford University has developed and tested on the ground the near perfect gyroscope. During the examination of inertial space however, to flight test the gyroscope, we realized that it was predicted to be curved by Professor Albert Einstein. As a matter of fact, this curvature will present a major error source in the absolute accuracy of a gyroscope. The Earth is predicted to warp inertial space for our experiment by 6.6 arc seconds in one year. An additional term was predicted which says that inertial space will be drug by the Earth's rotating coordinate frame by $.0\overset{\frown}{4}$ arc seconds per year (frame dragging).

Thus, we will fly the gyroscope to measure the relativistic effects on inertial space. (Reference 8)

NASA is sponsoring the project for a flight in 1996 aboard a Delta II Missile.

ACKNOWLEDGEMENTS
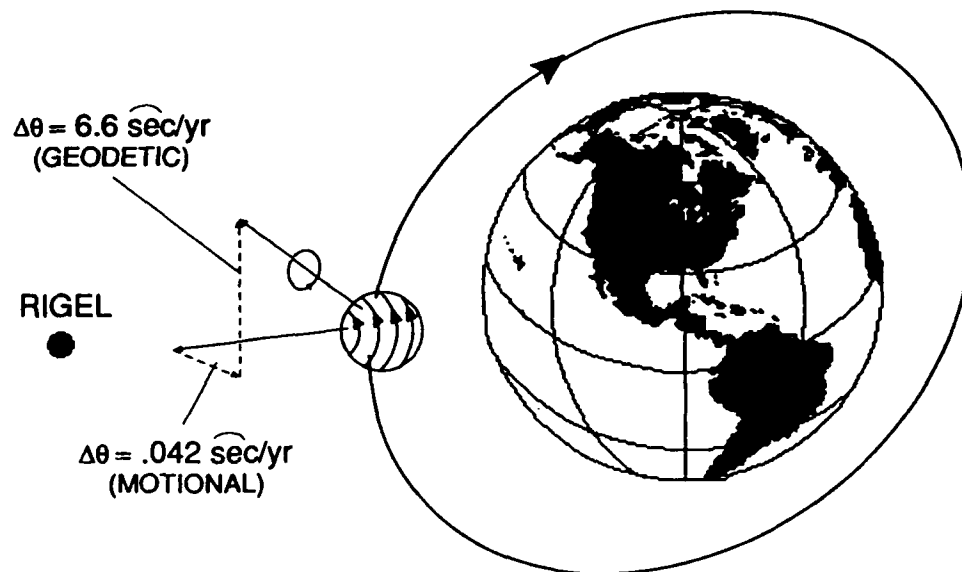
REFERENCES

1. G. Dunbar, Measurement of optical homogeneity of fused silica, M.Sc. Thesis, University of Aberdeen, Aberdeen, Scotland, U.K. (1981)

2. W. Angele, Finishing high precision quartz balls, Prec. Eng. 2, 119 (1980)

3. D.G. Chetwynd and G.J. Siddall, Improving the accuracy of roundness measurement, Phys. E: Sci. Instrum. 9, 537 (1976)

4. C. W. F. Everitt and B. W. Parkinson, Gravity Probe B, Program Brochure (1989)

5. J.P. Turneaure, C.W. F. Everitt, B.W. Parkinson, J.T. Anderson, D. Bardas, W.S. Cheung, D.B. DeBra, W.M. Fairbank, R.A. Farnsworth, D. Gill, R. Hacker, G.M. Keiser, J.A. Lipa, J.M. Lockhart, R.A. Van Patten, R.T. Parmley, R.H. Vassar, and L.S. Young, The Gravity-Probe-B Relativity Gyroscope Experiment: Approach to a Flight Mission, in: Proc. of the Fourth Marcel Grossmann Meeting on General Relativity, ed. R. Ruffini, North-Holland, Amsterdam, 1986, p. 411.

6. J.T. Anderson and C.W.F. Everitt, Limits on the measurement of proper motion and the implications for the relativity gyroscope experiment, GP-B Document No. S0020, W.W. Hansen Laboratories of Physics, Stanford University.

7. O. Yekutiel, GP-B In-flight Calibration, Mar 1, 1989, W. W. Hansen Laboratories of Physics, Stanford University.

8. L.I. Schiff, Motion of a gyroscope according to Einstein's theory of gravitation, Proc. Nat. Acad. Sci. 46, 871 (1960)

Vibration Isolation Technology

for the 1990's . . . and Beyond

October 1989

Prepared by:

Felix Morgan
Randy Goucher
John Gniady*
Richard Owen**

Applied Technology Associates, Inc.
1900 Randolph Road, SE
Albuquerque, NM 87106
505-247-8371
FAX 505-768-13781

Presented to:

Fourteenth Biennial Guidance Test Symposium
Department of the Air Force
Headquarters 6585th Test Group (AFSC)
Holloman Air Force Base, New Mexico 88330-5000

*Now with Aura Systems
6033 West Century Blvd
Los Angeles, CA 90045
(213) 337-1406

**Now with SBE Engineering
5301 Central Avenue, Suite 1500
Albuquerque, NM 87108
(505) 268-0405

Abstract

This paper describes two types of active vibration-isolation technology. The first relies on contact with a relatively large immobile mass while the second does not. The first technology[1] represents the first time that both long- and short-period seismometers have been used to close digital, vibration-isolation loops. Residual disturbance levels approaching 10 nano-g/$\sqrt{Hz}$ have been achieved over a five-decade range of frequencies with this first type of technology. The noncontacting technology[2] represents the first time that proof-mass actuators, common for modal damping of flexible structures, have been applied to rigid-body motion control. Stability levels approaching 10 micro-g/$\sqrt{Hz}$ are projected for the noncontacting, or fully inertial, approach to active vibration isolation over a three-decade range of frequencies. This paper reviews the fundamental vibration-isolation problem, the basics of active isolation, and Applied Technology Associates, Inc., (ATA) implementations for both isolation techniques. The paper concludes with a summary of the relative performance of the two techniques.

Vibration-Isolation Problem

As performance levels of a wide variety of equipment ranging from scientific instrumentation to industrial devices increase, so do the negative impacts of vibration on such equipment. Consequently, the surfaces upon which such equipment is to be operated must be increasingly free of vibration. The vibration-isolation problem shown in Figure 1 amounts to the attenuation of input disturbances which are generally of two classes: those impinging or originating on the surface to be isolated and those which reach the surface through its suspension system. The former are commonly referred to as direct disturbances; the latter, base disturbances. Two types of atmosphere-induced direct disturbances occur when the platform is used in nonevacuated space: 1) turbulent and laminar flows of the atmosphere surrounding the isolated element and 2) acoustic transmissions through the atmosphere to the element. Both disturbance mechanisms result in differential pressures across the isolated surface and thus their influence is governed by both the surface area and mass of the isolated platform.

A third type of direct disturbance depends only upon the dynamics of the equipment mounted on the isolated platform. If this equipment includes moving elements, then, in accordance with Newton's second law, motions of the elements are the result of action forces. As a consequence of Newton's third law, equal and opposite reaction forces will exist. If these reaction forces are not dissipated through the motion of inconsequential masses, undesirable motions of the isolated element, which in essence becomes a reaction mass for such forces, will occur. Given the nature of this latter disturbance, its influence is determined solely by the mass of the isolated element. It is interesting to note that this last disturbance mechanism can actually be employed to actively isolate the platform from unwanted vibrations.

The second class of input disturbances originates at the base of the isolated platform and is "passed" by the platform's suspension system. Additionally, while not part of the isolated element's suspension system, cables for data collection and equipment control, along with supply and return lines to support equipment on the isolated element, can also represent paths through which base disturbances can be transmitted to the isolated element. In demanding earth-based applications, the isolated element typically rests on a pier which is itself isolated from its surroundings. In space-based applications, the isolated element would be attached to its host vehicle. In both cases, base disturbances result from both natural and cultural mechanisms. As seen in Figure 1, the various types of base disturbances are distinguished by the frequency regimes in which they dominate.

---

[1] Performed under contract to the U.S. Air Force Central Inertial Guidance Test Facility, Holloman AFB, NM.

[2] Performed under contract to National Aeronautics and Space Administration, Lewis Research Center, Cleveland, OH.

- **Direct Disturbances**
  - Bulk Airflows ⎫
  - Acoustics   ⎬ (Pressurized)
  - Self Induced ⎭

- **Base Motion Disturbances**
  - Seismic (Earth)
    - - Earth/Moon Interactioni
    - - Geologic Motions (Plate & Microscopic)
    - - Micro-Seismic Earth Tides
    - - Cultural Disturbances
  - Shuttle/SpaceStation/Satellite (Space)
    - - Gravity Gradients
    - - Air Drag (Low Earth Orbit)
    - - Attitude Corrections
    - - Scanners/Positioning Devices
    - - Crew Motion

89M0073

Attenuating Effects of a Vibration-Isolation System

Two figures of merit can be used to quickly asses the relative performance of various vibration-isolation systems: the isolation system's corner frequency and the magnitude of the power spectral density (PSD) for the isolated elements' residual disturbance. Both quantities are best understood from a random point of view since most of the input disturbances shown in Figure 1 are random rather than deterministic. As such, while specific time histories for the disturbances cannot be predicted a priori, statistics for them can. As indicated, the particularly useful statistic is the PSD of a disturbance. While the PSD is usually defined in terms of the Fourier transform of a disturbance's auto-correlation function, the PSD is best understood in terms of its relationship to the mean square value or power associated with a disturbance. As indicated by Equation 1, the mean square value or power, X_{ms}, contributed by a disturbance's frequency components between f_{lower} and f_{upper} is simply the integral of the power spectral density, $G_{xx}(f)$, over this band of frequencies or:

$$X_{ms} = \int_{f_{lower}}^{f_{upper}} G_{xx}(f)\, df \tag{1}$$

The attenuating effect of a vibration-isolation system on a disturbance can be quantified in terms of its transmissivity for the disturbance according to Equation 2:

$$G_{yy}(f) = |H(f)|^2 G_{xx}(f) \tag{2}$$

where $|H(f)|^2$ represents the square of the magnitude of the transmissivity function. Simply put, the isolated element's residual disturbance PSD, or $G_{yy}(f)$, will be less than the original input disturbance PSD, $G_{xx}(f)$, at those frequencies where the magnitude of the isolation system's transmissivity is less than unity or zero decibel. Approximate transmissivities can be determined from frequency-domain models of the system. These transmissivities can also be empirically verified. From a mathematical point-of-view then, the goal of vibration isolation is transmissivities whose magnitudes are consistently less than unity over a broad range of frequencies.

Passive vibration isolation has long been used to attenuate base-motion disturbances without particular regard to direct disturbances. While passive isolation can be easily implemented using appropriately sized elastomeric or pneumatic "cushions" as the support or suspension system for an isolated element, passive isolation is not without its problems. As shown in Figure 2, while passive isolation attenuates base disturbances above the isolation system's corner frequency, it exposes the isolated surface to direct disturbances above this frequency and can amplify both base and direct disturbances within a narrow range of frequencies around the corner frequency. In certain critical applications, passive isolation of a surface can result in residual disturbances levels which are higher than those of the base upon which the isolation system rests; that is, it would have been better to have not isolated the surface. Corner frequencies for linear motion transmissivities are determined by the mass of the isolated surface and the stiffness or spring constant of the "cushions" in the direction of interest; rotational corner frequencies, by the moment of inertia of the isolated element and the rotational stiffness of the "cushions" about the axis of interest. Because all existing isolation systems are in some way attached to their surroundings, the passive transmissivities of Figure 2 represent starting points for gauging the improvements obtained through the addition of active isolation.

Active-Isolation Basics

The effects of augmenting a passive system with active isolation are also shown in Figure 2. For convenience, the six active loops, corresponding to three linear and three rotational degrees-of-freedom (DOF) are assumed uncoupled. Consequently, the block diagram and transmissivities of Figure 2 are representative of each of the six which occur in the multi degree-of-freedom case. With active isolation, a negative feedback loop is added which constantly seeks to drive the residual disturbances of the isolated surface to zero. This is accomplished by placing accelerometers on the surface, directing the accelerometer signals to compensation networks, and then using the compensated signals to drive actuators to exert forces on the surface in such a manner as to cancel surface disturbances. The accelerometers form, in essence, a "virtual" summing junction where the loop reference of zero and the actual residual motion of the platform are compared to derive an error signal for the associated active-isolation loop.

Compensation of accelerometer signals is required to achieve desired transmissivity improvements and ensure loop stability. While a variety of compensators can be employed, to date, only integral compensation has been explored in any great detail. The net effect of this particular compensation scheme is in essence the creation of viscous damping. Consequently, active isolation can also be thought of as resonance damping when loop gain is modest. As loop gain increases, active damping extends to well beyond the isolation corner frequency. Decreases in passive transmissivities can also be interpreted as increases in the apparent or dynamic mass of the isolated element. Therefore, the problems posed by purely passive isolation can in part be resolved through the application of active vibration-isolation technology.

The successful emergence of actively isolated platforms is a relatively recent occurrence. ATA has been engaged in the development of two types of state-of-the-art, active-isolation technologies. The first technology represents an evolution of existing methods which rely on the presence of a relatively large, immobile mass, typically the Earth, for the generation of forces to actively cancel platform disturbances. The second technique relies on small "action" or proof masses for the generation of "reaction" forces to
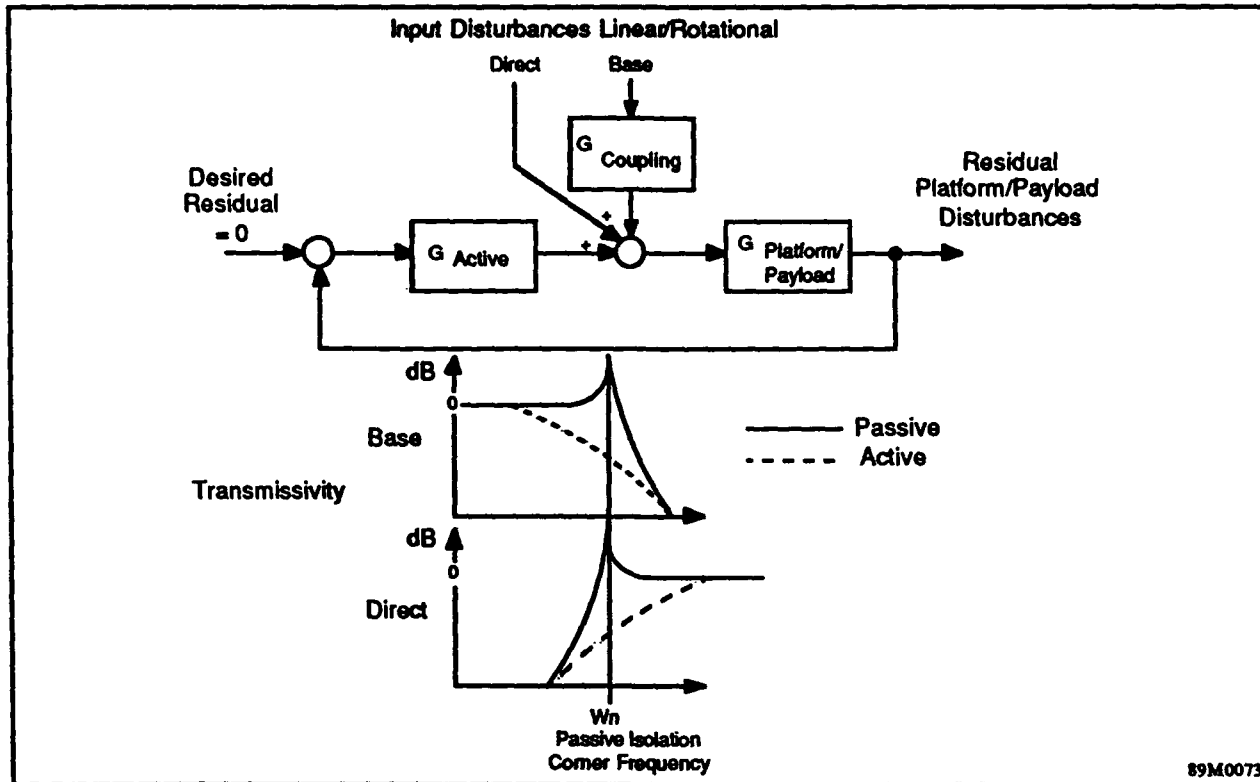
Figure 2. Active-Isolation Basics

cancel platform disturbances. The latter technique capitalizes on direct disturbances of the type resulting from motions of dynamic elements on the isolated platform. While proof-mass actuators have been proposed to damp structural modes of flexible bodies, it appears that this is the first instance in which they have been proposed for rigid-body motion control. Because of the "self-contained" nature of proof-mass actuators, the latter isolation technique can be readily used in situations where a relatively large, immobile mass is not immediately available. The latter technique can also be employed in situations where it is no longer desirable to apply reaction forces to the underlying entity, be it a rigid, seismically-isolated pier or a flexible space-structure.

Seismically Stable Platform (SSP)

ATA has been engaged in the development of the first technique for the Central Inertial Guidance Test Facility (CIGTF) at Holloman Air Force Base in southern New Mexico. In this application, depicted in Figure 3, an active-isolation system augments SSP's two-stage pneumatic, passive system. The corner frequencies for the two pneumatic stages are roughly equal, thus doubling the system's attenuation of base disturbances above the common corner frequency. Because the pneumatic system itself proved to be a disturbance source, its operation is limited to "inflation" of the cushions so as to "float" the two stages. Once the elements have been "floated," the pneumatic system is disabled so it does not compound the isolation problem.

Active isolation in the vertical axis is accomplished by the electromagnetic loop shown in Figure 3. Vertical axis disturbances are detected by both long- and short-period seismometers attached to the underside of the isolated element. The SSP's use of seismometers within control loops represents an innovative first. Seismometer signals are sequentially sampled and digitized to 16 bits of resolution. The

digitized seismometer signals are blended and compensated by algorithms within a high-speed, multiprocessor computer. Digital control signals generated within the computer are converted to the analog domain with 16 bits of resolution and applied, via low-noise audio amplifiers, to four moving voice-coil, electromagnetic actuators which are located immediately adjacent to the four pneumatic cushions supporting the isolated element. The actuators rest on tall columns or pedestals and generate disturbance cancellation forces by reacting or pushing against the large seismically-isolated pier underlying SSP.

DAMPER

The second active-isolation technique was conceptualized in the course of a Phase I Small Business Innovation Research (SBIR) contract performed for NASA's Lewis Research Center. The goal of that work, the Digital Active Materials Processing Platform Effort (DAMPER), was a top-level design for an actively isolated platform which would enable NASA to perform advanced, space-based materials-processing experiments in the 1990s. In the DAMPER situation, the principal concern was the platform's low-frequency isolation capabilities. Further, it was assumed that the principal sources of direct disturbances could be readily eliminated as the isolated element would have easy access to the vacuum of space. As a result, DAMPER concentrated on developing a top-level design which would exhibit superior low frequency base isolation. While the base transmissivity curves of Figure 3 suggest this can be accomplished through a combination of passive and active systems, the concept of passive isolation for extremely low-frequency disturbances does not make sense.
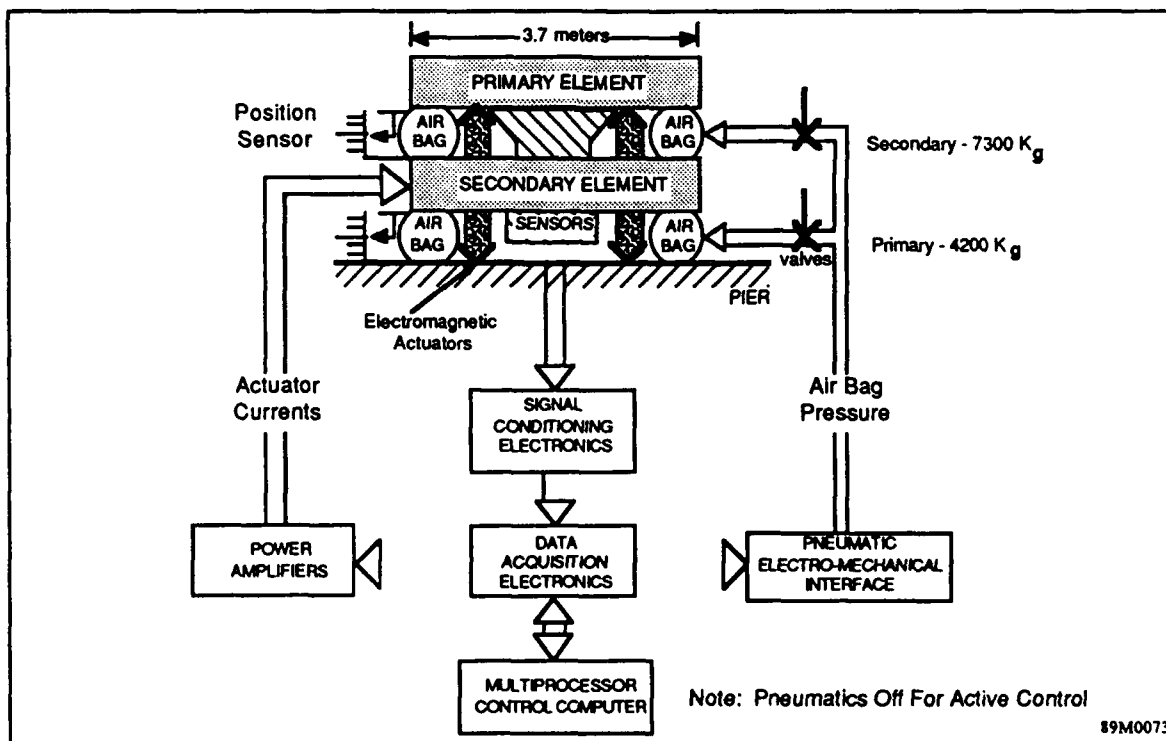

Figure 3. Seismically Stable Platform (SSP)

If passive techniques were to be employed to isolate an element against extremely low-frequency disturbances, the corner frequencies for the passive system would have to be extremely low for such isolation to be useful. Otherwise, not only would the passive system not contribute to an overall solution, but it would actually impede the operation of any active-isolation system which was added to augment the passive system.

Isolation from relatively modest disturbances at extremely low frequencies involves large displacements between the isolated element and its surroundings. For example, a 1 milli-g sinusoidal base disturbance at 0.01 Hz gives rise to 5.0 meters of base motion. If an element were to be isolated from such a disturbance, the element's isolation system would have to expand and contract by at least 5.0 meters. Clearly, the concept of passive isolation in the face of such large distances is no longer practical. If this difficulty is ignored and the corner frequency for the passive system is higher than the frequencies to be isolated, any active system which is added would have to produce extremely large forces just to overcome the spring forces of the passive system's "cushions" at these frequencies. Given these two considerations, the notion of passive isolation was completely abandoned as a solution to the extremely low-frequency isolation problem posed by DAMPER. In fact, the presence of base transmissivities was viewed as an artifact of the platform having to be attached to its surroundings for support services such as power, raw materials, and command and control information.

As a result of the large relative motions involved in the DAMPER isolation problem, the platform will appear to "free-float" with respect to its surroundings. Consequently, actuators for active isolation which depend on a relatively fixed relationship between the isolated element and its surroundings cannot be used. While g-off-loading or flotation techniques such as those being developed for terrestrial scale model testing of large space structures (LSS) may ultimately be applicable to the terrestrial isolation problem at extremely low frequencies, the feasibility of "free-floating" platforms with extremely low residual disturbance levels on the surface of the Earth remains dubious at best. However, in the near zero-g environment of space, it is feasible to consider "free-floating" platforms.

As the DAMPER actuation dilemma was pondered, work in the area of active suppression of LSS vibration proved to be a source of inspiration. Specifically, if proof-mass actuators similar in principle to those proposed for LSS modal damping could be developed for the suppression of low-level vibrations, the DAMPER isolation problem would be solved. Proof-mass actuators are based on straightforward applications of Newton's second and third laws of motion. In particular, if a proof-mass is to be moved, an action force must be exerted on it. As a result, an equal and opposite reaction force will be created. If, as is shown in Figure 4, the reaction force is exerted on the platform, action isolation occurs when the reaction force opposes the disturbance forces reaching the platform. When inertial proof-mass actuators are combined with inertial sensors, it will be possible to close vibration-isolation loops with respect to inertial space or the stars. That is, a method for noncontacting, active vibration isolation will have been realized. Figure 5 depicts a DAMPER materials processing platform which has been actively isolated in all six DOF with rectilinear proof-mass actuators. Active isolation of the platform's linear DOF will be accomplished through simultaneous motions of appropriate proof-masses which are in-phase, while control of rotational DOF will be achieved through opposed or "push-pull" motions of actuators.

Relative Isolation Capabilities

The significance of the active-isolation technology being developed for SSP and proposed for DAMPER is shown in Figure 6. Currently, the Newport Corporation's Electronic Vibration-Isolation System (EVIS) is the only system which contains active technology that begins to approach that of SSP and DAMPER. With active isolation, the Newport Corporation has achieved, in a compact table-top unit, what had only been previously possible with larger passive systems. With the technology discussed earlier for SSP, its apparent isolation corner frequency has been actively lowered by two orders-of-magnitude from approximately 1.0 to 0.01 Hz thus achieving what had been previously impossible. Further, the residual disturbance level of SSP's isolated element is approximately three orders-of-magnitude less than that of EVIS.
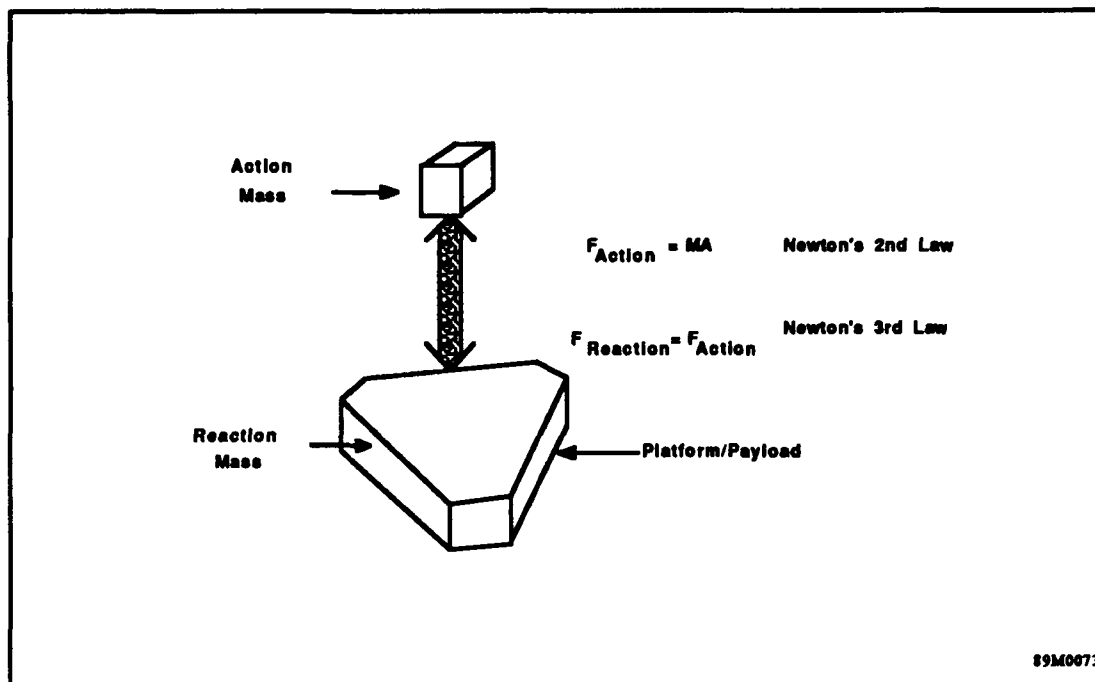
Figure 4. DAMPER Principle of Operation
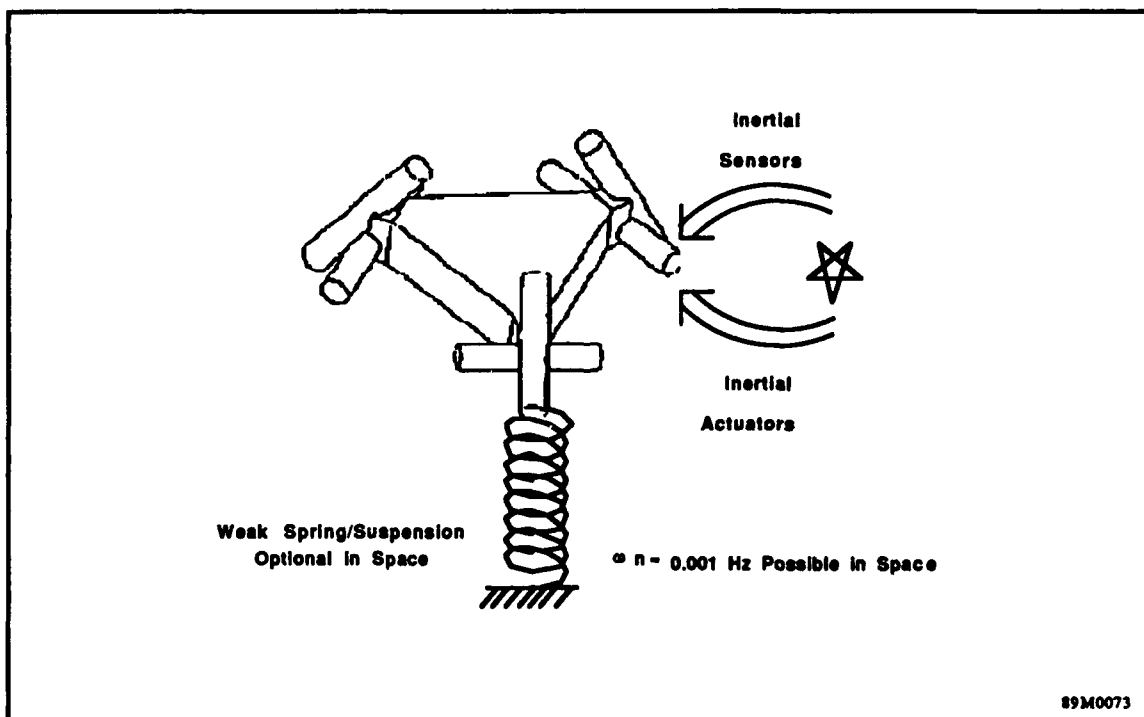
Figure 5. Six DOF DAMPER
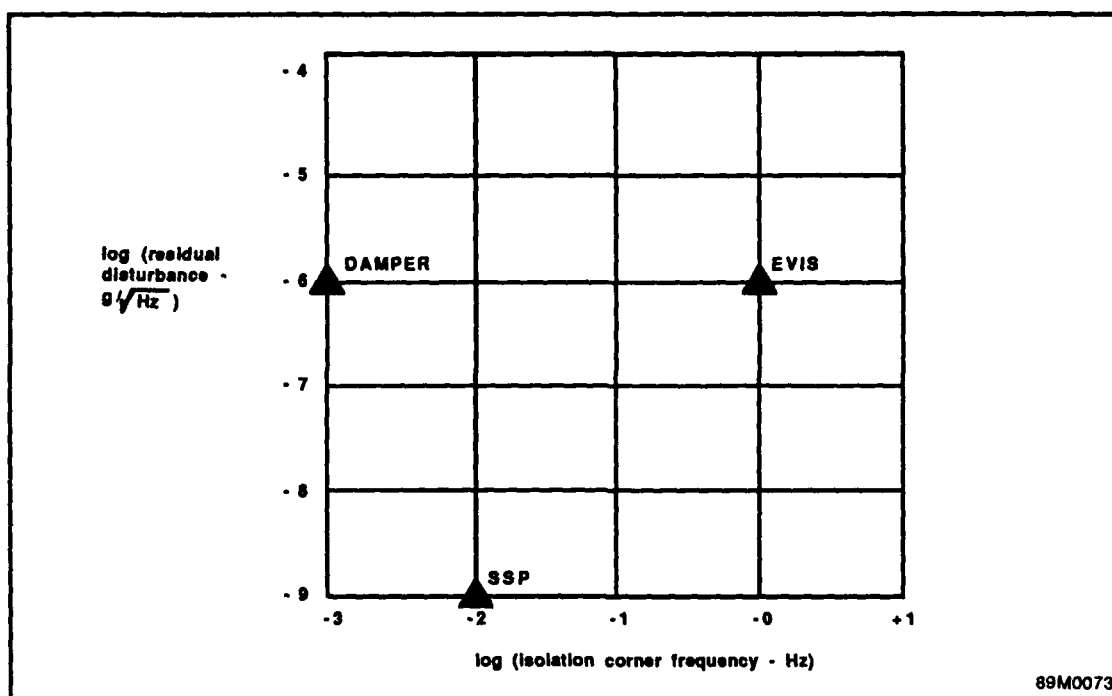
Figure 6. Relative Isolation Capabilities

The last data point of Figure 6 is that of a DAMPER system which is very loosely "tethered" to its host vehicle for a minimum of support services. In fact, a rough calculation of the spring constant associated with such a "tether" for a 100-kilogram platform indicates that a spring constant of 4×10^{-3} Newtons/meter will be necessary to achieve the 0.001 Hz corner frequency indicated. In the long term, such spring constants should not be unreasonable for isolated elements which are in essence, completely self-contained. Such an element would, at worst, be tied to its host vehicle by a fiber-optic strand for command, control, and status signals. In fact, whole constellations of such elements, each devoted to a specific materials process, can be envisioned floating about larger manufacturing facilities in space. Such an approach to space-based materials processing will significantly increase the yield of those processes requiring long-duration, low-disturbance environments. While the isolation corner frequency which should be ultimately achievable with DAMPER's completely inertial approach to vibration isolation will be an order-of-magnitude less than that of SSP, considerable sensor and actuator development work will be required before the residual disturbance levels of the DAMPER technology approach those of SSP.

Summary

Two active-isolation techniques have been described which rely on markedly different actuators. The first isolation technique uses conventional small-stroke moving voice-coils to push against a relatively large immobile pier; the second will rely on devices with significantly larger strokes. Isolation corner frequencies of 0.01 Hz with residual disturbance levels of 10 nano-g/$\sqrt{Hz}$ have been demonstrated with the first contacting technique in the course of SSP development. Isolation frequencies which approach 0.001 Hz with residual disturbance levels approaching 10 micro-g/$\sqrt{Hz}$ are projected for the second, fully inertial approach to active isolation when DAMPER development work is ultimately completed.

Site Selection and

Design Considerations

for an Advanced Guidance

Test Facility

October 1989

Prepared by:

Robert Thede*
Applied Technology Associates, Inc.
1900 Randolph Road, SE
Albuquerque, NM 87106
505-247-8371
FAX 505-768-13781

and

Richard Alexander
6585th Test Group/GDL
Holloman AFB, NM 88330
505-679-2151

Presented to:

Fourteenth Biennial Guidance Test Symposium
Department of the Air Force
Headquarters 6585th Test Group (AFSC)
Holloman Air Force Base, New Mexico 88330-5000

*Now with Litton Guidance and Control Systems Division
MS87, 5500 Canoga Avenue, Woodland Hills, CA 91367-6698
(818) 715-2625

Abstract

As the quality of inertial sensors increases, so must the quality of the facilities in which they are tested. Test-induced errors in current facilities are approaching, and in some cases already exceed, the accuracies of the devices being tested. Clever test and analysis techniques have been developed to overcome some of these limitations; however, these techniques generally require assumptions to reach their conclusions. Because assumptions leave unanswered questions a better alternative would be to provide an improved test facility.

A contractual effort has recently been completed which selected a site and developed a design for an Advanced Guidance Test Facility (AGTF). Because seismic and cultural disturbances at this facility must be at the lowest possible level, the selection of a quiet site was a key part of this task. This paper will review the techniques used to locate potentially quiet sites. Results obtained from the surveys, including seismic measurements made at five potential sites, will be presented, and the preferred site will be identified. The facility to be constructed at this site must be designed to maintain the quietness of the site. Passive and active isolation devices must be provided to reduce any motions to acceptable levels. The design which will be presented consists of a test facility buried 120 feet beneath the surface of the earth. Passive isolation techniques employed ensure that support equipment, which is located in an above ground control building, will not cause disturbances in the test cells. These techniques also isolate the test cells from each other so that activity in one cell will not disturb testing in an adjacent cell. The proposed facility is expected to provide an environment in which disturbance to the test item will be less than 10^{-9}g RMS at frequencies up to 100 Hz.

Introduction

The ability of a military system to perform a designated mission is often directly related to the performance limitations of inertial sensors employed as part of navigation, guidance, and reference systems. Historically, the testing and evaluation of inertial sensors had been done by accurately measuring the response of the sensor to known and/or controlled inputs and then comparing the measured outputs to the expected outputs. Implicit in this approach is the assumption that the tester has equipment, measurement techniques, and facilities which are more accurate than the component being tested. For many state-of-the-art sensors, and those being identified for future systems, this assumption is no longer always possible. To overcome this, clever test techniques and statistical inferences are often used to argue that a sensor is performing at the required level. While these procedures provide valuable information about system performance, they leave unanswered questions because of assumptions which are required to reach their conclusions. Clearly, a better alternative would be to test where the equipment and facilities are better than the instrument being tested. One of the fundamental test limitations at current facilities is the vibrational motions occuring within the facility. These motions, caused by seismic and cultural activities and by equipment in the facility, are in many instances as large or larger than the noise floor of the instruments being tested. A need therefore exists for a new Advanced Guidance Test Facility (AGTF) located in a seismically quiet, remote area and designed specifically to provide a quiet test environment. An effort has recently been completed which identified a suitable location and provided designs for such a facility. This facility, with test cells located underground, is designed to provide test beds where the input to the test device shall be less than 10^{-9}g RMS at frequencies up to 100 Hz. This facility is expected to provide capabilities for testing inertial sensors through 2010 and beyond.

The Need for Improved Facilities

The mission of the Central Inertial Guidance Test Facility (CIGTF) at Holloman Air Force Base, New Mexico, is to test state-of-the-art and developmental inertial sensors and systems. Two static test facilities are currently in use at CIGTF. The test laboratory in Building 1265 is part of a converted Atlas assembly building. The linear acceleration environment on test piers in this facility ranges from 10^{-5} to 10^{-6}g RMS in the low frequency band (dc - 10 Hz). The tilt environment is typically 0.5 arc second RMS in the low frequency band. The second facility is the Advanced Inertial Test Laboratory (AITL). It was built in 1971 to provide an improved static test facility. Low frequency accelerations in this facility are 10^{-6}g RMS and tilts range from 0.3 to 0.5 arc second RMS.

The need for an improved test facility has long been recognized. A study completed 14 years ago presented a preliminary design for such a facility (Reference 1). That study concluded that a nano-g environment was possible if the facility were located in a seismically quiet area, away from cultural disturbances, and if careful attention were paid to the minimization of noise transmission into the test laboratory. A second study (Reference 2) outlined the steps to follow in selecting a site for the facility.

A study completed in 1986 assessed the current test capabilities at CIGTF and projected the test requirements through 2010 based on an industry survey (Reference 3). That study concluded that current gyro and accelerometer test capabilities are marginal in many areas and will be deficient by several orders of magnitude in nearly all areas by 2010. The study stated that the current CIGTF facilities are not quiet enough to isolate the test areas from vibrations, regardless of whether the vibrations were from seismic activity or from the local environment. The solution recommended was to develop an Advanced Guidance Test Facility (AGTF) and to equip it with the latest in test equipment.

Site Selection

To achieve nano-g stability in the test facility, it must be located in a seismically and culturally quiet area. The identification of the best location for the AGTF was a two-step process. First, potential sites were identified, and then these sites were characterized. Five potential sites were characterized: three were selected based on criteria presented in Reference 2 and two were selected by the Air Force.

Identification of Potential Sites

Criteria presented in Reference 2 were used to select potential sites for the AGTF. The procedure was to identify noise sources and to exclude areas likely to be affected by those noise sources. The procedure was first applied on a regional level (continental United States), then on a subregional level (several hundred square miles), and finally on a site specific level.

The regional site selection criteria consisted of eliminating the following regions of the country:

1. Areas within 350 kilometers of any coast.
2. Seismically active regions of the country as established by the Modified Mercalli intensity scale (Reference 4). Only zones 0 and 1 were considered acceptable.
3. Fault zones.
4. Areas of high concentrations of earthquake epicenters.
5. Plate boundaries.
6. Areas of glacial uplift.
7. Areas of severe thunderstorms and tornadoes.
8. Areas in which the ground freezes below the uppermost soil level.

After applying these criteria, the acceptable regions of the country consisted of areas within southeastern New Mexico and western Texas. These regions are shown in Figure 1.

The subregional criteria consisted of avoiding the following:

1. Low-level military aircraft operations;
2. Heavily used roadways;
3. Railroads;
4. Rivers and other bodies of water;
5. Population centers;
6. Mining and oil pumping regions.

After applying these criteria the acceptable region was reduced from 42,000 square miles to 250 square miles. Site specific criteria were then applied to further define acceptable sites. This consisted of avoiding items such as ranches, buildings, windmills, and wells. The general principle was to stay at least 1 mile from these items. After applying these criteria the three sites selected were located near Elida, New

Mexico; Sunspot, New Mexico; and East Black Hills, Texas. The two sites selected by the Air Force were located on a remote area of Holloman Air Force Base, New Mexico, and in a potash mine located 20 miles east of Carlsbad, New Mexico. Figure 2 shows the five potential sites.
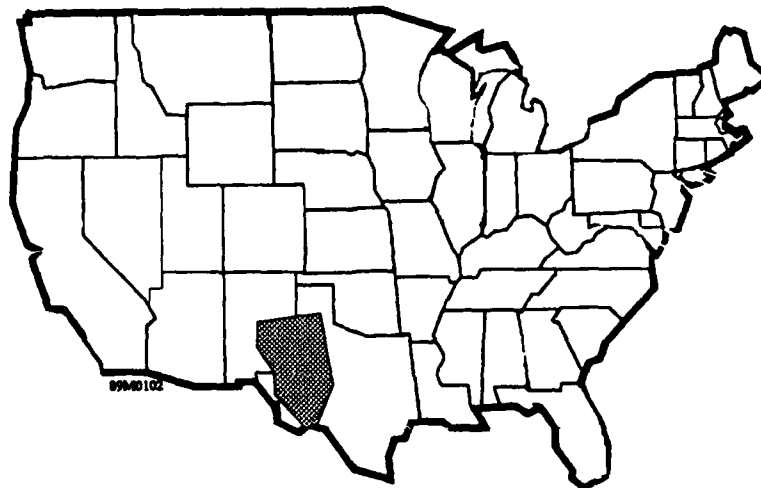
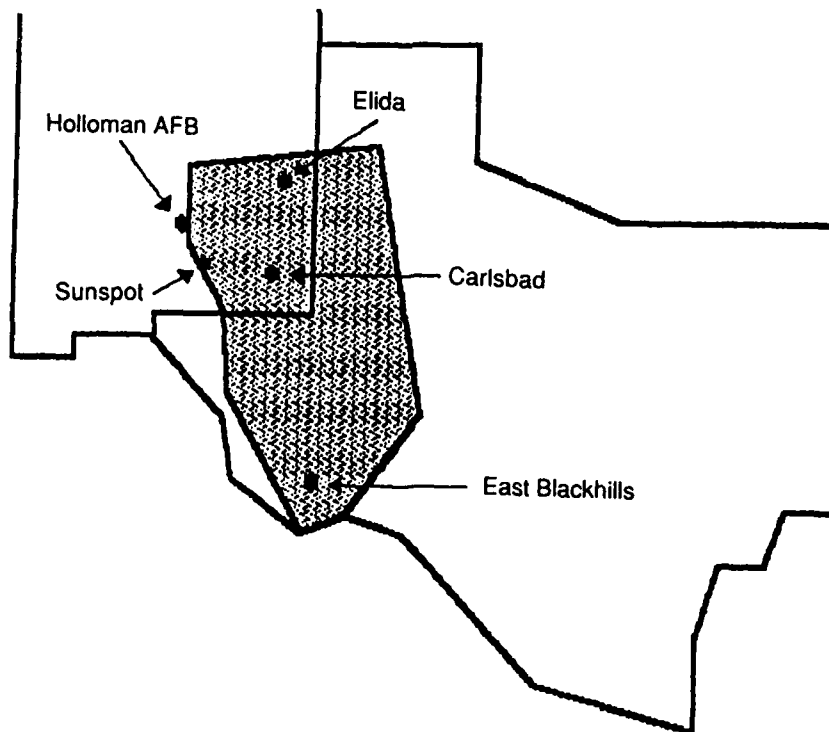Figure 1. Acceptable Regions for AGTF Siting

Figure 2. Potential Sites for AGTF

Site Survey Results

Following the selection of potential sites, the next step was to visit each of them to determine their suitability for an AGTF. During these visits the sites were examined to determine any undesirable characteristics, and seismic measurements were made to determine ground motion. The instruments used were Teledyne Geotech S500 Seismometers. These instruments have a noise floor of 10^{-17} g^2/Hz over a frequency band of 1.0 to 100 Hz. Data acquisition was provided by a Masscomp computer system with appropriate anti-aliasing filters, selectable signal amplification, and a 14-bit analog-to-digital converter. This system also provides quick-look data verification immediately after each test. Each test consisted of acquiring approximately 6 minutes of data at a 500 Hz sample rate. The anti-aliasing filters cutoff frequency was set at 150 Hz. Data were acquired simultaneously from two parallel triads of seismometers. This provided seismic measurements in the three orthogonal directions and by examining the coherence function between parallel instruments, data validity could be established. Test results were presented in the form of auto spectral densities, and RMS noise values were computed for frequency bands of 1.0 to 10 Hz and 10 to 100 Hz. Several sets of measurements were made at each site under slightly different conditions. Test results showed that a slight increase in wind speed (4 to 6 miles per hour) generally increased the noise level by 5 to 10 dB. Horizontal results were generally similar to vertical results in shape, but 3 to 5 dB lower in magnitude. Results will only be presented from vertical instruments under near ideal conditions, i.e., calm or very light wind.

Carlsbad, New Mexico Potash Mine

The site in this mine is 1,200 feet below the surface of the earth. The mineral mining conducted there creates long tunnels. These tunnels are approximately 32 feet wide by 10 feet high and as long as several miles. The tunnels are separated by 40-foot squares of unmined potash to provide ceiling support. The temperature in the mine remains constant at 70 °F and the humidity is 30%. Mining was being conducted 16 hours a day, 5 days a week. Other nearby mines operate 24 hours a day, 7 days a week.

The mine was generally noisy, with the tunnels providing a path for noise to be transmitted over great distances. Ceiling collapses in abandoned areas of the mine were common. The collapses transmit shocks throughout the mine. Power was available in the mine, but was of poor quality.

The cross spectral density obtained from the vertical seismometers is shown in Figure 3. These results were obtained when there was no mining activity and only a minimum of activity in a shop area in the mine. The noise is characterized by many spikes at various frequencies. These spikes are likely caused by activity in this mine or in other nearby mines. For example, spikes near 30, 60, and 90 Hz are most likely caused by drum miners operating in nearby mines. These are powered by 200-horsepower motors which turn at 1,775 rpm (29.6 Hz) and 80-horsepower motors which turn at 1,725 rpm (28.7 Hz). The power in the 50 Hz region is likely caused by the mine air handlers which operate at 3,200 rpm (53.3 Hz). The noise in the 2 to 7 Hz region is near the noise floor of the seismometers.

Construction of a test facility within a mine would require filling in many of the existing tunnels to ensure safety and stability. The size of the tunnels is not large enough to accommodate a test facility, therefore larger areas would have to be excavated. Additional ceiling supports would then be required to prevent cave-ins. Even if the mine were deactivated, activity nearby would cause vibrations in this mine. The mine is deep enough underground so that surface disturbances should have little effect.

Holloman AFB, New Mexico

The site at Holloman AFB is approximately 2 miles north of the Central Inertial Guidance Test Facility. The site is on the edge of an arroyo and the soil is a weak, sandy, clay material. Ground water is approximately 40 feet beneath the surface. Military aircraft landing patterns are close to this site and low-level helicopter fly-overs are common. The cross power spectral density obtained from vertical seismometers at this site is shown in Figure 4. The noise is relatively high at low frequencies and has a minimum between 20 and 30 Hz.
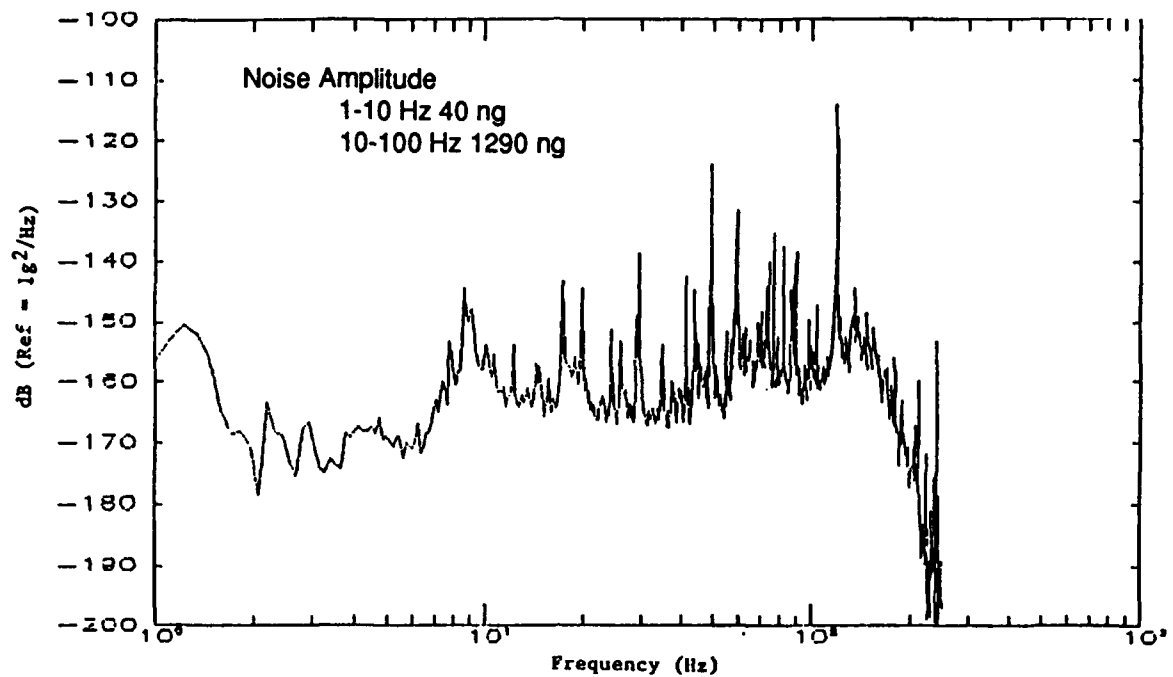
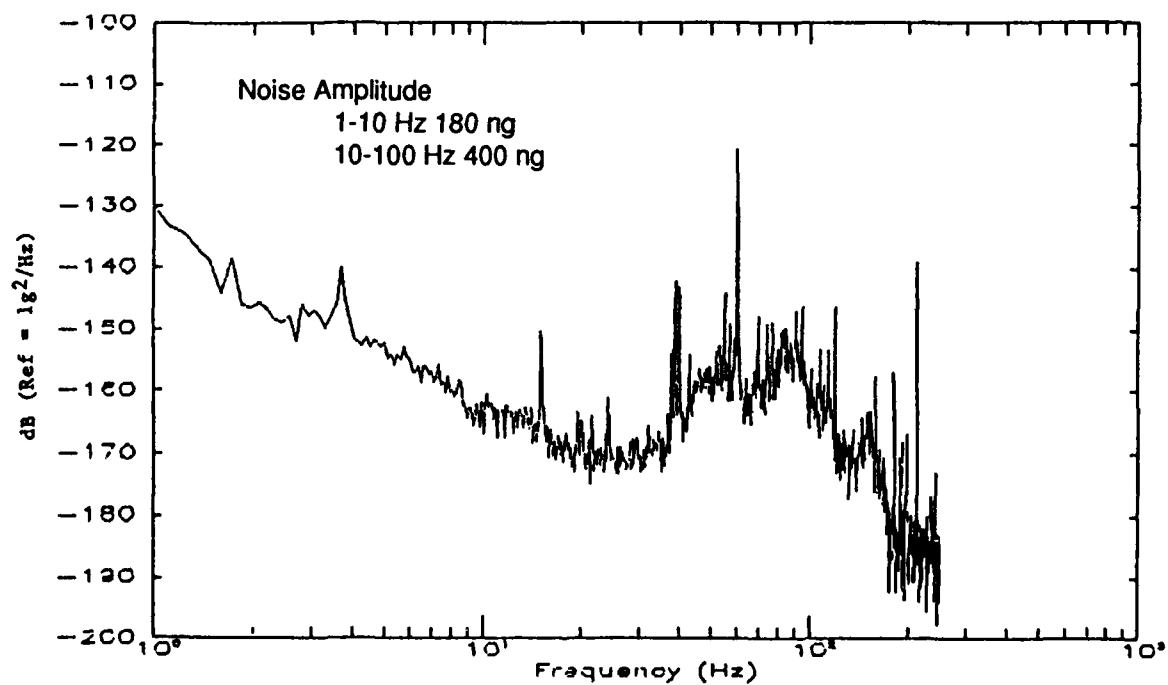Figure 3. Noise in the Carlsbad, New Mexico Potash Mine

Figure 4. Noise at Holloman AFB, New Mexico

89M0102 1

This site is not a desirable AGTF location because of the low-level aircraft activity, the poor soil type, and the high ground water level. A facility buried more than 40 feet would require extensive water proofing as well as some means to remove the ground water from the vicinity of the facility. Fluctuating ground water levels and the weak soil structure could cause low frequency building tilts, which are not desirable in a test facility.

East Black Hills, Texas

This remote site is used for ranching and grazing. The soil is very shallow with bedrock (limestone) present at 20 inches or less below the surface. Dominant hills, consisting of bedrock, protrude through the surface in several areas. Ground water is over 1,000 feet beneath the surface.

The cross spectral density obtained from vertical seismometers is shown in Figure 5. The noise is characterized by significant bands of power at 14, 24, 38, and 90 Hz. The horizontal noise was similar at low frequencies but peaked at 63 Hz and then decreased beyond that. These broad bands of power are believed to be caused by bedrock that transmits disturbances over large distances.

Because surface disturbances appear to be readily transmitted over great distances, a buried facility would be required here. The cost of excavating into the bedrock would greatly increase the cost of a facility at this location.

Sunspot, New Mexico

This tree-covered site is on top of a mountain at an elevation of 9,400 feet. It is on U.S. Forest Service land approximately 2 miles from the Sunspot Observatory. The soil is composed of fractured limestone extending many thousands of feet deep. Ground water is over 1,000 feet beneath the surface.

The cross spectral density obtained from vertical seismometers at this site is shown in Figure 6. The noise is at a low level, near the noise floor of the instruments across almost the entire frequency band. The large spike at 60 Hz signified an electrical problem with the data acquisition system. This power is not included in the noise amplitude numbers shown. Because of these problems a second visit was made to this site to verify results. S500 seismometers were again used, but a completely different data acquisition system was used. These results, shown in Figure 7, were almost identical to the original results except that the power at 60 Hz is not present.

The low noise floors exhibited in this area make this a preferred site for an AGTF. Some concerns exist because of the large number of tall trees in the area. These trees will transmit motion into the ground during windy periods; however, this disturbance will be minimized by burying the facility deeper than 70 feet and by removing trees from an area one third of a mile in radius around the facility.

Elida, New Mexico

This remote site consists of flat range land. The nearest occupied dwellings were over 5 miles away. The soil is deep, sandy, and well drained. The ground water depth is 50 to 100 feet.

The cross spectral density obtained from vertical seismometers at this site is shown in Figure 8. The noise is at a relatively high level across the entire frequency band. The noise at 60 Hz is again an electrical problem and is not included in the noise amplitude values.

The high ground water and the soil conditions at this site are similar to the conditions at Holloman AFB and therefore make this site undesirable for the same reasons. The measured noise level here was also significantly higher than at any other location.
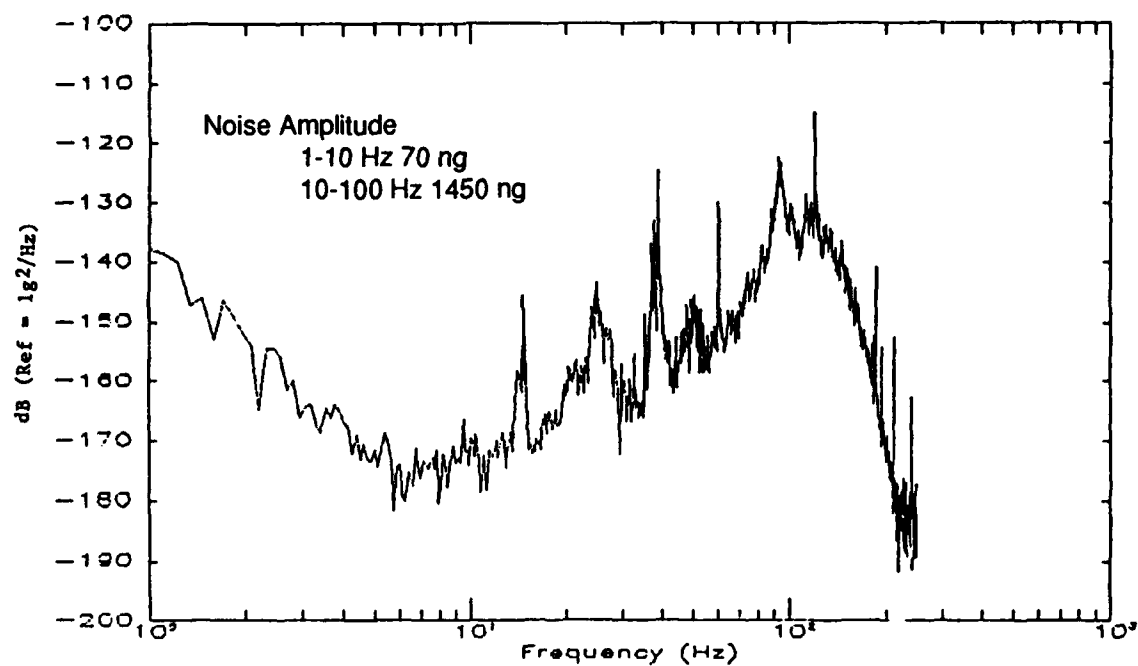
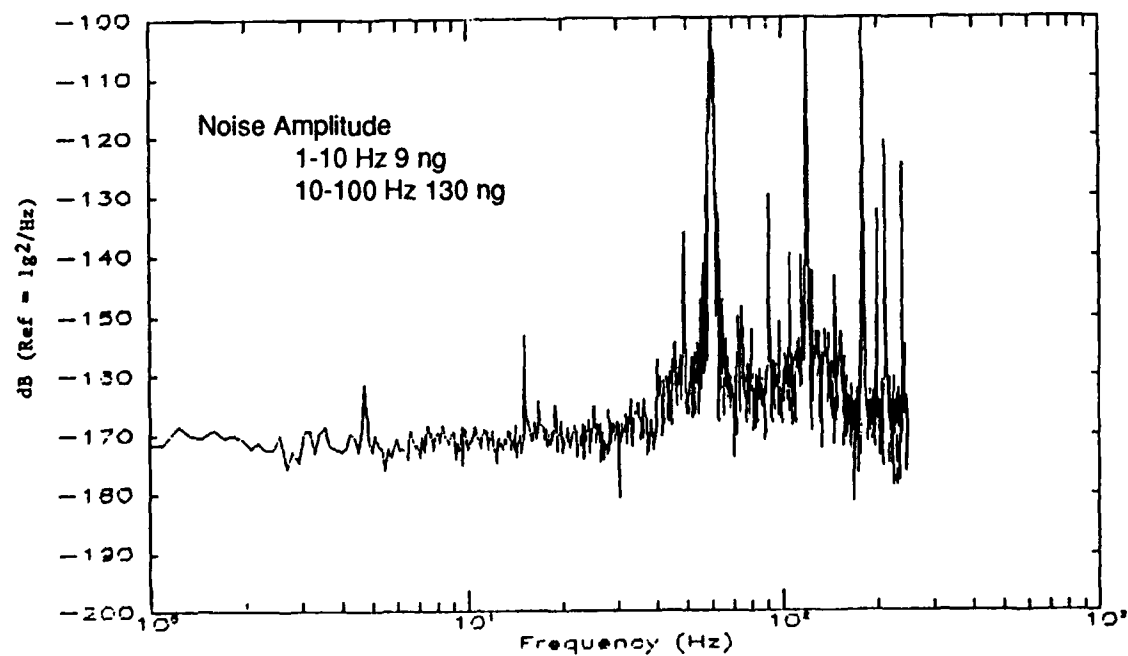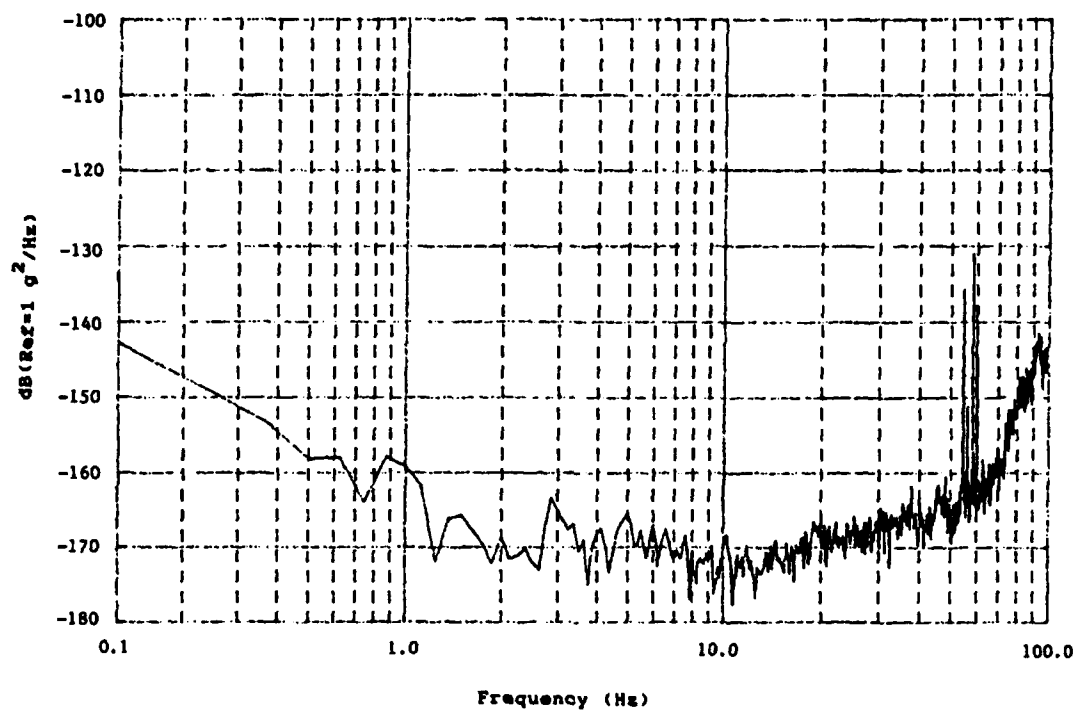Figure 5. Noise at East Black Hills, Texas

Figure 6. Noise at Sunspot, New Mexico

89M0102 2

- 33 -

Figure 7. Noise at Sunspot, New Mexico - Second Visit

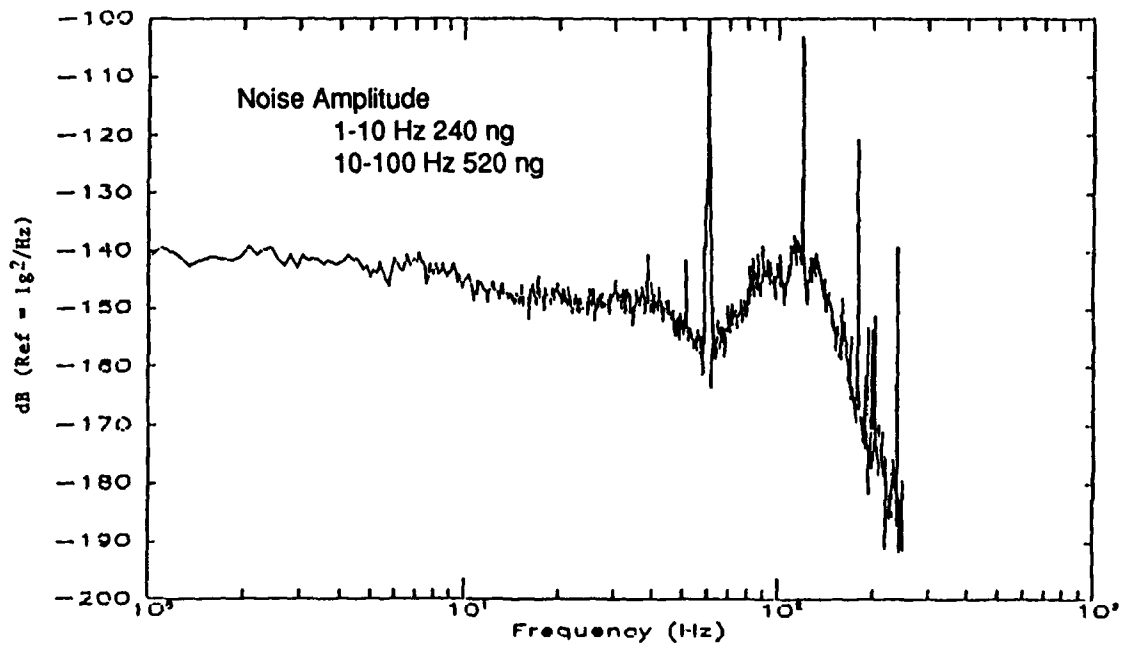
Noise Amplitude
1-10 Hz 240 ng
10-100 Hz 520 ng

Figure 8. Noise at Elida, New Mexico

89M0102 4

Overall Site Comparisons

To determine the best location for an AGTF the sites were compared on a basis of seismic noise, remoteness, site conditions, and climate. These comparisons are shown in Table 1. The data in this table were then used to prepare a site scorecard. The scorecard was prepared by assigning a score ranging from 1 to 10 to each parameter at each site based on how well that parameter met AGTF requirements at that site. Weighting factors were than assigned to each parameter as an indication of importance of the parameter to AGTF. The weighted score was determined by multiplying the score by the weighting factor. The weighted scores were then totaled for each site to provide an overall site comparison. The site scorecard is shown in Table 2.

Seismic noise was considered the most important parameter and accounted for almost half of the total score. The Sunspot location was significantly quieter than any other site and therefore received the highest score in this category. Site remoteness and site conditions were considered almost equal in importance and each contributed to approximately one fourth of the total score. The East Blackhills and Elida areas were the most remote and therefore scored highest in this area. The Holloman and Elida areas scored significantly lower than other sites in the category of site conditions because of the soil type and ground water depth. The climate at the site comprised only a small part of the total score because a buried facility would not be greatly affected by temperature or precipitation. In this area Sunspot rated somewhat lower than the other sites because of the amount of precipitation received there.

The overall comparison shows that Sunspot is the preferred site for an AGTF. The mine at Carlsbad and the East Blackhills areas are approximately 80% as good as Sunspot. A mine should only be considered if all mining activity has ceased and there are no active mines within 4 miles of the area. A buried facility in the East Blackhills area would be costly because of the need to excavate into bedrock. The Holloman and Elida areas both rate at about 60% of the Sunspot site. Construction of an AGTF at these sites that would meet the performance goals is considered risky because of the soil conditions and high level of ground water. It is therefore recommended that the AGTF be sited in the Sunspot, New Mexico area.

Table 1. Comparison of Site Parameters

Parameter	Units	Carlsbad, NM	Holloman AFB	E. Black Hills, TX	Sunspot, NM	Elida, NM
Seismic Noise (Measured)						
RMS 1-10 Hz	µg	0.04	0.18	0.07	0.01	0.23
RMS 10-100 Hz	µg	0.34	0.40	1.45	0.13	0.52
Remoteness						
Distance to Paved Road	mi	0.0	2.0	17.0	0.3	10.0
Distance to Railroad	mi	0.0	5.0	>10.0	>10.0	>10.0
Aircraft Activity		None	Heavy	None	Light	Med
Distance to Power Line	mi	0.0	2.0	1.0	0.0	4.0
Distance to Population Center	mi	25.0	12.0	32.0	2.0	20.0
Site Conditions						
Soil Type		Langbeinite	Sandy Loam	Limestone	Fractured Limestone	Sand & Silt
Ground Water Depth	ft.	0-50	35-70	1200-1300	1200	50-80
Land Use		Mining	Idle	Ranching	Laboratory	Ranching
Vegetation		None	Low Brush	Low Bush	Trees	Grass &Weeds
Topography		Underground	Near Arroyo	Low Hills	Mountain Top	Low Hills
Climate						
Avg. High Temp.	°F	95.8	94.9	94.2	73.3	91.3
Avg. Low Temp.	°F	27.7	28.0	36.2	19.1	22.9
Avg. Annual Prec.	in	12.7	10.9	13.0	26.2	14.3
Avg. Annual Snowfall	in	3.7	4.2	1.2	84.5	9.0

89M0102

Table 2　Site Score Card

Parameter	Wt. [*]	Carlsbad, NM		Holloman AFB		E. Blackhills, TX		Sunspot, NM		Elida, NM	
		Score[*]	Weight Score[x]	Score[*]	Weight Score[x]	Score[*]	Weight Score[x]	Score[*]	Weight Score[x]	Score[*]	Weight Score[x]
Seismic Noise (Measured)											
RMS 1-10 Hz	10	6	60	2	20	4	40	10	100	1	10
RMS 10-100 Hz	8	6	48	5	40	1	8	10	80	4	32
Weighted Total	180		108		60		48		180		42
Remoteness											
Distance to Paved Road	2	1	2	3	6	10	20	1	2	10	20
Distance to Railroad	2	1	2	5	10	10	20	10	20	10	20
Aircraft Activity	2	10	20	1	2	10	20	7	14	4	8
Distance to Power Line	1	5	5	10	10	10	10	3	3	10	10
Distance to Population Center	2	10	20	10	20	10	20	6	12	10	20
Weighted Total	90		49		48		90		51		78
Site Conditions											
Soil Type	2	10	20	4	8	10	20	10	20	6	12
Ground Water Depth	3	7	21	1	3	10	30	9	27	2	6
Land Use	1	5	5	10	10	8	8	1	1	8	8
Vegetation	1	10	10	8	8	8	8	1	1	8	8
Topograph	1	10	10	5	5	9	9	8	8	9	9
Weighted Total	80		66		34		75		57		43
Climate											
Temperature Spread	1	6	6	6	6	8	8	10	10	6	6
Precipitation	2	10	20	10	20	10	20	1	2	8	16
Weighted Total	30		26		26		28		12		22
Grand Total	380		249		168		241		300		185
% of Best			83		56		80		100		62

[*] Importance of parameter - 10 is most important
[*] Favorability of site for AGTF - 10 is most favorable
[x] Score times weight

AGTF Design

The primary design goal for the AGTF is that it shall provide the capability to test inertial instruments in an environment in which linear accelerations shall not exceed 1.0 nano-g at frequencies up to 100 Hz. A conceptual drawing of the proposed facility is shown in Figure 9. The facility consists of two buildings: a control building to house offices, test preparation areas, data acquisition and analysis functions, service needs, and mechanical and electrical equipment; and a below ground testing building where the actual testing will be performed. Even at the quietest site, both passive and active isolation techniques will have to be employed to meet the facility goal. Therefore, the test cells are designed to accommodate these isolation devices in as quiet an environment as possible. To maintain a quiet environment the test cell building is round in shape and dome covered to reflect any disturbances. Inside, seven triangular test cells, 50 feet on a side, surround a central reference cell (Figure 10). The test cells are separated from each other and from the circular corridor by at least 12 feet. This area between cells is filled with dirt to provide isolation as well as temperature stability. A cross section of the test building is shown in Figure 11. This shows that test tables will be located on passive and active control platforms which are located on massive concrete piers. These piers are further isolated from the undisturbed soil by a layer of attenuating soil. Trenches in the undisturbed soil provide further isolation of these piers from other building foundations.

Because air conditioning is a major source of disturbance in most facilities careful consideration must be given to minimize this noise. The air conditioning equipment is located in the above ground building and is designed to provide the required air conditioning with a minimum air flow rate. Ducts are treated with sound absorbing material and no hard connections are permitted between the ducts and the test building. Air flow through the test cells is laminar from top to bottom. Active duct isolators are employed both at inlet and outlet ducts to further attenuate the transmission of noise through the ducts.

The above ground control building comprises 21,000 square feet and houses all support equipment, computer equipment, buildup, and checkout areas and offices (Figure 12). To maintain a quiet environment in the test cells, only a minimum amount of activity and equipment will be permitted. All instrumentation buildup and instrument checkout will therefore take place in the control building. Only after it is fully checked out will it be moved into the underground laboratory for actual testing.

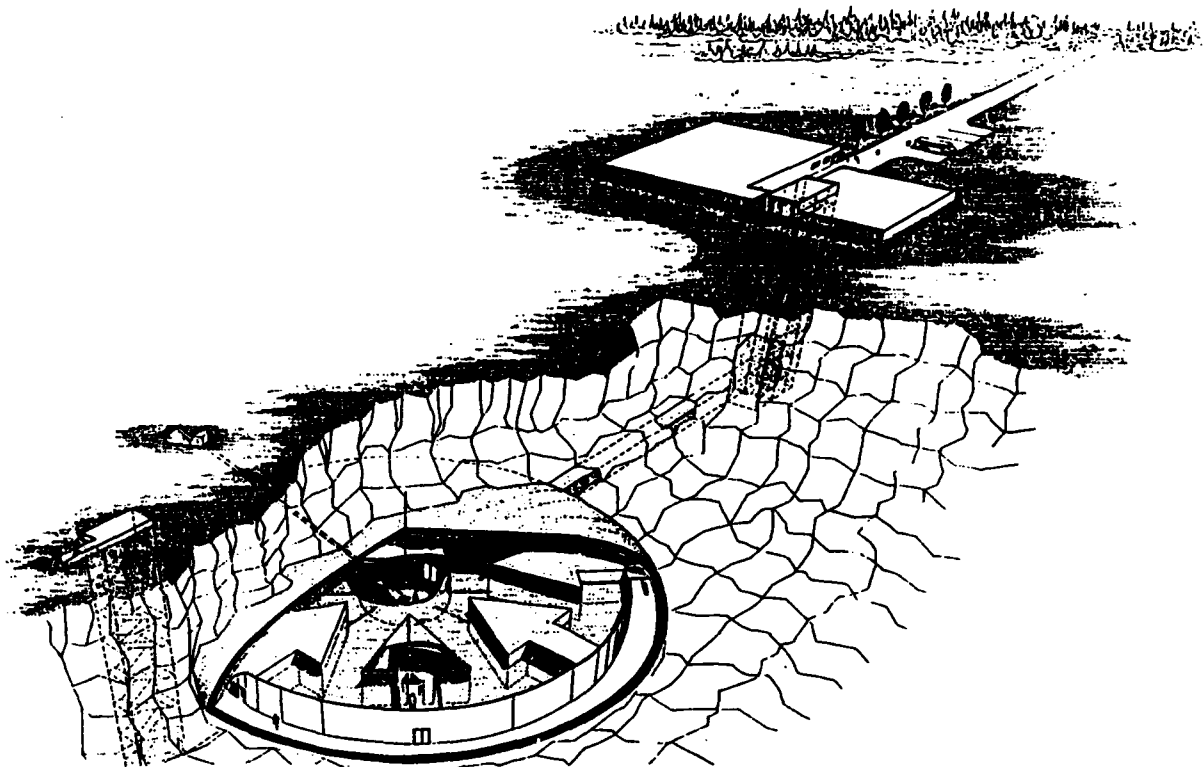Figure 9. Facility Design - Conceptual Drawing

FLOOR PLAN

TESTING BUILDING
FLOOR PLAN
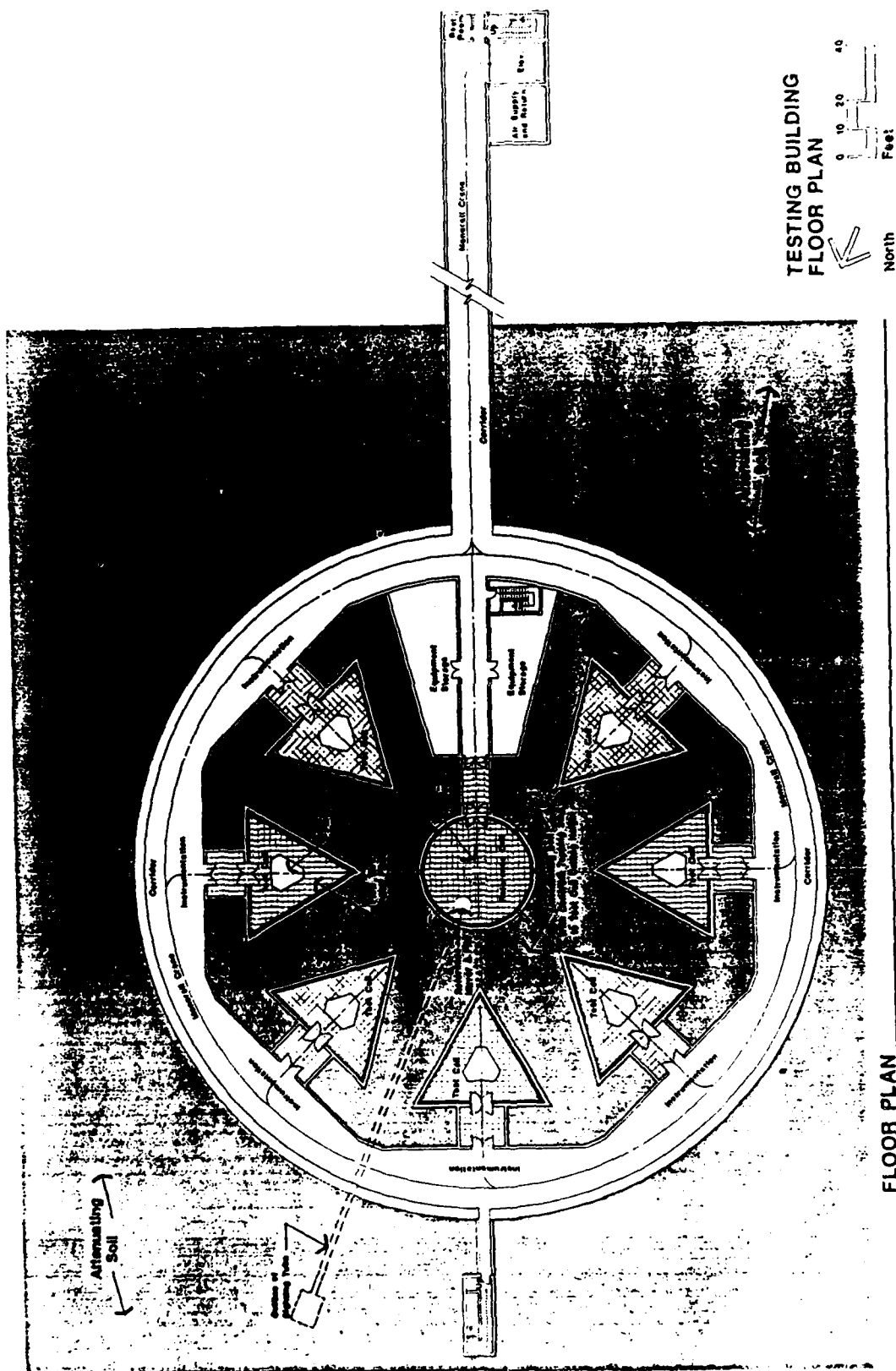
Figure 10. Testing Building Floor Plan
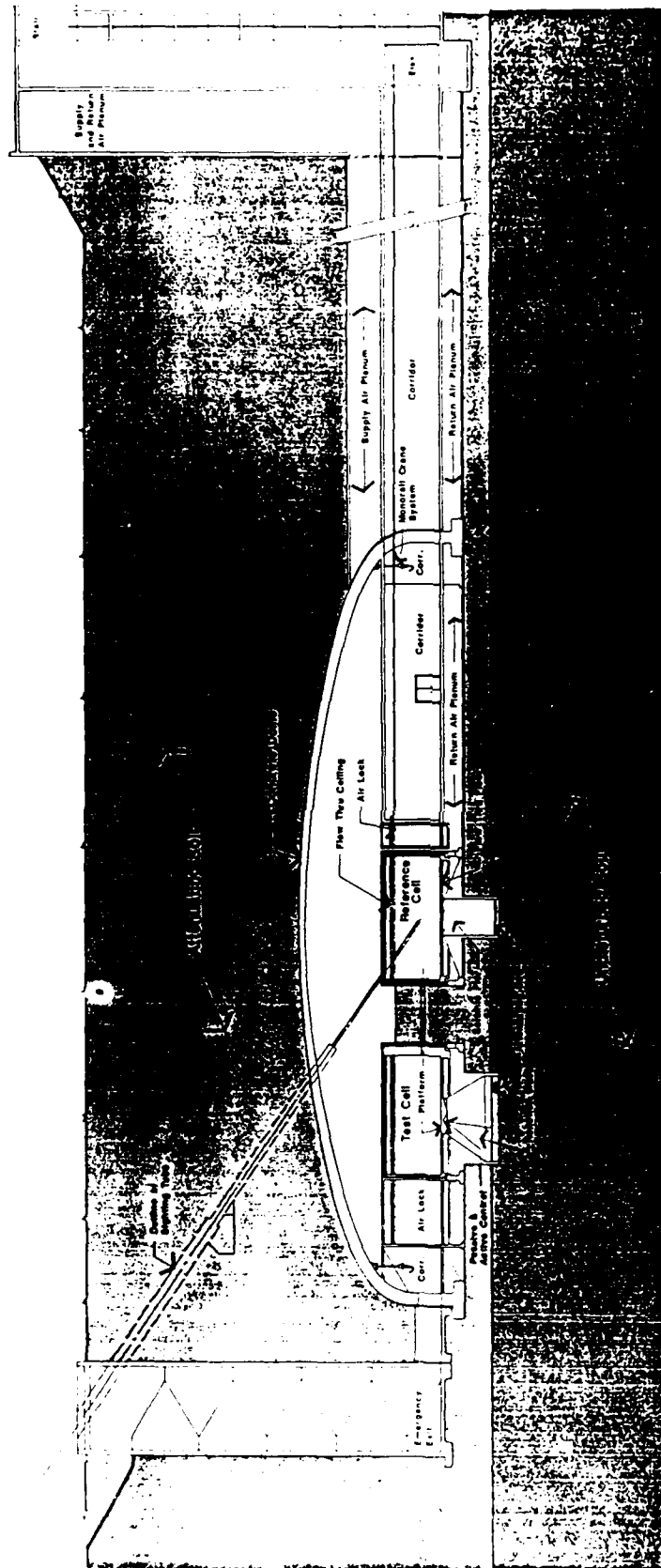
Figure 11. Testing Building Cross Section

CONTROL BUILDING
FLOOR PLAN

NORTH

Feet
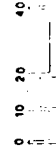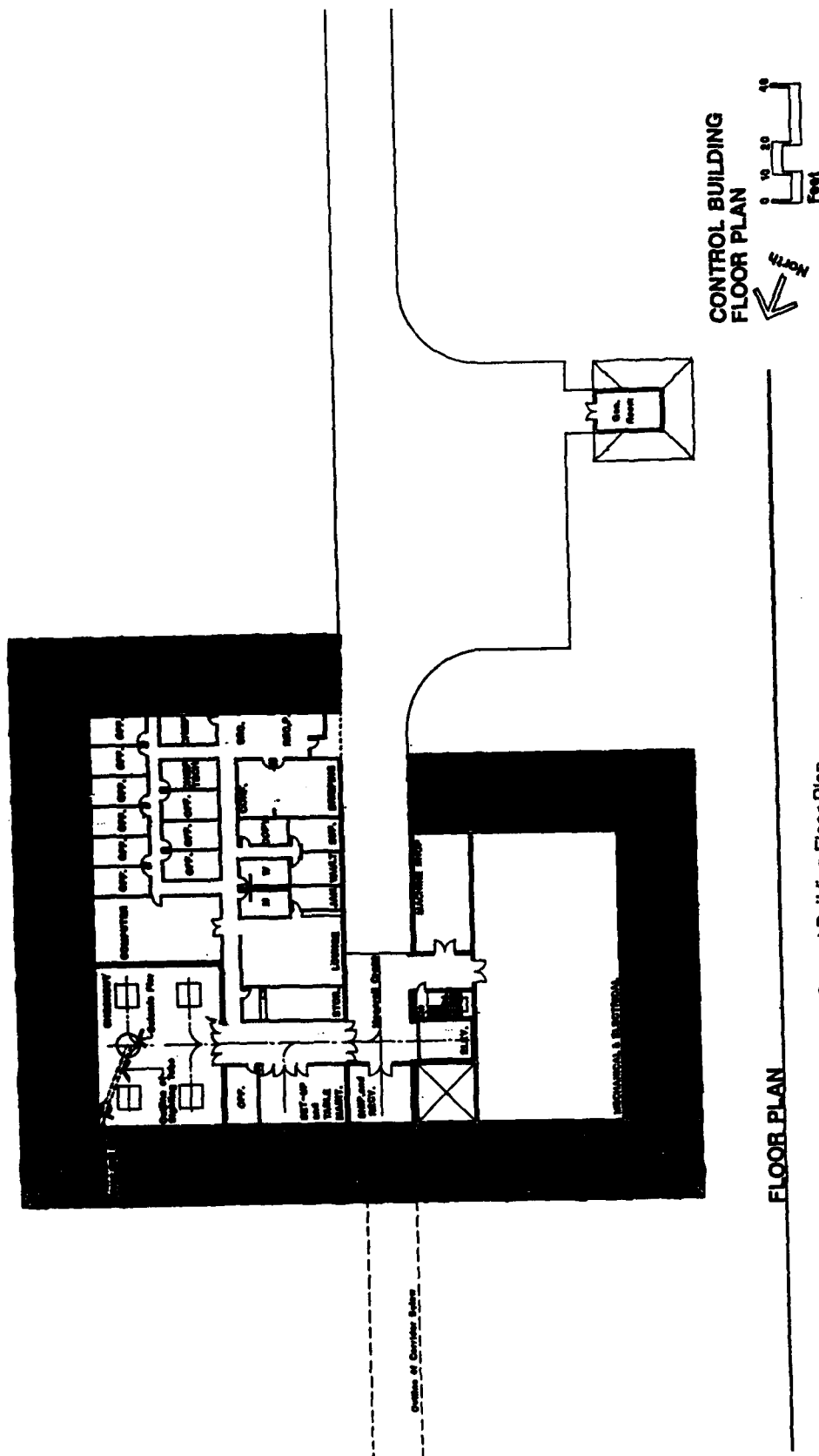
FLOOR PLAN

Figure 12. Control Building Floor Plan

Conclusions

The need for improved facilities to test inertial sensors has been long recognized. A study has now been completed which has identified a seismically quiet site in the Sacramento Mountains near Sunspot, New Mexico, as a location for such a facility. A design for this facility has also been completed. This design consists of an above ground support building and a round dome-covered test building buried at least 70 feet below ground. The design pays careful attention to isolating the test cells from seismic and cultural disturbances. Even in this quiet environment, passive and active isolation devices will be required to achieve the goals for this facility. The design presented is expected to provide a test environment for inertial sensors in which linear accelerations will not exceed 10^{-9}g RMS at frequencies up to 100 Hz. This facility should fulfill the inertial sensor test requirements through 2010.

References

1. Burns and Roe, Inc., Facilities Design Report, Precision Inertial Test Laboratory, 6585th Test Group, Holloman AFB, NM, Contract No. F29601-75-C-0091, November 1975.

2. Civil/Nuclear Systems Corporation, Search and Evaluation Techniques for Ultra-Low Earth Noise Sites, 6585th Test Group, Holloman AFB, NM, Contract No. F28601-78-C-8062, Project: 9333, November 1978.

3. Morgan, F. E., et al, Final Report for a Study of the Operational Need for an Advanced Guidance Test Capability, 6585th Test Group, Holloman AFB, NM, Contract No. F08635-85-C-0221, January 1986.

4. Algermissen, S. T., An Introduction to the Seismicity of the United States, Earthquake Engineering Research Institute, Berkeley, CA, November 1983.

THIS PAGE LEFT INTENTIONALLY BLANK

CSDL-P-2838

AN AUTOMATED SYSTEM FOR CONTAMINATION-CONTROLLED PROCESSING OF PRECISION INSTRUMENTS

by

T. M. Stepien, T.A. Hamilton,
D.S. Seltzer, J.M. Rourke*

November 1988

*Arthur D. Little, Inc.

The Charles Stark Draper Laboratory, Inc.

555 Technology Square
Cambridge, Massachusetts 02139

THIS PAGE LEFT INTENTIONALLY BLANK

AN AUTOMATED SYSTEM FOR CONTAMINATION-CONTROLLED PROCESSING OF PRECISION INSTRUMENTS

T. M. Stepien*, T. A. Hamilton*, D. S. Seltzer*, J. M. Rourke**

*The Charles Stark Draper Laboratory, Inc.

**Arthur D. Little, Inc.

ABSTRACT

The design and operation of an automated system for cleaning and assembly of precise electromechanical instruments in a clean room environment is described. Precision contamination-controlled automation implies automating those tasks that require process control that substantially exceeds the ability of humans and contamination control below the Class 100 level. The system described has demonstrated the capability to meet these requirements by successfully processing inertial instruments formerly processed by manual operators in a clean room. It is an integrated system comprised of modular workstations for freon and deionized water power spray cleaning, outgassing, precision assembly, epoxy bonding, epoxy curing, dry nitrogen storage, and testing. Workstations are linked by a four axis transport system. All stations are equipped with closed loop HEPA filtering which isolates the instruments from the workers, similar to a SMIF system. The system environment is maintained at a Class 1 clean room level. A network of workstation and supervisor computers controls, monitors, and documents system operations.

INTRODUCTION

Automated systems have been used to assemble many different electrical and mechanical products. IBM's PC Convertible [16], Sony's Walkman [18], and Seiko's watches [7] are examples of complex products that are assembled in a mechanized manner. Typical volumes of products assembled by these systems are high, averaging 800,000 units annually [6]. Automated systems are also used to process integrated circuits and disk drives for the semiconductor and computer industries. With these systems the principal limitation of volume production is quality. Production goals are becoming increasingly difficult to meet as line widths of ICs and flying heights of disk drives decrease; the salient limitation is contamination.

The automated system described in this paper shares attributes and goals from both types of systems. It is an assembly system, used to assemble tight tolerance, complex, three-dimensional parts. The system also controls contamination very rigorously, to a Class 1 clean room level. The parts processed by the system happen to form an inertial

instrument when assembled, but the assembly, cleaning, and contamination control technology can be applied to other electrical and mechanical products.

Inertial instruments are distinguished by having precise clearances, on the order of 0.000050 inch (1.5 micron), and cylindrical fits where the clearance is less than one-thousandth of the mating diameter. At these sizes, particles greater than 0.5 micron are significant (see Figure 1) and a potential source of failure. For some products yield losses attributable to particulate contamination alone are as high as 50% [9] [11]. The standard approach to battling these low yields is to upgrade clean room facilities and insist workers wear more restrictive garments. The costs for modified laminar flow cabinets, new filters, improved bunny suits, masks, and gloves can be prohibitively high and the results often uncertain.

A number of other difficulties arise due to the use of manual labor in such high precision manufacturing. Manual inconsistency is a significant problem. Different operators perform the "same" job in different ways. This results in variable quality and yields which lead to high unit costs. Training time for operators can be lengthy, and the results unpredictable. For some operations, only a few trainees will achieve high yield results. Manufacturers often rely on key personnel with years of experience to perform critical tasks. The loss of these seasoned operators can severely disrupt production capability.

An automated manufacturing system for the cleaning, assembly, and testing of inertial instruments is designed to combat these problems. It consists of computer controlled, modular workstations in which contamination is systematically controlled to a Class 1 level. The instrument parts are completely isolated from the workers during processing. They are introduced into the system on trays. The trays are automatically transported to different workstations for cleaning with freon and deionized water, outgassing, assembly, epoxy curing, dry nitrogen storage, and testing. Instrument assembly includes several difficult operations, including the mating of parts with extremely close clearance fits, accurate torquing of threaded parts, and application of precise amounts of epoxy.

The system was recently delivered to a manufacturer of inertial instruments and is in routine use. The following four sections describe the design and integration of the cleaning, assembly, and contamination control technologies.

SYSTEM REQUIREMENTS AND DESCRIPTION

The automated system was designed to perform final cleaning and assembly of an inertial instrument. The general requirements for these tasks are:

Contamination control Airborne particulates must be controlled; those greater than 0.5 micron in diameter potentially jeopardize the performance of the instrument. Parts enter the system dirty and must be cleaned in a mechanized

On this scale a human hair
is five feet in diameter

1 micron
line spacing

Integrated circuit

1.5 micron
clearance

Part A

Part B

PARTICULATES

Mating parts

- Class 100 cleanrooms have up to one hundred 0.5 micron diameter particles per cubic foot
- Draper's isolated environment is Class 1; less than one 0.3, 0.5, and 1.0 micron diameter particle per cubic foot.
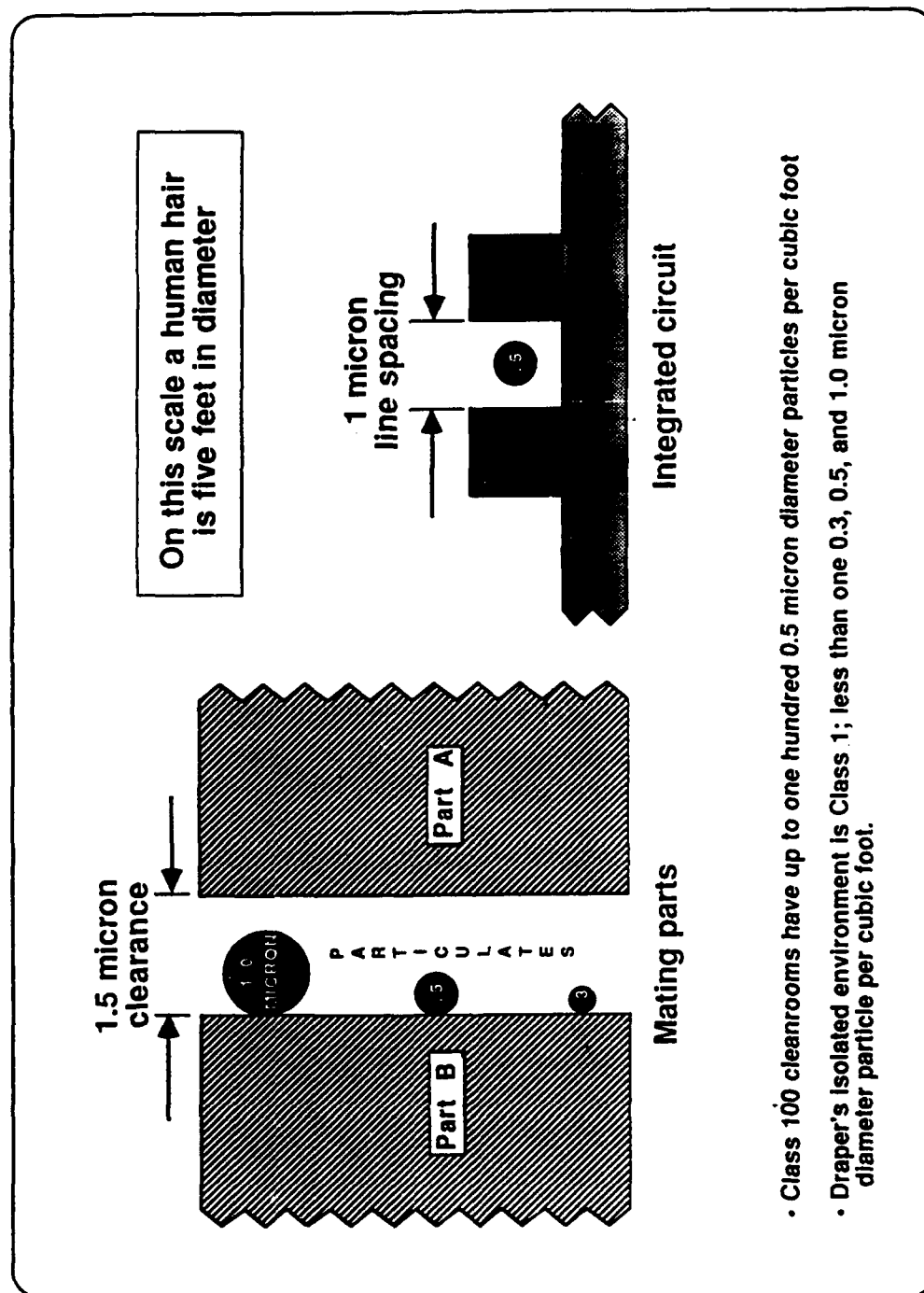
Figure 1: Particle sizes, part mating clearances, and line widths

manner. The instrument is susceptible to contamination until the final epoxy operation. Material outgassing must also be controlled.

Instrument assembly Assembly of the instrument requires precise control of assembly forces, to 0.1 grams, torquing operations, to 0.1 inch-ounce, and pick and place operations, to 0.001 inch open loop. Part clearances are as tight as 40 microinches (1 micron) and chamfers typically less than 0.005 inch. Parts are delicate; assembly forces must be minimized.

Special instrument operations The system is required to perform additional tasks during the processing of the instrument such as epoxy application, specialized test operations, and dimensional inspections.

Computer control The entire operation of the system is to be computer controlled and documented. Interface to the system by operators must be straightforward. Sensors necessary for process verification and error prevention are to be integrated with the control system.

The system is comprised of an interconnected group of special purpose automated workstations. The workstations are linked by an automated transport robot and controlled by a two level computer network. Figures 2 and 3 show perspective and plan views of the system. The workstations are:

Assembly Workstation This is the most sophisticated workstation. It includes all tooling required to perform instrument assembly and epoxy operations. The workstation has five axes of motion. Two linear axes (X and Y) carry the horizontal assembly base. A third linear axis (Z) carries a vertical tool changing wrist with special instrumentation that facilitates precision assembly. Two rotational degrees of freedom perform threading operations (about Z) and part inversion (about Y). The assembly base carries specialized assembly tooling, instrument parts, and trays upon which the parts reside. Assembly base tooling includes fixtures for torquing, epoxy application, and instrument testing.

Transporter The transporter links all the workstations. It is a four axis, rail mounted manipulator that transports trays between workstations over a 20 foot distance. There are three linear axes (X, Y, and Z) and one rotational axis (about Z). The manipulator arm contains a draw collet and an optical sensor that allows it to securely and accurately locate and pick up the trays. Figure 4 shows transporter reaching into the assembly workstation to deliver a tray of parts.

Freon Power Spray This is one of two cleaning stations. The freon power spray system is a spin rinser dryer which impinges instrument parts, held in part trays, with freon at up to 1500 psi, removing surface level particulates. The cleaning cycle is followed by a HEPA (High Efficiency Particulate Air) filter dry cycle.
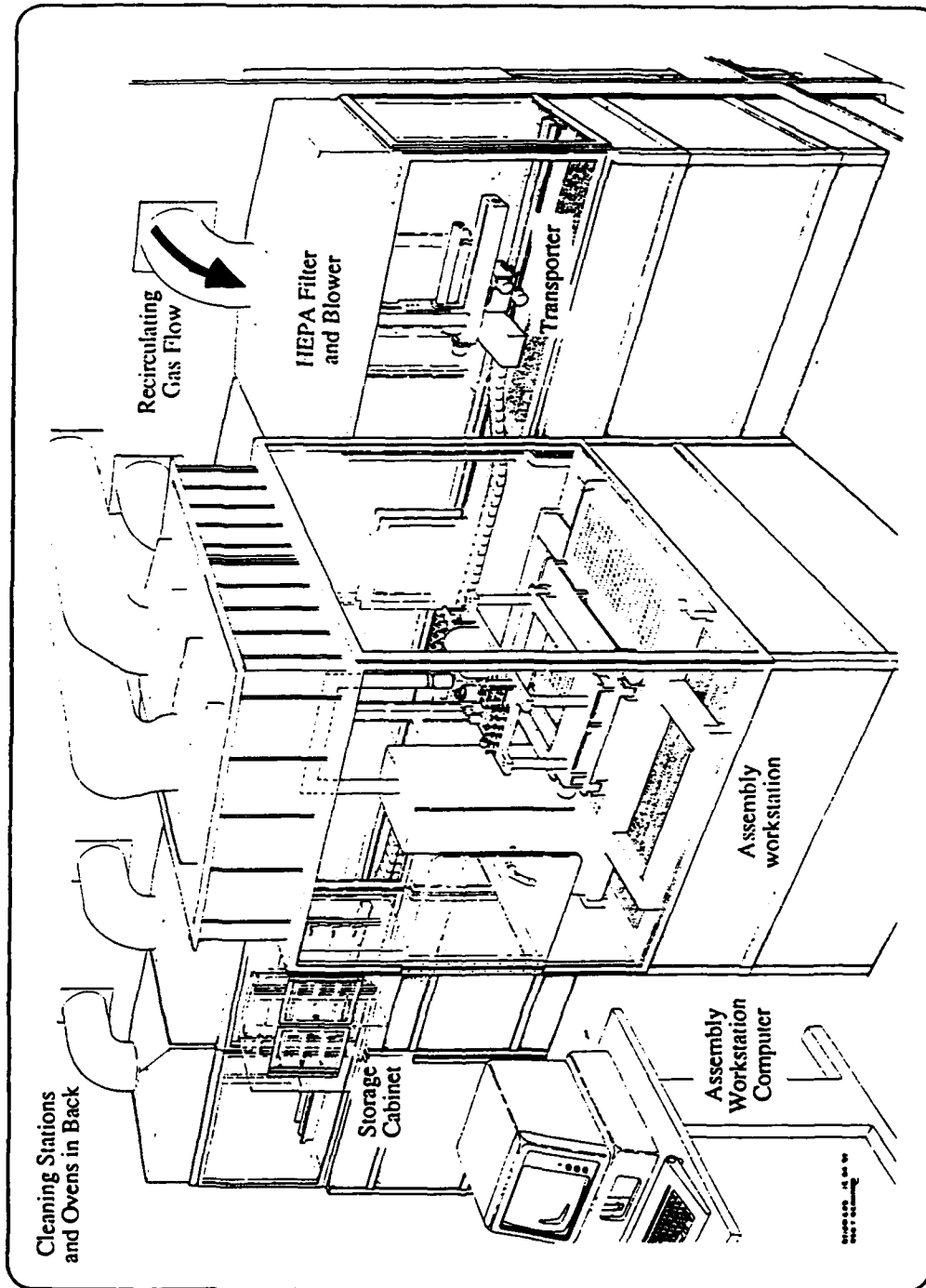
Figure 2: Automated Assembly System - Perspective View

Recirculating Gas Flow

HEPA Filter and Blower

Transporter

Assembly workstation

Cleaning Stations and Ovens in Back
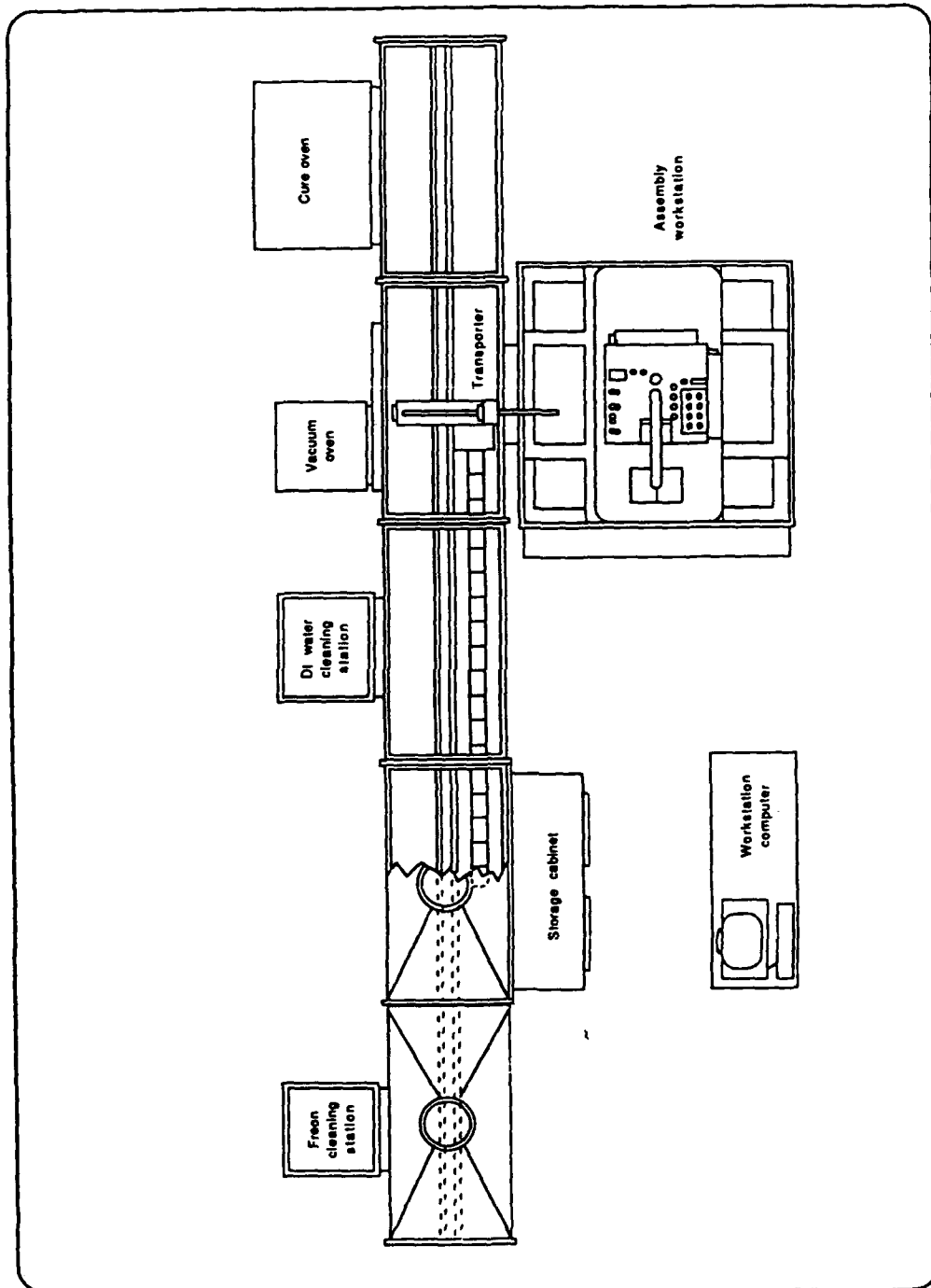
Storage Cabinet

Assembly Workstation Computer

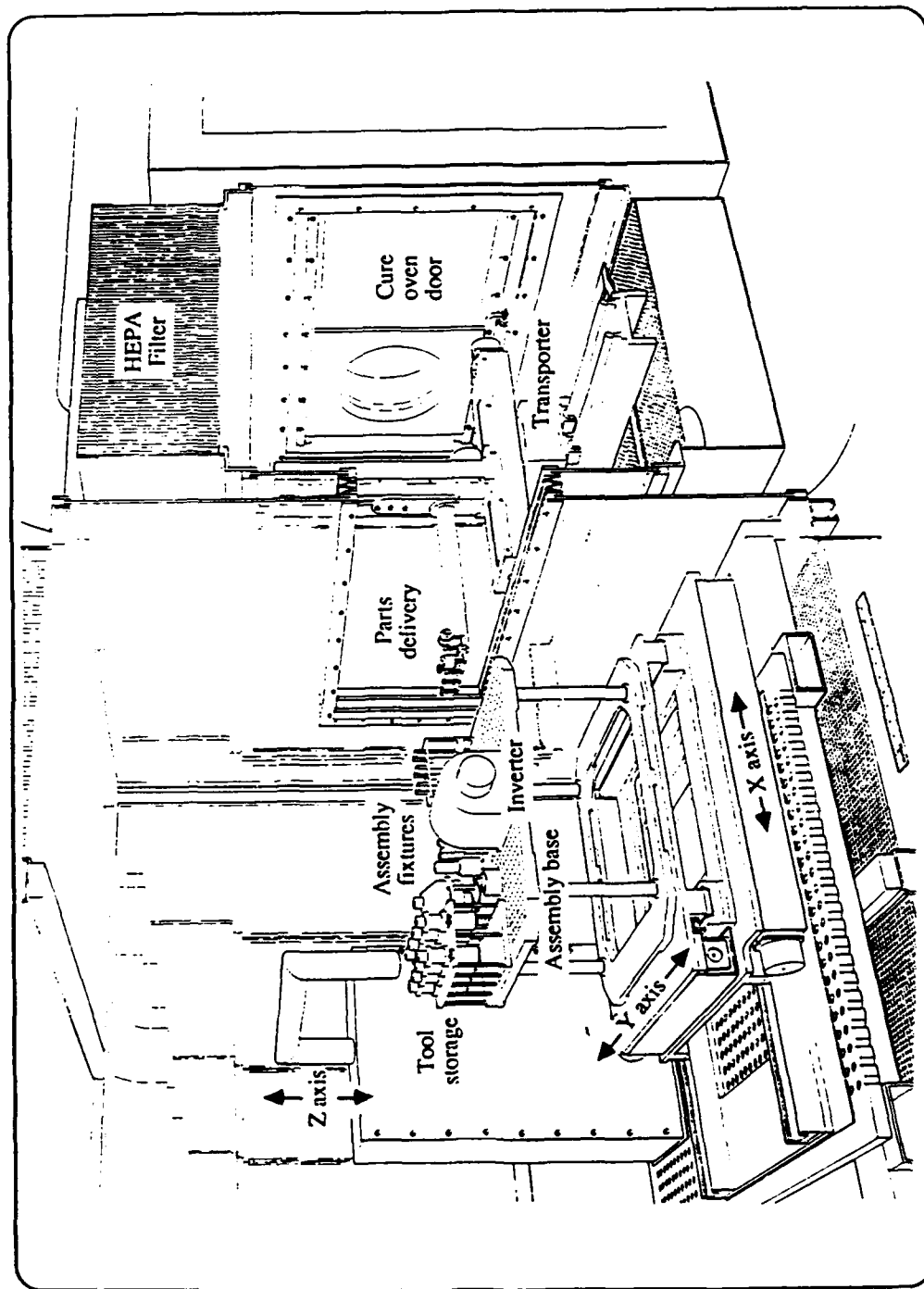Figure 3: Automated Assembly System - Plan View

Figure 4: Automated Assembly System - Section through Assembly
Workstation, Transport Compartment, and Curing Oven

Deionized Water Power Spray The second cleaning station is also a spin rinser dryer. It is similar to the freon system but cleans parts with deionized (DI) water, at pressures up to 300 psi.

Curing Oven The curing oven is a clean room oven with a HEPA loop. The oven is used for curing epoxy applied to instrument parts. It is equipped with an automated sliding door to interface with the transporter.

Vacuum Oven The vacuum oven is a standard model and is used for outgassing parts that have been cleaned with freon. It is also equipped with an automated sliding door to interface with the transporter.

Storage Cabinet All transportable trays and fixtures have dedicated storage locations in the storage cabinet. The cabinet is mounted to the side of the transport environment. It is physically divided into two sections of storage: Input/Output (I/O) and In-Process (IP). Trays that leave the system for loading or unloading are placed in the I/O cabinet for that purpose. This section of the cabinet has an interior sliding door for automated transporter access, and an exterior door for manual access. The IP section of the cabinet is for storage of clean trays and fixtures that are awaiting additional processing, including those trays and fixtures that permanently reside in the system.

Figure 5 is a simplified process flow for the instrument. The parts are manually loaded onto trays before they are introduced into the system. Once introduced, the parts remain internal to the system until they are assembled into a complete, sealed instrument. Sealing (with epoxy) insures that the instrument is impervious to contamination. An instrument is made up of twelve parts and requires approximately twenty-three hours to be processed. In the steady state the system, in its current configuration, can manufacture five instruments per 16 hour day. The instrument was not redesigned to be processed by the system.

SPECIAL TOOLING AND SENSORS

The automated system contains many specially engineered tools, fixtures, and sensors. Some of the more important ones are described in this section.

Tool Changing Wrist

The tool changing wrist at the end of the vertical arm of the assembly workstation performs all pick and place and assembly operations. It is a sophisticated engineering package which consists of three subassemblies: a tool socket, for attaching and detaching assembly base tools; a remote center compliance (RCC), a Draper designed mechanical device which accommodates misalignments during mating operations; and a sensor assembly, used for monitoring deflections of the tool. Figure 6 is a section drawing of the wrist showing these subassemblies. Figure 7 is a photograph of the wrist.
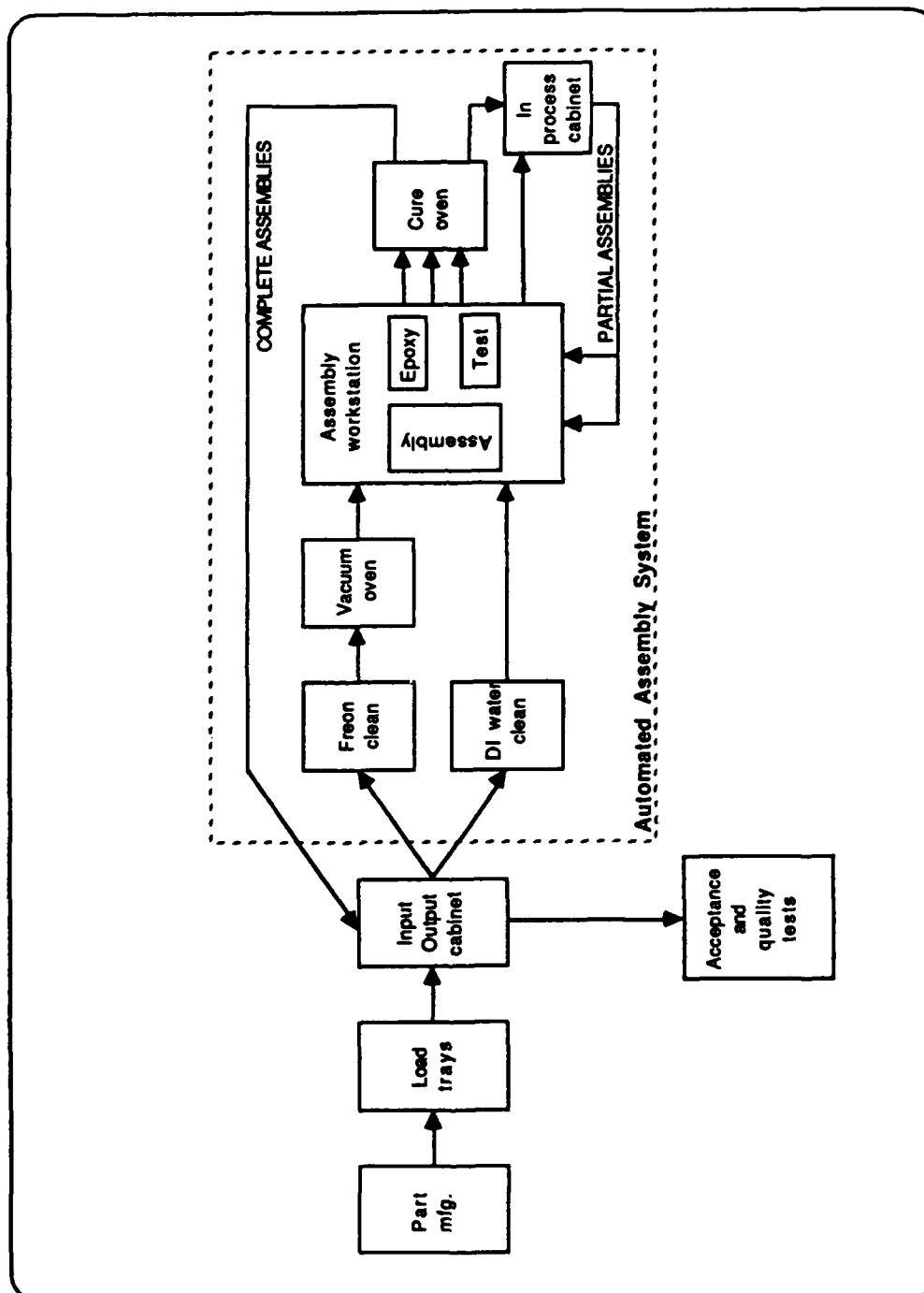
Figure 5: Process Flow for the Automated Assembly System

Four jacking screws for alignment capability

Air lines for tool attach/detach and finger open/close

Polished stainless steel exterior

Sensor assembly

Linear Variable Differential Transformer

Remote Center Compliance

Tool socket
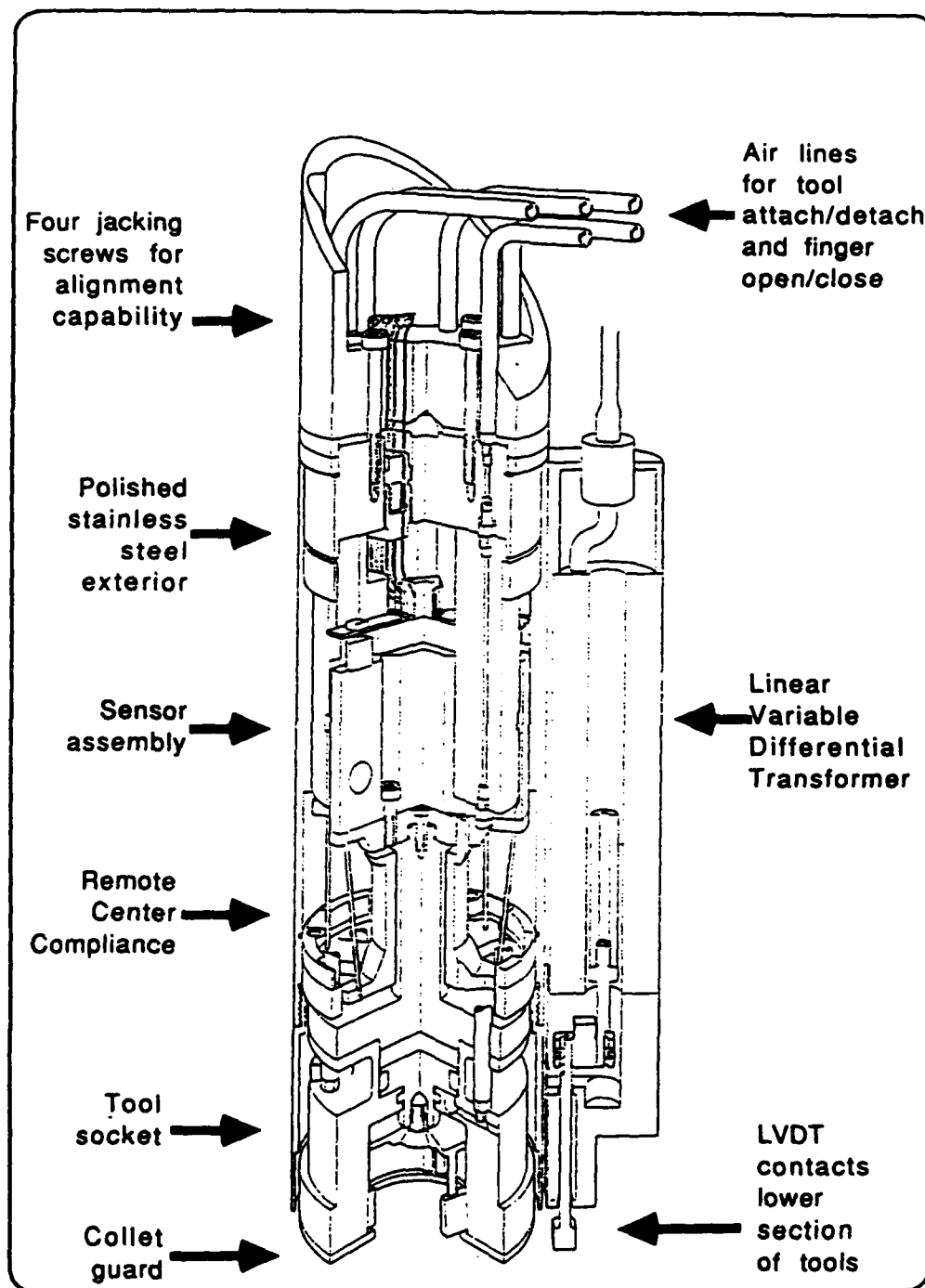
LVDT contacts lower section of tools

Collet guard

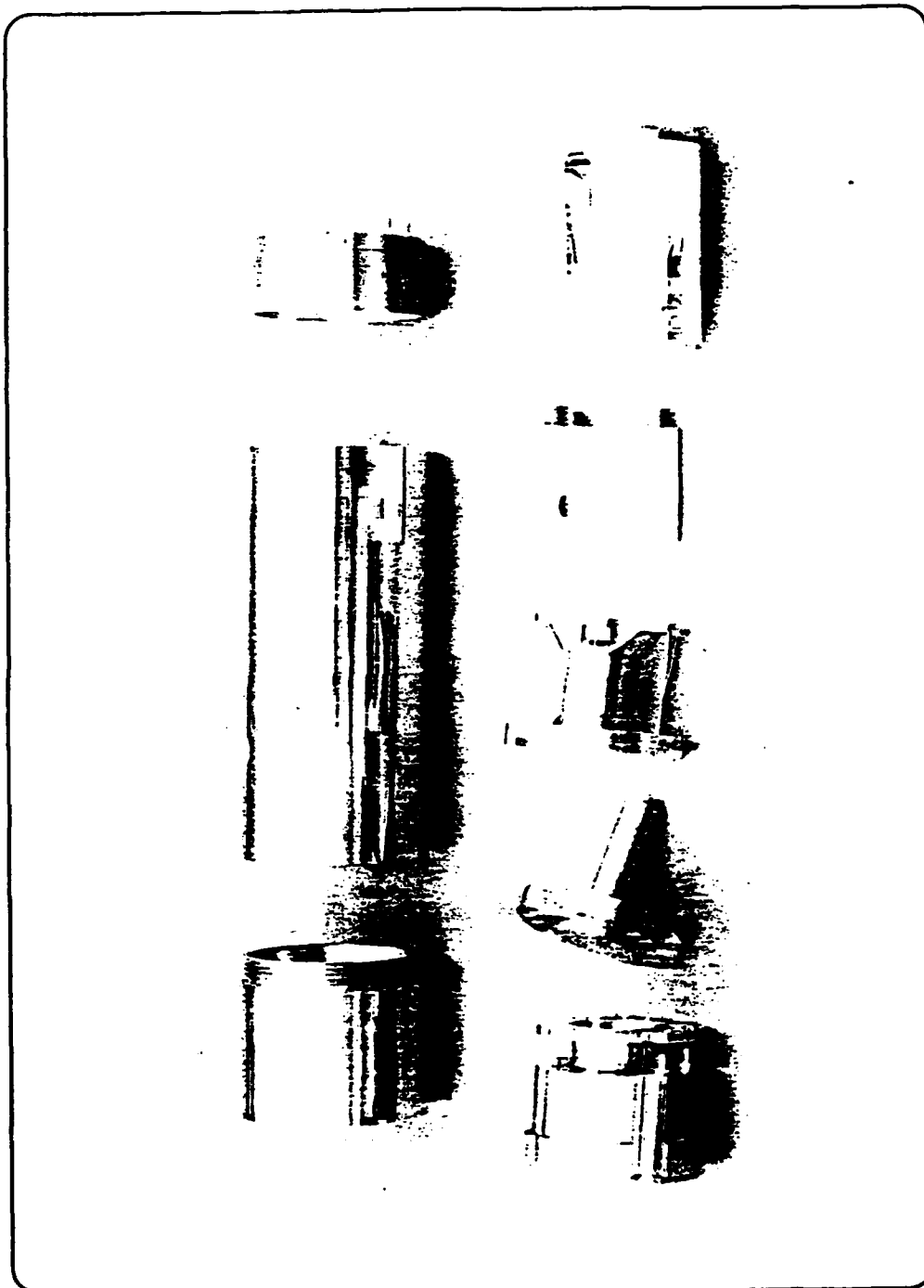Figure 6: Section Drawing of the Tool Changing Wrist

Figure 7: Photograph of the Tool Changing Wrist

Tool socket

The tool socket accurately secures tools, which are used to pick and place parts and fixtures. Securing or releasing a tool is performed with a pneumatically driven, dual acting draw collet. The design space of the collet was limited by a trade-off in stiffness: the flexible portion of the collet must be compliant so as to limit the draw force (the draw force is limited by the diameter of the piston cylinder, shaft diameter, air pressure, and seal friction) but must be stiff so it does not buckle when released. The design evolved into a short (0.5 inch), two fingered collet machined out of a stiff material (beryllium-copper).

Two additional design features of the tool socket are protection from collision and alignment capability. Our experience with similar tool changing robots [15] dictated that protection of the collet from vertical collisions was important. A guard ring whose internal diameter was slightly smaller than the undrawn collet diameter was added to the bottom of the tool socket. If, during a tool pick-up operation, the tool was located out-of-position, it would strike the guard ring before hitting the socket. The ring proved useful on more than one occasion. Alignment capability was provided with four jacking screws located at the top of the socket. The face of the tool socket is parallel to the assembly base to better than 20 microinches.

Remote Center Compliance (RCC)

The tool socket is supported by an RCC [21]. The RCC is a mechanical device which provides multiaxis compliance that accommodates positional and angular misalignments between mating parts. Compliance is provided with two pair of three 0.028 inch stainless steel wires bonded to the three level structure (see Figures 6 and 7). The RCC is instrumented; displacements are sensed electronically. The RCC was engineered to be lightly damped, having a damping ratio of approximately 0.3. Other specifications of the wrist are shown in Table 1.

Sensor Assembly

The sensor at the top of the tool changing wrist measures small deflections of the RCC and tool socket in six degrees of freedom. The sensor assembly consists of six Alnico VIII permanent magnets and nine linear Hall effect devices. The assembly measures horizontal deflection of the RCC along the X and Y (horizontal) axes, and rotational deflection about the X,Y and Z (vertical) axes. Vertical deflection along the Z axis can also be detected, but such deflection only occurs because of failure of the compliance structure. Range and sensitivity of deflection measurements are shown in Table 1.

The deflection sensors are extremely helpful during the teaching phase of the system setup. Teaching establishes the relationship of parts and fixtures (giving them names) to a multidimensional coordinate system. The axes are driven to the named locations during move operations. By sensing the tool socket deflections due to contact between a tool and a workpiece, a direct measure of positioning error of the assembly arm with respect to the workpiece is obtained. These errors are usually small (0.005) inch and difficult to detect visually. They are displayed on a computer screen and guide the operator during the teaching process.

Table 1: CSDL Precision Tool Changing Wrist Specifications

Feature	Lateral	Angular
Tool changing repeatability	0.0001 inch	0.1 milliradian
Compliance	20 lbs/inch	500 inch-lbs/radian
Compliance and deflection sensor range	0.020 inch	60 milliradian
Deflection sensor sensitivity	0.0001 inch	0.1 milliradian

The sensors are also a key element in error protection. The output signals are continually monitored by an electronic circuit set to trigger an alarm if excessive tool socket deflection occurs. Excess deflection can be caused by a misaligned workpiece or fixture, an improperly taught location, or an out of tolerance part. A horizontal deflection greater than 0.006 inch will immediately stop motion of all axes.

Another sensor, called the tool height sensor, is mounted at the end of the vertical arm. It is a linear variable differential transformer (LVDT) which measures the vertical deflection of tools (tool design is described in the next section). It measures tool deflection over a 0.2 inch range, with a resolution of 0.0001 inch. With no tool attached to the tool socket, the sensor is used as an inspection probe to measure the height of critical subassemblies.

The tool height sensor is also part of the error protection circuit, triggering an alarm in the event of excessive vertical tool deflection. The level at which the alarm is triggered is programmable over the entire range of the tool deflection. Each operation and each tool can be programmed to have a different protection level.

Tools

Assembly workstation tools have two main sections: an upper section, which mates with the tool socket; and a lower section, containing fingers which grasp parts and fixtures. A typical tool is illustrated in Figure 8. The lower section moves relative to the upper, travelling along a precision vertical spline. The spline maintains a constant angular orientation of the tool. The range of travel of the lower section is approximately 0.2 inch. A spring, located between the two sections, gives the tools vertical compliance. The philosophy behind this design is threefold:

Minimize assembly forces between parts. The instrument is a stack assembly; the majority of mates are performed in the vertical direction. When dealing with delicate parts, such as inertial instruments, it is desirable to minimize assembly forces. The deflection of the tool's spring can be adjusted to the point
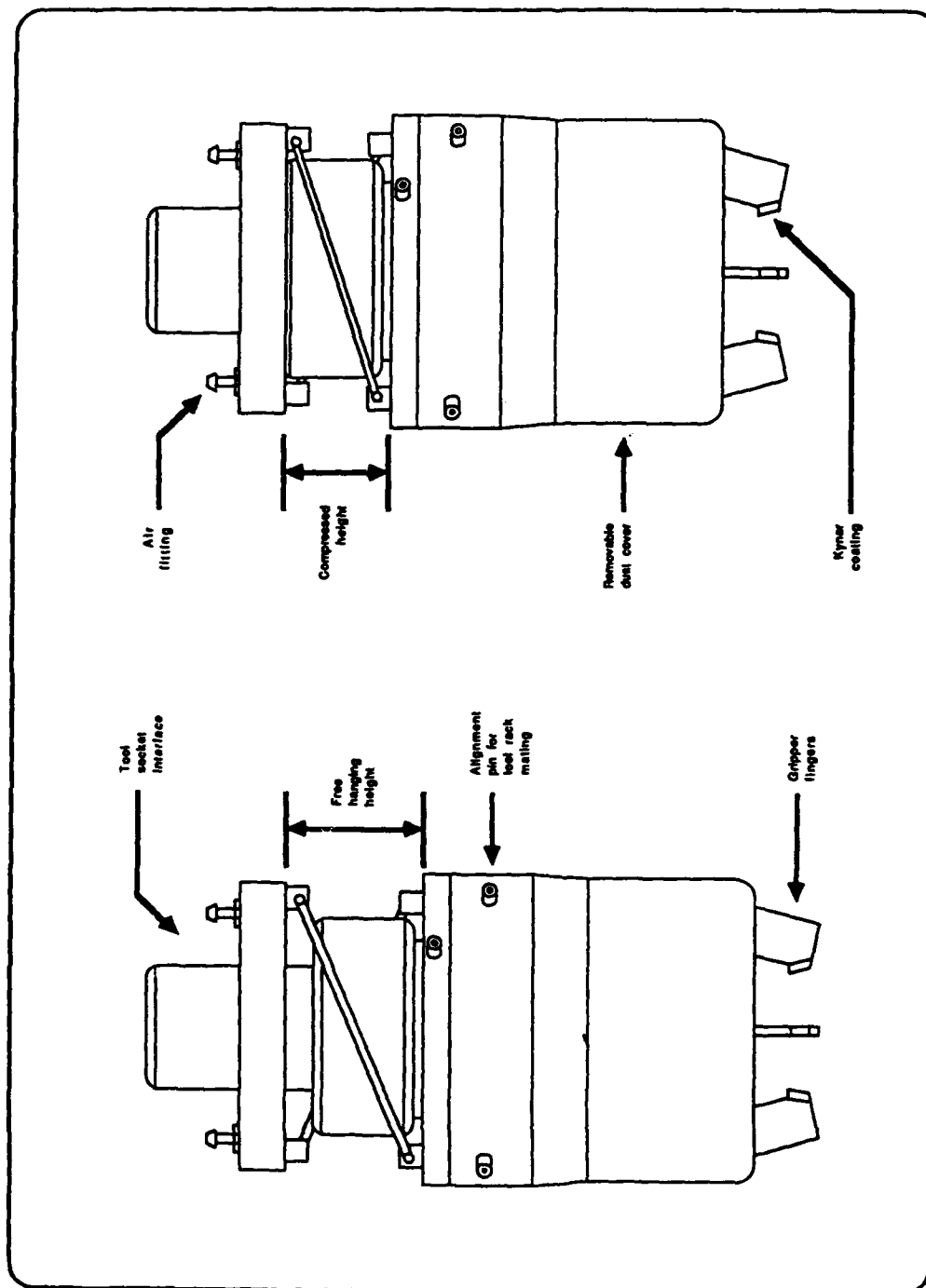
Air
fitting

Compressed
height

Removable
dust cover

Kynar
coating

Tool
socket
interface

Free
hanging
height

Alignment
pin for
tool rack
mating

Gripper
fingers

Figure 8: Assembly Workstation Tools

where the weight of the lower section balances upward spring force. By doing so, we can limit the vertical forces acting on any part held in the tool's fingers to the weight of the parts themselves, eliminating the weight of or force exerted by the tool, wrist assemblies, or vertical arm.

Allow threading operations to proceed in a clean and straightforward manner. Consider the example of threading a nut, held in the fingers of a tool, onto a rotating shaft. The advance of the threads could be accommodated in two ways: move the tool (and arm) vertically as threads advance; or displace the lower section of the tool (compress the spring) at the start of threading and allow the tool to advance (extend the spring) with threading. The second method has several advantages. It is easier to perform; allows thread advance to be monitored by sensing the movement of the lower section of the tool with the tool height sensor; and minimizes the forces acting on the parts during the potentially dirty threading operation.

Protect against errors. By providing compliance in the vertical direction the system will accommodate positioning errors in pick and place operations. If errors do occur, the spline of the tool is usually displaced first before parts, RCC, or other system components are contacted. The computer monitors the tool height sensor, which measures the tool spline deflection, and will stop the arm's vertical motion before damage occurs.

There are two basic finger mechanisms: pivoting and parallel motion. Pivoting fingers swing away from the workpiece. They are used for most operations. Parallel motion fingers translate away from the workpiece. They are employed when a feature of the part, such as a shoulder, does not allow for the down and away motion of the pivoting fingers. In both types of tools a pneumatically driven piston moves the fingers.

High Compliance Fixture

A second compliant fixture, called the high compliance fixture, is located on the assembly base. It is used for critical assembly operations, including the mating of parts with a clearance of 40 microinches (1 micron). The RCC could have been used to "push" these delicate parts together, but the resulting contact forces could have generated destructive particulates. The high compliance fixture is much softer (approximately ten times) than the RCC and keeps contact forces during assembly under 10 grams.

The high compliance fixture is instrumented. Three samarium-cobalt magnets and three linear Hall effect devices sense angular tilt about the X and Y axes, and vertical deflection along the Z axis. Angular resolution is 0.1 milliradian and vertical resolution is 0.0001 inch. The approximate vertical stiffness of the fixture is 0.001 inch/gram. The deflection profile is monitored and recorded during mates. The computer monitors the sensors and if contact forces exceed 10 grams the insertion is terminated before damage results.

Epoxy Application

An epoxy application subsystem within the assembly workstation is capable of delivering preprogrammed amounts of epoxy for bonding and sealing operations. The system includes an Electron Fusion Devices (EFD) epoxy dispensing device, 50 cc polycarbonate syringes, and syringe tips. Epoxy is loaded into the syringes prior to their introduction into the system. The EFD system controls the magnitude and duration of the pressure pulse to the syringe. The pressure, pulse width, and total number of pulses are computer controlled for each epoxy application.

A special tool is used to handle the epoxy filled syringes. Since the syringes and tips are not strictly controlled dimensionally, whereas the location of epoxy must be (to within 0.001 inch), the endpoint of each tip is located prior to each epoxy application. Locating the endpoint consists of sequentially passing the tip through an optical detector. The tip is located to within 0.001 inch in X, Y, and Z directions. The newly "found" tip location is compared to a known calibration location and the difference is accounted for in subsequent positioning operations. The system is capable of providing consistent and accurate applications of epoxy of two different viscosities.

Parts Trays

The parts trays, an example of which is shown in Figure 9, hold the instrument parts as they are transported throughout the system. A typical tray holds three or four instrument parts. Trays are loaded manually and introduced into the system through I/O box. They are also used to hold subassemblies and do not leave the system. The trays are carried by the transporter which grasps a dowel pin common to all trays.

The dowel pin is located by an optical sensor in the end of the transporter pickup arm. The sensor and search procedure of the pickup arm locate the end of the pin to within a few thousandths of an inch. A positioning error up to 0.050 inch can be accommodated by this method. Errors of this magnitude are allowed for tray transport since trays are manually placed in the I/O box and positions may vary from operator to operator.

The trays have a matrix of stainless steel 0.040 inch vertical pins that support the parts. There is a trade-off between the geometric location of the pins and the ability of the cleaning solvents to reach the parts. The pins must hold the parts accurately so they can be located by the assembly workstation and mated with other parts. However, the pins must allow access for cleaning solvents during cleaning operations. The trade-off was resolved by providing a 0.002 inch clearance between the part and pin. Pins are also designed to contact only noncritical surfaces of the parts.

The part tray pins are coated in a thin layer (0.0025 inch) of Kynar, a polyvinylidene flouride manufactured by Pennwalt. The Kynar coating is compliant and protects the parts from possible damage during cleaning operations. Fingers of some tools are also Kynar coated to protect the parts they handle and prevent possible contamination from metal to metal contact.

Figure 9: Part Trays

Transporter grips tray here

Top is lifted off to gain access to parts at assembly workstation

Top holds parts in tray during cleaning cycles and transport

part

Locating pins on bottom of tray accurately position tray at workstations

Pins coated in Kynar
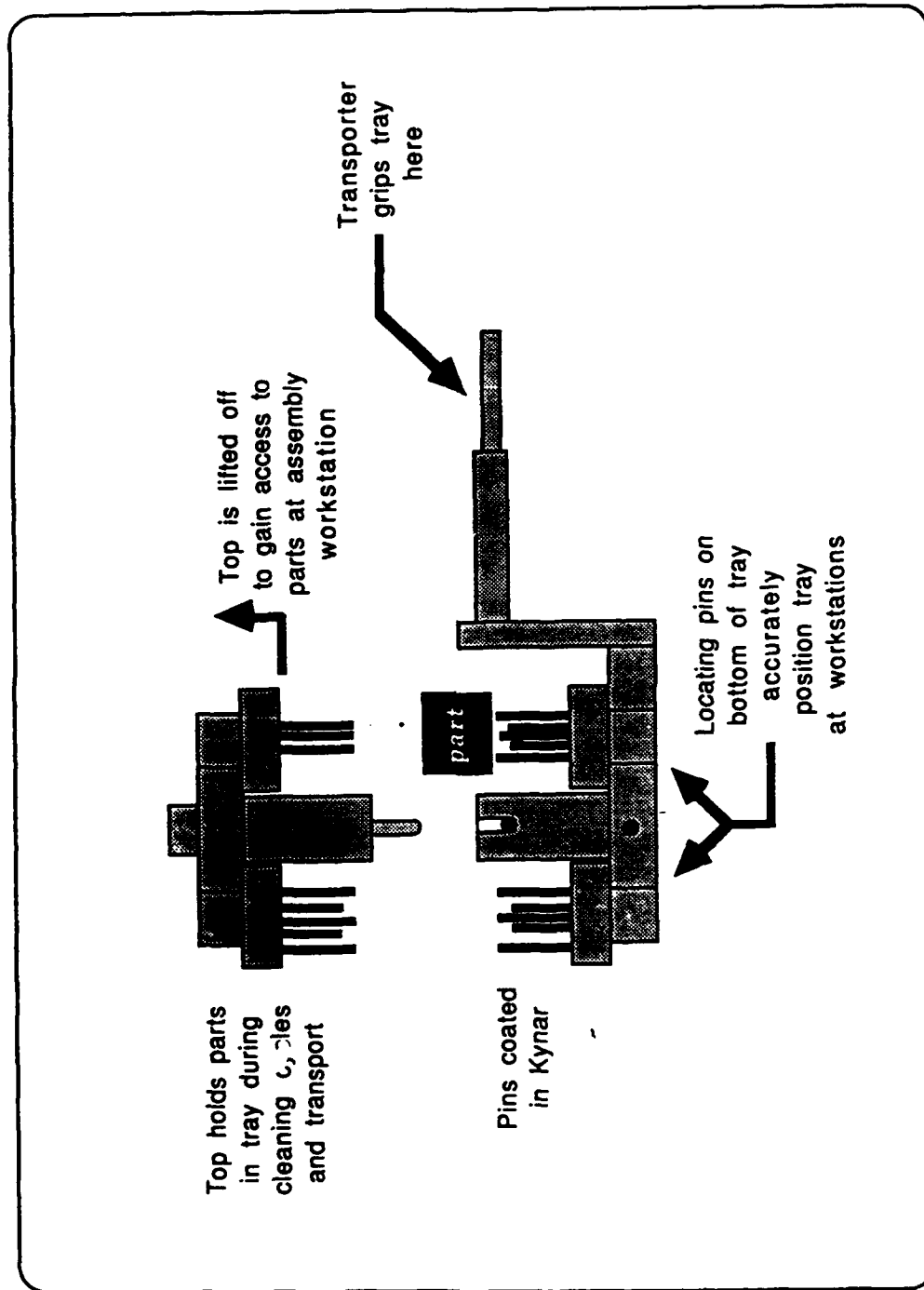
CONTAMINATION CONTROL

Draper's approach

The contamination control requirements for processing the inertial instrument are extremely rigid. The approach taken throughout the system is outlined in Table 2.

Table 2: Draper's Systematic Approach to Contamination Control

Isolation of instruments from human operators

Control of the system environment to eliminate airborne particulates

Monitoring of particulates with both airborne and liquid counters

Careful design of mechanical systems, tooling, and fixtures to minimize possible generation of contaminants

Selective choice of materials to minimize outgassing products

Development of rinser dryer systems to remove particulates from the surfaces of incoming parts

Several basic principles are applied throughout the design. The salient one is the isolation of the parts from human operators. Many studies have documented the contamination problems introduced by people in clean rooms. One stated that as many as 6000 particles per minute were emitted into an adjacent cubic foot by a fully suited clean room operator [3].

The approach taken is to enclose the system in its own closed loop, positive pressure, clean room. The modular workstations of the system are either connected together or sealed in glass. HEPA filters are located on top of each module. They have integral duct blowers which provide laminar downflow of gas at velocity of 50 ft/min. The system gas, typically dry nitrogen, is collected at the bottom of each module in a plenum. Standard ducting connects the plenums to the filters, recirculating the gas. Recirculation achieves a steady state level of cleanliness within a matter of minutes after system start-up.

Airborne particulate monitoring internal to the system is done primarily with a laser particle counter. The specific counter, a Particle Measurement System Model 101, resolves particles down to 0.1 micron in diameter. Particulate counts of the system environment verify that the system is a Class 1 clean room, as defined by Federal Standard 209D [20]. Particle measurements and statistics are detailed in Appendix A.

Several special design features were incorporated to accommodate the moving mechanisms of the system. The vertical axis of the assembly workstation is isolated from the other axes by enclosing the stepper motor and table inside a closed chamber. The

inverter axis, located on the assembly base, is also enclosed in a separate cover. The cartesian assembly base itself is raised above the stepper motors and lead screws to separate the critical assembly areas from the potentially contaminating mechanisms below. Any particulates that may be created by the drives are downstream of the instruments and are swept away with the wash of clean, downflow gas.

Basic chamber materials were selected to enhance cleanability and to avoid undesirable outgassing. The main structural members are fabricated out of either anodized aluminum or stainless steel. The diameter of the assembly arm is small (1.75 inches) and minimally obstructs airflow in the assembly workstation. The arm's exterior is highly polished (2 microinches AA) stainless steel. All mechanical and electrical fasteners are located inside to avoid possible contamination sources and disruptions to laminar gas flow. Assembly tools are sealed, and the gripping fingers are also polished stainless steel. Similar materials and packaging are incorporated in the design of the transporter.

The cleaning stations are commercially available rinser dryers manufactured by Semitool. They were originally developed for the semiconductor industry to clean boats of IC wafers prior to their processing. Draper personnel modified them to accept the part trays and operate with the desired cleaning solvents at the required pressures: freon up to 1500 psi and DI water up to 300 psi. The cleaning barrel is isolated from the transport environment with an automated sliding door. Rinse and dry cycles are computer controlled and easily modified.

The cleaning systems are extremely efficient and effective for precision instrument cleaning, especially when compared to the manual method of particulate removal using tweezers and suction under a binocular microscope. The viscous drag force generated by the high pressure cleaning solvents applies a shear stress greater than the adhesion force that holds particles to the surface of parts [12]. High pressure freon is supplied to the cleaning chambers by a spray unit manufactured by Quadrex HPS Inc. and modified by Draper. The effluent freon is returned to the Quadrex unit where is it filtered and distilled. None escapes to the atmosphere, insuring safety for workers and the environment.

Table 3 summarizes some of the features and benefits of Draper's approach to contamination control.

Comparison with SMIF

The most widely publicized contamination control standard is called the Standard Mechanical Interface (SMIF) developed by Hewlett-Packard [4] [5] [13]. Draper's approach is juxtaposed with SMIF in Table 4. The most salient advantage of the Draper approach is that the contamination control scheme is designed along with the processing equipment; they are integrated and controlled. SMIF systems control the environment of the products (integrated circuit wafers) up until the time they are handled by the processing equipment. They do not have the luxury of, nor have all semiconductor equipment designers recognized the importance of, controlling the internal environment of the processing machinery.

- 63 -

Table 3: Features and Benefits of Draper's Isolation Technology

Feature	Benefit
Provides a certified Class 1 clean room environment	Less production-limiting contamination
Completely separates critical instruments from workers	Reduces human-generated contamination
Isolates personnel from equipment and chemicals	Worker safety
Clean room facility not necessary	Less expensive, air handling costs greatly reduced
Garment standards can be relaxed	More comfortable working environment

Table 4: Comparison of SMIF and Draper Contamination Control Approaches

SMIF	Draper
Strive for Class 10. No published data to confirm or deny	Class 1 at 0.3 and 0.5 micron diameter particles per FS 209D
3 to 10 fold reduction in particulates on wafers. Size of these particulates unknown	Insufficient data to quantify particulate reduction
"least amount of particle fallout occurs inside a small enclosed space with a still air environment"	Based on 50 fpm laminar downflow of gas
Controls wafer transport and transfer	Controls assembly, testing, epoxying, curing, outgassing, as well as transport
Applications principally directed at semiconductor industry	Applications directed at precise electromechanical products
Handles mostly two-dimensional parts	Handles complex, close-clearance three-dimensional parts

COMPUTER CONTROL

Hardware

The seven automated workstations are controlled by a two level computer network as illustrated in Figure 10. The computer at the upper level is the supervisory computer (SC). The two computers connected to the SC are the workstation computers. The SC is an IBM PC/AT, the workstation computers are IBM PC/XT's. The SC communicates with the workstations over standard serial interfaces. All workstation hardware is connected to the workstation computers.

The following design rules govern the configuration of the workstations and computer network and the operation of the software:

The workstation computers control all real-time processes.
The SC only supervises activities at the workstations on a task basis. The SC initiates and monitors tasks by downloading commands to workstation computers to execute particular programmed sequences, and by checking workstation status flags. The SC handles system control tasks such as operator interface, database management, and workstation scheduling.

The SC initiates all communications. The workstation computers set status flags that allow the SC to determine their status.

The workstation computers only communicate with the SC, not with each other. No direct communication between workstations or real-time synchronization of multiple workstation activities occurs.

The workstation computers and their workstation hardware are fundamentally stand-alone systems. The SC serves only to initiate, coordinate, and document system activities and is not required for workstation level operations. For development or error recovery purposes each workstation can be operated independently.

The two workstation computers are the Assembly Workstation Computer (AWC) and the Transport & Cleaning Workstation Computer (TCWC). The AWC controls all instr ment assembly operations. It is interfaced only with hardware located within the assembly workstation. This creates a stand-alone assembly environment. The assembly workstation can perform assembly, test, and epoxy operations autonomously without any interaction with the SC or other workstations.

The AWC controls the axes of the assembly workstation through a Compumotor 3000 Indexing System. The 3000 indexer also provides interface channels for axes limit switches and pneumatic solenoids used for tool functions. A variety of tooling is interfaced directly to the AWC through digital and analog channels. The key tooling includes the wrist sensors, high compliance fixture, hotplate, and epoxy dispensing system.
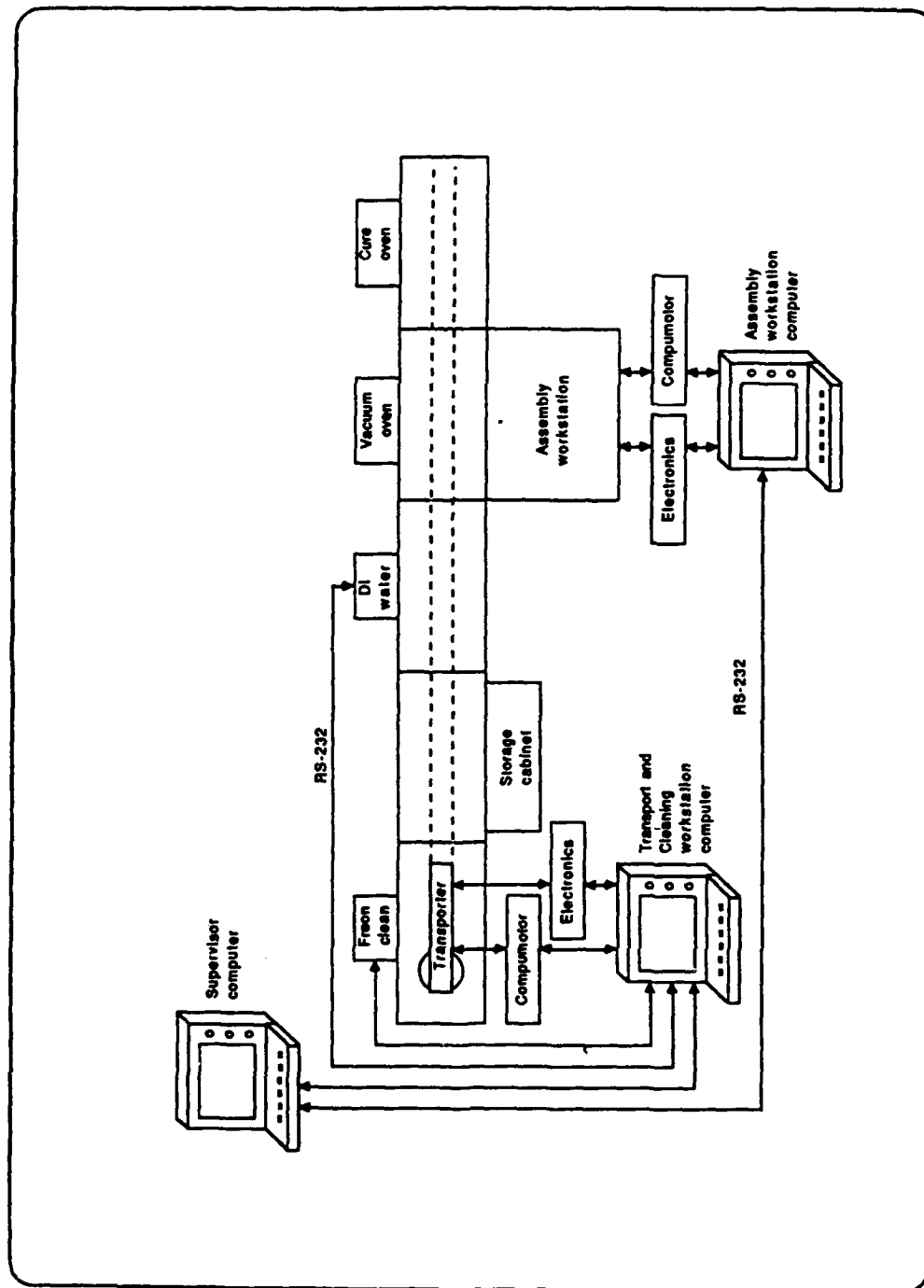
Figure 10: Computer Network for the Automated System

The TCWC is responsible for all tray and fixture transport between the individual workstations, and initiation and termination of cycles at the two cleaning stations. The configuration of the TCWC is different from the AWC in that it interfaces with all the workstations. These interfaces allow the TCWC to open and close the sliding doors on the ovens, storage, and cleaning stations during tray transport operations.

The TCWC is interfaced to the transporter through a second Compumotor 3000 Indexing System. The optical sensors in the end of the transporter arm and the axes limits are also interfaced through the 3000. As with the AWC, the TCWC has additional analog and digital interfaces to door control solenoids for the ovens and storage cabinet.

The SC directs the TCWC to make a transport move after it verifies that both the origin and destination stations for a tray are in an appropriate state. The SC also keeps track of the time that trays have been in ovens, and commands the transporter to remove them when appropriate.

Software

The system software is divided into two distinct packages: DAPL and Supervisor. DAPL (Draper Assembly Programming Language) is the operating software for the workstation computers. It has been under development for over three years and was employed on an earlier generation automated assembly system [15]. DAPL allows all workstations to be operated as stand-alone systems, or as part of a networked system. It is written almost exclusively in the C programming language using an off-the-shelf compiler and additional commercial libraries. Two versions were developed: one controls the assembly workstation from the AWC; the other controls the transporter and cleaning systems from the TCWC.

DAPL operates in two modes: manual and automatic. In the manual or interactive mode an experienced operator changes the state of a workstation by entering a single command at the keyboard of the workstation computer. An example of this interaction is the development of an assembly sequence. An operator would assembles parts in a step by step manner by entering a series of DAPL motion commands and tool operations. With the aid of displacement sensors, displayed visually on the computer screen, he can teach and name locations, pick and place parts and fixtures, and develop an assembly scenario. This is analogous to programming a standard robot with a teach pendant. Figure 11 is the primary computer screen of the AWC that an operator interacts with. A complete state description of the workstation is displayed to the operator.

Once the individual steps of an assembly sequence are established, they are coalesced into a separate, compiled program called an application program. These programs reside and run on a workstation computer in the automatic mode. They perform a specific task with little or no operator input. The application program "INSTRUMENT BOND", for instance, is a separate program that runs on the AWC to bond a portion of the instrument. Application programs can be developed off-line by experienced operators who use symbolic constants for locations. This separates the name of a location from the actual

Figure 11: Operator Interface of the Assembly Workstation Computer

multidimensional coordinates in space, allowing coordinate changes to be independent of the application programs.

DAPL commands were designed to be English-like. DAPL is most similar to numerical control and other robot programming languages like VAL developed by Unimation. Typical examples of DAPL commands for the AWC and TCWC are shown in Tables 5 and 6.

**Table 5: Typical DAPL Commands
for the Assembly Workstation Computer**

Command	Action
ATTACH and DETACH	pick up or return a tool
GRIP and RELEASE	actuate the fingers of a tool
MOVE, APPROACH, and DEPART	perform a move operation
SCREW and UNSCREW	perform a threading operation

**Table 6: Typical DAPL Commands
for the Transport & Cleaning Workstation Computer**

Command	Action
FETCH and PUT	pick up or drop off a tray
START and STOP	initiate or terminate a cleaning cycle
OPEN and CLOSE	actuate a workstation door
MOVE, REACH, and ROTATE	move the transporter

The supervisor software has four principal functions:

Task scheduling The supervisor directs the workstations to perform application programs.

Database management Data logged during the performance of an application program by the workstations are sent to the supervisor where they are managed in a database. Typical data include assembly forces, torque levels, part serial numbers, dates, and times.

Workstation polling The supervisor polls the workstations to determine their status.

Operator communications The supervisor is the principal conduit between the system and operators. Operators can schedule tasks, enter and determine piece part information, and determine status of each of the workstations.

The supervisor was written in C and KnowledgeMan, a database package which interfaces well with C.

CONCLUSION

The automated system has processed over a dozen instruments. All cleaning, transport, assembly, and epoxy operations were reliably and repeatedly performed by the system. Instruments made from "flight-quality" parts subsequently passed all the required quality control and instrument performance tests. The system was delivered to a vendor of inertial instruments and is in routine use.

Many of the technologies developed for the automated system can be applied to products other than inertial instruments. The cleaning techniques are suitable for many small mechanical parts such as bearings, gauges, and other complex electrical and mechanical parts and assemblies. The contamination control concepts can be applied to many industries including aerospace, computer and disk drive manufacture, medical testing, and pharmaceutical instruments. The precision assembly techniques have and will continue to be developed to handle tight clearance fits for critical parts.

ACKNOWLEGEMENTS

References

[1]   Austin, P.R., *Design and Operation of Clean Rooms*, Business News Publishing Company, Troy, MI (1970).

[2]   Cooper, D.W., "Statistical Analysis Relating to Recent Federal Standard 209 (Cleanrooms) Revisions," *Journal of Environmental Sciences*, Vol. 31, No. 2, pp. 32-36 (March/April 1988).

[3]   Dahlstrom, M., "Clean Room Garments: Where from Here?" *Semiconductor International*, Vol. 4, No. 4, pp. 110 (April 1983).

[4]   Gunawardena, S., Haven, R., Kaempf, U., Parikh, M., Tullis, B., and Vietor, J., "The Challenge to Control Contamination: A Novel Technique for the IC Process," *Journal of Environmental Sciences*, Vol. 27, No. 3, pp. 23-30 (May/June 1984).

[5]   Gunawardena, S., Kaempf, U., Tullis, B., and Vietor, J., "SMIF and Its Impact on Cleanroom Automation," *Microcontamination*, Vol. 3, No. 9, pp. 54-62 (September 1985).

[6]   Harrington, S.J., and Sackett, P.J., "A Study of Robotic Assembly Systems", *Assembly Automation*, Vol. 7, No. 3, pp. 122-126 (August 1987).

[7]   Hartley, J., "Seeing the Faces, Moving the Hands," *Assembly Automation*, Vol. 5, No. 2, pp. 97-100 (May 1985).

[8]   Hoenig, S.A., "The Clean Room as a System for Contamination Control," *Solid State Technology*, Vol. 28, No.9, pp. 129-135 (September 1985).

[9]   Hughes, R.A., Moslehi, G.B., and Castel, E.D., "Eliminating the Cleanroom: Experiments with an Open-Area SMIF Isolation Site (OASIS)," *Microcontamination*, Vol. 6, No. 4, pp. 31-37 (April 1988).

[10]   McDonough, J., and King, G., "An In-Depth Review of Federal Standard 209C: Defining Cleanroom Performance for the VLSI Era," *Microcontamination*, Vol. 5, No. 1, (January 1987).

[11]   Mittal, K.L., "A Multidisciplinary Approach to Surface Contamination Control," *Microcontamination*, Vol. 6, No. 5, pp. 16-24 (May 1988).

[12]   Musselman, R.P., and Yarbrough, T.W., "Shear Stress Removal of Submicron Particles from Surfaces," Presented at the 9th Contamination Control Working Group Meeting of the Inertial Guidance and Navigation Community, Los Angeles (1985).

[13] Parikh, M., and Kaempf, U., "SMIF: A Technology for Wafer Casette Transfer in VLSI Manufacturing," Solid State Technology, Vol. 27, No. 7, pp. 111-115 (July 1984).

[14] Peck, R.D., "The Proposed Revision of Federal Standard 209B," *Journal of Environmental Sciences*, Vol. 29, No. 5, pp. 42-46 (September/October 1986).

[15] Rourke, J.M., Seltzer, D.S., and Stepien, T.M., "Precision Automated Assembly in a Clean Room Environment," *Proceedings* , Robots 11/17th International Symposium on Industrial Robots, Chicago, pp. 4-49 - 4-57 (April 26-30, 1987).

[16] Saparito, B., "IBM's No-Hands Assembly Line," *Fortune*, pp. 10-12 (September 15, 1986).

[17] Schreiber, R.R., "Mechanical Assembly: Robots Carve Their Niche," *Robotics Today*, Vol. 8, No. 5, pp. 25 - 32 (October 1986).

[18] Sony Corporation's "Flexible Assembly Center System: FX-1 System," presented at The Fifth Annual Seminar on Robotics and Advanced Assembly Systems, The Charles Stark Draper Laboratory, November 6-8, 1984.

[19] Tolliver, D.L., "Insights into Contamination Control for VLSI Processing," *Proceedings*, Third International Symposium on VLSI Science and Technology, Vol. 5, pp. 3-32 (1985).

[20] U.S. General Services Administration, "Federal Standard Clean Room and Work Station Requirements, Controlled Environment," Federal Standard No. 209D, Washington, DC (June 15, 1988).

[21] Whitney, D.E., "Remote Center Compliance," *International Encyclopedia of Robotics: Applications and Automation* , Dorf, R.C., editor, John Wiley & Sons, New York, pp. 1316-1324 (1988).

[22] Wiesler, M., "Robotic Automation within the Semiconductor Industry," *Solid State Technology*, Vol. 31, No. 7 (July 1988).

Appendix A
Airborne Particulate Measurements and Class Level Calculations

The general system characteristics important for airborne particulate measurements, as outlined in Federal Standard 209D [20], are shown in Table A1. The particulate counts for the eight sample location are shown in Table A2. Figure A1 shows the positions of the locations within the automated system.

Table A1: System Characteristics for Airborne Particulate Measurements

Volume of system:	201 cubic feet
Entrance plane area:	28 square feet
Number of sample locations:	8
Particle counter:	Particle Measurement Systems Model 101

Table A2: Average Particulate Measurements and Calculations

Location	Volume (ft^3)	Particle Sizes (micron)			
		0.1	0.3	0.5	1.0
1	247	70.9	0.1	0.1	0.1
2	32	48.6	0.2	0.1	0.0
3	533	95.4	0.1	0.1	0.0
4	96	73.7	0.1	0.0	0.0
5	94	85.4	0.3	0.0	0.0
6	159	63.1	0.1	0.0	0.0
7	75	57.6	0.2	0.1	0.0
8	72	79.7	0.4	0.0	0.0
Mean of the averages		71.8	0.2	0.0	0.0
Standard deviation		15.2	0.1	0.0	0.0
Standard error		5.4	0.0	0.0	0.0
Upper confidence limit		82.0	0.3	0.1	0.0

Standard error of the mean of the averages, as defined by FS 209D, is the quotient of the standard deviation and the square root of the number of locations:
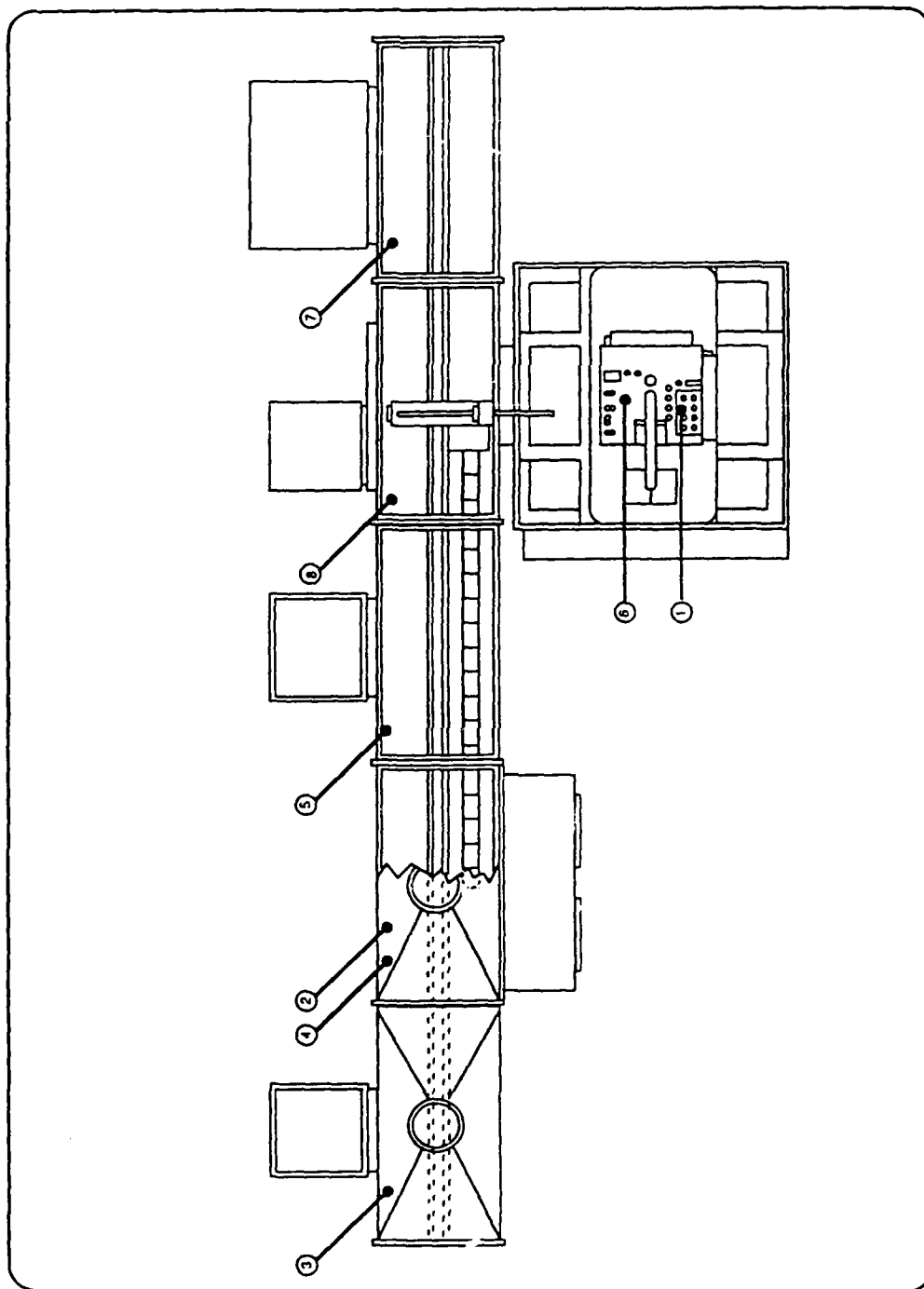
Figure A1: Sampling Locations within the Automated System

$$SD = \frac{SE}{\sqrt{L}}$$

(A1)

The 95% upper confidence limit (UCL) of the mean of the averages is the sum of mean and the product of the UCL factor and standard error:

$$UCL = M + (UCL\ Factor \times SE)$$

(A2)

The UCL factor is dependent on the number of sample locations and is found in Table III of FS 209D. For eight sample locations the factor is 1.9.

The conclusions from the calculations are:
1) Airborne particulate measurement data meet the acceptance criteria for Class 1 at 0.3 and 0.5 diameter particles.
2) Data meet the acceptance criteria for Class 10 at 0.1 diameter particles.

These conclusions are shown diagrammatically in Figure A2.

Data meet the Federal Standard 209D acceptance criteria for Class 1 at 0.3 and 0.5 micron diameter particles.

Data meet the acceptance criteria for Class 10 at 0.1 micron diameter particles.

Figure A2: Average Particulate Levels within the Automated System

QUBIK INERTIAL MEASUREMENT UNIT

TEST RESULTS

Prepared by,

Melvin Mark Morrison
President of QUBIK CONSULTANTS
P.O. Box 272460
Concord, California   94527

PRESENTATION

of the

QUBIK INERTIAL MEASUREMENT UNIT

at the

FOURTEENTH BIENNIAL GUIDANCE TEST SYMPOSIUM

October 3,4,5, 1989

6585th TEST GROUP
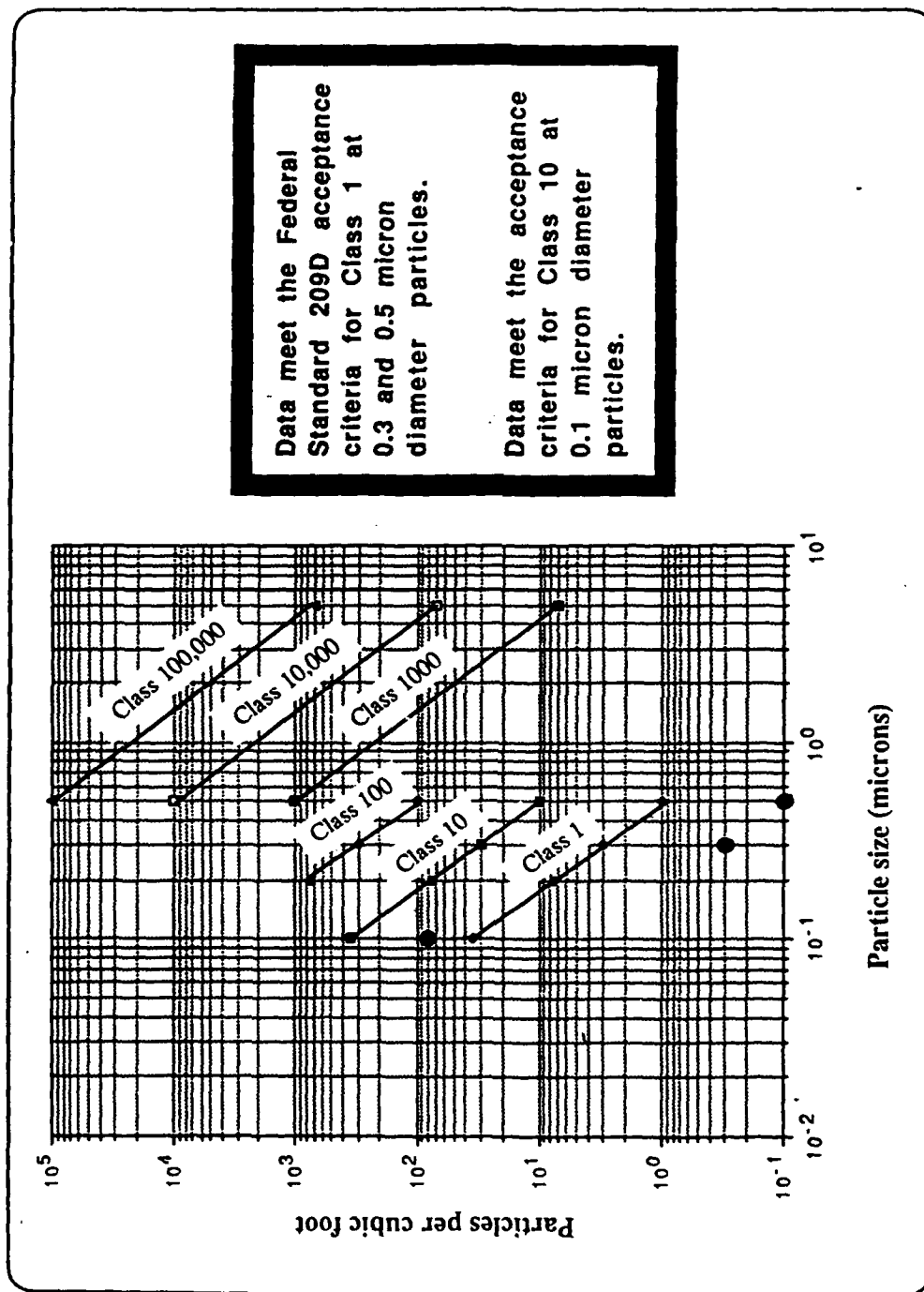
CENTRAL INERTIAL GUIDANCE TEST FACILITY

HOLLOMAN AIR FORCE BASE, NEW MEXICO 88330-5000

by,

Melvin Mark Morrison
P.O. Box 272460
Concord, California 94527

ABSTRACT
This paper will cover test and evaluation results of the
QUBIK Inertial Measurement Unit (IMU). A qualification test
plan will be discussed in detail. One test was designed to
verify this instrument can be used to locate North. Testing
of breadboard models indicates this technology has obtained a
useful dynamic range of ten to the fourth power, which is
more than adequate for tactical mission requirements.
Further test and evaluation will undoubtedly reveal design
improvements unveiling a dynamic range of ten to the fifth
and possibly a ten to the sixth power is obtainable.

The breadboard sensor, excluding electronics is a one inch
cube that weighs less than 25 grams. A complete one incn
cube IMU with associated electronics will weight less than 50
grams. High accuracy variable capacitance sensing and
electromagnetic restoring servo techniques are employed.
Three orthogonal linear and three orthogonal angular degrees
of freedom are all derived from one proof mass system design.
It can withstand over 100,000 g's of shock without
performance degradation. The linear channels can be designed
to capture 100 g's steady state. The angular channels can
capture 15 radians per second squared. Thermal and vibration
dynamic environments will not cause mechanical bias errors
because the sensor is completely magnetically levitated with
no mechanical attachments to it. This technology achieves
the ultimate design goal of being a small, lightweight,
rugged, high accuracy, and low cost IMU. Patent # 4711125
was issued by the U.S. patent office on December 7, 1987 for
this new innovative technology.

1.0 INTRODUCTION

End item system designers and users of sub-munitions need a dramatic breakthrough in IMU technology. The size, weight, durability, accuracy, and cost of ownership for existing IMU technologies have limited their effectiveness in some applications. The QUBIK IMU technology achieves the ultimate design goal by meeting the small, lightweight, rugged, accurate, and low cost requirements for new sub-munition applications. Testing of the breadboard models verify that this technology has a useful dynamic range of ten to the fourth power. This is more than adequate for the sub-munitions requirements. Further test and evaluation should reveal design improvements that will unveil that a dynamic range of ten to the fifth and possibly a ten to the sixth power is achievable. Putting any IMU through a qualification test program will establish a baseline of performance specifications and knowledge needed to determine future applications and design goals. This paper will describe a qualification test plan for the QUBIK IMU.

2.0 BACKGROUND

The breadboard sensor, excluding electronics, is a one inch cube sensor that weighs less than 25 grams. A complete one inch cube strapdown IMU, with associated servo loop electronics attached to it will weigh less than 50 grams as shown in Figure 1. Three orthogonal linear and three orthogonal angular motion signals are derived from a single cubic proof mass design shown in Figure 2. This system requires six identical conventional electronic servo loops as shown in Figure 3. High accuracy variable capacitance is used for sensing the position of the cubic proof mass in its cavity. Electromagnetic forces are used to levitate the cubic proof mass at its null position. These force levels measure the vehicle motions in all six degrees of freedom. A unique feature of this system is that it completely isolates the sensing and restoring signals in all six degrees of freedom. Each servo loop has its own individual set of variable capacitors and electromagnetic forces that are not shared with the other servo loops as shown in Figure 4. The close physical relationship of the sensor with the outer housing is shown in Figure 5. Design studies indicate that the sensor can withstand over 100,000 g's of shock without performance degradation. The steady state capture range, with proper design, can be 100 g's steady state. Temperature and vibration environments will not cause mechanical bias errors because the sensor is completely magnetically levitated with no mechanical attachments to it.

3.0 DEVELOPMENT BREAKTHROUGHS

The major breakthroughs in the evolution of the proof mass are shown in Figure 6. The overall system design performance was improved and the fabrication was simplified by eliminating the soft iron return paths. This is not the most efficient magnetic circuit but it is the most efficient from the entire system standpoint. Higher g's can be captured with the inefficient magnetic circuit beca··se the proof mass

is lighter and the coils can handle higher current levels.
The coils are mounted on the ideal heat sink. The sensor
weight was further reduced after discovering that the angular
magnets could be smaller while still maintaining a
sufficiently high capture range. The development activity of
the entire system is realized by the cross section of the
close physical relationship between the inner and outer plate
assemblies shown in Figure 7.

4.0 QUBIK IMU TEST RESULTS

Test and evaluation of IMU's are the stepping stones toward
system applications. Breadboard models have demonstrated a
dynamic range of ten to the fourth power. The performance of
these models are limited by the bubbles present in the fluid
fill. The fluid provides damping and velocity storage for
the servo loops. It is a design goal to eliminate the fill
fluid.

4.1.0 TUMBLE TESTING

A typical tumble test is shown in Figure 8. Six position and
tumble testing helped in discovering the mass unbalance
effects of the sensor. The sensor mass unbalance acts like a
pendulosity and is torqued by the angular servo loops. The
tumble test also proved that the linear servo scale factor is
linear by nature as indicated by least squares residuals as
low as 216 micro-g's rms. This tumble test data has been
verified by two different accelerometer manufacture's.
Tumble testing at various temperatures showed a bias
temperature coefficient of 30 micro-g's per degree F and
scale factor temperature coefficient of 200 ppm per degree F.
The six position and tumble test results will improve when
the instrument is tested on a stable pier with thermal
control.

4.2.0 DRIFT TESTING

Drift testing showed that a dynamic range of ten to the fifth
power is obtainable even without mounting the instrument on a
stable pier with no temperature control. The linear
accelerometer drift is 0.014 micro-g's per second. The
angular accelerometer drift is 0.027 micro-radians per second
squared per second. The drift residuals are as low as 15
micro-g's rms for the linear channels and 20 micro-radians
per second squared rms for the angular channels. These
results will improve if there are no bubbles present in the
fill fluid and the instrument is tested on a stable pier with
temperature control. A significant improvement is also
expected when the instrument has no fluid fill medium.

4.3.0 FREQUENCY RESPONSE TESTING

The instrument went through vibration testing to evaluate the
servo loop bandwidth. The first experiment revealed a
bandwidth of about five hertz. A sub-munitions application
requires a minimum bandwidth of 50 hertz. A second vibration
test sequence was conducted after using smaller capacitors on
the integrator stage of the servo loops. This increased the
bandwidth to 23 hertz. A third test sequence included some

more adjustment to the integrator stage and raised the
bandwidth to 75 hertz as shown in Figure 9. There is some
peaking at the 67 hertz which can be reduced by increasing
the resistance in series with the integrating capacitor. A
little transmisability peaking is good from a system
standpoint. At the very best, the computer Kalman filter
updates will provide late position information in a dynamic
situation. Having some transmisability peaking of the
instrument output versus frequency in a dynamic situation
will increase the accuracy of the Kalman filter updates.
Repeated testing for the servo bandwidth while making
modifications to the integrator capacitor showed excellent
correlation with a PC circuit analysis program. More work in
this area will keep increasing the bandwidth. This frequency
response development would have been speeded up if a network
analyzer were used. A network analyzer would interpret the
results much faster and could be used for evaluating the
bandwidth for the linear and angular servo loops. The
vibrating method is slow to interpret and only tested the
linear servo bandwidth. The angular servo loops use the same
electronics are the same as the linear's.

4.4.0 RATE TABLE TESTING

The angular scale factor was tested for using a rate table.
The instrument was rotated CW and CCW while real time data
was collected. This test sequence and data reduction
development activity are in process. A quick look at the
raw data proves that the angular servo channel acts like an
angular accelerometer as expected. When the instrument was
rotated at a constant velocity the angular channels,
detected the variations due to going in and out of earth
rate. The angular channels dynamic range and repeatability
is expected to be consistent with the linear servo results.

5.0 FUTURE DEVELOPMENT

The knowledge gained so far from testing has revealed some
significant improvements in the overall system design. The
next most significant improvement will be occur by packaging
the pre-amps closer to the pick-offs. The breadboard pick-
offs have a one inch lead before the pre-amp non-inverting
input. This makes the electrical null susceptible to stray
capacitance. Just waving your hand close to the sensor will
cause an offset. The best solution would be to package the
pre-amps inside the housing on the outer plates right beside
the pick-offs. There is plenty of room inside the one inch
cube to package the pre-amps. The differential and
integrator stages of electronics will all have to be packaged
on the cube to get this technology through a qualification
program and into system applications.

5.1.0 FINITE ELEMENT ANALYSIS STUDY

A Finite Element Analysis (FEA) study will make significant
discoveries and increase the knowledge base of this
technology. The FEA will prevent over-design of the sensor
to meet the 100,000 g survivability for sub-munitions
applications.

5.2.0 FLIGHT SIMULATION
A flight simulation for the IMU is starting, based on a five second sub-munition application. The IMU must have a transfer alignment capability. The breadboard model test data for scale factor, bias, and alignment are being used for this simulation.

5.3.0 INCORPORATING MAGNETIC BEARING MOMENTUM WHEEL
The angular channels of the system can be converted from detecting angular accelerations to angular rates by adding a momentum wheel to the proof mass. The momentum wheel design incorporates a new magnetic bearing technology. The addition of the momentum wheel would raise the cost of the system but it would provide pure angular rate versus angular acceleration. The momentum wheel is expected to double the cost of the instrument. The system would be more suitable for aircraft navigation but would be difficult to design for the high g low cost requirements for sub-munition applications.

6.0 QUALIFICATION TEST PLAN
The intent of the qualification test plan is to evaluate the present and future performance specifications. Improvements are expected to be made at every level of testing. Test scenarios are intended to make discoveries about this technology and are intended to be exhausting. An Acceptance Test Procedure (ATP) will be developed from data collected during this qualification program. The testing sequence will most likely be improved upon after actually conducting the tests. Some tests will be modified and some different tests may be developed during this type of development.

A Finite Element Analysis (FEA) model must be used to support the qualification program. The FEA model will provide knowledge of the instrument behavior in thermal and vibration environments. The FEA model would take about one month to generate. The FEA model of the proof mass would take about one week. The complete symmetry of system design will make the FEA model easier develop and perform analysis work on.

More than one instrument will need to go through qualification testing. Catastrophic failures are expected in the qualification test sequence. The environmental exposure levels are intended to find the envelope of the instrument. The Temperature Sensitivity, Sine Sweep, and Drop Shock testing may also cause instrument failure. The first qualification unit would take about six months to produce. The qualification instruments would need the pre-amps packaged inside the housing and the remaining servo electronics packaged on the outside. The test sequence below needs to be conducted after qualification instruments are fabricated.

6.1.0   Frequency Response
6.2.0   Scale Factor, Bias, Alignment

6.3.0   Tumble Test
6.4.0   Locating North
6.5.0   Scale Factor Non-Linearity
6.6.0   Cross Axis Sensitivity
6.7.0   Long & Short Term Drift
6.8.0   Static Temperature Sensitivity
6.9.0   Dynamic Temperature Sensitivity
6.10.0   Magnetic Sensitivity
6.11.0   Radio Frequency Sensitivity
6.12.0   Acoustic Sensitivity
6.13.0   Shielding Sensitivity
6.14.0   Drop Shock
6.15.0   Sine Sweep
6.16.0   Random Vibration
6.17.0   Radiation Hardenability

6.1.0 Frequency Response:
The frequency response should be checked using a network
analyzer. The bandwidth of the breadboard linear servo loops
have already been tested for using a shaker. The network
analyzer is preferred because it is a quicker and more
accurate method of determining the bandwidth. The network
analyzer can also measure the angular servo loop bandwidth.
When one channel is being checked for servo bandwidth using
the network analyzer, the other five channels should be
recorded with a strip chart recorder.

6.2.0 Scale Factor, Bias, Alignment:
This test sequence will determine all the scale factors,
bias, and alignments for all six servo loops. The three
orthogonal linear servo loops can be tested using gravity.
The three orthogonal angular servo loops must be tested using
a rate table. Calibrating these coefficients should be
performed using a three axis rate table. These parameters
will be tested before, during, and after all environmental
test exposures.

Note: The scale factor, bias, and alignment will be checked
      pre and post all environmental testing.

The linear scale factor and bias coefficients can be
calibrated by testing the gravity effects in twelve cardinal
positions. The angular scale factor, bias, and alignment
will have to tested for using a rate table. The rate table
would input a CW and CCW angular rotation at different (TBD)
frequencies. This test sequence must be carefully planned.
However changes may be required in test procedures in order
to get competent data.

6.3.0 Tumble:
The tumble test will verify the linear scale factor, bias,
and alignment. The test will consist of measuring all six
signal levels with the instrument positioned in 36 rotational
positions per axis. The data collection will start at steady
state with the index table in the 0 position. The data will
be collected with the index table rotated in ten degree

increments until 360 or the initial zero position is reached.
The data collection will then be stepped backwards from 360
to 0 decreasing by steps of 10 degrees. The scale factor,
bias, and alignment will be evaluated by performing a least
squares regression analysis on the data.

6.4.0 Locating North:

The instrument has a feature that allows it to locate north.
The instrument will be rotated at a constant (TBD) velocity
with all six channels recorded on a strip chart. The angular
servo loops will be cycled in and out of earth rate. Their
outputs will be investigated and are expected to be sine
waves that are out of phase with each other. The linear
channels will also be monitored and are expected to have no
significant deviations during this test. The rate table data
already taken has verified these effects on the linear and
angular channels when the system is rotated at a constant
velocity.

6.5.0 Scale Factor Non-Linearity:

The scale factor non-linearity coefficient (micro-g's per g
squared) for the linear servo loops can be tested using the
three axis rate table as a centrifuge. The maximum g level
for each linear channel will be verified. The angular scale
factor non-linearity is evaluated by conducting the scale
factor test at different amplitudes.

6.6.0 Cross Axis Sensitivity:

The cross axis sensitivities can be determined from the scale
factor, bias, and alignment test sequence. They should also
be evaluated during the Tumble, Locating North, and scale
factor non-linearity test sequence.

6.7.0 Long & Short Term Drift:

After the scale factors are known for all six channels a
drift test can commence. The drift test can include any warm
up trend or can be conducted at constant temperature. The
turn on transient for all six channels will modeled to a
first order fit. After any turn on transient has settled out
and the instrument has reached steady state, a first order
fit will be applied to output for all six channels. The
linear accelerometer drift will be reported in micro-g's per
second and the angular accelerometer drift will be reported
in micro-radians per second squared per second.

6.8.0 Static Temperature Sensitivity:

The scale factors, bias, and alignments coefficients will be
tested by performing tumble tests at temperatures ranging
between -60 and +200 degrees F. The test should start at -60
and increase in steps of 20 degrees F until 200 is reached
and back down to -60 in decrements of 20 degrees. This will
show the hysteresis of the scale factors, bias, and
alignments.

6.9.0 Dynamic Temperature Sensitivity:

The instrument will then be subjected to rapid temperature

changes from -60 to +200 degrees F. The temperature will be
increased from -60 to 200 degrees at a ramp of 10 degrees per
minute. If the instrument does not have a catastrophic
failure then the static temperature will be checked for
again. The temperature ramp from for this test sequence will
be increased to 20, 30, 40, etc degrees per minute until a
catastrophic failure occurs.

6.10.0 Magnetic Sensitivity:
The scale factor, bias, and alignment magnetic sensitivity
must be checked between the range of plus and minus twenty
gauss.

6.11.0 Radio frequency sensitivity:
The instrument must be checked for any scale factor, bias,
and alignment changes due to the effects of low and high
frequency radio signals.

6.12.0 Acoustic sensitivity:
The instrument must be checked for scale factor, bias, and
alignment changes due to background acoustic sounds.

6.13.0 Shielding sensitivity:
This test will be conducted to verify that the effects of
stray capacitance have been eliminated by locating the pre-
amps either inside the cube housing or by putting them right
on the pick-off feedthroughs.

6.14.0 Drop Shock:
The intent of this test is to determine the non-operating g
level survivability of the instrument. The drop shock level
will be incremental from 100 to 1000 g's in steps of 100 g's
with a (TBD) millisecond pulse width. If the instrument is
still operational then it the will be drop shocked from 1,000
g's incremental by 1,000 g's up to 10,000 g's. If the
instrument is still operational then it will be drop shocked
from 10,000 g's incremental by 10,000 g's until 100,000 g's
is obtained. If the instrument is still operational then the
instruments will be continually shocked at increasing levels
until a catastrophic failure occurs.

Note: The test will end if the test fixture cannot
      perform the required test.

6.15.0 Sine Sweep:
The sine sweep will search for all resonances up to 2000
hertz while the instrument is running. If a resonance is
found in this range, this frequency will be dwelled on for
(TBD) minute; at a g level of (TBD). If a frequency is
dwelled on, the sine sweep will be repeated to verify if the
discovered resonance has changed. If a frequency shift is
noticed then the dwell test will be repeated at the new
frequency.

Note: The test will end if the test fixture cannot
      perform the required test.

6.16.0 Random Vibration:
The random vibration will be conducted for various system
application requirements. Random vibration is not expected
to be critical.

6.17.0 Radiation Hardenability:
Radiation hardenability is a consideration for military
applications. Exposure levels are (TBD).

7.0 SUMMARY
Qualification test results are needed to bring this
technology into operational service for sub-munitions.
Testing will provide system engineers with information they
need to meet their application requirements. The test
sequence is intended to establish a baseline of conditions
that the QUBIK IMU can be subjected to. The results of the
qualification test scenario will also be used to determine
future design goals.

BIBLIOGRAPHY
Mr. Morrison has been developing the QUBIK Inertial
Measurement Unit (IMU) for the past six years. He is
pioneering this technology by building, testing, and
demonstrating working models. He has presented papers at the
Institute Of Navigation (ION) National Technical meetings in
Santa Barbara January 1988 and in San Mateo in January 1989.

FIGURE 1: QUBIK IMU FINAL ASSEMBLY

SMALL   one inch cube

LIGHT   25 grams (excluding electronics)
               50 grams (including electronics)

RUGGED   100,000 G survivability (-60 to 200 F)

ACCURATE   dynamic range of ten to the fourth power

LOW COST   simple and easy to fabricate
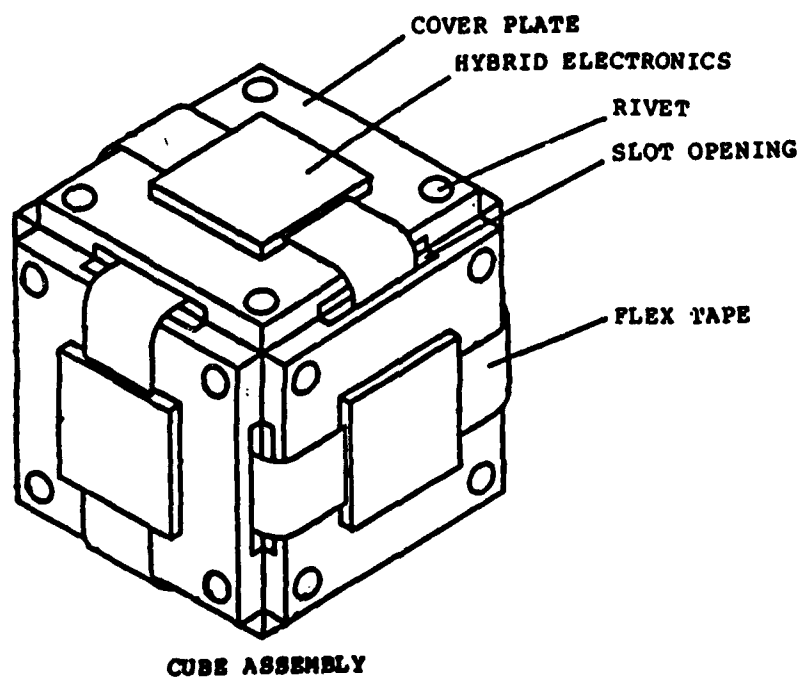

CUBE ASSEMBLY

FIGURE 2: QUBIK IMU PROOF MASS

1/2 INCH CUBE   (less than 5 grams)

THREE PAIRS of LINEAR, PARALLEL, ORTHOGONAL ARRAYS of

    Magnets & variable capacitors

LINEAR ACCELERATIONS

    Detected by middle pick-offs

    Force rebalanced by larger magnets

ANGULAR ACCELERATIONS

    Detected by side pick-offs

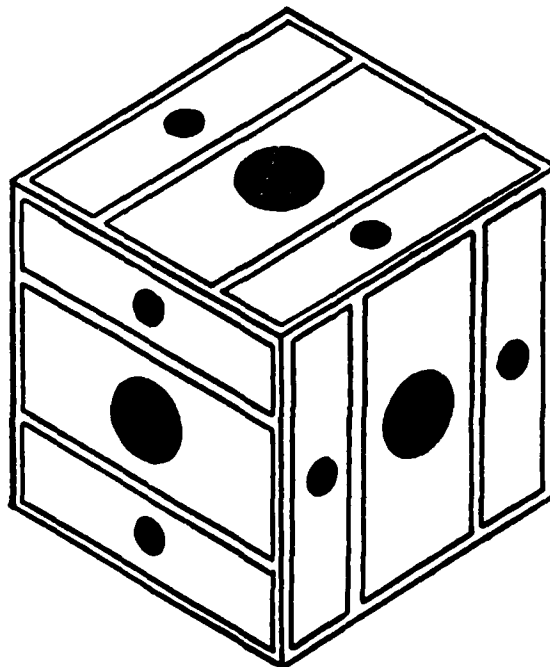   Force rebalanced by smaller side magnets

FIGURE 3: QUBIK IMU SERVO LOOP ELECTRONICS

SIX REDUNDANT CIRCUITS

PREAMP GAIN   Pick-off signals

RECTIFIED   Clipped by diodes

DIFFERENTIATED   1/2 wave rectified

FILTERED   Filter to DC

INTEGRATED   Keeps proof mass at null

CURRENT GAINED   NPN/PNP

PRECISION RESISTOR   Current measurement
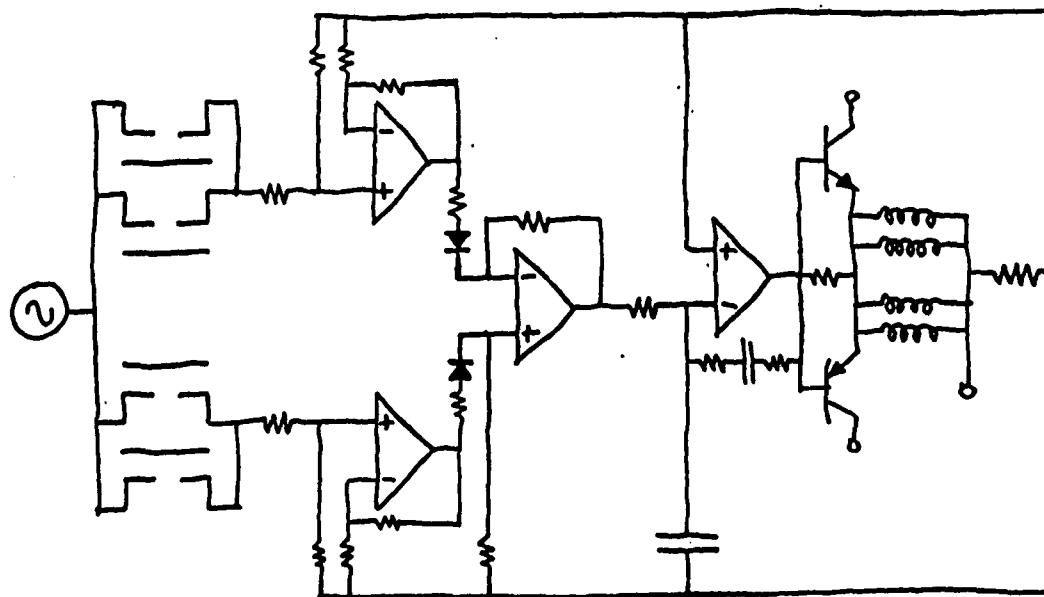   (voltage drop across 1 ohm)

FIGURE 4: QUBIK IMU BLOCK DIAGRAM

SYMMETRICAL DESIGN

Three orthogonal linear accelerations.

Three orthogonal angular accelerations.

High accuracy variable capacitance sensing with electro-
magnetic nulling force rebalance servo's.

Each servo has its own set of variable capacitors and
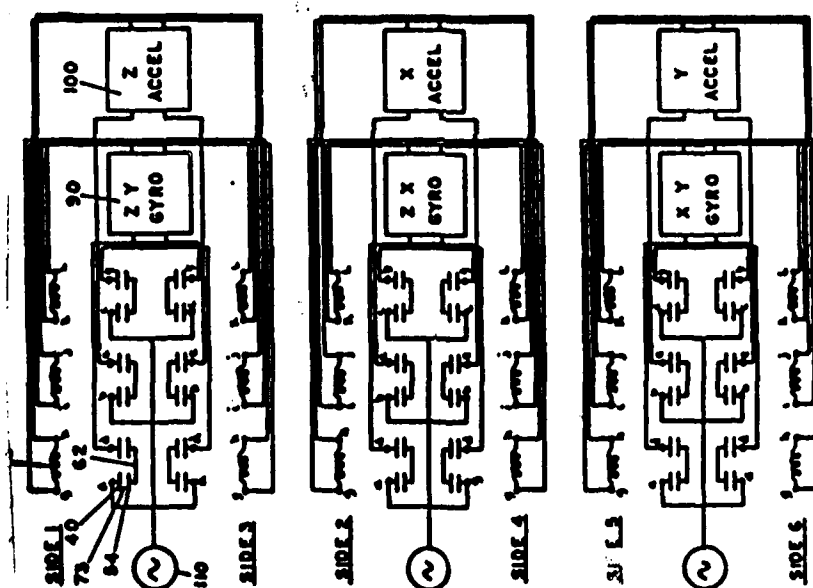magnets that are shared with any other servo.

FIGURE 5: CROSS SECTION OF QUBIK IMU MAGNETIC CIRCUIT

RELIABILITY

Magnets are flush with surface

Coils are heat sinked

Rugged construction

It would take over 100,000 g's to shear of linear magnet

$$\text{Maximum G level} = \frac{F}{W} = 271,166 \text{ g's}$$

$$F = SA = (7,000 \text{ psi})*(pi)*(0.125)^D*(0.05)^L = 137.375 \text{ lbs}$$

$$W = \text{Weight of magnet} = 0.23 \text{ grams} = 0.000506607 \text{ lbs}$$
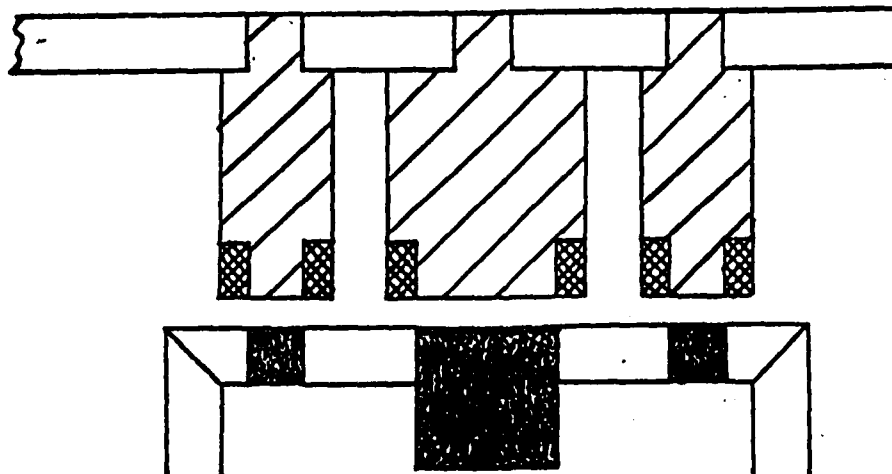
FIGURE 6: QUBIK IMU PROOF MASS EVOLUTION

RELIABILITY

Reduction in parts

Simplified parts

Improved performance (higher capture, survivability)
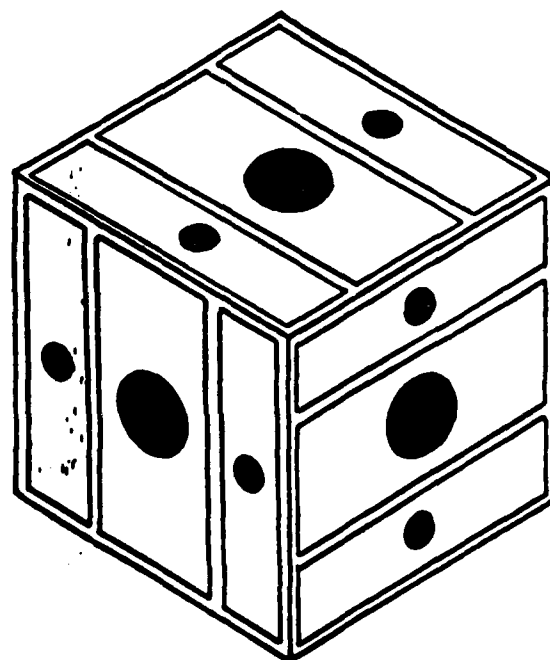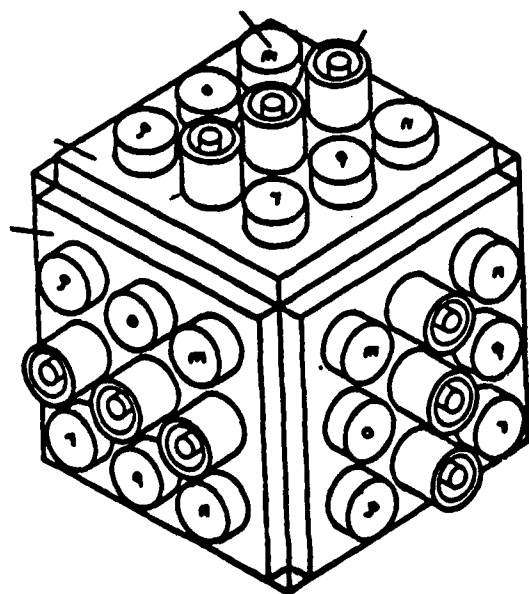
FIGURE 7: QUBIK IMU CROSS SECTION EVOLUTION

RELIABILITY

Reduction in parts

Simplified parts

Improved performance (higher capture, survivability)
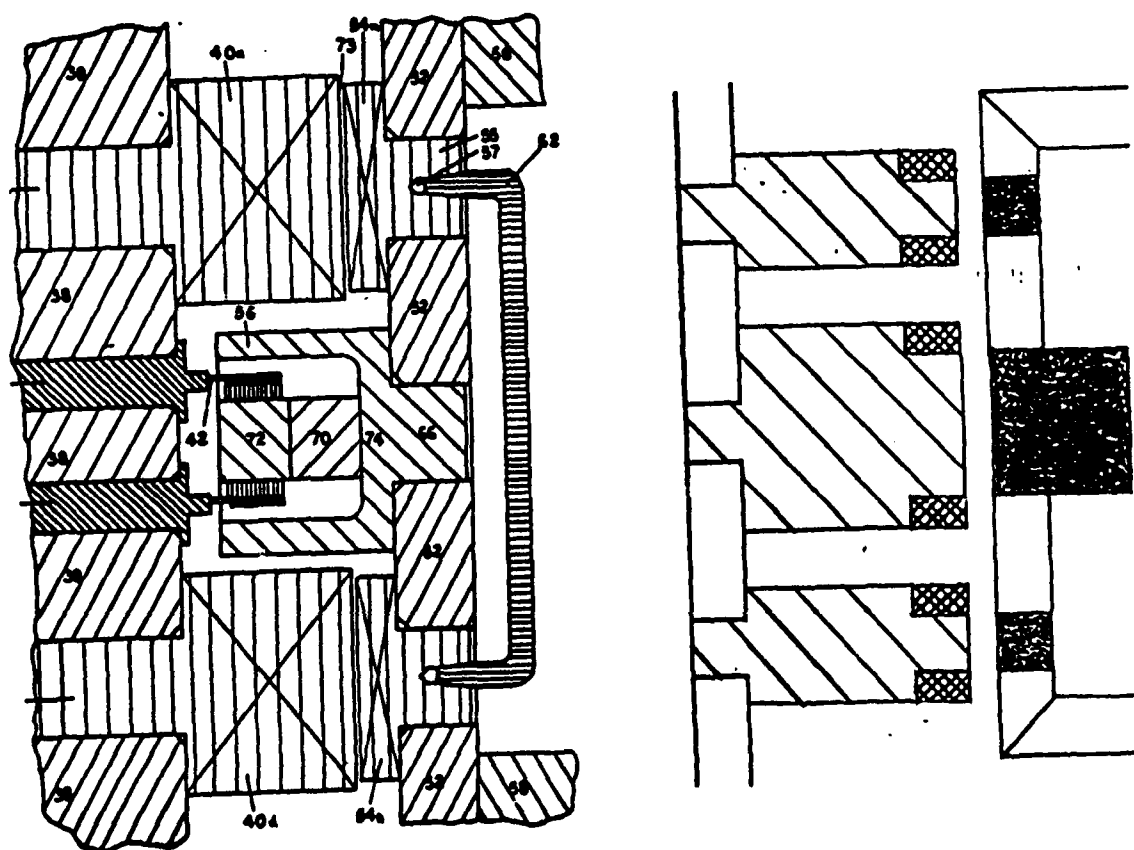
FIGURE 8: TUMBLE TEST RAW DATA

QUBIK IMU TUMBLE TEST DATA
X CHANNEL

FIGURE 9: QUBIK IMU FREQUENCY RESPONCE

"Z" AXIS FREQUENCY RESPONSE OF QUBIK
Figure 1 (Test date: 4/14/89)

The Micro Inertial
Measurement Unit (mIMU)
Using Advanced Inertial Sensors

Prepared by
Anthony Lawrence

NORTHROP
Precision Products Division

Abstract

The micro IMU (mIMU) is an inertial measurement unit (IMU) concept using two new inertial sensors now in development: the micro Optic Gyro (MOG) and the Micro Silicon Accelerometer (MSA). The mIMU will be cheaper, smaller, and lighter than any ot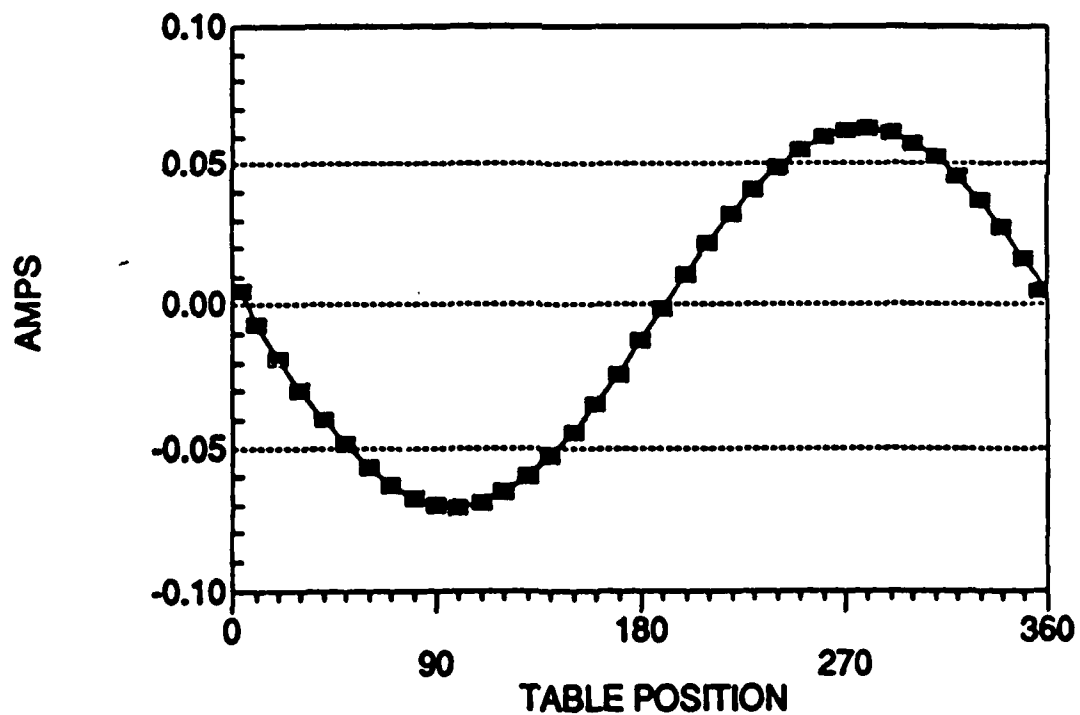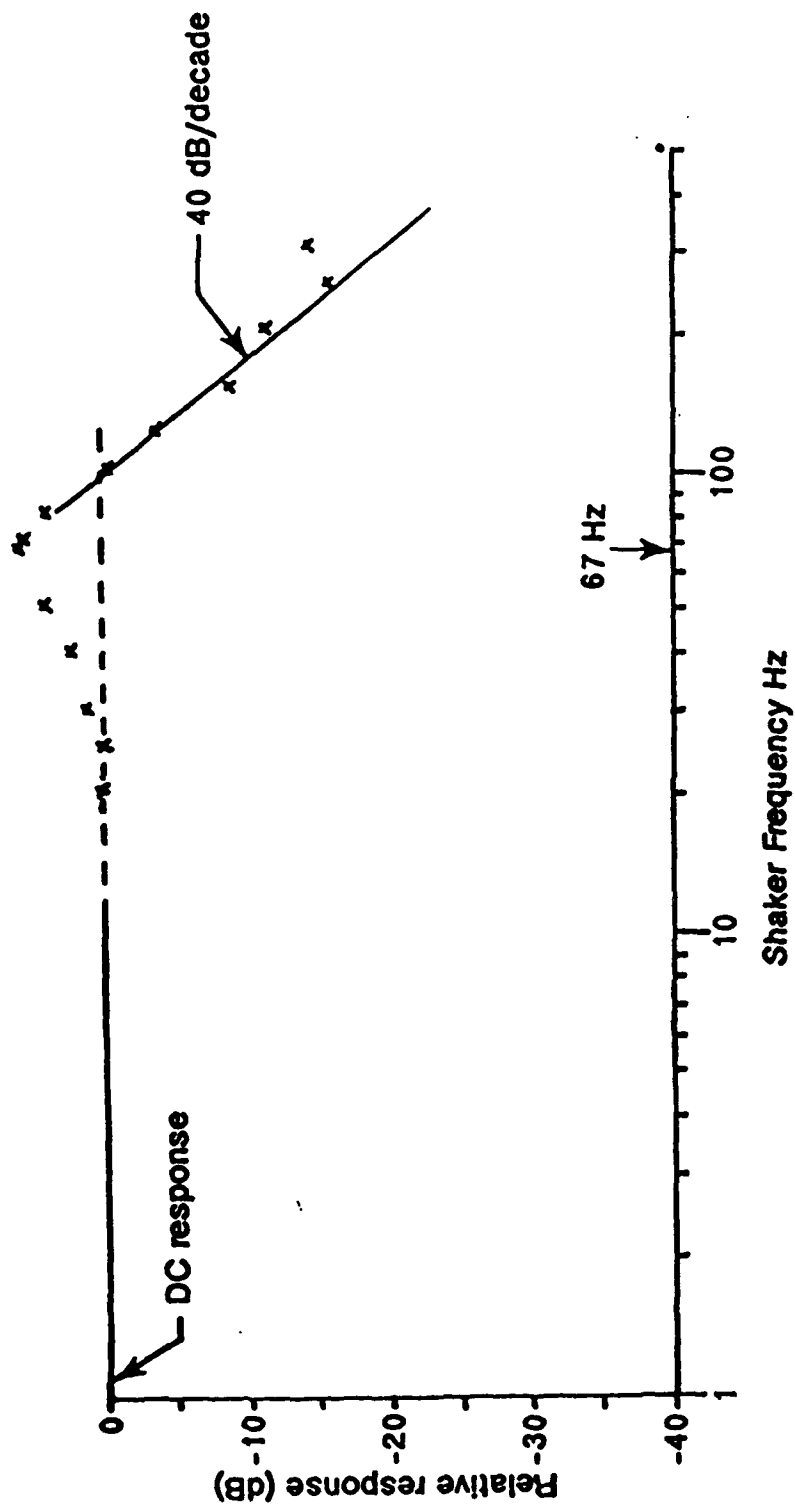her IMU in the 1°/hr class because its sensors are planar, integrated devices. Unlike gyros and accelerometers made from conventional bulk components (SDF gyros and RLGs, and magnetically rebalanced pendulum accelerometers), the MOG and MSA design concepts come from the field of integrated circuits, leading to inherently low cost production. We forecast an IMU production cost close to $5000.

The MOG is an integrated optics passive ring resonator gyro (formed from a diode laser and a waveguide resonator), and the MSA is a finger-nail sized, electrostatic force rebalanced, silicon micromachined accelerometer. This paper gives the MOG theory, construction, and performance limits and outlines MSA construction.

We also forecast the effects of integrated optics technology evolution over the next decade on the IMU field, especially for kinetic energy and hypervelocity projectile IMU applications.

1 The Strapdown IMU

Strapdown inertia measurement units can provide information about a body's attitude, position, and velocity. Gyroscopes measure the angles turned; accelerometers measure the changes in velocity of the moving body. The gyros' function is to keep track of the directions in which the accelerometers point, so that the indicated accelerations can be resolved to an inertially stable set of axes. Then, integrating the accelerations twice provides dead reckoning of the body's position. This is the kind of IMU we are considering in this paper, consisting of three orthogonal gyros, three orthogonal accelerometers, and a coordinate transformation computer whose output is a sequence of changes in angle (body rates) and changes in speed over the last few milliseconds.

Further, we are considering here IMUs for tactical missiles such as air-to-air midcourse guidance, kinetic energy weapons, and hypervelocity projectiles, applications with times of flight less than five minutes.

Tactical IMUs generally need small, rugged, cheap sensors with characteristics like those in Table 1-1.

IMUs for kinetic energy weapons fired from a gun will need 20,000 g or more shock capacity, while those for hypervelocity projectiles will need shock load tolerance of 100,000 g or more.

Table 1-1
Tactical Sensor Specifications

Gyro

Day-to-day bias stability, deg/hr	10
Rate resolution or random drift, deg/hr	1
Maximum rotation rate, deg/sec	400 - 1000
Scale factor error, %	0.01
Bandwidth, Hz	100
IA alignment stability, mr	0.5

Accelerometer

Day-to-day bias stability, mg	1
Resolution or in-run drift, mg	0.1
Maximum acceleration, g	50
Scale factor error, %	0.05
Bandwidth, Hz	100
IA alignment stability, mr	0.5

Environment

Operating temperature, min, °C	-55
max, °C	+85
Vibration, g^2/Hz to 2000 Hz	0.1
Shock, g for 0.5 mS.	400

Gyros for spinning projec*, ›s will need a much lower scale factor error. A gyro measuring roll angle to 1 degree, with a spin rate of 20 Hz, for a flight 200 seconds long must have less than 0.7 ppm scale factor error.
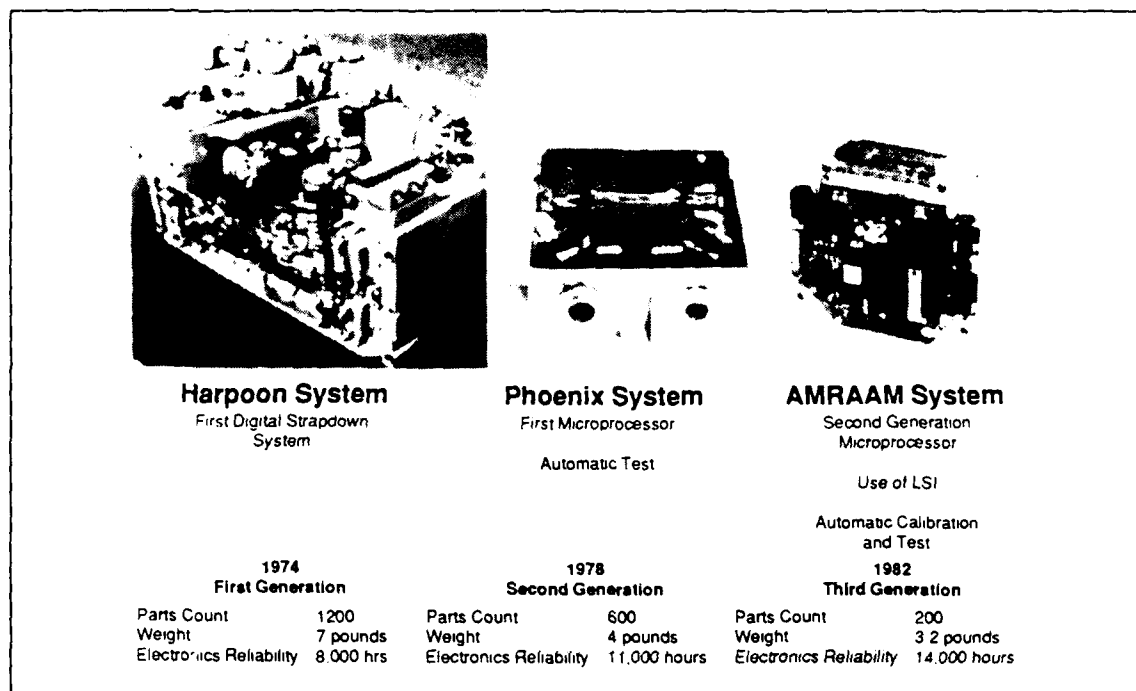

Harpoon System	Phoenix System	AMRAAM System
First Digital Strapdown System	First Microprocessor	Second Generation Microprocessor
	Automatic Test	Use of LSI
		Automatic Calibration and Test
1974 First Generation	1978 Second Generation	1982 Third Generation

Parts Count	1200	Parts Count	600	Parts Count	200
Weight	7 pounds	Weight	4 pounds	Weight	3 2 pounds
Electronics Reliability	8.000 hrs	Electronics Reliability	11,000 hours	Electronics Reliability	14.000 hours

Figure 1-1
The Evolution of PPD's Tactical Strapdown System

Tactical IMUs have evolved over the last 15 years or so, and three Northrop products clearly show this evolution, Figure 1-2. The 1974 Harpoon missile system has a mass of 3.2 kg (7 lb), while the 1980 Phoenix system has a mass of 1.8 kg (4 lb), followed by the 1985 AMRAAM system's 1.4 kg (3lb). This trend will continue; we forecast that the microIMU mass will initially be 0.4 kg (1 lb), with a potential of 70 gm as MOG technology matures.

So far, fielded tactical IMUs have used single-degree-of-freedom (SDF) gyros, dynamically tuned gyros (DTG), and pendulous accelerometers, all electromechanical sensors. While their drift performance is satisfactory and their shock tolerance might be extended to 10,000 g, they cannot be g-hardened enough for hypervelocity projectiles, nor can their size and cost be pushed significantly lower. But the pendulous accelerometer is still a viable approach, particularly if constructed using silicon micromachining, a fallout from integrated circuit technology.

High environmental tolerance will be provided in the microIMU by the use of modern "planar" instrument technology. Northrop is using techniques from the electronic integrated circuit industry to make a solid state laser gyro, the Micro-Optic Gyro and a silicon micromachined pendulous accelerometer, the Micro-Silicon Accelerometer.

2 General Description of the MicroIMU

The microIMU performance wil) depend on the specific angular rates and accelerations of the application, but Table 2-1 gives one possible error budget for a tactical mid-course guidance system flying a three-minute mission.

Table 2-1
MicroIMU Performance

IMU Error Source		Value	Navigation Error Position meters	Attitude degrees
MOG	Drift			
	Day-to-day	4°/hr	45.7	0.17
	Random walk	$0.2^\circ/\mathrm{h}^{1/2}$	24.1	0.07
	G sensitivity	0.1°/h/g	5.9	0.02
	Scale factor (all sources)	550ppm	58.9	0.11
	Misalignment	200 μrad	20.6	0.05
MSA	Bias			
	Day-to-day	1 mg	36.8	
	In-run noise	0.1 mg	1.73	
	Scale factor (all sources)	520ppm	82.5	
	Misalignment	520 μrad	85.9	
	TOTAL (rss)		130.7	0.22

The values are three sigma maxima on any axis at the end of three minutes.

Figure 2-1 shows how the first generation microIMU can look. It is not definitive, for one big advantage of strapdown systems is that they can be specifically tailored to the space the customer has available. Each sensor is individually packaged with its own servo electronics. The system electronics shown in the block diagram (Figure 2-2) comprises an interface controller for taking sensor data and presenting it to the processor where temperature and other deterministic compensations (such as scale factor non-linearity) are made.

The processor takes the gyro outputs, which are the increments in the angles turned since the last computation cycle, and uses them to compute the vehicle attitude and the matrix of its direction cosines. These are then used to transform the accelerations (incremental velocities) into "North/local level" axes using the strapdown coordinate conversion algorithms. The interface controller also sends this data to the output port, for the navigation computer. The processor carries out self-test on demand, and reports IMU status, but the system design has not yet progressed enough for the data formats, data rate, and quantization to be specified. The microIMU is being designed to operate over the full military temperature range (-55C to +100C).
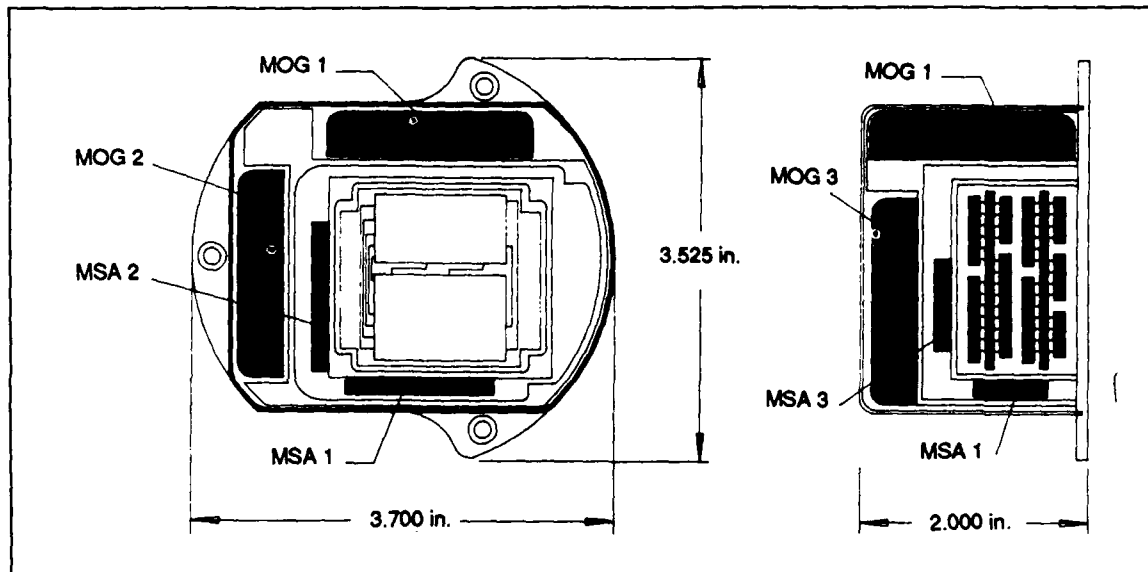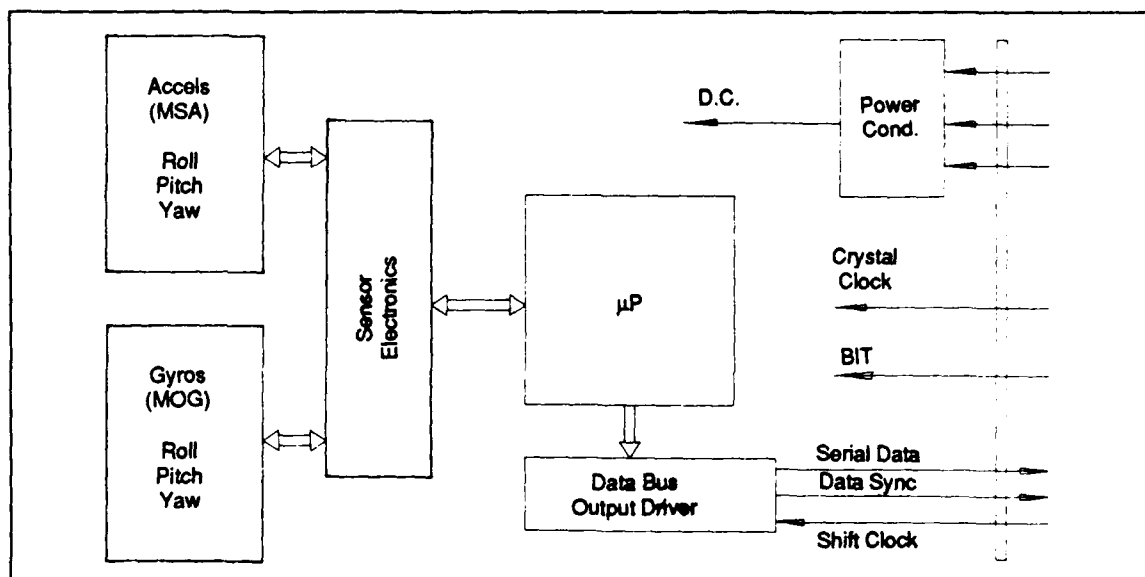
Figure 2-1
An Example of MicroIMU Construction

Figure 2-2
MicroIMU Block Diagram

3 The Micro-Optic Gyro

The MOG is a passive ring resonator laser gyro that relies for its operation on the Sagnac effect -- the fundamental principle underlying all optical gyros, which states that a beam of light traveling around a closed path experiences a path length change if the path rotates in its plane, by an amount proportional to the rotation rate. Therefore, after traveling around the path, there will be a phase change in the light at the output, depending on rotation rate. In ring resonator gyros the Sagnac phase shift causes a shift in resonant frequency, increasing the frequency of the beam traveling against the direction of rotation, and decreasing the frequency of the other beam. The MOG principle was first described by Ezekiel[1].

To relate this effect to the MOG, see Figure 3-1 which shows the MOG in schematic form. Light from the laser divides and passes through two surface acoustic wave frequency shifters which each add a controllable frequency to the laser frequency. Light couples into the resonator in the two directions (through the directional coupler), and the intensity in the ring is sampled at the opposite coupler and measured by the detectors. A servo tunes the laser to maintain resonance in the clockwise path around the ring, that path having a fixed bias frequency fed to its frequency shifter (f1). Resonance in the counterclockwise direction comes from tuning its frequency shifter with the output from a voltage controlled oscillator, frequency f2. The difference frequency f1-f2 is the desired measure of rotation rate. The MOG does not suffer from the lock-in problem which limits ring laser gyro performance, for the clockwise and counterclockwise oscillators couple weakly (if at all) in a passive resonator.
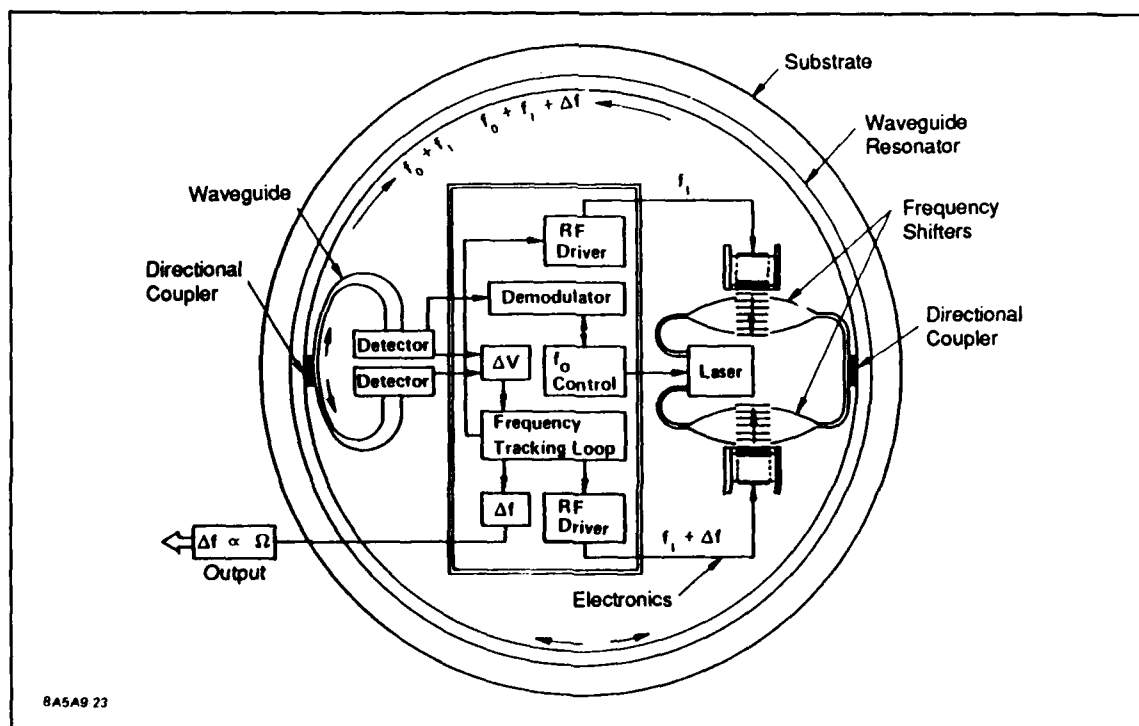

Figure 3-1
MOG Schematic

The solid state laser is like those used in Compact Disk players, a production component with well characterized properties. These lasers are the size of a sugar crystal, of the order of 0.5 mm on a side. The laser is butt-coupled to the input port, and detectors are surface mounted on the output waveguides. The waveguides that form the resonator are regions of increased refractive index in a glass substrate; they are a few microns wide and deep, while the resonator may be 25 mm diameter or larger. The frequency shifter can be a surface acoustic wave device (Bragg cell). In the Bragg cell, the light wave is diffracted by a traveling surface acoustic wave (SAW), so that it changes direction (by about one degree) and undergoes a Doppler frequency shift. The change in direction is beneficial because not all the incoming light is shifted, so there is a spatial separation between the shifted and unshifted light, and we can choose only the shifted light.

The optical components are fabricated by planar processes like those used to make integrated circuits, and can use much of the same equipment. For instance, the waveguide patterns are defined photolithographically by printing a mask pattern onto the glass substrate. The waveguides are then formed by ion exchange, a process in which the alkali metal ions (sodium or potassium) in the glass are exchanged for silver ions. This creates channels about 3 x 2 micron in section along which the light travels. Once the complete waveguide pattern has been formed, a piezoelectric film for the SAW frequency shifter is sputtered onto the substrate locally where the SAW will be generated. Aluminum transducer fingers four microns wide are deposited on the film, which is then excited by an RF signal at about 200 MHz to create the traveling SAW wave. The laser and detectors are cemented to the substrate (or optical chip). The servo loops to control the laser and the frequency shifters complete the gyro. An alternate design using a single coupler is shown in Figure 3-2; the detectors here see a minimum signal when the ring is in resonance, for then the ring absorbs energy from the input guides.
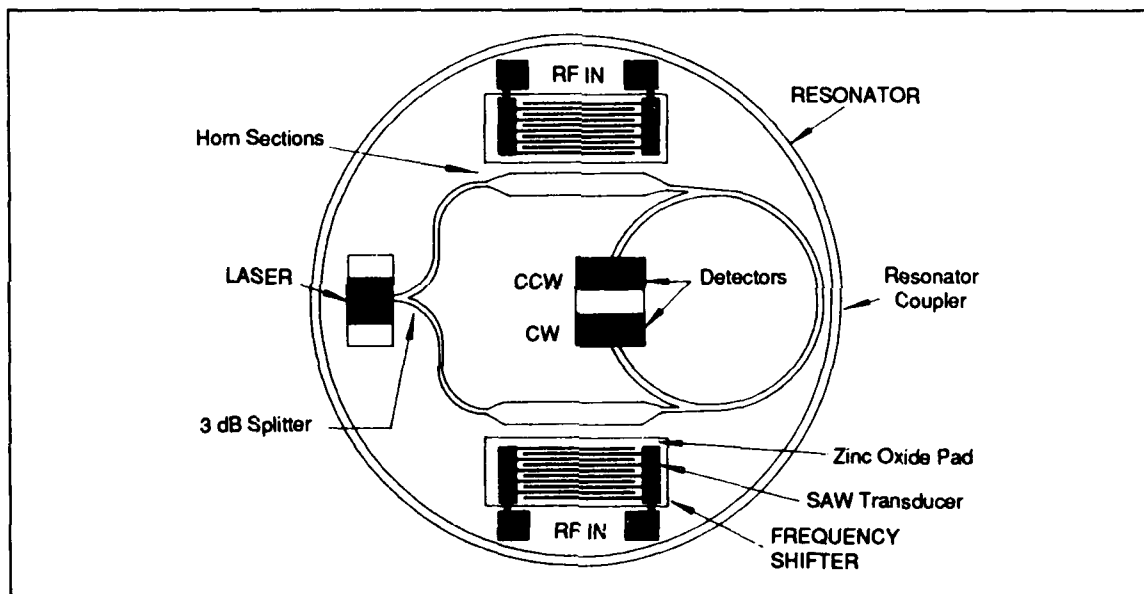

Figure 3-2
MOG Schematic -- Alternate Design

The simplicity and degree of integration of the MOG make it easy to see that it will be inexpensive. MOG is the first gyro whose design makes it inherently mass-producible; it will be fabricated on an automated production line like those being used for integrated circuit

manufacture. We have already ascertained that much of the IC fabrication equipment can be used for MOG (and, indeed, for MSA). Similar optical devices are already in mass production; Sharp reportedly fabricates 800,000 semiconductor lasers per month using a similar automated line, at a cost below $5 each. Using 6-inch diameter substrates, up to ten gyros can be made at a time, as shown in Figure 3-3.
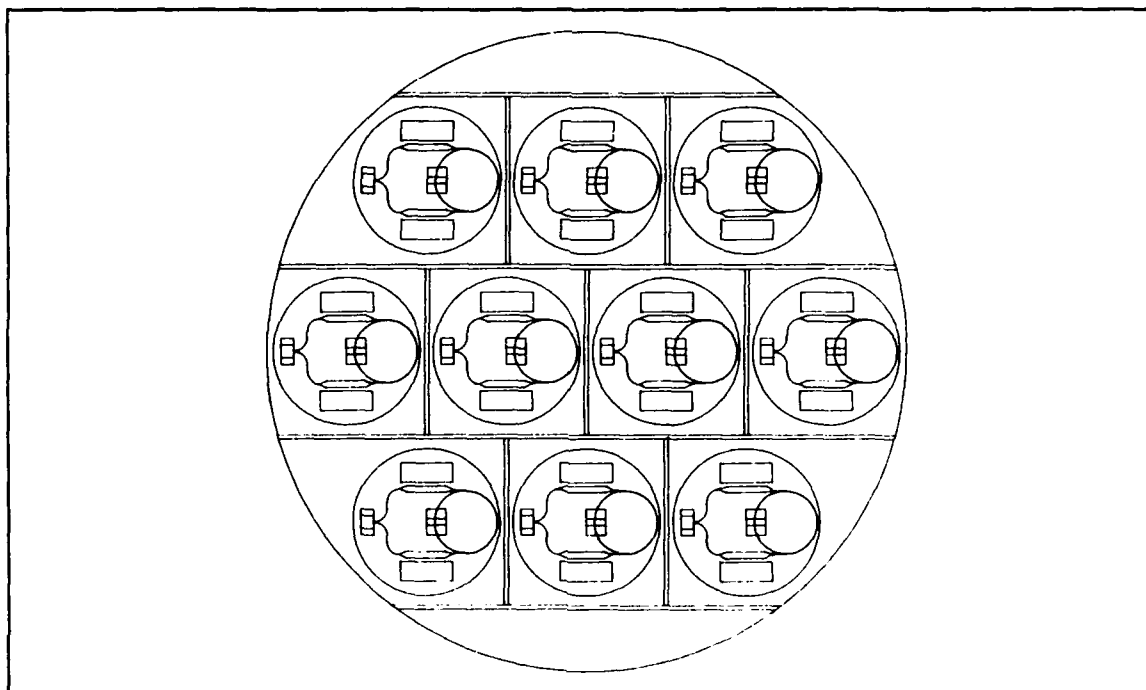

Figure 3-3
Ten MOGs on a Six-Inch Wafer

The MOG's minimum detectable rotation rate depends on the wavelength of the laser, the laser power output and the amount of laser energy coupled into the optics chip, the resonator diameter, and the frequency shifter insertion loss. There is an optimum value for coupling to the resonator, and the gyro rate resolution at the optimum coupling is:

$$\Delta\Omega \ = \ \frac{312.\lambda. \ \alpha p}{n.d\sqrt{P_{LD}.T_{chip}.R.t}}$$

where

T_{chip}	=	$10^{-(Loss/10)}$;
Loss	=	$L_{LC} + L_{FS} + 9$ dB;
L_{LC}	=	laser to chip coupling loss, dB
L_{FS}	=	frequency shifter insertion loss, dB
n	=	refractive index
αp	=	waveguide loss, dB/cm
d	=	resonator diameter, cm
P_{LD}	=	laser output power, mW
R	=	detector responsivity, A/W
t	=	sample time, sec
λ	=	free space wavelength, micron

The gyro performance is better if the rate resolution is lower, so for best performance the gyro needs the lowest possible waveguide loss, the largest possible diameter, and as much laser power as possible. Laser-to-chip coupling and frequency shifter insertion loss reduce the effective laser power at the resonator. Some typical values are used in Figure 3-4, which shows the performance possible for gyros with different diameter resonators.

It is almost always necessary to make the gyro as small as possible to keep the guidance system small. Waveguide loss is caused by scattering and absorption in the material, and radiation from the guides if the bend radii are small or the guide edges too rough. For success, the MOG needs low loss waveguides but not as low loss as found in fibers. Presently, integrated optics waveguides have losses of 0.05 to 0.1 dB/cm. Reducing losses to fiber losses, 10^{-5} dB/cm, has little advantage, since once the loss reaches 0.001 dB/cm, other error sources have a greater effect. Backward scattered light captured in the waveguide gives rise to gyro scale factor non-linearity, whose magnitude is roughly equal to twice the backscat-

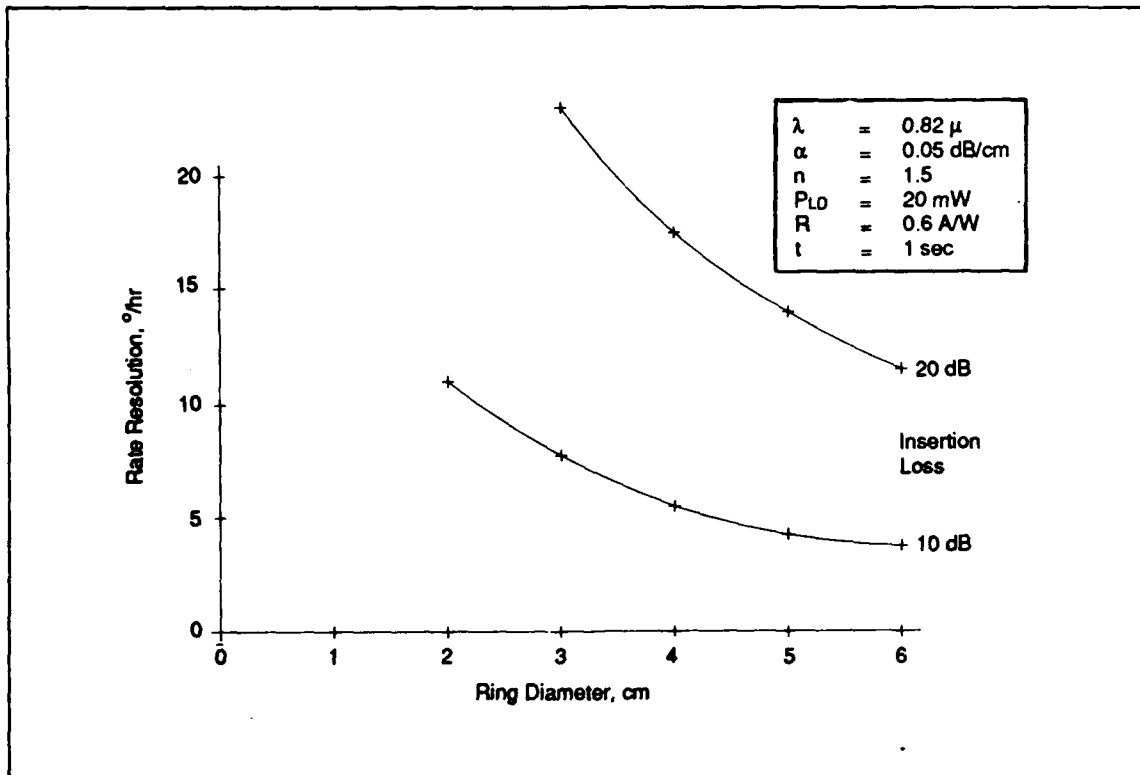

Figure 3-4
MOG Rate Resolution

ter for small rotation rates and small backscatter. That is, for scale factor linearity of 100 parts per million, backscatter must be less than 50 ppm.

Table 3-1 shows the physical parameters needed to meet initial microIMU goals compared with the goals of Table 1-2, which we believe to be achievable in a few years as integrated optics technology improves.

Table 3-1
Gyro Performance Near Term and 1990's

	Near Term	1990's
Gyro day-to-day stability, deg/hr	50	10
Gyro resolution, deg/hr	10	1
Maximum rotation rate, deg/sec	1000	1000
Scale factor error, %	0.05	0.01
Bandwidth, Hz	200	200
IA alignment stability, mr	0.5	0.5
Waveguide loss, dB/cm	0.05	0.01
Laser power, total, mW	15	40
Total insertion loss, dB	15	10
Ring diameter, cm	5	4
Resonator linewidth, MHz	37	7

The laser linewidth must be less than the resonator linewidth. We can purchase commercial diode lasers with linewidths less than 20 MHz, at 10 mW nominal output power, and linewidth decreases with increasing power. Our experiments have shown that we can additionally reduce laser linewidth by 1 to 2 orders of magnitude by actively controlling the phase of light coupled back into the laser[2].

The tactical gyro needs to withstand military temperature ranges, vibrations, and shocks typical of guided missiles, and conventional packaging approaches will be acceptable. But gyros for precision guided munitions and kinetic energy missiles IMUs will need to be g-hardened against launching accelerations up to 100,000 g. We are currently developing suitable technology under DoD contract.

4 The Micro Silicon Accelerometer

The Micro Silicon Accelerometer (MSA) is a closed loop acceleration sensor micromachined in a silicon wafer. Micromachining makes use of the anisotropic chemical etching properties of single crystal silicon to form structures a millimeter or so in size; Angell et al.[3] have given an excellent review of this field. Silicon forms the same type of crystal as diamond; it is harder than most metals and has higher elastic limits than steel in both tension and compression. It is brittle and can be cleaved; it has negligibly small hysteresis and virtually infinite fatigue life. These mechanical properties make it very suitable as the structural material for an accelerometer, as Table 4-1 shows.

Table 4-1
Mechanical Properties of Silicon Referred to Steel[4]

	Yield Strength (10^{10}) (dyn/cm^2)	Young's Modulus (10^{12}) (dyn/cm^2)	Density (g/cm^3)	Thermal Conductivity $(W/cm.C)$
Silicon	7.0	1.9	2.3	1.57
High strength steel	4.2	2.1	7.9	0.97

Any accelerometer consists of three fundamental parts:

1. A mass, whose inertia causes a force when it is accelerated.

2. An elastic member of some kind, often a hinge, which allows the force to do some kind of work.

3. A pickoff which senses the work done by the force.

The performance is better if the accelerometer is used in a force feedback arrangement (closed loop), when a fourth element is necessary: a force generator that provides an equal and opposite force to the inertia force, and that is excited by a servo which seeks to maintain the elastic member in an undisplaced state by driving the pickoff signal to null.

In the MSA the mass is a part of the structural silicon, freed from the structure by a through-cut well around three sides. The fourth side carries the elastic hinge, also part of the silicon structure, but thinned symmetrically top and bottom to reduce its mechanical stiffness. The pickoff is capacitive and the forcer electrostatic. The position of the proof mass is sensed by a capacitive pickoff, and any movement of the proofmass from pickoff null produces an error signal that is amplified and fed back to electrodes to restore null. In the electronic system the feedback voltage is proportional to the acceleration.

The MSA is being developed to meet the microIMU specification given in Table 1-2. Figure 4-1 shows an isometric sketch of the MSA, in which in the proof mass, elastic hinge, pick-off, and forcer are clearly distinguishable. The MSA consists of a sandwich of glass top and bottom plates anodically bonded to a central silicon part, fabricated from integrated circuit silicon, and electrically grounded. The proof mass is slightly thinner than the starting wafer and is chemically etched free of the wafer on three sides leaving the hinge on the fourth side only three microns thick. The outside dimensions of the mechanical part are 8 mm x 4 mm, by 2 mm thick.
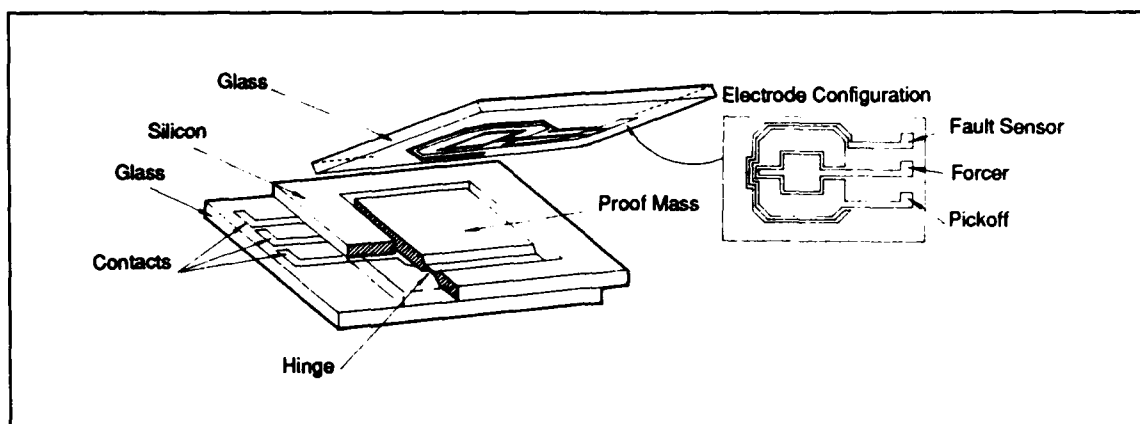

Figure 4-1
Micro Silicon Accelerometer

The pickoff and forcer system consists of three concentric electrodes on each glass plate and the silicon itself. The middle electrodes on the top and bottom glass plates and the silicon proof mass form two pickoff capacitors. When the proof mass is at its null position, the values of these capacitors are equal and are compared in the capacitive comparator, Figure 4-2. Should one of the capacitors be larger than the other, the comparator produces a signal with proper polarity that is amplified in the operational amplifier, voltage shifted and applied to the top and bottom driver electrodes to drive the pickoff capacitances to equality.
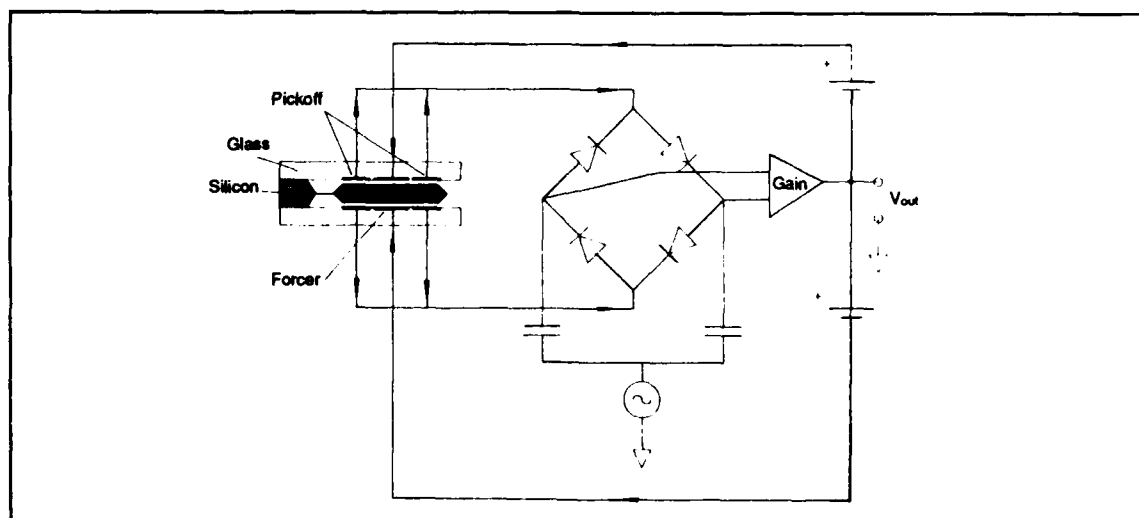

Figure 4-2
MSA and Electronics

The fault sensing electrode is used to signal that the proof mass is deflected "to the stops", such that it is touching a glass plate. This feature is necessary to achieve system turn on under acceleration, such as might be found when the microIMU is used in a tactical missile. Providing the electrostatic sensing and forcing functions on separate electrodes allows each function to be separately optimized.

A self-test feature included in the electronic feedback system provides a short electrical pulse as an "error signal" to the operational amplifiers, causing the proof mass to deflect with a known momentum. After the pulse, the feedback system will act to restore the proof mass and thus establish its operational status.

The MSA will be very cheap to produce, and will be fabricated alongside the MOG. Silicon is readily available for integrated circuits, and mass production equipment for the processes common to ICs, like photolithography, dry etching, and metallizing are sophisticated and available with automated batch processing capabilities. IC wet etch equipment can be readily modified for the micromachining operations, and the MSAs are cut from the wafer using an IC saw. Automatic test requires specific equipment for inertial sensors (like precision rotary stages and centrifuges) which is now available. But the dominant cost savings occur because each wafer can hold 80 or more MSAs (Figure 4-3), a proliferation of devices unthinkable in the usual inertial sensor production factory.
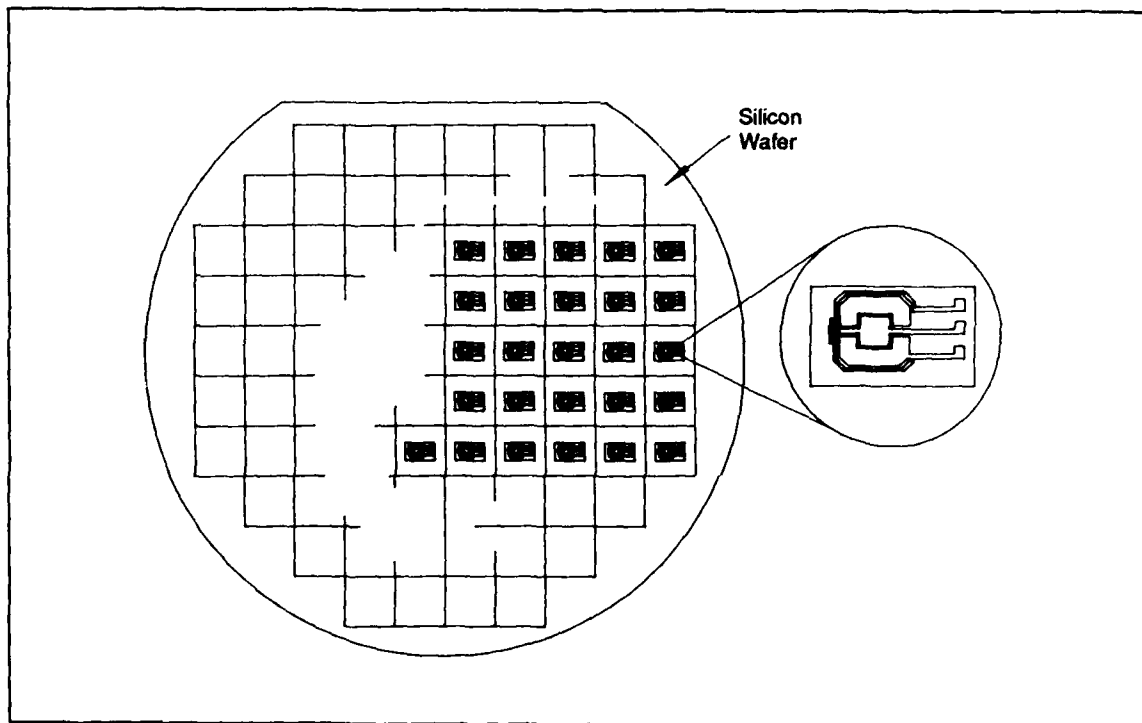

Figure 4-3
80 MSAs on a Six Inch Wafer

5 Integrated Optics Advances and MIMU Evolution

The field of integrated optics is still developing, being drawn on by the communications industry which sees it as a way of making communications devices faster, cheaper, and more reliable. Integrated optics involves the processing of light waves by modulators, switches, and amplifiers in devices made (perhaps by different but compatible processes) on the same substrate. It is the photonic analog to the electronic integrated circuit, and is moving toward the integration of devices on gallium arsenide and silicon. There is work in progress on growing GaAs devices like lasers on silicon wafers, and electronic processing might be incorporated into the same chip. Semiconductor laser development is proceeding at full tilt across a broad front, from 1.5-micron GaAsInP devices for telecommunications, to GaAlAs 0.82-micron lasers for CD players and WORM (Write Once, Read Many) optical storage disks, to GaInAs 0.6-micron lasers to replace the HeNe gas laser - a vast and profitable market opportunity.

All these technology advances are being pursued for large markets other than gyros, yet all benefit the MOG. Higher power lasers improve drift performance, GaAs phase modulators reduce gyro power if used to replace the Bragg frequency shifter, and GaAs grown on silicon could lead to even less expensive, entirely integrated MOGs with the very highest of shock and vibration tolerance, even to the 150,000 g acceleration required of electromagnetic rail gun launched projectiles. Perhaps GaAs laser-phase modulator macrochips will be coupled to waveguides grown on silicon wafers (glass, after all, is mostly silicon dioxide).

The whole field of smart weapons will demand cheap, small gyros and accelerometers, and all these advances in integrated optics are going to supply technology that can be used to develop later MOG generations. No matter how much one tries, the attachment of a fiber optic gyro's fiber to its processing chip is going to need a mechanical joint, not easily made rugged and stable, not easily automated. While it is true that the fiber gyros may have better drift performance than the MOG, the tactical weapon field does not need higher performance, it needs low cost, small size and reliability, all best achieved by total integration.

Today's MOG and MSA are really the start of a generation, even a dynasty of new sensors, which will lead to the capability of inertially controlling tactical projectiles and vehicles with the broad capabilities being conceived today. When coupled to the global positioning system (GPS) by a tightly integrated GPS receiver, the microIMU will offer inexpensive tactical navigation which will aid IR and optical radar sensors in creating tomorrow's smart weapons.

References

1. S. Ezekiel, S. R. Balsamo, "Passive Ring Resonator Laser Gyroscope", Applied Physics Letters, 30, 9, 1 May 1977, p.478.

2. S. T. Ho, S. Ezekiel, J. R. Haavisto, J. J. Danko, "Optical Feedback Stabilization of a Semiconductor Laser", J. Lightwave Tech., LT-4, 3, 3/1/86, p.312.

3. James B. Angell, Stephen C. Terry, Phillip W. Barth, "Silicon Micromechanical Devices", Scientific American, 248, 4, pp. 44-55, April 1983.

4. Kurt E. Petersen, "Silicon as a Mechanical Material", Proc. IEEE, 70, 5, pp. 420-457, May 1982

5. Chapter 1 in S. Ezekiel, H. R. Arditty (Eds), *Fiber Optic Rotation Sensors*, Springer-Verlag, 1982.

THE MICROMECHANICAL INERTIAL GUIDANCE SYSTEM AND ITS APPLICATION

by

Burton Boxenhorn
Brock Dew
Paul Greiff

The Charles Stark Draper Laboratory, Inc.
Cambridge, Massachusetts

1. INTRODUCTION

This paper will present the results of designing, building, and testing micromechanical inertial instruments at the Charles Stark Draper Laboratory (CSDL). These instruments were built from silicon, using semiconductor fabrication techniques. Their size is minute, of the order of 1 square millimeter; they consume negligible power and are of negligible weight. In large quantities, their cost will be very low.

Studies have shown that their potential performance is adequate for many tactical applications. This combination of factors provides a breakthrough in applications such as smart bombs or shells, guided rockets, and other applications in areas such as aircraft controls and structural damping.

The presentation is in the following order: (1) Instruments: A discussion of the micromechanical gyro and accelerometer and their per-formance; (2) Architecture: A discussion of how they are put together in a system, and finally; (3) An example application.

2. INSTRUMENTS
2.1 Accelerometer

The accelerometer is a monolithic structure (no assembly of com-ponent parts) consisting of a torsional pendulum with capacitive readout and electrostatic torquer. A sketch of the configuration is shown in Figure 1. The active area of the device is about 300 by 600 μm in size. The pendulum is supported by a pair of flexure pivots. The readout and torquing electrodes are built into the device beneath the tilt plate. Figure 1 also shows a side view of the device. The device is made on a silicon wafer, and is all silicon except for the electroplated gold on one side of the tilt plate which provides the pendulosity. The elec-trodes are separated electrically from the body of the device by p-n junction isolation. Construction details are presented elsewhere[1]. Figure 2 shows a SEM photo of an accelerometer.
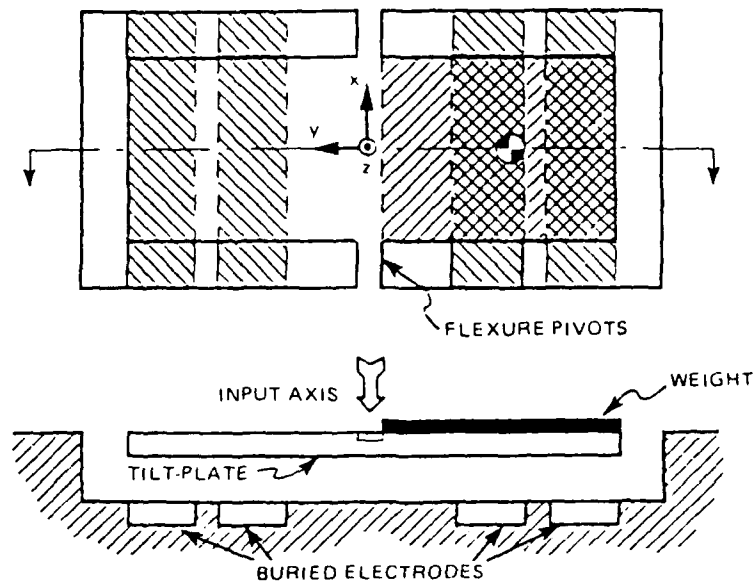
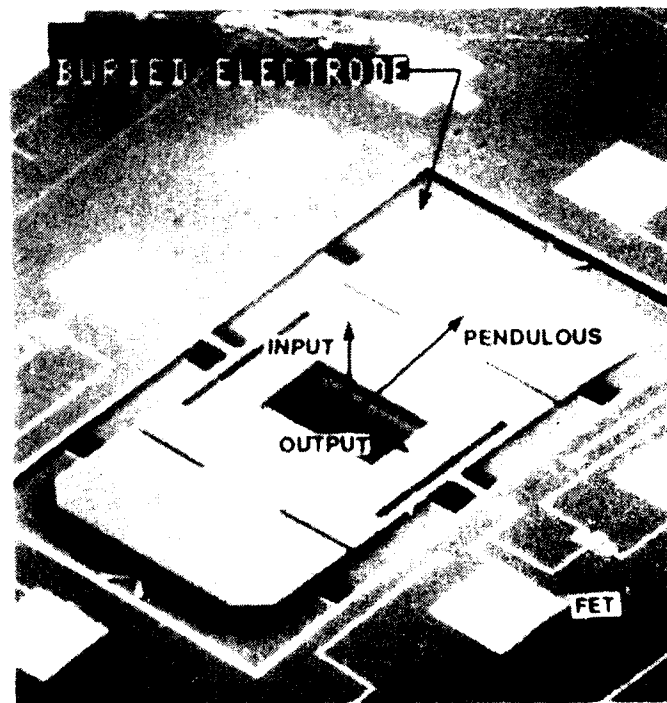Figure 1.   Micromechanical accelerometer.

Figure 2.   Accelerometer: SEM photo.

The angular position of the tilt plate is sensed by measuring the capacitance difference between one side of the plate and the other. One pair of electrodes is dedicated to this purpose; the other pair is used for torquing the plate. The output of the angle sensor is integrated and fed back to the torquer to maintain the tilt plate in a fixed angular position. The torque required to maintain this balance is then proportional to the input acceleration.

The components of the instrument are discussed next.

2.1.1 Angle Readout

The implementation of the buried electrodes depends on the appropriate doping of the device. The doping is indicated in Figure 3. The tilt plate and the buried electrodes are doped P. The substrate is doped N. The device can then be modeled as the circuit shown in Figure 4. By properly biasing the substrate or the plate, the buried electrodes and the tilt plate can be electrically isolated from the surrounding substrate. The final equivalent circuit is shown in Figure 5. This is the small signal equivalent circuit. The readout electrodes are driven by two amplifiers. These in turn are driven by an excitation oscillator, Ex, at some suitably high sinusoidal frequency. The amplifier configuration is such that the sense electrodes are driven 180 degrees out of phase from each other. Thus, when the tilt plate is level, and the two sense capacitors are equal, there is no net current driven into the summing junction of the output amplifier, and thus no output voltage Eo. As the plate tilts, the sense capacitors are unbalanced, and there is a net current into the summing node, resulting in an output ac voltage.

The result is an output voltage proportional to the change in the differential capacitance of the sense electrodes. The capacitive feedback configuration of the output amplifier shown makes the output voltage independent of the excitation frequency. For small gaps, it is easy to show that the change in capacitance is a linear function of the tilt angle for small angles.

2.1.2 Torquer

The basic equation for the force on a capacitor shows that it is proportional to the square of the applied voltage. The problem is to linearize the net torque as a function of the input voltage. This is done by using the following relationships:

$$\text{net torque:} \quad T = k[V_1{}^2 - V_2{}^2] \tag{1}$$

where

V_1 = the voltage applied to one torquing electrode

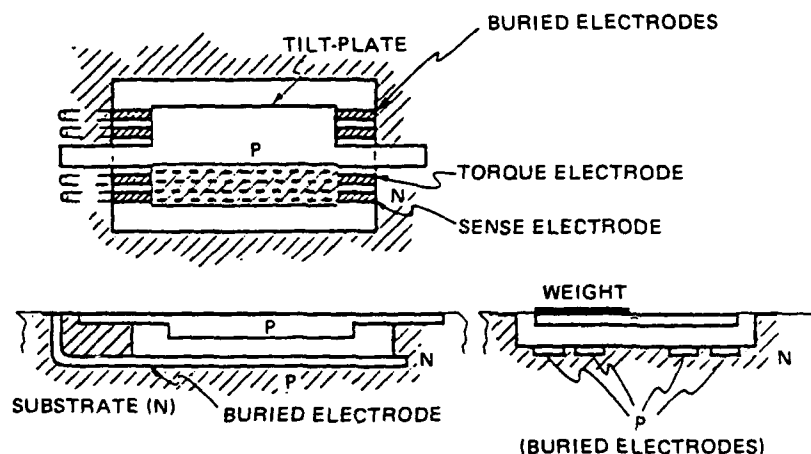V_2 = the voltage applied to the other electrode

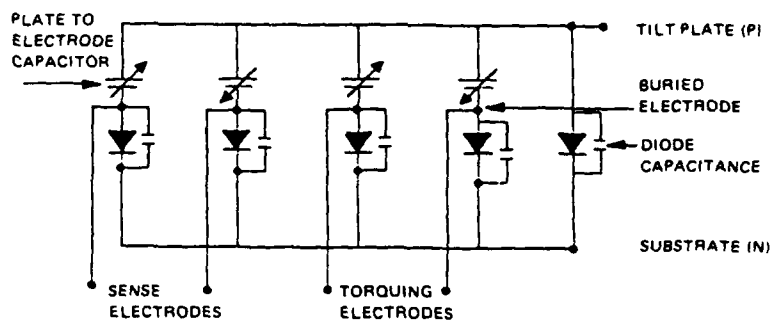Figure 3.   Sketch of tilt plane with buried electrodes and doping.

Figure 4.   Circuit model of buried electrodes.

k   -   a constant depending on the geometry, the dielectric con-
        stant, and the gap between the tilt plate and the torquer
        electrode

Let:

$$V_1 = B + E_t \qquad (2)$$
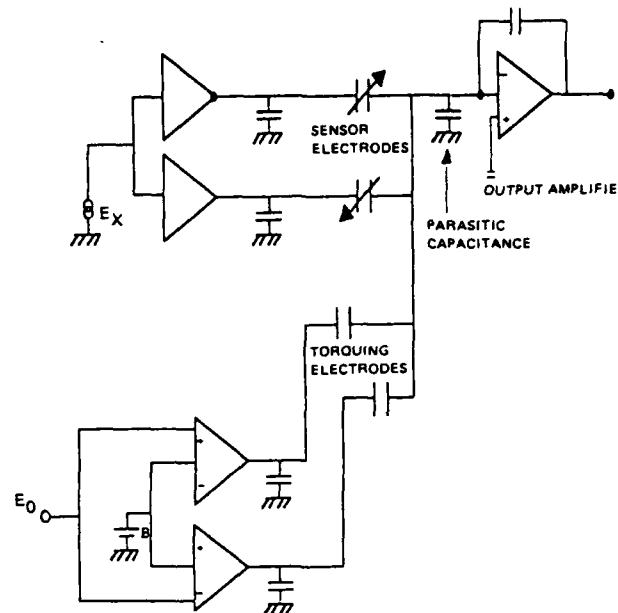
$$V_2 = B - E_t \qquad (3)$$

Figure 5. Sense and torquer circuit.

where B is a fixed bias. Then, combining these three,

$$T = k[(B + E_t)^2 + (B - E_t)^2]$$

$$= k[B^2 + 2 E_t B + E_t^2 - (B^2 - 2 B E_t + Et^2)] \qquad (4)$$

$$= 4 k B E_t$$

The torquing circuit shown in Figure 5 implements the above equation, resulting in a linear relationship between the applied voltage Et, and net torque, T, applied to the tilt plate. The bias voltage also serves to bias the p-n junction appropriately.

2.1.3 Rebalance Loop

The above circuit configuration is used in a feedback loop to rebalance the tilt plate. A functional block diagram of the loop is shown in Figure 6.

The output of the angle readout, θ, is demodulated with respect to the excitation signal of the sensor. The dc output of the demodulator is then passed through servo compensation to an integrator. The output of the integrator is fed back to the torquer network, previously described, which serves to drive the tilt plate back so as to zero the output angle θ. Any acceleration, A_{in}, will apply a torque to
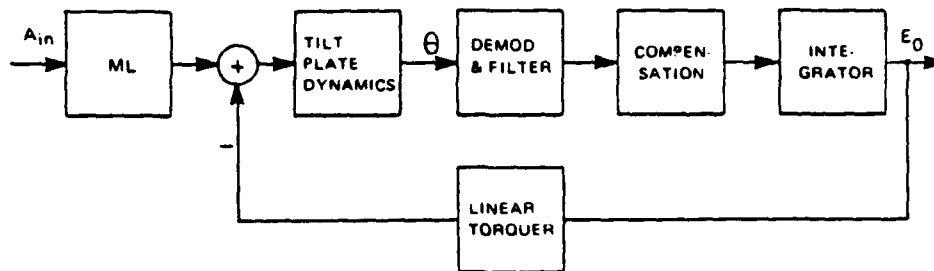
Figure 6. Rebalance loop.

the tilt plate equal to $A_{in}*M*L$, where M is the pendulous mass and L the pendulum length. The loop then serves to rebalance the tilt plate, resulting in a voltage on the integrator output. This voltage, required to hold the plate against the acceleration torque, is the instrument output in volts, and is proportional to the input acceleration for a perfectly linear torquer.

2.2   Gyro

The micromechanical gyro, called simply the "gyro", has no continuously rotating parts, but instead is vibrated about flexure pivots. Vibratory gyros are not new[2], but the particular configuration described here is novel, and has been patented.

Driving and readout for this device is performed electrostatically and capacitively. This is done by mounting electrodes above the outer and inner plates (or gimbals) for torquing and sensing. The development program required major innovations in the areas of device fabrication, ultrasensitive capacitive sensors and linear electrostatic torquers.

Figure 7 shows a schematic of the gyro. It is a double gimbal structure, with a vertical bar mounted on the inner gimbal. The inner gimbal can be thought of as the gyro, and the outer gimbal as the motor. Each gimbal is attached to the other through a set of orthogonal flexure pivots. These pivots are relatively weak in torsion, but strong in all other directions. When the outer gimbal vibrates through a small angle θy, at a frequency w, the inner gimbal becomes sensitive to angular rates about the axis normal to the plane of the gimbals. In the presence of an angular rate about the axis normal to the plane of the gimbals, the inner gimbal responds by vibrating at the outer gimbal
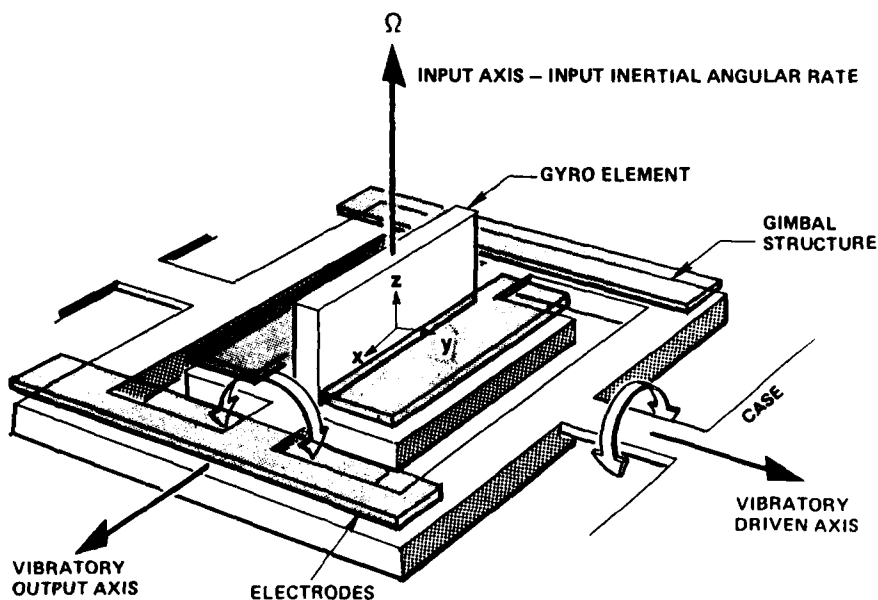
Figure 7. Vibratory rate gyro.

vibration frequency and at an amplitude proportional to the input
angular rate.

Gyro Equations:
A detailed mathematical derivation of the pertinent equations is
given is Ref. 2. The final open-loop equation for the output angle, θ,
is

$$\theta_{1x} = \frac{I \; \theta_{2y} \; Q}{I_{1x} \; \omega_N} W_z$$

$$I = (I_{1x} + I_{1y} - I_{1z}) \qquad\qquad (5)$$

$$Q = \frac{1}{2\zeta}$$

where

θ — the outer gimbal vibratory angle, Q is the mechanical
quality factor
ζ — the damping factor
ω_N — the resonant frequency of inner
W_z — the input rate and I--, I--, and I-- are moments of
inertia about the x, y, and z inner axes

The above is one form of the governing equation, in terms of resonant quality factor Q and the vibration frequency ω. Another form of the above is obtained by retaining the damping factor, D, explicitly. This results in another form for the mechanical angle as shown next.

$$\theta_{1x} = \left[\frac{I \, \theta_{2y}}{D} \right] W_z \qquad (6)$$

Eq. (6) shows that the sensitivity, the term within the parenthesis, is independent of Q or ω, but depends inversely on the damping coefficient, D. For practical operation, D must be as small as possible. Since D is inversely proportional to pressure, the gyro is vacuum packaged to maximize sensitivity.

This gyro operates as an AC-modulated suppressed carrier system. The information is carried on the envelope of the output vibration, at the vibration frequency. This raises the question of what is the transient response, or bandwidth of the instrument. As is shown in Ref. 2, the open loop bandwidth of the gyro is:

$$\theta_{1x} = \frac{I \, \theta_{2y}/I_{1x}}{2(s + \omega_N/2Q)} \, W_z \qquad (7)$$

where s is the Laplace transform variable.

The open loop is not the major mode. In steady state, when s = 0, the result becomes equal to Eq. (5). The bandwidth, ω_N/Q becomes small for high Q. This means that the gyro looks more and more like an integrating gyro rather than a rate gyro as the Q becomes very large. Control loops have been devised to rebalance the inner gimbal output. This will enable the bandwidth to be adjusted to a value appropriate to the application.

Fabrication:

A photomicrograph of the active element of the gyro, including typical dimensions, is shown in Figure 8. The gyro and accelerometer devices are made by chemical etching from a wafer of single crystal silicon. This accounts for the high values of Q obtained experimentally (greater than 2000 at 3 mTorr). The geometrical control is obtained by selective boron doping and anisotropic etching with Ethylene diamine Pyrochatechol-water to undercut and free up the desired geometry. Although some novel processing is required, (patents have been applied for) the general nature of the technology has been described in literature on micromechanical devices[2]. The vertical member, which is the gyroscopic element, is a mass of gold that has been electroplated though an opening patterned in photoresist.
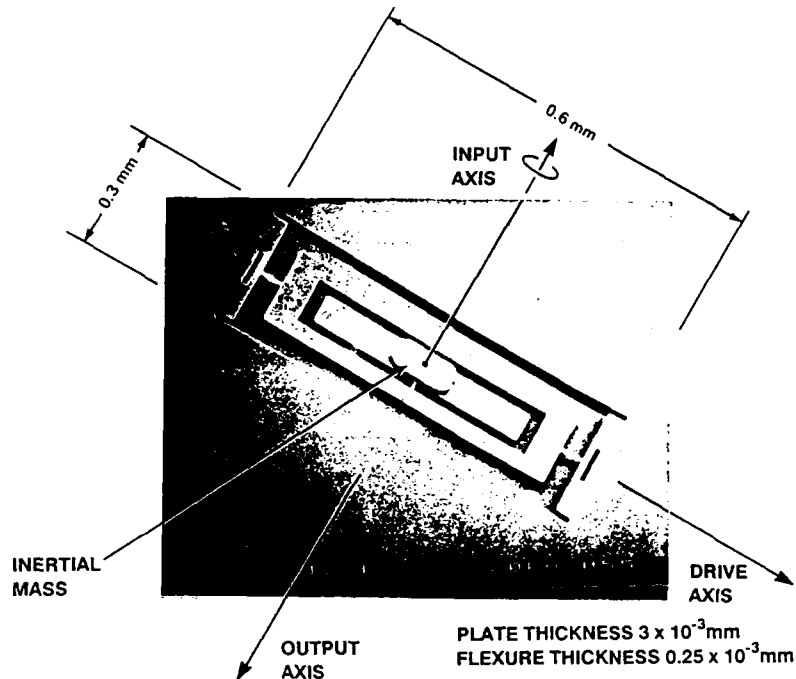
Figure 8. Micromechanical gyro.

In the version of the gyro shown here, an unsymmetrical vertical member was used. This simplified the fabrication process. The asymmetry does not change the equations of motion. Future instruments will incorporate a symmetric vertical member, to reduce vibration susceptibility.

The gyro fabrication process is not yet completely monolithic as is the accelerometer, however, this is expected to be accomplished in the near future.

A model was developed to account for the mechanics of the flexure pivot, vibration sensitivity and stresses, as well as the gyro dynamics given here. This model was integrated in a computer program that computed all important mechanical factors and resonant frequencies, and predicted the performance of a design.

2.3   Gyro and Accelerometer Test Performance
2.3.1 Accelerometer Test Results

The accelerometer performance was measured using a tumble test, as described in detail in Ref. 3. The goal was to achieve a Scale Factor Error less than 500 ppm and a Bias Stability less than 500 μg. Initial results are promising; they are summarized in Table 1.

Table 1. Accelerometer performance parameters (best run, 203 minutes).

Bias Stability - BS (micro-g): 261

Scale Factor Error - SFE (ppm): 480

Since these tests were run, an improved set of electronics has been built and tested. This considerably improved the temperature sensitivity and long-term stability. A new improved device is in the process of being fabricated, and is expected to demonstrate improvement in thermal sensitivity and stability.

2.3.2 Gyro Test Results
The gyro performance was measured both open loop and closed loop. The results of the open loop test are given in Ref. 2, and summarized in this subsection.

To simulate a vacuum package and to attain high Q, the device was tested in a vacuum chamber. The gyro, along with its AC amplification stages and torquing network, was mounted inside the vacuum chamber on a rotatable platform. This was rotated by a synchronous motor through a rotating vacuum seal. The signals were brought in and out through a slip-ring assembly.

The resonant frequency of both inner and outer gimbals was measured with a spectrum analyzer. The outer gimbal was driven at the resonant frequency of inner, an input rate W_z was applied and the resulting rate sensitivity was observed on a strip chart recorder. Table 2 shows tabulations of the pertinent data for a sample experiment.

Table 2. Data for gyro experiment.

Inner resonant frequency	1596 Hz
Outer resonant frequency	1883 Hz
Input rate	10.5 rad/s
Output voltage	0.60 mV
Predicted output voltage	0.97 mV

The above results were obtained in the initial experiments to demonstrate feasibility. They were obtained by operating the gyro open-loop. This results in an instrument with very low bandwidth, and great sensitivity to resonant frequency. Later tests were run in which the

gyro was operated in a closed-loop rebalanced mode, as described later in this paper, with encouraging results. Thus far, a resolution of 2300 deg/h has been achieved, with a 20-second filter on the output.

3.   ARCHITECTURE
3.1   Rebalanced Closed Loop System
        A block diagram of the gyro loop with transfer functions is shown in Figure 9. This shows the gyro dynamics along with various disturbance elements. A discussion of this block diagram follows.

        A sinusoidal vibratory torque, M_2, is applied to the outer gimbal at a frequency equal to the resonant frequency of the inner member. This results in an output angle, θ_{2y}, and an output angular rate, $d\theta_{2y}/dt$. The product of angular rate, inertia term I, and applied angular rate, W_z, produces the gyroscopic torque that is applied to the torque summing junction and drives the inner gimbal. For a fixed vibratory drive torque, the angular rate of the outer gimbal is a fixed sinusoid, 90 degrees out of phase with the driving torque (assuming the phase shift through the outer gimbal dynamics is negligible). Since the geometry is fixed, the moment of inertia term, I, is fixed. Then the gyroscopic coupling from outer to inner is a function only of the inertial angular rate, W_z.

        In addition, there are several other forces exerted on the inner gimbal. One is the effect of unbalance of the inner gimbal. This causes dynamic forces on the inner gimbal from the oscillation of outer. As shown, it is proportional to the mass, M_1, of the inner gimbal, and the distance, L_x and L_y, of the center of gravity from the x and y axes of the inner. The important point to note is that this is 90 degrees out of phase from the gyroscopic term. Another term is due to the misalignment or nonorthogonality of the two axes. This causes a certain percentage of the outer drive to couple directly in to the inner axis. Note that this, too, is in quadrature with the gyroscopic torque.

        There are two noise torques: one due to Brownian motion, and the other due to linear acceleration. The first is proportional to the damping, and the other is a function of the unbalance of the vertical member. If the center of gravity of the inner gimbal is not at the center of the coordinate axis, then one has a pendulum, and there is a sensitivity to acceleration. The first is minimized by increasing the moment of inertia of the inner member, and the other is minimized by building the gyro with precise symmetry.

        The net torque is applied to the inner gimbal, which is a highly resonant system, with very small damping. This small damping is achieved by operating the gyro in a vacuum, and by nature of the fabrication and design, uses single crystal silicon and a monolithic gimbal structure to minimize the inherent physical damping within the flexure pivots. The sensor output is a sinusoid whose amplitude is

OUTER GIMBAL DYNAMICS

APPLIED TORQUE M_2

INNER GIMBAL DYNAMICS

n_b = BROWNIAN NOISE

n_a = READOUT NOISE

DC OFFSETS

$\angle 90°$

QUADRATURE PATH

w_z = INPUT RATE

GYROSCOPIC COUPLING

W_z

$\angle 0$

DC OFFSETS

GYRO

UNBALANCE

θ_{2y} (FROM OUTER GIMBAL)

MISALIGNMENT

ACCEL

K_1

K_2

$I = I_{1x} + I_{1y} - I_{1z}$

$S = jw_0$ WHEN M_2 IS SINUSOIDAL

DEMOD FILTER COMP. $\int dt$ REMOD
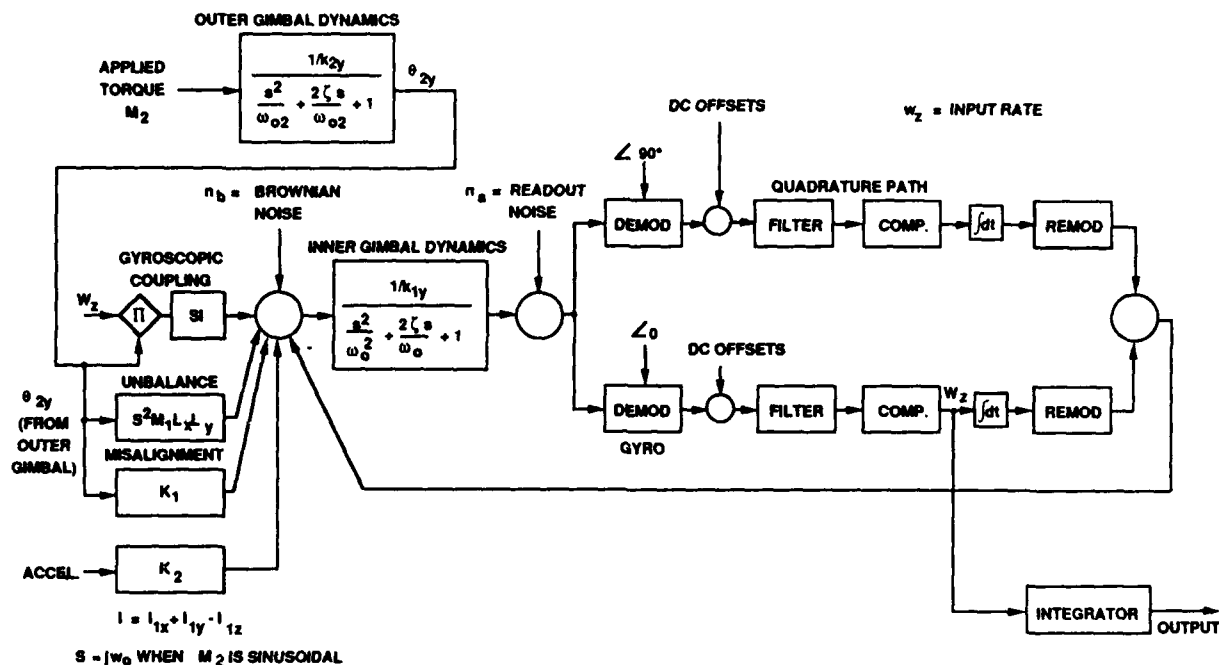
INTEGRATOR OUTPUT

Figure   Rebalanced vibratory gyro control loop.

proportional to the input rate, plus the effect of the terms discussed previously.

This output is demodulated in phase and in quadrature, to produce two parallel paths, as shown in Figure 9. Each path is filtered, servo compensation is applied, and then remodulated. The servo is designed to be type 1 system, which integrates the error. The remodulated output of the compensation of the two paths is then summed. This is then fed back through a torquer to rebalance the inner gimbal, both in phase and in quadrature. The output is a dc voltage proportional to the input rate. The output is taken from the final integrator of the gyro path before remodulation. To obtain angle, an external integrator would be necessary.

Aside from Brownian motion discussed above, the other major noise term is due to the readout noise, contributed by the amplifiers, primarily from the input noise of the signal generator preamplifier. There is no inherent bias term in the gyro itself. In order to have such a term, a signal synchronous with the resonant frequency and of the proper phase would have to be applied to the torque summing junction. However, an apparent bias will appear due to the dc offsets of the amplifiers in the servo. This will cause an offset in the output, which would be interpreted as bias in the instrument. This effect can be

minimized by designing the servo with high ac gain, and using low offset operational amplifiers.

This loop has been built, and shown to work, however, the 2300 deg/h rate resolution, quoted previously, was obtained with it. Device and electronics improvements are expected to produce a gyro at least tenfold better. Calculations have been made that indicate that a goal of 10 deg/h at 100 Hz bandwidth should be achievable with further development.

3.2 Packaging Concepts

In this section, the configuration of a micromechanical IMU will be presented and discussed.

3.2.1 Single Axis Sensor

The initial goal is to package a single accelerometer and gyro and attendant electronics in a single flatpack. A three-axis IMU would consist of three packages in an orthogonal configuration. A conceptual sketch of this is shown in Figure 10. The loop electronics for the gyro and accelerometer will be on separate analog/digital chips that will be implemented using configurable arrays. Included within the package will be an oscillator, thermal controller, VCO pulse integrators, precision reference voltage source and attendant digital circuitry. The electrical input will be the DC power lines. The output will be incremental velocity and angle in digital form, as well as analog output of rate and acceleration.
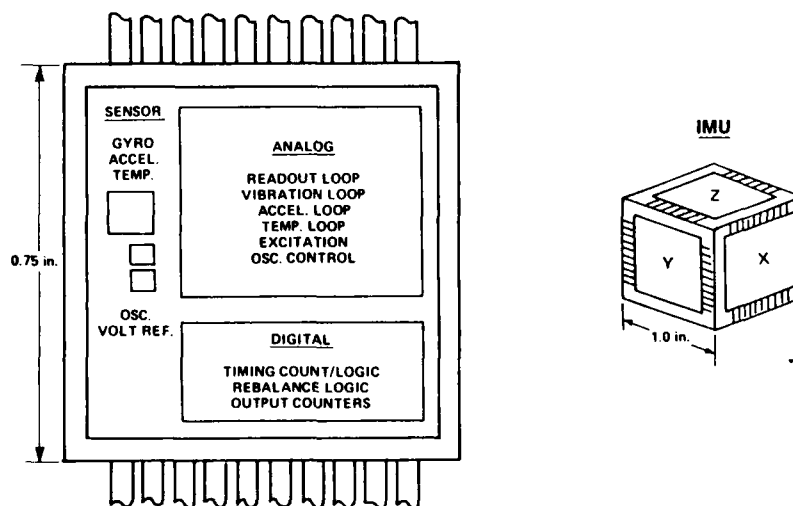

Figure 10. Single-axis inertial sensor.

All of the electronic functions required to support a single-axis IMU are shown in Figure 11. It is clear that due to the multiplicity of functions, only monolithic circuits will make possible the
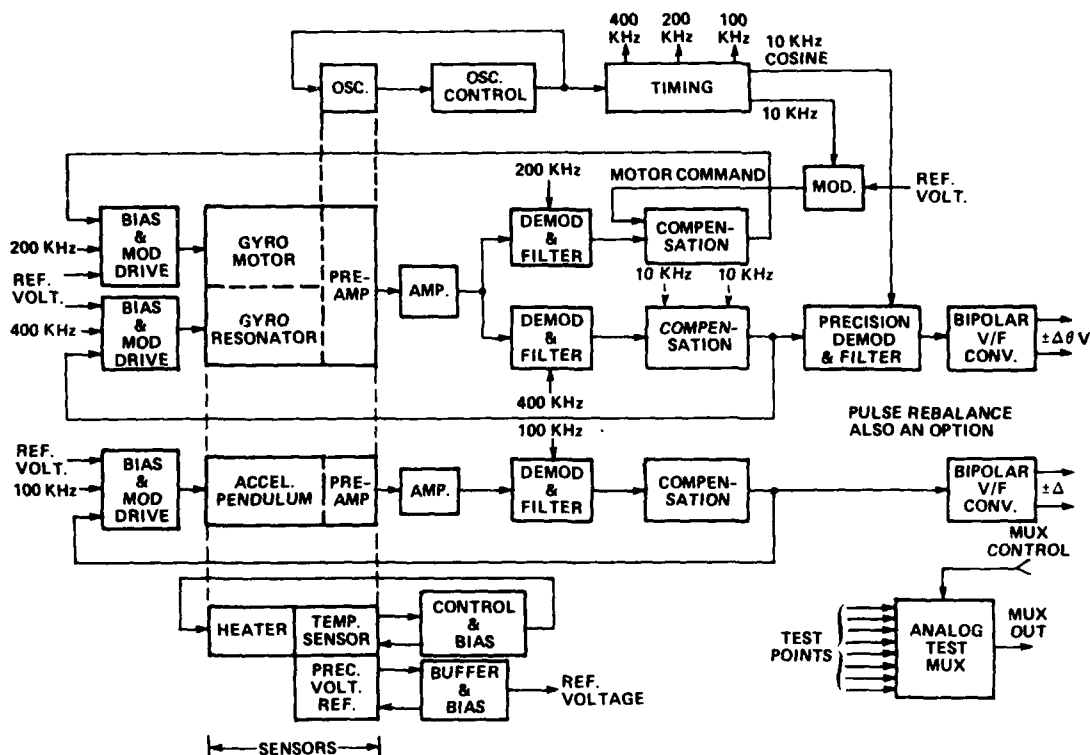
Figure 11.   Integrated micromechanical single-axis sensor.

implementation of circuits comparable in size and cost to the instruments possible.

Preliminary estimates are that such a package would weigh 10 grams; have a volume of 2 cubic centimeters; and cost in large quantities, $200 per package. An initial goal of 100 deg/h for gyro, 500 ppm; μg for the accelerometer, would allow application to many tactical systems.

3.2.2   Single Package IMU

The ultimate goal is to build an IMU in a flatpack. This can be done with the same inertial devices as in the single-axis package: by mounting three device chips orthogonally inside the package. The attendant electronics etc., would be further miniaturized using custom chip designs. Such a concept is shown in Figure 12. The device chips are mounted on the faces of the corner of a cube. The instruments would then be orthogonal to each other, but would have a form factor that would simplify assembly, trim, and test within the package. The package would have all that is electronically necessary to operate the inertial devices. The output interface is assumed to be digital. A complete system would then consist of this instrument package and another system
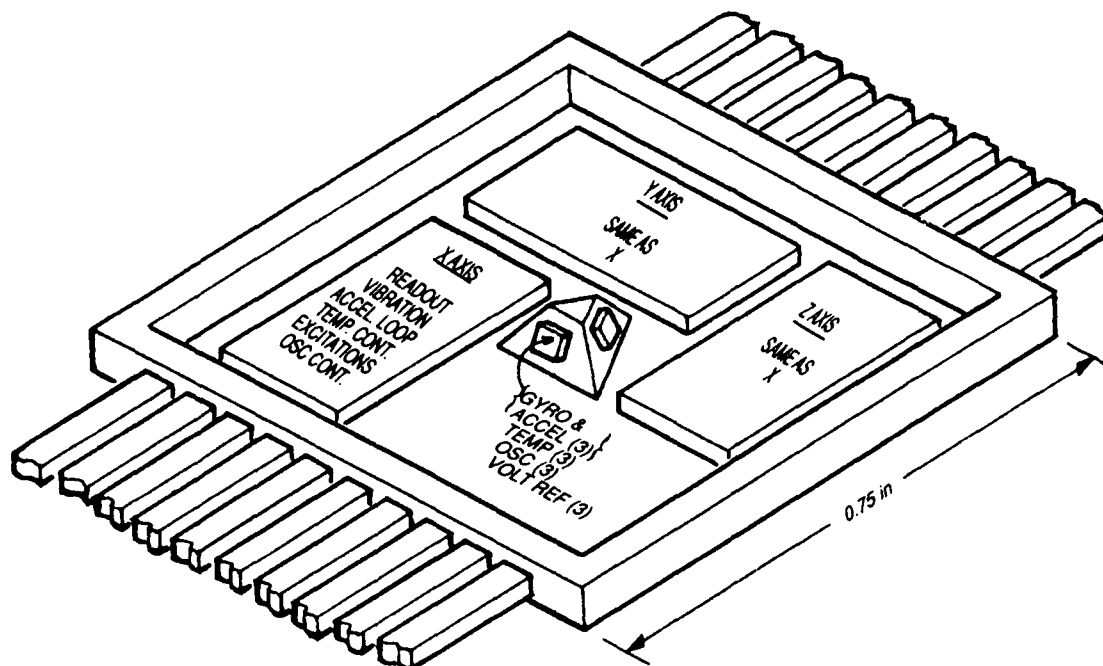
Figure 12. Three-axis micromechanical IMU.

package that is customized to the application system requirements. It would be the same size and weight as the single-axis package, and cost about $200-$500 in large quantities.

4.   APPLICATIONS

Possible application of an IMU as described above run the gamut from tactical, to strategic, to control systems. At present, inertial guidance systems are too large, heavy, and expensive for application to small tactical weapons. The availability of a micromechanical IMU of small size weight and cost will make inertially guided tactical rockets, shells, and bombs feasible. It can also be used in many control situations. As the performance improves, the spectrum of weaponry to which this can be applied widens enormously.

4.1   Detailed Example: An Anti-Armour Weapon

This section will present the performance requirements of a Light Anti-Armour Weapon. This is envisaged to be an inertially guided rocket, that can be launched by one person.

The advantage of using an inertially guided rocket over a conventional rocket weapon is that it provides closed-loop guidance to the rocket. This means that it can be told where to go and where it is, and it gets there in the presence of any disturbances, so long as there is adequate thrust capability. There is no need to depend on a lengthy

launch tube for proper aim, and the thrust can be scheduled so that the initial blast effects are minimized.

The rocket will be aimed at a tank (see Figure 13), during which time the inertial guidance system will be initialized, and launched. It will then fly straight to the target, independent of trajectory disturbances or thrust perturbations. It will weigh about 15 lb (see Figure 14), and will require a light launching tube.
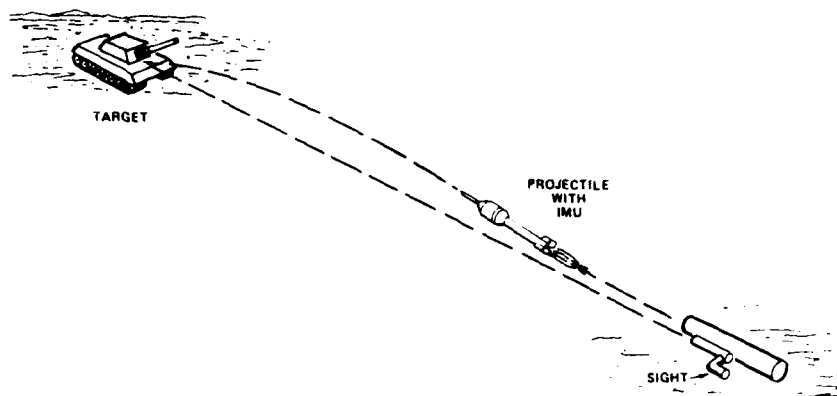

Figure 13.   Inertially guided light anti-armour weapon.

Table 3 shows the projected performance requirements of this weapon. The weapon system requirements were assumed to be 1 m miss 50-percent probability at one kilometer. The time of flight was assumed to be 3 seconds. A soft launch was assumed of 5 g, and the projectile accelerated as the fuel was consumed according to a fixed schedule.

The gyro requirements of 100 deg/h is modest, and the accelerometer requirements of 15000 for SFE and Bias has been proven to be readily achievable (see Ref. 1). The gyro bias is the largest contributor to the error budget. The second largest is the aiming error, which is the accuracy of the initial conditions. An optical transferal between the sighting mechanism and the guidance system within the projectile was assumed.

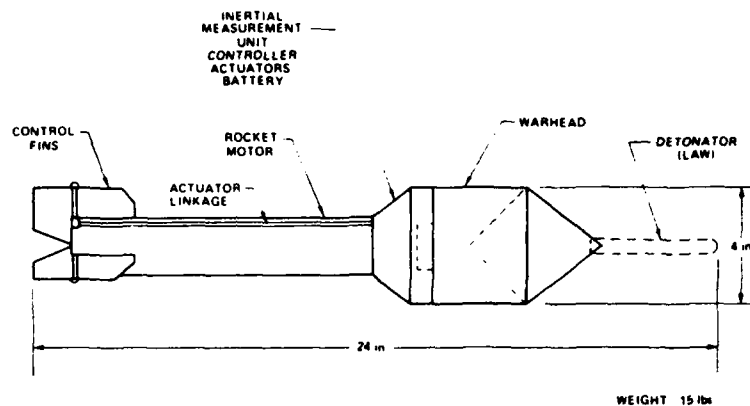Figure 14.   Inertially guided rocket projectile.

Table 3.   Light anti-armor weapon performance.

Acceleration profile: a ≈ g*(5+17.7*t) for 3 seconds.

Term	Error	Miss
Gyro Bias	100 deg/h	0.61 m
Gyro S.F.	15000 ppm	0.22
Aiming Error	100 arcsec	0.49
Accel. Bias	15000 μg	0.22
Accel S.F.	15000 μg	0.22

RSS = 0.87 m
CEP = 1.03 m

References

1. Boxenhorn, B. and P. Greiff "Monolithic Silicon Accelerometer,"
    5th International Conference on Solid-State Sensors and
    Actuators, June 1989.

2. Boxenhorn, B. and P. Greiff, "A Vibratory Micromechanical Gyro
    scope," AIAA Guidance and Control Conference, August 15-17, 1988,
    Minneapolis, Minnesota, paper 88-4177, p. 1033.

3. Boxenhorn, B., and P. Greiff, "An Electronically Rebalanced
    Micromechanical Accelerometer," AIAA Guidance and Control Confer-
    ence, August 1989, Boston, paper 89-3438.

NOMENCLATURE

A_{in}	Input acceleration
B	Bias
BS	Bias stability
CG	Center of gravity
D	Damping coefficient
E_t	Applied torquing voltage
I	Moment of inertia parameter
I_{1x}	Moment of inertia about x of inner
I_{1y}	Moment of inertia about y of inner
I_{1z}	Moment of inertia about z of inner
k	Constant
L	Length
L_x	Distance of CG from x-axis
L_y	Distance of CG from y-axis
M	Mass
M_1	Driving torque
M_2	Mass of inner gimbal
Q	Quality factor
S	Laplace transform parameter
SFE	Scale factor error
T	Torque
$V_{()}$	Voltage
W_z	Input inertial rate
ς	Damping ratio
θ_x, θ_{1x}	Tilt angle, inner gimbal
θ_y, θ_{2y}	Tilt angle, outer gimbal
ω_N, ω_o	Natural frequency of inner
ω_{oz}	Natural frequency of outer

THIS PAGE LEFT INTENTIONALLY BLANK

TEST EQUIPMENT CORRELATION

Testing and Analysis Techniques in Test and Evaluation of Guidance and Navigation Systems

Author

John Budzinski

Company

Kearfott Guidance and Navigation Corporation
A Subsidiary of Astronautics Corp. of America

Date: July 8, 1989

CONTENTS

INTRODUCTION

Getting different data results of end product parameters from two or more seemingly identical pieces of test equipment is an issue that can only be resolved by utilizing a correlation testing process as part of an overall reliability program. A program of test equipment correlation ensures the consistency of measurements taken and assesses variabilities among "like test stations".

The Kearfott Guidance and Navigation Corporation began a correlation program in 1977. This program was implemented by a contractual obligation to the Navy Strategic Systems Program Office, (SSPO) to ensure that when more than one test and inspection station is used for verifying conformance to specification requirements of identical products, the contractor develops a plan for conducting a correlation program to detect and correct conditions contributing to significant differences in test results between stations. The correlation plan includes:

a. A description of the test stations.

b. Schedules.

c. Criteria for selection of parameters to be evaluated.

d. Parameters to be evaluated.

e. Methods for evaluating parameters.

f. Data recording requirements.

The contractor performs test station correlation in accordance with it's plan. A summary report delineating problems encountered and action taken shall be submitted for information to the appropriate agencies.

DEFINITION OF TEST EQUIPMENT CORRELATION

Correlation is the process of ensuring that like test equipment has a complementary and parallel relationship of structure, function, or qualitative correspondence of data between two or more comparable test set's.

Correlation testing is the systematic means of test equipment data accumulation and operation performance by evaluation and analysis of data.

Simply stated like test equipment testing like end products shall yield like test results.

PURPOSE OF CORRELATION TESTING

The purpose of correlation testing is to ensure that each piece of test equipment is performing within acceptable limits and that the variation between identical test sets are within acceptable limits. In addition, correlation testing will determine test set degradation and malfunctions due to:

* Aging.

* Subtle test set defects.

* Test data measurement repeatability.

* Configuration changes.

* Environmental affects (temperature, humidity, vibration, and shock).

* Overall design integrity problems

Test Equipment correlation programs should provide evidence of the capability of the test equipment to furnish the necessary data to ensure that they are within specific tolerance limits and functionally alike.

Implementing a well conceived correlation program increases the confidence level in the test equipment used and the products tested. This also improves overall program reliability.

CORRELATION OBJECTIVES

The objectives of a correlation program are as follows:

* To determine test equipment defects.

* To determine test equipment degradation due to aging.

* To analyze environmental affects of temperature, humidity, vibration, and shock.

* To analyze the effects of line voltage and frequency variations.

* To identify the need to tighten tolerances and/or frequency of calibrations.

* To provide evidence of functional similarity.

* To verify that the test equipment maintains specified source and measurement requirements.

* To verify that the test equipment yields long term repeatability and that statistically stable data are obtained at various site locations.

* To verify software funtionality.

* To validate acceptance test procedures and calibration procedures.

* To provide necessary data to establish that like test sets are within specific tolerance limits and are functionally alike.

* To observe under continuous testing the long term degradation of the end product used for correlation testing.

* To determine test equipment accuracies that cannot be derived through theoretical analysis.

FORMULATION OF THE CORRELATION PLAN

A plan must be systematically generated to accomplish the established set of correlation objectives. The following are provisions to be considered to obtain those objectives.

* Selection of correlation methods.

* Guidelines for test procedures.

* Critical parameters selected for correlation testing.

* Test scheduling.

* Software considerations.

* Statistical analysis.

* Correlation summary and reporting.

SELECTION OF CORRELATION METHODS

Consideration for selection of the most suitable methods began at Kearfott with a comprehensive examination of the advantages and disadvantages of different methods. The following are methods considered most suitable for correlation data collection.

1) **Production Data** - This may include production acceptance test data of the unit being analyzed. This data is derived from production testing.

2) **Calibration Data** - This data is obtained during normally scheduled periodic calibration from the established criteria for the test set calibration limits.

3) **Special Software** - Correlation software may be generated as applicable for special test scenarios and data collection. Critical circuitry may be exercised and functionally tested. The test set's self testing capabilities may also be examined. Correlation software may verify the test equipment operation in various modes. The software itself may be used as the medium for correlation collection and data storage.

4) **Reference Standards and Measurement Devices** - Standards are used to simulate the unit under test (UUT). The use of standards eliminates the unit under test as a contributing factor to the test equipment correlation results. Such standards will duplicate the UUT loads and also the stimulus supplied to the test equipment from the UUT. The category of standards references are Black Boxes. This simulates product loads and stimuli that are normally provided by the UUT. Accuracy of such equipment should be maintained at ten to one ratio between the test equipment data accuracy requirements and the instrumentation used. Special purpose test instrumentation is used to measure the end-item inputs/outputs or provide product stimuli. Adaptors and

instrumentation may be utilized during correlation
testing. Input/output stimuli (such as voltage, current,
frequencies, waveforms, etc.) are measured with the inputs
properly loaded. The correlation interval of test
equipment calibration should be long enough to allow
correlation of all test equipment prior to recalibration.

5) **Permanently Dedicated Production Unit** - This requires
   production units of known stability (gold plated) that are
   available for the life of the program. The use of a
   production unit for correlation offers the advantage of
   supplying all the required signals and loads. Selecting a
   production unit of proven stability requires a careful
   evaluation of the products test data. While a production
   unit of proven stability must be selected for correlation
   use, the production unit acceptance data need not be in
   specification limits. It may be advantageous to exercise
   the test equipment with a known out of limit product to
   ensure that the test equipment recognize such conditions.

GUIDELINES AND PROCEDURES

Guidelines and procedures are essential in applying the
correlation methods or combination of methods selected.

* The "Round Robin" approach first obtains correlation
  data on a stationary test set for comparison to all
  other test set's. Baseline station correlation testing
  is then accomplished on all other subsequent test set
  criteria. It is then repeated on the baseline standard
  and will provide data concerning drift or change in
  correlation standards and measurement equipment.

* Only calibrated, functionally operational test equipment
  will be correlated.

* Correlation should exercise the test equipment as
  thoroughly as possible within economic and time
  considerations.

* Correlation test equipment should be portable, such that
  it can be readily moved from facility to facility.

Correlation test procedures also establish criteria to
correlate the test equipment under test and should include
the following:

* Test set present configuration.

* Test set and pertinent subassembly part number and
  serial number, also latest revision number

* Test set site location

* Correlation test set operator's name

* Applicable software part number and serial number

* Describes designated test to be performed

* Correct sequence of procedural steps

* Correlation data results

* Specified environmental conditions (temperature,
  relative humidity, etc.)

* Line voltage and frequency applied to test equipment

* Test failure criteria and tolerances

* Relative documents

* Test Station log book information pertinent to
  configuration change, last date calibrated, due date of
  next calibration, failure occurrences, test set
  modifications or any other test set anomalies

* Specified and uniform warm-up time

INTERVAL OF CORRELATION TESTING

Interval of correlation testing should be a maximum
period between correlation events on a particular serial
number test set of 180 days.

Consideration for the intervals of correlation testing
are influenced by the availability of the test equipment and
calibration cycles of the test station. A work around
schedule should also be put into place as not to interfere
with the production schedule, end of month deliveries, etc.
Also correlation that is scheduled soon after calibration may
mask data deterioration by readjustments of the test station.
Correlation just prior to calibration will indicate if
parameters have held to specification and identify the
possible need for shorter calibration cycles or more

stringent calibration parameters.

SELECTION OF THE CRITICAL PARAMETERS AND DATA ANALYSIS

While it is desirable to measure all parameters during correlation, the correlation test time may be excessive. If test time is determined to be excessive, only critical parameters should be selected for data collection. Determination of critical parameter selection is a team effort and should be given to the responsible parties concerned with the particular needs for test equipment correlation data retention.

* **Test Equipment Engineers** (Test Equipment Builder)
  Critical parameters submitted by test equipment engineering will provide the data required to determine the need for modifications that will correct test equipment anomalies. The collection of these parameter data points will also assist in the building of future test equipment.

* **End-Item Product Engineers** (End-Item Designers)
  Parameters called for by end-item engineering should provide product performance data essential to establishing long term stability of that product when a "Gold Plate" product unit is used for correlation testing. This data is especially important in determining the effects of long term wear and the environmental effects to the product under test by the test equipment.

* **Field Service Engineers** (Test Equipment Maintenance)
  Parameter submitted by field engineering provide data to identify calibration drifts over calibration cycles as well as data affecting test set functions. These parameters also identify maintainability requirements regarding component/subassembly replacement and spacing. The need for test equipment refurbishment and periodic component replacements can be determined through analysis of the correlation parameter data selected. Correlation parameter results can also show the need for the development of preventive maintenance procedures such as test equipment filter replacement, fixture alignments, etc.

* **Quality Assurance Engineers** (Q.A. Engineers)
  Parameters of interest to Q.A. Personnel concerns the overall test station quality in its relationship to

products accepted by the test equipment. This data may also identify problems associated with the test operator's procedures that affect test set performance. Test equipment located at vendor sites both in the field and in house, often requires comparison of product acceptance data by Q.A. engineers. Correlation will provide the needed data for this analysis.

CORRELATION STATISTICAL ANALYSIS

The correlation sample must be large enough to limit statistical error to that which is defined by end-item quality assurance requirements. Thus, enough samples are taken from each test equipment to establish a mean value for the given standard. Essentially, the statistical analysis will determine the ability of a given equipment type to maintain a standard of measurement accuracy for established test limits. Again, the relationship of measurement accuracy to test limits is determined by quality assurance requirements. For example, the test limit for a given current measurement test might be 1.5 amps ± 500 milliamps. If the measurement accuracy to test limit ratio is 10:1, then all test equipment means that are within 100 milliamps of each other (± 50 milliamps) are considered to be statistically equal. The test limit tolerance covers a range of 1 amp. Therefore a 100 milliamp measurement accuracy is needed to meet the 10:1 ratio established by quality assurance requirements.

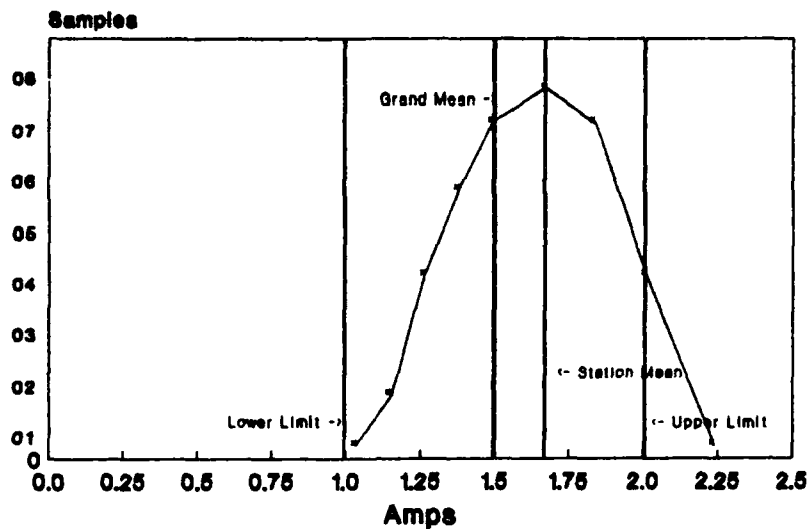# CURRENT MEASUREMENT TEST
Station 1

Figure X

The distribution of correlation test samples for each equipment are expected to be fairly represented in a bell curve (figure X) centered around a nominal value (station mean). The grand mean is an average of individual equipment means. Over a period of time, after many samples, the bell curve may shift. This may be an indication of component or circuit degradation within a given equipment.
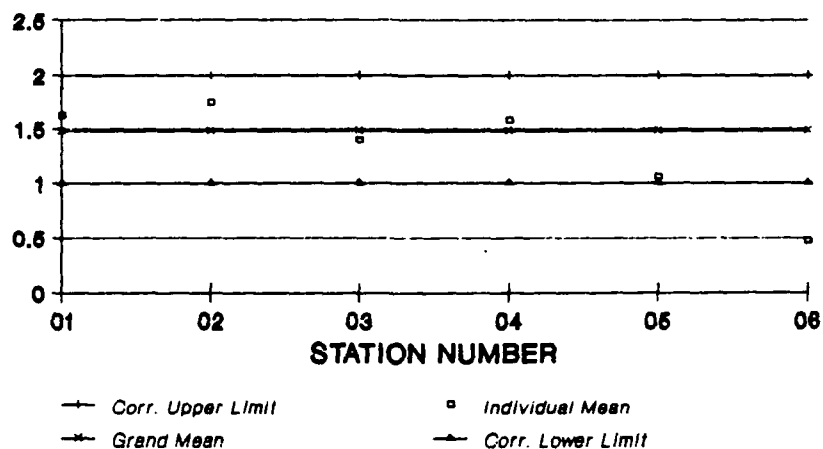
CORRELATION
Current Measurement Test

Figure Y

Correlation data for each equipment are compared to determine individual equipment differences and commonalties (figure Y). Note that the grand mean is determined only by those equipments whose means are within acceptable measurement accuracy.
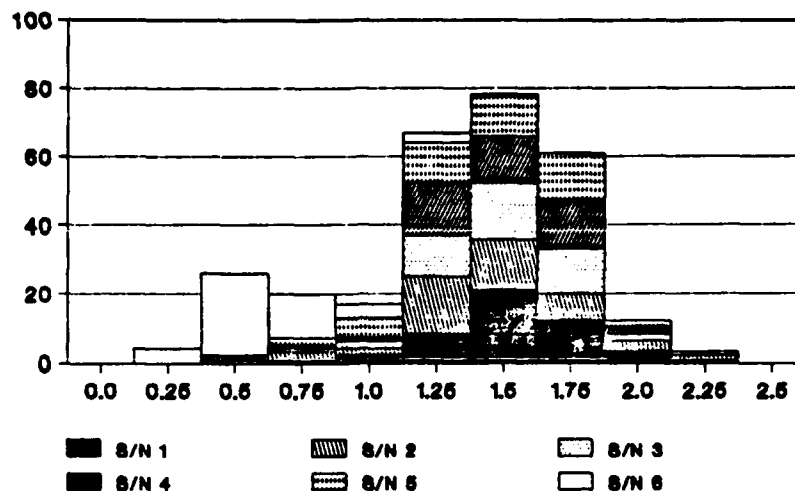
CURRENT MEASUREMENT TEST
Histogram

Figure Z

Histogram analysis (figure Z) illustrates the general trend of data across all the correlated equipments. Again, a bell curve becomes apparent. Changes in this bell curve indicate the commonalties of degradation. This type of information can indicate the need for design or procedural changes that affect all the correlated equipment.

SUMMARY

A correlation program ensures that like test equipment testing like products yield like results.

Correlation provides evidence that test equipment are within specific tolerance and are functionally alike.

Correlation testing is a part of an overall reliability program to ensure consistency of measurements and to assess variabilities among test sets.

No single correlation plan applies in all cases. Therefore, any correlation plan should be tailored to the particular test equipment functionality and end-item

specifications. A team effort is required in evaluating methods, guidelines, procedures, critical parameter, selection, etc.

REFERENCES

* Test Equipment Correlation; Blum, Martin P.
  by: Kearfott Guidance and Navigation
  Reprinted from 1979 IEEE Test Conferences,
  Cherry Hill, New Jersey
  CH1509-0/79/0000-0074

* Test Equipment Correlation Report for the Trident I
  Mark 5 Guidance Program
  by: Kearfott Guidance and Navigation
  on: September 30, 1981
  document number: Y251A168
  contract: N00030-81-C-0088
  Prepared for: Strategic System Project Office (SPN)
  Department of the Navy, Washington D.C. 20376

* Test Equipment Correlation Report for the Trident I
  Mark 5 Guidance Program
  by: Kearfott Guidance and Navigation
  on: September 30, 1988
  document number: Y257C211
  contract: N00030-88-C-0008
  prepared for: Strategic System Program Office (SPN)
  Department of the Navy, Washington D.C. 20376

* Correlation Plan Requirements for SKD System Monitor
  Acceptance Test Set (SMATS)
  by: Kearfott Guidance and Navigation

* Kearfott Guidance and Navigation Internal Memorandums
  by: Senausky, P.V.   on: December 13, 1976

ABOUT THE AUTHOR

John Budzinski is a Senior Field Engineer with Kearfott Guidance and Navigation Corporation, Wayne, New Jersey. Among his accomplishments he has over 13 years of experience involving correlation testing of guidance and navigation test equipment. He is currently working on the TRIDENT II Fleet Ballistic Missile Program.

Before coming to Kearfott, John's responsibilities included data acquisition systems for research and development of rocket and missile propulsion systems at Thiokol Chemical Corporation.

John served 4 years in the United States Air Force maintaining aircraft navigational equipment and flight instrumentation.

John received a Certificate of Merit Award from the United States Navy's Strategic Programs Office in recognition of significant contributions during ten years of service in support of the United States Navy Fleet Ballistic Missile Program.

THIS PAGE LEFT INTENTIONALLY BLANK

A TECHNIQUE FOR THE FORMULATION OF CONSTRAINTS
IN DYNAMIC FILTER STATE EQUATIONS

by

JAMES B. GOSE
PHYSICAL SCIENCE LABORATORY
NEW MEXICO STATE UNIVERSITY

INTRODUCTION

This paper is intended to show a procedure for incorporating constraints into the estimation process. The first part of the paper derives the necessary equations for including the constraints in the estimation process, while the latter half includes an example of such constrants.

DERIVATION

NOTATION – The matrix notation to be employed in this paper is quite ordinary:
Vectors are noted by bold face lower case e.g. x,
Arrays are noted by bold face capitols e.g. A,
Scalars are noted by regular lower case e.g. c.

INDIRECT MEASUREMENTS: From least squares theory, a set of simultaneous equations may be written in the matrix form:

$$z = Bx + e_z$$

wherein: x = dependent variable (to be estimated)
z = measurements
B = coefficient matrix (the Jacobian).
e_z = error in in the measurements.

The least squares estimate may be expressed as:

$$x = (B^t W B)^{-1} B^t W z$$

for $W = P^{-1}$ a weight matrix

and having variance-covariance matrix

$$P = (B^t W B)^{-1}.$$

DIRECT MEASUREMENTS: Similarly for direct measurements, the simultaneous equations may be written:

$$x' = Ax + e_x$$

wherein: x' = external estimates of the solution parameters,
x = variables to be estimated,
A = an identity matrix,
e_x = error in the external estimates.

the least squares estimate for this set of equations may be written:

$$x = (A^t U A)^{-1} A^t U x'$$

for U = a weight matrix
and, again, having variance-covariance matrix:

$$P = (A^t U A)^{-1}$$

for the special conditions that

$$U = P^{-1}, \text{ a diagonal matrix}$$

CONSTRAINTS - conditions may be written in an analogous form as:

$$g = Cx + e_g$$

wherein, again; g = constraint value,
$\quad\quad\quad\quad$ x = the variables to be estimated,
$\quad\quad\quad\quad$ C = a coefficient matrix,
$\quad\quad\quad\quad$ e_g = error values

this latter value is taken as very small, approaching zero, for the constraint case. Again, as before, the estimate of the unknowns may be found as:

$$x = (C^t V C)^{-1} C^t V g, \text{ with weight matrix } V \text{ very large.}$$

CONSIDERING INDIRECT, DIRECT AND CONSTRAINT EQUATIONS SIMULTANEOUSLY leads to a similar equation:

$$z = Bx + e_z$$

wherein: $z = \begin{pmatrix} z \\ x \\ g \end{pmatrix}$

$$B = \begin{pmatrix} B \\ A \\ C \end{pmatrix}$$

$$x = x$$

with solution

$$x = (B^t W B)^{-1} B^t W z$$

wherein now: $W = \begin{pmatrix} W & 0 & 0 \\ 0 & U & 0 \\ 0 & 0 & V \end{pmatrix}$

The solution equation may also be written as:

$$x = \left[(B^tA^tC^t) \begin{pmatrix} W & 0 & 0 \\ 0 & U & 0 \\ 0 & 0 & V \end{pmatrix} \begin{pmatrix} B \\ A \\ C \end{pmatrix} \right]^{-1} (B^tA^tC^t) \begin{pmatrix} W & 0 & 0 \\ 0 & U & 0 \\ 0 & 0 & V \end{pmatrix} \begin{pmatrix} z \\ x \\ g \end{pmatrix}$$

Upon reducing this array equation we arrive at a Least Squares form for a unified estimation process:

$$x = (B^tWB + A^tUA + C^tVC)^{-1}(B^tWz + A^tUx + C^tVg)$$

with error variance-covariance matrix:

$$P = (B^tWB + A^tUA + C^tVC)^{-1}$$

These last two equations are the matrix formulation of a weighted average of the three types of estimates.

A RECURSIVE FORMULATION The recursive formulation of the Least Squares require that the A matrix of the previous equations be an identity matrix. For which case, one may write:

$$x = x' + (B^tWB + U + C^tVC)^{-1}[B^tW(z - Bx') + C^tV(g - Cx')].$$

EXAMPLE

While examples of indirect measurements and direct estimates from the integration of a differential equation are relatively available; an example of a constraint condition imposed from the physics or mathematical consideration is by no means easy to find. The example chosen here is one arising from work in the field of meteorology. It is chosen principally because it has a defineable constraint condition.

The direct measurements are measurements of atmospheric pressure taken from three different instruments. The differential integration integrated to provide an estimate is the integral of the pressure lapse rate. The constraint conditions are that the pressure to temperature ratio for all instruments should be equal, as they are all in the same volume of air.

Presented here are the residuals from the direct measurement least squares estimate on Figure 1.; the constraint estimate condition residuals in Figure 2.; and finally the residuals from the unified estimate shown in Figure 3.

The least squares estimate shows a minimum bias about each time point.

The constrained estimate residuals show an overall systematic bias; however, these also emphasize the curious error at TIME = 300.

The unified estimate residuals show a more reduced systematic bias than

the constrained estimate residuals, but considerably amplify the occurrance at TIME = 300.

CONCLUSION

The example well illustrates the usefullness of constraints in a Kalman filter algorithm for identifying systematic bias and highlighting an anomolous event in the data.

It should be noted that the occurrence at TIME = 300 was in fact an inflection in the pressure lapse rate due to passage of the sensors thru a mountain wave. One of the sensors utilizing a strong Kalman filter type smoothing to remove noise, also removed the effect of the mountain wave on its pressure data outputs.

BIBLIOGRAPHY

Mikhail, E.V.; Observations and Least Squares; 1976; IEP

Searle, S.R.; Matrix Algebra Useful for Statistics; 1982; John Wiley and Son Inc.

Gose, J.B.; A cause of Divergence in the Kalman Gain Equation; 1987;Thirteenth Biennial Guidance Test Symposium Proceedings Vol. I; AD-TR-87-08 Vol.I; HAFB, NM.

Guard, K.; Estimation of Variane in a Kalman Filter, Doctorial Dissertation; 1972;University of Delaware.

Aoki, M. and Huddle, J.R.; Estimation of the State Vector of a Linear Stotastic System with a Constrained Estimator; IEEE Trans. on Automatic Controls, Vol. AC12, No. 4; Aug. 1967
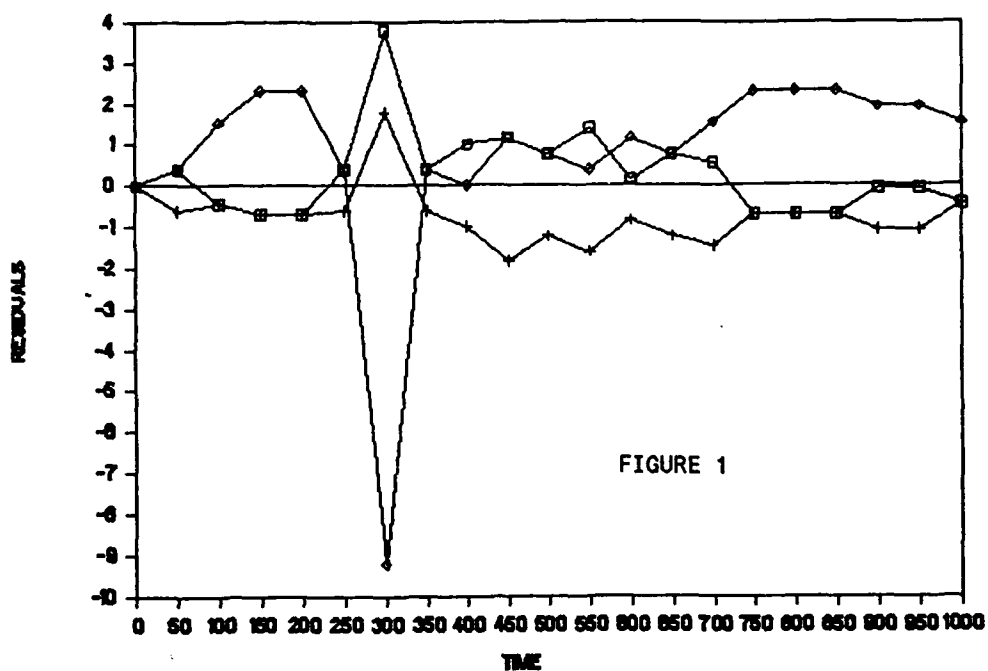
MEASUREMENT STATE SOLUTION RESIDUALS

FIGURE 1
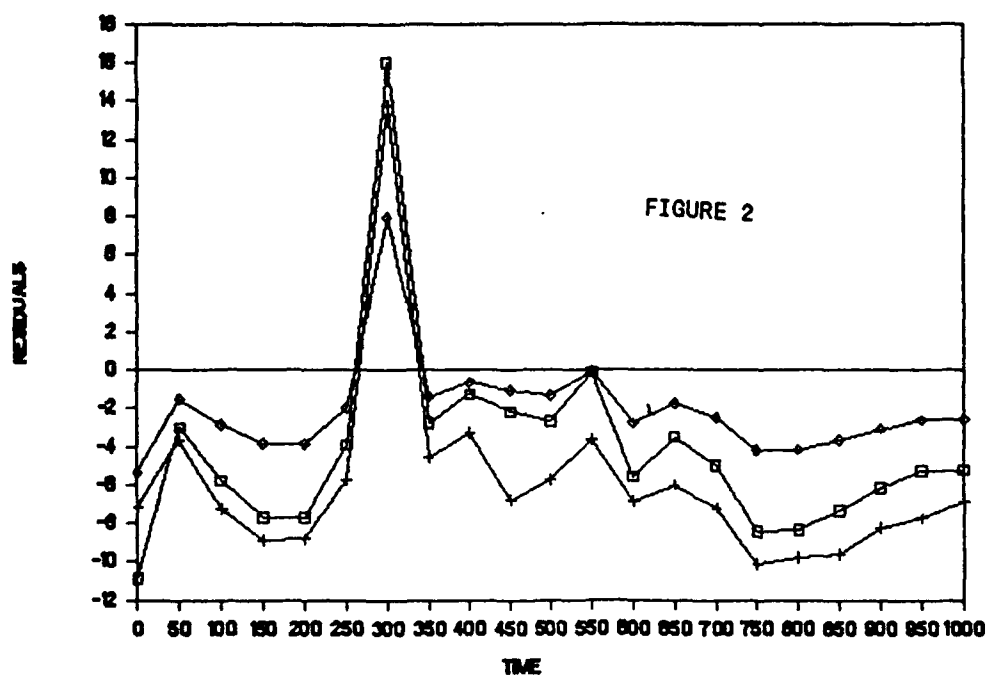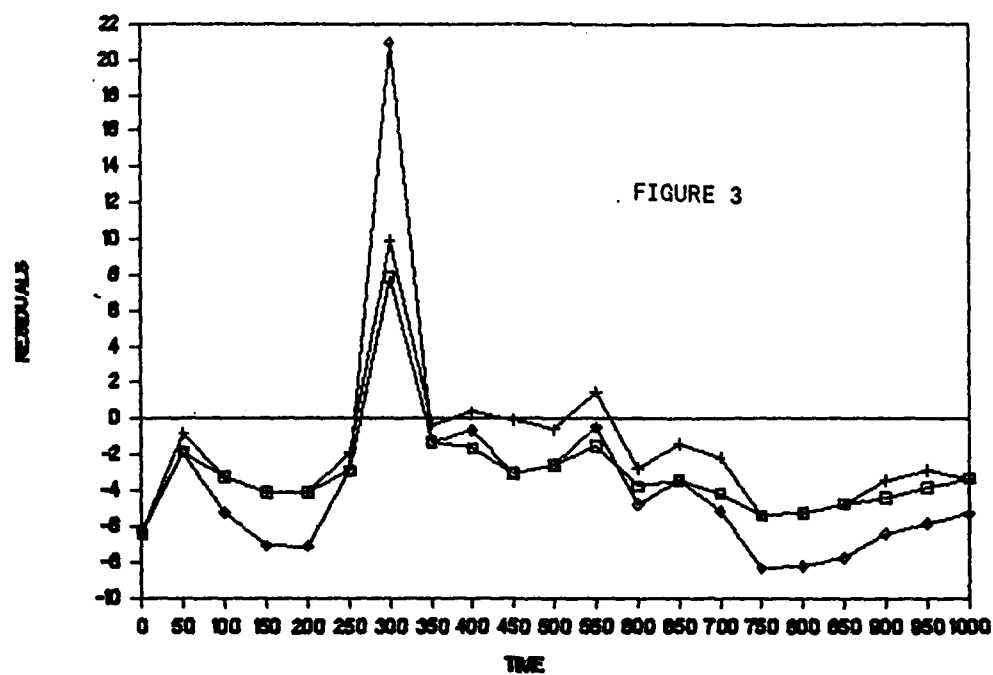
CONSTRAINED SOLUTION RESIDUALS

FIGURE 2

UNIFIED ESTIMATES RESIDUALS

FIGURE 3

Multirate Controller Realizes Three

Degree-of-Freedom Stabilization

of a Seismically Stable Platform

October 1989

Prepared by:

Randy Goucher
Andrew Ardaman
Richard Owen*

Applied Technology Associates, Inc.
1900 Randolph Road, SE
Albuquerque, NM 87106
505-247-8371
FAX 505-768-13781

Presented to:

Fourteenth Biennial Guidance Test Symposium
Department of the Air Force
Headquarters 6585th Test Group (AFSC)
Holloman Air Force Base, New Mexico 88330-5000

*Now with SBE Engineering
5301 Central Avenue, Suite 1500
Albuquerque, NM 87108
(505) 268-0405

Abstract

As the accuracy and noise performance of inertial instruments and navigation systems continue to improve, so must the capabilities of the test facilities used to characterize them. The role of the Central Inertial Guidance Test Facility (CIGTF), part of the 6585th Test Group at Holloman AFB, is to provide the Air Force with such a test capability. The goal of the Seismically Stable Platform (SSP) contract, sponsored by CIGTF, is to develop and demonstrate the technology necessary to provide an ultra-quiet test platform suitable for testing next generation inertial instruments and systems. This requires that the SSP be stabilized in both translation and rotation over the bandwidth of 0.001 Hz to 100 Hz. The translational acceleration seen on the platform must be below 10^{-8} gs and the tilt environment must be below 10^{-8} radians over this bandwidth. This type of stabilized testbed will be an integral part of more advanced test facilities planned to support characterization of systems and instruments through the year 2010. Applied Technology Associates, Inc., (ATA) made substantial progress toward realizing this capability during 1988.

Introduction

The SSP provides a low motion test environment by isolating the test package from seismic inputs and providing active cancellation of direct disturbances. Dominant low frequency seismic inputs, known as microseisims, arise from wave action on the coasts of the continent. These forces propagate through the earth's crust and give rise to both vertical and horizontal accelerations in the 0.1 Hz region of the bandwidth. In the Holloman AFB area these acceleration levels are on the order of several tenths of a micro-g. High winds and rain generate ground-coupled disturbances at higher frequencies. Cultural activities, such as traffic on roads and highways, machinery, and aircraft activity generate higher frequency disturbances that also couple through the ground to the test site. In addition to seismic inputs, acoustic characteristics of the test chamber can cause unwanted motion on the platform. Air flow resulting from environmental controls and equipment cooling acts directly on the platform and generates motion in the frequency range above 10 Hz. The platform motions induced by these direct disturbances are typically larger than those generated by the seismic inputs.

A variety of acoustic treatment methods are available to reduce the direct disturbances mentioned above. Passive systems can be used to attenuate both seismic and direct disturbances. Passive isolation techniques to attenuate seismic disturbances include the use of massive concrete piers resting on crushed granite, or a similar material. The pier typically extends well below the foundation level of the building and is not coupled to the floor system. The test platform then rests on the isolated pier. Additionally, a pneumatic isolation system may be used to further reduce seismic inputs from the pier to the test platform.

While passive systems are effective in reducing induced motions on the test platform, residual motions can still exceed the levels required for testing next generation instruments. However, an active stabilization system can be used in conjunction with the passive techniques to reduce these motions to acceptable levels.

System Components

Figure 1 shows the major components that make up the SSP system. The large isolated concrete pier provides the base for the platform. The platform consists of a two-mass steel structure. The lower, or secondary mass, is supported by four pneumatic isolators which set on the pier. The upper, or primary mass, is also supported by four pneumatic isolators which set on top of the secondary mass. This arrangement provides a dual-stage passive isolation system to attenuate seismic disturbances to the primary mass, which would support the test package. Note that this portion of the system does not act to reduce the motions induced by direct disturbances.
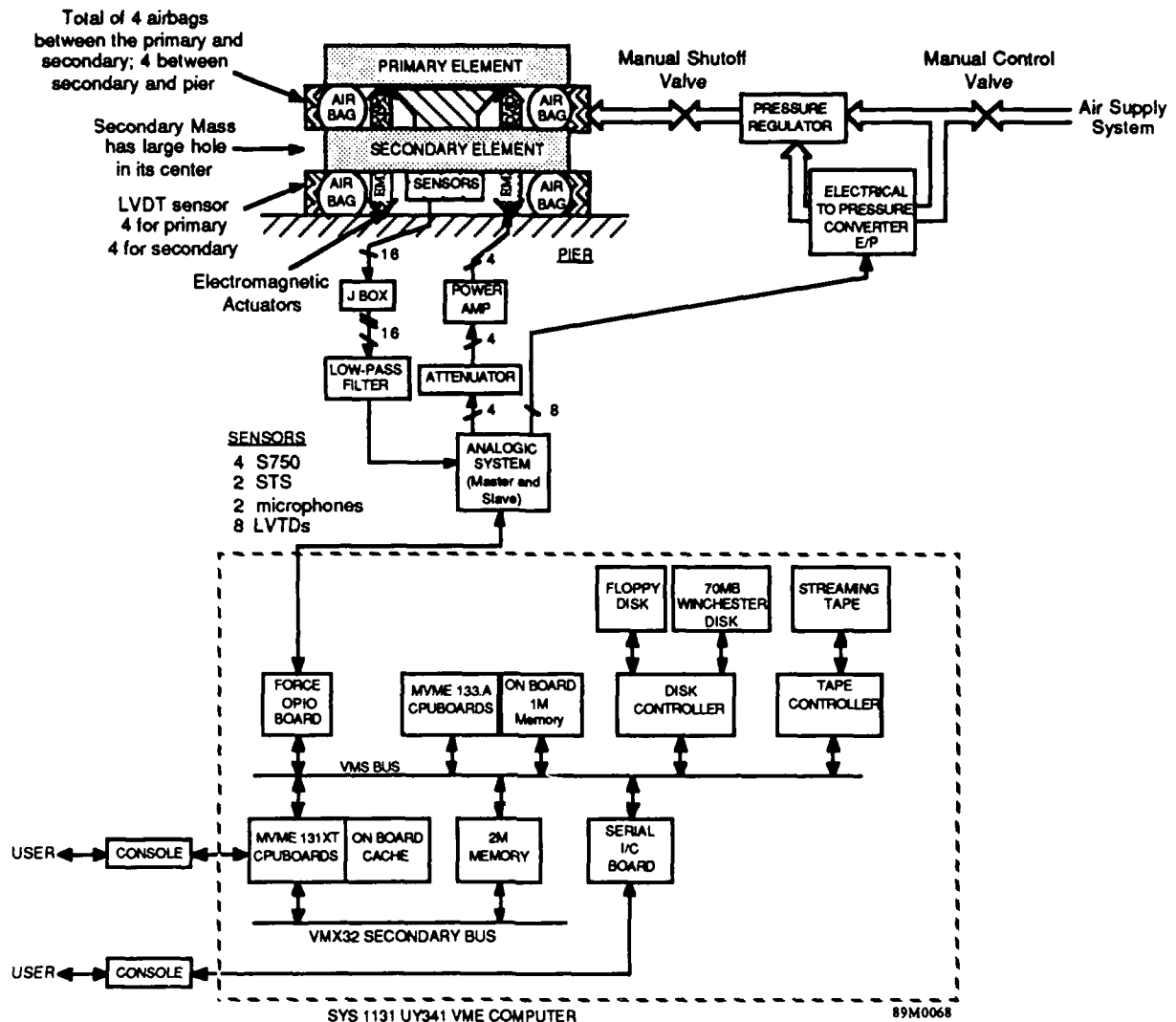
Figure 1. Major Components of the SSP System

The platform is instrumented with a variety of sensors that measure the motion of the primary mass. An array of horizontal and vertical seismometers provides acceleration measurement over the desired bandwidth. Seismometers were chosen because of their excellent noise performance. Linear variable differential transformer (LVDT) sensors provide relative displacement measurements between the seismic pier and the secondary mass, as well as between the secondary and primary masses. Rotational sensors with acceptable noise performance for use in the control system could not be identified. Therefore, the linear sensors are used as inputs to the control computer, which calculates angular motion based on these inputs and the geometry of the sensor layout.

Four electromagnetic (EM) actuators, which are attached to the primary mass, allow stabilization forces to be applied to the platform. The actuator control signals from the control computer are amplified by a set of power amplifiers to provide the necessary current to drive the EM actuators. Eight electrical-to-pressure (E/P) transducers interface the control computer to the pneumatic system. Control signals to the E/P transducers allow the primary and secondary masses to be raised to the proper operating point by the

computer. Electrically operated valves in the pneumatic lines are then closed to float the two masses, while control commands to the EM actuators stabilize the primary mass.

The sensor outputs are signal conditioned and digitized by a data acquisition subsystem and then input to the control computer. A VME-bus based multiprocessor system using Motorola 68020 CPUs is used to provide the real-time computational resources to implement the control algorithm. This algorithm is implemented as a series of digital filters. The filter outputs are sent to the data acquisition subsystem for conversion to analog form and conditioning. The signals are then amplified to drive the EM actuators, which stabilize the platform.

Controller Development and Implementation

The current phase of the SSP contract calls for the implementation and demonstration of a three degree-of-freedom (DOF) controller. This controller must stabilize the vertical axis and the two horizontal tilt axes of the primary mass. The next phase of the contract will call for the implementation of a full six DOF controller which adds stabilization of the remaining horizontal translation axes and the azimuth axis.

ATA's approach to solving the three DOF controller problem was to first design and implement a single DOF controller to stabilize the vertical axis and then add loops to stabilize the horizontal tilt axes. A block diagram of the vertical axis controller is shown in Figure 2. The compensator acts to reduce the resonant peak of the platform at 1 Hz, caused by the platform and pneumatic system dynamics. The notch filter acts to reduce a 150 Hz platform resonance that causes instability in the controller at high gains. The stretcher and blender filters act to provide a single estimate of the platform vertical acceleration based on multiple and dissimilar sensor outputs. As Figure 2 shows, the frequency responses of the Strekeisen STS seismometer and the Teledyne-Geotech S-750 cover different frequency bands, with a region of overlap in the 0.03 to 5 Hz band. The output of the vertical STS is fed to the stretcher which acts to move the low frequency corner of its response from 0.05 to 0.01 Hz (stretching its response). The outputs of the four S-750s are first averaged and then input to the blender filter. The blender combines the S-750 and STS outputs, taking into account the sensor dynamics at their corner frequencies, to provide a single velocity (integral of acceleration) estimate over the desired frequency band. This provides a Type 1 control loop with respect to acceleration.

This controller was implemented using a Motorola SYS1131 computer system. The basic system provides a 12-slot VME bus chassis containing a 16 MHz 68020/68881 processor with 2 Mbytes of main memory and 16 Kbytes of cache memory. A 71 Mbyte hard disk, 40 Mbyte cartridge tape, and 360 Kbyte floppy provide storage and backup capability. Serial and parallel ports provide connections for terminals and printers. The SYS1131 comes configured with the UNIX System V operating system, which was used for all software development. To provide more capable real-time support, ATA added Emerge Systems' real-time UNIX (RTUX) executive software to the system. A FORCE OPIO card was also added to the SYS1131 to provide a 16-bit parallel I/O port for communication with the data acquisition subsystem. This card also provided programmable timers that were used to generate the required timing interrupts to synchronize the controller operations.

The controller sequencing proceeded as follows: the programmable timer generated a VME-bus interrupt at the desired sample rate (every 2.5 msec for the vertical controller). The controller software was entered in response to this interrupt, suspending all UNIX system activity. The vertical S750 and STS sensors were sampled using the OPIO card/Analogic hardware. The controller computations associated with the current sample were then performed, resulting in a set of actuator commands. These commands were sent out the OPIO/Analogic path to the EM actuators. The controller computations associated with past samples were then performed in preparation for the next cycle. The interrupt service routine was then completed, returning processor control to UNIX tasks needing attention, until the next interrupt from the timer. Figure 3 shows the vertical axis stabilization performance achieved with this controller.
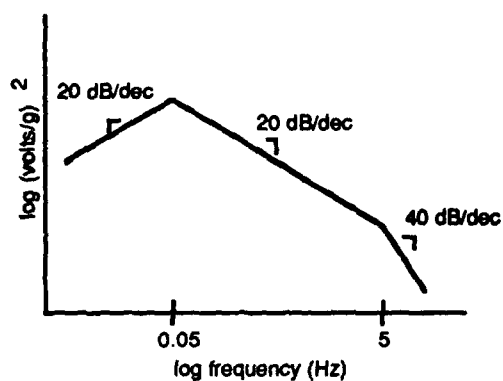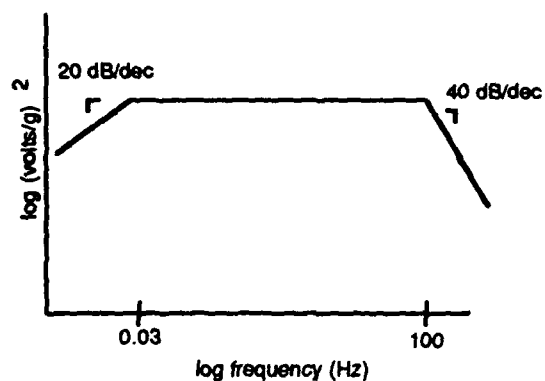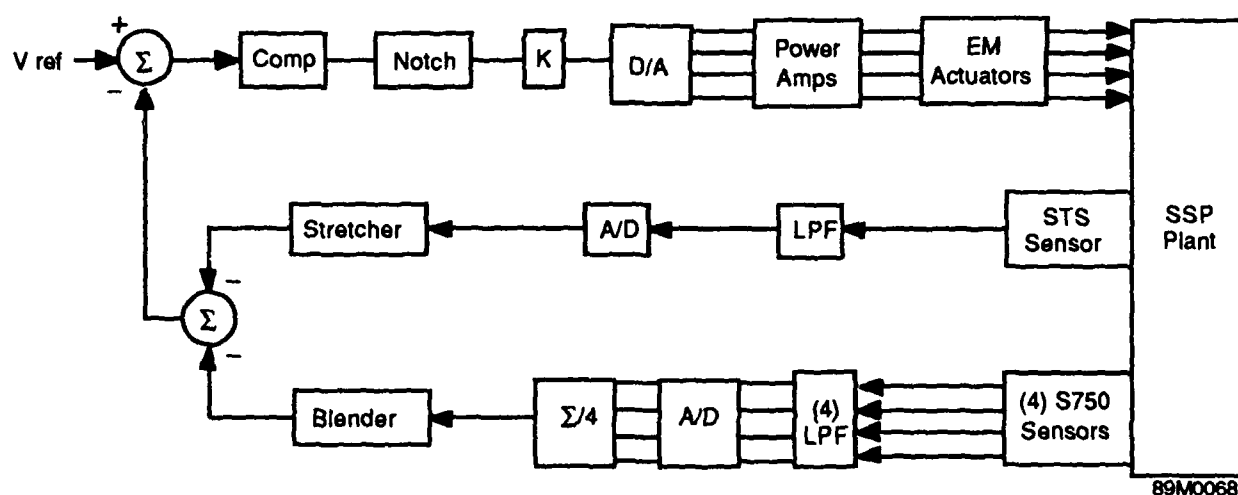
Figure 2. Sensor Frequency Response and Vertical Axis Control Loop Block Diagram. The stretcher and blender filters combine the sensor signals so that the result is an acceleration term which is nulled.
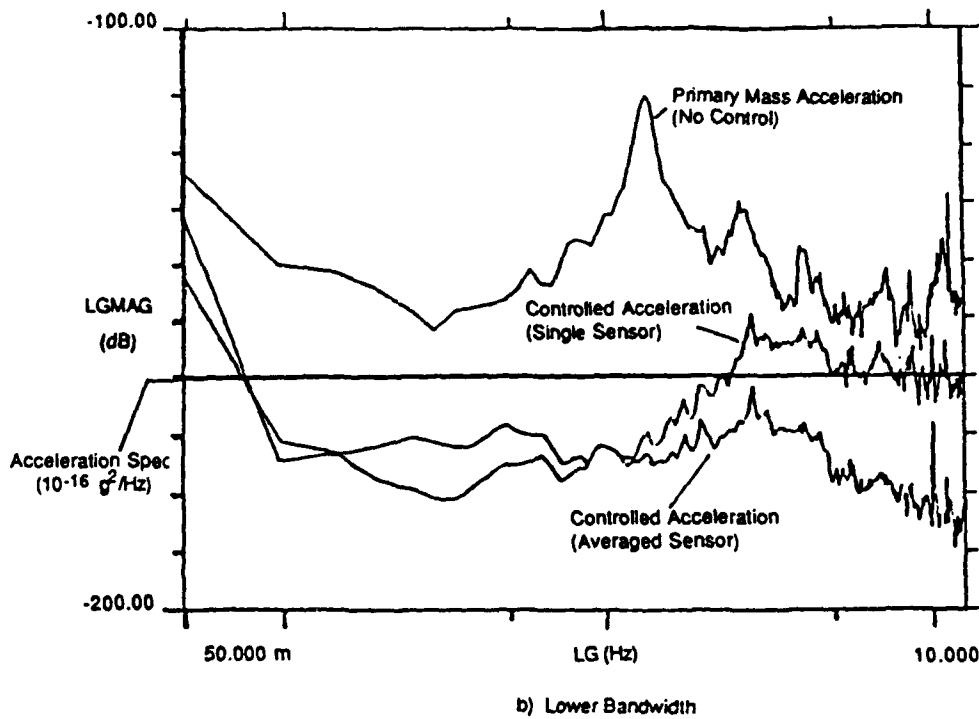
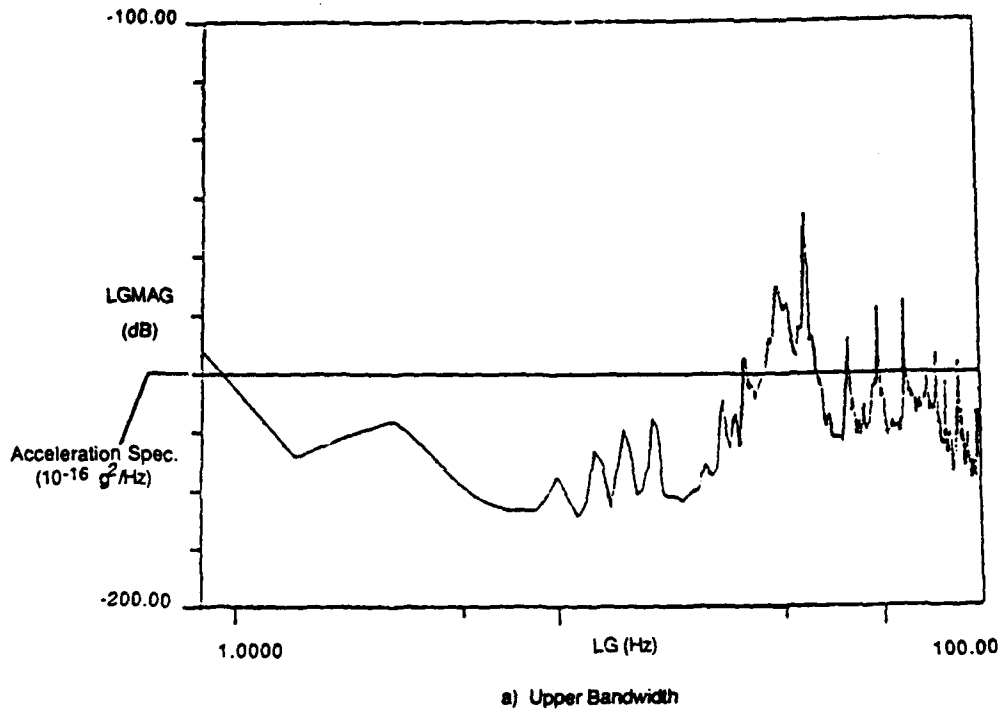a) Upper Bandwidth

b) Lower Bandwidth

Figure 3. Multirate Controller Performance Based on Averaged S750s (Semi-Quiet Environment)

Timing measurements made to characterize the resource utilization of this controller indicated that two problems would arise in adding the tilt control capability for the three DOF controller. First, the execution time of the controller would not allow for the additional computations needed to compute the tilt algorithms. This problem had been anticipated in the design and would be solved by adding a second 68020/68881 processor card to the system. Secondly, the sampling time required to input the additional sensor data needed for the three DOF controller would introduce an unacceptable delay in the control cycle, reducing the controller bandwidth. This problem would become even more critical in going to the six DOF version.

To overcome the I/O problem, ATA decided to use a multirate sampling technique based on the frequency response of the control sensors. Rather than sampling all of the sensors every control cycle, the low frequency sensors would be sampled in multiples of the control cycle. Like sensors would be sampled in the same control cycle to maintain phase relationships between them. This approach had the added benefit of reducing the number of digits needed to represent the control coefficients associated with the lower frequency sensors. Because the coefficients are a function of the sample rate, this reduces the likelihood of roundoff errors and instability. While design of the three DOF controller was underway, the one DOF controller software was modified to implement the multirate sampling and to incorporate a second processor into the system. Testing of the vertical controller with these design changes was successful and showed only a minor difference from the original controller's transfer function at the Nyquist frequency.

The implementation of the three DOF controller involved adding the additional sensor inputs, the tilt compensators, and a set of geometry computations to compensate for the off-axis locations of the sensors and actuators. Preliminary testing of the controller has shown acceptable performance above 10 Hz. Below this frequency, the controller needs to be refined to account for horizontal acceleration effects. This work is expected to be completed this summer.

To the best of our knowledge, the results of this effort represent the state-of-the-art in active stabilization control performance. The development of this capability has applications in a variety of industries. It is also being considered by NASA for use in space-based materials processing. ATA will be leading the development of this technology in the future.

THIS PAGE LEFT INTENTIONALLY BLANK

SMALL COMMON INERTIAL NAVIGATION SYSTEM (SCINS) DEVELOPMENT STATUS AND TEST RESULTS

A Technical Paper
For The Fourteenth Biennial
Guidance Test Symposium
October 3-5, 1989
Central Inertial Guidance Test Facility
Holloman Air Force Base, New Mexico

By Michael J. Hadfield, Sr. Project Staff Engineer
and Alan J. Hasselbring, RLG Systems Engineer
Telephone Number: 813/579-6604 or 6642

Honeywell

ABSTRACT

Major program and system decisions by DoD agencies, and thorough evaluation testing by CIGTF, have led to widespread introduction of Ring Laser Gyro inertial systems in the mid-to late 1980s. The standard INUs per SNU 84-1 and FNU 85-1 are proving their value to user programs, and are expected to continue doing so well into the 1990s. However, needs are also developing for smaller, lighter, lower power, and lower cost RLG INUs. In CIGTF '87, the commonality virtues of the current standard INUs were presented and discussed.

This paper addresses the newly emerging needs and the ongoing preference for standardization and commonality. It introduces the 20 lb class, 60-75 W, 500-700 in^3 Honeywell H-764 SCINS, with performance initially in the 2.0–5.0 nm/hr class, and growth potential to SNU 84-1 levels. This system has been under development during the past two years and will be ready for flight test demonstration testing in late '89. With mature MTBF levels of 2900 hours (AUF) to 7000 hours (AIT), the H-764 SCINS should continue the tradition of high reliability in RLG systems.

Functional descriptions and performance features are discussed, along with results of laboratory testing from the 1988-89 efforts at Honeywell. Multifunction aspects of the H-764 SCINS design are also presented since its use can vary widely from an AHRS, to a full-up aircraft navigator, to a land navigation system for ground combat vehicles. Some of the design tradeoffs and unique design features of the evolutionary H-764 SCINS concept are also covered. Future plans conclude the scope of the paper.

INTRODUCTION

Honeywell has continued the evolution of Ring Laser Gyro (RLG) Inertial Navigation Systems (INSs) and now introduces the H-764 Small Common Inertial Navigation System (SCINS). The H-764 SCINS is designed to meet small, lightweight, low-cost applications for helicopter and fixed-wing aircraft platforms with Attitude Heading Reference System (AHRS), full navigation, and Radar/EO sensor stabilization/motion compensation capabilities. The H-764 is also adaptable to land vehicle applications. Growth provisions include the incorporation of an integrated, closely coupled Global Positioning System (GPS) receiver.

The current model of SCINS incorporates instruments and circuit card assemblies (CCAs) that are in high volume production, thus benefiting substantially from the economy of scale inherent in on-going programs with established performance capabilities. The SCINS is designed to benefit from the Honeywell RLG systems that have demonstrated high reliability in millions of hours of commercial airline service, and thousands of hours of military service. They are standard equipment on the commercial Boeing 757, 767, 737-300 and Airbus A320, as well as most business aviation aircraft. In the military applications, the parent systems to SCINS include the Honeywell Military Laser Inertial Navigation System (MIL-LINS) RLG H-770 systems for the F-15 A through E upgrade, and the H-423 INU for the SNU 84-1 Form, Fit, and Function (F^3) Standard Inertial Navigator program. The H-764 SCINS is also related to the H-726 Dynamic Reference Unit used in the U.S. Army Modular Azimuth Position System (MAPS) and the H-700-3A used in the Army Tactical Missile System (ATACMS) FSD and Production programs.

RLG systems are displacing conventional gyro systems throughout the world for many reasons, including:

- Their demonstrated reliability and large production base offer the highest availability as well as the lowest acquisition and life cycle costs.

- Their heaterless design provides "instant-on" reaction time from "power on" and fully rated performance over the military operational temperature range without the need for temperature control.

- Their performance is consistently good over a variety of applications and for many years of operational use.

These benefits are inherent in the new H-764 SCINS, and are shown in Table 1 along with other key features for present and future H-764 models.

H-764 SCINS OVERVIEW

The 1991 production model H-764, shown in Figure 1, uses the same Honeywell GG1328 RLG and Sundstrand QA2000 accelerometer as used in the ATACMS Inertial Guidance Unit (IGU). The H-764 prototype line replaceable unit (LRU) currently weighs 28 lb, but a 1991 production unit goal of 23 lb has been established. Package size is nominally a 3/4 ATR short (14 in. length for the prototype and 12 in. for the production model). Production unit power consumption is 75W of 28 Vdc power. The unit operates without cooling air throughout a full range of MIL SPEC environmental variations.

Table 1. H-764 SCINS Features and Benefits

	1991 Production	1992-93 Growth	Units
• Performance			
Position Accuracy	2.0 – 5.0	0.8 – 1.0	nmi/hr CEP
Velocity (per axis)	11.0	<3.0	fps, rms
Heading	0.2	0.05	deg, rms
Roll and Pitch	0.15	<0.05	deg, rms
• Reaction Time			
GC Align	8.0	<8.0	min
Stored Heading Align	1.5	<1.0	min
• Reliability — MTBF			
Fighter	2000	2900	hr
Helicopter	3000	4000	hr
Transport/Cargo	4000	>6500	hr
• Size (3/4 ATR Short)	7.5x7.5x12	7x7x11	inches
• Weight (<1/2 SNU 84-1)	23	<20	lbs
• Power (No cooling air needed)	75	<70	watts
AND ... LOW COST FOR ACQUISITION AND LIFE CYCLE!			

Near-term navigation performance is in the 2.0 to 5.0 nmi/hr CEP, category, with a three-to four-year goal of better than 1.0 nmi/hr, CEP. Predicted mature MTBF of the production units in high volume usage is 2884 hours in the Airborne Uninhabited Fighter environment, 3989 hours in the Airborne Rotary Wing (helicopter) environment, and 6531 hours in the Airborne Inhabited Transport environment.

Although designed initially to provide an Attitude Heading Reference System capability, the H-764 now also has resident software and functions to provide a total navigation capability. Its operating modes include:

- Alignment

- Navigation (pure inertial)

- Airborne Alignment and Aided Navigation (future option)

- Ground Test

Future growth can include at-sea align capability.

Primary signal/data interface with other avionics is via dual MIL-STD-1553B multiplex data buses, but a variety of other interfaces can be provided to accommodate customer application needs.

Extensive Built-In Test (BIT) capability, consistent with that used in MIL-LINS type systems, is included in the H-764 hardware and software mechanizations.

Honeywell pioneered the two technologies brought together in the H-764 — strapdown inertial system products, and the ring laser gyro. In over 26 years of engineering development and production effort, the RLG has been converted from a laboratory development to a practical, producible inertial sensor.
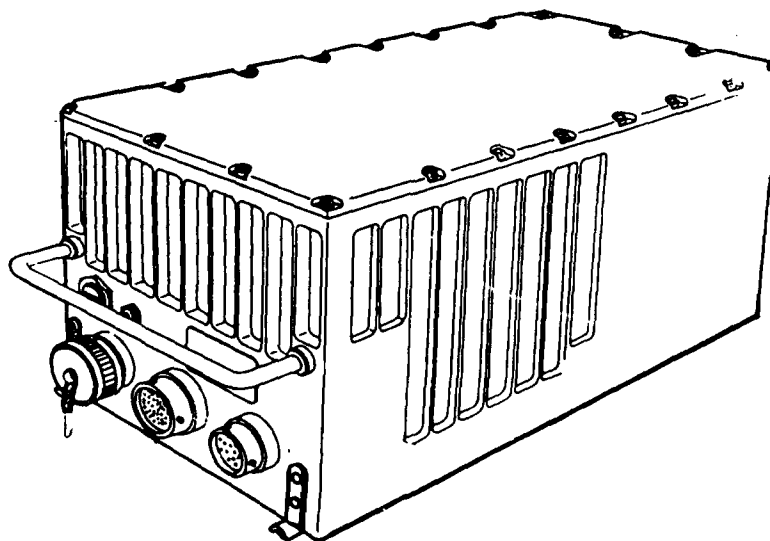
0389-39

Figure 1. SCINS Unit — The Small, Lightweight, Low Cost SCINS

The Honeywell GG1328 RLG is the heart of the H-764 SCINS. Solid-state construction, high accuracy rate sensing, and repeatability of performance are inherent characteristics of this device. Proven reliable in all types of aircraft and missile environments, the Honeywell RLG has demonstrated itself to be a rate sensor highly suited for strapdown inertial system mechanizations. With the performance accuracy of a strapdown system directly related to the speed of algorithm processing, Honeywell has combined the simplified system hardware design offered by the RLG with the features of the low cost, high speed, solid-state MIL-STD-1750A microprocessors available today.

In inertial systems, the RLG offers a singular advantage not available in electromechanical rate sensors — fast, "instant-on" reaction. The RLG does not require long thermal warmup before rated performance is available. The solid-state RLG applied in the Honeywell H-764 takes advantage of the simplified electronic needs of the strapdown inertial design and the "instant-on" features of the RLG to provide an advanced and practical inertial system design approach.

The H-764 SCINS evolution from the H-700-3/Army TACMS IGU and the H-423/USAF standard INU is illustrated in Figure 2. To further this evolution, in addition to the 1991 production system capabilities, we have a planned H-764 product improvement to a smaller, GG1320 RLG-based system, weighing less than 20 lb., and using less than 70W, with a goal of <1.0 nmi/hr performance.

GPS Compatibility. While the H-764 SCINS currently has no embedded GPS, we have implemented (and verified by test) both GPS augmentation and embedded GPS/INS on previous programs. In 1987-88, Honeywell successfully van tested an integrated INS/GPS using the GG1328, and, in 1982, we were the first to flight test an INS/GPS-aided configuration. We therefore have the potential for future INS/GPS integration, either with embedded or stand-alone GPS.
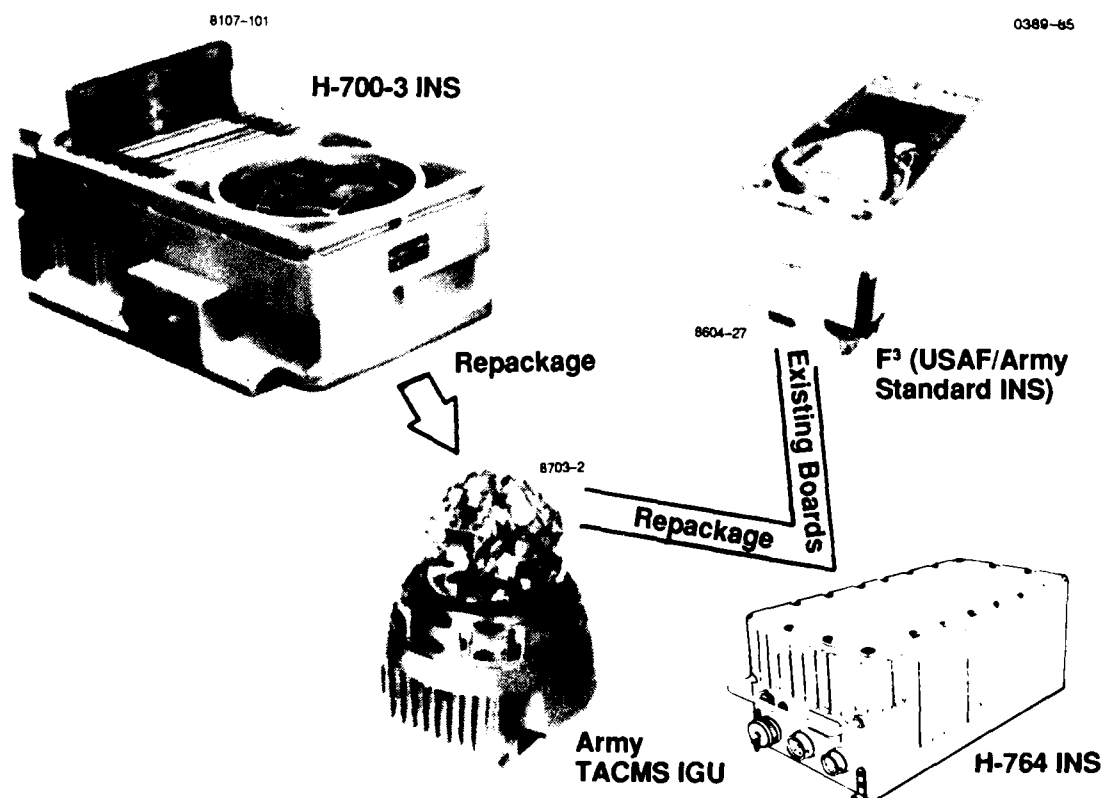

Figure 2. H-764 SCINS Evolution

SYSTEM HARDWARE DESCRIPTION

As stated above, the H-764 SCINS is an RLG-based strapdown inertial navigation mechanization. The strap-down sensor assembly (SSA) is made up of:

- Three mutually orthogonal Honeywell GG1328 RLGs

- Three orthogonal Sundstrand QA2000 single axis accelerometers

- High voltage power supply (HVPS)

- Three identical gyro current control/gyro readout boards

- Gyro drive board

- Temp-Cal programmable read-only memory (PROM) board

- Aluminum alloy component mounting block.

The SSA Electronics Cards are shown in Figure 3. The SSA is housed in a 7.50-in wide x 7.50-in high x 12.00-in long aluminum chassis that also includes gyro and accelerometer electronics, two MIL-STD-1750A digital processors and memories, input/output (I/O) electronics, and a low-voltage power supply (LVPS). By incorporating large-scale integrated circuit (LSIC) technology and other miniaturization in the future, we can achieve a Line Replaceable Unit size goal of 7.00-in x 7.00-in x 11.00-in.

For ease of maintenance, full access to the LRU's plug-in replaceable assemblies is provided via removal of the top cover. Figure 4 shows the individual CCAs that plug into the chassis. These are common with the H-423/F3 and H-770/F-15 INSs. They are:
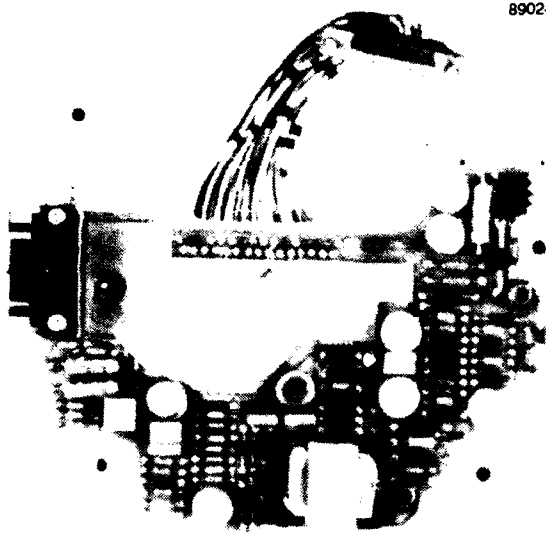
- Gyro electronics

- Accelerometer electronics

- Analog-to-Digital (A/D) pulse accumulator module (PAM) card

- Inertial processor (IP)

- Navigation processor (NP)

- 1553 MUX bus Interface.

The H-764 low voltage power supply is similar to the H-423 LVPS. The internal architecture of the H-764 system is shown in the Figure 5 block diagram.

Gyro Electronics (A1). The gyro electronics CCA provides all electronic input and output interfacing functions for the three RLGs, with the exception of the dither motor drive circuits and the path length control (PLC) differential drive stages which are contained in the SSA. Circuit functions contained on the A1 CCA are readout and the balance of path length control circuitry.
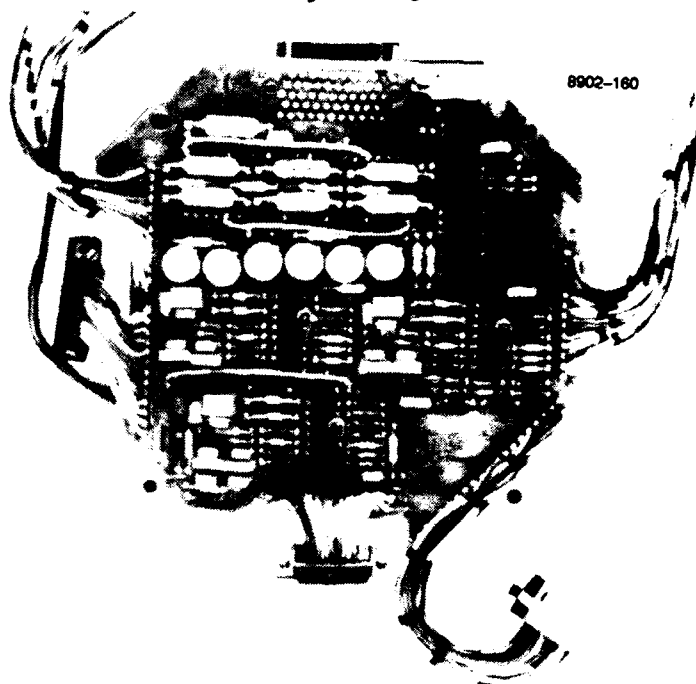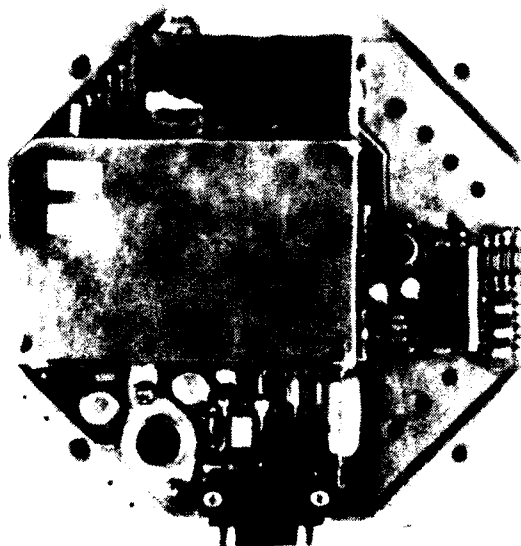
Discharge Current Control

8902-163

Gyro Drive

8902-160

High Voltage Power Supply

8902-165

Temp/Cal Prom
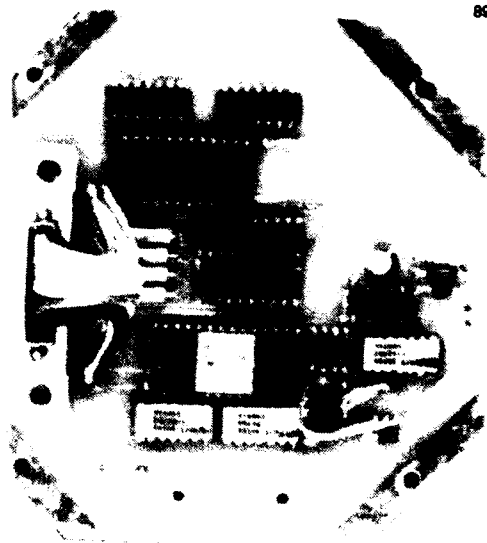
8902-161

Figure 3. SSA Electronics Cards
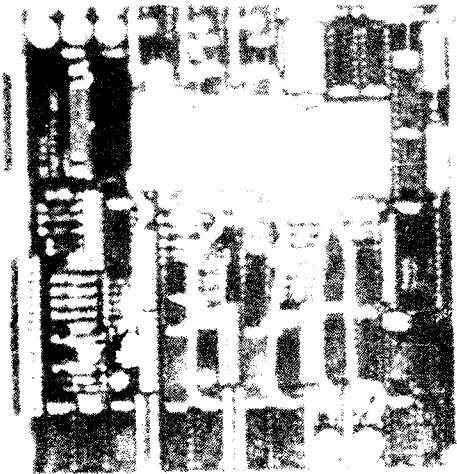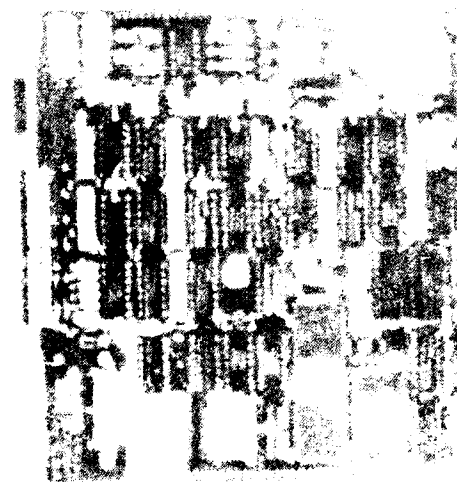
0389-92
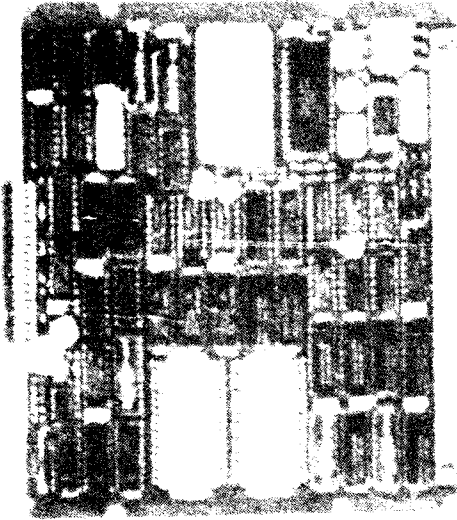
8902-167

A/D PAM

8902-169

1553 MUX

8902-173

Accel Elex

8902-17

Nav. Proc.

8902-177

Gyro Elex
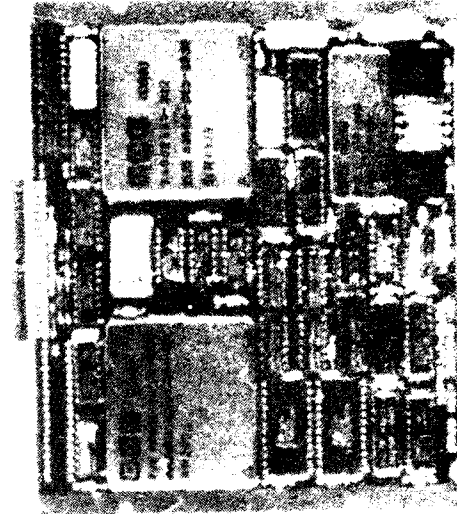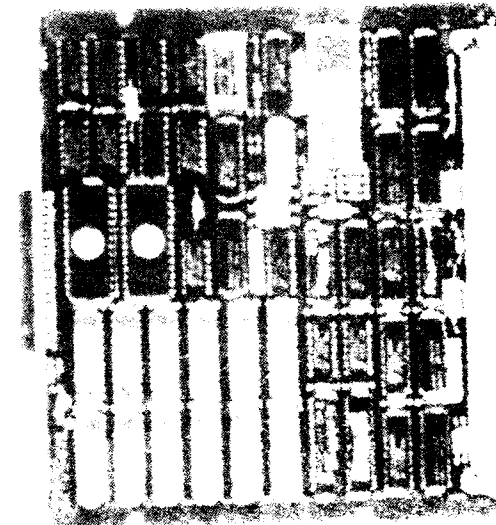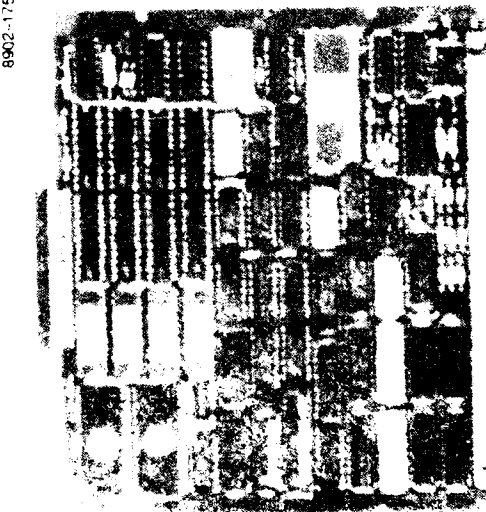
8902-175

Inertial Proc
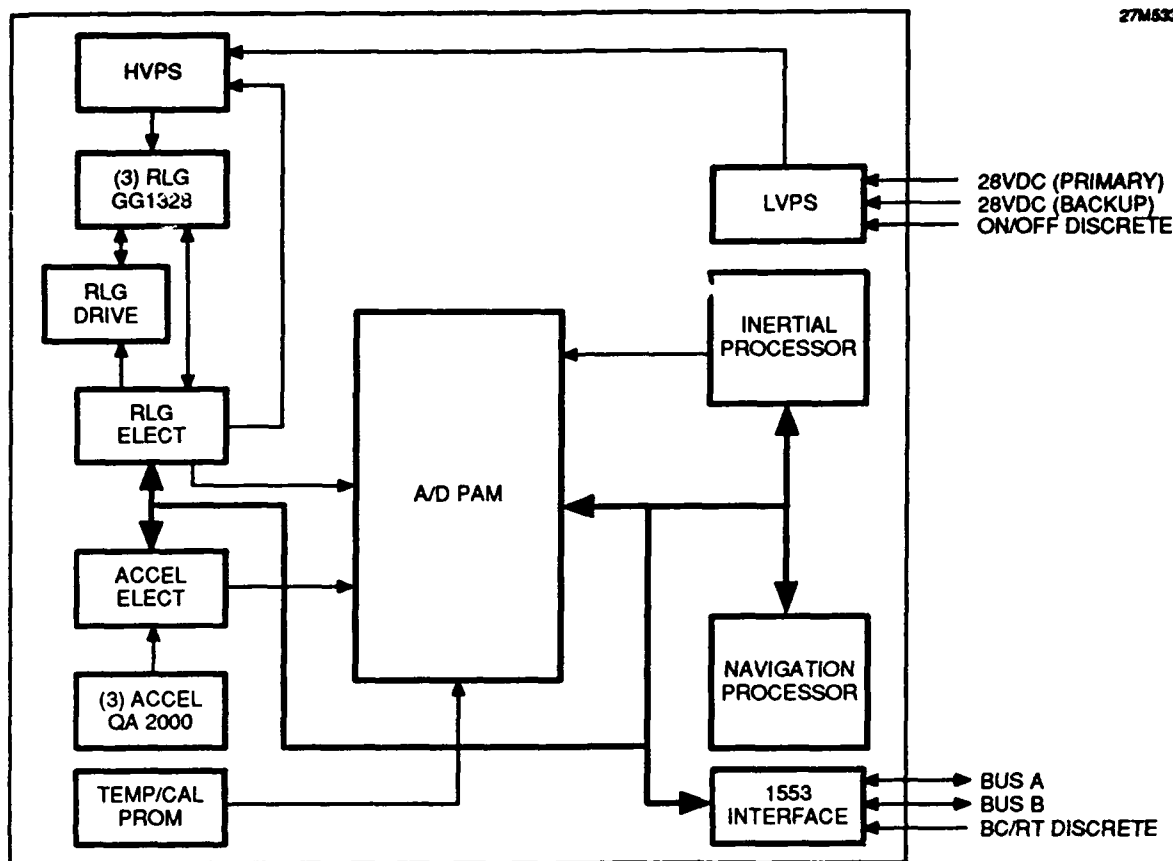
Figure 4. Common Electronic Cards

Figure 5. H-764 Functional Block Diagram

Accelerometer Electronics (A2). The accelerometer electronics card (A2) provides both digital pulses and analog outputs as a function of the outputs from each of the three accelerometers mounted on the SSA.

A/D-PAM Card (A3). The A/D-PAM card provides the functions of analog-to-digital conversion, BIT discrete inputs, pulse accumulation, calibration PROM interface, real-time interrupt generation, system timing, and interfaces to the IP and the NP.

Digital Data Processors (A4 and A5). The H-764 INS configuration features a data processing architecture that has proven highly successful and reliable in Honeywell RLG strapdown inertial systems (both military and commercial). The configuration is characterized by a set of clearly partitioned dual microprocessors. The dual processing approach provides ideal modular flexibility by implementing the high-speed data accumulation and compensations required by a strapdown inertial system mechanization on one circuit board — the IP (A4) card. The slower, standard inertial navigation algorithms are handled on the NP (A5) card. The IP processes sensor data. The NP receives compensated rate and velocity data from the IP, computes navigation parameters, monitors other system functions, and formats the 1553B data messages. With each processor contained on its own plug-in card, automatic BIT fault isolation is improved, as are rapid removal and replacement, if required.

MIL-STD-1553B Multiplex Data Bus (A6). The circuitry for the generalized avionics dual multiplex data channels is located on A6 card and provides a discrete interface to manage the operation of the dual channels as an RT, or as a backup bus controller (BBC).

Built-In-Test. Built-in test provides a failure detection capability of more than 96 percent, based on our experience with U.S. Air Force (USAF) Standard Navigator (H-423)/F-15 (H-770) systems with similar BIT mechanizations.

Electrical Power Description

Power is supplied by a single input of 28Vdc. An alternate backup power source connection is provided for battery backup. Automatic switchover to battery power occurs when the line voltage drops below +20 Vdc. Power quality is defined by MIL-STD-704A and SNU 84-1. For all environmental conditions, the maximum power consumption does not exceed 75 watts.

An on-off input discrete controls the on-off state of the SCINS low voltage power supply. When the on-off discrete input line is open, the LVPS is "off". When the on-off discrete line is shorted to primary power return, the LVPS is "on".

Packaging and Thermal Control

The H-764 SCINS is a self-contained unit that houses the inertial sensor and navigation electronics (see Table 2). Size reductions are planned in future years, and mounting modifications may be adapted to meet the needs of various applications.

Table 2. Functional Assemblies

- Chassis assembly and covers
- Strapdown Sensor Assembly (gyros, accelerometers, and supporting SSA electronics)
- Accelerometer electronics assembly
- Gyro electronics assembly
- A/D-PAM assembly
- IP assembly
- NP assembly
- 1553B MUX assembly
- Master interconnect board (MIB)
- Low voltage power supply

The H-764 SCINS is designed for natural convection and conduction thermal transfer and does not require forced air cooling.

H-764 HARDWARE/SOFTWARE FUNCTIONS

The H-764 SCINS offers an optimized systematic distribution of functions between the hardware and software programmed into two microprocessors — the Inertial Processor and the Navigation Processor. This configuration has proven most effective in the Honeywell laser inertial system product line. Benefits include·

- Circuit mechanizations with fewer parts

- Use of the full library of functions available in a MIL-STD-1750A microprocessor

- High speed computations isolated to the IP

- Low speed computations and I/O control performed on the NP.

GENERAL SYSTEM ARCHITECTURE

Figure 6 is a block diagram showing the partitioning of functions between the hardware and software within the H-764 INU. The hardware is composed of the inertial sensors and the bus communications. The software is composed of the compensation algorithms, BIT, mode selection and processing for navigation, and data communication.

HARDWARE FUNCTIONS

The hardware within the INU is composed of the sensors, pulse accumulators, and other electronics. As shown in Figure 6, the laser gyros and accelerometers mounted within the inertial sensor assembly (ISA) provide precision angular rate information about the aircraft roll, pitch and yaw axes, and linear acceleration information along the same axes.

The sensors have excellent parameter stability and repeatability, allowing each sensor to be characterized at the time of manufacture for bias, scale factor, misalignment, and thermal model coefficients. This data is stored in the Temp/Cal EEPROM at the time of SSA calibration. This design approach simplifies the overall mechanical and electrical configuration of the sensors.

The accelerometer and gyro outputs, which are initially serial pulse trains, are hardware converted to parallel words for use in processors. The initial accelerometer analog outputs are converted to pulses by the digitizer.

Interface with the INU is accomplished with bus communication hardware. The INU is a remote terminal on the 1553B bus during normal operation but may become the bus controller. Communication exists on two networks.

SOFTWARE FUNCTIONS

At system turn-on the contents of the EEPROM are transferred to the NP memory. The temperature of each sensor is measured, and (together with calibration data stored in the NP memory) used to compensate for start-up ambient conditions.

The BIT software consists of a comprehensive set of tests and checks that provide not only BIT test performance for the H-764 Organizational level and inflight test environments, but also provide the essential core test coverage for H-764 production test environments.

Based on external inputs to the INU, the mode of the INU can be selected. During the alignment and navigation modes, the two INU processors apply systematic error compensations for known fixed biases, scale factor errors, misalignments, and thermal effects. The compensated data is used in a three-axis attitude integration algorithm to compute aircraft attitude relative to locally level navigation coordinates. Aircraft angu-
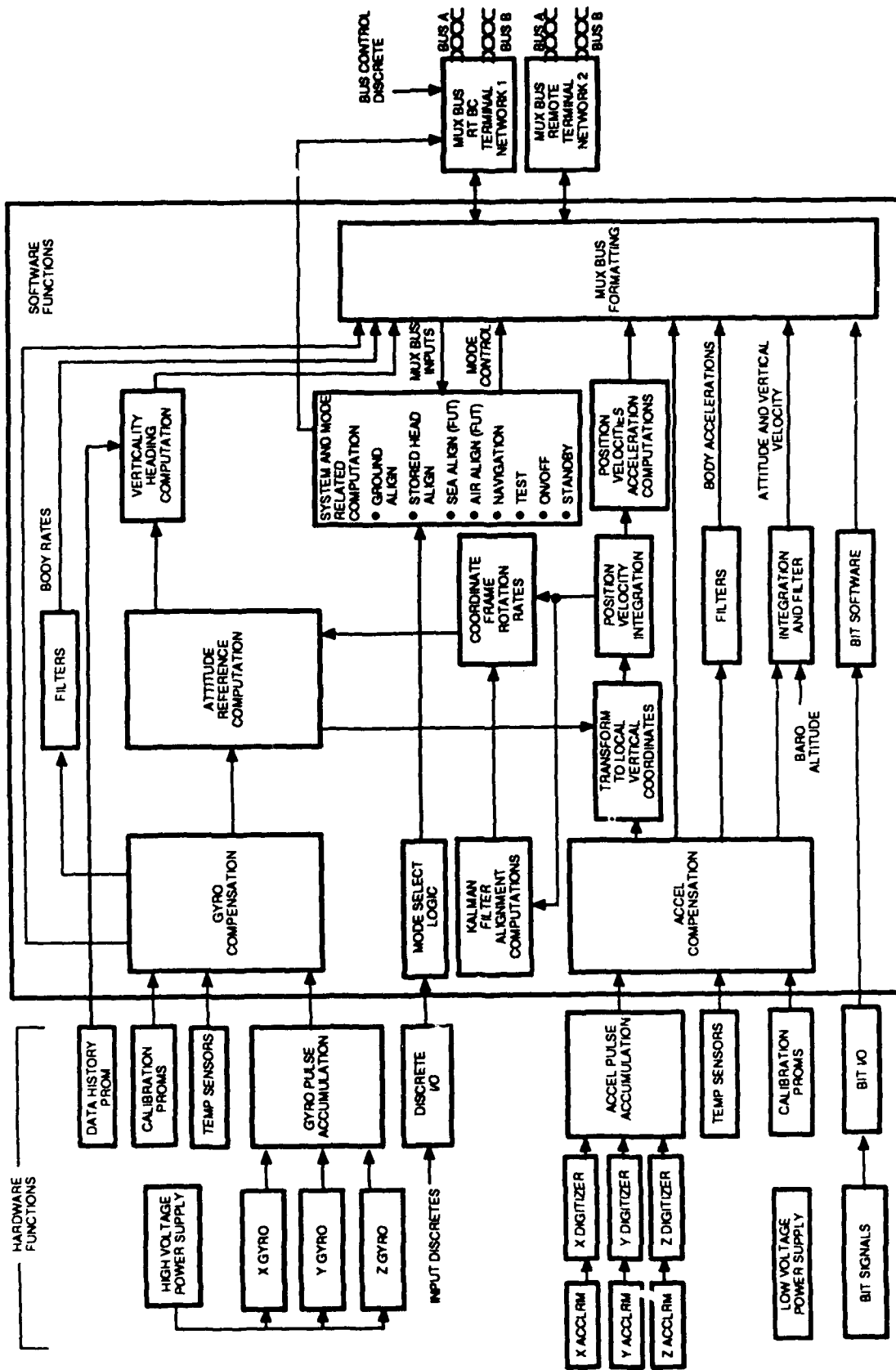
Figure 6.11-764 Hardware/Software Functions Diagram

lar rate over the surface of the earth (due to the earth's rotation and the aircraft's velocity) is included in this computation to account for the rotation of the local vertical. Aircraft attitude data is used first to resolve the acceleration data into the local-level coordinate frame. Computed horizontal and vertical acceleration components are then integrated in an inertial velocity/position algorithm to calculate the aircraft's horizontal and vertical velocity and position. Barometric altitude is used to filter and stabilize the vertical channel.

Verticality, heading, body rate, and body acceleration outputs in filtered and unfiltered forms are available for output on the 1553B data bus, as required by the particular avionics. As a minimum, the output data requirements of U.S. Air Force specification SNU 84-1 are available.

SCINS 1988–89 TEST RESULTS SUMMARY

System level testing with the Honeywell H-764 (Small Common INS) prototype unit began in October 1988. The following paragraphs summarize the results of this development test program. The development program effort increased in the first quarter of 1988 and by October 1988, laboratory tests had begun on the first prototype. Testing of the first preproduction SCINS unit began in early 1989 and the second preproduction unit in April 1989. A third preproduction unit was scheduled to complete build and begin testing in the summary of 1989. Testing of the first two units has gone extremely well. Performance under all of the test environments has been well under the 2.0 to 5.0 nm/hr goal set for the SCINS program.

DITHER STRIPPING

Since the SCINS unit uses the GG1328 (block-mounted readout) gyro rather than the GG1342 (case-mounted readout) gyro, some method of removing dither from the gyro output signal is required. The software dither stripping method was chosen. This method uses the dither pickoff signal as a reference. The new dither stripping method used on SCINS has been very successful. The advantages of dither stripping over dither filtering include elimination of phase and gain distortion which can degrade navigation performance in dither filter mechanizations.

MINIMIZED RANDOM WALK ERRORS

The measured random walk errors in the SCINS units have consistently been very low. Several different system level methods of measuring gyro random walk were used, and the results were all similar. For a variety of reasons, the GG1328 random walk measurements were expected to be worse than similar system level measurements made on GG1342 gyros. However, measurements made on the two SCINS units tested thus far have yielded gyro random walk performance nearly as good as that measured on GG1342 systems. We believe this random walk performance is a combination of better dither random noise and a better dither stripping method.

GYRO COMPASS ALIGNMENT — EXCELLENT HEADING CONVERGENCE

The major factors which determine how fast an INS can accurately find the correct heading are:

1. Gyro channel random walk

2. Accelerometer channel trending

With the very low gyro random walk measured so far and the excellent trending data from our Accelerometer Electronic cards, heading convergence has been exceptional. A plot of heading scatter as a function of align time is shown below. This was derived from multiple alignments on the H-764 SN 001 system at room temperature. The plot in Figure 7 indicates excellent heading convergence (the filter is well converged after about four minutes).
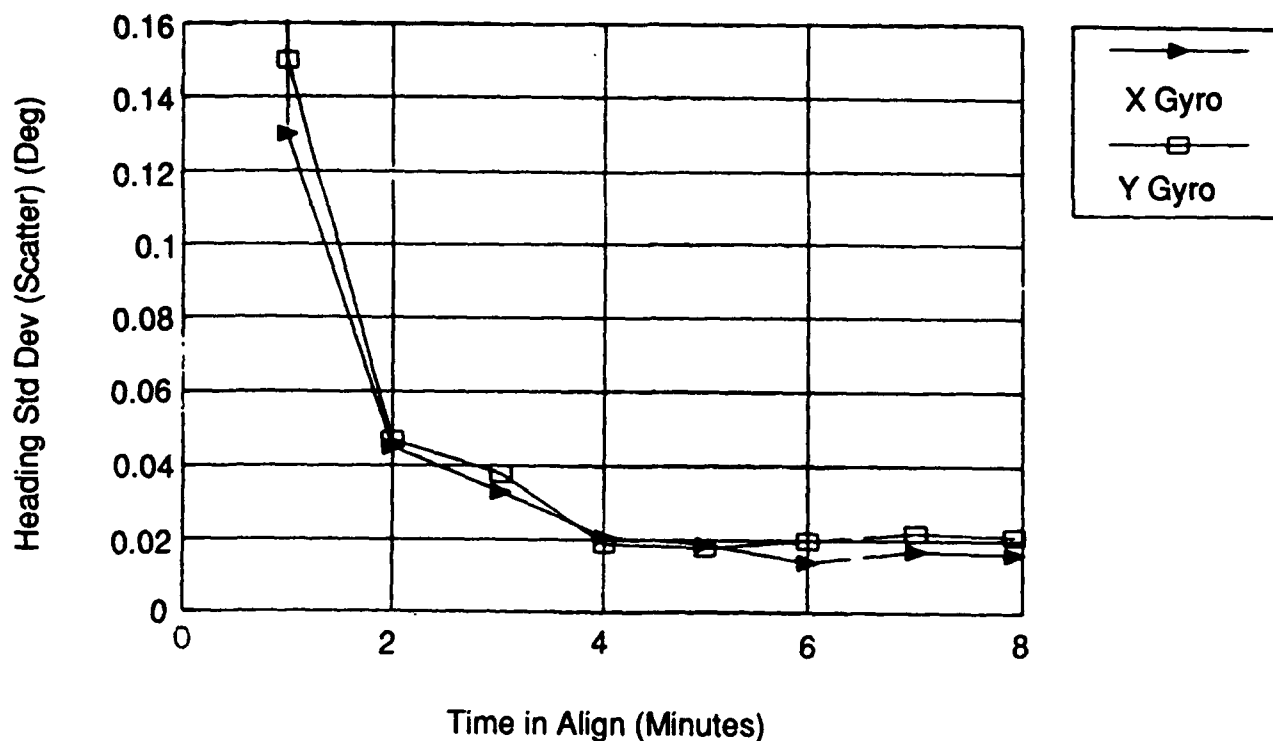
Figure 7. Heading Scatter Over 10 Alignments H-764 SN 001 — GG1328 Gyros

For 2.0 to 5.0 nm/hr performance, SCINS SN 001 heading scatter is performing much better than required. SN 002's heading scatter is also well below the allocated budget.

DYNAMIC PERFORMANCE

Navigation performance, even with 90 and 180 degree rotations during the navigation run, has been quite good. Figure 8 shows a set of four different 60 minute navigation runs, all with rotations. These runs were performed on SCINS SN 001. The average radial position error rate for the four runs was 0.68 nm/hr (well below the SCINS performance goal of 2.0 to 5.0 nm/hr).

MAGNETIC EFFECTS

Tests were performed on H-764 SN 001 to measure the effects of magnetic fields on gyro bias. Stresses in RLG mirrors can lead to gyro bias errors which are somewhat proportional to the magnetic fields surrounding the gyro.

Figure 8. *Room Temp Nav Runs with 90 and 180 Degree Rotations During Nav 0.68 nmph Average RPER for 60 min Nav Runs*

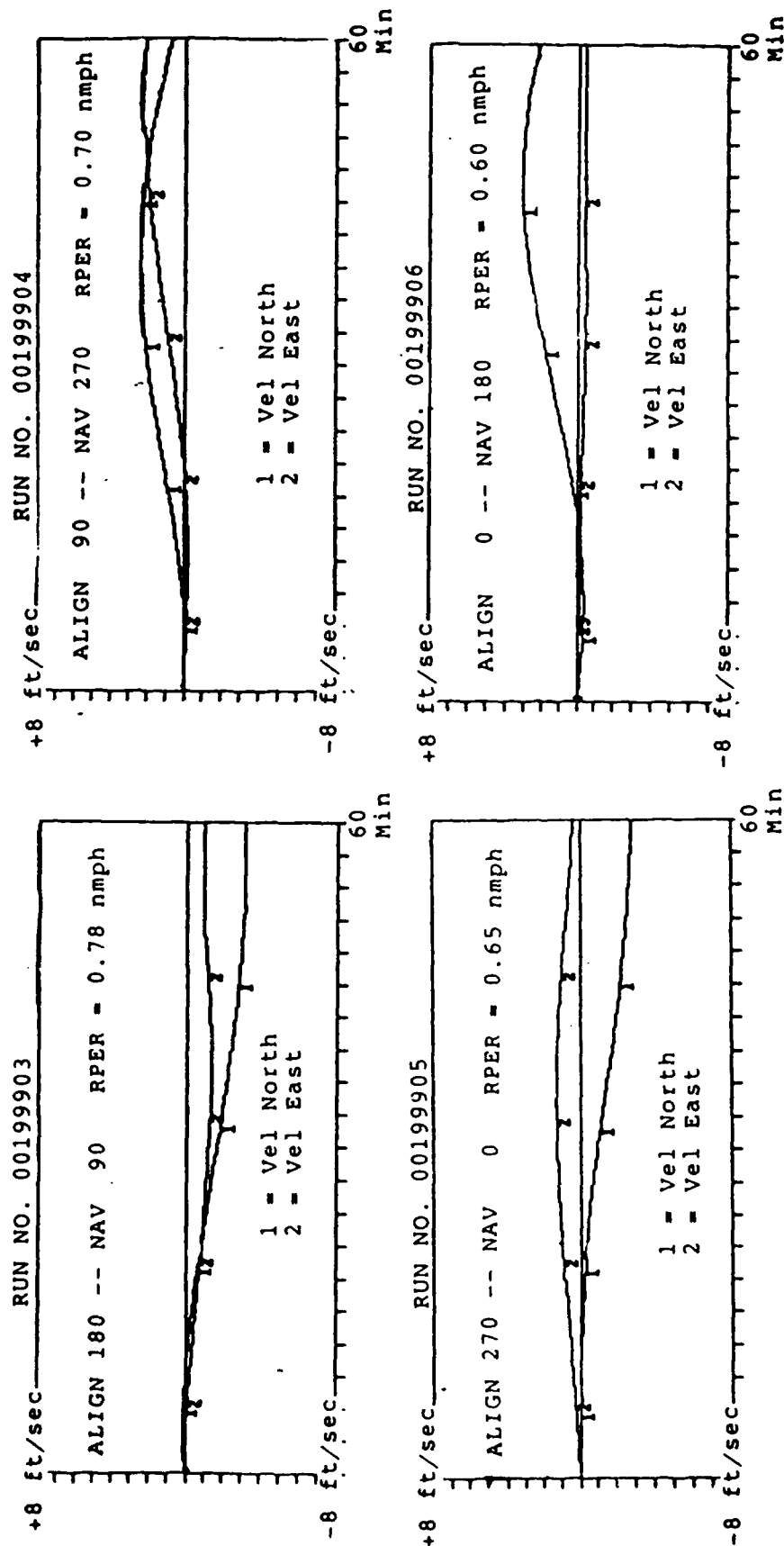As a result of the SCINS magnetic effects testing, an effort was initiated to design and build a SCINS chassis electro-plated with a Ni-Fe magnetic shield material. This effort resulted in a shielded chassis which virtually eliminated all magnetic sensitivities.

All SCINS units now have a shielded chassis. The plating ads approximately 0.7 lb to the weight of the unit, but for most of the potential applications, the performance improvement is well worth the slight weight penalty.

GYRO THERMAL RATE SENSITIVITY

As with all Honeywell strapdown RLG systems, the sensors in the SCINS unit are not thermally stabilized. Instead they are thermally compensated over the entire military temperature range using a three term model which relates gyro temperature to gyro bias. These terms are called K1, K2 and K3.

Analysis of factory GG1328 gyro data indicated a bias error which is proportional to the thermal rate being experienced by the gyro. (This term is referred to as "K4.") K4 type gyro channel errors were also observed at the system level. Once the K4 value for each gyro is determined, software in the INS can be used to compensate for the effect of this error.

In early 1989, the H-764 program developed an improved method of measuring both gyro bias and K4 errors at the system level. By compensating for K4 effects, as well as bias effects, navigation performance during hard thermal ramps over the full military temperature range; i.e., ambient temperature thermal ramps from +70°C to –60°C and visa versa, improved from 2.8 nm/hr without K4 compensation to approximately 1.1 nm/hr with K4 compensation. The thermal profile for this test is shown in Figure 9.

EXTREME HOT AND COLD TEMPERATURE TESTING

SCINS is specified to provide performance from –40°C to +55°C ambient temperature (plus half hour transients to +70°C) with no forced cooling air required.

The H-764 system has repeatedly operated as low as –54°C (well below its required limit) with excellent results. The gyros all started within five seconds, the unit aligned and then navigated normally after being soaked at –54°C for over five hours with power removed. The performance of the unit at this temperature was approximately 2.0 nm/hr, even though the system had not yet been calibrated at temperatures that low.

A limited (30 point) thermal survey was performed on the system in May 1989. The test showed that the unit's components all operated below their derating temperatures with ambient temperatures of +55°C and 30 minute transients to +70°C, even without cooling air.

SENSOR MISALIGNMENTS VERSUS TEMPERATURE

A major design goal for the new SCINS "cube" sensor assembly block was to reduce sensor coning motion. This effort was successful as coning motion errors, even under unrealistic "worst case" conditions, have been virtually eliminated.

Another improvement over the blocks used for larger gyros, however, was the "cube's" orthogonality stability over temperature. The total sensor-to-sensor IA instability over the entire military temperature range was reduced significantly. This improvement comes from the compactness of the main block on which the sensors are mounted (a by-product of the GG1328s small size).
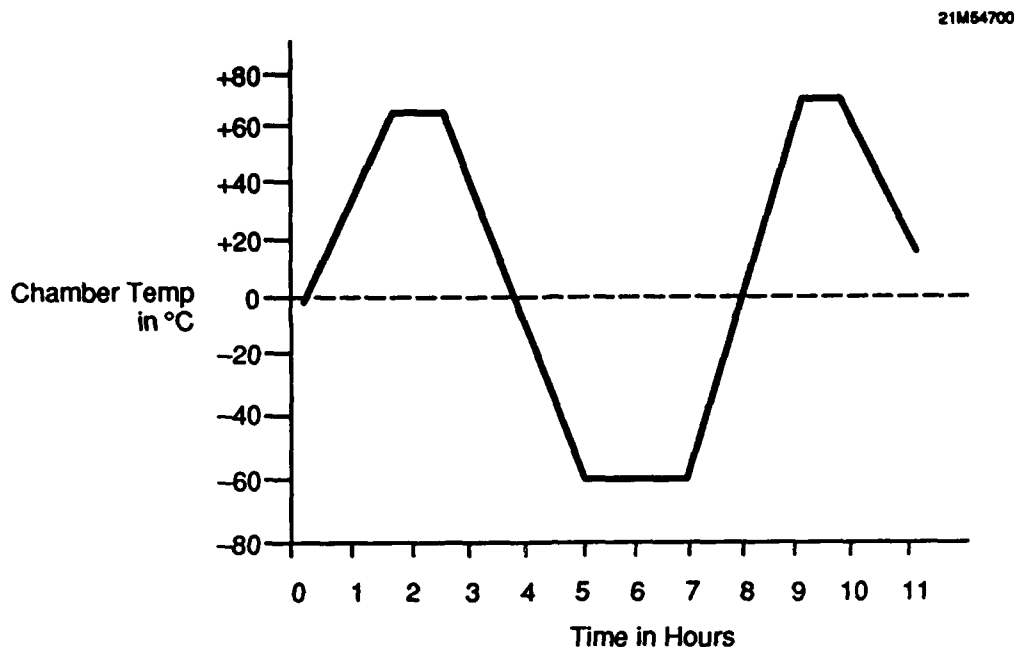
21M54700

Figure 9. SCINS SN 002 K4 Test Ambient Temp Profile

FLEXURE AND VIBRATION TESTING

The rigidity of the new SCINS sensor block should also reduce sensor-to-sensor misalignments under high-g loads (flexure), which, in turn, should improve performance during vibration. Vibration testing of the SCINS units and measurement of actual flexure magnitudes are scheduled for the fall of 1989.

H-764 VAN TESTING

The SCINS unit can easily be transformed into a unit that can be tested in a van. This is done by removing the SCINS 1553 card, replacing it with an RS-422 card, and placing a Discrete I/O card in the spare card slot. We also install a slightly modified version of Honeywell's standard land navigation software in the Navigation Processor.

At the time this paper was written, these modifications were scheduled to be made to one of the SCINS units in the summer of 1989. That unit was to be extensively tested in the lab, as well as in a Honeywell van.

GG1320 GYRO TESTING IN THE SCINS UNIT

In late 1989 or early 1990, Honeywell's new GG1320 gyro is scheduled to be tested in a SCINS unit. The GG1320 gyro has many advantages over the GG1328 including smaller size, lower power, lighter weight, and, eventually, lower cost and better performance, as well.

The SCINS program team is currently determining what modifications will be required (mechanical, electrical, and software) to allow the H-764 unit to use the GG1320 gyros.

THIS PAGE LEFT INTENTIONALLY BLANK

STRAPDOWN ASTROINERTIAL NAVIGATION (SAIN)

- AN IDEA THAT HAS COME OF AGE

Paper No. 89-15

CENTRAL INERTIAL GUIDANCE TEST FACILITY (CIGTF)
Holloman Air Force Base, New Mexico

Primary Author

Seymour Levine - Northrop Electronics Systems Division

Co-authors

Ronald Dennis - WRDC/AAA-1
Kenton L. Bachman - NADC

27 June 1989

COPYRIGHT TRANSFER AGREEMENT
Form C-299 (R11-87)

NORTHROP

TITLE OF PAPER: STRAPDOWN ASTROINERTIAL NAVIGATION (SAIN) - AN IDEA THAT HAS COME OF AGE

AUTHOR(S): SEYMOUR LEVINE (NESD), RON DENNIS (AFWAL) KEN BACHMAN (NADC)

Northrop Corporation hereby transfers its copyright interest in the above work to:

CENTRAL INERTIAL GUIDANCE TEST FACILITY (CIGTF) HOLLOMAN AFB, NM 88330-5000

effective if and when the work is accepted for publication, subject to the following rights reserved:

(1) All proprietary rights other than copyright, such as patent rights.

(2) The right to use all or a portion of the above work in future works prepared by or for all company elements of Northrop Corporation.

(3) The right to reproduce, or have reproduced, a reasonable number of copies of the above work for the author's personal use, and for company use.

(4) The right to distribute a reasonable number of abstracts and reprints of the above work, or portions thereof, prior to publication.

(5) Where the above work was created in the course of or under a contract with the United States Government, publisher grants the United States Government the royalty-free right to reproduce all or portions of the above work, and to authorize others to do so, for governmental purposes.

Was the above work performed under a U.S. Government contract?

☐ YES   ☐ IN PART   ☐ NO

DATE: 07 JUNE 1989   AUTHOR(S):
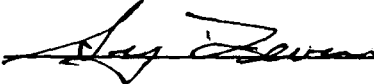
CLEARANCE STATEMENT

This work is UNCLASSIFIED and has been cleared by the appropriate authority for release and publication.

DATE: 07 JUNE 1989   AUTHOR(S):

NORTHROP CORPORATION

ELECTRONICS SYSTEMS DIVISION
COMPANY ELEMENT

DATE: 6/16/89

BY: TECHNICAL PAPER COORDINATOR

ABSTRACT

This paper discusses strapdown astroinertial navigators as an autonomous high precision terrestrial navigation aid that approaches GPS position and velocity performance without dependence on electromagnetic radiation. It discusses its lens systems, accuracy, applications, and testing. Other items discussed are cloud coverage, star-to-sky density, vehicle motion, and focal plane array minimization. The paper's conclusion is that inertial systems augmented with optical aids provide a high precision position, velocity, and angular navigation capability to a vast quantity of diverse vehicles.

I.   INTRODUCTION AND BACKGROUND TO STELLAR INERTIAL SYSTEMS

The majority of today's high performance terrestrial, in-air vehicles employ pure inertial navigation systems. These navigation systems have errors which grow with time at typical values of 1.0 nautical mile per hour, although some grow at tenths of a mile per hour. Such performance is inadequate for many of today's missions. The accuracy can be improved, and has been over the last thirty years, by the utilization of a number of man-made, electromagnetic radiation navigation system aids (e.g., radio, radar, or satellite position and doppler velocity fixes) that augment the inertial systems. Autonomous navigation, which does not depend on man-made electromagnetic radiation, is still required in a high technology, hostile environment and furthermore may be the desired mode of operation, even in non-hostile environments, to insure vehicle safety and mission success.

Natural, visible spectrum aids, such as celestial bodies and landmarks have been utilized since ancient times to augment man's dead-reckoning navigation systems. These natural, visible spectrum data are as valuable to navigation now as they were in ancient times. In many of today's navigation environments, the magnetic compass has been relegated to a backup mode, and the inertial navigator has emerged as the twentieth century's dead-reckoning navigation system. Furthermore, the advent of the laser gyroscope has made non-gimballed, or strapdown, inertial navigation precision reasonable. In fact, due to low cost, low weight, and high reliability, the use of strapdown inertial navigation has proliferated in the low and medium accuracy inertial navigation field. One natural augmentation device for these dead-reckoning strapdown inertial navigation systems is a strapdown solid state astro tracker. It is the Strapdown Astroinertial Navigator (SAIN) that is the subject of this paper.

Figure I.1 shows a projection of both gimballed and strapdown inertial and astroinertial systems for a ten hour flight. It should be mentioned that the devices used to achieve terrestrial strapdown astro-tracking are as revolutionarily different from space and gimballed trackers as the optical gyroscopes are from the angular momentum, iron wheel gyroscopes. Thus, the field of autonomous navigation is destined to go solid-state optical, both for its inertial gyroscopes and its augmentation aids. Unlike the ancients, Twentieth Century man has extended his optical sensors from the visible into the infra-red spectrum. In addition, terrestrial trackers not only track stars in the dark background of space and at night, but also track stars in daylight at sea level. It is this feature that allows high precision strapdown stellar-inertial navigation technology to be employed in a plethora of vehicles ranging from ships and planes through ballistic and cruise missiles.

Figure I.1
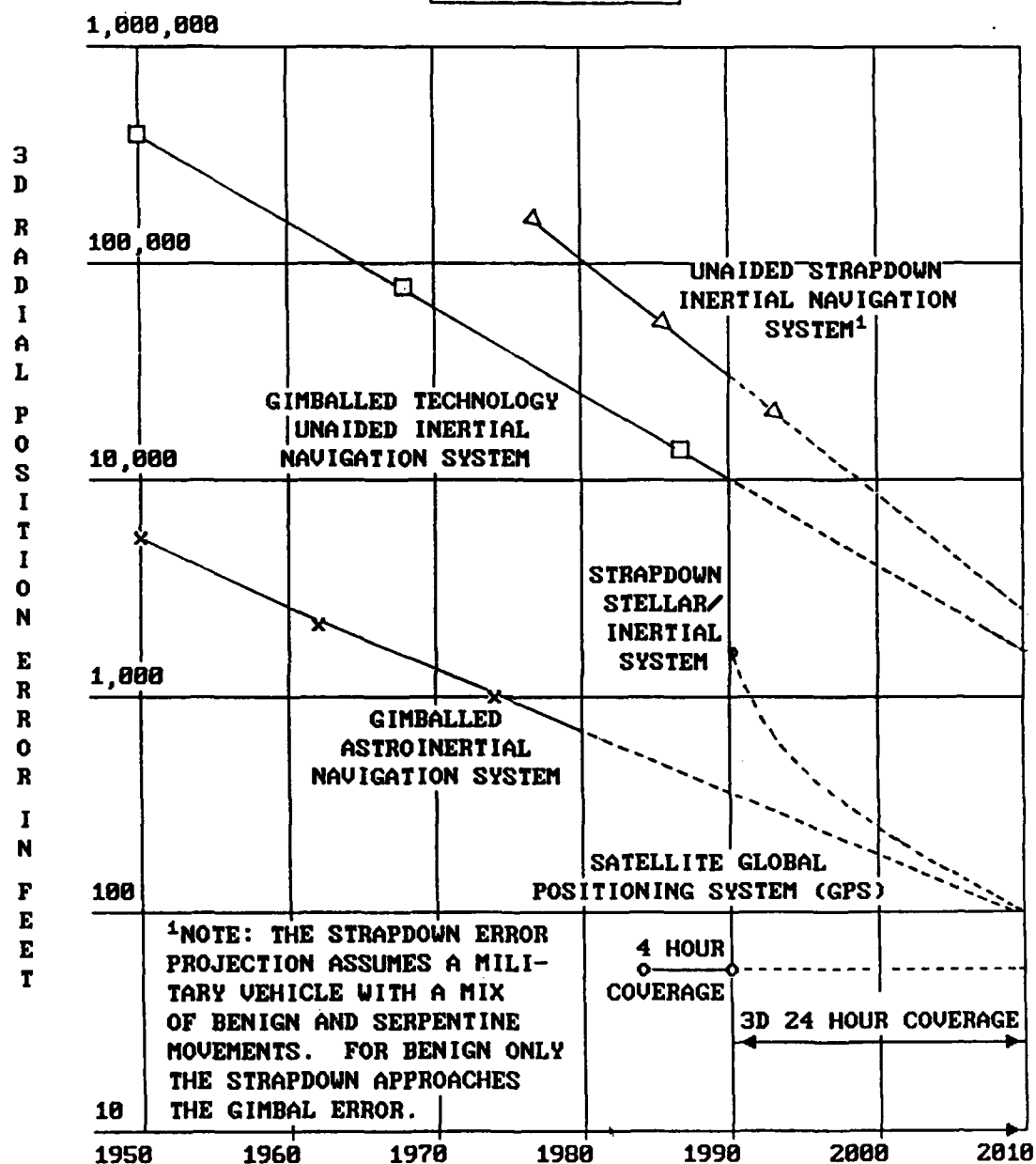
PROJECTION OF NAVIGATION SYSTEM PERFORMANCE FOR GPS, ASTROINERTIAL AND UNAIDED INERTIAL NAVIGATION SYSTEMS FOR 10-HOUR FLIGHT.

The Air Force and Navy, recognizing the potential of this technology, have agreed to develop jointly a Strapdown Stellar Sensor/Inertial System (SSSIS) for advanced airborne applications in the 1990s. Under this agreement, a two-phase program has been initiated to develop and demonstrate a highly modular, mission adaptive, and passively aided inertial system employing strapdown stellar technology. The SSSIS will be designed for use in a variety of vehicles, including strategic/reconnaissance aircraft, hyper-velocity vehicles, and strategic missile applications.

The Wright Research and Development Center (WRDC), operating under a memorandum-of-agreement (MOA) with the Naval Air Development Center (NADC), awarded two design feasibility study contracts in 1988. The contractors, working independently to the same set of design goals, conducted trade-off studies of candidate stellar and inertial sensor designs, performed analytical simulations, and postulated various system configuration options. The recommended final system configurations were presented to the Air Force and Navy for consideration and concurrence.

Under Phase 2 of the program, an Advanced Development Model (ADM) contract will be awarded in 1990 to fabricate and test a proof-of-concept demonstration model SSSIS. System test plans and schedules will be coordinated by both services prior to the start of the government performance evaluation. The test center supporting WRDC in the flight test evaluation will be the Central Inertial Guidance Test Facility (CIGTF) at Holloman AFB, NM. Initial bench testing by the Navy will be conducted at the Strapdown Navigation Systems Development Laboratory of the NADC.

II. SAIN CANONICAL, SIMPLEX, AND HEURISTIC MODELS AND
     SIMULATIONS

Figure II.1 shows the canonical model of a stellar inertial
navigation system. This can be shown in a simplex model, Figure
II.2. The strapdown inertial system, utilizing its gyroscopes
and accelerometers, provides estimates of the vectors of position
(e.g., latitude, longitude, and altitude); velocity (e.g., north,
east, and vertical); and Euler angles (roll, pitch, and heading).
The raw inertial vectors are combined with a self-contained
ephemeris and chronometer (an error of one second of time in the
chronometer represents a 1500 foot position error) to predict a
star fix angle. The astro-tracker then utilizes this estimated
coordinate location to find the actual star and to provide an
error vector that represents the difference between the predicted
star angular coordinates and the astro-tracker's measured star
angular coordinates. This error vector is then processed
optimally in a Kalman filter to yield the best estimates of the
vectors of position, velocity, and Euler angles as well as
gyroscopic (e.g., bias, scale factor, misalignment, etc.) and
observable accelerometer errors.

It should be pointed out that the astro-tracker is similar to a
marine sextant in that it looks at the star angle with respect to
the horizontal level, but unlike the sextant's observed horizon,
the astroinertial system utilizes the inertial system's estimated
vertical. This deviation leads to a lack of observability of
certain errors. Figure II.3 is a heuristic error model of an
astroinertial system. As can be seen by the model, the star
tracker cannot distinguish between a tilt in the inertial system
and an error in star location when both are equal and opposite.
This leads to the inability of the tracker to damp Schuler
oscillation. Uncompensated gravity horizontal deflections have
the same response to tilt errors as they do to position errors,
but with opposite signs. Due to the equal but opposite sign
responses, the astrotracker is unable to sense these errors.
As a result of this lack of observability, astroinertial systems
exhibit the identical error responses to uncompensated gravity
horizontal deflections as do the pure inertial navigators. The
errors can be minimized by accurate gravity compensation that
takes into account spherical harmonics, terrain data, and
geological information. Horizon sensor and velocity reference
systems can also minimize these errors, as shown in Figure II.4.

On the other hand, gyroscopic drift terms are easily distin-
guished, since the response to tilt (one integration) is much
faster than the three integration processes for the error to go
into position. This yields one of the major advantages of
astroinertial systems, in that they can observe and compensate
for gyroscopic drift. Figure II.5 shows a strapdown inertial
aircraft system during a sixteen hour flight with 4 cm path
length ring laser gyroscopes (RLGs), both with and without an
astro-tracker. The dramatic improvement illustrates one of the

values of the astroinertial navigator. Figure II.6 shows how
the size of the RLG, which is a measure of its pure inertial
component performance, can be reduced and still yield superb
navigation performance in an astro-tracker application. The
strategic penetrator navigation performance was essentially
the same for a 16 to 1 reduction gyroscopic random walk. The
astro-tracker compensates gyroscopic drift by monitoring the
navigator's tilt and azimuth angles and by providing tilt,
azimuth, and gyro drift corrections.

Another major attribute of astroinertial systems is the ability
to observe north directly. In inertial systems, the initial
azimuth determination process is corrupted by effective east
gyroscopic drift. Furthermore, the azimuth error vector may be
changed by effective azimuth gyroscopic drift. Star trackers
have excellent observability of these vectors. This allows
astroinertial systems to have excellent response times for
accurate performance, since they can correct these quantities in
the sky. Stellar inertial systems also provide a high level of
self monitoring and healing. For example, a pure inertial system
cannot observe an initial or updated Longitude insertion error
during flight, but a stellar-inertial can detect this potentially
catastrophic problem. This is because the pure inertial
navigator's dynamic response is transparent to longitude data,
while the stellar inertial star ephemeris depends on longitude.
When the star detection probability is high, the stars should be
in the field of view. This feature could either trigger a self
corrective action response or a mission safety abort mechanism.
The choice of action can be programmed into the flight computer
and depends on subsequent self tests.

Thus, astroinertial systems provide an excellent augmentation for
the inertial navigator. Furthermore, the addition of a velocity
correlator or horizon sensor can provide performance that
approaches GPS inertial performance without the utilization of,
or dependence on man-made radiation devices. If GPS were
available, it would be integrated into the navigation suite as
another inertial navigator augmentation device. This augmented
navigation suite provides a level of navigation position and
velocity redundancy. Nevertheless, the mission's performance
goals need not be jeopardized by the dependence on satellite data
availability. Therefore, the astro-inertial system yields a high
performance autonomous mission capability.

Figure II.1
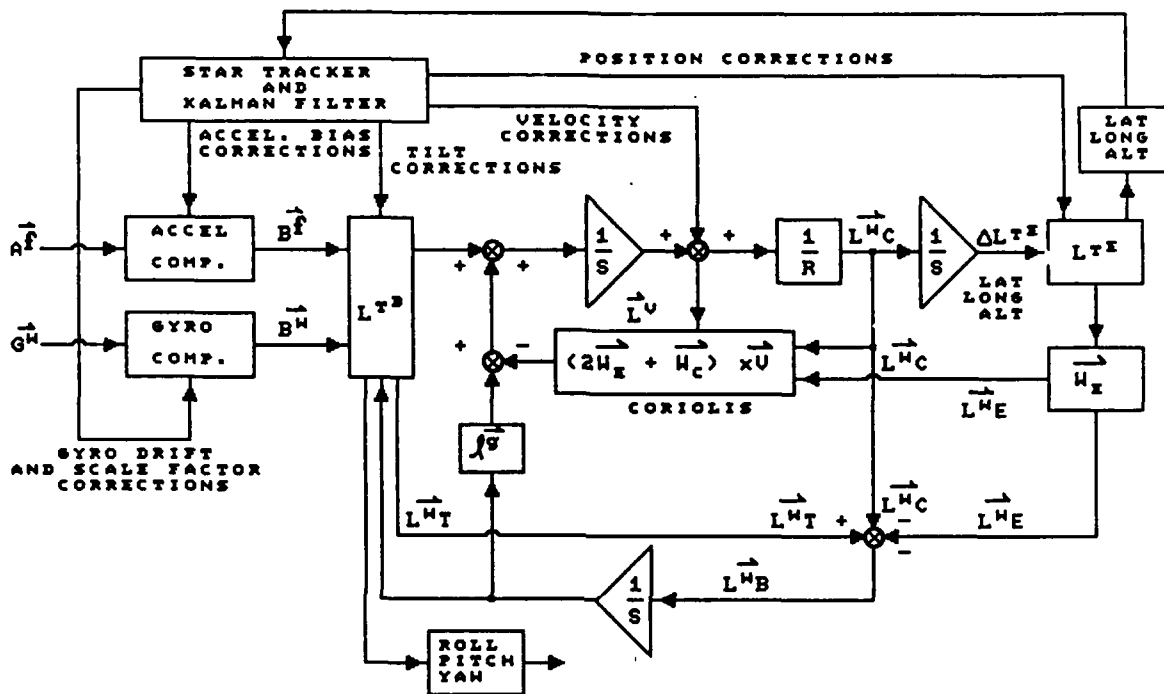
f = SPECIFIC FORCES	U = VELOCITY	
W = RATES	$\int\vec{g}$ = GRAVITY	
L^{TB} = BODY TO LEVEL TRANSFORMATION	W_T = TOTAL INERTIAL RATE	
L^{TE} = EARTH TO LEVEL TRANSFORMATION	R = EARTH RADIUS	
	$_A()$ = ACCEL FRAME	
W_E = EARTH RATE	$_G()$ = GYRO FRAME	
W_B = BODY RATE	$_B()$ = BODY FRAME	
W_C = CRAFT RATE	$_L()$ = LEVEL FRAME	

STRAPDOWN STELLAR INERTIAL NAVIGATION SYSTEM, CANONICAL MODEL

FIGURE II.2

STRAPDOWN INERTIAL SENSORS

GYROSCOPES ⟶

ACCELEROMETERS ⟶

INERTIAL SENSOR PROCESSOR

o DIRECTION COSINES
o CONING COMP., ETC.

ALTIMETER

INTEGRATION PROCESSOR

o KALMAN FILTER
o EPHEMERIS, ETC.

CHRONOMETER ⟶

OPTIMUM ESTIMATED
NAV SYSTEM OUTPUT
o POSITION
o VELOCITY
o EULER ANGLES
o ANGULAR RATES

STRAPDOWN IMAGE SENSORS

STELLAR ⟶
TERRESTRIAL ⟶
HORIZON ⟶

IMAGE SENSOR PROCESSOR

o CORRELATOR
o ENHANCERS, ETC.

SIMPLEX STRAPDOWN STELLAR INERTIAL SYSTEM MODEL
WITH TERRESTRIAL AND HORIZON IMAGE OPTIONS

FIGURE II.3
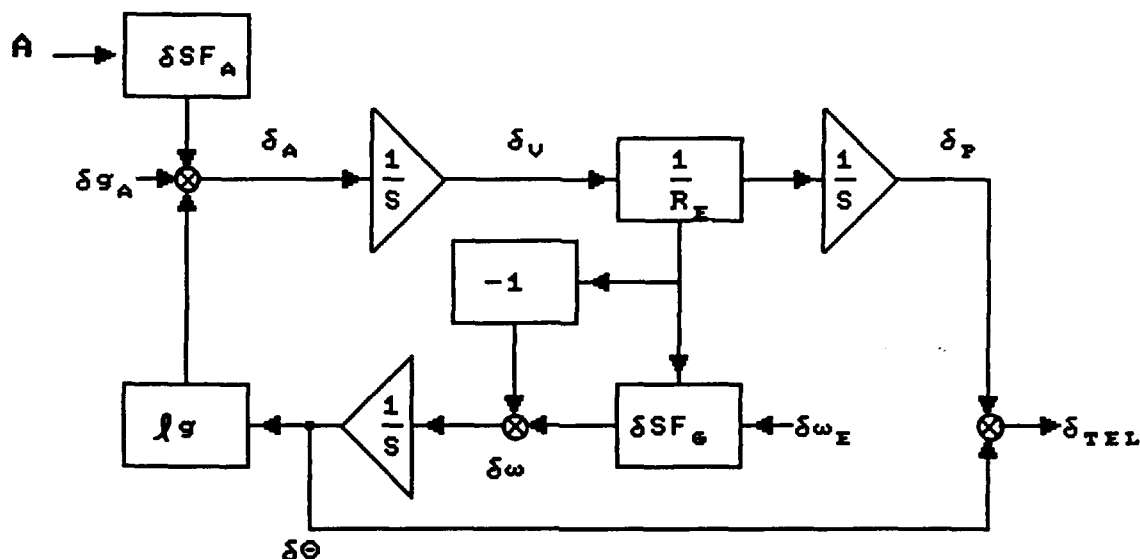
*NOTE: LAPLACIAN OPERATOR 1/S IS USED
FOR AN INTEGRATOR.

$\int g$ =	ACCELERATION OF GRAVITY
δ_A =	ACCELEROMETER ERROR
δ_V =	VELOCITY ERROR
δ_P =	POSITION ERROR
$\delta\Theta$ =	TILT ERROR
$\delta\omega$ =	ANGULAR RATE ERROR
$\delta\omega_E$ =	ERROR IN EARTH RATE COMPENSATION
δg_A =	ERROR IN GRAVITY HORIZONTAL COMPONENT
δSF_A =	ACCELEROMETER SCALE FACTOR ERROR
δSF_G =	GYROSCOPE SCALE FACTOR ERROR
δ_{TEL} =	TELESCOPE ANGULAR ERROR

HEURISTIC ASTROINERTIAL ERROR MODEL (THE ASTROINERTIAL SYSTEM CANNOT COMPENSATE FOR SOME ACCELERATION ERRORS)

Figure II.4
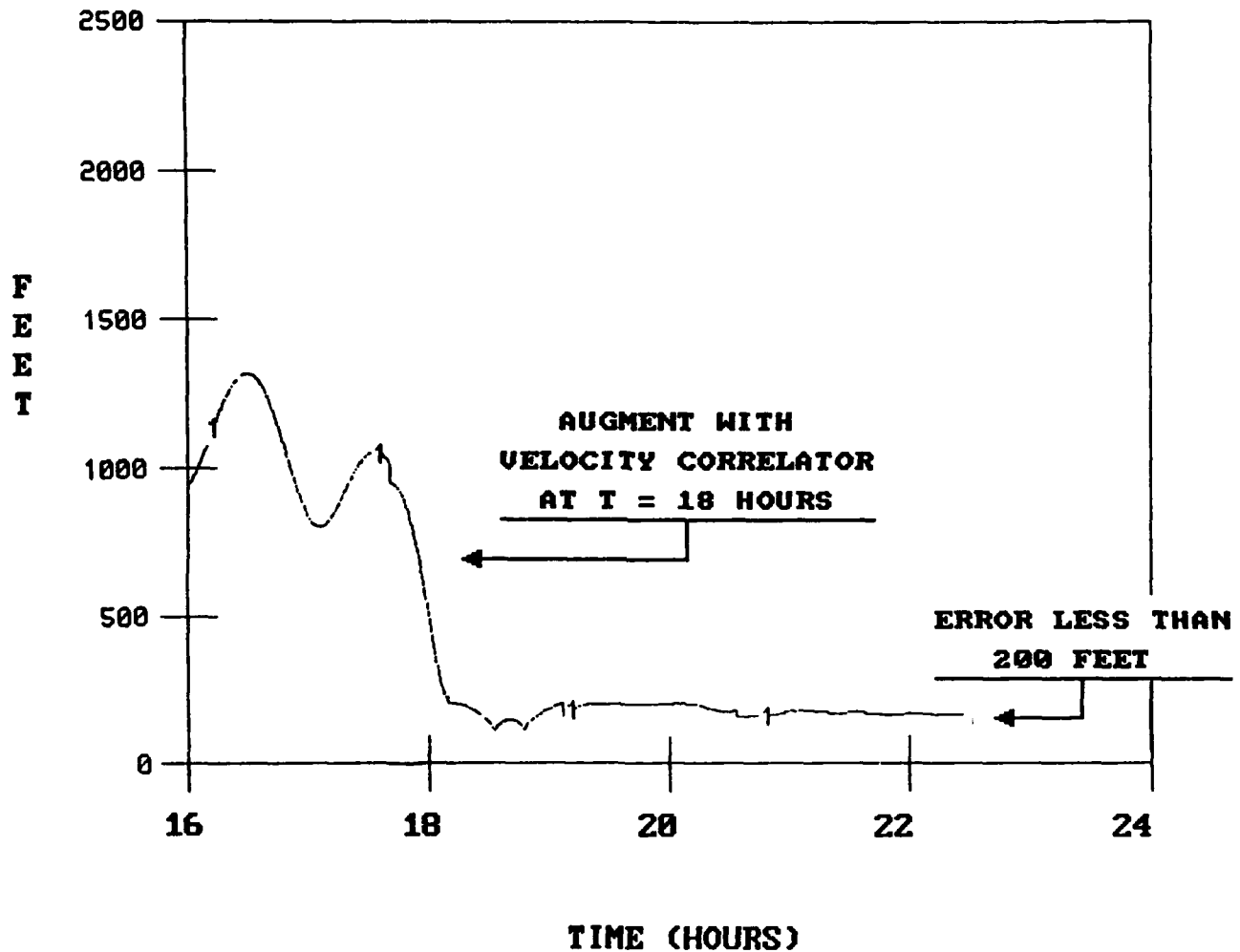
STRATEGIC PENETRATOR POSITION CEP
SUMMARY (IN FEET) - INERTIAL PERFORMANCE WITH LOW
RATE STELLAR AND VELOCITY CORRELATION AUGMENTATION

Figure II.5

INERTIAL WITH
ALTIMETER AUGMENTATION

INERTIAL WITH ALTIMETER
AND STELLAR AUGMENTATION

CEP
IN
FEET

MISSION TIME IN HOURS
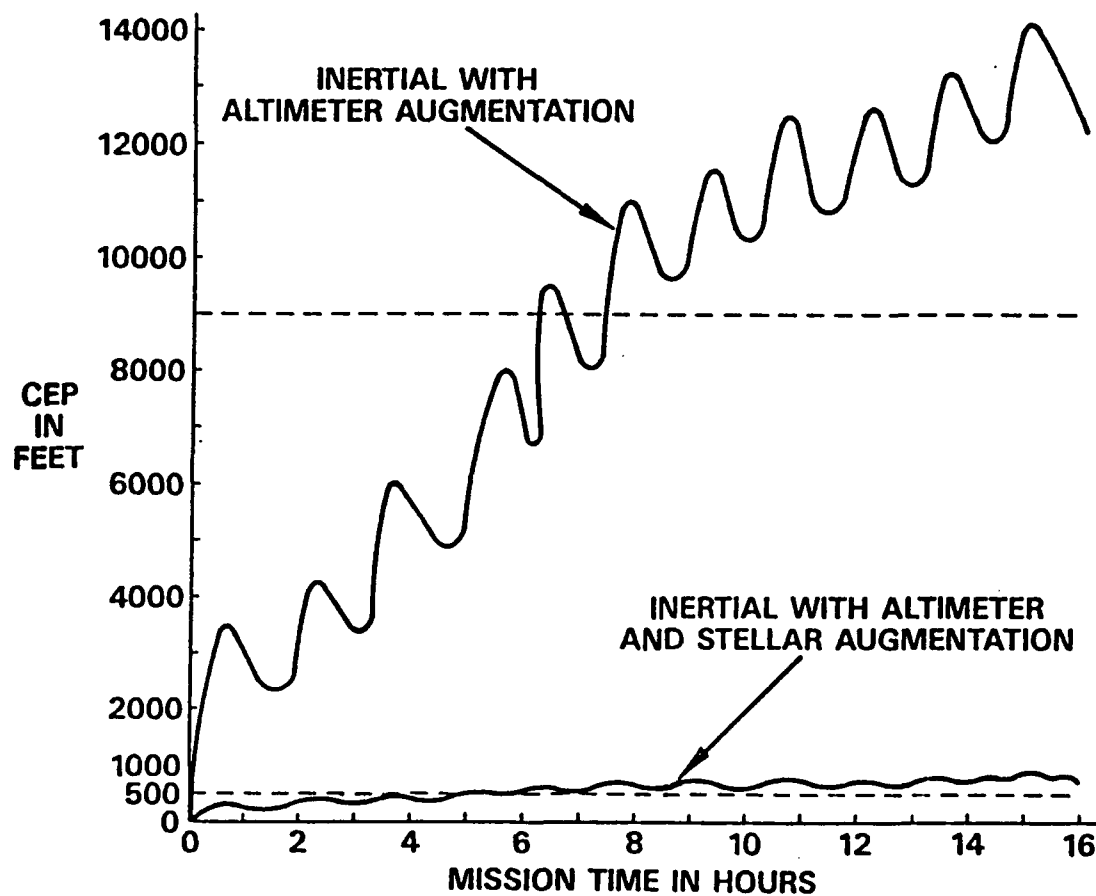
STRAPDOWN STELLAR INERTIAL SYSTEM PERFORMANCE
STRATEGIC PENETRATOR MISSION WITH 40 cm RLGs
(CEP vs. MISSION TIME)

Figure II.6
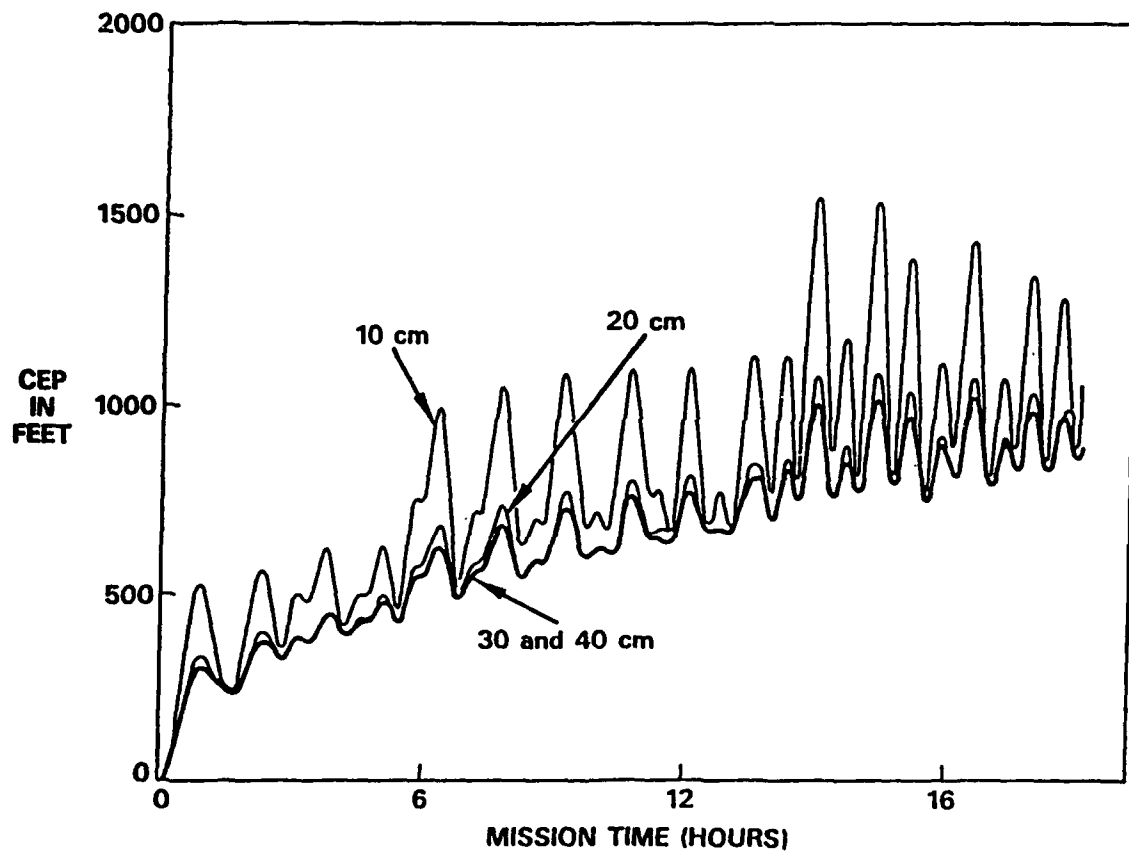
STRATEGIC PENETRATOR
STRAPDOWN STELLAR INERTIAL SYSTEM
10cm, 20cm, 30 cm, and 40 cm RLGs (CEP vs. MISSION TIME)

III.   STAR IMAGE CONSIDERATIONS

Image stabilization is a major problem with solid state astro-trackers.   Figure III.1 shows how a vehicle's motion causes a star's image to transverse a fixed-to-vehicle focal plane array (FPA).   Due to the motion of the vehicle, a high speed snapshot of the star's image must be taken to avoid blurring.   Once the image snapshot is taken, the data in the image processor is transformed into stabilized coordinates with the aid of the inertial navigator's direction cosine matrices.   The image data integration for signal-to-noise enhancement as shown in Figure III.2 is a complex process where the shutter is being operated at 100 to 1000 microseconds to prevent star image blurring.   This high speed shuttering of data is necessary even for vehicle rates as low as one degree per second.

Figure III.3 shows that a mega-pixel array (i.e., 1000 x 1000 pixels) is required for sky background noise reduction and for the estimation of star image centroids.   A telescope with a three degree field of view (FOV) and a mega-pixel FPA will have a ten arc-second per pixel sensitivity.   The centroid algorithm would then estimate the star's image to a tenth of a pixel for a one arc-second (100 foot) astro-tracker.

The sky background, the FPA's pixel current and gain variations, the image processor space stabilization techniques, etc., all force the strapdown astro-tracker to employ a pixel-to-pixel noise reduction mechanism in order to achieve high fidelity star angular information.

Star-to-sky density (i.e., the number of stars per steradian) and star magnitude are major design parameters for a terrestrial strapdown tracker.   This is because the tracker is not a steerable gimballed tracker with the concomitant costs and reliability problems.   Nevertheless, it should have the field-of-regard of a full 60° (0.84 steradians) cone angle.   In order to increase the star-to-sky density, the strapdown astro-tracker must have a sea level capability of tracking magnitude five stars in daylight. This is because the magnitude 5 star density for a silicon detector in the R band is only 0.075 stars per square degree (0.0003 steradians).

Figure III.1

TIME   T1
VEHICLE:
ROLL   R1
PITCH P1

TIME   T2
VEHICLE:
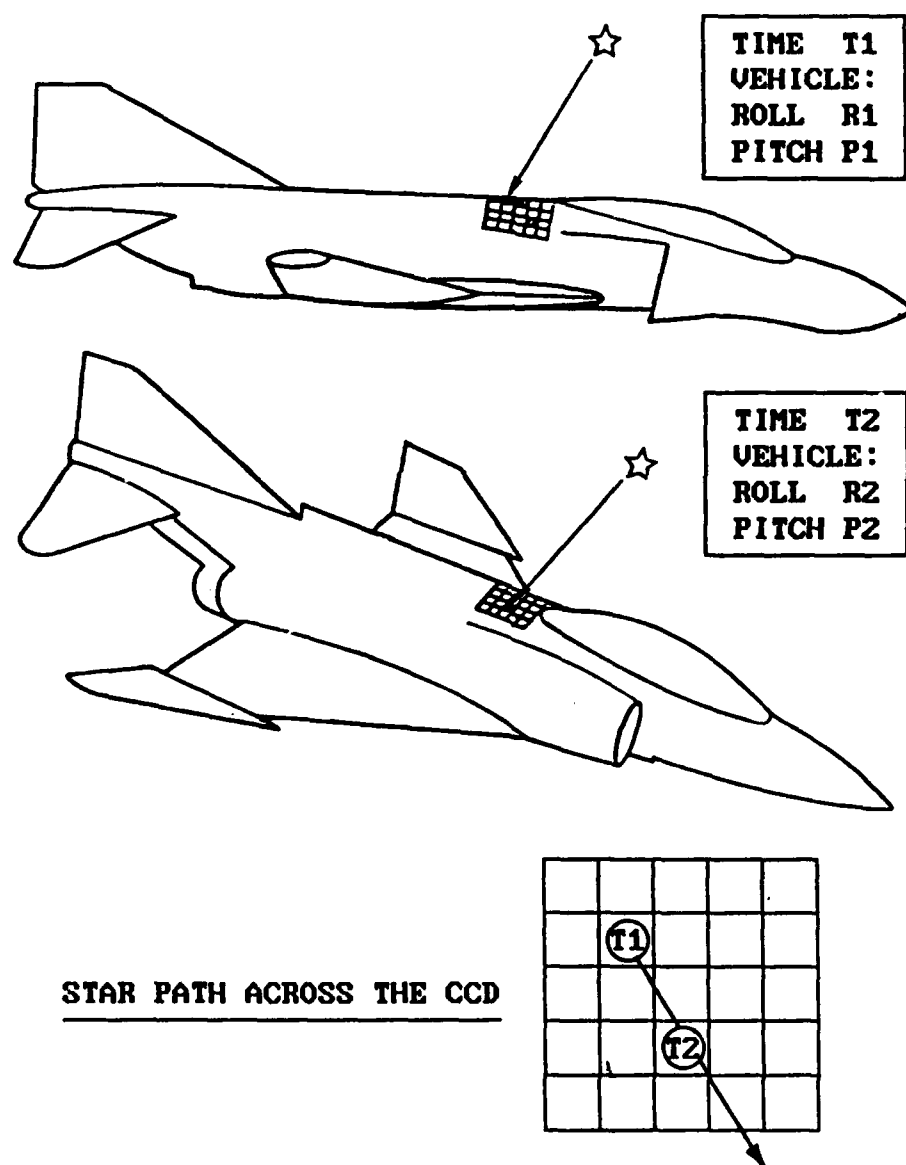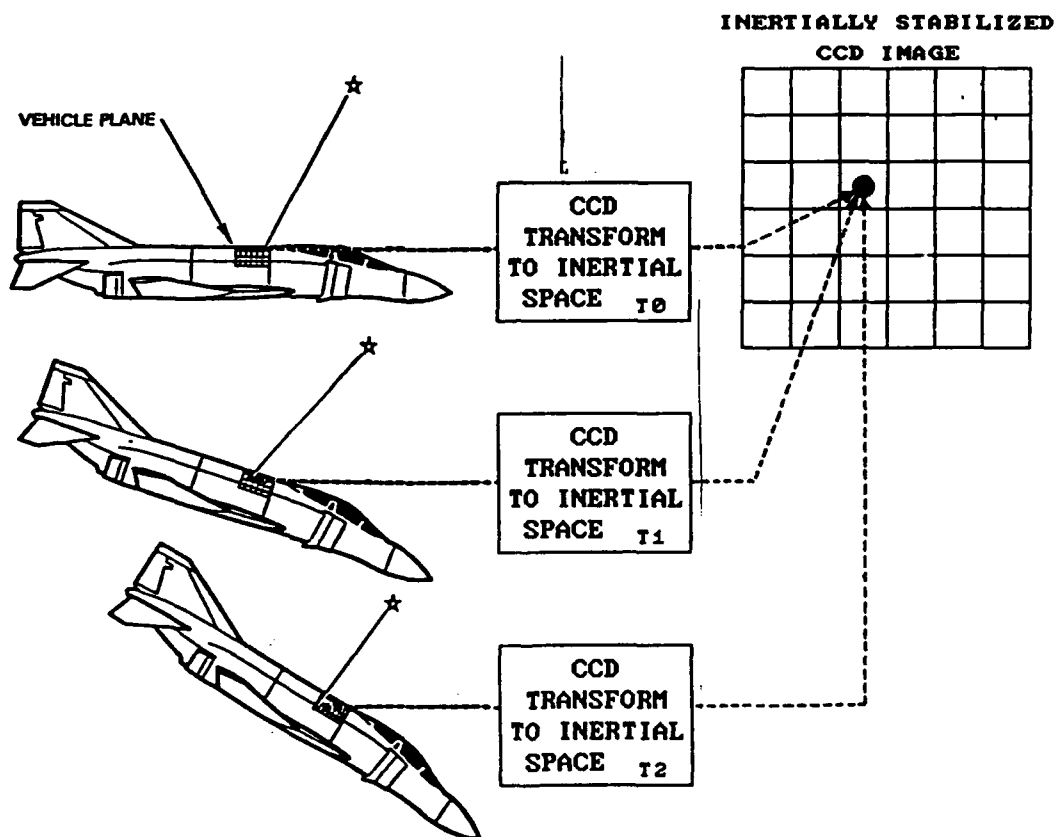ROLL   R2
PITCH P2

STAR PATH ACROSS THE CCD

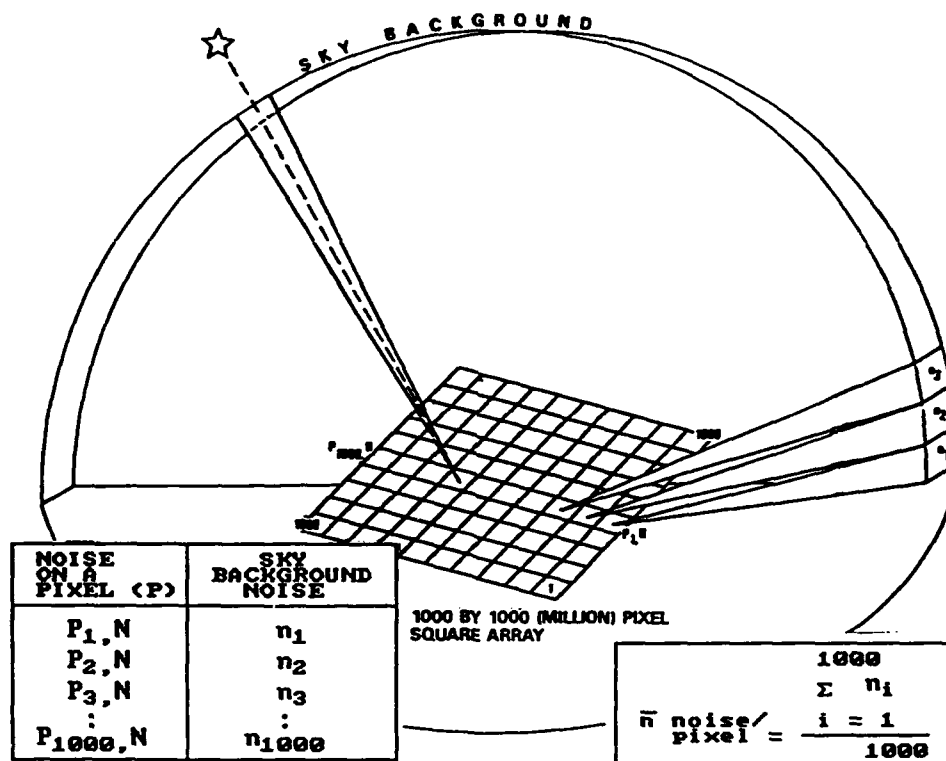IMAGE TRAJECTORY ACROSS AN UNSTABILIZED CCD STAR DETECTOR

Figure III.2

TOTAL PHOTON ENERGY = ARTIFICIALLY STABILIZED IMAGE X TIME

STRAPDOWN CCD CHARGE ENHANCEMENT

Figure III.3

SKY BACKGROUND NOISE FOR A 1000 x 1000 PIXEL
[ONE MILLION PIXEL] SQUARE ARRAY

IV. STELLAR, GROUND, AND HORIZON VISIBILITY

The probability of seeing a star is a critical parameter of
terrestrial stellar-inertial. Furthermore, if a velocity
correlator or horizon sensor is utilized as an inertial
augmentation aid, its visibility probabilities must also be
accounted for in arriving at an optimum autonomous navigation
system.

Figure IV.1 shows the Northern Hemisphere probability of a clear
line-of-sight for the sky, horizon, and ground visibilities. By
factoring this data for a 480-knot vehicle, a 99% probability of
seeing a star at sea level is achieved in one tenth the Schuler
period (or eight minutes--see Figure IV.2). When the vehicle
altitude is increased, there is a twofold improvement in star
visibility. The clear line-of-sight probability increases, and
the number of independent field-of-view (FOV) observations also
increases. As such, the 99% probability of seeing a star for a
480-knot vehicle operating at 25,000 feet is reduced to only 1.8
minutes, or 2 percent of the Schuler period. This 25,000 foot
altitude flight is illustrated in Figure IV.3. In addition, the
probability of seeing the ground at low altitude is very high.
The horizon visibility at high altitude is sufficient to provide
excellent vertical damping information for an inertial navigator.

Sky brightness is another impediment to seeing the stars in
daylight at sea level. The sky brightness ratio from sea level
to 100,000 feet ranges from 100:1 to 1000:1. This inhibited the
ability of the ancients to engage in stellar navigation during
daylight. Sun navigation occurred during daylight hours. Modern
man, so far, has not been effective in utilization of the sun as
an automated terrestrial inertial navigation augmentation aid.
Several attempts at this type of inertial navigation failed to
provide a sun and moon augmentation of one arc-second residual
error. The reason for this failure is that the sun, which has an
angular spread of about one-half a degree, could not be read in a
single snapshot by the previously utilized photo-multiplier
tubes. In addition, the gimbal readouts and their concomitant
errors prohibited this kind of accuracy.

The advent of mega-pixel FPAs high-speed shuttering and Optical
Wide-angle Lens Star-trackers (OWLS) and advanced image
processing algorithms has now permitted the sun to join up with
its brother stars as an inertial navigation aid. The integration
of the sun into the family of astroinertial stars has many
advantages, but it also carries a severe problem in that the sun
represents 1400 watts per square meter. The temperature effects
of optical-imaging the sun must be minimized for its practical
utilization.

The sky background is frequency dependent. When one looks at the
sky, it appears blue. At the 0.7 micron (deep red) wavelength,
the sky background irradiance is reduced by a factor of two.

Silicon FPAs operate at the 0.7 micron region; therefore, they offer some advantage over the previous photo-multiplier tubes by their reduction in sky background effects. As low cost mega-pixel infra-red FPAs are developed, they will be integrated into astroinertial systems. This is because several infra-red bands offer not only minimum star signal attenuation but also substantial reductions in sky background irradiance.
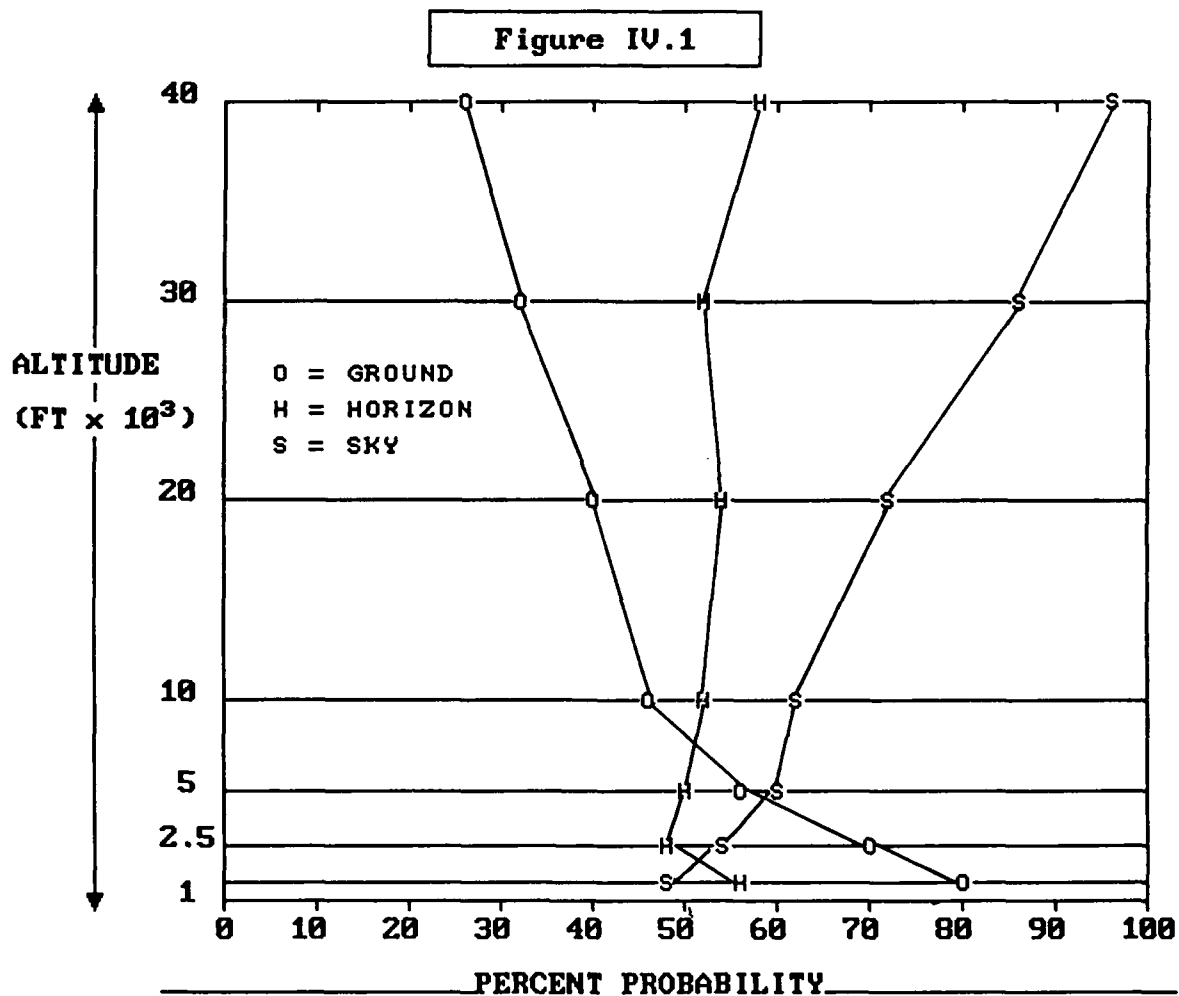
Figure IV.1

PROBABILITY OF CLEAR LINES-OF-SIGHT OVER THE NORTHERN HEMISPHERE FOR ALL SEASONS COMBINED (72,000 OBSERVATIONS)

Figure IV.2
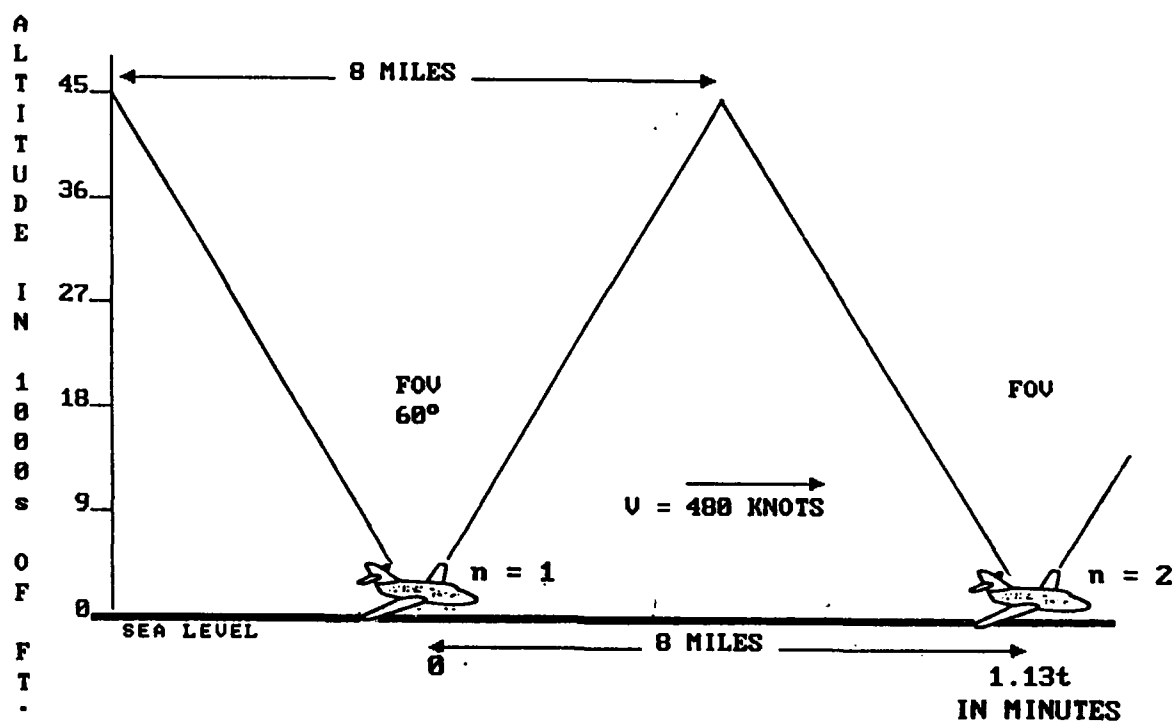
P_1 = 50%
P_7 = 99%
  n = 7
  t = 8 MINUTES

P_n = 1 - [1 - P_1]^n
P_7 = 1 - [1 - 0.5]^7 ≅ 99%

SEA LEVEL FLIGHT AT 480 KNOTS

Figure IV.3

$$P_n = 1 - [1 - P_1]^n$$

$$P_n = 1 - [1 - 0.75]^3 \cong 99\%$$

25,000 FOOT FLIGHT AT 480 KNOTS

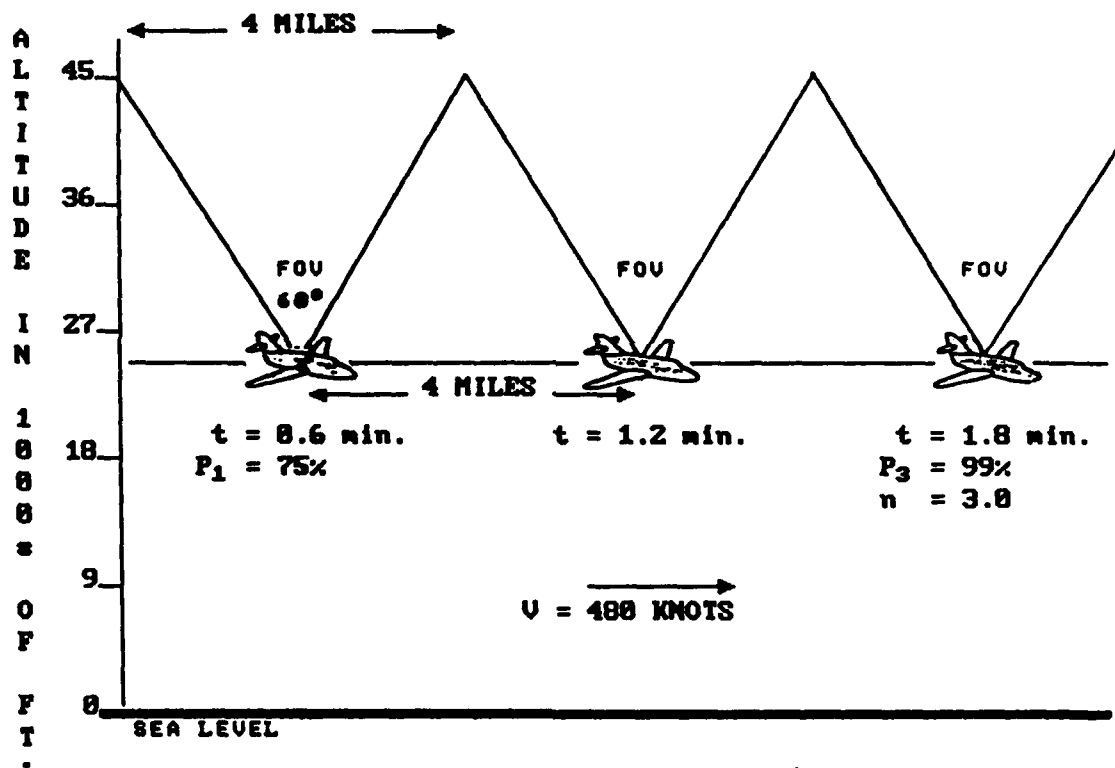## V. OPTICAL WIDE ANGLE LENS STARTRACKER (OWLS)

The probability of seeing a magnitude five (or less) star in the red band with a 3° field of view (FOV) is only 0.675. This 0.675 probability is unacceptable for a sea level tracker designed into a stellar-inertial system whose errors are to be less than 1000 feet. In order to enhance the star detection system, either additional telescopes need to be employed, or an Optical Wide-angle Lens Startracker (OWLS) needs to be utilized. In addition, one narrow FOV lens does not permit the utilization of low performance and moderate performance gyroscopes in a strapdown inertial system. Using more than one telescope (like a fly's eye in principle) appears to be a reasonable star detection solution, but this approach proves to be limited as far as star signal detection is concerned. This is because each additional telescope must divide up the maximum vehicle window area available to collect stars. Any division of the telescope's star signal collection area via an aperture reduction directly lowers the star signal collection power. In a practical solid state system, between four and eight 3° FOV telescopes need to be utilized. This allows for a reasonable amount of cloud coverage while still maintaining some clear lines-of-sight to the stars that are not in the angular vicinity of the sun.

The OWLS system avoids the fly's eye multi-telescope problem in that it provides a 60° field-of-regard and embeds a number of 3° lenses distributed throughout the aperture. This concept utilizes the irradiance of the star over the full aperture. In order to maintain a one arc-second array, 3° FOV sections of the lens are focused on mega-pixel arrays. In the studying of lens systems, only two lenses meet the requirements of a terrestrial OWLS. One is the Monocentric Ball Lens (Popeye) that has been utilized in the SDI Brilliant Pebbles, and another is a Northrop developed holographic lens. Each lens offers some unique advantages, but for low cost, light weight, and mass producibility optics, it is felt that the holographic OWLS is superior. The holographic OWLS utilizes Holographic Optical Elements (HOEs) embedded on a multiple exposure hologram in order to achieve multi-angular telescopes, each of which has the full aperture collection area. Thus, it provides simplicity of manufacture, since the lens system is essentially made by a photographic process. Figure V.1 shows one simplex version of this OWLS system. In this picture, one 3° FOV lens is pointed in one direction in space and focuses on an FPA. Similarly, a different FOV lens superimposed upon the first collects light from another direction in space and focuses on another FPA. Variations of the lens are made to focus all light on one FPA. The choice of the number of FPAs utilized in the focus plane is dependent on the sky background reduction factor, which is a

function of the vehicle's altitude. The star-to-sky density is sufficiently sparse to permit the mapping of the sky onto a small area. As a result, the stellar-inertial system has enough information to re-map the star fix in its proper coordinate frames, thus minimizing FPAs. In high altitude only applications, a single FPA will suffice.

Figure V.1

THE HOLOGRAM LENS KEEPS THE WIDE-ANGLE FULL APERTURE BUT DIRECTS LIGHT INTO SUBSET SOLID-ANGLE MULTI-LENS BUNDLES
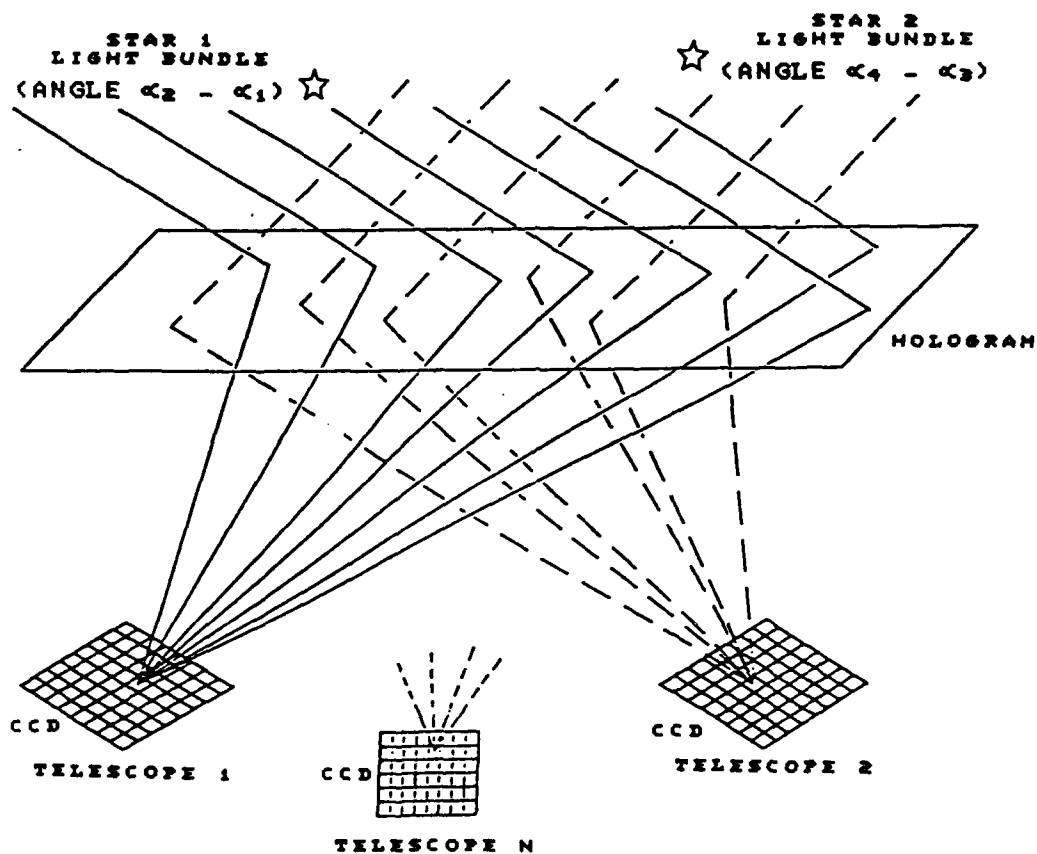
SIMPLEX HOLOGRAM LENS MULTIPLE CCD FOCUS

VI. STELLAR-INERTIAL SYSTEM VALIDATION, PRODUCTION, AND DEPOT TESTING

Just as in any other product, stellar-inertial systems require a total quality management approach to insure product integrity. As such, the quality of the system begins with the designer's calculations and extends through the manufacture of the product. Engineering calculations and high fidelity simulations must be utilized as the initial process to insure that the stellar-inertial system is a high quality product. Modern computer-aided design and simulation tools adapted to electrical, mechanical, optical and inertial systems provide a necessary and invaluable aid in minimizing design flaws. Nevertheless, errors of theory, omission, and commission can and will occur. In order to weed out these design errors it is necessary to validate the design via physical product testing over the specified environment and during system field testing. Starting at the component level and extending to the buildup of the components into subassemblies and assemblies, extensive validation testing must be done. As the sub-arc-second OWLS is integrated with an inertial system, more complex testing must occur. Figure VI.1 shows an astroinertial system undergoing dynamic star tracking and inertial integration testing utilizing a special table fixture. This type of table can provide simulated variable angle stars and strapdown angular platform rates. Figure VI.2 shows some simpler fixed angle star simulator tests that provide variable magnitude stars and sky background. Yet with all this in-situ factory testing the product validation must culminate in an in-vivo flight test program of the entire stellar inertial system over a fiducial high performance tracking range. Since the aim of the flight test program is to validate the design utilizing actual vehicle dynamics and environments as well as stars and sky conditions (e.g., clouds, irradiance, rain, etc.), the fiducial quality of the test range and the gravity grid accuracy and density are of great importance. The horizontal gravity deflections must be known to sub-arc-second levels so that the inertial system can compensate for this phenomenon. Peeling away the gravity errors allows the flight test program to unmask other subtle error sources. During the flight test program, the total system performance, the stellar-inertial system, and the vehicle window (Figure VI.3) must function as a single entity for a successful program. Figure VI.4 shows a matrix of system parameters as a function of time, and Figure VI.5 shows one embodiment of a typical modular stellar-inertial system.

A variant of this design that is applicable to high precision ballistic missiles is a configuration where the Strapdown Stellar-inertial Sensor Unit (SSSU), which is a line-replaceable unit (LRU), gets mounted into a two gimbal simplex calibration controller unit. The controller unit would have no slip rings or angular readouts. It would only be utilized to rotate the sensor assembly during infrequent calibration intervals. During flight,
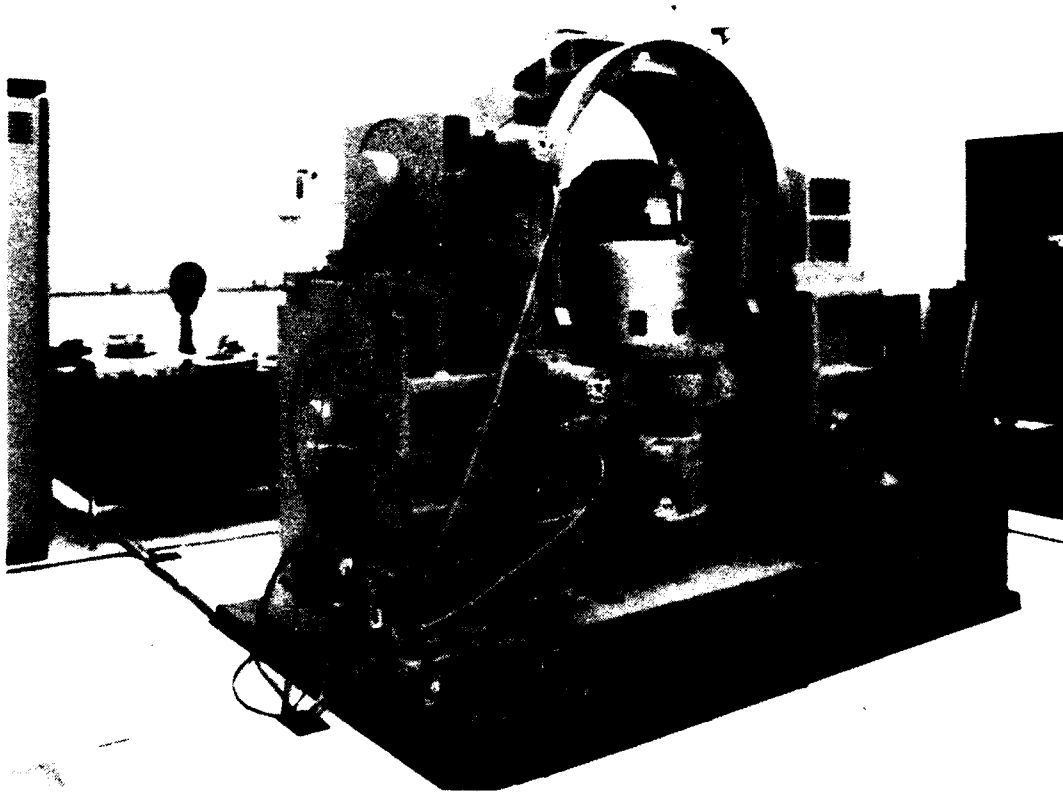
the SSSU would be locked into fixed position with respect to the vehicle. This would allow for a selection of high precision inertial components along the thrust axis and moderate precision components along the cross thrust axis. By utilization of this configuration, angle and angular rate come directly out of the strapdown inertial package without the need for shaft angle encoders. The OWLS provides a wide FOV and thus can optimally compensate for three axes of gyroscopic drift and their effects on navigation during flight. The design, as previously mentioned, provides a high level capability for self checking, since the stellar measured errors should be commensurate with the inertial error propagation. It should be mentioned that the calibration controller unit is not required for most other applications, and its purpose is to provide variable earth rate and gravity effects for a stationary vehicle. This configuration provides the reliability, simplicity, and cost savings of a strapdown system while maintaining a ballistic missile self calibration mode.

Once the flight test program is successfully completed, the task of production testing must be re-evaluated. This is necessary since the economics of production testing forces the minimum testing that insures the quality of the product from a workmanship point of view. The concept of the design being already validated must be accepted, and yet, because of a number of factors, (i.e., shrinking vendors forcing substitute parts, subtle process changes, etc.) a more stringent lot sampling system test must also be incorporated. These sub-arc-second tests (they represent tolerances of one inch in three miles) are are not simple to make, yet they are possible and can yield the benefits of autonomous high performance terrestrial navigation. Furthermore, when the stellar-inertial system is integrated with an electromagnetic navigation system, a high performance position and velocity redundant navigation process occurs that aids in mission success. It should be noted that GPS cannot provide vehicle Euler angles and angular rate information; yet when the electromagnetic radiation navigation is not available, the mission can still be successful via the unaided stellar inertial platform.

Since the SSSU, by virtue of its modularity, has many applications, a low cost depot approach to testing can be made. Sub-arc-second star signal simulators can be shared across many programs. Calibration procedures and personnel training share a common thread of learning. Standard Electronic Modules can be developed for a broad range of applications. This commonality will substantially cut into the proliferation of test equipment and test program sets with their concomitant high costs. The OWLS will allow gyroscopes ranging from fiber optics to ring lasers to be utilized in the SSSU for high performance systems. The choice would depend on the mission scenario. As such, SAIN provides an avenue for substantial reduction in high performance autonomous system life cycle cost.

In summary, the advent of low cost digital computers has made strapdown inertial navigators and OWLS both economical and practical. This combination eliminates gimbals and superfluous components and provides an all optical gyroscope and tracker system. This high reliability, low cost technology offers navigation advances for surface ships, commercial aircraft, strategic bombers, cruise missiles, ballistic missiles, remote piloted and hypersonic vehicles. In fact, where high performance autonomous navigation is desired, modern man, like the ancients, can still depend on the stars.

Figure VI.1

DYNAMIC STAR TRACKING SIMULATOR

THIS PAGE LEFT INTENTIONALLY BLANK

STRAPDOWN STELLAR-INERTIAL
SENSOR UNIT (SSSU)

HOLOGRAPHIC
OPTICAL
ELEMENT (HOE)

INERTIAL
ASSEMBLY UNIT
(IAU)

OPTIONAL - VELOCITY CORRELATOR
MODULE (VCM) AND/OR GLOBAL
POSITION SYSTEM MODULE (GPSM)

UNIVERSAL SENSOR
ELECTRONICS UNIT
(USEU)

POWER SUPPLY
MODULE (PSM)

CG SHOCK MOUNT
(4 PLACES)

OPTICAL WIDE-ANGLE LENS
STARTRACKER (OWLS)

DIGITAL
CORRELATOR
MODULE
(DCM)

COMPUTER PROCESSOR
MODULE (CPM)

INSTRUMENT
ELECTRONICS
UNIT (IEU)

I/O MODULE
(I/OM)

STRAPDOWN ASTROINERTIAL SYSTEM
UTILIZING A HORIZONTAL OWLS ASSEMBLY

THIS PAGE LEFT INTENTIONALLY BLANK

Design, Test and Evaluation of a Canadian
Strapdown Gyroscope (CSG-2)-Based AHRS

By

M. Vinnins
L.D. Gallop
F. Paquet

Defence Research Establishment Ottawa

1.0 INTRODUCTION

1.1 BACKGROUND

In 1977, Litton Systems Canada Limited (LSL) produced an experimental strapdown two-degree-of-freedom (TDF), dry tuned-rotor gyroscope using a blend of existing and developing technologies. A new rotor and suspension system with potential to meet the performance requirements of a strapdown inertial navigation system were integrated with the motor and case from the Litton G1200 gyro used in the LTN-72 gimballed inertial navigation system.

This gyro, referred to as the G-2 1/2, was tested extensively at LSL, and the results highlighted several areas still requiring development to provide a gyro suitable for flight evaluation.

At that point, LSL proposed a strapdown design and demonstration program to improve the gyroscope's performance. This proposal led to the award of a Canadian Government contract sponsored by DREO, for the design and demonstration of an improved strapdown gyroscope to be known as the Canadian Strapdown Gyroscope (CSG-2). The CSG-2 Phase 1 program undertaken under this contract was successful and involved the manufacture of four tuned rotor gyroscopes, two of which were delivered to DREO in July, 1983. The DREO gyroscopes have been extensively evaluated in a closed loop (strapdown) configuration and the results presented in DREO reports and papers [1,2,3].

At that time, the development of the CSG-2 was considered to be at a point where accumulation and evaluation of performance data in a system environment was feasible. This led to a proposal to demonstrate the CSG-2 as a closed-loop strapdown unit in an existing Attitude and Heading Reference System (AHRS). The demonstration program consisted of several phases of development for both the gyroscope and the system.

1.2 Gyroscope: Design and Performance

The CSG-2 gyroscope has several unique features, the most significant of which are the "machined-from-solid' flexure mechanization and the use of sophisticated laser welding techniques during the assembly process. The overall design promises high instrument performance at low cost due to the ease of manufacturing techniques employed.

Random drift of the gyro has been shown to be less than 0.01 deg/hr and the use of laser welding rather than epoxies has resulted in excellent long term stability.

As a result of the success of Phase 1, very few gyroscope design changes were required for integration into the AHRS. The modifications included:

- redesign of the rotor magnetic circuit to reduce the torquer scale factor, thus increasing the output signal for a given rate,

- use of Samarium Cobalt (Sm_2Co_5) magnets to reduce costs,

- thermal modelling to reduce temperature sensitivity and improve stability, and

- use of laser welding to improve gyro cover seals.

CSG-2 performance specifications are shown in Table 1-1.

2.0 System Design

LSL proposed the use of a development system, the LTN-73, as a test-bed into which the CSG-2 would be installed. The LTN-73 is a modified LTN-72 package from which the sensor block and gimbals have been removed and replaced by a triad of ring laser gyros (RLG's) with appropriate modifications to the system software. The LTN-73 is intended to be a "universal" AHRS within which almost any combination of strapdown sensors could be installed. This unit is referred to as the Performance Evaluation Unit (PEU). In order to interface the CSG-2 to the LTN-73, several system design modifications/developments were necessary:

- assessment of gyro power supply requirements to provide appropriate start and run sequence, and variable frequency to tune the gyros,
- assessment of rebalance loop requirements for the CSG-2,
- development of rebalance electronics,
- development of the digital interface between the AHRS and CSG-2 rebalance electronics,

PARAMETER	UNITS	DESIGN GOAL	TYPICAL INERTIAL GYRO GRADE	COMMENTS
Random Drift	°/Hr	< 0.005	< 0.005	
Non-G Sensitive Drift	°/Hr	< 3.0	< 4.0	System Compensation
Non-G Drift Repeatability	°/Hr	< 0.01	< 0.007	Turn-On to Turn-On
Non-G Drift Temperature Sensitivity	°/Hr/°C	< 0.018	< 0.0252	60 °C to 74 °C
G-Sensitive Drift (R.S.S.)	°/Hr/G	< 10.0	< 0.5	System compensation with G level info.
G-Sensitive Drift Repeatability	°/Hr/G	< 0.02	< 0.02	Turn-On to Turn-On
G-Sensitive Drift Temperature Sensitivity	°/Hr/G/°C	< 0.05	< 0.04	60 °C to 74 °C
Torquer Scale Factor	°/Hr/mA	750 - 1800		Application dependant
Torquer Resistance	Ohms	50		
Torquer Axis Alignments	mRads	< 19.39		
Wheel Speed (Resonant Frequency)	Hz (mech)	100 ± 5		4-Pole Motor Driven By ≈400 Hz
Motor Power - Start	Watts	< 8		
- Run	Watts	< 3		
Wheel Run-Up Time	Sec.	< 30		
Operating Temperature	°C	68.3		

Table 1-1   CSG-2 Design Specifications

- development of software compensation for thermal parameters and gyro/accelerometer scaling, and
- design and integration of a sensor block for the AHRS package.

2.1 REBALANCE ELECTRONICS

2.1.1 Rebalance Loops

The rebalance loop design used in the PEU is a relatively standard phase lag control design, using a phase lag of $180°$ for nutation control, and precision resistors in series with the torquer coils of the gyroscope to obtain a voltage signal directly proportional to the rate input of the gyro. The rebalance loop electronics for each gyroscope include only the "direct-axis loops", that is, the loops producing the X and Y torques from the Y and X pickoff signals respectively. No scheme for the elimination of the closed loop acceleration sensitivity was used since phase lag loops do not normally include any cross-axis decoupling.

The transfer function of the loop electronics has a proportional plus integral term with a third order low-pass filter response for the phase lag. No wheel spin frequency notch filtering is included.

The "torquer driver" stage is a transconductance push-pull amplifier capable of driving currents of up to ± 0.3 A into 56 Ω torquer coils and with 30 Ω current sensing resistors (a total load resistance of 86 Ω). With gyroscopes having torquer scale factors of ≈ 850 °/hr/mA, this translates into rates of up to ± 67 °/sec.

At start-up, while the gyroscopes are getting up to speed, the torquer currents are suppressed with electronic switches shorting the feedback RC network of the integrated circuits serving for the integrating function of the loops.

Further information on rebalance loops, a dynamic analysis and a description of RL-3, the DREO-developed rebalance loop, are given in appendix A.

2.1.2 Analog to Digital Converter

The analog to voltage converter includes 3 precision voltage integrators each having a feedback closed with a multiplexed precision reference current source digitally controlled as a function of the output of the integrators. The integrators continuously sense the rate voltage signals on 3 axes, and these signals are sequentially rebalanced by precision pulses from the

current source. The average output of the integrators is zero and therefore, the integral of the feedback current pulses (pulse count) is equal to the integral of the sensed rate voltage signal. The digital signals that control the multiplexed current source serve also as the 3 axis digital output for this digitizer.

2.2 System Design Specifications

A synopsis of the system design specifications is contained in Table 2-1. System performance goals are shown in Table 2-2.

The proposed performance goals are to be considered as 'minimum' by industry standards and higher performance should be expected using CSG-2 gyroscopes. The PEU was delivered to DREO in 1987 and extensive tests commenced in the DREO Inertial Navigation Laboratory (Navlab).

3.0 The DREO Inertial Test Facility

The DREO Inertial Navigation Laboratory was developed between 1977 and 1981 as a complete gyroscope and inertial system test facility for the evaluation of strapdown components and systems. The laboratory's purpose is twofold: it provides the department with the ability to evaluate various manufacturer's navigation components or systems; and acts as a flexible independent facility for experimental research and development.

Computer control of the laboratory has been a major emphasis from 1986 to the present. The software design is modular in concept and has been written as individual tasks that can stand alone, run concurrently, or be coordinated by a controlling task. This takes advantage of the multi-tasking capabilities inherent in the RSX11M operating system on the Digital PDP 11/73 computer. Automation of experiments and data acquisition from short transient tests of milli-seconds to long term tests running several hours has been the goal.

The Navlab is capable of simulating a wide range of environments including 0, 1 and 2-axis motions, earth rate compensation and temperature analysis. Tests include drift coefficients, instrument integrity, drift stability and repeatability, thermal sensitivity, torquer scale factor linearity, and rate transients. Motion control of navigation components for testing purposes is made possible through the use of a Contraves Goerz 2-axis precision motion table.

Spin Motor Supplies

Two three-phase square wave fixed voltage supplies with independent software frequency control.

a) Voltage (start):   14 VAC line to line.
b) Voltage (run):   8.5 VAC line to line.
c) Frequency:(electrical)   390 to 410 Hz (Actual
                            value depends on gyro)
d) Frequency Resolution: 0.01 Hz
e) Frequency Stability: ±0.01%

Pickoff Excitation

Constant voltage primary excitation requirements for all gyro pickoffs.

a) Voltage: 5 VAC rms ±0.05 VAC
b) Voltage Stability: ±1%
c) Frquency: 54 KHz ±1%
d) Frequency Stability: ±0.1%
e) Pickoff Load(2 gyros):   12.5+j70 Ohms ±20%

Pickoff Output

a) Nominal Scale Factor: 1.45 VAC rms/milliradian
b) Scale Factor Tolerance: ±20%
c) Pickoff Output Impedance: 25 Ohms max.

Pickoff Amplifier Supplies

a) Voltage: ±15 VDC ±1.2 VDC
b) Current (both gyros):

Table 2-1: System Design Specifications

	Pitch	Roll	Heading
Rate Range (deg/sec)	70	70	40
Drift (deg/HR)	5	5	5
Dynamic Range (deg)	0 to 85	0 to ±180	0 to 360
Accuracy (deg)	0.5	0.5	1° (Slaved) $\begin{bmatrix} 5°/\text{HR} - \text{Free} \\ \text{DG Drift} \end{bmatrix}$

Table 2-2: System Performance Goals (ARINC Standard 705)

Remote motion table control is achieved by an in-house developed Motion Table Language (MTL) interpreter written in Fortran 77. MTL includes features that initiate data collection by user specified logging routines, independent of the MTL application, at any desired point in the MTL program, providing coordination of data collection with table motion. A library utilising various forms of coordinated data collection MTL programs has been established for routine laboratory test procedures. This automation of the table through the use of MTL eliminates much of the test supervision requirement and at the same time increases the accuracy, repeatability and reliability of both the experiment and the data collected without limiting the flexibility of the system.

The laboratory sensors utilize the IEEE 488-1978 general purpose instrument bus (GPIB) for communications and interface with the Digital PDP 11/73 computer. As well, custom hardware and software drivers have been developed to handle the ARINC 429 digital data.

A number of software logging tasks have been developed to aid in data collection both in a coordinated manner in conjunction with MTL and in a stand alone mode. These logging routines include: a) Log Datron (precision multimeter) b) Log ARINC, c) Log A2D d) Log Scope e) Log Temp, and f) Log Table. All of the tasks have similar data logging formats and include block averaging and a basic statistical summary of the data points collected.

With the degree of automation currently developed in the Navlab comes the problem of keeping track of the coordinate relationships of devices under test and the parameters being measured. The intensity of this problem appears directly proportional to the time lapse between the collection and analysis of the data.

Once a navigation package is secured to the motion table platform, the axes coordinates and their interrelationships are set. A task has been developed to aid in documenting this relationship for later referral. This task prompts the user through a series of menus to create, based upon user response, a file tabulating the various coordinate relationships and "tombstone" information of device under test. The file, once created, can be merged into any of the logging task data files discussed earlier, thus providing a future reference of the Cartesian coordinates to be used during data analysis.

Data analysis including importation of ASCII data files, data reduction to engineering units, statistical tests and data summaries, curve fitting, and graphic presentation of the data generated from the "logging" routines is handled by the commercial software application RS/1.

4.0 SYSTEM TESTS

4.1 TEST DESCRIPTION

To evaluate both gyroscope and system performance, the PEU was designed with a spare test connector which permitted access to the analog torquer current signals from each gyroscope. This enabled direct measurement of the gyro outputs for comparison to ARINC outputs. The system output is standard ARINC 429 with the following data parameters (only) available:

LABEL	PARAMETER	UPDATE RATE (Hz)	RESOLUTION
324	Pitch Angle	64	0.005493°
325	Roll Angle	64	0.005493°
334	Platform Heading	16	0.005493°
331	Body Longit. Accel.	64	0.000122 g
332	Body Lateral Accel.	64	0.000122 g
333	Body Normal Accel.	64	0.000122 g

Both raw (analog, gyro output) data and system (digital, ARINC 429) data were recorded for each test for comparison purposes.

Upon delivery, the PEU was mounted on the 2-axis motion table as shown in Figure 4-0. The top cover was modified to create a breakout panel where all connections could be tested or monitored. In addition, several temperature sensors were installed within the sensor block for recording purposes.

4.2 Drift Coefficients (Multiposition Test)

As was shown in Figure 4-0 the Litton PEU, when mounted on the motion table, is too large to be oriented in some positions. This prevents the performance of a complete set of multi-position tests for each system axis. As a result, the individual CSG-2 gyros were tested, after being removed from the PEU, to determine the drift coefficients. The DREO-developed rebalance loop, RL-3, was used for these tests. No ARINC data was available.
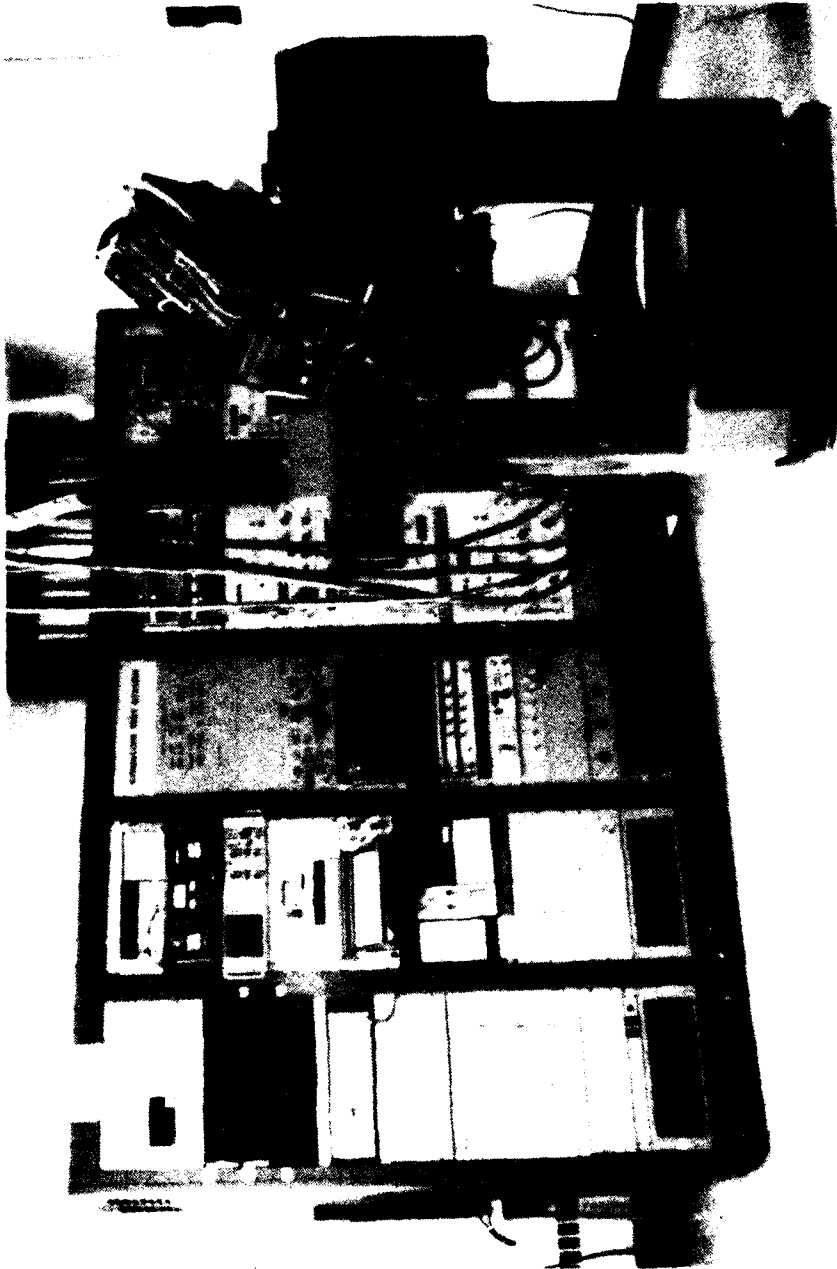
Figure 4-0 DREO Inertial Navigation Laboratory

A comparison between LSL and DREO results is shown in Table 4-1.

The following points should be noted:

- Torquer Scale Factor for these gyros was originally specified to be 750 deg/hr/ma. The actual scale factor is higher due to lower tuned wheel speed resulting from decreased suspension flexure thickness.

- Scale Factor Repeatability is worse than expected (0.01%). The errors are most likely accumulated from gyro, loop closure and thermal control repeatabilities.

- Scale Factor Temperature Sensitivity was found to be 550 ppm/$^\circ$C; comparable to other gyros employing Samarium Cobalt magnets and similar to earlier gyros with Platinum Cobalt magnets

- Random drift values are all inertial grade.

- Non-G sensitive (Bias) repeatability is better than specifications and compatible with high accuracy inertial navigation requirements.

- G-sensitive drifts are as expected. Of special note is the quadrature mass unbalance Q_x, Q_y. This term is less than 0.5 deg/hr/g and is a good measure of suspension flexure quality.

- G-sensitive (mass-unbalance) repeatability values are good, demonstrating the importance of laser welding over adhesive techniques for rotor assembly.

- Anisoelasticity continues to be an elusive property to control in that it is a function of the machining of the suspension rings and flexures. These parts are already so tightly toleranced that the cost to improve production control is large.

- The time constant for both gyros is lower than expected. According to Litton, numerous refills achieved no improvement. The extra thickness of the magnet rings due to plating is the probable cause due to reduced air gaps (windage).

4.3 Random Drift

Figures 4-1 to 4-4 are plots of random drift for both the pitch and roll axes. Figures 4-1 and 4-2 are raw instrument outputs. The random drift stability in both cases is 0.02 deg/hr or better.

DATE: 07 FEB 89	GYRO DATA SOURCE		LITTON	DREO	LITTON	DREO
PARAMETER	SYMBOL	UNITS	GYRO 13	GYRO 13	GYRO 17	GYRO 17
TORQUER SCALE FACTOR	Kx	°/Hr/mA	873.11	871.82	869.17	863.62
	Ky	°/Hr/mA	870.02	867.84	860.74	854.85
SCALE FACTOR REPEATABILITY	Kx	%	0.0097	0.0230	0.0242	0.0428
	Ky	%	0.0230	0.0150	0.0136	0.0983
SCALE FACTOR TEMPERATURE SENSITIVITY	T Kx	ppm/°C	481	-	506	516
	T Ky	ppm/°C	499	-	470	447
TUNED FREQUENCY (Horizontal)	FRh	Hz (Mech)	85.31	85.30	84.62	84.75
	FRh	Hz (Elec)	341.25	341.20	338.48	339.00
RANDOM DRIFT (Horizontal)	σXh	°/Hr	0.0021	0.0110	0.0023	0.0100
	σYh	°/Hr	0.0027	0.0030	0.0039	0.0030
NON-G SENSITIVE DRIFT	Bx	°/Hr	-3.2402	-3.3317	-0.7496	-0.6386
	By	°/Hr	-1.5554	-2.8843	-2.2434	-3.1354
NON-G SENSITIVITY REPEATABILITY	σBx	°/Hr	0.0027	0.0080	0.0043	0.0400
	σBy	°/Hr	0.0060	0.0040	0.0170	0.0220
G-SENSITIVE DRIFT	MUx	°/Hr/g	-0.4628	0.1704	3.4359	7.3368
	MUy	°/Hr/g	-0.4656	0.1557	3.4243	7.3412
	Qx	°/Hr/g	0.1669	-0.2183	-0.2791	0.1509
	Qy	°/Hr/g	0.1065	0.2728	-0.1427	-0.2219
G-SENSITIVITY REPEATABILITY	σMUx	°/Hr/g	0.0093	0.0020	0.0340	0.0350
	σMUy	°/Hr/g	0.0185	0.0050	0.0240	0.0360
ANISOELASTICITY (G²-SENSITIVE)		°/Hr/g²	0.398	0.015	-0.383	0.022
MOTOR START POWER (10 V)		Watts	4.89	-	5.43	-
MOTOR RUN POWER (5 V)		Watts	0.906	-	0.906	-
TIME CONSTANT		sec.	97	75 ±2	80	68 ±5
PICKOFF SCALE FACTOR	K POx	V/mRad	1.084	-	1.059	-
	K POy	V/mRad	1.108	-	1.061	-

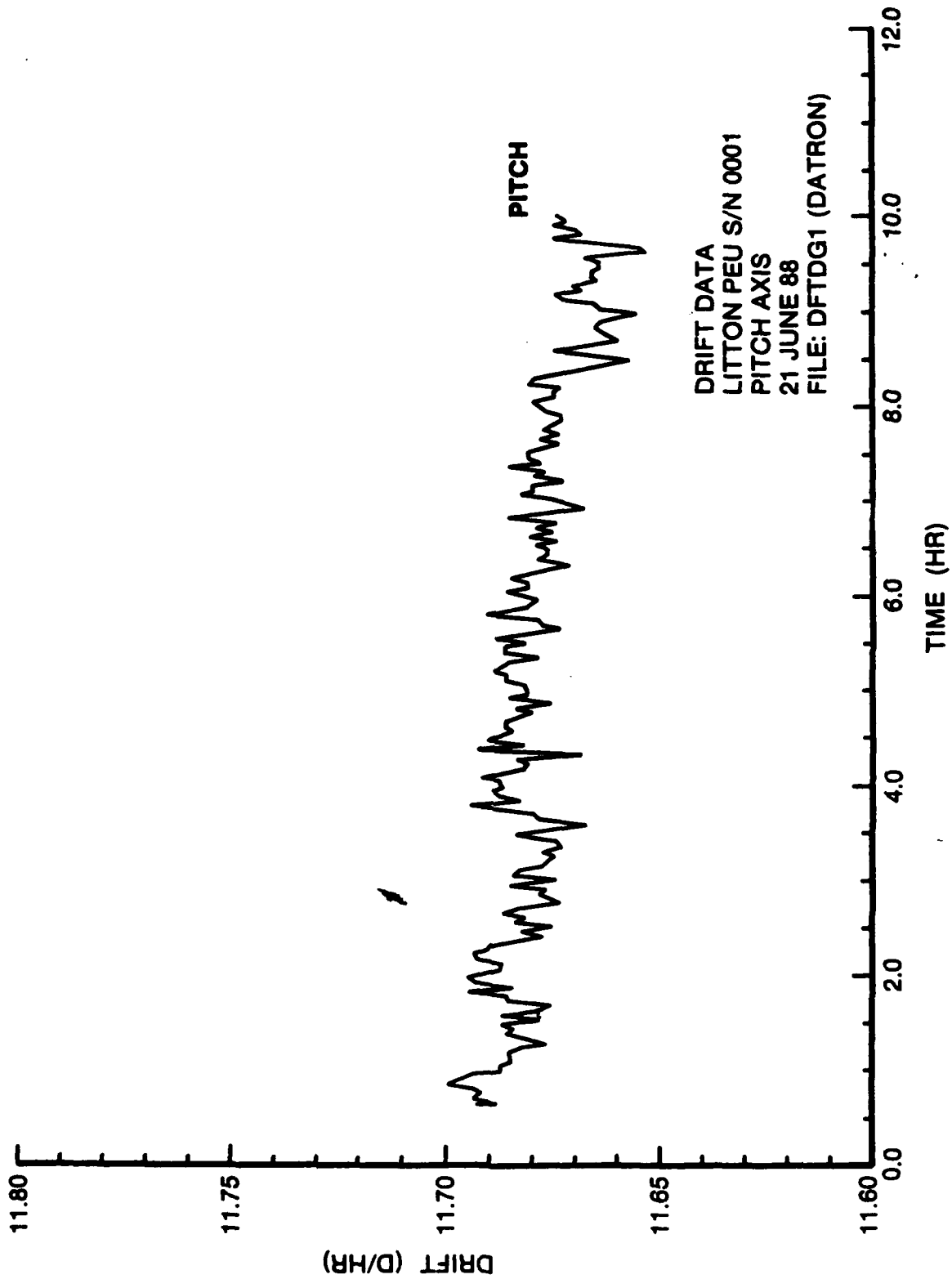Table 4-1:   Drift Coefficients for PEU Gyros

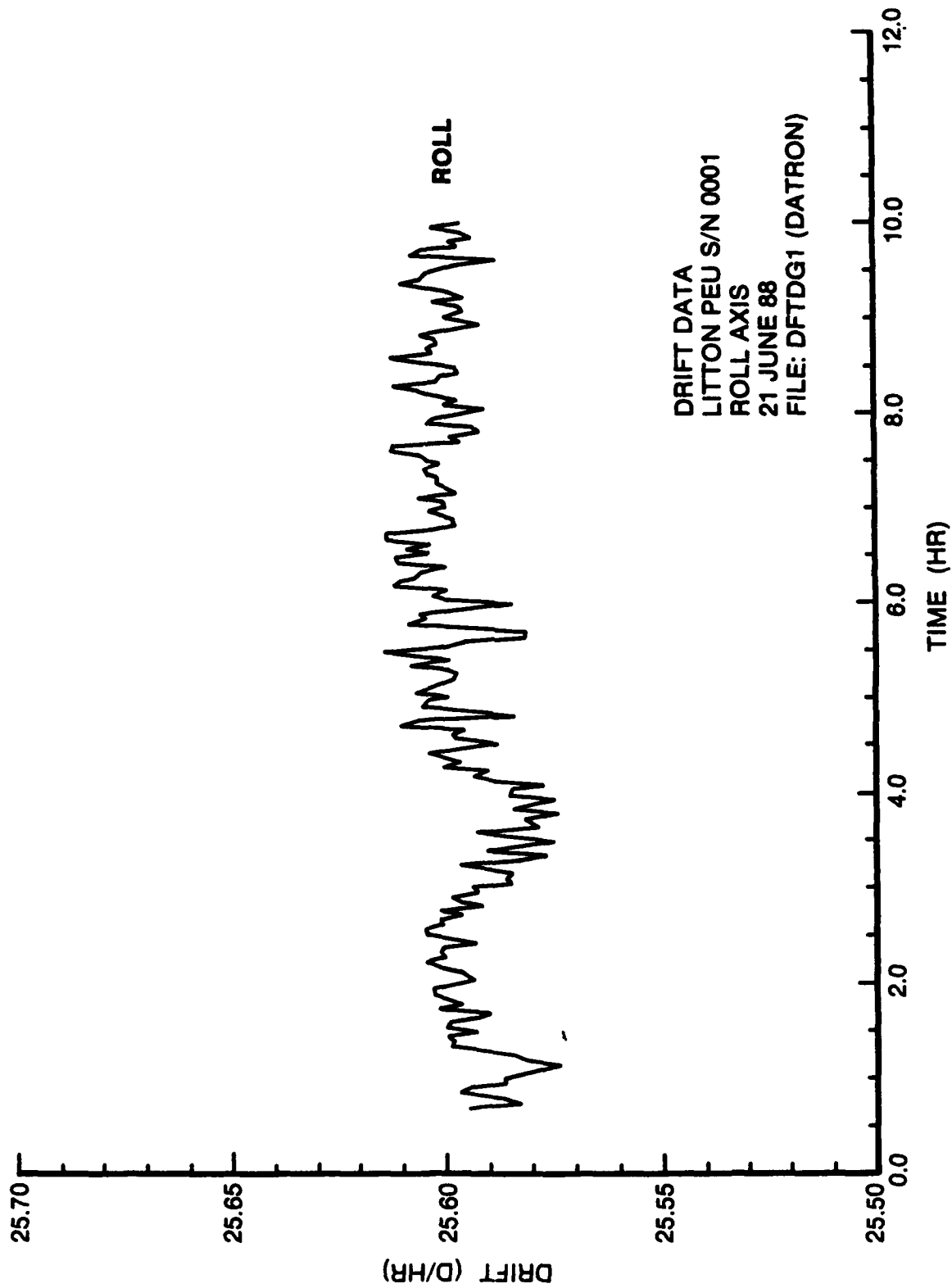Figure 4-1: Random Drift, Pitch Axis (Analog)

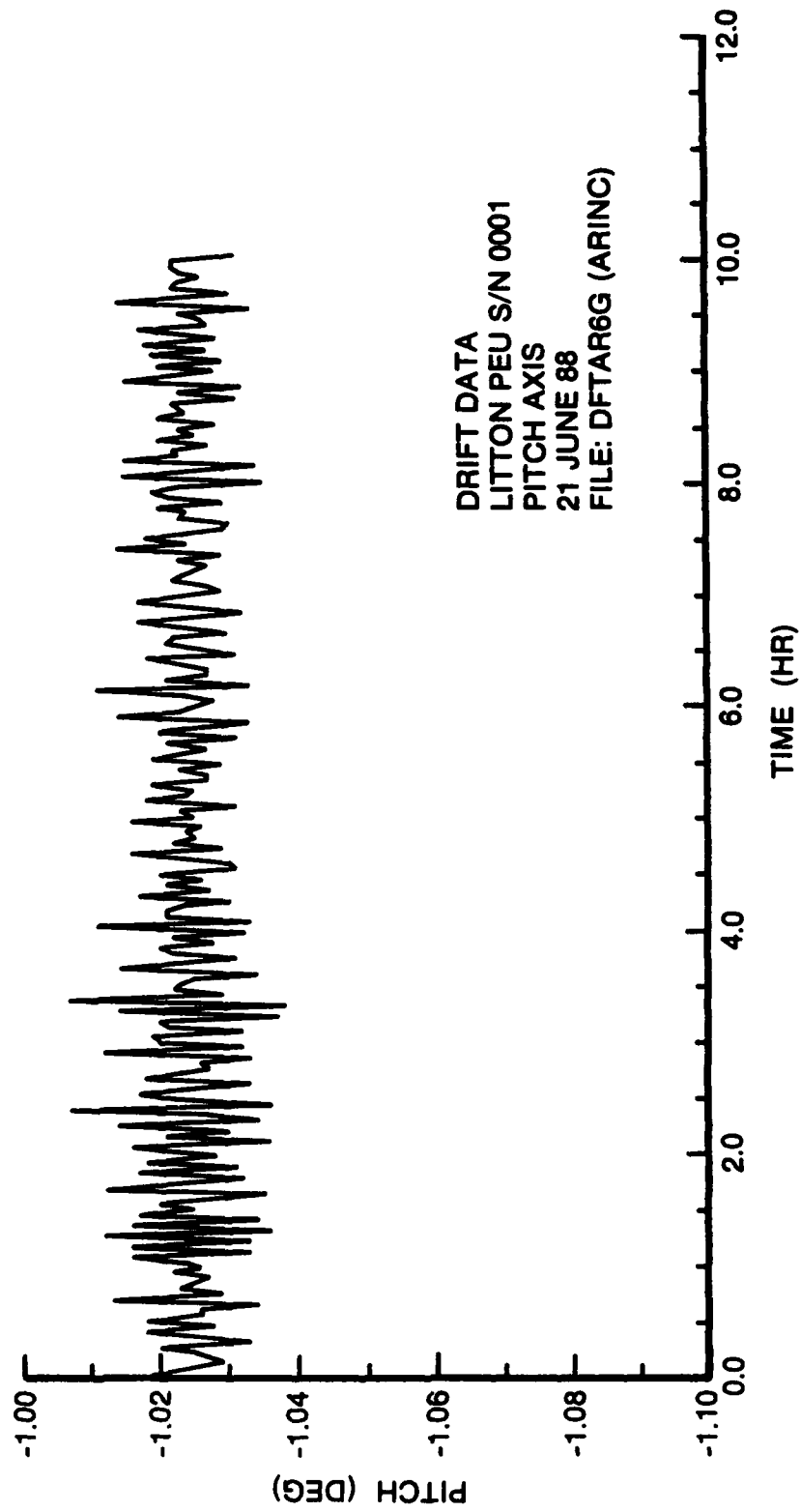Figure 4-2:   Random Drift, Roll Axis (Analog)
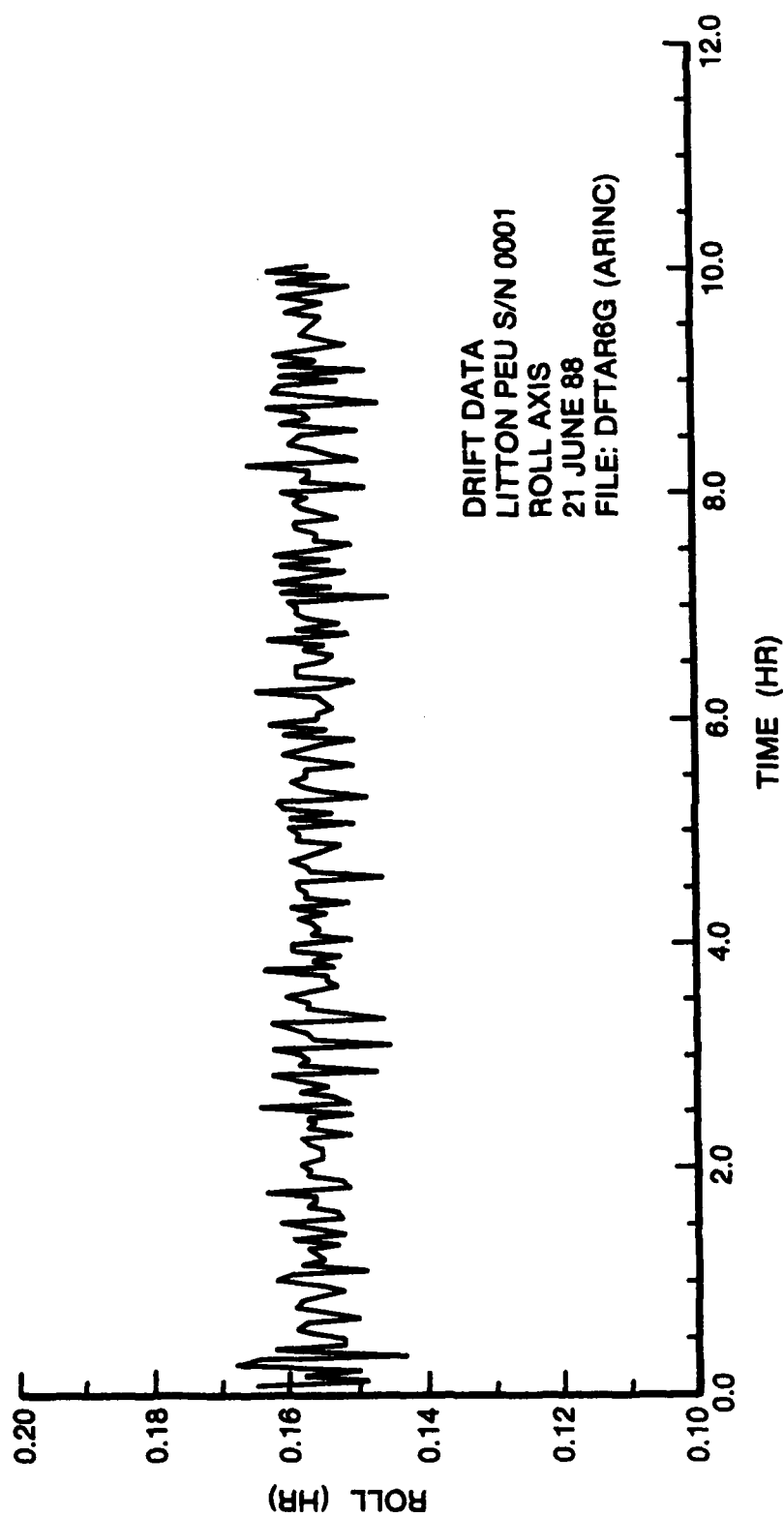
Figure 4-3:   Random Drift, Pitch Axis (ARINC 429)

Figure 4-4:   Random Drift, Roll Axis (ARINC 429)

4.4 Scale Factor Deviation

Figure 4-5 is a plot of scale factor deviation (from nominal) over a rate range of ± 1 radian/second for the azimuth axis. The deviation is ≈ 7700 ppm.

This result is consistent with the changes made in scale factor as compared to earlier gyros. The original CSG-2 design called for a torquer scale factor of ≈ 1700 deg/hr/mA. Tests performed on those instruments showed a scale factor deviation of 1800 ppm over ± 1 rad/sec due to torquer heating effects.

The gyros used in the PEU have a much lower torquer scale factor but this results in a proportionately higher current demand over a given rate range. Since torquer heating is proportional to the power in the torquer (I^2R), the actual temperature changes as the square of the current. As a result, since the scale factor deviation for a gyro with a scale factor of 1700 deg/hr/mA has been shown to be ≈ 1800 ppm over ± 1 rad/sec, then for a torquer scale factor of 850 deg/hr/mA, the actual deviation can be expected to be four times as large or ≈ 7200 ppm. This is, indeed, the case as shown in Figure 4-5. (Note, also, that the curve fitted to the data is a second order polynomial, consistent with the I^2R effect). The plot also shows a 'skew' between the positive and negative rates. This is believed to be due to a pickoff misalignment about that axis in the gyroscope.

To verify this, a scale factor linearity test was repeated after the gyroscope was removed from the PEU. A laboratory rebalance loop (RL-3) was used for this test to eliminate any possible rebalance loop errors which might have affected results in the PEU. A plot of the scale factor deviation is shown in Figure 4-6. Note that the apparent 'skew' still exists; it is independent of the rebalance electronics. It is likely that this effect is due to pick off misalignment; the electrical and mechanical 'null' points are not coincident.

Similarly, the pitch axis gyroscope was tested. As is shown in Figure 4-7, there is no "skew' effect, but rather, good symmetry.

In addition, scale factor deviation data as recorded from the ARINC 429 data bus is shown in Figure 4-8. Note that due to the low resolution (>1000 ppm), the data is of questionable value in determining sensor capabilities and performance.
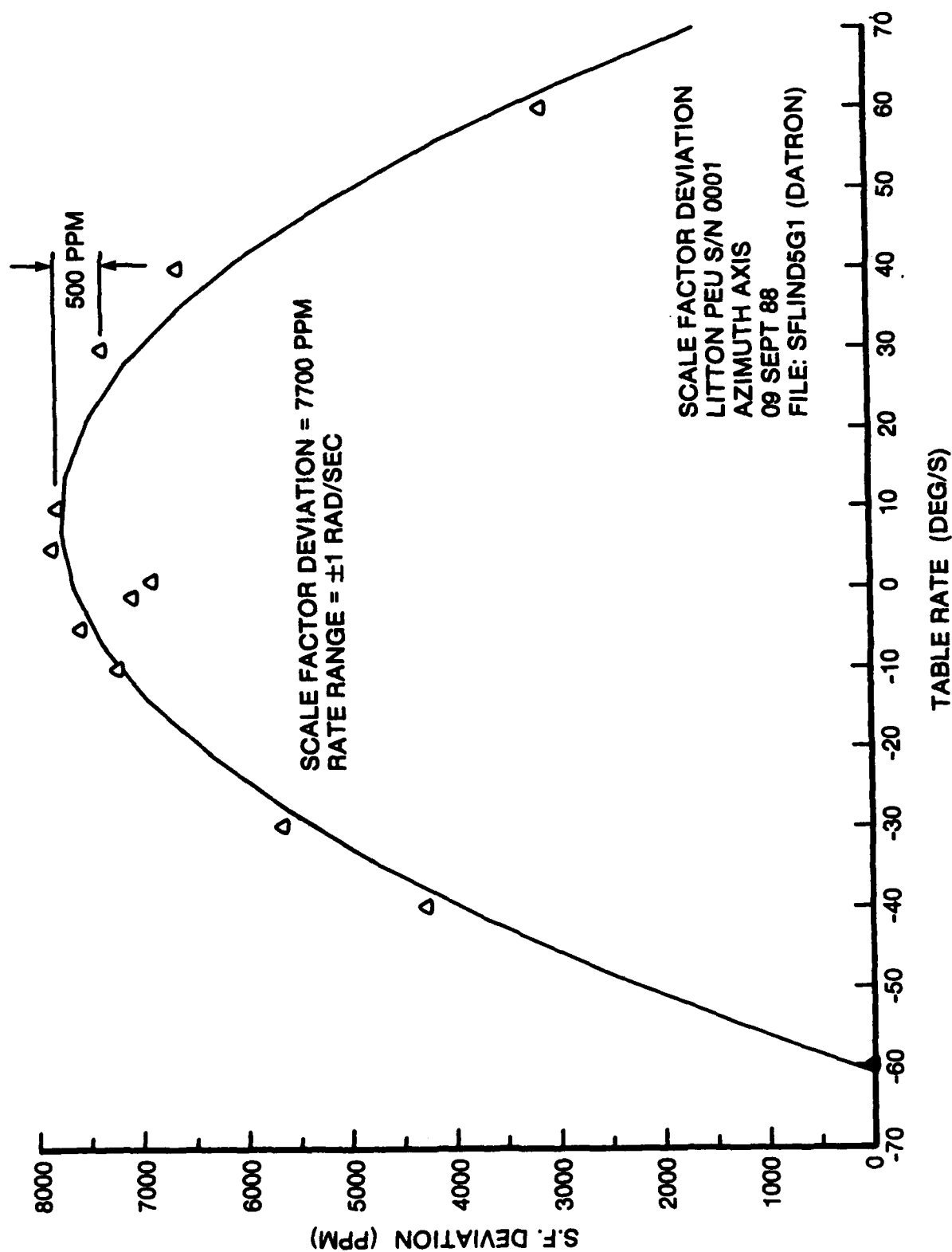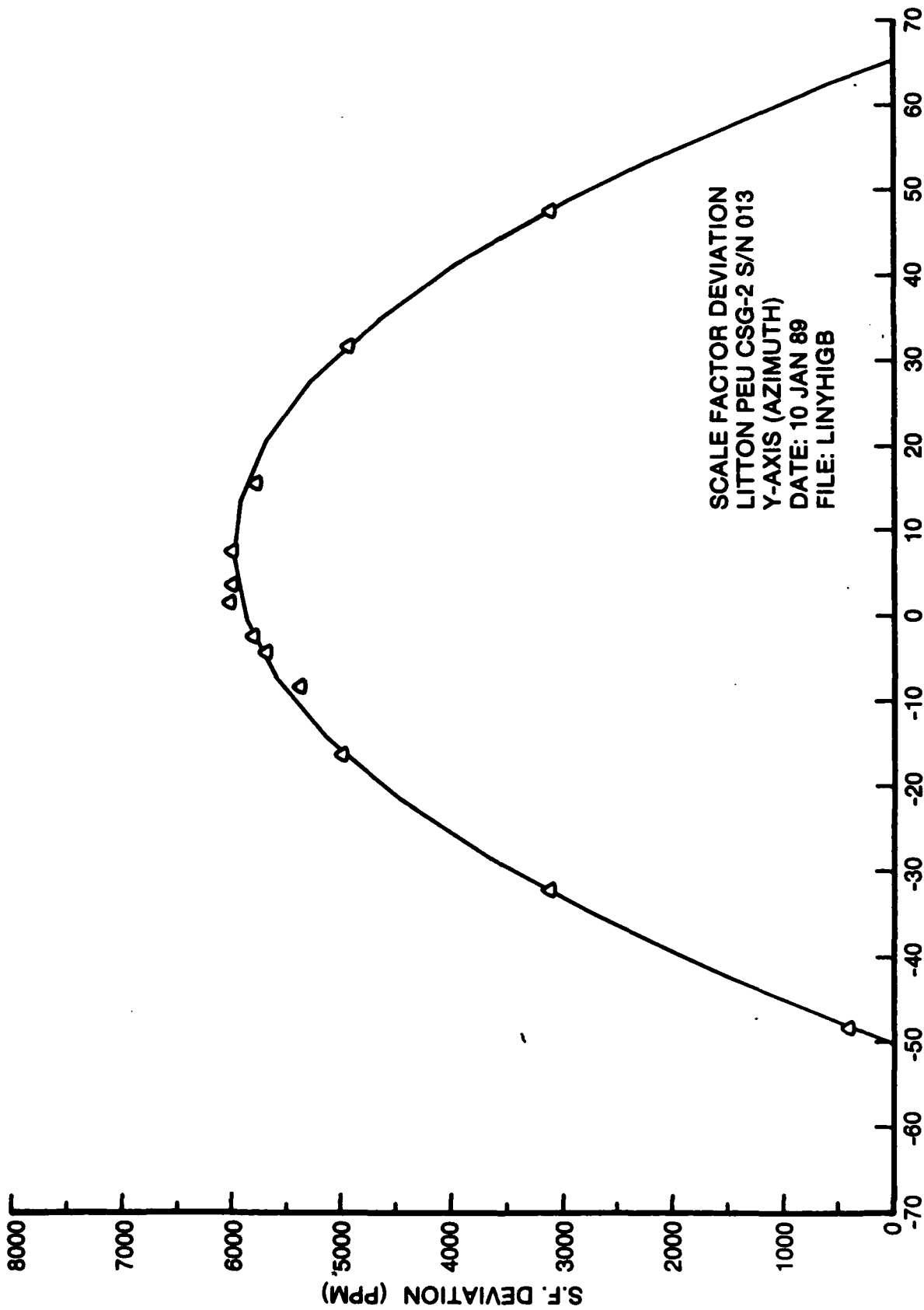
Figure 4-5: Scale Factor Deviation

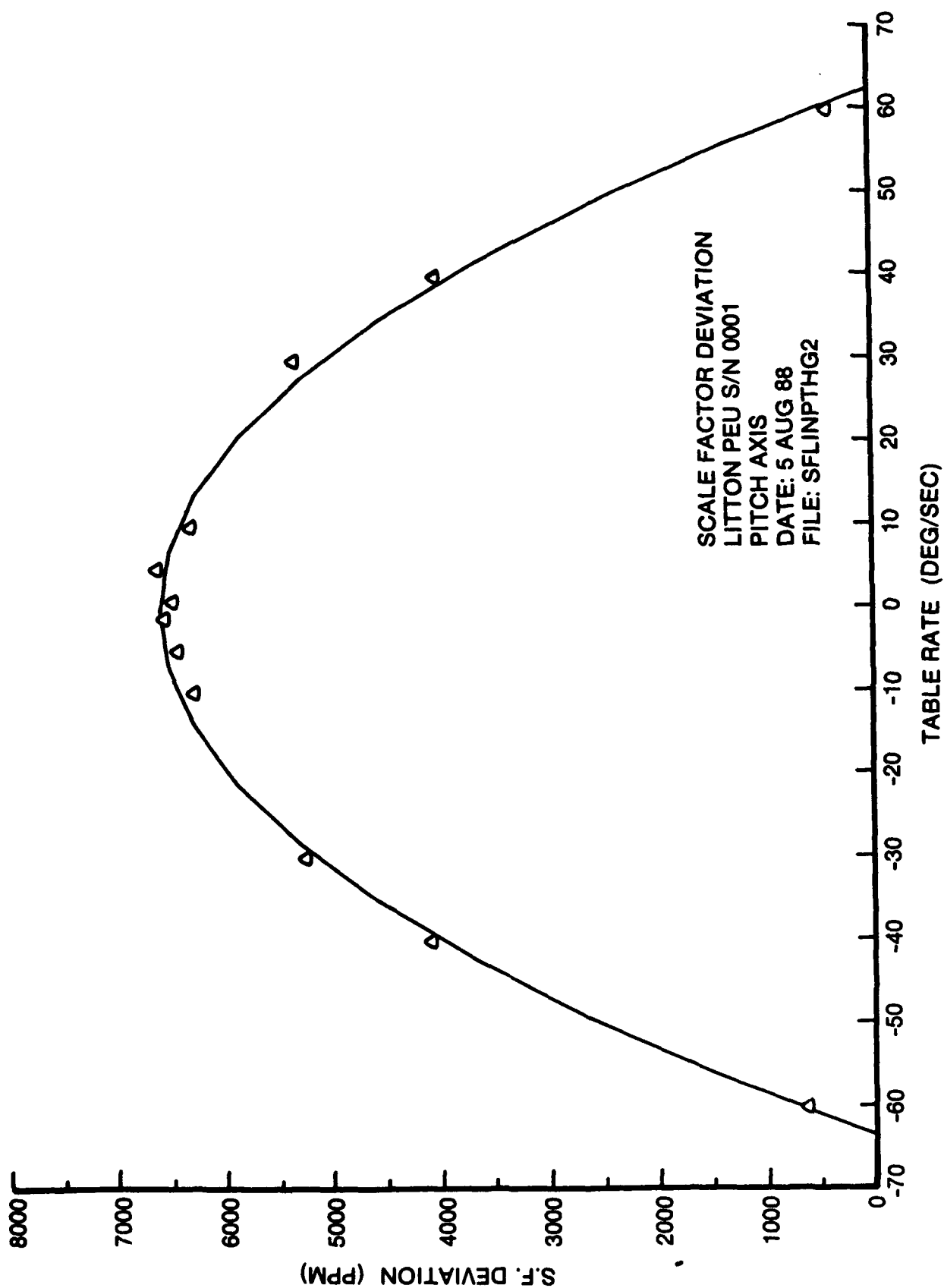Figure 4-6: Scale Factor Deviation, Azimuth Axis

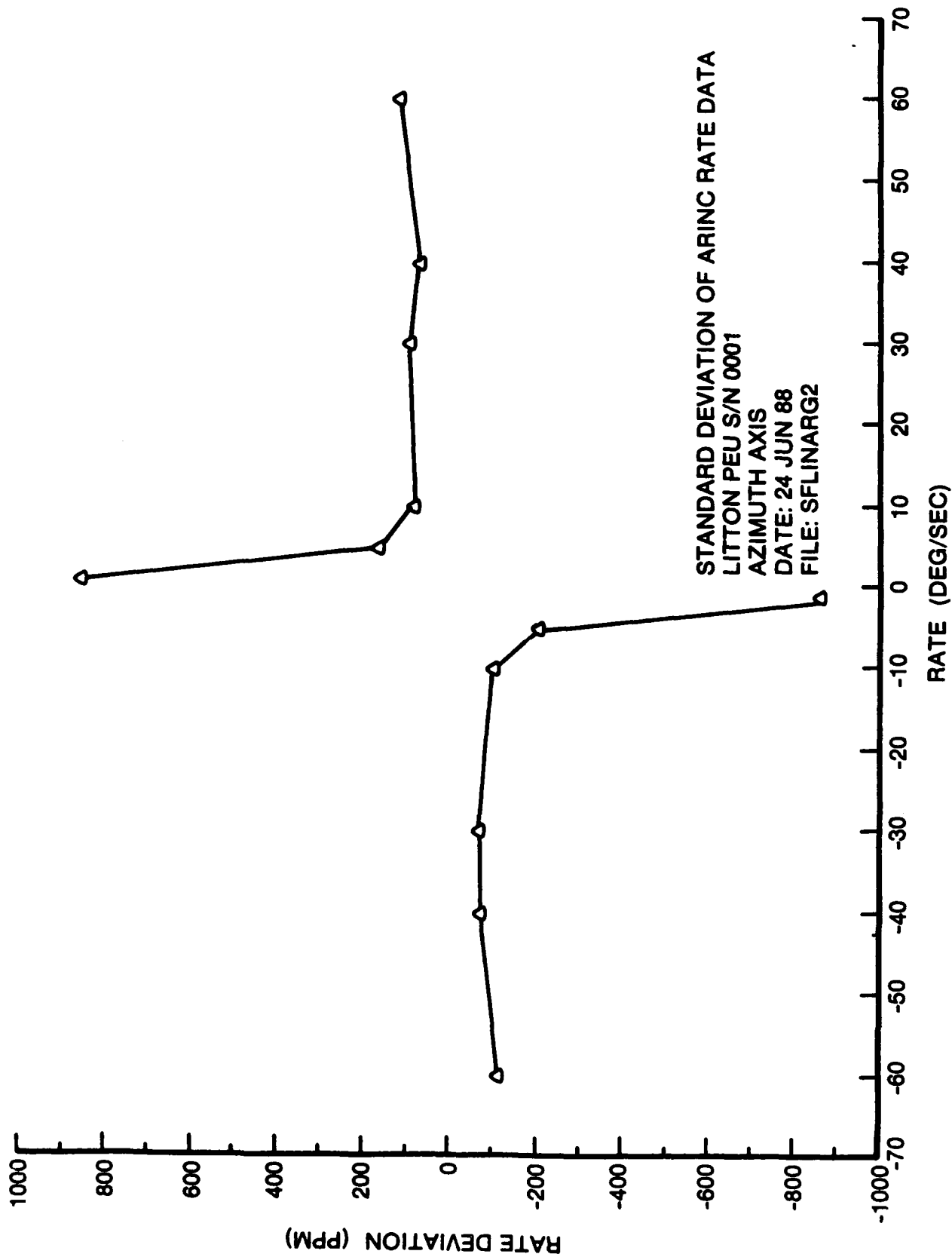Figure 4-7:   Scale Factor Deviation, Pitch Axis

Figure 4-8: Rate Deviation, ARINC 429

4.5 Scale Factor Stability

Plots of scale factor stability are shown in Figures 4-9 to 4-11. Figures 4-9 and 4-10 are raw azimuth axis data at rates of 2 and 20 deg/sec respectively. Peak-to-peak stability is better than 50 ppm in both cases. Figure 4-9 also shows a long term drift in scale factor which is most likely due to a slow thermal change.

Figure 4-11 is a plot of ARINC data for the azimuth axis at 6.0 deg/sec. Note that the ARINC data is far noisier; stability is approximately 400 ppm peak-to-peak.

4.6 Rate Changes

A series of rate change tests were performed to study thermal effects and verify scale factor deviations. A plot of a rate change test is shown in Figure 4-12. The change in scale factor between 10 and 30 deg/sec is approximately 500 ppm; in agreement with the scale factor deviation plot in Figure 4-5. Scale factor stability is, again, 30 ppm and the decreasing scale factor at each rate is due to thermal effects. The apparent 'jumps' of 100 ppm during the 30 deg/sec segments are due to instability of the temperatures controller; by pure chance, the temperature controller is on the borderline of cycling on and off and the inherent torquer heating present in the gyro causes the controller to cycle resulting in a small temperature change which results in a scale factor variation. A 100 ppm change is equivalent to $\approx 0.2°C$ temperature change at the torquer coil.

4.7 TEMPERATURE TESTS

4.7.1 Warm-up/Cool-Down

The original PEU specification called for temperature control at the sensor block to be $68°C \pm 0.2°C$ with ambient temperature controlled to $\pm 1°C$.

On system turn-on from cold start, a 'fast warm-up' is initiated. At $30°C$, the gyros are turned on and the heating continues, changing to 'fine' temperature control until operating temperature is achieved. In addition, over-heating protection is supplied whereby an increase of $11°C$ over steady-state results in a shutdown of the temperature controller.

RTD's were attached to the end-cover of the azimuth gyro to monitor and record temperature variations during tests.

As a baseline, a static 'turn-on' test was performed to record sensor warm-up. A plot of the turn-on transient and settling time is shown in Figure 4-13.

SCALE FACTOR STABILITY
LITTON PEU S/N 0001
AZIMUTH AXIS (CW)
RATE = 2.0 Deg/s
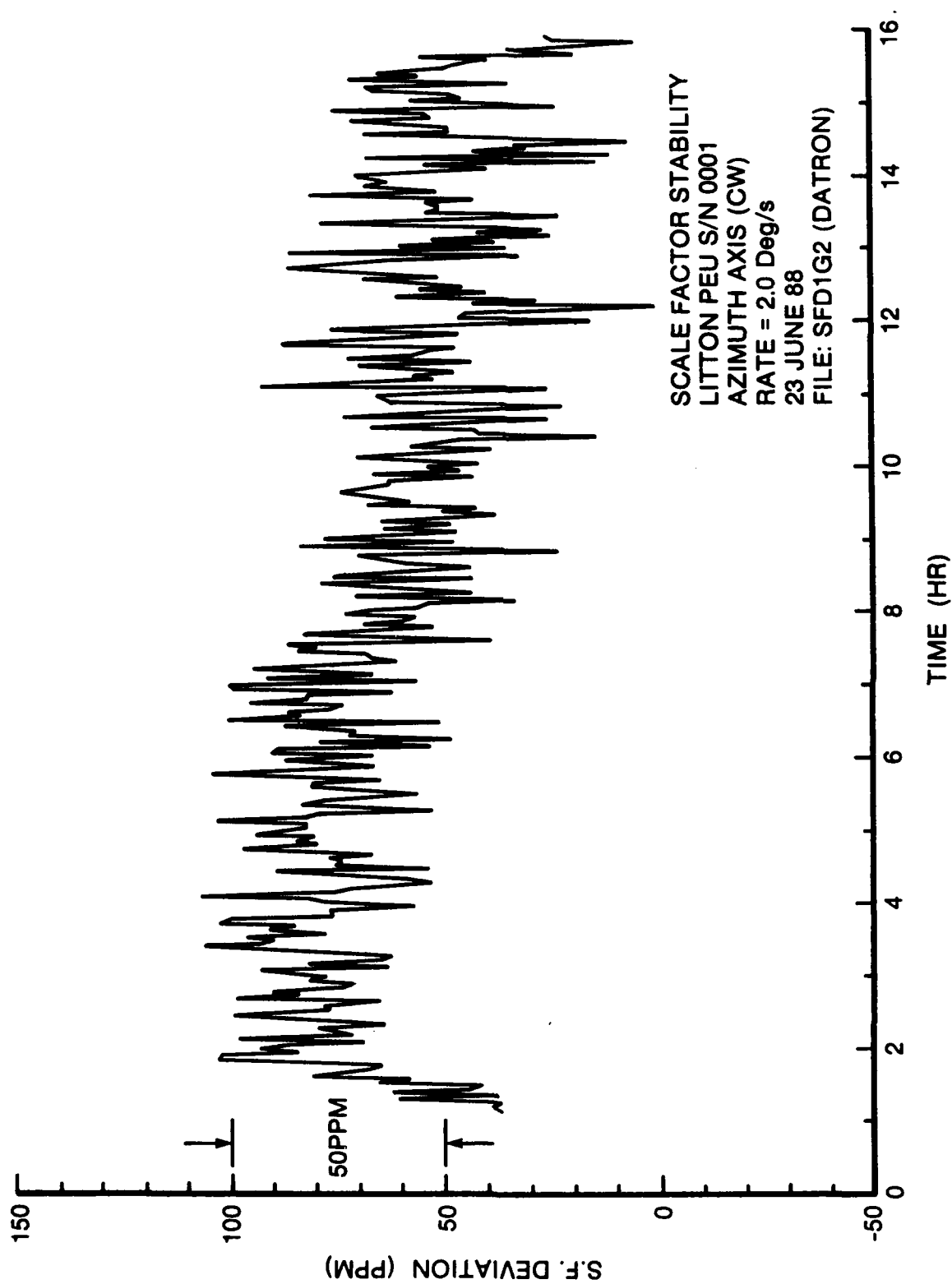23 JUNE 88
FILE: SFD1G2 (DATRON)

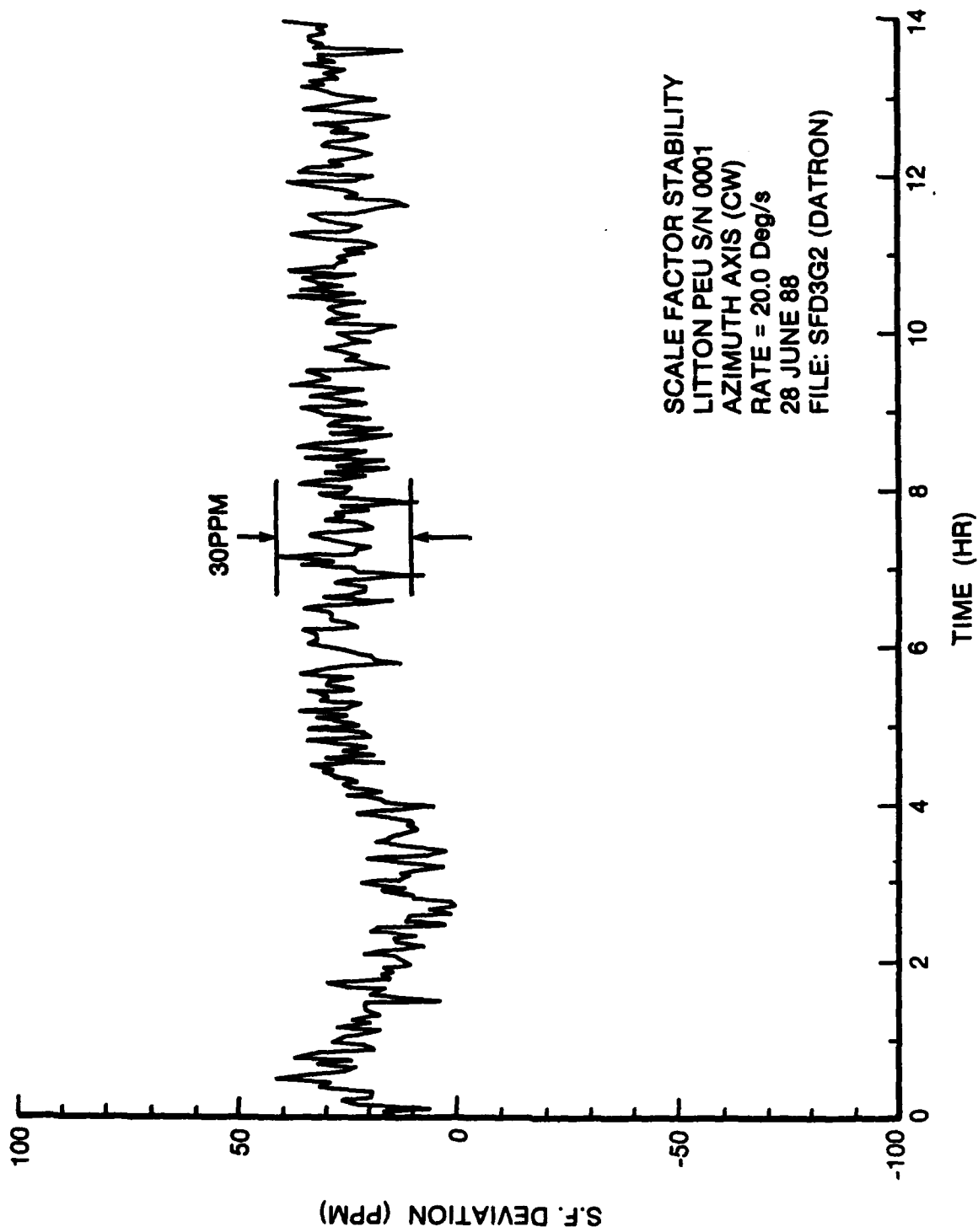Figure 4-9: Scale Factor Stability, 2.0 deg/sec
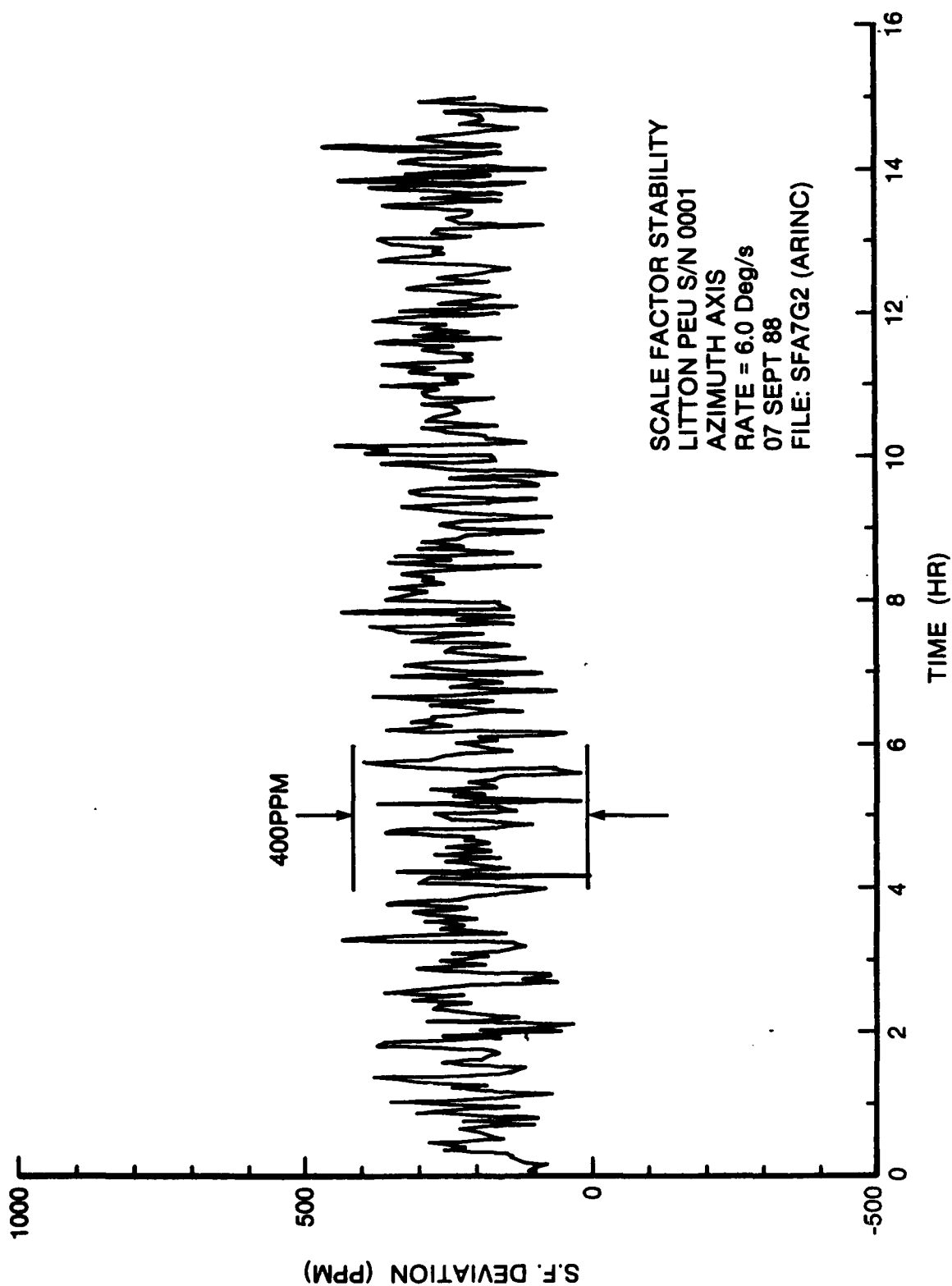
Figure 4-10: Scale Factor Stability, 20 deg/sec

Figure 4-11: Scale Factor Stability, 6.0 deg/sec, ARINC 429

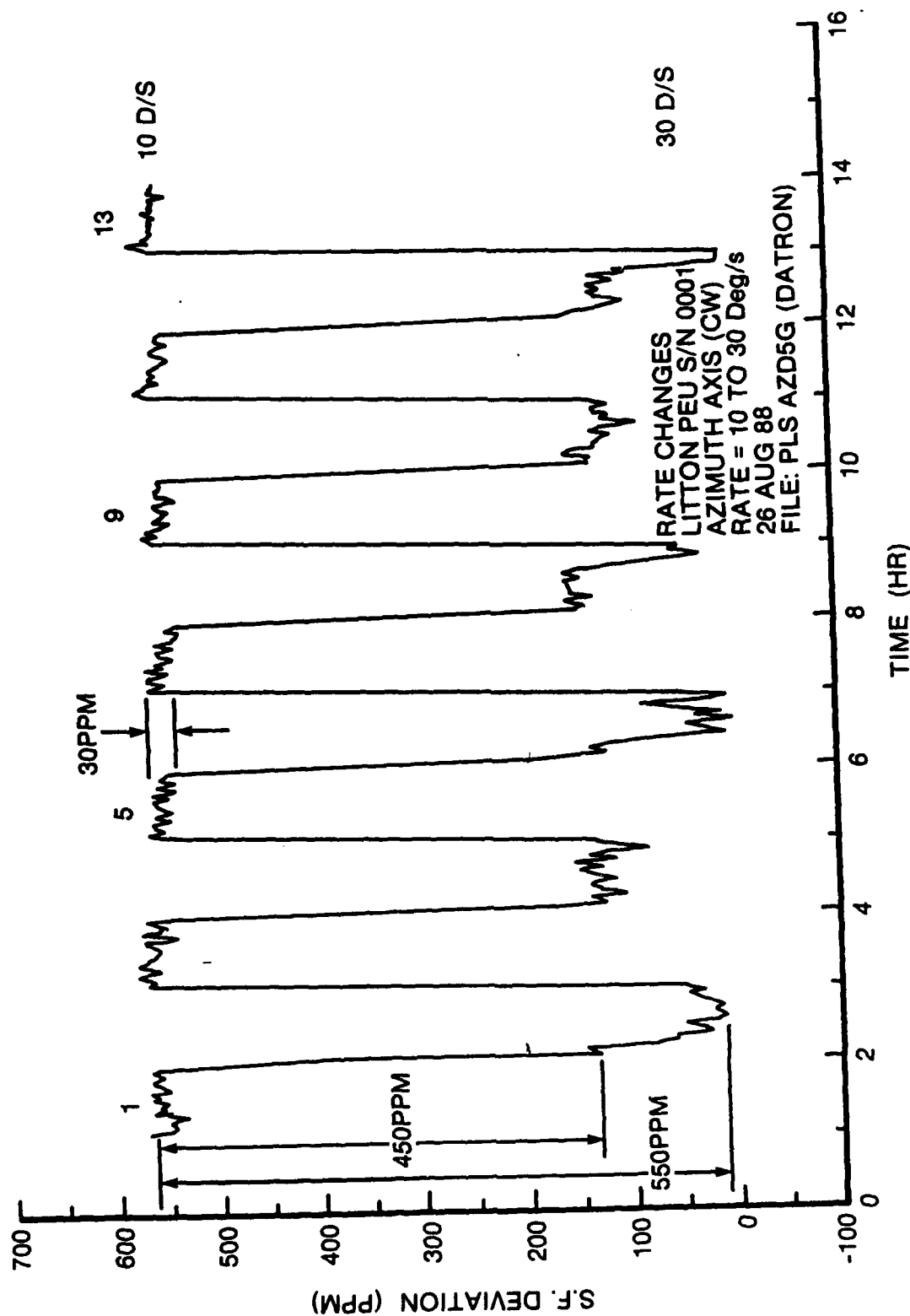Figure 4-12:   Scale Factor Deviation Due to Rate Change

TURN-ON TEMPERATURE TRANSIENT
AND TEMPERATURE STABILIZATION
PROBE ATTACHED TO I.D. COVER
OF CSG-2 GYRO S/N 013 (AZ)
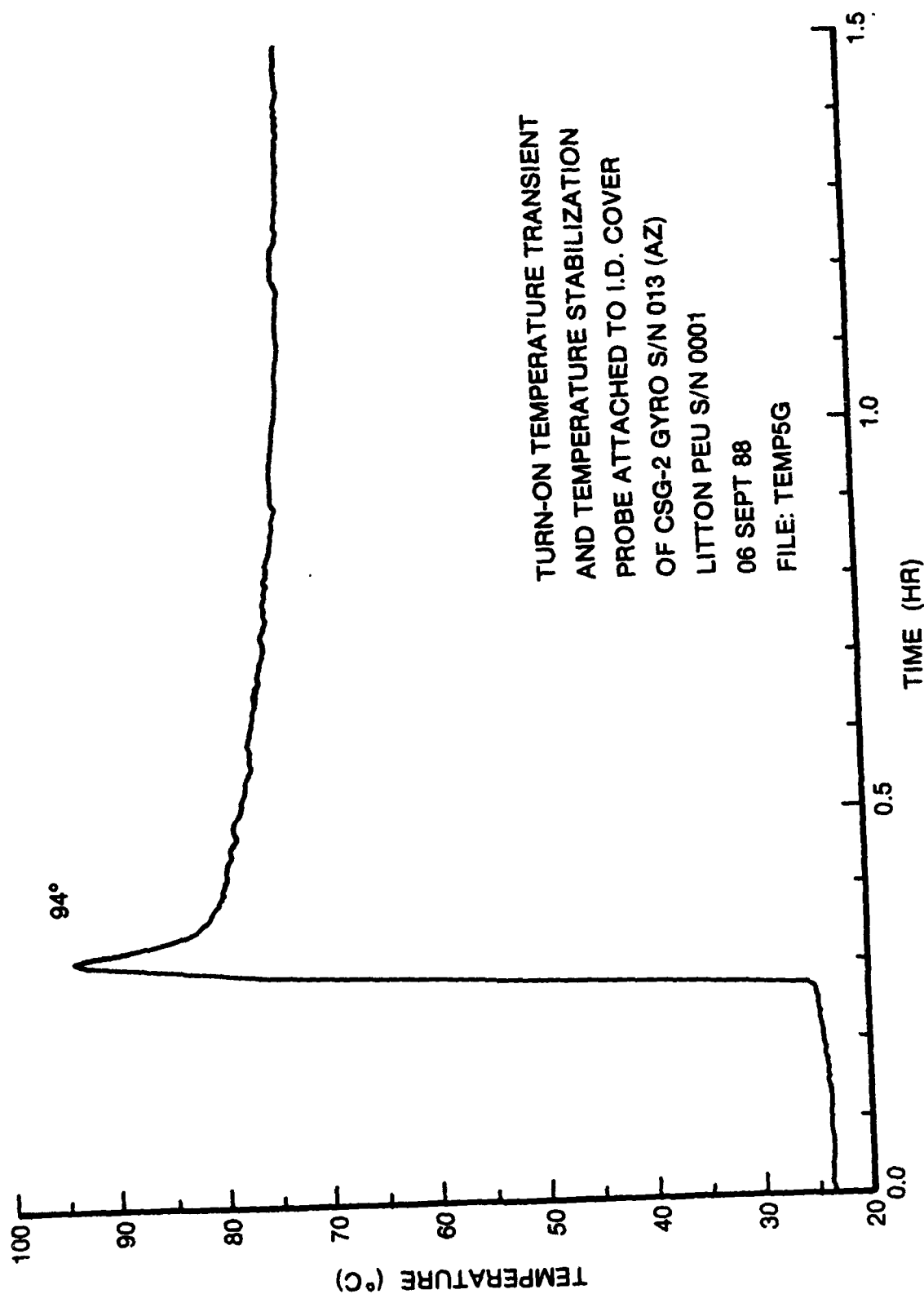LITTON PEU S/N 0001
06 SEPT 88
FILE: TEMP5G

Figure 4-13: Turn-On Temperature Transient

Two important effects should be noted here; firstly, the large temperature overshoot at turn-on. The temperature <u>at the gyro</u> peaks at ≈ 94°C; 26°C above nominal operating temperature.

Secondly, as a consequence, the settling time to reach operating temperature is almost 2 hours. This is illustrated in Figure 4-14 (an enlarged view of Figure 4-13).

4.7.2 Thermal Variation with Rate Changes

Since we have already seen the effect of temperature changes on scale factor deviation (≈ 550 ppm/°C), it is obvious that system thermal control at turn-on could cause serious problems.

This was verified by performing a rate test during system warm-up. Figure 4-15 illustrates the change in scale factor when the system is turned on and immediately rated at 2.0 deg/sec. If compared to Figure 4-14 over the time period of 1 to 2 hours, the change in scale factor is ≈ 900 ppm for a temperature change of 1.5°C or 550ppm/°C; very closely in agreement with the predicted value.

In comparison, the equivalent system data recorded from the ARINC 429 bus is quite different. Figure 4-16 is a plot of output rate vs time for the same test as in Figures 4-13 to 4-14. Since the PEU employs a <u>constant</u> scale factor in its compensation software, the result of an actual scale factor change in the gyros will appear as an apparent rate change to the system and will be directly proportional to the scale factor deviation.

The plot seems to indicate a cycling effect, most likely an internal compensation for thermal changes. Unfortunately the peak-to-peak deviation is > 2500 ppm; a crude compensation, and cannot, therefore, be directly related to thermal variations at the sensors.

5.0 SYSTEM EVALUATION

5.1 DATA SUMMARY; GYROSCOPE VS. SYSTEM PERFORMANCE

A comparison between the individual sensors and the overall system performance is a somewhat difficult task and must be limited to only a few areas. The reason for this is the fact that very little work was performed on 'system' development; digitizers, A/D converters, noise reduction, software compensation, etc. Most efforts were expended in sensor block design, thermal control and rebalance electronics development. In addition, only a small
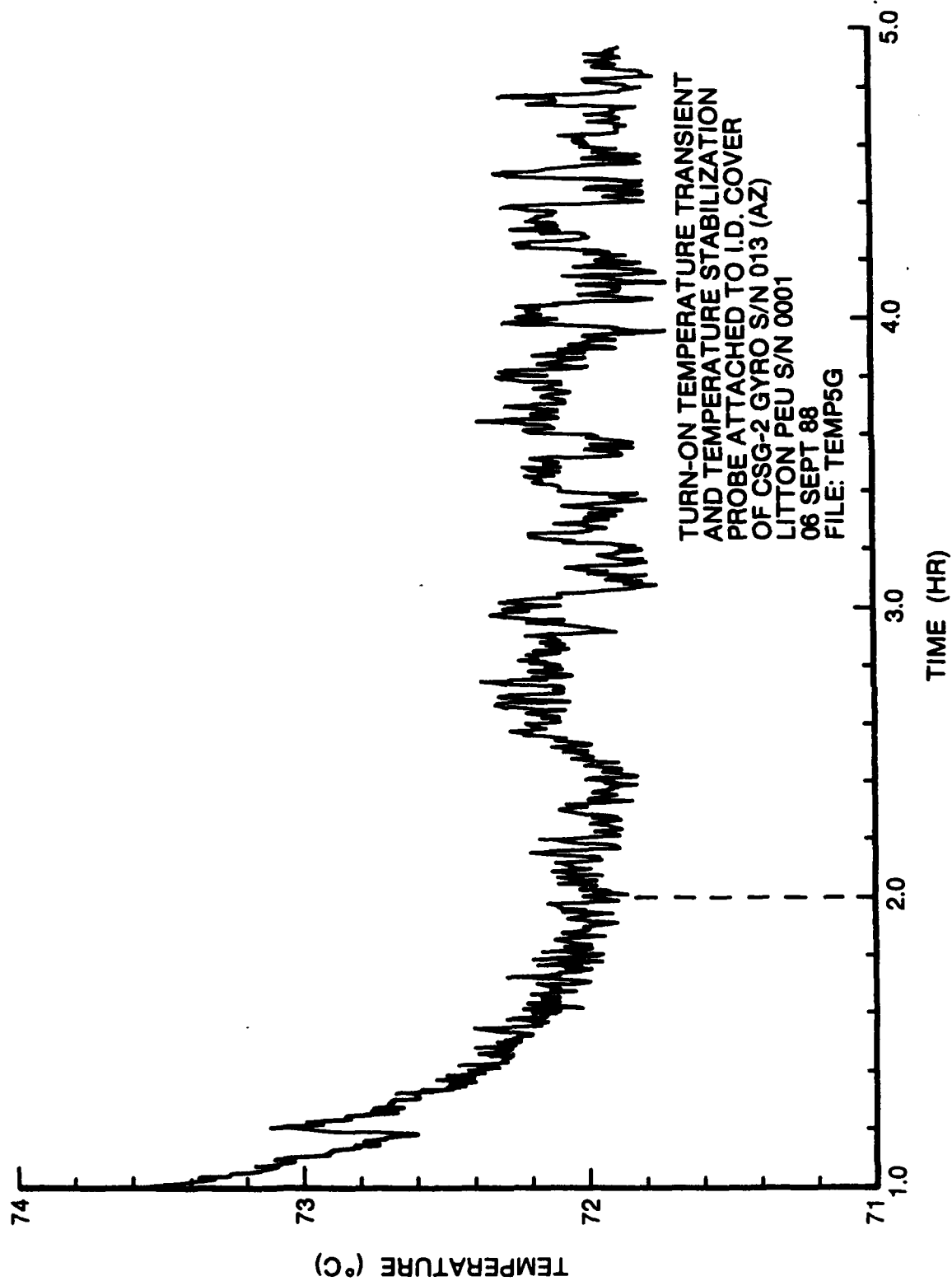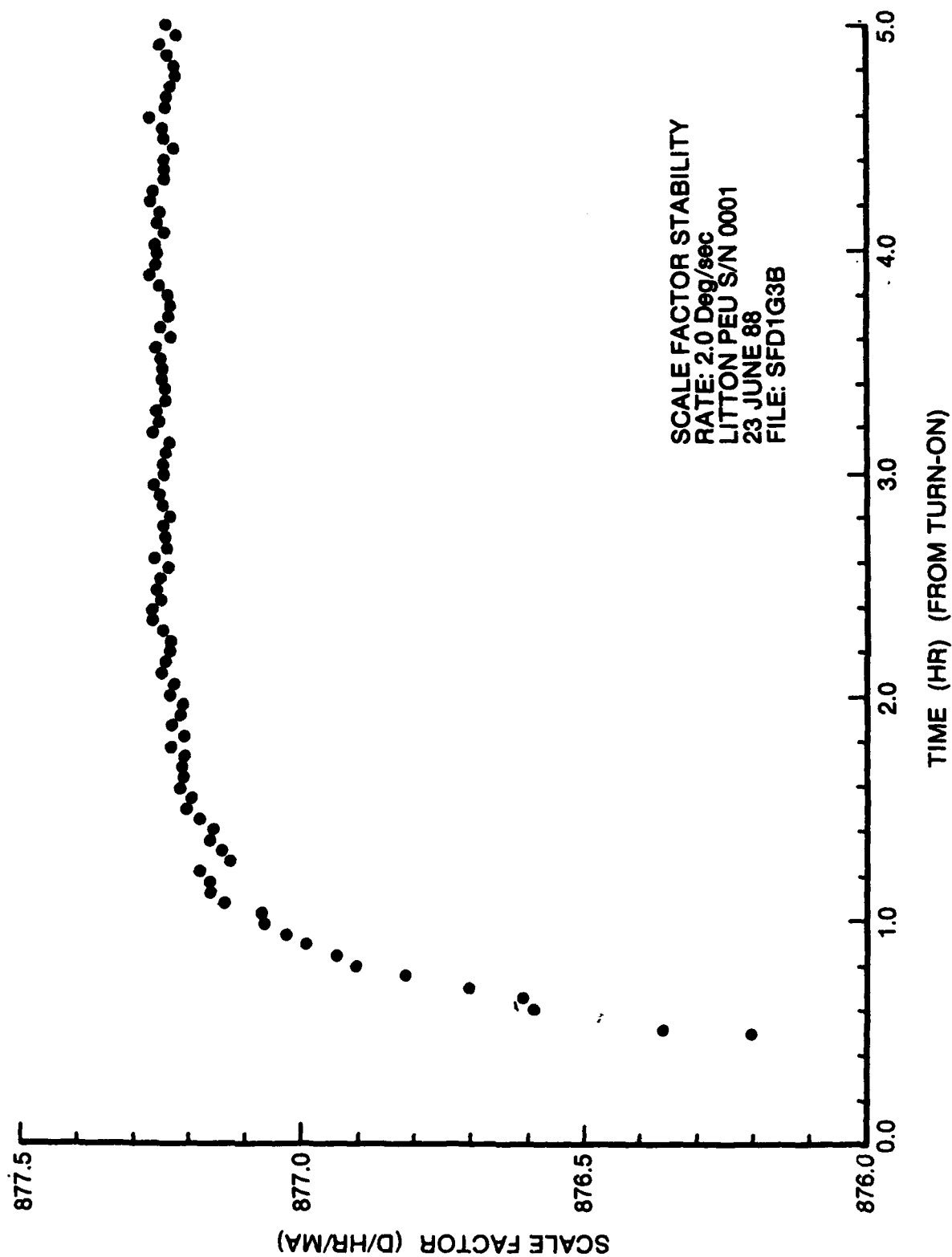
Figure 4-14: Turn-On Temperature Transient

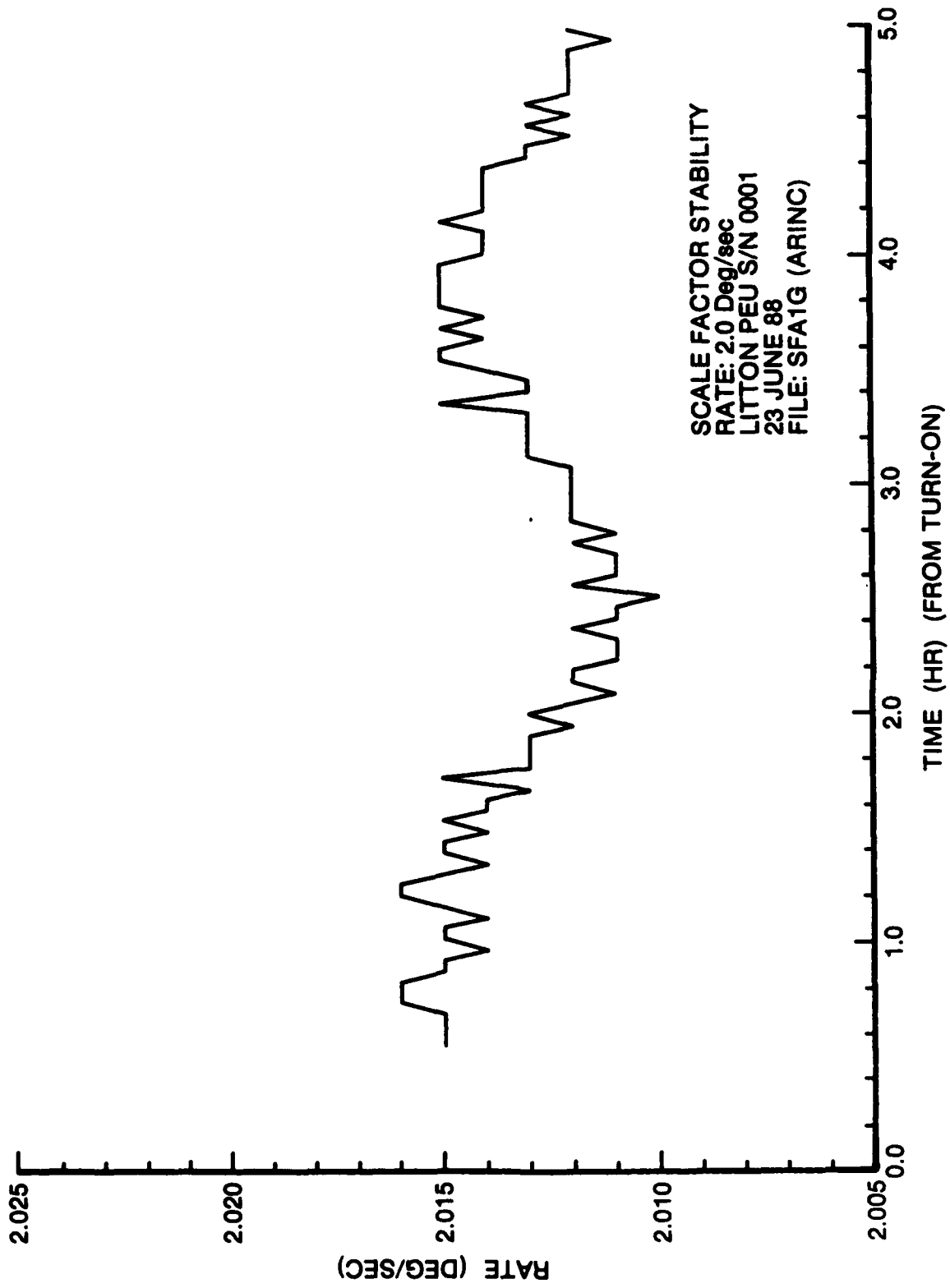Figure 4-15: Scale Factor Variation due to Temperature Settling

Figure 4-16: Scale Factor Variation due to Thermal Settling (ARINC 429)

amount of data was made available on the ARINC 429 bus, limiting the information available during testing.

Nonetheless, several comments can be made. In particular, the drift stability of the system is $\approx$ 400 ppm as compared to individual gyro stabilities of 50 ppm or better. This is due to the large amount of wheel noise which is not filtered within the PEU as well as A/D instability.

An additional problem is the large temperature overshoot at turn-on. This was not recognized during early tests and, as demonstrated previously, results in scale factor deviation and a very prolonged settling time.

In general, the higher noise levels of the system impaired accurate and consistent data performance comparisons with the raw sensor outputs.

5.2 COMPARISON WITH DESIGN SPECIFICATIONS/GOALS

System design specifications/goals were discussed in Section 2.2. Most elements of the system met specifications except for the temperature controller. The large overshoot and long settling time inhibited good system performance.

The system performance goals of 5 deg/hr drift in each of heading, pitch and roll were achieved but were toleranced and specified for a very low performance system.

The development of the PEU was originally intended as a demonstration of the performance capabilities of the CSG-2 gyroscope in a system environment. Individual gyroscope performance was well within specification although the relatively low torquer scale factor as compared to earlier designs resulted in a predictably large scale factor deviation over the desired rate range due to torquer heating effects.

System performance was impaired due to (wheel) noise and poor temperature control as discussed.

Since little effort was put into sensor modelling, software error compensation within the PEU is inadequate to demonstrate the instrument performance capabilities in a convincing manner.

6.0 **FUTURE WORK**

As discussed, the performance of the PEU did not completely satisfy the intent of proving CSG-2 performance in a system environment. To this end, on-going work at DREO is centering on development of an AHRS for land vehicle navigation applications while Litton Canada is continuing to pursue helicopter and drone/RPV applications.

References

1. 'The CSG-2 Canadian Strapdown Gyroscope; Rate and Dynamic Tests", M. Vinnins, L.D. Gallop, J.S.S. Sinkiewicz, 1987 Symposium Gyro Technology, Stuttgart, FRG, Sept. 1987.

2. "Analysis of Rate and Dynamic Tests on the Litton (Canada) Canadian Strapdown Gyroscope (CSG-2), M. Vinnins, L.D. Gallop, DREO TN # 88-22, April 1988.

3. "Test Evaluation of the Litton (Canada) Canadian Strapdown Gyroscope (CSG-2)' M. Vinnins DREO Report # 914, 1984.

APPENDIX 'A'

ANALOG REBALANCE LOOP

A.1 GENERAL

The function of the analog rebalance loop is to keep the angular position of the gyro rotor stationary with respect to the case for the purpose of producing analog electrical signals for the measurement of the applied rates. In a TDF gyro, the applied rates are not mechanically coupled to the rotor. Rather, a rebalance loop creates the required torquing currents to produce the rotor rates. The output rate information is obtained from the torquing currents which are proportional to rate, and the sensing components for this servomechanism are the "pickoff" coils in the gyro, from which the angular difference information is obtained.

A.2 DYNAMIC ANALYSIS

For all purposes in this analysis, the TDF gyro can be assumed to be totally undamped. The essentials of the rotor dynamics are given by:

$$T_x = H\omega_y + I\dot{\omega}_x \qquad (A.1)$$

$$T_y = -H\omega_x + I\dot{\omega}_y \qquad (A.2)$$

where:

H = angular momentum

I = transverse moment of inertia

T_x, T_y = torques applied on the rotor

ω_x, ω_y = absolute angular rates of the rotor

A-1

These equations suggest that the application of a torque on one axis only will create angular motion on both axes, and that to create angular motion on one axis only, torques on both axes must be applied.

By using the Laplace transform and by rearranging equations A.1 and A.2, it is possible to express the rotor rates in terms of torques:

$$\omega_x(s) = \frac{\left[\dfrac{s}{(H/I)}\right]\dfrac{T_x(s)}{H} - \dfrac{T_y(s)}{H}}{\left[\dfrac{s}{(H/I)}\right]^2 + 1} \qquad (A.3)$$

$$\omega_y(s) = \frac{\left[\dfrac{s}{(H/I)}\right]\dfrac{T_y(s)}{H} + \dfrac{T_x(s)}{H}}{\left[\dfrac{s}{(H/I)}\right]^2 + 1} \qquad (A.4)$$

These equations show that the rotor response to torques are second order undamped responses with a natural frequency equal to H/I. This is the "nutation frequency" of the gyro.

A.2.1 Closed loop transfer functions

Figure A.1 is an equivalent block diagram of a system comprised of one TDF gyro and its rebalance electronics. The rates "ω_{cx}, ω_{cy}" are those that are applied on the gyro case. The blocks "D(s)" and "C(s)" contain the transfer functions of the rebalance loop, for the "direct-axis loops" and the "cross-axis loops" respectively. The outputs "$H\omega_{ox}$, $H\omega_{oy}$" represent the voltage drop on precision resistors through which flows the torquing current produced by the direct-axis

A-2

loops. For this general configuration, the scaling factors of
any actual gyro are ignored and the inputs and outputs of the
loops are assumed to be angle and torque respectively. As
indicated by equations A.3 and A.4, a factor 1/H can be used
to scale the output signals into the output rates ω_{ox} and
ω_{oy}. To simplify the determination of the closed loop
direct-axis and cross-axis transfer functions shown below,
the nutation frequency H/I is set to 1 rad/s, and the factor
1/H is placed inside D(s) and C(s). For clarity, the (s)
notation is not shown:

direct-axis:
$$\frac{\omega_{ox}}{\omega_{cx}} = -D \left[\frac{s(s^2+C+1)+D}{(s+D)^2+(s^2+C)^2} \right] \qquad (A.5)$$

cross-axis:
$$\frac{\omega_{ox}}{\omega_{cy}} = -D \left[\frac{C-sD}{(s+D)^2+(s^2+C)^2} \right] \qquad (A.6)$$

The closed loop transfer functions for the other output
(ω_{oy}/ω_{cy} and ω_{oy}/ω_{cx}) are identical to those shown above
except for the polarity of the cross-axis transfer function
($\omega_{oy}/\omega_{cx} = -\omega_{ox}/\omega_{cy}$).

A.2.2 Sensitivity to angular accelerations

Because the outputs ω_{ox} and ω_{oy} are a measurement of
ω_{cx} and ω_{cy} respectively, the cross-axis response must
ideally be zero. This is achieved when C(s)= sD(s)/(H/I), or
simply C= sD in the transfer functions A.5 and A.6. It can be
seen from equations A.1 and A.2 that to obtain angular motion
of the rotor on one axis only, a torque proportional to the
acceleration is required on that axis. This torque is
supplied by the cross-axis loops, and if no cross-axis loop

A-3

are used (C= 0), it is supplied by the direct-axis loop serving for the measurement of the rates on the other axis, leading to a rate measurement error (acceleration sensitive).

A.2.3 Stability considerations

When C= sD, several terms cancel out in the closed loop transfer functions, and when D is a proportional gain, the direct-axis closed loop transfer function becomes a simple first order function. Unfortunately, the response curves in the frequency domain will exhibit sharp discontinuities at the nutation frequency which indicates instability (at the nutation frequency, the closed loop transfer functions are equal to 0/0). This problem may go unnoticed during experimentation because the frequency bandwidth where the discontinuities occur is infinitesimal. Stability will exist when C> sD (that is, C= ksD with k> 1) but the cross-axis closed loop response would no longer be zero, and with C only slightly larger than sD, the stability margin would be insufficient. Another means of obtaining nutation stability in the system is to include a phase lag of 180° at the nutation frequency in the direct-axis loops, and have C< sD, or C= 0 (no cross-axis loops).

A.2.3.1 Phase lag nutation control

A popular scheme of nutation control is one that uses only the direct-axis loops but with a phase lag of 180° at the nutation frequency. With this scheme, a wide margin of stability is possible without the use of cross-axis loops. However, when the cross-axis loops are used, the nutation instability problem associated with C= sD still exists,

A-4

except that with the phase lag scheme, the condition for nutation stability is reversed, that is, $C < sD$. The advantage of this is that it is possible to design the circuits so that C is essentially equal to sD in the closed loop bandwidth for the elimination of the acceleration sensitivity, and that $C = 0$ at the nutation frequency for maximum nutation stability. This is accomplished by including in the cross-axis loops a notch filter tuned at the nutation frequency and having approximately the same low frequency phase lag response as that of a low-pass filter used in the direct-axis loops. A precision rebalance loop using this scheme and designated RL-3 was recently developed and built at DREO for the purpose of testing TDF gyros under static (constant rate input) and dynamic excitations.

A.3 THE RL-3 REBALANCE LOOP

A functional block diagram for the circuits of RL-3 is shown in Figure A.2. The phase lag for the direct-axis and cross-axis loops is obtained from the low-pass filters and from the nutation notch filters. The phase lag from these circuits must compensate the small phase lead from the spin notch filter at the nutation frequency so that the total phase lag may be 180°. To eliminate the high frequency noise normally obtained from pure differentiation, the differentiators are actually second order band-pass filters having a natural frequency well above the nutation frequency. One of the nutation notch filters is inverting, the other is non-inverting. All of these filters each have a second order response and the damping ratios are 0.7 for the low-pass filters, 0.3 for the spin notch filters and 0.8 for the nutation notch filters and the differentiators. Except for

A-5

the differentiators, the closed loop performance is essentially insensitive to the voltage drifts of the operational amplifiers which can be the "all purpose" types.

A.3.1 Closed loop response

Figure A.3 shows the closed loop amplitude response in the frequency domain obtained from a software simulation of the closed loop transfer function A.5. The software must also include the transfer functions of each filters in C(s) and D(s) in the Laplace form. The software first calculates the response for C(s) and D(s) for a discrete frequency, and then calculates the closed loop response for that frequency using the transfer function A.5. This cycle is repeated for each of the discrete frequency increments of the curve. The gain margin can be tested by increasing the gain of C(s) and D(s) until the closed loop response curve shows a very large peak. A similar approach is used to test the phase margin.

A.3.2 The torquer driver circuit

The functions of the torquer driver is to generate the torquer current over a range of ± 0.4 A and to produce the rate voltage output on a precision resistor. A simplified diagram of the circuit is shown in Figure A.4 which illustrates how the torquing current from the direct-axis loop (proportional to the rate) is combined to the torquing current from the cross-axis loop (proportional to acceleration on the other axis) to form the total current for the torquer coils while none of the torquing current from the cross-axis loop flows through the sensing resistor R2. The circuit behaves as a voltage follower for the rate voltage

A-6

output $(= V_d)$ and as a voltage-to-current converter and a summing junction for the torquer current output. The current from the cross-axis loop can not flow into the sensing resistor R2 because of the action of the feedback of the operational amplifier which regulates the voltage drop on R2.
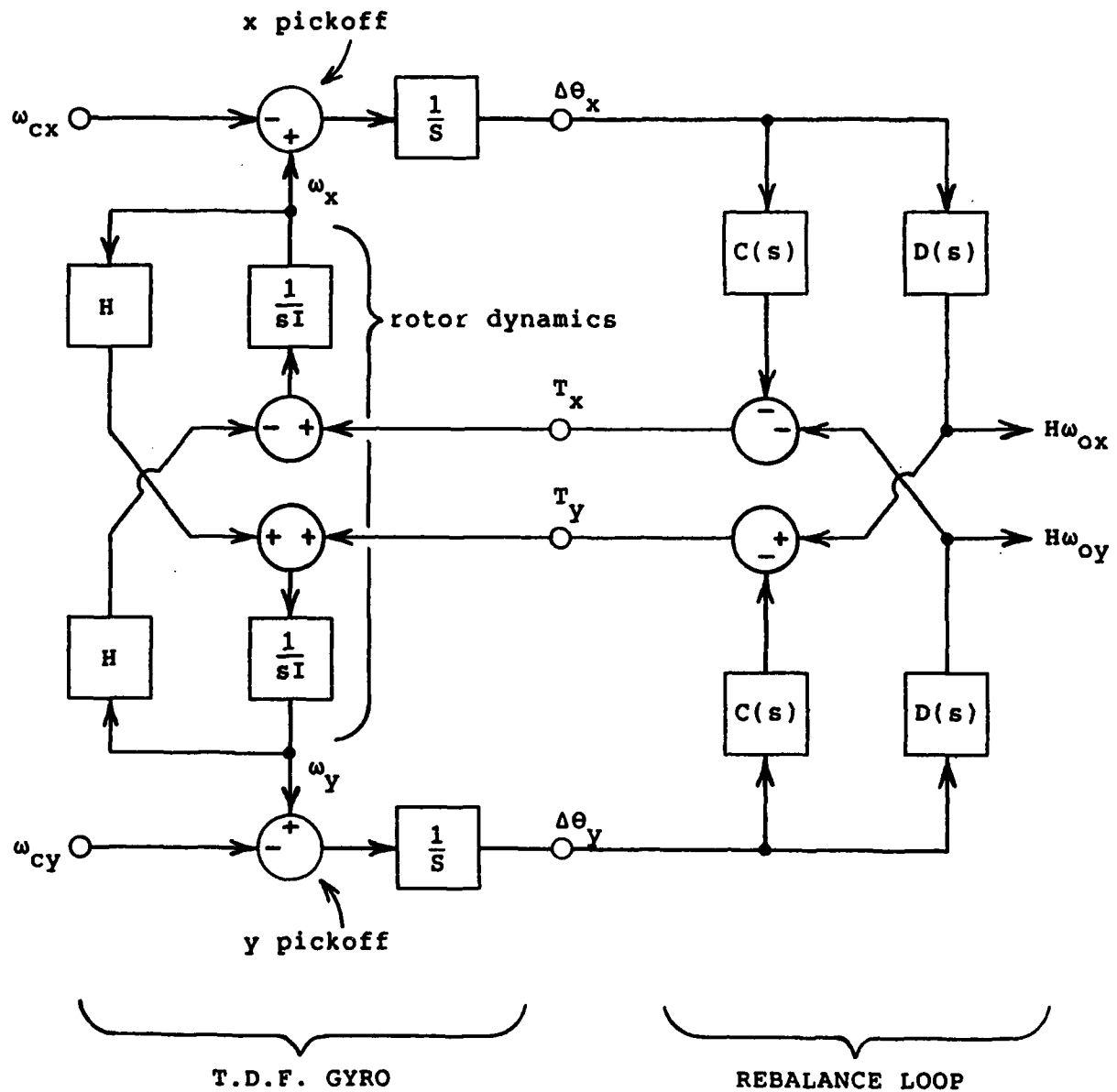
A-7

Fig. A.1   Servomechanism for a T.D.F. Gyro
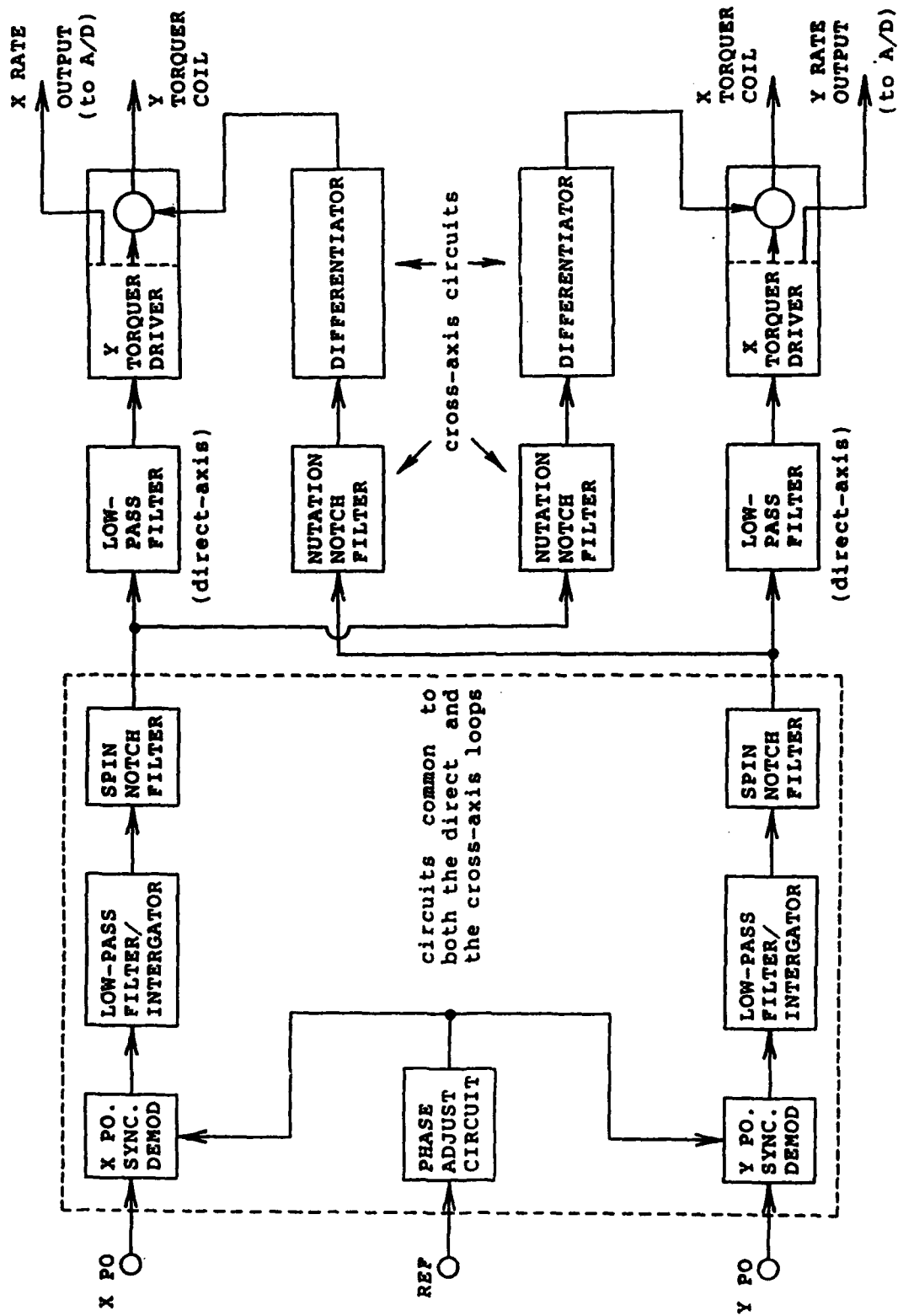
Fig. A.2 Block diagram for RL-3
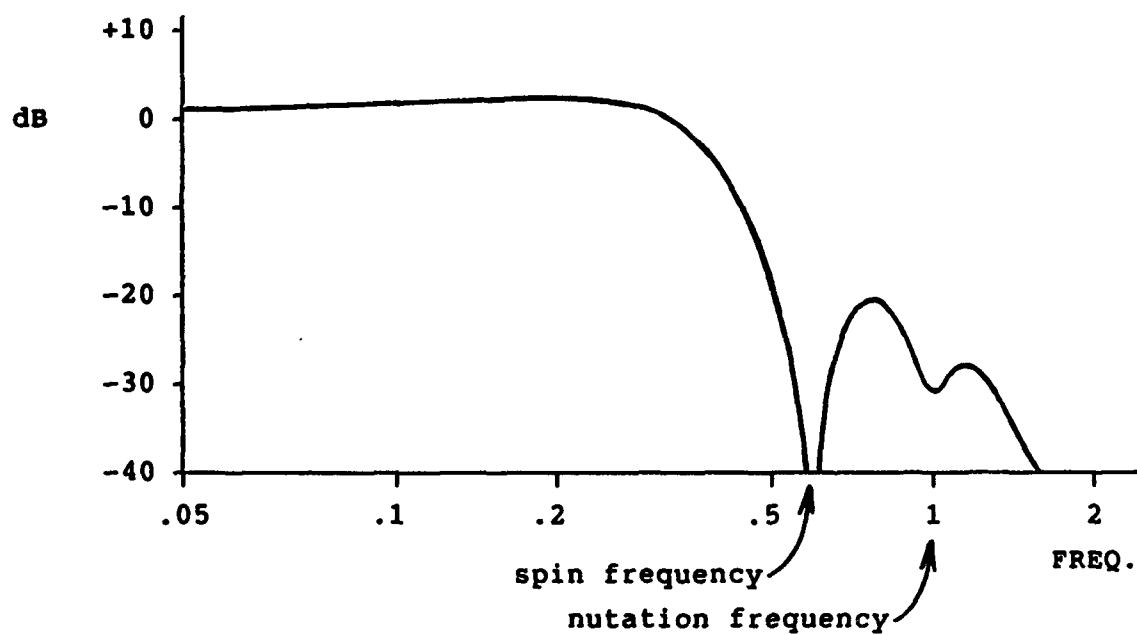
Fig. A.3   Direct-axis closed loop response

push-pull stage

"V_d"

direct-axis loop

"I_t"

TORQUER
COIL

"V_c"

cross-axis loop

R1 (500Ω)

R2
(15Ω)

RATE OUTPUT

(to A/D)
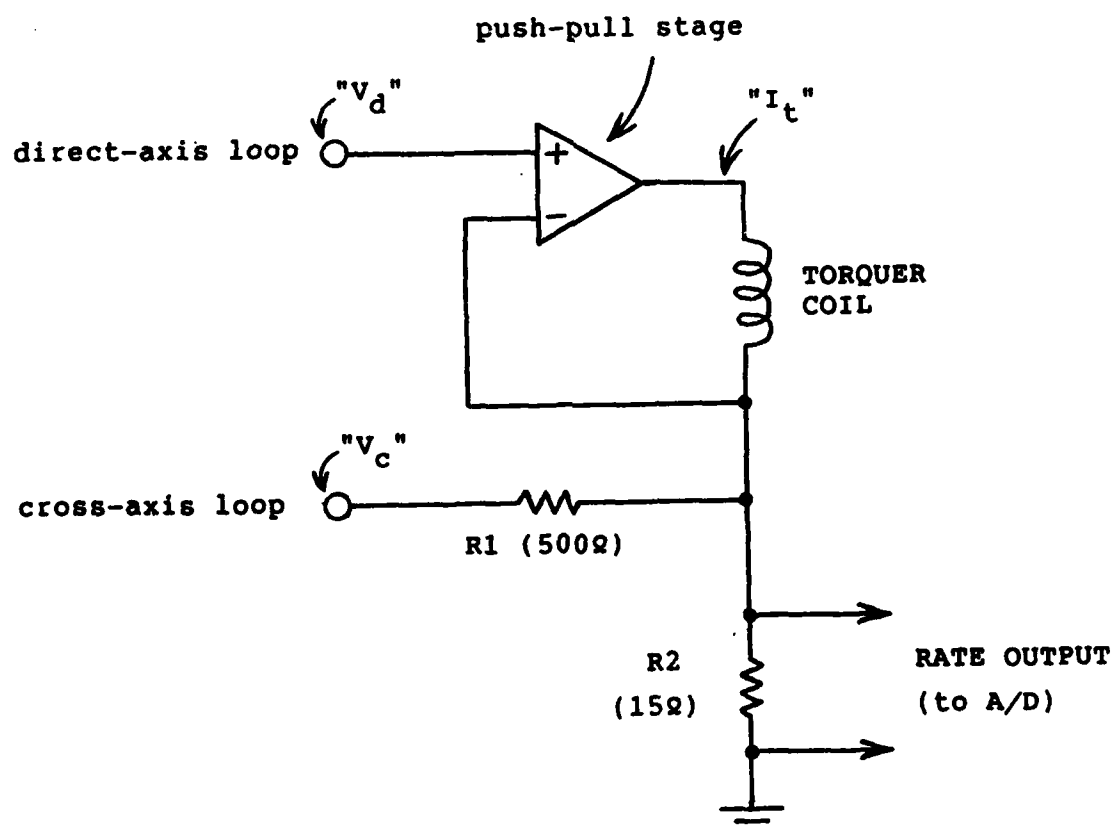
$$I_t = \frac{V_d}{\frac{R1\ R2}{R1+R2}} + \frac{(-V_c)}{R1}$$

Fig. A.4   TORQUER DRIVER

DESIGN, DEVELOPMENT, AND TEST OF A 3-INCH OPEN LOOP ALL FIBER GYRO

Jim Blake, Jim Cox, John Feth, Randy Goettsche

HONEYWELL
P. O. Box 21111, Phoenix, Arizona 85036

INTRODUCTION

The interferometric fiber-optic gyro (IFOG) along with its cousins, the resonator fiber gyro (RFOG) and the ring laser gyro (RLG), measure rotation in inertial space by means of the Sagnac effect, named after its discoverer, the French physicist, Georges Sagnac in 1913.[1] The effect is relativistic; counter-propagating light waves in a closed optical path experience a differential phase shift proportional to the rotation rate of the path in inertial space. The relationship between the rotation rate, Ω, and the associated induced phase shift, ϕ_R is given by:

$$\phi_R = (8\pi A/\lambda c)\Omega \qquad (1)$$

where A is the area enclosed by the loop, λ is the free space wavelength, and c is the free space propagation velocity of light.

The scale factor $8\pi A/\lambda c$ is very small for reasonable areas. The RFOG and the RLG overcome this problem by utilizing resonant structures; the effective area enclosed by the loop is greatly amplified by the number of passes the light makes before exiting. In the IFOG, the scale factor is magnified by winding many turns of fiber on the relatively small mandrel. The IFOG is advantageous in this respect in that it does not rely on a high finesse cavity for its operation. Expression (1) for an IFOG becomes:

$$\phi_R = (2\pi LD/\lambda c)\Omega \qquad (2)$$

where L is the length of the fiber coil and D is its diameter. For example, the gyro discussed in this paper has a 100 m coil with an average diameter of 6.6 cm and a source wavelength of .83 μm. These choices yield a scale factor of .8 μrad phase shift per deg/hr rotation rate.

OPTICAL CIRCUIT

In order to detect sub-microradians of rotation induced phase shift between the counter-propagating optical beams, great care must be taken to ensure all other sources of differential phase shift between the two beams are suppressed. This task can largely be accomplished by making use of reciprocity; the counter propagating beams travel the same optical path, traversing the coupler on the coil in an identical manner and the coil in opposite directions. The opposite directions taken in the coil ensure that one beam will transit the phase modulator on entry and the other beam on exit of the coil, thus allowing a phase difference (i.e., modulation) to be introduced between the beams during the coil transit time. Figure 1 shows a diagram of the minimum optical circuit [2] which allows reciprocity and the basic means of signal recovery. A polarizer in the common input/output port of the sensing loop ensures that only one mode can enter or exit the loop. A perfect polarizer thus provides perfect reciprocity between the counter propagating waves, allowing only non-reciprocal phase shifts due

to time varying thermal gradients, magnetic field sensitivities, and of course, the rotation induced Sagnac phase shift. In the absence of a perfect polarizer, an additional non-reciprocal phase shift arises at polarization cross coupling points in the optical circuit. We have elected to use polarization maintaining fiber and polarization maintaining couplers in conjunction with a broad linewidth light source to decorrelate the signals in the two polarization modes, and thereby reduce the polarizer requirements. Alternative schemes make use of depolarizers and standard fiber components.[3]

A phase modulator is added to one side of the loop for the purpose of biasing the gyro to a sensitive operating point. Without this bias, at low rotation rates the gyro is operating in the middle of a fringe where the sensitivity to change is minimum and the direction of rotation cannot be determined. Given a net phase modulation between the counter propagating beams of $\phi_m \cos \omega t$, the light intensity at the detector, I_d, is:

$$I_d = (I_0/2)[1 + \cos(\phi_R + \phi_m \cos \omega t)] \qquad (3)$$

where I_0 is the light power returning to the detector in the absence of non-reciprocal phase shift or modulation. The intensity of this detected light at the first harmonic of the modulation signal, I_ω, is given by (4) where J_1 is the Bessel Function of the first order.

$$I_\omega = I_0 J_1(\phi_m) \sin(\phi_R) \cos \omega t \qquad (4)$$

For low rotation rates, i.e. small values of ϕ_R, $\sin(\phi_R) \approx \phi_R$ and the amplitude of I_ω signal is proportional to the rotation rate; for all rates the direction of rotation is defined by the sign of I_ω.

OPEN LOOP VS. CLOSED LOOP OPERATION

Two different techniques exist to extract the rotation rate information from the interference signal (3); "open" and "closed" loop operation.[4] In the "open loop" schemes, the I_ω signal amplitude is measured and the rotation rate is computed. In the "closed loop" schemes, a phase shift between the counter propagating beams is added to effectively null the Sagnac phase shift. The I_ω signal is driven to zero and the rotation rate is proportional to the added non-reciprocal phase shift.

Each of these schemes has its advantages and disadvantages. Open loop gyros depend on accurate demodulation of the output signal. It is a difficult electronic task to obtain good linearity over six orders of magnitude of dynamic range. Closed loop gyros, on the other hand, make use of complex modulation schemes requiring large bandwidths, or use some sort of acousto-optic modulation. These schemes, though elegant, require optical components that are not ready for large scale production. Closed loop gyros are the better option in the long run for obtaining good scale factor

linearity and dynamic range, however, Honeywell sees many applications for lower grade open loop gyros which can be produced **now**.

OPEN LOOP IFOG STATUS AT HONEYWELL

Honeywell has been involved in both open loop and closed loop IFOG research since 1983. Good success was achieved on a 670 m, 10.2 cm diameter open loop gyro in 1986.[5] The bias drift was measured to be less than 0.1 deg/hr from 0 °C to 40 °C and scaled for fiber length and loop diameter, was better than any other fiber gyro published in the literature at that time. The scale factor linearity achieved was a bit less than 2000 ppm. This gyro was scaled down for commercial AHRS application with the rationale that the bias stability scales inversely with diameter and fiber length, and the scale factor could be improved with minimal risk. The AHRS gyro has 100 m of fiber packaged in a 6.6 cm diameter. The target performance is bias drift less than 1 deg/hr and scale factor repeatability better than 500 ppm over the temperature range -55 °C to +90 °C.

To reduce the product risk, only mature component technologies were incorporated in the design. Thus a PZT ring phase modulator was chosen over an integrated optic phase modulator. This choice forced the gyro to be open loop as the PZT ring only operates with minimum complexity as a narrow band device. All the fiber and components are polarization maintaining in order to keep polarization error to a minimum and thus realize the drift performance goals. This latter choice required an in-house development of fused polarization maintaining couplers. We currently manufacture couplers with greater than 20 dB extinction ratio and less than .5 dB loss over the full temperature range in a package 1.25 inches long. These couplers have better performance for their length than any fused couplers reported in the literature to date. The polarizer, optical source, and detector are all off the shelf items and have proven performance.

PERFORMANCE DATA

In this section we describe the most recently available AHRS gyro data on bias stability, scale factor stability, and random noise performance. We also discuss the gyro's performance while subjected to magnetic fields and vibration. Details of the gyro design are changing and performance is improving on successive gyros. At this writing, 14 AHRS gyro prototypes have been built and tested.

BIAS STABILITY

The bias stability requirement of this gyro is 1 deg/hr over the temperature range -55 to +90 °C. At room temperature, the gyro exhibits 0.25 deg/hr 1σ (0.2 μrad) drift performance. Figure 2 shows a fourteen hour section of a room temperature drift run chosen because it exhibits the maximum drift observed on this gyro. Figure 3 shows a bias drift run as the temperature of the sensor was ramped from -30 to 50°C. The uncompensated bias stability performance is seen to be about 2.5 deg/hr 1σ. The small oscillation of the bias with temperature can be explained as a consequence of either polarization error or thermal gradient error [6]; we believe the oscillation is due to polarization error as the extinction ratio of the loop coupler in this sensor was only 12 dB. Using couplers noted above, we expect the bias drift over temperature to depend on the variability of electronic pickup and offsets in the demodulating circuitry.

SCALE FACTOR STABILITY

The scale factor accuracy requirement of the gyro for the AHRS application is < 1000 ppm over the rotation rate range of 0 to 150 deg/sec. Scale factor asymmetry needs to be < 100 ppm to minimize bias errors which result from rectification of the asymmetric scale factor in a vibrating environment.

The AHRS fiber gyro operates in two rate ranges, a low rate range (up to 15 deg/sec) and a high rate range (15 to 150 deg/sec). Figures 4 and 5 show the scale factor deviation from linearity after correction by a fifth order polynomial for each rate range. The compensated scale factor is linear to about 15 ppm 1σ in the low range and about 100 ppm 1σ in the high range. The same polynomials were used in successive runs for high and low input rates and the results are shown in Figures 6 and 7. The scale factor repeatability is approximately 60 ppm 1σ in the low range, and approximately 200 ppm 1σ in the high range.

The scale factor deviation from linearity of the sensor has also been measured from -30 to 50°C with results similar to those above when fitted with fifth order polynomials for both rate ranges. The demodulation electronics show some temperature dependence, however, and as of this writing have become the focus of our efforts towards scale factor stability.

RANDOM WALK

The random noise requirement for this gyro is .05 deg/$\sqrt{\text{hr}}$. For interferometric fiber gyros, the random noise performance is typically limited by the shot noise of the light impinging on the photo detector. The AHRS gyro operates very close to the theoretical shot noise limit of 0.03 deg/$\sqrt{\text{hr}}$. We have verified that the noise

is indeed white (as one would expect for shot noise performance) in that the peak to peak noise varies as $1/\sqrt{\tau}$ where τ is the integration time.

MAGNETIC FIELD SENSITIVITY

At the date of this writing, magnetic field sensitivity has not been tested on the AHRS gyro. Comprehensive data has been taken on the 670 m gyro mentioned earlier.[5] That gyro had no magnetic shielding and exhibited a 10 μrad non-reciprocal phase shift per gauss of magnetic field. However, because of smaller dimensions, better fiber, and the use of magnetic shielding, this sensitivity will be limited to .2°/hr/gauss for this application.

VIBRATION TESTING

Preliminary vibration testing of the gyro has begun. Testing consisted of a 2g sine sweep from 7 Hz up to 2000 Hz and back to 7 Hz in a 20 min time span, and 9 g rms random vibration within a 16 to 2000 Hz band for 1 hour. Tests were run for each of the three orthogonal axes of the gyro with the gyro operating. No physical damage or degradation in bias drift was observed either during or after testing. To illustrate the performance under vibration, figure 8 shows raw, unfiltered gyro output for the beginning and end of a 1 hour 9 g rms random vibration test.

AHRS IFOG STATUS

We believe that Honeywell's commercial AHRS gyro will be the first fiber gyro to be produced on a large scale basis. Honeywell is presently gearing up for production which is scheduled to begin in early 1990. Over 50 pre-production gyros will have been completed by the end of 1989. First sales have been made of the AHRS system using this gyro.

Figure 9 shows a photograph of a complete engineering brassboard AHRS IFOG system. The gyros are contained in a 3.0 in. diameter by 0.9 in. high package. The processing electronics for all three gyros occupies one 11 in. × 14 in. circuit card. The performance specs of 1 deg/hr bias drift, 1000 ppm scale factor stability and .05 deg/$\sqrt{hr}$ random noise are met quite easily at room temperature. Over temperature, the bias drift is still 2.5 deg/hr, however, with further improvements in the optics and the electronics we fully expect to meet the AHRS system requirement.
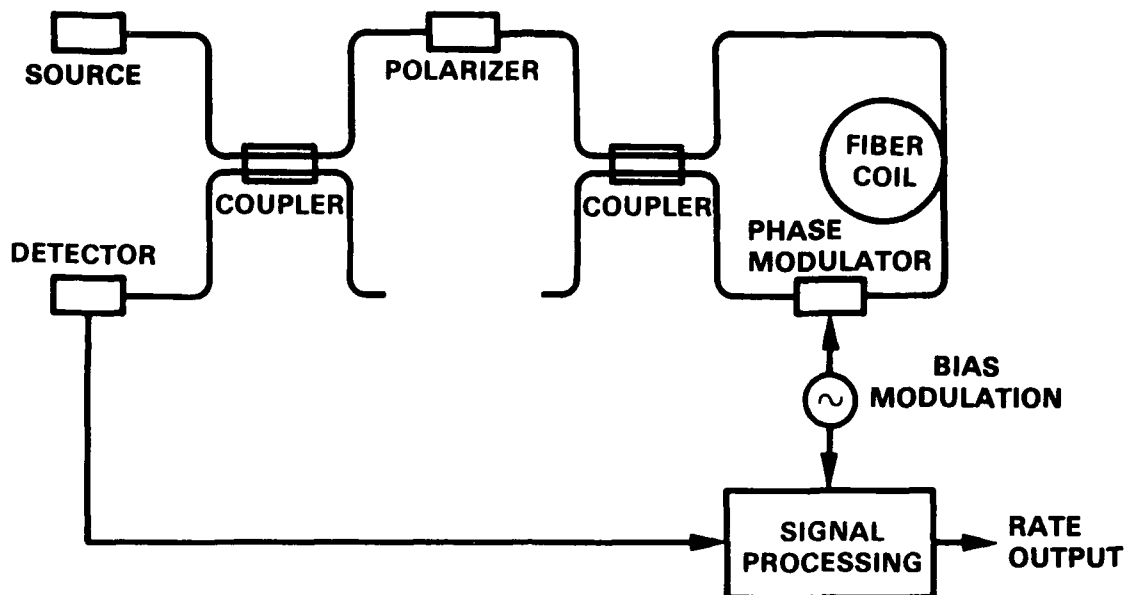
FIG. 1. Minimum interferometric fiber-optic gyro configuration.

14 HOUR BIAS RUN (LABORATORY ELECTRONICS)
(100 TC)

CUMULATIVE DATA
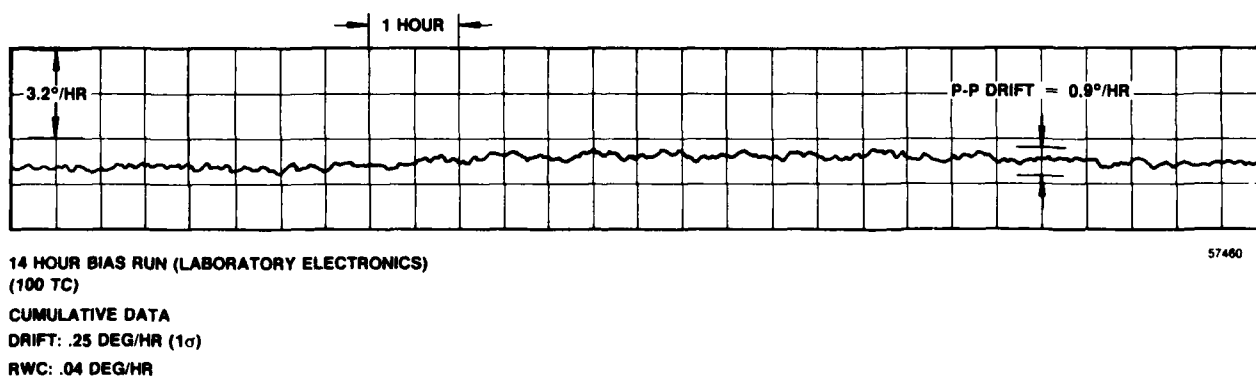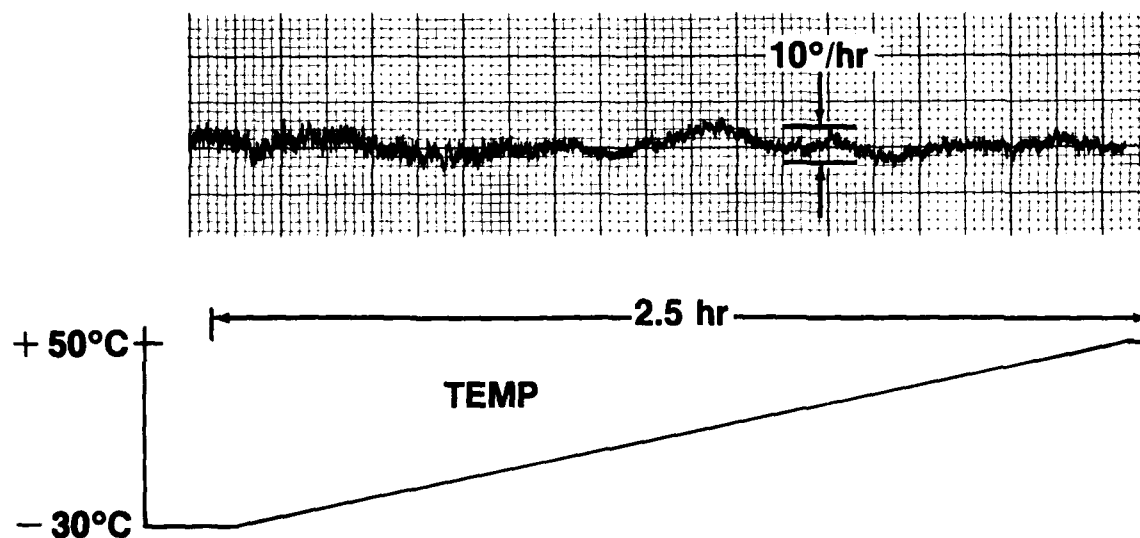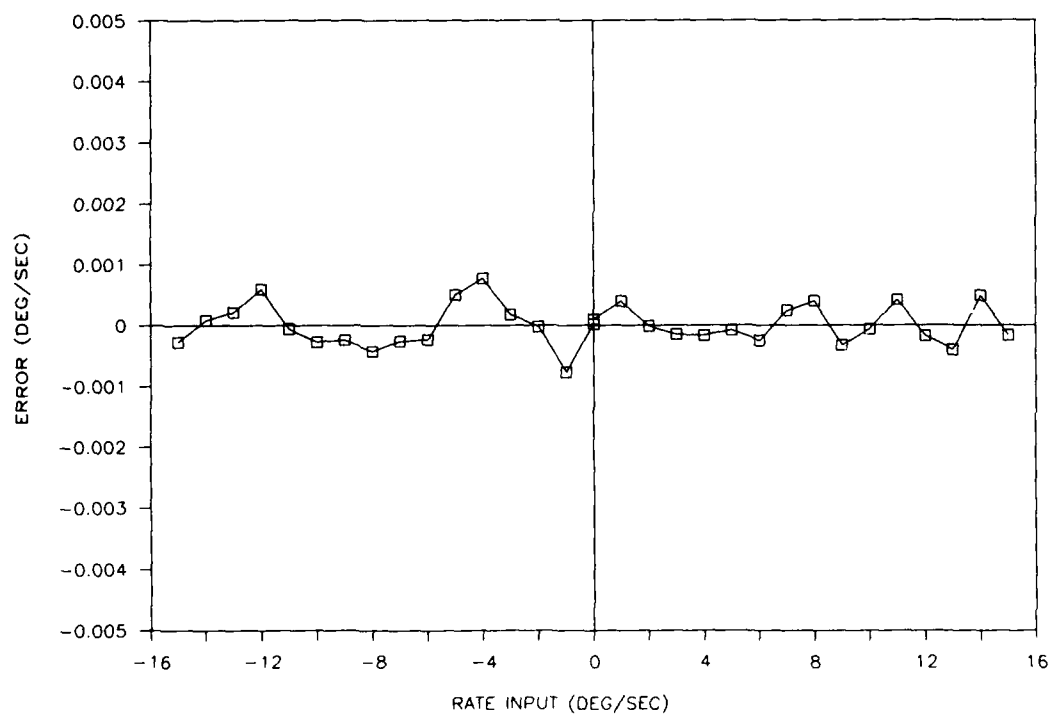DRIFT: .25 DEG/HR (1σ)
RWC: .04 DEG/HR

FIG. 2. 14 hour room temperature bias run.

FIG. 3. Bias run over temperature.

FIG. 4. Low rate scale factor deviation from linearity.
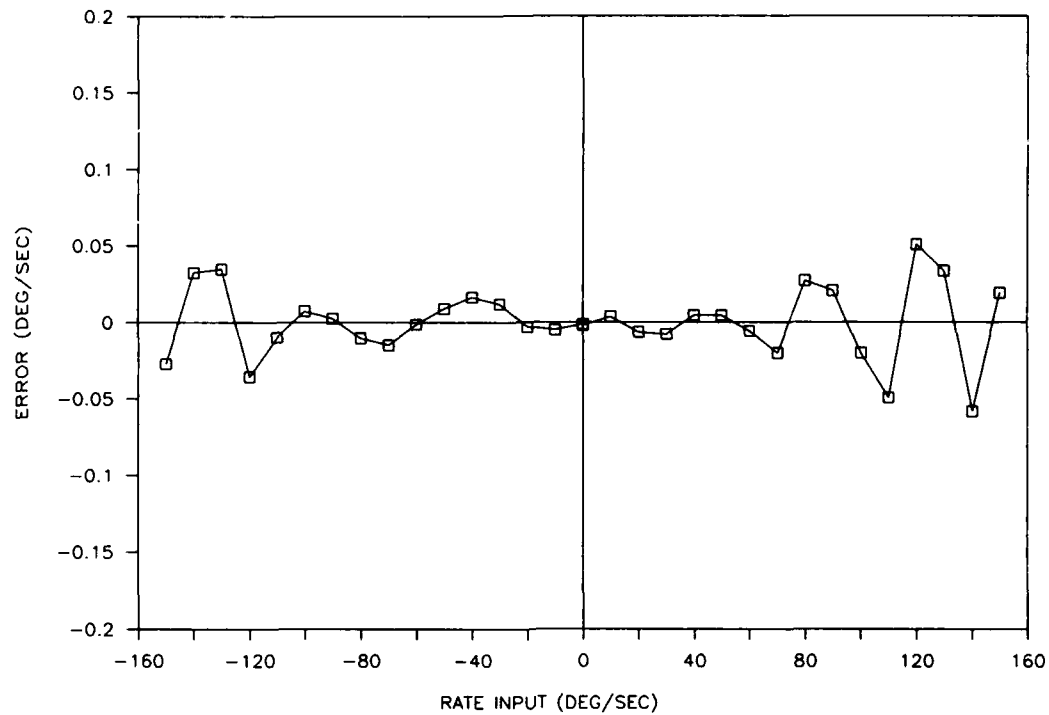
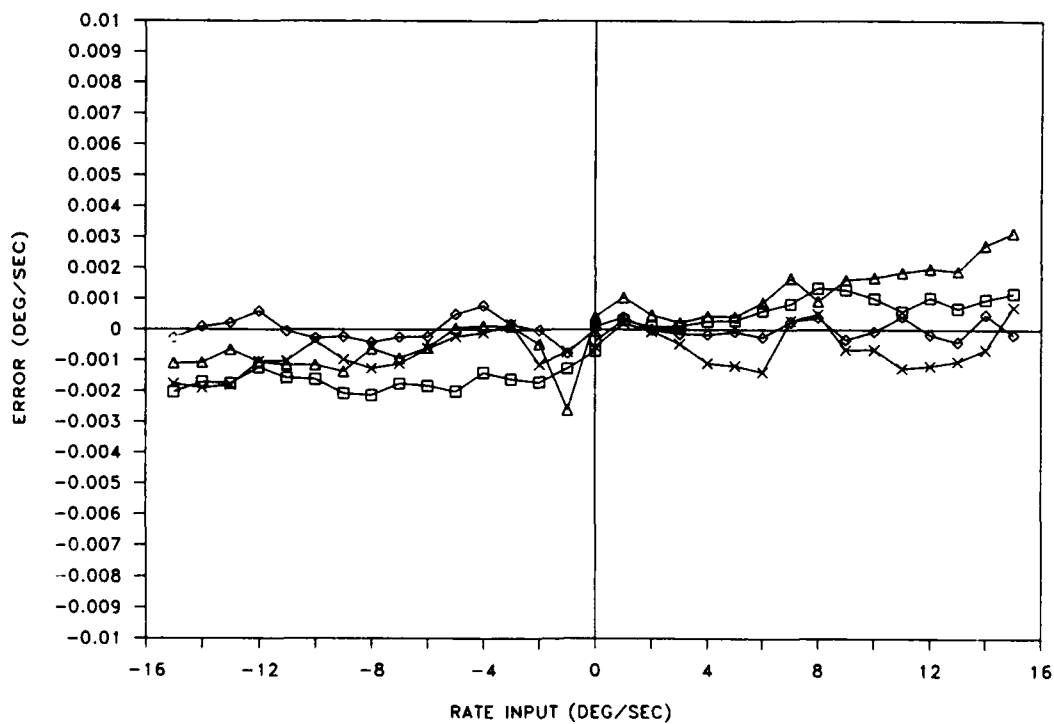**FIG. 5.** High rate scale factor deviation from linearity.

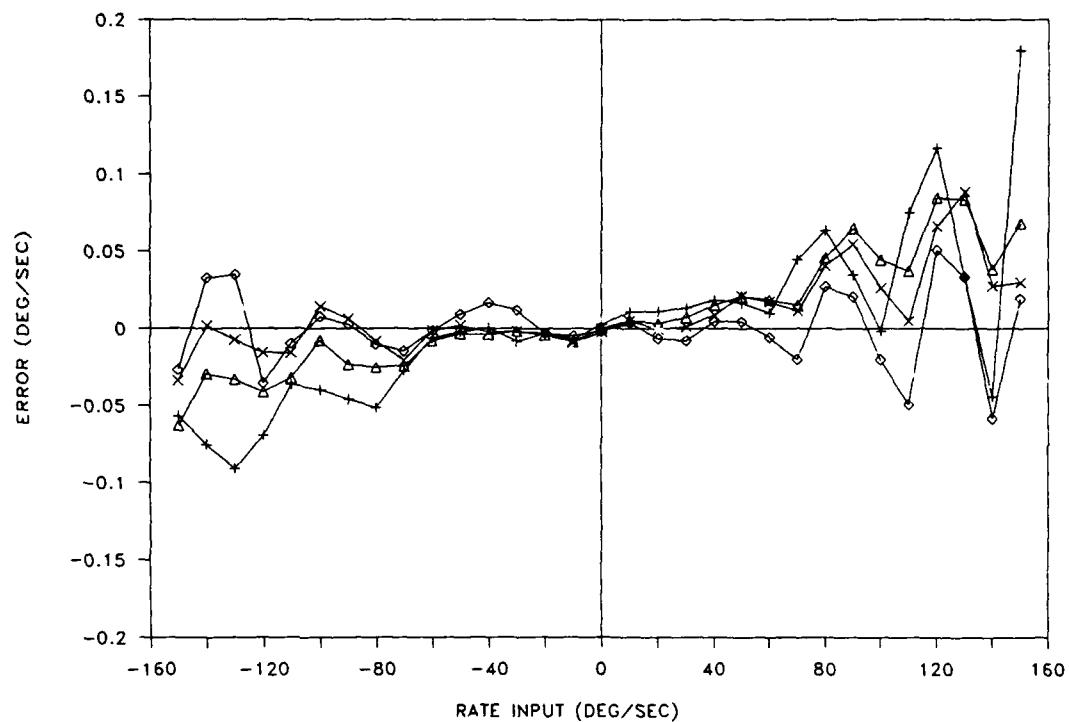**FIG. 6.** Low rate scale factor repeatability.

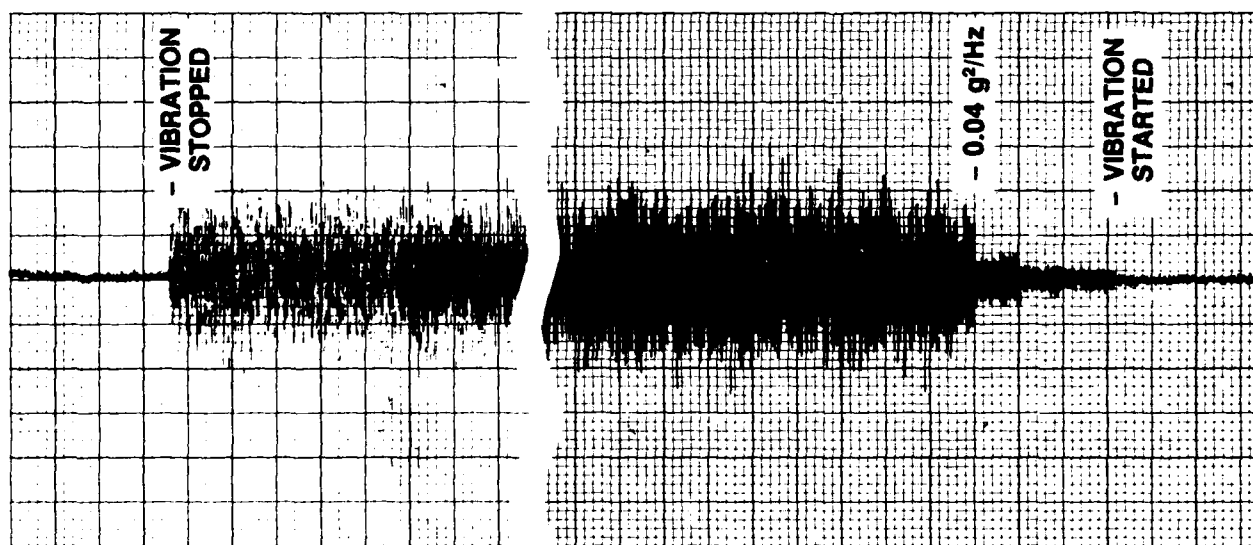**FIG. 7.** High rate scale factor repeatability.

FIG. 8. Gyro performance under vibration

FIG. 9. Engineering brassboard IFOG AHRS system.

REFERENCES

1. G. Sagnac, "L'ether lumineux demontre par l'effet du vent
    relatif d'ether dans un interferometre en rotation uniforme,"
    C.R. Acad. Sci. 95, 708 (1913)

2. R. Ulrich, "Polarization and depolarization in fiber-optic
    gyroscopes," in **Fiber-optic rotation sensors and related**
    technologies, Springer Series in Optical Sciences 32, 2,
    Springer-Verlag, New York (1982)

3. R. J. Fredricks and R. Ulrich, "Phase error bounds of fiber
    gyro with imperfect polarizer/depolarizer," Electron. Lett.
    20, 330 (1984)

4. H. J. Arditty, "Modulation and signal processing for the
    fiber optic gyro," Proc. SPIE, 719, 254 (1986)

5. L. F. Stokes, "Enviromental testing of a prototype open-loop
    fiber optic gyro for space applications," Proc. SPIE, 838, 98
    (1987)

6. D. M. Shupe, "Thermally induced nonreciprocity in the fiber
    optic interferometer," Appl. Opt. 19, 654 (1980)

THE IEEE/AESS GYRO AND ACCELEROMETER PANEL

presented by
THOMAS C. LEAR
Jet Propulsion Laboratory
NASA/CALTECH

The Aerospace and Electronics Systems Society is within the framework of the Institute of Electrical and Electronic Engineers. It is composed of members with a similarity of professional interests. All IEEE members are eligible for participation.

The Gyro and Accelerometer Panel is a technical panel of the AESS. Its charter is as follows:

1. To create standard terminology, specifications, formats, and test procedures for, and to promulgate understanding of components for detection or measurement of linear or angular motion.

2. The panel is composed of representatives of industry, government laboratories, educational institutions and professional societies who are knowledgeable of the characteristics, operating principles, sources of error, and areas of application of these components.

The panel meets six times a year, for two days each meeting. The members' supporting organizations host the meetings, providing meeting rooms and limited support logistics. The members provide their own per diem and travel expenses, as supported by their organization.

The standards written by the panel are the result of many hours of work by many different people from many different organizations. The average time is about two and a half years of deliberation to bring a standard to submittal for publication. The documents, as published, are standard FORMATS. That is, the user is able to use as much or as little of the document as he wishes, depending on the application. The panel tries hard to make the format complete. Specification terms are included where there is a recognized application which requires them, and usually omitted when an application is obscure. The test procedure section is treated in the same manner. Again, the documents are specification FORMATS, not finished specifications. Most of the newer documents contain appendices consisting of a mathematical model of the instrument described, a discussion of its physical components, and a discussion of special data-reduction considerations.

In addition to the specification formats, the panel also maintains a document titled, "IEEE Standard Inertial Sensor Terminology." This standard is a listing of terms and definitions relating to inertial sensors. When necessary, the needs of the inertial sensor community have been given preference over general technical usage. For example, degree-of-freedom, rotor angular momentum, and pendulosity are defined in a restricted sense, as applied to inertial sensors. In general, standard textbook definitions have not been included; for example, damping ratio and orthogonality.

Advantages of participation in such a panel are important. People from all aspects of the inertial community take part. The discussions between the panel members give a broad exposure to the many applications of gyros and accelerometers, and to new and exciting developments in their technology. While the members from the producing industry are very

careful about protecting their company's proprietary interests, they are equally careful to be sure that the unique capabilities of their sensors are represented in the specification formats. The latest in testing and data reduction techniques are fully explored. The panel's deliberations are sometimes contentious, but they are always interesting.

The panel would welcome anyone who may care to join us.

The 1989 officers of the Gyro and Accelerometer Panel are:

Panel Chairman
Thomas C. Lear
Jet Propulsion Laboratory

Panel Vice-Chairman
Menno G. Koning
Northrup Corp. PPD Div.

Gyro Committee Chairman
Cleon H. Barker
6585 Test Group (CIGTF)
            USAF

Accelerometer Committee Chairman
Harold D. Morris
Systron Donner Corp.

These documents may be ordered from:

IEEE Service Center
445 HOES Lane
Piscataway, NJ   08854

GYRO AND ACCELEROMETER PANEL

IEEE STANDARDS

Specification Format for Single-Degree-of-Freedom Spring Restrained Rate Gyros	IEEE Std 292-1969 $5.00
Test Procedure for Single-Degree-of-Freedom Spring-Restrained Rate Gyros	IEEE Std 293-1969 $5.00
Specification Format Guide and Test Procedures for Linear, Single-Axis, Pendulous, Analog Torque-Balance Accelerometer	IEEE Std 337-1972 $10.00
Standard Specification Format Guide and Test Procedure for Linear, Single-Axis, Digital, Torque-Balance Accelerometer	IEEE Std 530-1978 $17.50
Standard Specification Format Guide and Test Procedure for Single-Degree-of-Freedom Rate-Integrating Gyros	IEEE Std 517-1974 $25.00
Standard Inertial Sensor Terminology	IEEE Std 528-1984 $6.00
Supplement for Strapdown Applications to the IEEE *Standard Specification Format Guide and Test Procedure for Single-Degree-of-Freedom Rate Integrating Gyros*	IEEE Std 529-1980 $15.00
Standard Specification Format Guide and Test Procedure for Laser Gyros	IEEE Std 647-1981 $15.00
Standard Specification Format Guide and Test Procedure for Non-Gyroscopic Inertial Angular Sensors: Acceleration, Velocity and Displacement	IEEE Std 671-1985 Avail Aug 1985 $12.00
Guide to the Characteristics and Application of Inertial Angular Sensors (Gyro, Accelerometer, and other)	Project P761 (In Process)
Standard Specification Format Guide and Test Procedure for Two-Degree-of-Freedom (Dynamically Tuned) Gyros	Project P813 (In Process)
Recommended Practice for Precision Centrifuge Testing of Linear Accelerometers	Project P836 (New Assignment)

Comparative Analysis for Improved Attitude Estimates

from

Global Positioning System receiver RCVR3A

by

Robert M. Rogers

Presented at the

Fourteenth Biennial Guidance Test Symposium
Holloman Air Force Base, New Mexico
3-5 October 1989

Rogers Engineering & Associates
Gainesville, FL 32605

Abstract

The GPS RCVR3A's Kalman filter is analyzed to evaluate potential performance improvements afforded by adjusting the filter's tuning parameters. The objective of the improvements are: 1) to obtain better short term position accuracy in the event of an outage by improved attitude estimates, and 2) to improve the RCVR3A's capabilities for airborne alignment. The analysis is based upon a simulation using models of a strapdown INU and the GPS RCVR3A. The results of the analysis shows that improved attitude estimates can be obtained by adjusting the RCVR3A's filter velocity plant noise tuning parameters.

Introduction

The Global Positioning System (GPS) receiver RCVR3A is the primary receiver for airborne dynamic fixed wing aircraft. This receiver operates in several modes depending on the aircraft's on-board velocity sensor availability. The mode addressed in this paper is the INS aiding mode in which the Inertial Navigation Unit (INU) data is used within the receiver's processing. The interface between the INU and the RCVR3A is the MIL-STD-1553B data bus [Reference 1]. The INU state information is passed via the I06 bus message to the receiver and is used in the receiver's 12 state Kalman filter. The filter processes both pseudo range and delta range/pseudo range-rate measurements at a 1 Hz rate. This Kalman filter, implemented in earth-centered earth-fixed (ECEF) coordinates, provides corrections to the INU data, in local level navigation coordinates, which is then output in several forms via the G07 and G09 bus messages.

The objective of this paper is to examine, via simulation, modifications to the receiver's Kalman filter that can improve the filter's estimates and maximize the receiver's stand-alone utility during intermittent outage operations. This was suggested by earlier workers who used test data for evaluation [Reference 2]. The improvements sought are in improved attitude estimates while maintaining quality position and velocity estimates. The velocity and attitude errors will dominate position error growth in the short time period following an outage. Contribution of component errors, i.e. gyro and accelerometer biases, will contribute to position error growth for longer time periods; however, these contributions have not been included at the current time.

Other approaches to minimizing the impact of outages include the implementation of a second, or cascaded, Kalman filter which uses the receiver's corrected velocity and/or position estimates as new measurements. There are several filter design considerations if this approach is used and these considerations have been addressed in other forums [Reference 6]. It is the objective of this work to eliminate the need for a second filter if only short time period outages are anticipated.

Simulation Description

The simulation program uses a modular structure representing logical segmentation of the processes modeled. The main program flow generates a reference dynamic environment for a maneuvering aircraft and GPS satellite position/velocity data. The main program flow and reference dynamic equations solved are shown in Figures 1 and 2 respectively. The maneuver specifications are those from Reference 7.

Separate modules represent models for a strap-down INU and the GPS RCVR3A receiver with it's Kalman filter. The module for the INU is self-contained and computes a navigation solution based on sensed accelerations and rates from the main program reference dynamics. The INU model is based on a whole value dynamic representation for wander azimuth navigation frame quantities: attitude quaternions, velocities, and position direction cosines. The dynamic equations implemented for the INU model are shown in Figure 3. Outputs representing the appropriate MIL-STD-1553B output messages are formed and quantized.

Likewise, the GPS RCVR3A model in contained within a separate module. The outputs of the INU model, as specified in the MIL-STD-1553B message, are used in the RCVR3A's Kalman filter. The RCVR3A Kalman filter is shown in Figures 4 and 5 [References 3 and 4]. The filter tuning parameter values are summarized in Table 1 [Reference 2]. True values for the relative range and velocity between the aircraft and the satellites are generated in the main program reference dynamics. Estimates of these values, formed from INU and the RCVR3A's Kalman filter estimates, are used to form the residuals for the pseudo range and delta range/pseudo range-rate measurements. The outputs from this module are the estimates of corrections to be applied to the INU data received from the INU module. These corrections are then compared to the differences between the INU module outputs and the truth data from the main program reference dynamics and should be identical if the RCVR3A's Kalman filter estimates were perfect.

The modular structure and the whole value INU model permits the evaluation of the RCVR3A's Kalman filter without the limitations imposed by using a linearized simulation tool [Reference 5]. Large errors and data latencies can be introduced into a more realistic processing environment. This simulation was used to generate outputs for a comparative analysis, using different values of "tuning" parameters documented in Reference 2 for the RCVR3A's Kalman filter. Known values for INU errors were introduced. Estimates of these errors by the RCVR3A's Kalman filter are then compared with the known values to assess the resulting performance.

Simulation Results

The GPS RCVR3A's Kalman filter design was evaluated using a 10 minute flight segment along a 45 degree heading and with two 70 degree heading changes during the first 5 minutes. The original heading was maintained after the two opposite direction heading changes. The heading change maneuvers were benign using a 30 degree bank. The GDOP value was approximately 3.5 during the segment.

In the cases examined, the INU data is corrupted with known additive attitude errors. No other errors are interjected into the simulation. The difference between the main program reference dynamics and the outputs of the INU model show this error. For all cases, the roll and pitch error added to the INU initial conditions is 0.01 degrees. Two variations of azimuth error are considered. A small value of 0.05 degrees and a larger one of 0.5 degrees. These azimuth error levels are used to evaluate the ability of the RCVR3A's Kalman filter to complete an alignment while airborne.

Shown in Figures 6 and 7 are the velocity component differences between the reference dynamics and the outputs of the INU model for the two values of azimuth error and includes the roll and pitch errors above. The significance of the larger azimuth error is reflected in the larger induced INU velocity error shown in Figure 7 when a heading change maneuver occurs. These errors should be estimated by the RCVR3A's Kalman filter. How well the filter estimates these values and the attitude errors interjected into the simulation will be examined below. For each of the two azimuth error values, ensitivities to levels of reduced horizontal velocity, N_{hv}, plant noise are examined.

CASE 1: Azimuth error = 0.05 degrees:

Shown in Figures 8 and 9 are the differences between the RCVR3A filter's estimates of the INU velocity errors and the values presented in Figure 6. These figures show that the velocity error in the RCVR3A's estimates are significantly reduced with the indicated reduction in N_{hv} to 1.E-4. Shown in Figures 10 and 11 are comparisons between the estimated roll and pitch errors and the actual error computed from the difference between the reference dynamics and the INU model. Noticeable in Figures 10 and 11, near the end of the time segment simulated, is the beginning of a divergence in the roll and pitch error estimates. This divergence is suspected to be the result of too small a value for N_{hv} while prior to that point the much improved estimates are evident. The azimuth error estimates are shown in Figures 12a and 12b. In these figures, the plus and minus one sigma uncertainties associated with the azimuth error estimate are also presented. These figures show the potential improvement with the lower value of N_{hv} if the divergence did not occur.

Using an intermediate value of N_{hv} reduction to 1.E-3, the RCVR3A's estimates are again compared. Shown in Figures 13 and 14 are the differences between the RCVR3A model's estimates for INU velocity errors and the values presented in Figure 6. This value of N_{hv} yields a reduced level of velocity error oscillation while no evidence of divergence is present. The roll, pitch and azimuth error estimates shown in Figures 15, 16, and 17a and 17b are also much improved.

CASE 2: Azimuth error = 0.5 degrees:

Shown in Figures 18 and 19 are the differences between the RCVR3A filter's estimates of the INU velocity errors and the values presented in Figure 7. These figures show that the velocity error in the RCVR3A's estimates are significantly reduced with the indicated reduction in N_{hv} to 1.E-4 with a slight increase in the peak error during the heading change maneuver. Shown in Figures 20 and 21 are comparisons between the estimated roll and pitch errors and the actual error computed from the difference between the reference dynamics and the INU model. Again, noticeable in Figure 20, near the end of the time segment simulated, is the beginning of a divergence in the roll error estimate. As mentioned above, this divergence is suspected to be the result of too small a value for N_{hv}. Prior to that point the much improved estimates are evident. The azimuth error estimates are shown in Figures 22a and 22b. In these figures, the plus and minus one sigma uncertainties associated with the azimuth error estimate are also presented. These figures show the potential improvement with the lower value of N_{hv} if the divergence did not occur.

Using an intermediate value of N_{hv} reduction to 1.E-3, the RCVR3A's estimates are again compared. Shown in Figures 23 and 24 are the differences between the RCVR3A model's estimates for INU velocity errors and the values presented in Figure 7. This value of N_{hv} yields a reduced level of velocity error oscillation and lower peak error while no evidence of divergence is present. The roll, pitch and azimuth error estimates shown in Figures 25, 26, and 27a and 27b are also much improved.

Discussion of Simulation Results

Improved velocity and attitude error estimates result from using lower values of the horizontal velocity plant noise parameter N_{hv}; however, values that are too low may result in divergence. An intermediate value between that in Table 1 and that recommended in Reference 2 exhibits the best overall performance and desireable characteristics.

The results presented show that the attitude error estimates can be improved significantly compared to those provided by using the current filter tuning parameters. However, with large values of initial psi error, the estimates tend to lag behind the actual error values. This indicates the importance of correcting the INU errors. This can be done via the F02 correction vector in standardized INUs.

While these results, using simulation, are insightful, the best values of the tuning parameters should the result of evaluating flight data over a spectrum of flight conditions. This additional step in the evaluation is recommended.

References

1. Greenspan, R.L., et al, "The GPS User's Integration Guide", ION Meeting, January 1988.

2. Soltz, J.A., et al, "An Option for Mechanizing Integrated GPS/INS Solutions", ION Meeting, June 1988.

3. Krishnamurti, G., et al, "The Design and Performance of GPS Phase II User Equipment Navigation Software", Navigation, Vol 32, No 3, 1985, pp 263-281.

4. Bartholomew, R.G., et al, "Software Architecture of the Family of DoD Standard GPS Receivers", ION Meeting, September 1987.

5. Sinha, P.K., "Integrated GPS/Strapdown Inertial Simulator Computer Program", Intermetrics Report IR-253, December 1977.

6. Bletzacker, F.R., et al, "Kalman Filter Design for Integration of Phase III GPS with an Inertial Navigation System", ION Meeting, January 1988.

7. Musick, S.H., "PROFGEN - A Computer Program for Generating Flight Profiles", AFAL TR-76-247, November 1976.
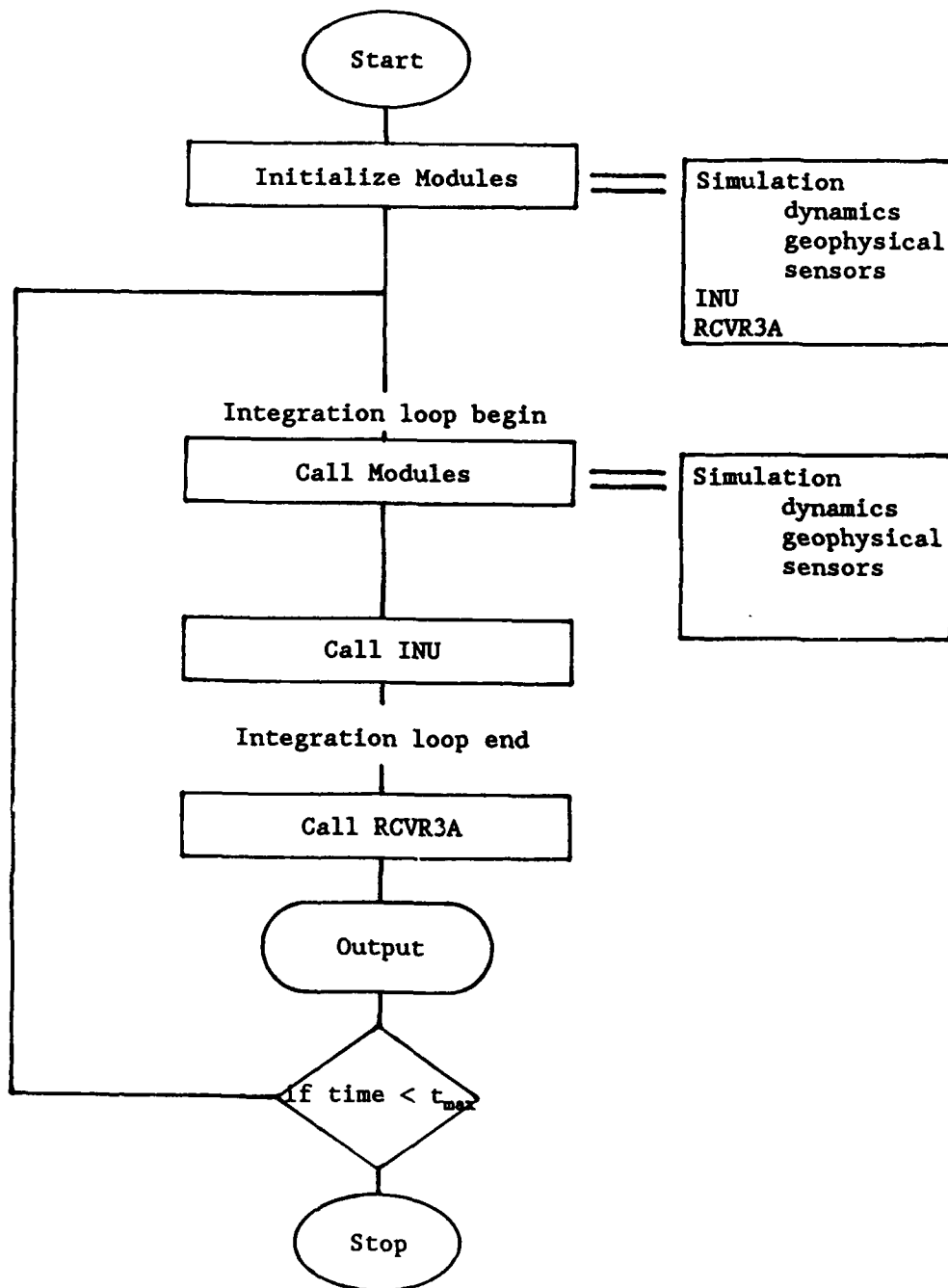
Figure 1: Main Program Flow

$$^{V}\dot{C}^{B} = {}^{B}\Omega^{B/V}\; {}^{V}C^{B}$$

$$\dot{\underline{V}}^{V} = {}^{B}\Omega^{B/V}\; \underline{V}^{V}$$

$$\dot{\phi} = V_{north}/R_{m}$$

$$\dot{\lambda} = V_{east}/(R_{n}\; \cos(\phi))$$

$$\dot{h} = -V_{down}$$

where

$^{V}C^{B}$ — body to local vertical direction cosine matrix

$^{B}\Omega^{B/V}$ — skew symmetric matrix vector cross product equivalent of relative body rotation rates, roll, pitch, and yaw, coordinatized in body frame

$\underline{V}^{V}$ — velocity vector whose components, north, east and down, are defined in local vertical coordinates

ϕ — latitude

λ — longitude

h — altitude

R_{m} — local meridional earth radius of curvature

R_{n} — local normal earth radius of curvature.

Figure 2: Main Program Reference Dynamics

$$\dot{q} - \tfrac{1}{2}\,\omega\,q$$

$$\dot{\underline{V}}^N - \underline{a}^N - (\underline{\rho} + 2\underline{\Omega})^N \times \underline{V}^N + \underline{g}^N$$

$${}^E\dot{C}^N - {}^E C^N \; {}^N\Omega^{N/E}$$

where

q - quaternions defining the body to navigation frame, wander azimuth, direction cosine matrix

ω - skew symmetric matrix composed of compensated relative body rates coordinatized in the navigation frame

$\underline{V}^N$ - velocity vector whose elements, x, y, and z, are defined in the navigation frame

$\underline{a}^N$ - navigation frame referenced acceleration vector

$\underline{\rho}$ - navigation frame transport rate vector; ρ_z is defined as zero

$\underline{\Omega}$ - navigation frame earth rate vector

$\underline{g}^N$ - navigation frame gravity vector

${}^E C^N$ - navigation to earth center direction cosine matrix; position

${}^N\Omega^{N/E}$ - skew symmetric matrix vector cross product equivalent composed of transport rate vector elements.

Figure 3: INU Dynamic Equations

Dynamics Model:

$$\dot{\underline{x}}(t) = F(t)\, \underline{x}(t) + G(t)\, \underline{w}(t)$$

State Vector:

$$\underline{x} = \begin{array}{lll}
\epsilon\underline{P} & = & \text{ECEF nominal position error vector (3x1)} \\
\epsilon\underline{V} & = & \text{ECEF nominal velocity error vector (3x1)} \\
\Psi & = & \text{ECEF INS platform tilt error vector (3x1)} \\
\epsilon h & = & \text{baro altimeter bias} \\
b & = & \text{range bias (clock phase error * c; speed of light)} \\
d & = & \text{range drift (clock frequency error * c)}
\end{array}$$

Dynamics Matrix:

$$F = \left[
\begin{array}{c|c|c|c}
-k_1\,\Pi & I_{3x3} & 0_{3x3} & k_1\,\underline{e}\ \begin{smallmatrix}0&0\\0&0\\0&0\end{smallmatrix} \\
\hline
\begin{array}{l} -\omega_s\,I_{3x3} \\ -(k_2-3\omega_s)\,\Pi \end{array} & \begin{array}{ccc}0&2\Omega&0\\-2\Omega&0&0\\0&0&0\end{array} & \begin{array}{ccc}0&-f_3&f_2\\f_3&0&-f_1\\-f_2&f_1&0\end{array} & k_2\,\underline{e}\ \begin{smallmatrix}0&0\\0&0\\0&0\end{smallmatrix} \\
\hline
0_{3x3} & 0_{3x3} & \begin{array}{ccc}0&\Omega&0\\-\Omega&0&0\\0&0&0\end{array} & 0_{3x3} \\
\hline
0_{3x3} & 0_{3x3} & 0_{3x3} & \begin{array}{ccc}-1/\tau_h&0&0\\0&0&1\\0&0&0\end{array}
\end{array}
\right]$$

where

k_1 = INS vertical velocity damping coefficient

k_2 = INS vertical acceleration damping coefficient

ω_s = Schuler frequency

Ω = earth rotation rate

$\underline{f}$ = ECEF specific force vector with components, f_1, f_2 and f_3

$\underline{e}$ = unit local level vertical vector at position $\underline{P}$

Π = local level vertical projection operator ($\underline{e}\ \underline{e}'$)

τ_h = baro altimeter bias Markov time constant

Figure 4: GPS Kalman Filter State Vector and Dynamics Matrix

Noise Distribution Matrix:

$$
G = \begin{bmatrix}
{}^{E}C^{L} & 0_{3x3} & 0_{3x3} & 0_{3x3} \\
0_{3x3} & {}^{E}C^{L} & 0_{3x3} & 0_{3x3} \\
0_{3x3} & 0_{3x3} & I_{3x3} & 0_{3x3} \\
0_{3x3} & 0_{3x3} & 0_{3x3} & \begin{matrix} 1 & 0 & 0 \\ 0 & 1 & 0 \\ 0 & 0 & 1 \end{matrix}
\end{bmatrix}
$$

where

${}^{E}C^{L}$ — local level to ECEF direction cosine matrix computed from INS supplied latitude, longitude, and wander angle

Measurement Model:

Pseudo Range:

$$PR(\underline{x}) = r + b$$

$$H = [\quad -\underline{e}' \quad | \quad 0_{1x3} \quad | \quad 0_{1x3} \quad | \quad 0 \quad 1 \quad 0 \;]$$

Delta Range/Pseudo Range-Rate:

$$DR(\underline{x}) = r_f - r_b + d \, \Delta t$$

$$H = [\quad 0_{1x3} \quad | \quad -\underline{e}' \, \Delta t \quad | \quad 0_{1x3} \quad | \quad 0 \quad 0 \, \Delta t]$$

where

r — range from vehicle to satellite

$\underline{e}'$ — unit line of sight vector from vehicle to satellite

Δt — difference between final time, t_f, and beginning time, t_b for doppler integration interval.

Figure 5: Plant Noise Distribution and Measurement Matrices

Table 1

Plant Noise (Tuning) Parameter Values [Reference 2]

Parameter	Units	Description	Values
N_{hp}	m^2/s	horizontal position plant noise	1
N_{vp}	m^2/s	vertical position plant noise	1
N_{hv}	m^2/s^3	horizontal velocity plant noise	1.E-2*
N_{vv}	m^2/s^3	vertical velocity plant noise	1.E-2
N_{ℓ}	$1/s$	specific force-dependent plant noise	1.E-6
N_{ψ}	rad^2/s	misalignment ψ plant noise	1.E-12
$N_{alt}:a_1$	m^2/s	baro altimeter bias plant noise	1.E+1
$N_{alt}:a_2$	s	velocity-dependent baro altimeter plant noise	1.E-3
N_b	m^2/s	clock plant noise	0.25
$N_d:d_1$	m^2/s^3	clock rate plant noise	2.E-4
$N_d:d_2$	s	acceleration-dependent clock rate plant noise	1.E-4
R_{pseudo}	m^2	Nominal pseudo range measurement noise	2.25
R_{delta}	m^2	delta·range measurement noise	95.E-4
k_1	$1/s$	baro inertial coupling constant	1.E-4
k_2	$1/s^2$	baro inertial coupling constant	1.E-6
r_h	s	baro altimeter bias correlation time	1.E+3

*This value is changed to be consistent with other documentation

note:

$N \underset{=}{\Delta} E\{ \underline{w}(t) \underline{w}'(r) \}$ where E{} is the expectation operator.
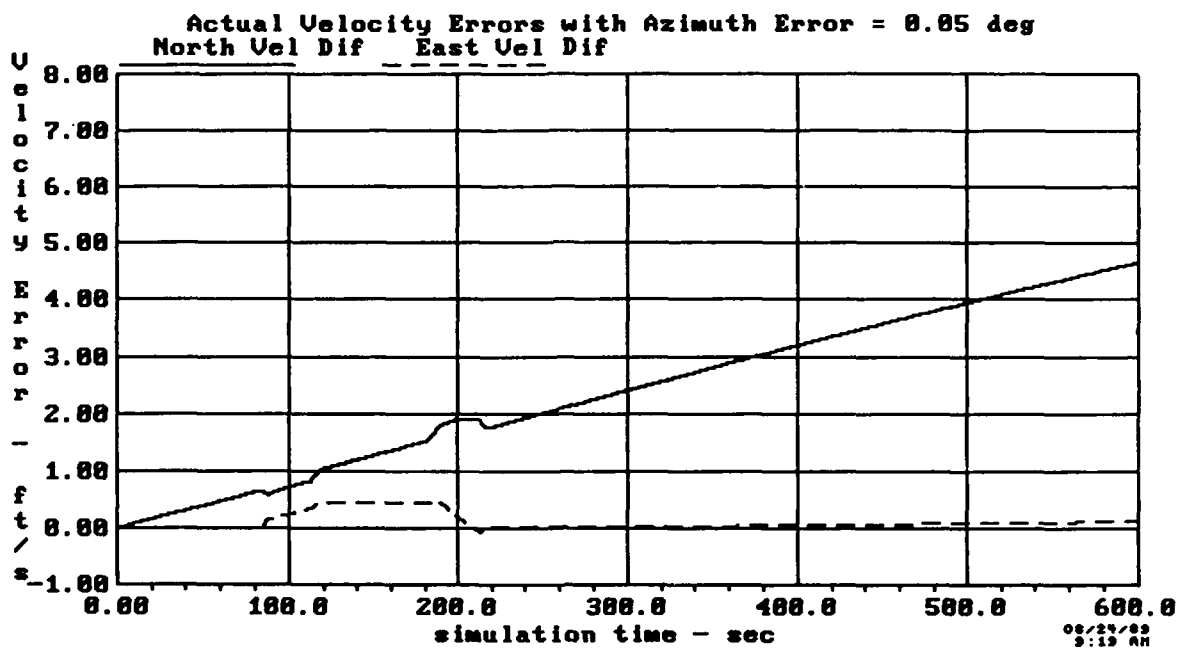
Figure 6: Velocity Differences; Reference Dynamics and INU Model-Psi=0.05 deg.
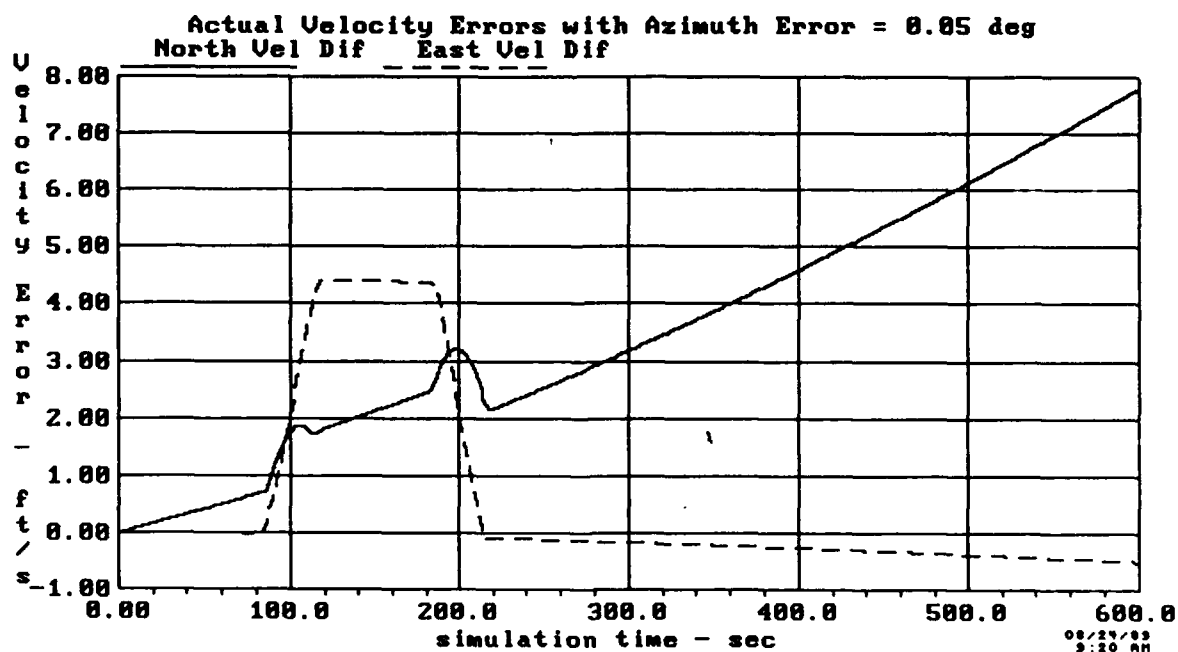

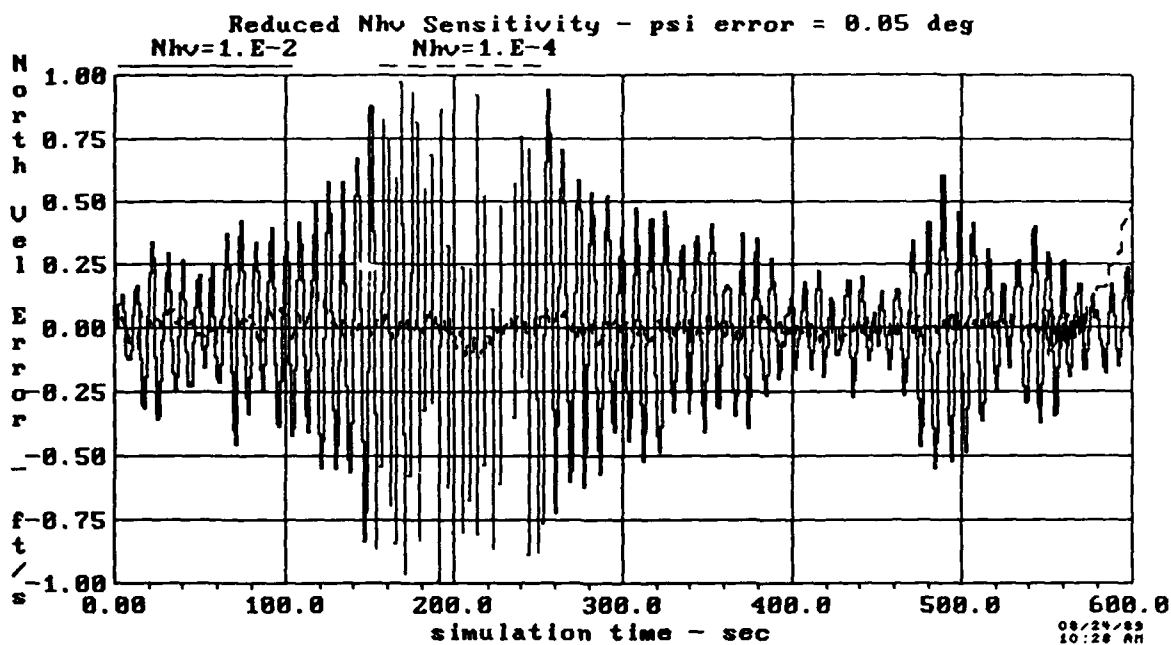Figure 7: Velocity Differences; Reference Dynamics and INU Model-Psi=0.5 deg.

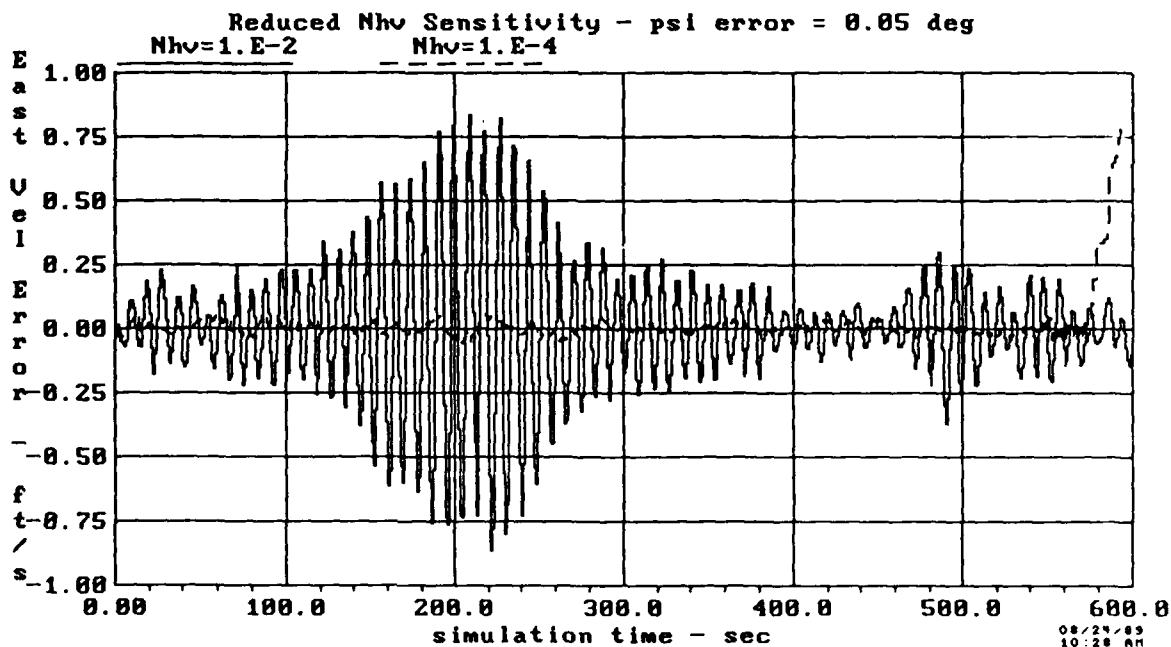Figure 8:   North Velocity Error with Reduced Nhv-Psi=0.05 deg.

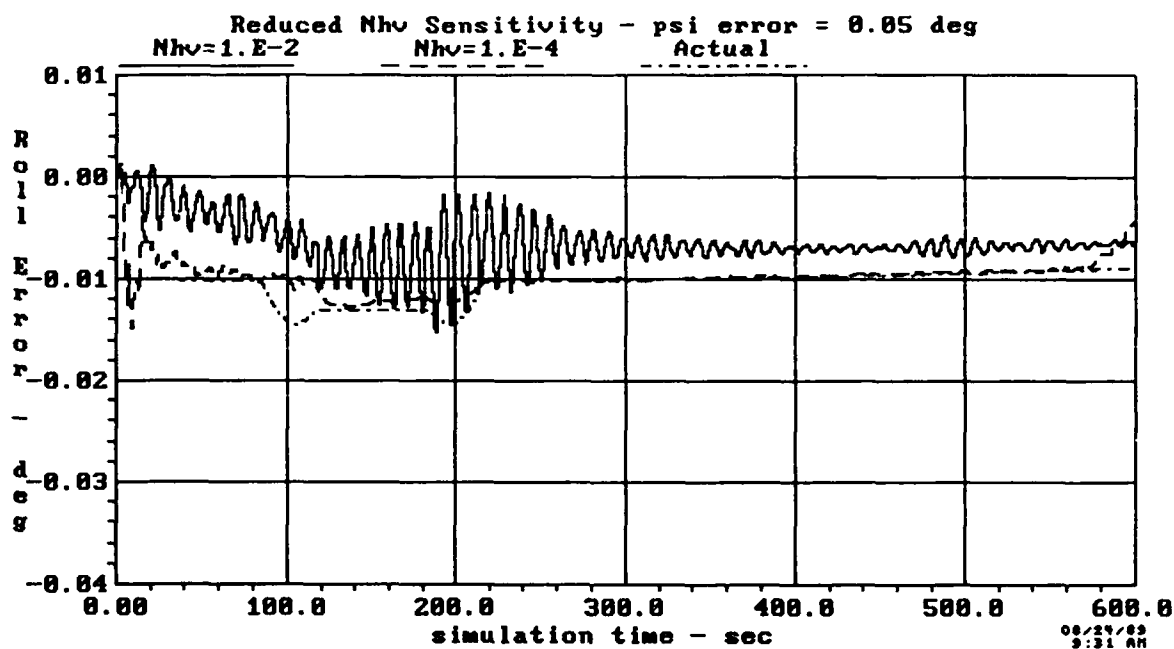Figure 9:   East Velocity Error with Reduced Nhv-Psi=0.05 deg.

Figure 10: Roll Error Estimates with Reduced Nhv-Psi-0.05 deg.

Figure 11: Pitch Error Estimates with Reduced Nhv-Psi=0.05 deg.

Figure 12a: Azimuth Error Estimates with Reduced Nhv-Psi=0.05 deg.

Figure 12b: Azimuth Error Estimates with Reduced Nhv-Psi=0.05 deg.

Figure 13:   North Velocity Error with Reduced Nhv-Psi=0.05 deg.

Figure 14:   East Velocity Error with Reduced Nhv-Psi=0.05 deg.

Figure 15:   Roll Error Estimates with Reduced Nhv-Psi=0.05 deg.
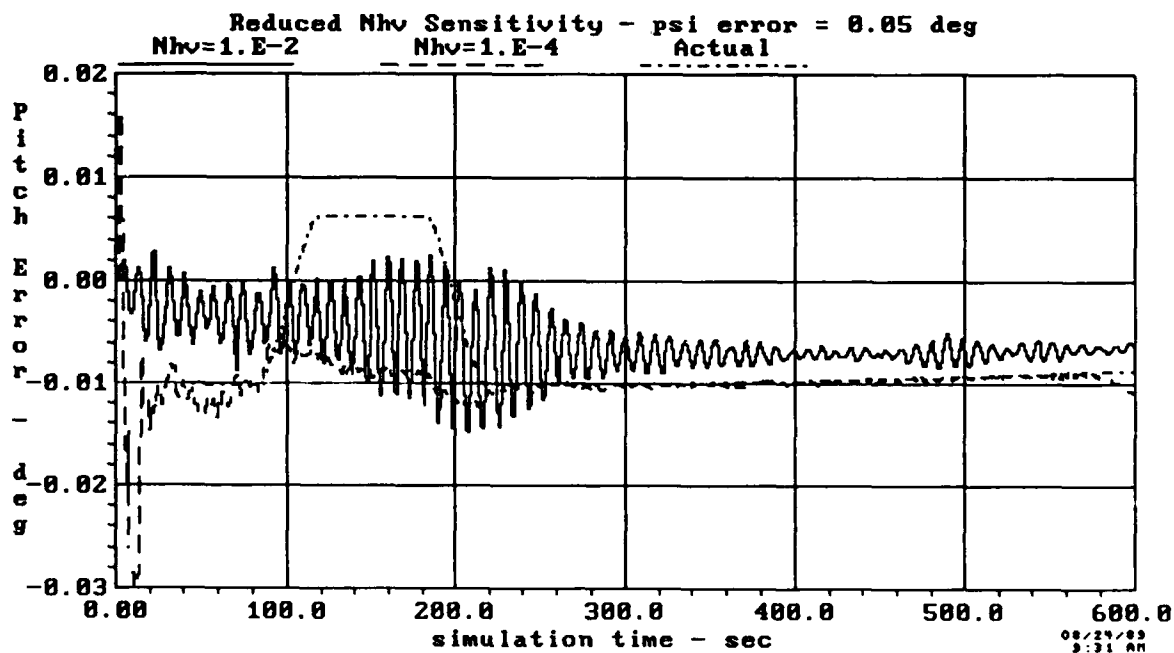

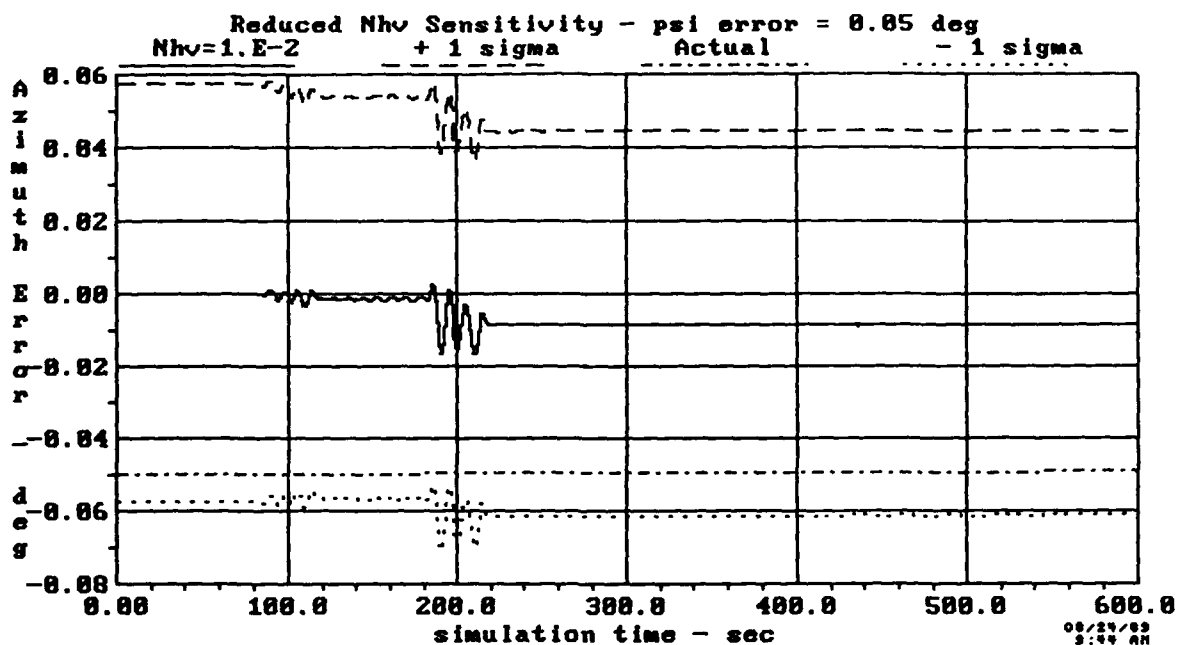Figure 16:   Pitch Error Estimates with Reduced Nhv-Psi=0.05 deg.
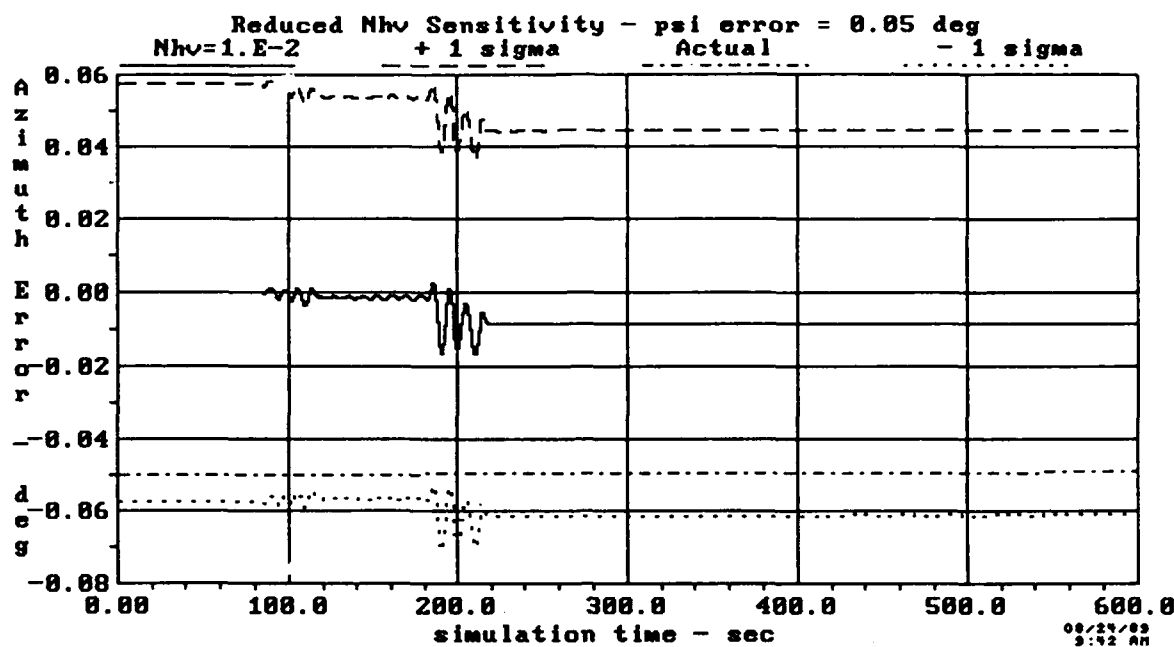
Figure 17a: Azimuth Error Estimates with Reduced Nhv-Psi=0.05 deg.
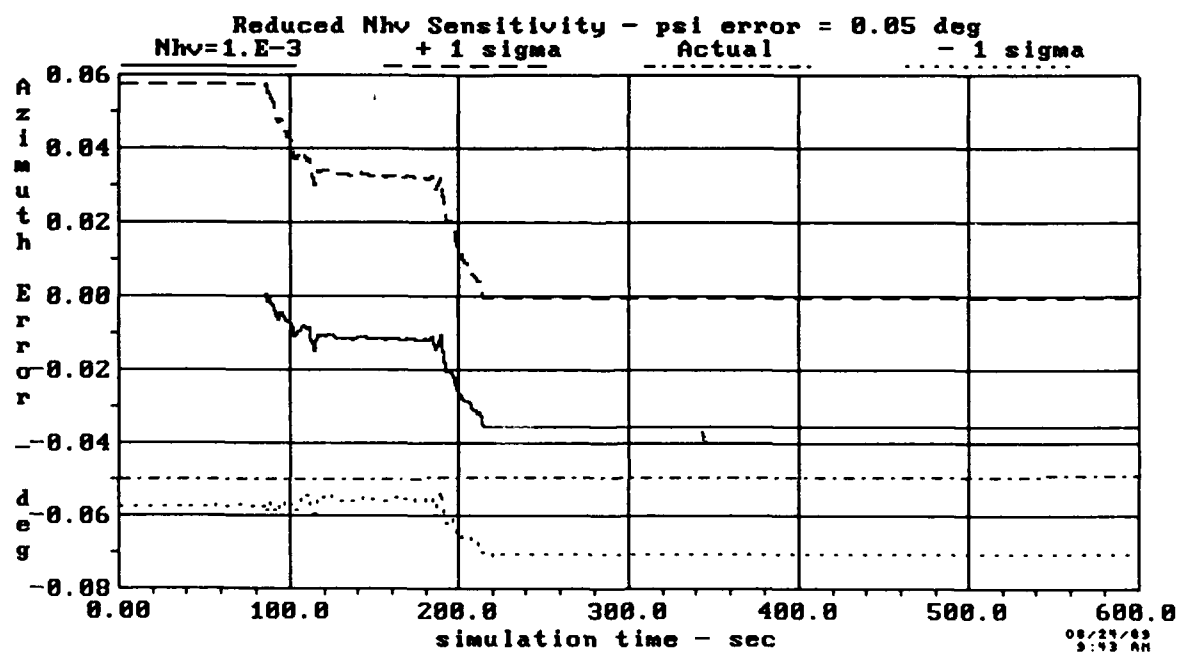
Figure 17b: Azimuth Error Estimates with Reduced Nhv-Psi=0.05 deg.
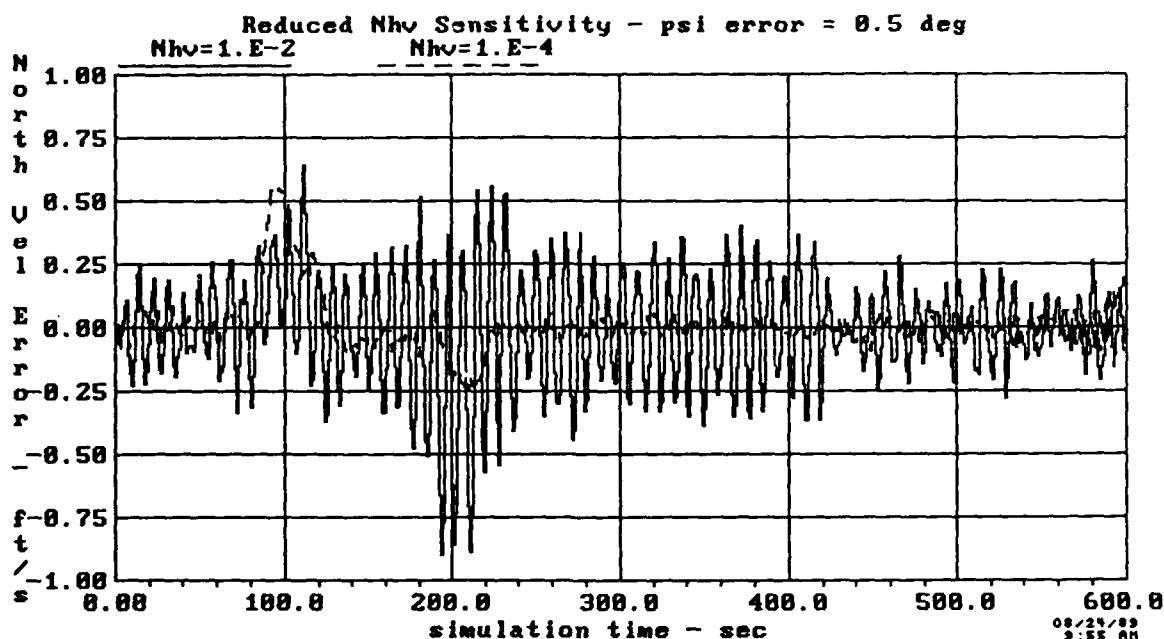
Figure 18: North Velocity Error with Reduced Nhv-Psi=0.5 deg.
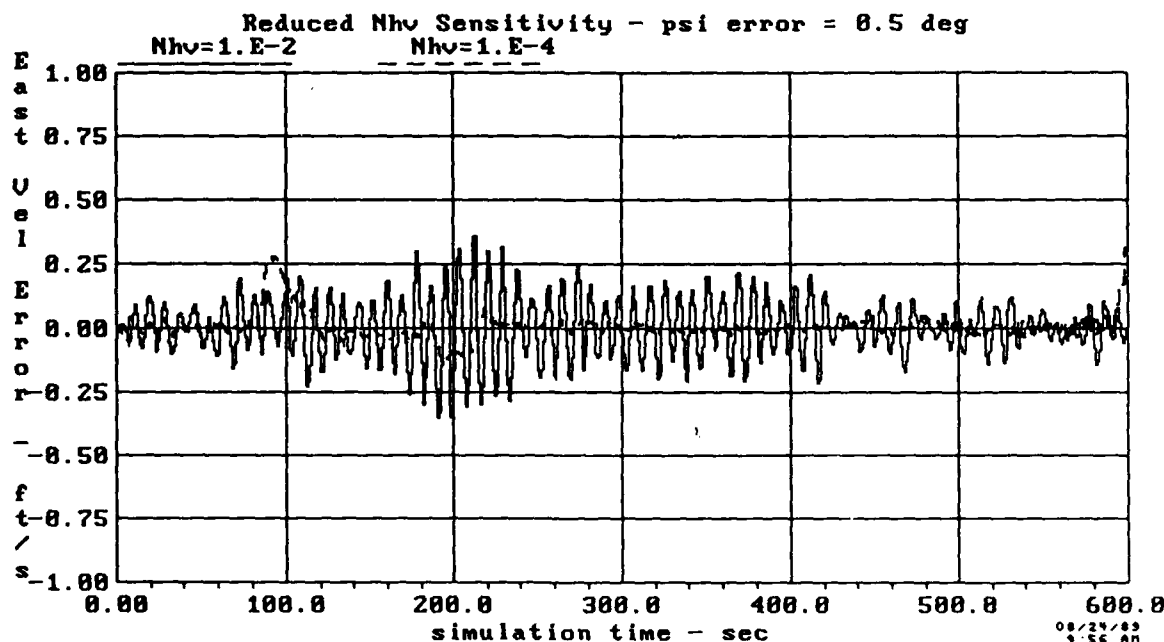
Figure 19: East Velocity Error with Reduced Nhv-Psi=0.5 deg.
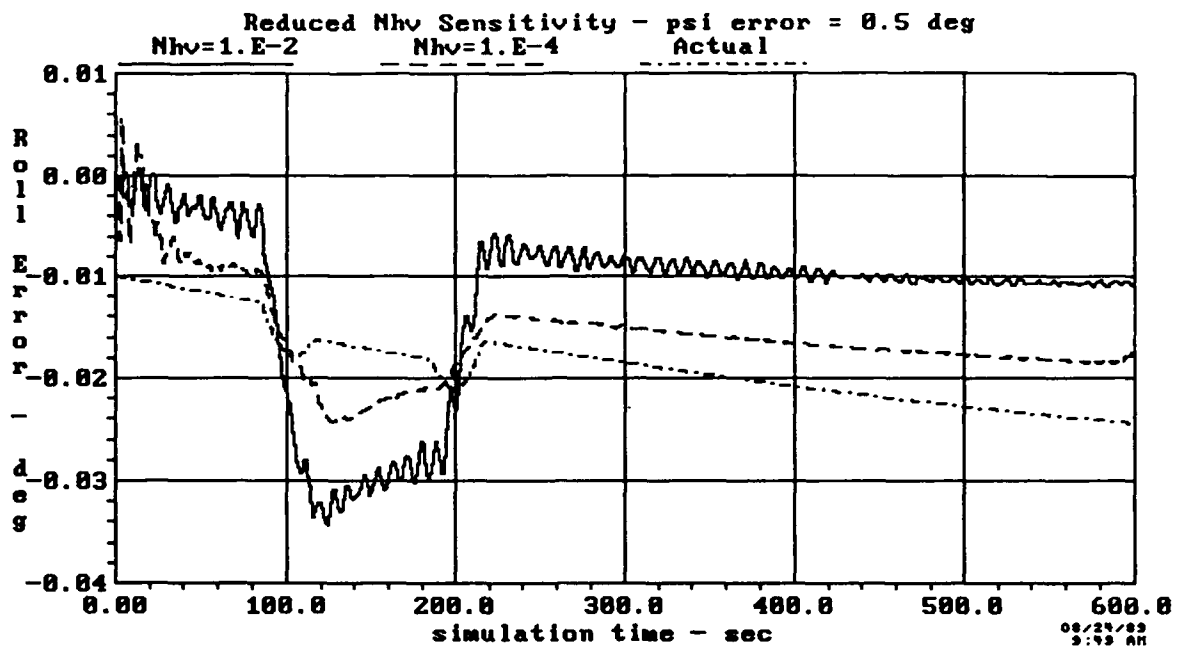
Figure 20: Roll Error Estimates with Reduced Nhv-Psi—0.5 deg.
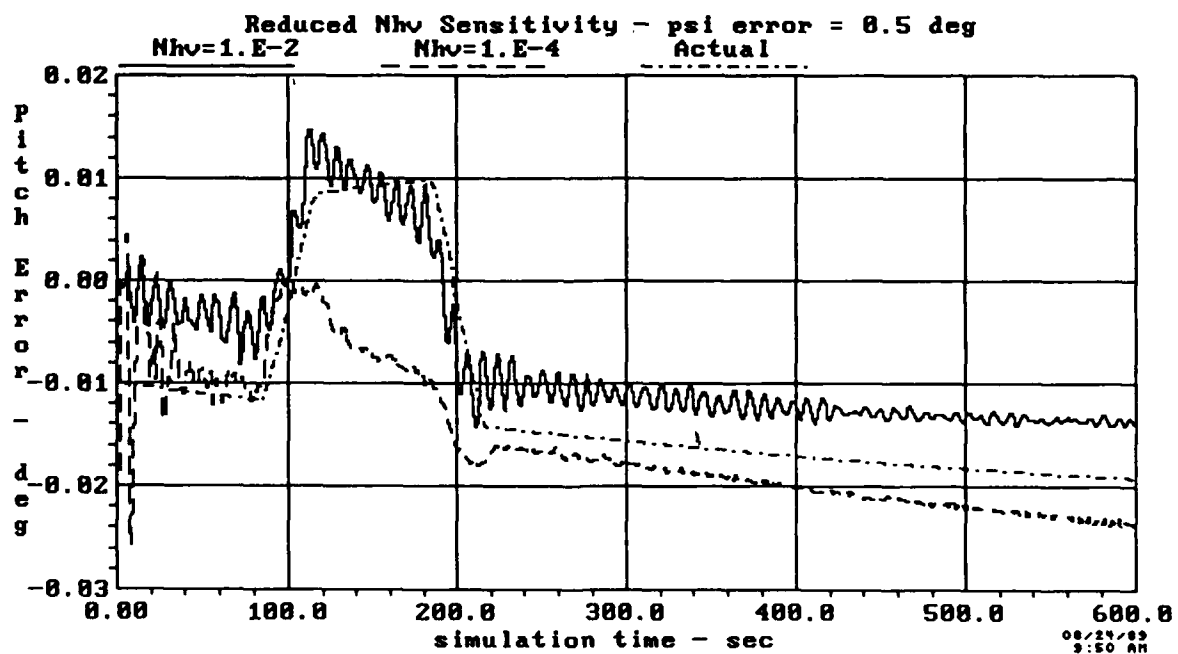
Figure 21: Pitch Error Estimates with Reduced Nhv-Psi—0.5 deg.
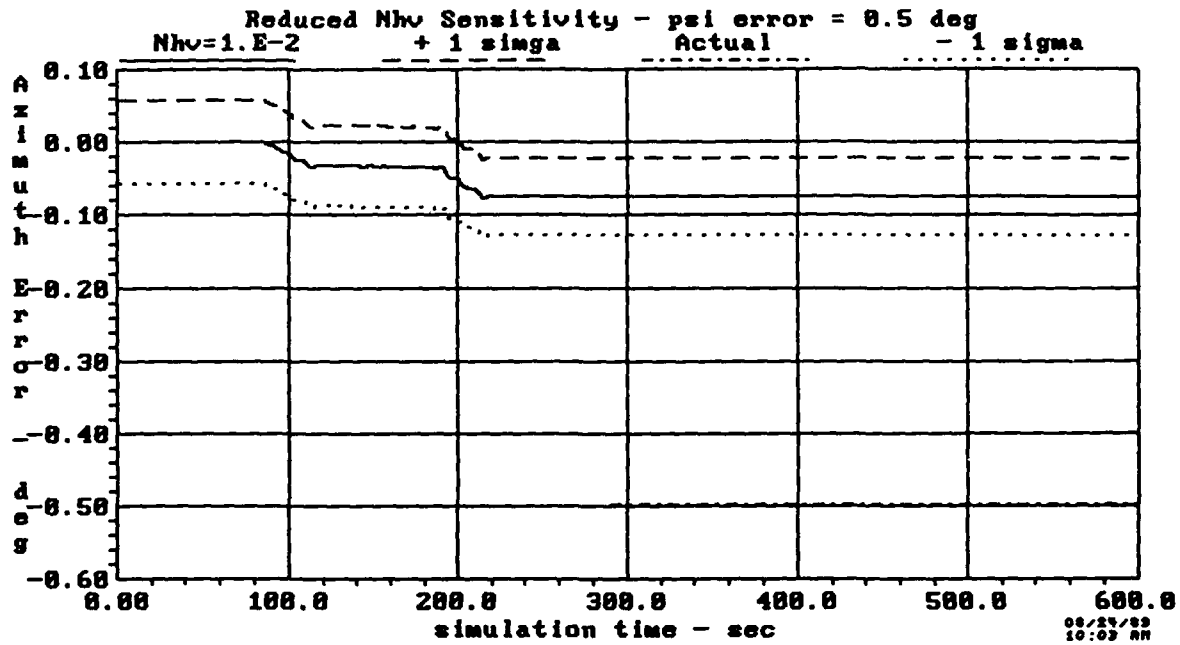
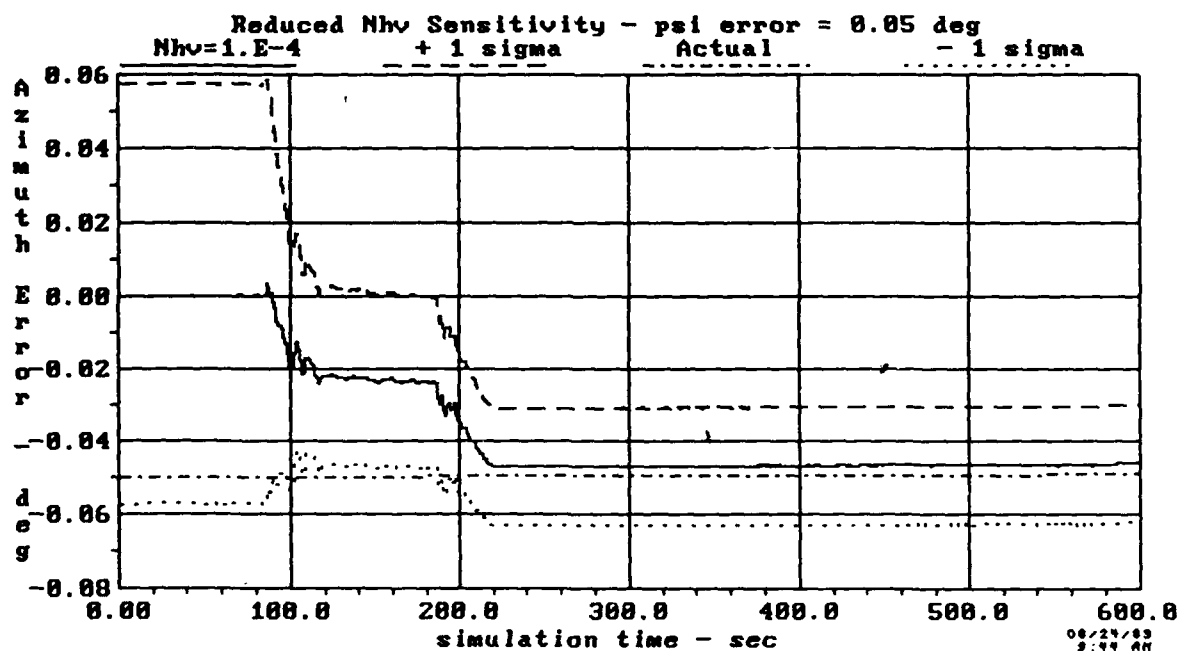Figure 22a: Azimuth Error Estimates with Reduced Nvv-Psi=0.5 deg.
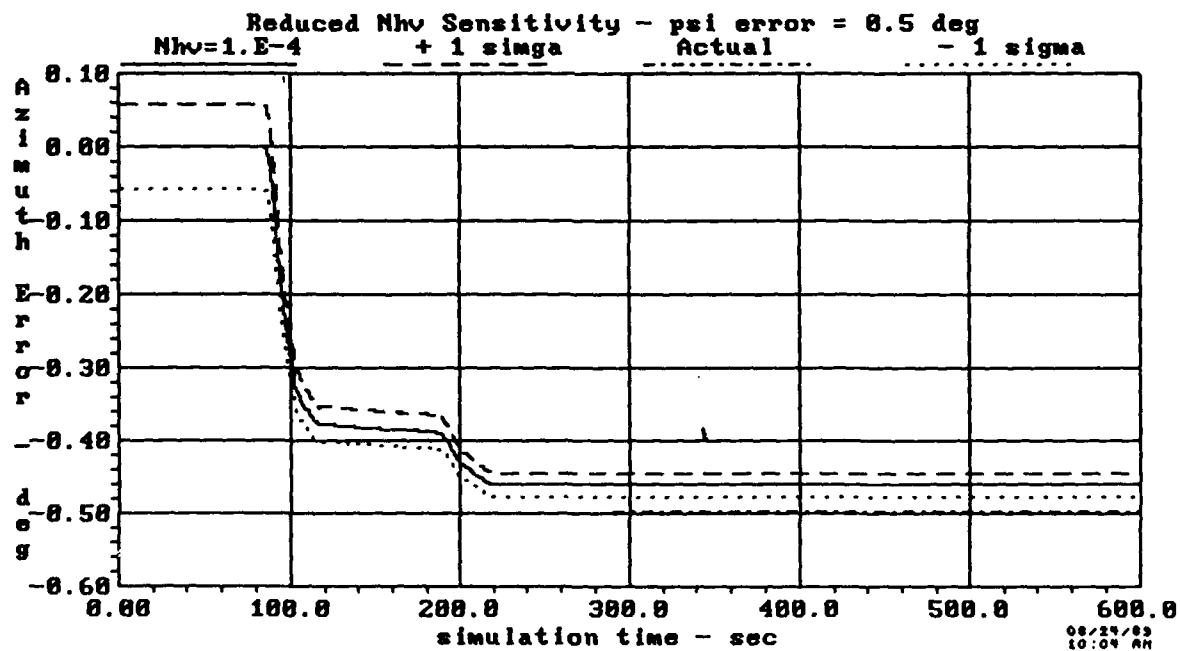
Figure 22b: Azimuth Error Estimates with Reduced Nvv-Psi=0.5 deg.
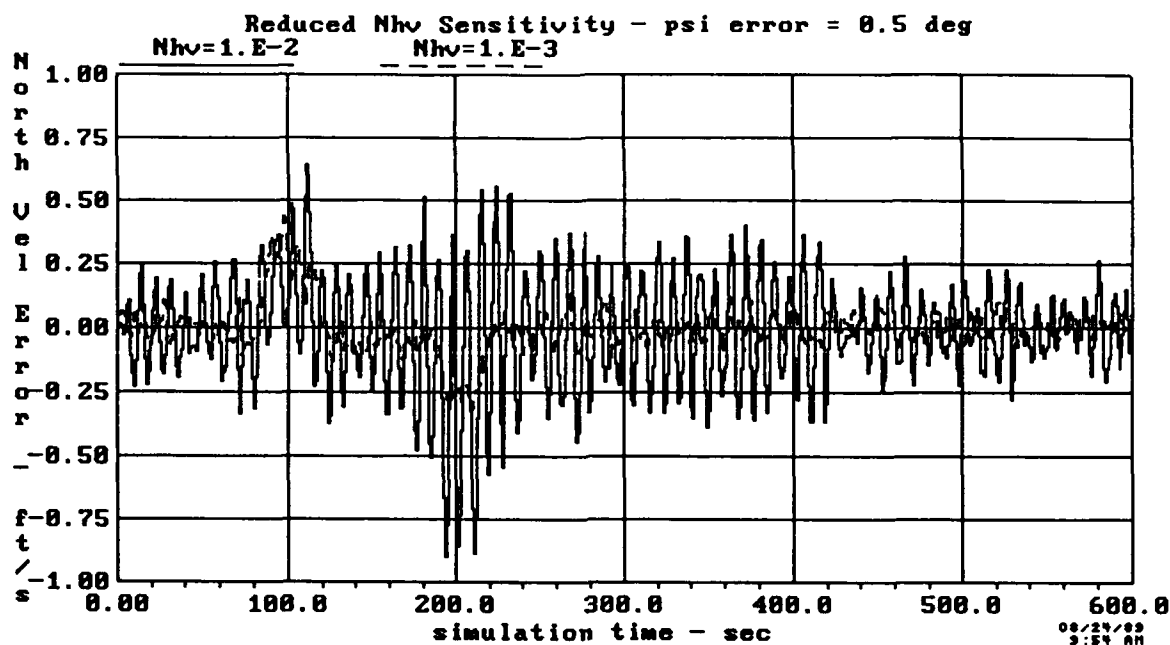
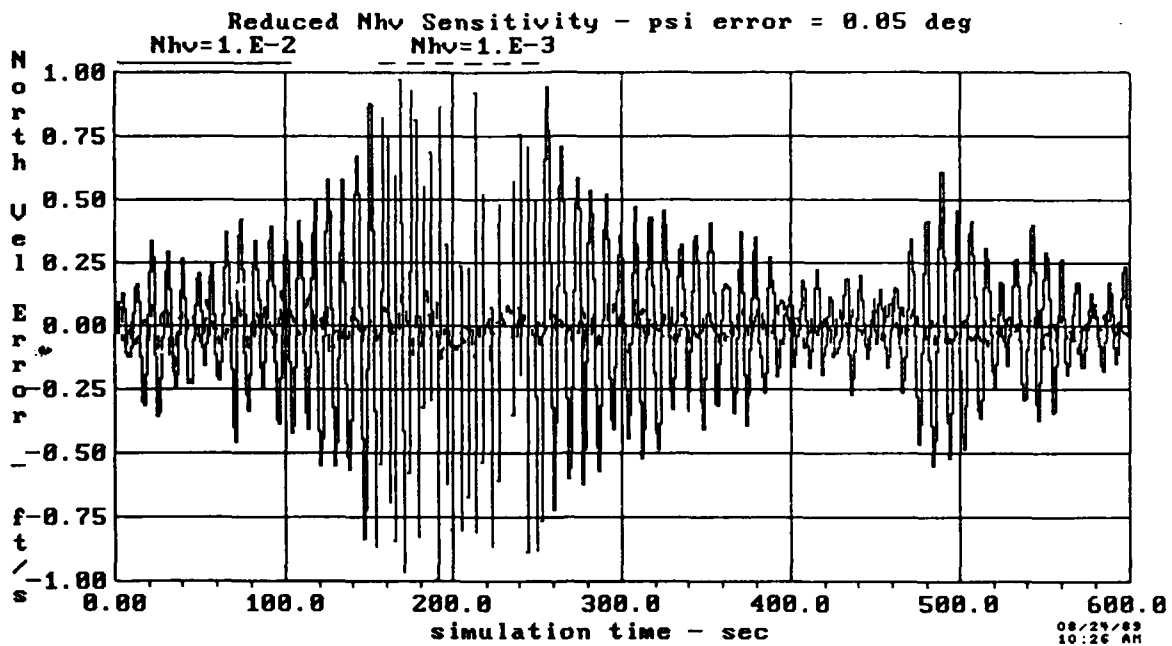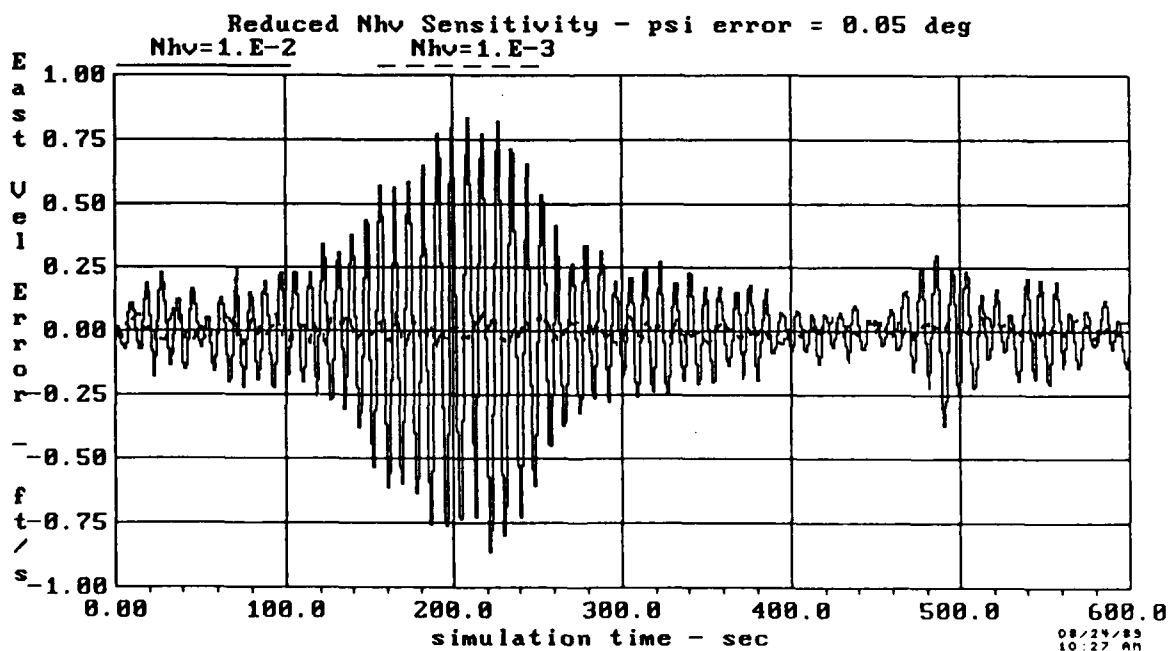Figure 23:   North Velocity Error with Reduced Nhv-Psi-0.5 deg.
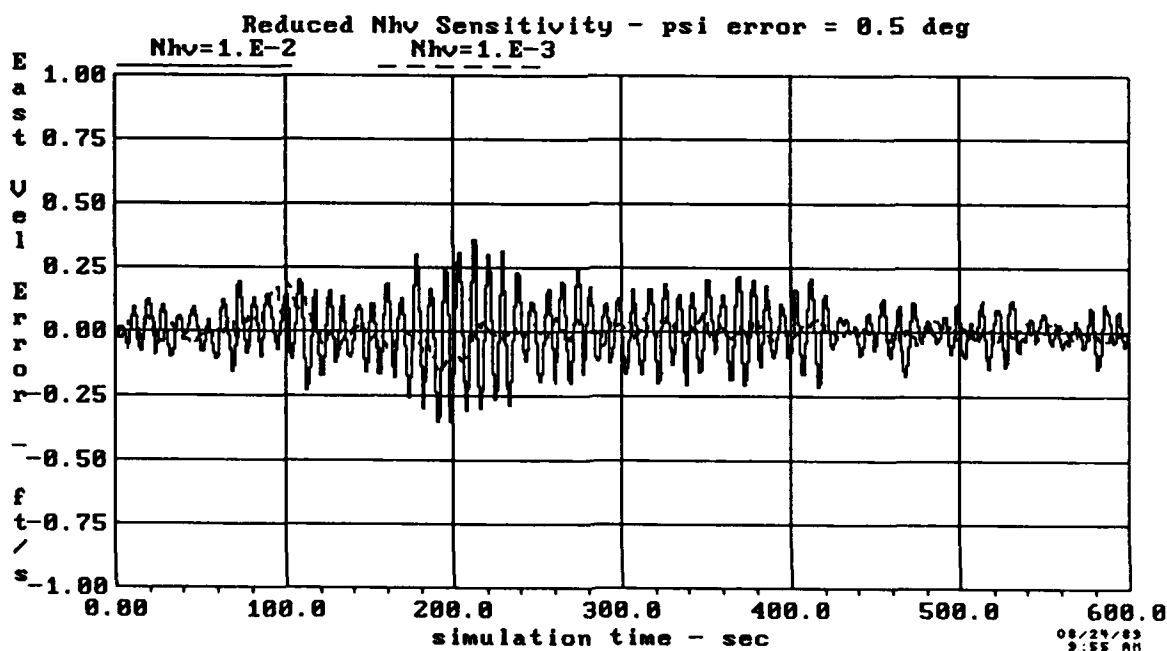
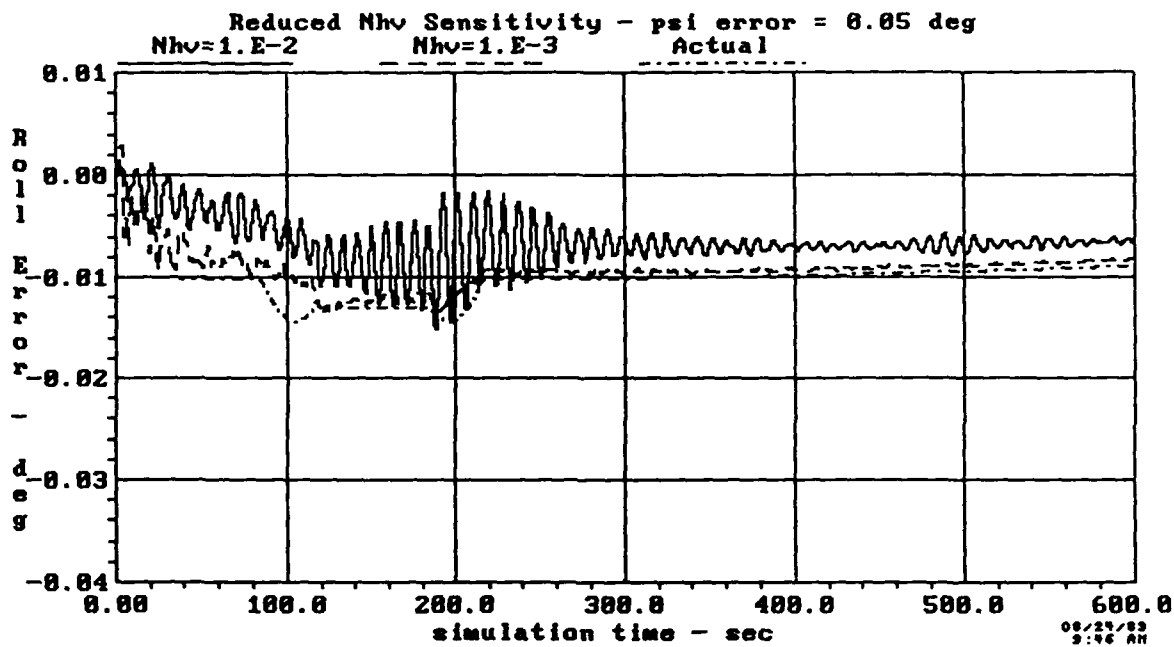Figure 24:   East Velocity Error with Reduced Nhv-Psi-0.5 deg.

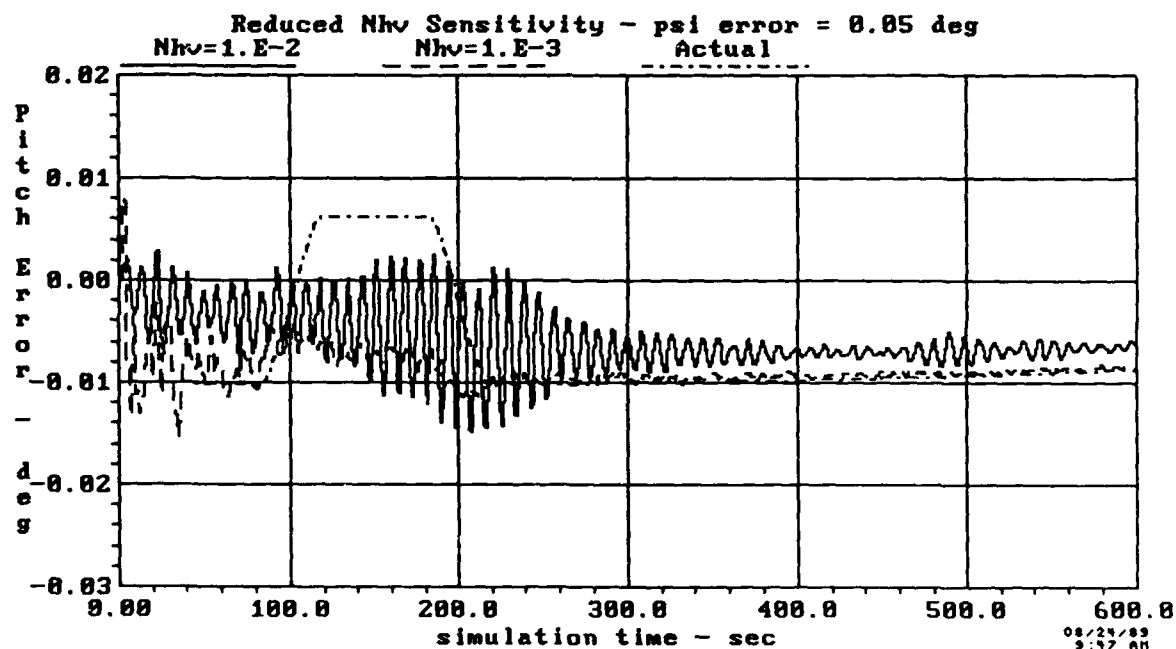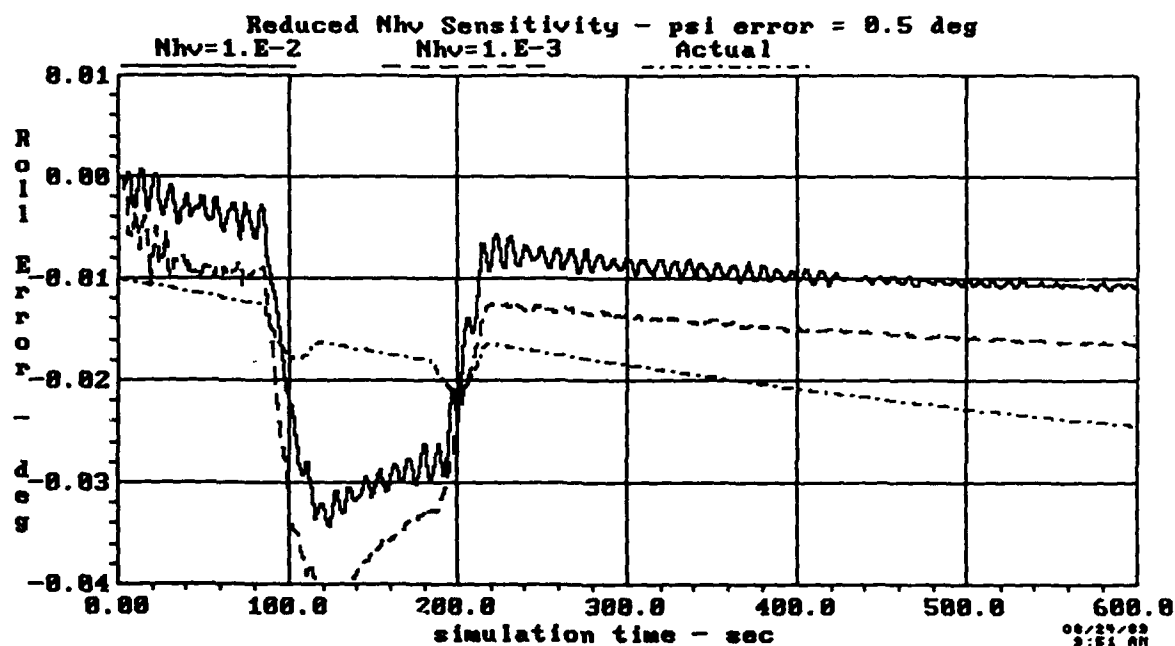Figure 25: Roll Error Estimates with Reduced Nhv-Psi=0.5 deg.
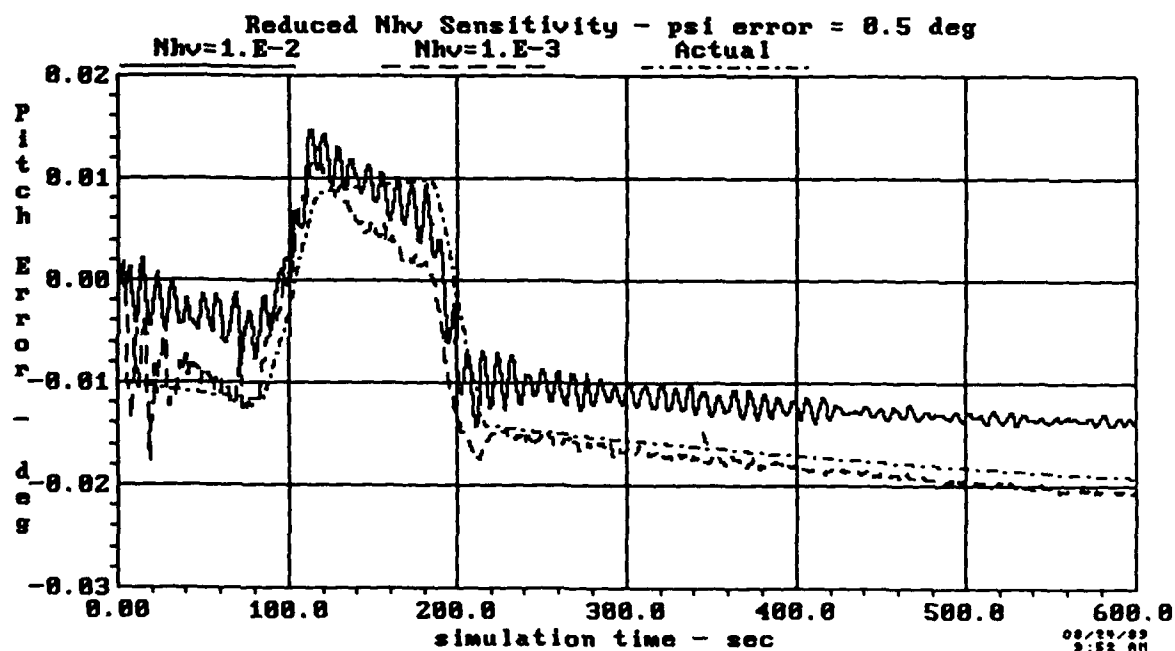
Figure 26: Pitch Error Estimates with Reduced Nhv-Psi=0.5 deg.
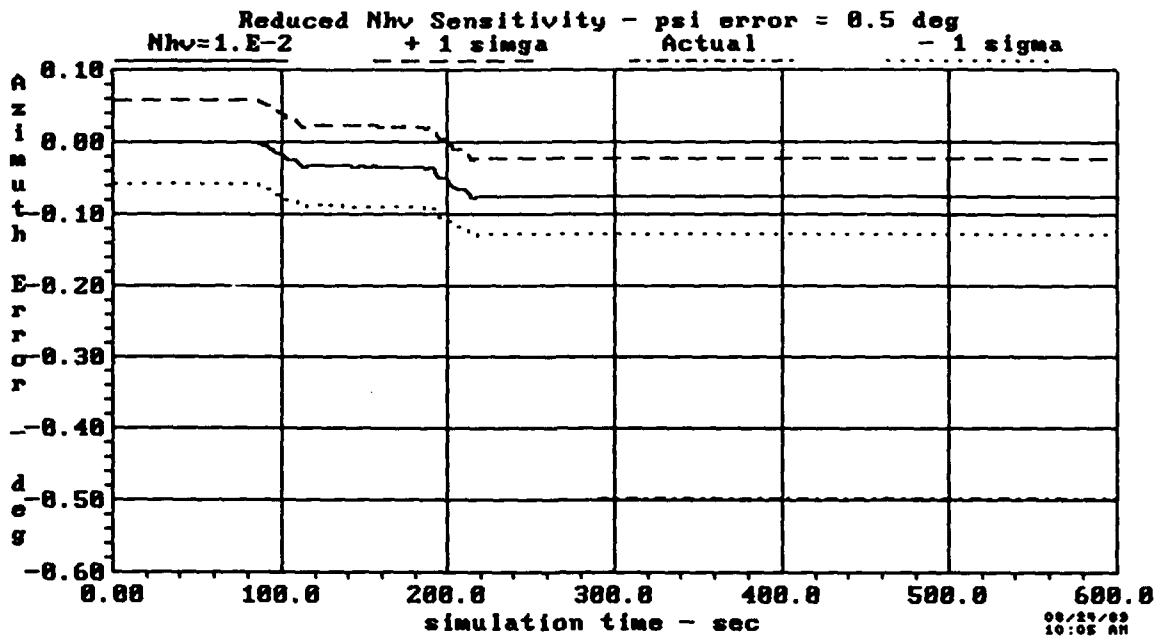
Figure 27a: Azimuth Error Estimates with Reduced Nhv-Psi=0.5 deg.
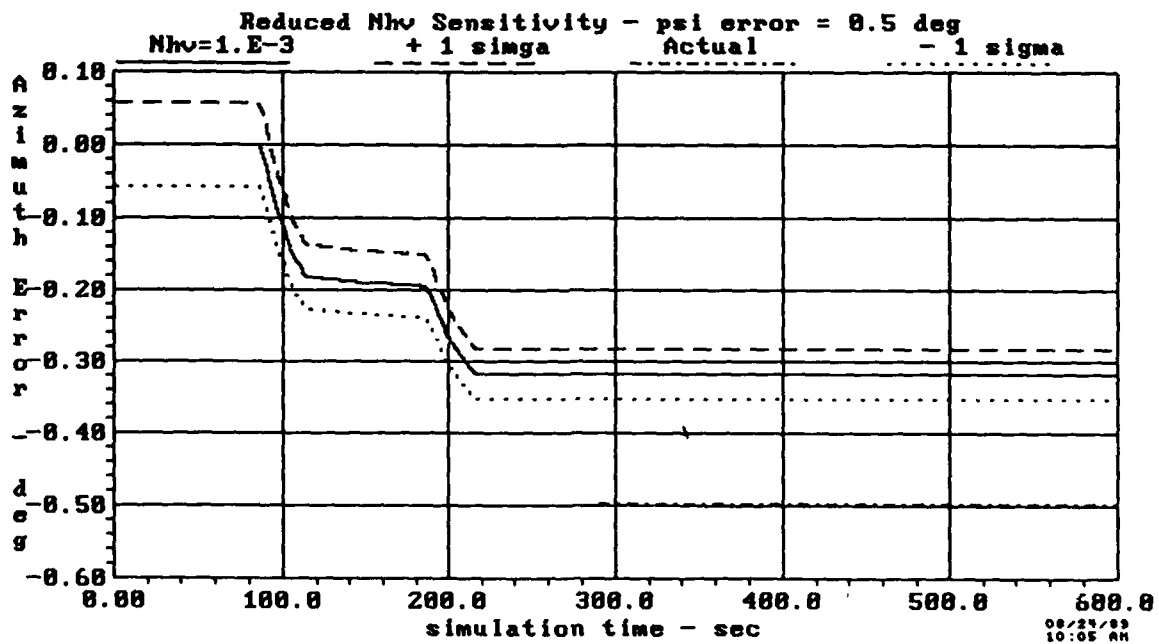
Figure 27b: Azimuth Error Estimates with Reduced Nhv-Psi=0.5 deg.

THIS PAGE LEFT INTENTIONALLY BLANK

THIS PAGE LEFT INTENTIONALLY BLANK

GPS AS A TSPI SOURCE FOR
NAVIGATION SYSTEM TEST AND EVALUATION

By
CARL E. HOEFENER
Director of Business Development, Range Systems

and

ROBERT VAN WECHEL
Senior Chief Scientist

Prepared for Presentation at

FOURTEENTH BIENNIAL GUIDANCE TEST SYMPOSIUM

October 3-5, 1989
Central Inertial Guidance Test Facility
Holloman Air Force Base, New Mexico

GPS AS A TSPI SOURCE
FOR NAVIGATION SYSTEM TEST EVALUATION

Carl Hoefener and Robert Van Wechel
Interstate Electronics Corporation
Anaheim, California

Abstract

Although GPS was developed as a precision radionavigation system, it has been successfully applied as a precise source for time and space-position information (TSPI) in the evaluation of test vehicles. Even though the advertised standalone accuracy of GPS is not sufficient for sophisticated guidance system evaluation, the accuracy obtained from differential GPS applied in post flight analysis falls well within that required. A thorough review of accuracy obtainable from GPS was performed in a paper entitled "Accuracy Considerations for GPS TSPI System Design" presented at The Institute of Navigation, Satellite Division, International Technical Meeting in Colorado Springs in September 1988. This paper indicated that a one sigma position accuracy of 1.36 meters could be obtained from a differential P-code instrumentation system with atmospheric corrections utilizing post-flight analysis with a PDOP of 2. A differential GPS P-code instrumentation system of this type has been developed for the Range Applications Joint Program Office at Eglin Air Force base and will be undergoing tests in 1989. The hardware required to provide this type of instrumentation consists of an instrumentation P-code receiver coupled to an inertial reference unit, together with a datalink to receive the differential corrections from a GPS reference station located at a surveyed ground site. This paper provides a complete description of the hardware required and an analysis of potential error sources.

Precise position must be known in order to perform guidance system evaluation. Rather than just knowing precise position at the start and completion of a test exercise, it would be ideal to have a precise position reference throughout the test, even under conditions of high dynamics. The Global Positioning System (GPS) should be considered for this reference source.

GPS was designed as a precision navigation system itself, but it has been adapted as a precision source for time and space-position information (TSPI) on test and training ranges.

In fact, because of the delay in the launching of the GPS satellites, GPS is not yet used as an operational navigation system. On the other hand, on test ranges where flight tests can be timed to optimize existing satellite coverage, or pseudosatellites can be used, GPS is currently applied as a precision source of TSPI.

There has been much discussion as to what position accuracies can be realized with GPS. This is because there are so many ways in which GPS can be implemented that there are a myriad of figures quoted for GPS accuracy. A brief review of GPS error sources is in order. For a

user of the system to obtain precise position, one's precise position must be measured from at least three satellites. The technique used to measure this distance is to locally generate the identical satellite code (for the satellite being observed) within the receiver and then shift it in time until correlation is obtained with the satellite signal. This measurement is called pseudorange because one's own precise time is unknown. Therefore, pseudorange measurements from four satellites must be taken to solve for four unknowns in the navigation equations; these are X, Y, and H defining one's position plus T, the precise time. The error in one's position then depends upon how well the position of the satellite is known, the geometry of the satellites (as in any trilateration system), and how accurately pseudorange can be measured and a position solution made.

There are really four major sources which affect the accuracy of a GPS TSPI system. These are the satellite's clock and ephemeris errors, signal transmission time errors from the satellite to the user equipment, the user receiver measurement errors, and errors caused by the dynamics of the vehicle being tracked. As mentioned previously, the geometry of the satellites used for making the position solution will also have a dominating effect on system accuracy. There are techniques available for minimizing the effects of all of these potential error sources. These techniques are particularly applicable when operating within a designated area such as a test and evaluation range. The potential error source and methods available to minimize the error source are presented below.

1. Space and Control Segment (Satellite) Errors

The major error contributed by the space and control segment is attributable to satellite clock noise. Where post–flight data analysis can be used, as in the case of navigation system evaluation, clock correction data, such as obtainable from the U.S. Naval Observatory, can be applied to remove a significant portion of the space and control segment error. Other techniques are also available for minimizing the effect of space and control segment errors.

The most common technique takes advantage of the fact that these errors appear nearly the same at all user sites, especially the closer together they are. Therefore, by the use of differential or relative GPS where these bias error sources appear as common mode at both receivers, they essentially cancel out. Differential GPS (see figure 1) also tends to minimize the effects of signal transmission time errors.
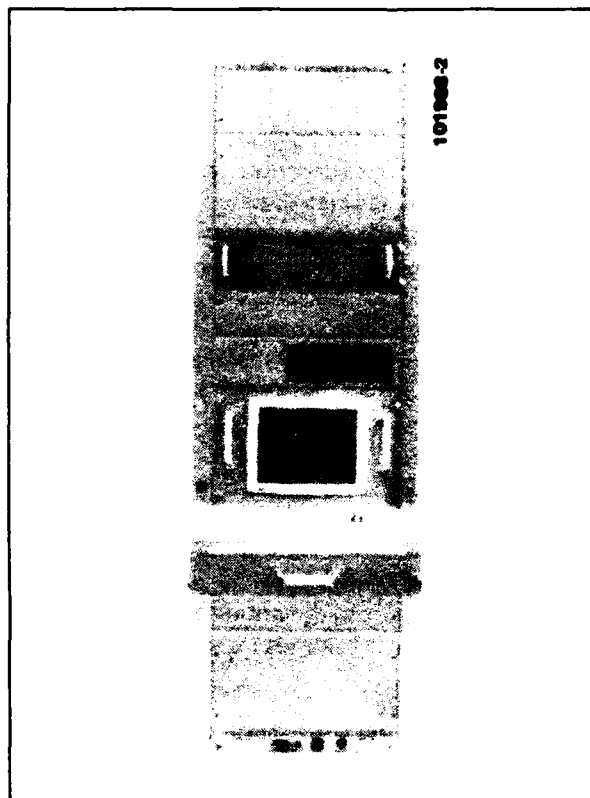
Figure 1. GPS Differential Ground System with Datalink Tropospheric Correction

2. Transmission Time Errors

As mentioned above, one of the major methods of minimizing transmission time errors is to utilize differential GPS. This, of course, is practical on test and evaluation ranges where the receiver on the test vehicle and the reference receiver are no more than a few hundred miles apart. There are other techniques also used for minimizing the effects of signal transmission time uncertainty. These range from simple elevation angle measurements of the satellite, to

tropospheric error corrections (figure 1) (made by taking water vapor and temperature measurements), to the utilization of two transmission frequencies (L1 and L2) from the satellites to measure the transmission time, to the utilization of ionospheric models. All of these techniques help in the reduction of uncertainty of signal transmission time caused by propagation characteristics of the troposphere and ionosphere.

3. Receiver Measurement Errors

The receiver measurement errors are primarily random errors and tend to be much smaller than the bias errors discussed previously. Also, since they are random, they can be reduced by lowpass filtering. A variety of GPS receivers can be selected for instrumentation purposes. These can be either C/A-code or P-code and single channel or multichannel. For instrumentation purposes P-code is generally selected because both the L1 and L2 signals are received from the satellites, enabling ionospheric correction, and the chip rate is higher than transmitted on C/A-code. The number of channels to be selected depends largely upon the dynamics of the vehicle aboard which the measurements are being made.

4. Errors Caused by Vehicle Dynamics

The difference between a single channel GPS receiver and a multichannel receiver is that in a single channel multiplexed receiver, only a single processor is used, and it measures pseudorange from one satellite at a time sequentially. In a multichannel receiver, at least four tracking processors are used to measure pseudorange from four satellites simultaneously. The tracking loop bandwidths of both types of receivers must be adjusted to a bandwidth such that they can track the dynamics of the satellite signals without dropping lock. For low dynamic applications, narrow loop bandwidths can be used so that more signal-to-noise margin is available. This extra margin can be traded off to obtain a lower cost receiver by multiplexing.

However, in the process of multiplexing, a multiplexing duty cycle power loss is incurred, which can be offset against the improved signal-to-noise margin obtained from the narrower loop bandwidths due to the lower dynamics. Because of this, a single-channel multiplexed receiver is generally limited to about one G dynamics, and a four channel or five parallel channel GPS receiver (see figure 2) will operate to higher dynamics, in the four to ten G range. In order to operate in the 10 G level, an inertial reference unit (IRU) is used. This allows narrowing the loop bandwidths again, since the tracking loops can then be aided by the IRU. When the vehicle dynamics exceed ten Gs in acceleration and ten Gs per second in jerk, more exotic techniques are necessary to maintain satellite signal lock. Fast Fourier tracking processors can be used in place of conventional tracking loops, allowing track to be maintained under conditions of extreme vehicle dynamics.

Figure 2. 5 Channel P-Code GPS Receiver

The overriding ultimate determination of GPS position accuracy is geometric dilution of precision (GDOP), or the geometry of the GPS satellites being used. For optimum position determination, three satellites are selected just above the horizon, spaced 120 degrees apart in azimuth. A fourth satellite is chosen directly overhead, and pseudo-range measurements would be made from these satellites. The worst choice would be to select four satellites in a cluster. Even with optimum satellite selection, accuracy in H measurement tends to be less than in X and Y. Receivers are preprogrammed to select those satellites in the best locations providing the least GDOP. Two techniques are available to optimize

GDOP: the test operation may be scheduled for a time when the existing GPS satellites are in a desirable position, or pseudo-satellites can be installed to augment the satellite coverage before the full constellation is in place. Even then, on test ranges, a pseudosatellite may be used under the operation in order to improve the H measurement.

Now that the various GPS error sources have been discussed, and techniques for minimizing these error sources have been presented, what then are the typical accuracies which could be expected with various types of GPS systems? Table I displays typical position accuracies which might be expected with various types of GPS system implementation. You will notice that the random portion of the user equivalent range error (UERE) ranges from plus or minus 4.44 meters to 2.04 meters depending upon the GPS

system implementation. Filtering will reduce the random portion of this error by a factor of three. Therefore, when using differential GPS and the bias errors have been eliminated, the resulting UERE errors will be one third of that shown. As these errors will be multiplied by the experienced GDOP, the expected position error of a differential P-Code receiver with atmospheric and post flight time and ephemeris corrections will be in the neighborhood of plus or minus 1.36 meters for a position dilution of precision (PDOP) of 2. This low magnitude of PDOP can be obtained by augmenting the planned satellite constellation with one or two pseudosatellites, or by selecting the operation time to optimize the GDOP obtained from the existing satellite constellation.

The PDOP obtained will vary with the number of satellites in orbit, as well as the time of day. When the full constellation is in place in late

TABLE 1. TYPICAL ACCURACIES EXPECTED WITH VARIOUS TYPES OF GPS SYSTEMS (IN METERS)

Error Source	Standalone C/A Receiver Iono Model		Standalone P Receiver L1/L2		Differential C/A Receiver		Differential P Receiver		Differential P Receiver Atmos Meas Post Mission	
	Bias	Random	Bias	Random	Bias	Random	Bias	Random	Bias	Random
Satellite Ephemeris	2.1	0	2.1	0	0	0	0	0	0	0
Satellite Clock	3.0	2.7	3.0	2.7	0	2.7	0	2.7	0	1.3
Ionospheric Delay	6.0	0	0	1.5	0	0	0	0	0	0
Tropospheric Delay	1.4	1.4	1.4	1.4	0	1.4	0	1.4	0	0.2
Receiver Noise	0	3.0	0	1.0	0	3.0	0	1.0	0	1.0
Multipath	0	1.2	0	1.2	0	1.2	0	1.2	0	1.2
RSS UERE (1–Sigma)	7.17	4.44	3.92	3.73	.00	4.44	.00	3.42	.00	2.04
Pos Error – PDOP = 2.0 (1–Sigma Meters)	14.34	8.88	7.84	7.46	.00	8.88	.00	6.84	.00	4.08
Filtered Pos Error (1–Sigma, PDOP = 2)	14.64		8.22			2.96		2.28		1.36
Pos Error – PDOP = 6.0 (1–Sigma Meters)	43.02	26.64	23.52	22.38	.00	26.64	.00	20.52	.00	12.24
Filtered Pos Error (1–Sigma, PDOP = 6)	43.93		24.67			8.88		6.84		4.08

1991, typical PDOP will be from 2 to 4. At this time, however, it is sometimes higher because satellites are not in their optimum positions.

The U.S. Air Force has developed a family of GPS TSPI systems for use on test and training ranges. These systems have been developed by Interstate Electronics Corporation under contract to the U.S. Air Force AD/YI at Eglin Air Force Base. This development has yielded the GPS instrumentation hardware necessary to implement TSPI systems which can be applied to guidance system test and evaluation.

There are many ways in which such a system could be implemented, depending upon the type of vehicle and navigation system under test. Examples of various GPS TSPI system implementations are given below.

1. Dedicated Test Aircraft

In this case, the test system could be flown inside the test aircraft. The GPS instrumentation system would consist of a multichannel P-code GPS receiver, an inertial reference unit, a solid state recorder, and necessary power supplies. The GPS L-band antenna would be mounted on the exterior of the aircraft. It is assumed that post flight analysis of the guidance system would be sufficient. If realtime TSPI were needed aboard the aircraft or at a ground station, a datalink could be added to the system. With the use of a datalink, the differential corrections could either be made in the aircraft or on the ground. Utilizing a real time GPS solution does not take advantage of post flight analysis, however.

Whether an on-board recorder or datalink is utilized, a ground station will be required. This ground station will contain a GPS reference receiver, playback capability for the solid state recorder, recording capability to record the reference receiver output, tropospheric measurement capability, a datalink if desired, and computational capability to perform the differential corrections, tropospheric corrections, and post flight ephemeris and clock corrections.

2. Using an Aircraft of Opportunity

If a dedicated test aircraft were not available, the GPS instrumentation could be placed in an AIM-9 POD (see figure 3) and attached to the aircraft wing station. This POD would contain the same equipment as that internally mounted in the dedicated test aircraft described above. The same ground station would also be utilized.

3. Missile Guidance System Testing

When testing missile guidance systems, there is generally very little space available for test instrumentation on the missile. For this reason, a GPS frequency translator (see figure 4) is recommended. The translator receives the L band signals from all of the satellites in view and retransmits them at S band to a ground station (see figure 5) for TSPI solution. This ground station would contain a translator processing system in addition to the ground station equipment described above. As a GPS frequency translator, TSPI system utilizes C/A-code instead of P-code, the post flight differential accuracy realized is slightly less than that obtained with P-code.

Nose Cone with
GPS and Data Link
Antenna Subassys

Pod to Launch Rail
Umbilical/EMI Filter

Pod Structure/
Tube Assy

Pod
Hangars

103086-11

Nose
Cone
Interconnection

Space for Air Data Sensing Subsystem

Data Link
Transceiver

Inertial
Reference
Unit

GPS
Receiver
and Solid-
State
Recorder

GPS
Power
Supply

Encryption
Unit

GPS
Battery
Power Assy

111987-44
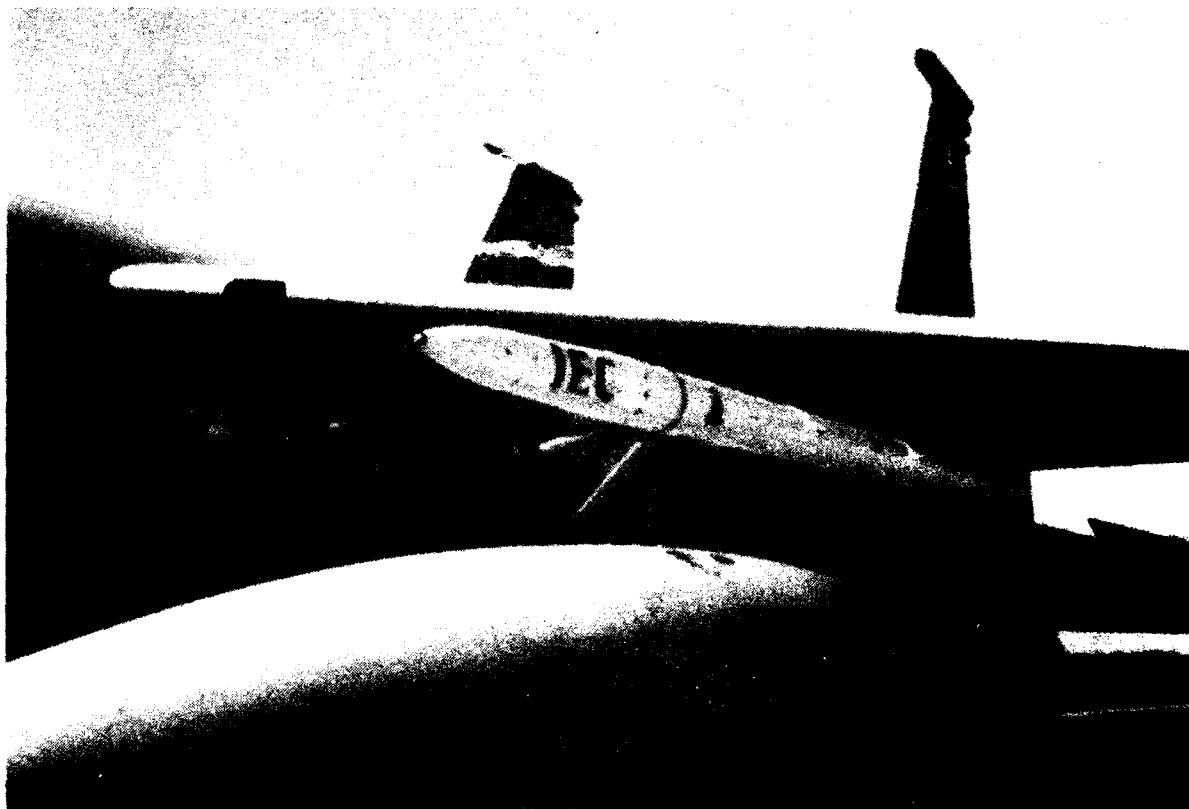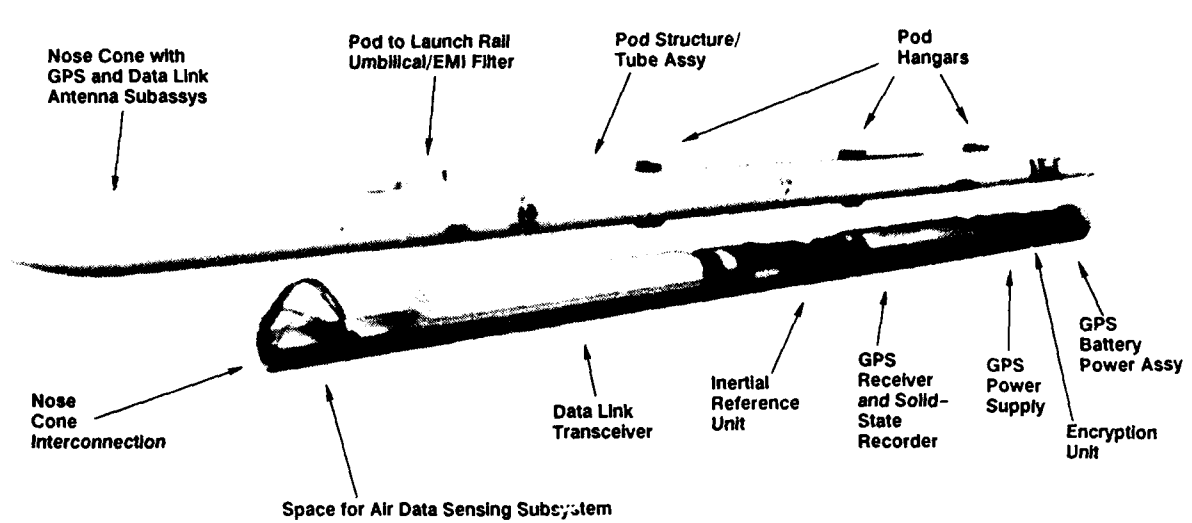
Figure 3. AIM-9 GPS Instrumentation POD
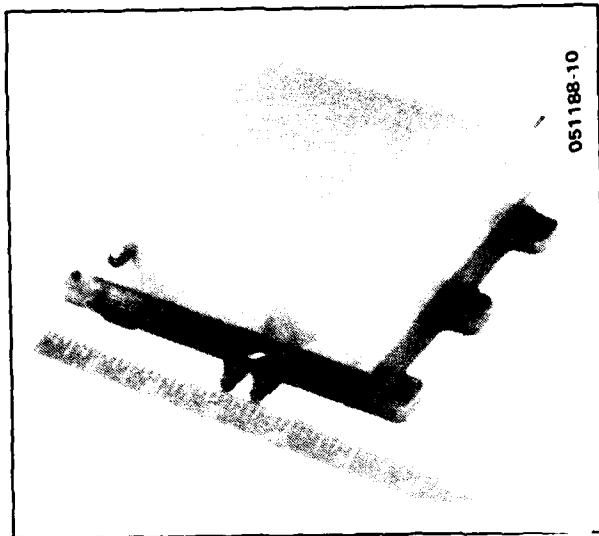
Figure 4. GPS Frequency Translator

The hardware required to provide these systems is becoming available at this time. It was developed by Interstate Electronics Corporation on contract to the U.S. Air Force Range Applications Joint Program Office at Eglin Air Force Base. The following figures show the equipment described above.
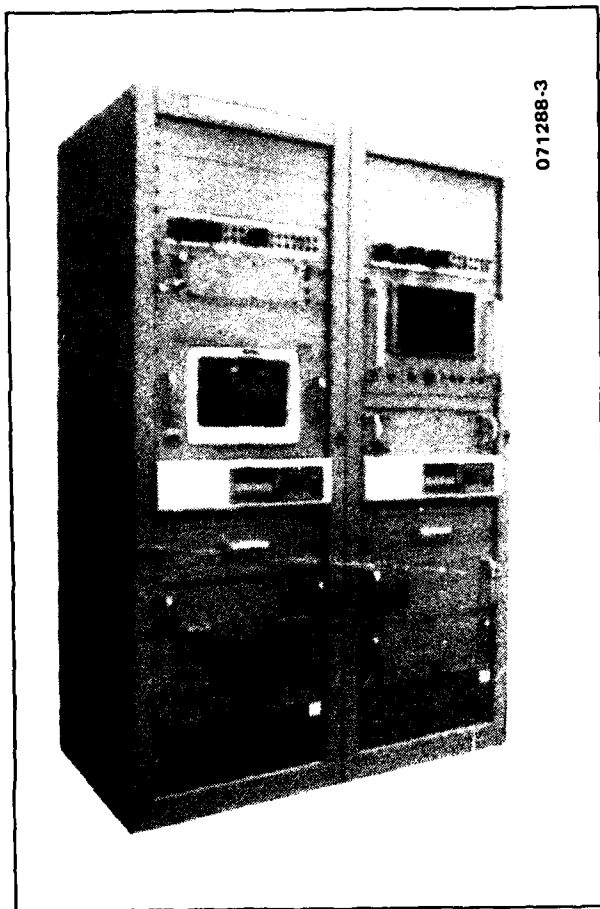
Figure 5. GPS Translator Processing System

GPS and Transponder Aided

Completely Integrated Reference Instrumentation System

(CIRIS II)

Joseph K. Solomon

and

Zdzislaw H. Lewantowicz

Air Force Institute of Technology
Department of Electrical and Computer Engineering
Wright-Patterson AFB, OH 45433-6583

1. ABSTRACT

The Completely Integrated Reference Instrumentation System (CIRIS) is an airborne inertial navigation system (INS) aided with range and range-rate measurements from precisely surveyed ground transponders. The CIRIS system with Litton LN-39 Standard INS is called CIRIS II. The goal of this research is to substantially improve performance by optimally integrating CIRIS II with the Global Positioning System (GPS). The first two steps toward this larger goal are the development and validation of adequately correct dynamic and stochastic error models of the INS, transponder, and GPS measurements. The INS, transponder, and GPS error models are analytically integrated in a full-ordered Kalman filter "truth" model to define the baseline performance of this system. This truth model baseline serves as the foundation for the development of a CIRIS system aided with Global Positioning System (GPS) measurements.

This paper describes the development of the 85 state INS, 42 state transponder, and 30 state GPS error models. The validation of these "truth" error models is an ongoing process using analytic and empirical methods. Next, the INS and transponder error models are analytically integrated in a Kalman filter and a baseline full "truth" model performance is established. The transponder errors include the atmospheric propagation errors and the transponder survey errors. This full 127 state Kalman filter is used to process the empirical data recorded during a CIRIS flight. The performance of the filter is quantified by analyzing the characteristics of the transponder line-of-sight range and range-rate residuals and by comparing the estimated position and velocity error estimates to the current CIRIS filter estimates.

Next a 70 state reduced order filter is derived from the full ordered INS/transponder model. This state reduction process is described and the reduced order filter model defined. The reduced order filter is designed to decrease the required computation time for the processing of a 4 hour CIRIS flight without a significant loss in error estimation performance.

Finally the correlated GPS range measurement error model, consisting of 28 states is added to the INS/transponder 70 state filter. The defined 98-state filter accommodates four satellite error models. The GPS measurement errors modeled are the receiver clock bias and drift errors and the satellite correlated clock bias and drift; each satellite trajectory errors; code loop tracking errors; and atmospheric (tropospheric and ionospheric) errors. This 98-state filter is used in a covariance analysis of the position and velocity estimation errors for a representative CIRIS flight trajectory using four static satellites. To quantify the increase in performance, the covariance estimates for the position and velocity error states are compared to the current CIRIS filter estimates.

2. INTRODUCTION

The Office of Primary Responsibility (OPR) for the CIRIS system is the Central Inertial Guidance Test Facility (CIGTF), 6585th Test Group, Air Force Systems Command (AFSC), Holloman AFB, NM. The navigation system to be tested, the test article, and the CIRIS system are flown aboard a host vehicle over an aircraft trajectory of interest through the CIRIS transponder range. The data from both systems is recorded during flight. The CIRIS system is much more accurate than the tactical navigation systems currently being tested, thus the CIRIS generated trajectory is used as a reference.

The current CIRIS system (using an LN-15 INS) provides aircraft latitude and longitude with an accuracy of 13 feet (ft) 1σ; altitude with an accuracy of 40 ft 1σ; north and west velocity with an accuracy 0.1 ft/sec (fps) 1σ; and vertical velocity with an accuracy of 0.4 fps 1σ. The 1σ value indicates a 68.3% probability that the position/velocity true error lies in the interval between $[m - \sigma, m + \sigma]$, where m is the mean. The high accuracy of the CIRIS system is due to high accuracy of the transponder measurement aiding.

Ground based transponders are installed over a test range covering the length and width of the continental United States. The transponder locations are surveyed precisely; CIGTF estimates the accuracy of these surveys at approximately 3-6 ft 1σ. During a test CIRIS system receives accurate range and range-rate measurements to each of the transponders within receiving parameters which are combined with the INS data in an extended Kalman filter to produce an accurate estimate of the INS errors. The INS data is corrected to produce a highly accurate estimate of the aircraft position and velocity. Currently this data is much more accurate than the standard aircraft navigation systems (15).

To further increase the accuracy of the CIRIS system, increase its coverage to global capability, and improve the vertical channel position and velocity it has been proposed that Global Positioning System (GPS) pseudorange and delta-range measurements be added to augment the transponder measurements. This concept is shown in Figure 1. The positions of the satellites are known precisely and accurate pseudorange and delta-range measurements from available GPS satellites can be provided to the CIRIS system. In effect, the GPS constellation simply becomes an additional transponder set.
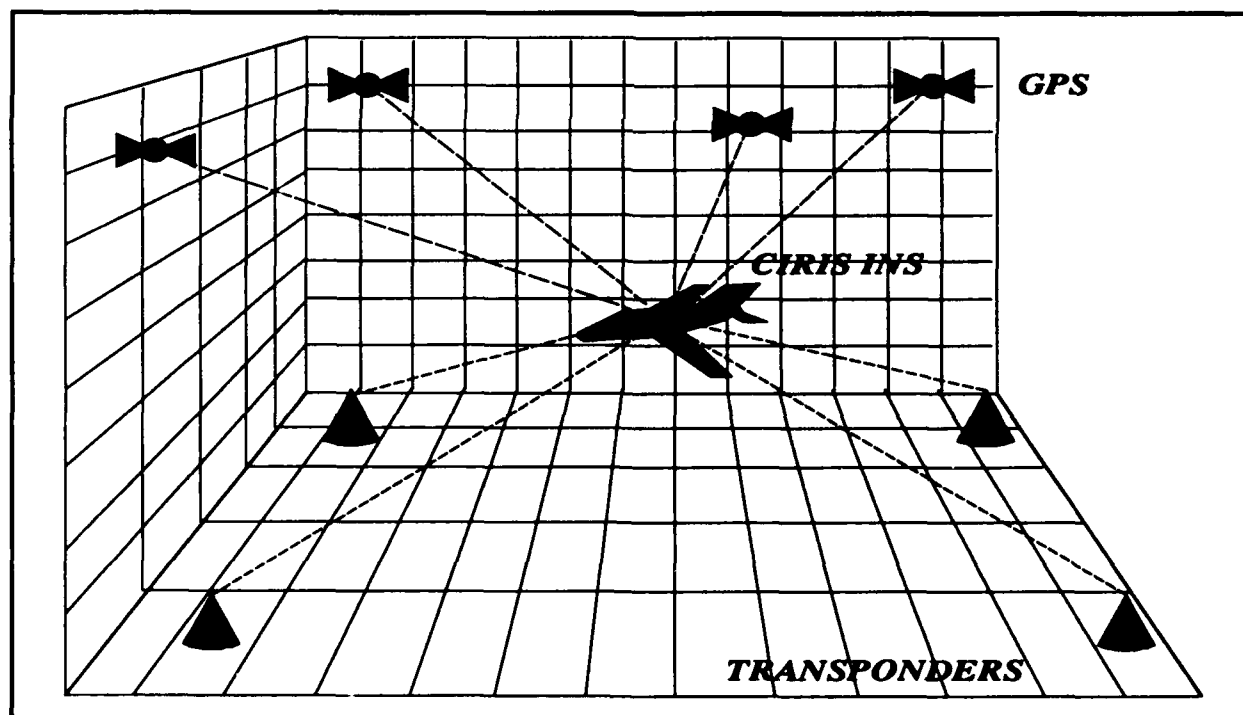
Figure 1. Physical Concept of GPS Aided CIRIS

The GPS range (R_{SAT}), GPS range-rate (V_{SAT}), transponder range (R_{TRANS}), transponder range-rate (V_{TRANS}), and baro-altimeter (H_B) measurements are optimally combined with INS position (P), velocity (V), and acceleration (A) data, through the use of an extended Kalman filter.

An important point of emphasis the this is a **jointly solved, single Kalman filter**, to estimate the error in the CIRIS INS and transponder measurement errors. This filter concept is shown in Figure 2. The CIRIS INS data is corrected, resulting in an accurate estimate of aircraft position and velocity. This estimate is expected to be more accurate than that of the current CIRIS system (15).
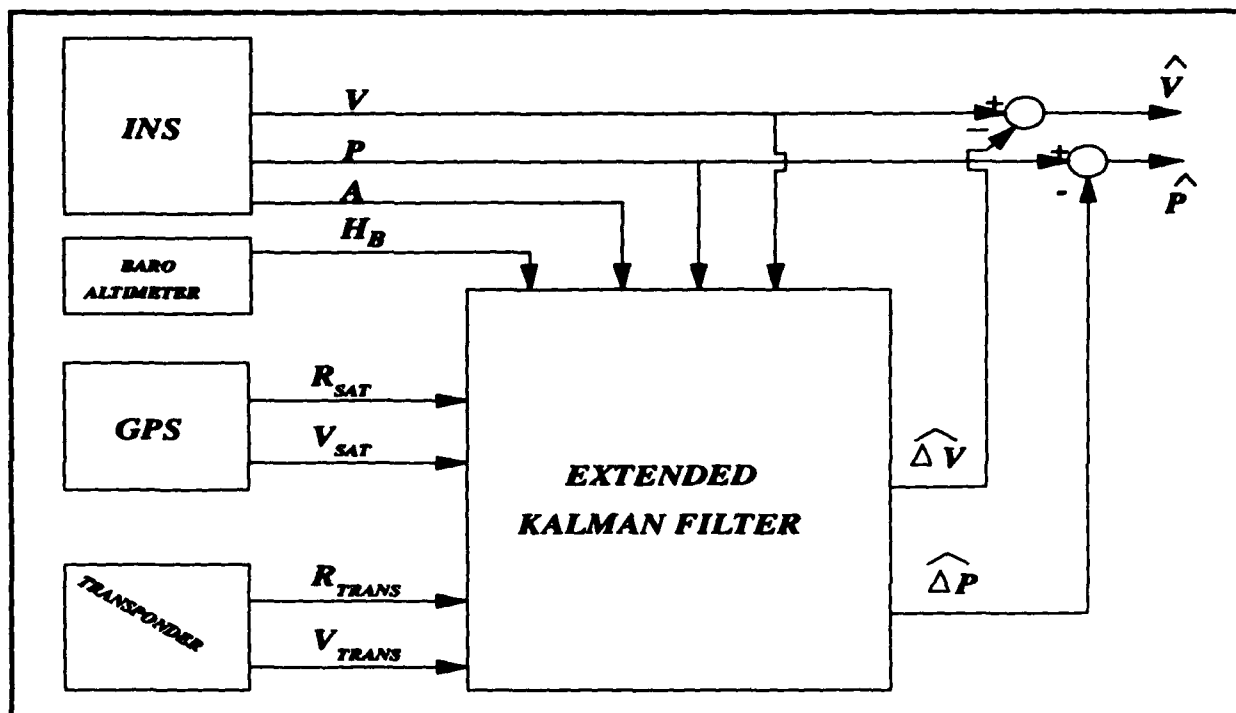
Figure 2. Advanced CIRIS Indirect Kalman Filter

3. BACKGROUND

The original CIRIS system is based on a reduced-order Kalman filter consisting of 14 states. This filter is based on the 9 primary error states of the Litton LN-15 INS, two vertical channel aiding states, and 3 error states reserved for estimating errors in Doppler velocity aiding measurements. The Kalman filter is structured for maximum 14 states, however the Doppler velocity error states currently are not used, thus it is an 11-state filter. This system is designated CIRIS I by CIGTF (19). In another CIRIS version the Litton LN-15 INS has been replaced by the Litton LN-39 INS. The main reason for this change was to increase the overall reliability of the CIRIS system. This system is designated CIRIS II by CIGTF, and the current CIRIS system data referred throughout this thesis is from the CIRIS II system (19).

Due to the low number of states, limitations exist in the Kalman filter model used by CIRIS I. A higher ordered Kalman filter model, including the correlated transponder measurement errors, is required to increase the CIRIS filter's accuracy. Current computational capabilities allow higher ordered filters to be implemented, if not as a real-time filters then as post-processors. A new Kalman filter design based on the CIRIS II with GPS range and range-rate aiding measurements, promises to achieve a maximum increase in the accuracy and stability of the CIRIS velocity and position.

The majority of current research in this area has been directed towards the integration of GPS measurements with INS systems. Among the papers published on this topic the paper by D. B. Cox (6:144-153) is most representative. This paper explores advantages of GPS integration with INS and is the basis for integrating CIRIS with GPS and transponders. Other studies designed GPS/INS integrated systems, such as the 15-state Kalman filter by R. Butler and G. Rhue (4).

The idea of aiding an INS with GPS and transponders is unique to CIRIS and there are no known current papers published in this area. C. Smith designed a 13-state Kalman filter for the INS/GPS data integration in 1985 (20). Although his filter performed well, Smith did not include a sufficiently accurate model of all the dominant errors in the GPS measurements. The advanced CIRIS Kalman filter initially is based on the complete error model of the Litton LN-39 standard INS and a Kalman filter of approximately 100 states. Emphasis is placed on detailed system error models of the INS, transponder measurement system, and the GPS, with the expected increase in accuracy and stability over the current CIRIS.

3.1 Research Objectives

The step in designing a reduced-order Kalman filter is the development of a full-ordered "truth" model. This "truth" model must realistically model all major error sources in the real world. This research effort concentrates on the development and verification of the "truth" model for the CIRIS II system (INS/Transponder/GPS). This goal is defined by the following objectives:

1. Establish the LN-39 INS, transponder, and GPS "truth" models.

2. Predict the baseline performance for a particular flight using the full-ordered Kalman filter, based on the CIRIS II (without GPS) "truth" model.

3. Process the data from this CIRIS test flight with the full-ordered Kalman filter based on the "truth" model (no GPS). Compare with the analytic prediction and with CIRIS I results. Primary objective is the LN-39 and transponder error model validation using the Kalman filter residual analysis.

4. Design a reduced-order filter (70 states) to reduce filter computation time while maintaining the accuracy nearly that of the "truth" model.

5. Design a CIRIS II Kalman filter including the transponder and GPS measurements. Using covariance analysis predict the overall system performance.

Initial research on the INS/GPS/Transponder integrated model is presented in Reference (21).

3.2 Research Approach

The Multimode Simulation for Optimal Filter Evaluation (MSOFE) software package is used (5). The MSOFE has been developed by Wright Aeronautical Development Center (WRDC), Avionics Laboratory. It is a powerful and flexible analysis tool capable of covariance, Monte-Carlo, and time simulations. The 85-state LN-39 "truth" model is defined in a Litton engineering analysis report (23). This report also defines the INS error growth statistics using a 10-run Monte-Carlo analysis for several different flight trajectories. The 10-hour static and 2-hour fighter flight profiles are chosen for the INS "truth" model verification. The flight profile is generated using the Profile Generator (PROFGEN) simulation package, a companion of MSOFE. Using the flight data from PROFGEN and MSOFE, the covariance of the INS "truth" model's stochastic differential equation is propagated over the 2-hour flight profile. The 1σ error growth plots for position, velocity, and tilts are compared with the applicable Monte-Carlo 1σ plots in the Litton engineering report (23).

Next the transponder measurement "truth" model is developed. The correlated errors in the range measurement are modeled as a random bias for the receiver/transmitter calibration error, random biases for the transponder Defense Mapping Agency (DMA) survey data errors, and a first order Markov atmospheric propagation delay error. One random bias state is required for the aircraft transponder receiver/transmitter bias, 3 states for each transponder's 3-dimensional survey error, and 1 state for each transponder's line-of-sight atmospheric error.

The CIRIS system works with a window of 5-10 transponders which it samples at a 1 Hertz (Hz) rate. Therefore, 10 sets of transponder bias/atmospheric states are used. This results in 41 additional states. The correlated error in the range-rate measurement is modeled with only a random bias error for the receiver/transmitter calibration error. This requires 1 additional state. The overall filter "truth" model consists of 127 states (85 INS and 42 transponder measurement).

Next the 127-state "truth" model is verified using actual CIRIS flight data. A direct comparison is made between the "truth" model and the current CIRIS position and velocity error state means. If the "truth" model filter is operating correctly, the "truth" model error state means fall within the 1σ bounds on the CIRIS error state means; since the current CIRIS system accuracies have been independently verified. A comparison is also made between selected transponder range and range-rate residuals. The error growth reflected in the transponder atmospheric and survey error state means and covariances is analyzed to determine if the states are fully observable and the error magnitudes warrant inclusion in the "truth" model.

The design of a reduced-order Kalman filter is based on this "truth" model. This reduced-order filter is not a candidate filter for real-time applications, but an intermediate step in the overall system error model development and validation! The "truth" model states with insignificant error contribution magnitudes are deleted until the computation time is reduced to an estimated 8-12 hours of CPU time, for a 4.5 hour CIRIS flight data record, on a VAX 8650 computer system. A final comparison is made between the reduced-order filter, "truth" model filter, and the current CIRIS filter. The final analysis of INS/transponder integration quantifies the differences between these models. The conclusions and recommendations are based on the results of this analysis.

The final goal of this effort is to develop a GPS system measurement error model, integrate it in the INS/transponder/GPS Kalman filter, and validate the entire analytic error model. This validated error model will become the basis for further CIRIS II development, analysis, and subsequent design of a Kalman filter for real-time applications.

4. INS/TRANSPONDER ERROR MODELLING AND ANALYSIS

4.1 Kalman Filter Equations

The Kalman filter is the navigation system analytic integration framework. The INS, transponder, and GPS error models are represented in terms of stochastic error differential equations. The specific models will be presented in subsequent sections. This section presents the Kalman filter equations with only a brief comment. The reader is referred to texts such as Maybeck (6) for further explanation and detail. The stochastic error differential equation is in the form:

$$\delta \underline{\dot{X}}(t) = F(t)\,\delta\underline{X}(t) + \underline{W}(t) \tag{1}$$

$$E\{\underline{W}(t)\} = \underline{0} \tag{2}$$

$$E\{\underline{W}(t)\underline{W}^T(t+\tau)\} = Q(t)\,\delta(\tau) \tag{3}$$

The vector $\delta\underline{X}(t)$ represents the navigation system stochastic error variables which are defined as the difference between the true and the indicated or measured states. The matrix $F(t)$ represents the time varying, linearized system error dynamics (1). The vector $\underline{W}$ is a gaussian, "white," zero-mean noise vector with strength $Q(t)$ (6:275). The linearized measurement error equation is in the form:

$$\delta Z_k(t_i) = H_k(t_i) \; \delta\underline{X}(t_i) + V_k(t_i) \tag{4}$$

$$E\{V_k(t_i)\} = 0 \tag{5}$$

$$E\{V_k(t_i) V_k(t_j)\} = \begin{cases} R_k(t_i) & t_i = t_j \\ 0 & t_i \neq t_j \end{cases} \tag{6}$$

The time-varying matrix $H(t)$ relates the measurement to the error states. V is a Gaussian, "white," zero-mean noise with strength R. In this application the measurement is represented by a scalar equation (6:275). For the filter presented $k=1,2$; where $k=1$ is the range aiding measurement and $k=2$ is the range-rate aiding measurement. The Kalman filter propagation equations, in continuous time form, are (6:275):

$$\delta\dot{\underline{X}}(t/t_{i-1}) = F(t) \; \delta\hat{\underline{X}}(t/t_{i-1}) \tag{7}$$

$$\dot{P}(t/t_{i-1}) = F(t) \; P(t/t_{i-1}) + P(t/t_{i-1}) \; F^T(t) + Q(t) \tag{8}$$

These are integrated from initial conditions $\delta\hat{\underline{X}}(t_{i-1}^+)$ and $\delta P(t_{i-1}^+)$, where t_{i-1}^+ is the last Kalman filter update time. The algorithm is started from an appropriate set of initial values. Finally, the standard form of the Kalman filter update equations is (6:275):

$$\underline{K}(t_i) = P(t_i^-) H^T(t_i) [H(t_i) P(t_i^-) H^T(t_i) + R(t_i)]^{-1} \tag{9}$$

$$\delta\hat{\underline{X}}(t_i^+) = \delta\hat{\underline{X}}(t_i^-) + \underline{K}(t_i) [\delta Z_k(t_i) - H(t_i) \delta\hat{\underline{X}}(t_i^-)] \tag{10}$$

$$P(t_i^-) = P(t_i^-) - \underline{K}(t_i) H(t_i) P(t_i^-) \tag{11}$$

The $[\delta Z_k(t_i) - H(t_i) \delta\hat{\underline{X}}(t_i^-)]$ in Eq (10) is commonly referred to as the residual.

4.2 Current CIRIS Kalman Filter

This section describes the major characteristics of the current CIRIS filter model. The current CIRIS system uses a 11 state EKF where the states represent 11 errors shown in the error state vector in Eq (12). The error states modeled in this filter represent a subset of the error states required to completely model the CIRIS INS linearized error dynamics and baro-altimeter aiding error states. Note that this subset of error states does not include any of the correlated errors in the INS (gyro drift, gyro bias, accelerometer bias, etc.) or the range measurement (transponder survey, atmospheric, etc.) (1).

$$\delta \underline{X} = \begin{bmatrix} \delta L \\ \delta \lambda \\ \delta H \\ \phi_N \\ \phi_E \\ \phi_Z \\ \delta V_N \\ \delta V_E \\ \delta V_Z \\ S_1 \\ S_2 \\ S_3 \\ S_4 \end{bmatrix} = \begin{bmatrix} \text{Latitude Error} \\ \text{Longitude Error} \\ \text{Altitude Error} \\ \text{North Tilt} \\ \text{East Tilt} \\ \text{Vertical Tilt} \\ \text{North Velocity Error} \\ \text{East Velocity Error} \\ \text{Vertical Velocity Error} \\ \text{Baro Aiding 1} \\ \text{Baro Aiding 2} \\ \text{Baro Aiding 3} \\ \text{Baro Aiding 4} \end{bmatrix} \tag{12}$$

The effect of this low order EKF limitation is illustrated by examining the transponder line-of-sight range residuals. The Kalman filter residuals are a direct indication of how well the selected Kalman filter model represents the physical reality. If the model perfectly matches all the spectral characteristics of the real world data, the residual data process will be a "white" Gaussian sequence of mean zero and covariance $H(t_i)P(t_i)H^T(t_i) + R(t_i)$ (6). Since it is a function of the filter's covariance, it is independent of the real world measurements and can be calculated "a priori" if the flight trajectory were known. The square root of each diagonal covariance matrix element is designated the 1σ value (6:226-231).
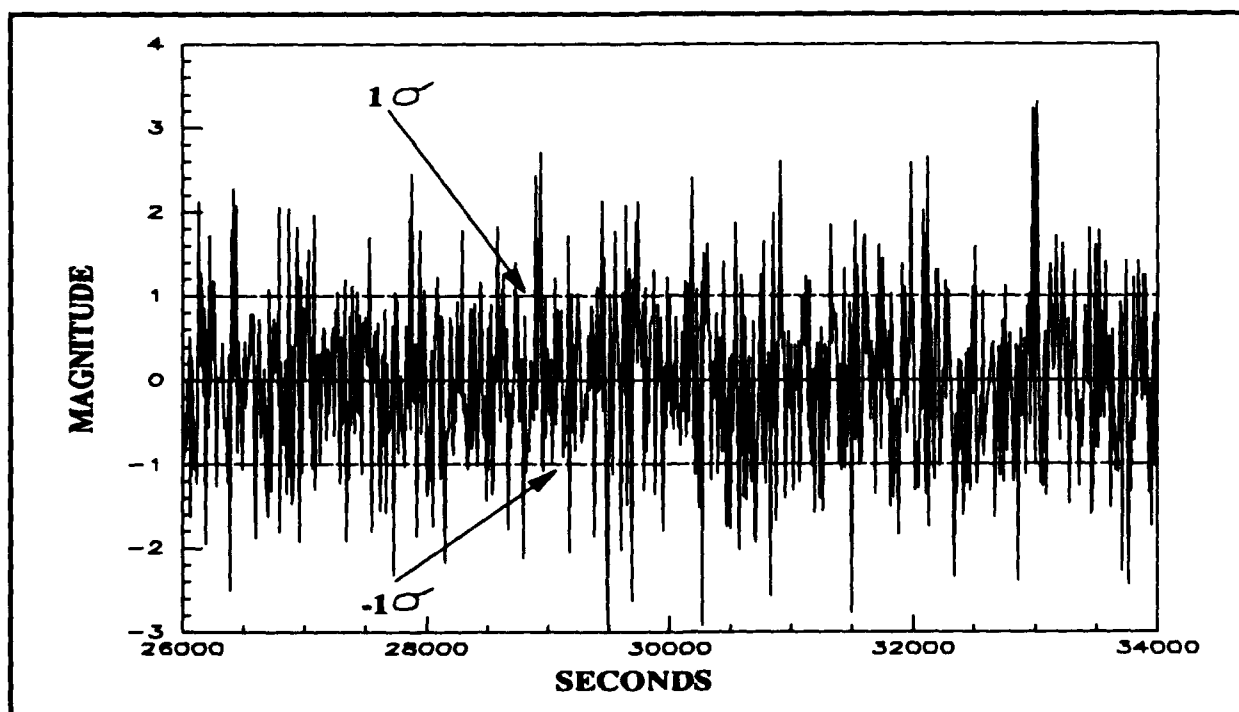
Figure 3. Gaussian "White" Noise

An example of a "white," zero mean Gaussian noise and unit strength is shown in Figure 3. In the physical world a "white" residual can not be attained. However, the closer the Kalman filter residuals approach this "white" process model, with the applicable 1σ magnitude, the better the Kalman filter performance, which in turn implies higher accuracy of the system error model.

The current CIRIS filter output for the aircraft trajectory used in this analysis, presented later in this paper, is available. One representative transponder range residual is presented. This transponder is also used in the analysis of the full-ordered filter performance. The range residual for the transponder designated T-185 is shown in Figure 4.
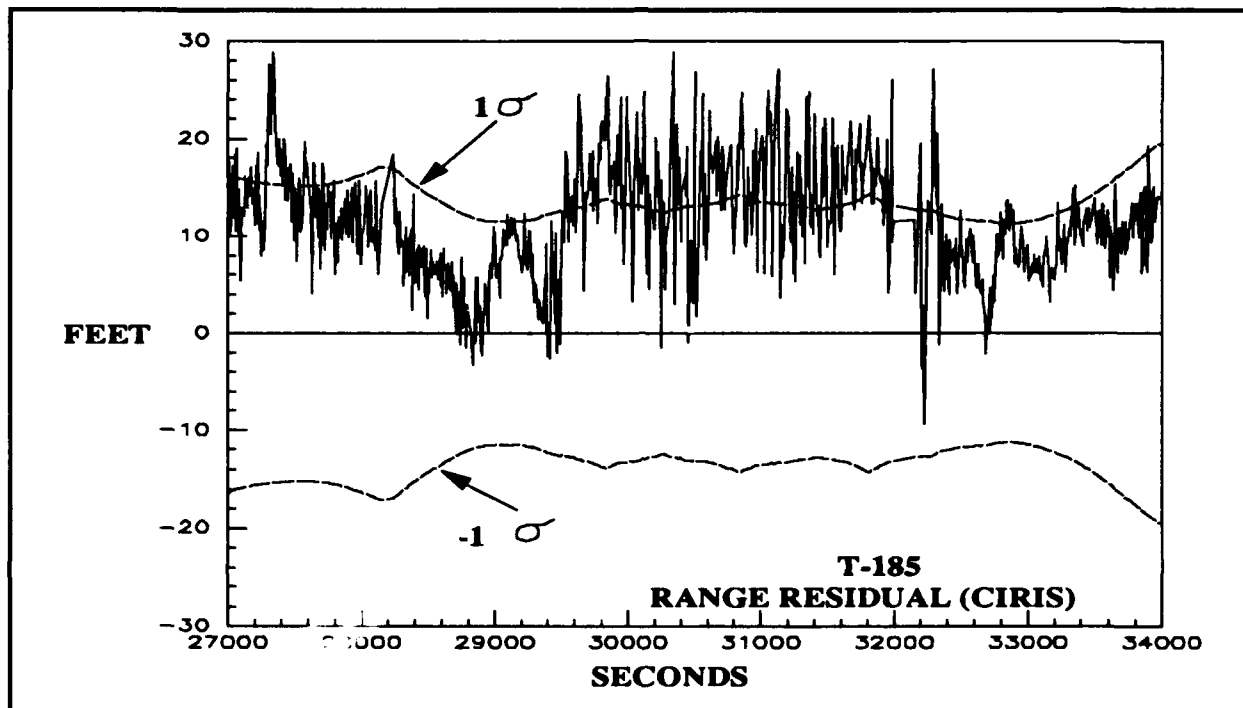
Figure 4. Typical Current CIRIS Transponder Residual

The 1σ value designated in the plot is predicted by the filter for each measurement update. This quantity is:

$$1\sigma(t_i) \;=\; \sqrt{H(t_i)P(t_i)H(t_i)^T \;+\; R(t_i)} \tag{13}$$

where:

H = Filter measurement gradient row-matrix
P = Filter covariance matrix
R = Scalar filter measurement noise strength

The predicted statistics for the range residual shown in Figure 4. are a mean of zero and a 1σ value of approximately 14 ft. The actual statistics of the range residual shown are a mean of +11.02 ft and a 1σ value of 5.51 ft; the residual is biased and exhibits significant correlated errors indicating a lack of "whiteness" (as compared to Figure 2). It is clear that filter performance is degraded by unmodelled correlated errors. The bulk of these correlated error effects, exhibited by the current CIRIS filter residuals, are attributed to the unmodelled transponder-survey and atmospheric errors.

A partially successful attempt is made in the current CIRIS computer algorithm to remove some of the atmospheric error. A deterministic open-loop correction is made to the line-of-sight range measurement data before it is processed by the filter. This correction is:

$$R_M = R'_M - e_R \qquad (14)$$

R_M = Corrected Range Measurement
R'_M = Raw Range Measurement
e_R = Error Due To Atmospheric Effects

The atmospheric error (e_R) is attributed entirely to the nonzero refractivity of the troposphere. The troposphere is defined as the region of the atmosphere from sea-level to about 70,000 ft. In the current CIRIS filter, the refractivity above sea level is approximated with an exponential function based on altitude above sea level (H), atmospheric scale factor (H_S), and sea level refractivity (N_S). This equation is:

$$N = N_S \ e^{-\frac{H}{H_S}} \qquad (15)$$

The CIRIS range correction (e_R) calculation is based on a complicated function relating refractivity, altitude, and length of measurement cycle. This algorithm description can be found in Reference (5:6.3-14, 6.3-15). However, as indicated by the residual characteristics defined in Figure 2, this open-loop correction is inadequate for the desired estimation accuracies. Developing a stochastic atmospheric error model and allowing the EKF to estimate this error can improve the system performance.

4.3 Transponder Survey-Error Model

The transponder survey-error is a highly correlated measurement error and must be modeled with a stochastic shaping filter. All correlated measurement errors present in the range measurement are depicted in the Earth-Centered-Earth-Fixed (ECEF) frame (E-frame) in Figure 5. The transponder survey-errors are designated $\delta X'_T$, $\delta Y'_T$, and $\delta Z'_T$.

The transponder survey-errors represent the limitations of Defense Mapping Agency (DMA) geodetic survey accuracy. The resulting errors are constant in time and relatively small in magnitude. In this research the survey-errors are modeled in the X', Y', and Z' (E-frame) axes. This error is "best" represented by a random bias (constant) shaping filter. The three transponder survey-errors coordinatized in the E-frame are represented by the vector defined:

$$\delta \underline{P}_T = \begin{bmatrix} \delta X'_T \\ \delta Y'_T \\ \delta Z'_T \end{bmatrix} \qquad (16)$$

The stochastic differential equations are now developed for the errors shown in Eq (16). The transponder position errors (δX_T, δY_T, δZ_T) are modeled as random biases with an initial mean of 0 ft and initial 1σ value of 5 ft. The describing stochastic differential equation is:
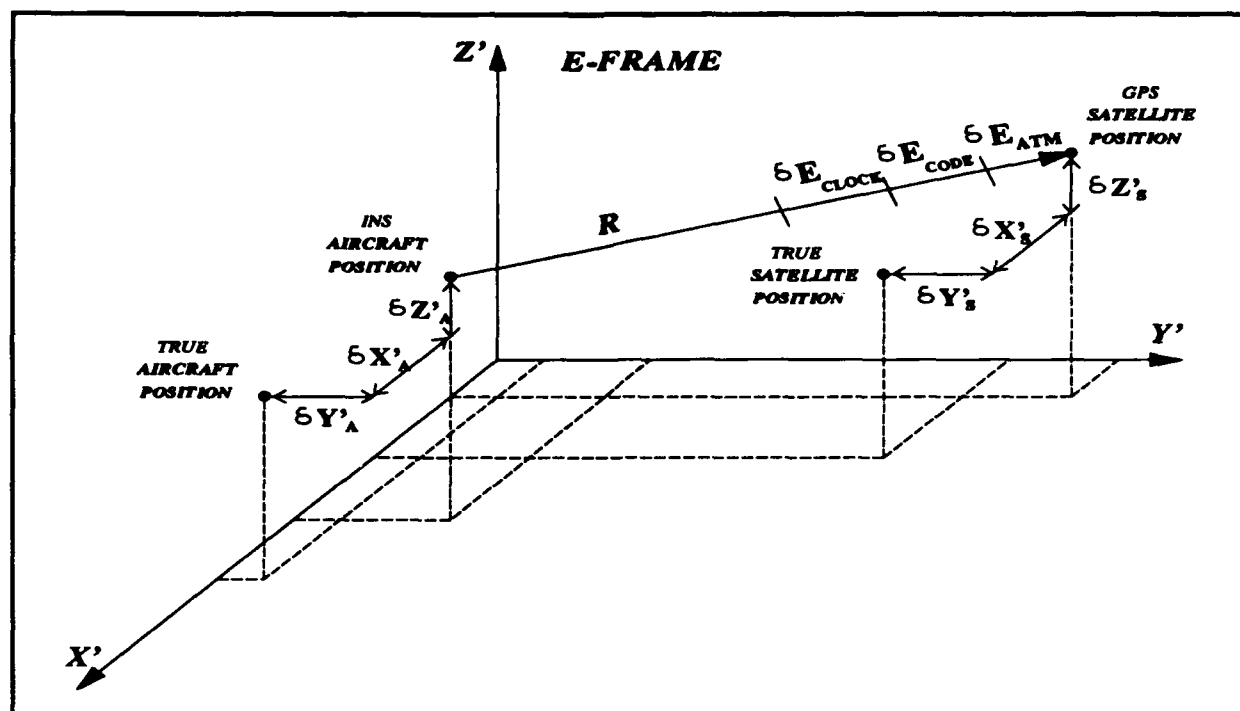
Figure 5. Depiction of Correlated Measurement Errors

$$\delta \dot{\underline{P}}_T(t) = \underline{0} \tag{17}$$

$$\delta \hat{\underline{P}}_T(t_0) = \underline{0} \tag{18}$$

$$P_{\delta \underline{P}_T}(t_0) = \begin{bmatrix} 25 & 0 & 0 \\ 0 & 25 & 0 \\ 0 & 0 & 25 \end{bmatrix} \tag{19}$$

The Kalman filter identifies and estimates these errors based on the modeled spectral characteristics. The initial mean is designated m_0 and the initial covariance by P_0. These three states are augmented to the INS error vector and included in the filter's range measurement equation. The measurement error correlatedness dynamics are augmented to the INS F(t) matrix. The full-ordered model is defined in a later section.

4.4 Atmospheric Error Model

The atmospheric propagation error is another correlated measurement error which requires a stochastic shaping filter model. This error is depicted as a line-of-sight range error in Figure 5. This error is attributed to the nonzero refractivity of the troposphere integrated along the line-of-sight path. The range measurements are deterministically corrected as presented in Eq (14). The Kalman filter then estimates the error residue in this correction. The refractivity (N) is a function of the atmospheric index of refraction (n):

$$N = (1-n) \times 10^6 \tag{20}$$

A nonzero refractivity (N) corresponds to an index of refraction (n) greater than 1 and a decrease in the electromagnetic wave propagation velocity (v) from the speed of light (c). This decrease in velocity results in an erroneous increase in the line of sight range measurement. The basic equation is (5:6.3-1, 6.3-3):

$$v = \frac{1}{n} c \tag{21}$$

The refractivity is a time varying quantity based on the atmospheric temperature (T), water vapor content (e), and atmospheric pressure (P). This quantity is (5:6.3-4):

$$N(t) = \frac{77.6 \; P(t)}{T(t)} + \frac{37,300 \; e(t)}{T(t)^2} \tag{22}$$

A line of sight error occurs in the range measurement due to atmospheric conditions changing the index of refraction and resulting in propagation delays. The resulting time-varying error magnitude is relatively small. This error is "best" represented by a first-order Markov process shaping filter. It is modeled as a first order Markov time varying error with a correlation time of approximately 300 seconds, noise strength of 0.1667 ft^2/sec, initial mean of 0.0 ft, and initial 1σ value of 5 ft. The correlation time for this model is derived from data obtained in a static test at CIGTF. Range data was recorded from several transponders at different distances. After removing the true range, the power spectral density (PSD) on this error data indicated an average correlation time of 300 seconds. The stochastic differential equation and the filter initial conditions are:

$$\delta\dot{E}_{ATM}(t) = -\frac{1}{300} \; \delta E_{ATM}(t) + W_{ATM} \tag{23}$$

$$\delta\hat{E}_{ATM}(t_0) = 0.0 \tag{24}$$

$$P_{\delta E_{ATM}}(t_0) = 25 \tag{25}$$

$$E\{ W_{ATM}(t) \} = 0.0 \tag{26}$$

$$E\{ W_{ATM}(t) W_{ATM}(t+\tau) \} = 0.1667 \; \delta(\tau) \tag{27}$$

This is an exponentially time-correlated process. The correlation time is represented by T, the mean is zero, and the initial covariance by σ^2. This state is augmented to the INS dynamic system stochastic differential equation and included in the filter's range measurement equation. The full-ordered model is defined in a later section.

4.5 Full-Ordered Kalman Filter Structure

The first 85 states of the full-ordered EKF represent the errors in the CIRIS II Litton LN-39 Air Force standard INS. This 85 state error model is taken directly from the comprehensive Litton engineering analysis report defining the error characteristics of this system (7). The error states contained in this model consist of the three position errors, three platform tilts, three velocity errors, one wander angle error, three baro-altimeter INS aiding channel errors, 10 sensor correlated errors, 21 gyro bias errors, 29 accelerometer and bias errors, 9 thermal transient errors, and three gyro turnaround drift errors. The details of this INS model are not presented in this paper, but can be found in Reference (8).

An additional 42 states are required to model the correlated errors in the range and range-rate measurements. These error states consist of two transponder interrogator/receiver calibration errors (range loop and range-rate loop) common to all transponders, three transponder survey-errors (three axes of E-frame) and a line-of-sight atmospheric error for each transponder. These errors are augmented to the INS error model to form the full-ordered "truth" model vector stochastic differential equation. The range and range-rate random bias calibration errors are assumed to be in the aircraft interrogator. Therefore, these errors are common to all the transponders interrogated and require only two states. The transponder survey- and atmospheric errors are unique to each transponder. Although the atmospheric propagation error is expected to be somewhat correlated from one transponder line-of-sight to another, it is neglected in this analysis. Therefore, each transponder interrogated requires 4 unique states.

A typical CIRIS flight uses from 10 to 30 different transponders. It normally sequences through a 5-10 transponder window at a 1 Hz rate. It deletes/adds transponders to this window to optimize the transponder geometry. Providing 4 states for each transponder is computationaly burdensome. To keep the computational load manageable, 4 states are provided for only 10 different transponders (maximum number possible in a window) for a total of 40 additional states. When a transponder is deleted and replaced with a new one, the four rows and columns of the covariance matrix for the respective transponder error states are set to zero. The mean for each of the respective states is set to zero when the transponder is first used in the flight. However, the algorithm saves the mean estimates of the current transponder before switching to a new transponder. If the same transponder is encountered again in the flight, the algorithm re-initializes the error state means with the saved values. The covariance diagonal element for each of the four states is re-initialized to its initial value of 25 ft^2. With this procedure, any number of transponders encountered during a flight are accommodated without requiring additional Kalman filter states. The 127-state (85+42) augmented stochastic differential equation is:

$$\delta \underline{\dot{X}}(t) = F(\underline{\hat{X}}, t) \, \delta \underline{X}(t) + \underline{W}(t) \tag{28}$$

$$\underline{\delta X} = \begin{bmatrix} \delta X_{INS} \\ \delta X_{MEAS} \end{bmatrix}, \qquad F = \begin{bmatrix} F_{INS} & 0 \\ 0 & F_{MEAS} \end{bmatrix}, \qquad \underline{W} = \begin{bmatrix} W_{INS} \\ W_{MEAS} \end{bmatrix}$$

$$\delta \underline{\hat{X}}(t_0) = [0] \tag{29}$$

$$P_{\underline{\delta X}}(t_0) = \begin{bmatrix} P_{INS} & 0 \\ 0 & P_{MEAS} \end{bmatrix} \tag{30}$$

$$E\{\underline{W}(t_0)\} = \underline{0} \tag{31}$$

$$E\{\underline{W}(t_0)\,\underline{W}(t_0+\tau)\} = Q(t_0)\delta(\tau) = \begin{bmatrix} Q_{INS} & 0 \\ 0 & Q_{MEAS} \end{bmatrix}\delta(\tau) \tag{32}$$

Note that the F matrix is calculated based on linearization about $\hat{X}$, which is the current best estimate of the true states. This full state vector is defined as:

$$\underline{\hat{X}} = \underline{X} - \delta\underline{\hat{X}} \tag{33}$$

The details of this model are found in Reference (8). The measurement equations are defined as:

$$\delta Z_1(t_i) \;=\; \delta Z_{RANGE}(t_i) \;=\; H_R(\hat{\underline{P}}_A, \hat{\underline{P}}_T, t_i)\, \delta\underline{X}(t_i) \;+\; V_R(t_i) \tag{34}$$

$$\hat{\underline{P}}_A \;=\; \underline{P}_A \;-\; \delta\hat{\underline{P}}_A$$

$$\hat{\underline{P}}_T \;=\; \underline{P}_T \;-\; \delta\hat{\underline{P}}_T$$

$$E\{ V_R(t_i) \} \;=\; 0$$

$$E\{ V_R(t_i)\, V_R(t_j) \} \;=\; \begin{cases} R_R & t_i = t_j \\ 0 & t_i \neq t_j \end{cases}$$

$$\delta Z_2(t_i) \;=\; \delta Z_{RATE}(t_i) \;=\; H_{RR}(\hat{\underline{P}}_A, \hat{\underline{P}}_T, \hat{\underline{V}}_A, t_i)\, \delta\underline{X}(t_i) \;+\; V_{RR}(t_i) \tag{35}$$

$$\hat{\underline{V}}_A \;=\; \underline{V}_A \;-\; \delta\hat{\underline{V}}_A$$

$$E\{ V_{RR}(t_i) \} \;=\; 0$$

$$E\{ V_{RR}(t_i)\, V_{RR}(t_j) \} \;=\; \begin{cases} R_{RR} & t_i = t_j \\ 0 & t_i \neq t_j \end{cases}$$

Eqs (34) and (35) are scalar equations. Again note that the best estimates of the full states are used to calculate the measurement gradient matrices (H_R and H_{RR}). The definitions of the H_R and H_{RR} matrices are not presented in this paper, but can be found in Reference (8). The Kalman filter is updated once a second with a measurement from one of the transponders.

The final topic of the Kalman filter structure is the residual generated during the update process. Because the measurements are nonlinear, the extended Kalman filter form of the residual equation is used. This equation replaces the residual quantity defined in Eq (10). This form is defined as:

$$r_1(t_i) \;=\; \hat{R}_C(\hat{\underline{P}}_A, \hat{\underline{P}}_T, t_i) + \delta\hat{E}_{CALR}(t_i) + \delta\hat{E}_{ATM}(t_i) - R_M(t_i) \tag{36}$$

$$r_2(t_i) \;=\; \dot{\hat{R}}_C(\hat{\underline{P}}_A, \hat{\underline{P}}_T, \hat{\underline{V}}_A, t_i) + \delta\hat{E}_{CALRR}(t_i) - \dot{R}_M(t_i) \tag{37}$$

The variables $\hat{R}_C$ and $\dot{\hat{R}}_C$ are the nonlinear calculations of aircraft range and range-rate to transponder based on the optimal estimate of aircraft and transponder positions and aircraft velocity. The variables R_M and $\dot{R}_M$ are the measurements from the RRS. The range and range-rate nonlinear equations are used with the best estimate of the full states. This form of the residual calculation takes into account the nonlinearities and results in a better estimate of the true residual when compared with the linearized error residual update form (6).

The overall structure of the full-ordered filter is defined in this section to illustrate the complexity of the model and the method of augmenting the transponder survey and atmospheric errors. The details of this model are found in Reference (8).

4.6 Simulation

A CIRIS flight tape was provided by CIGTF. This data tape contains the INS position and velocity, barometric altimeter, range measurement, and delta range measurement data for the flight of approximately 4.5 hours. The tape also contains the error state means, error state covariances, and measurement residuals from the current CIRIS I filter for this flight. The flight trajectory for this data is illustrated in Figure 6.
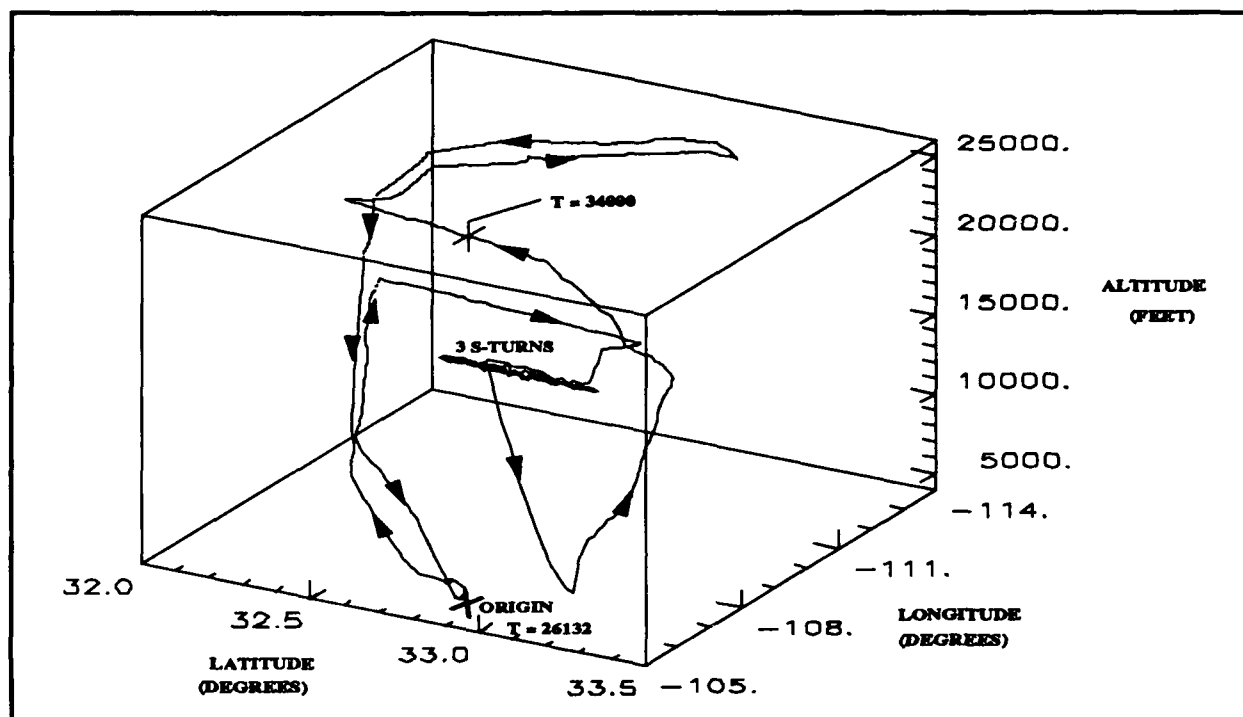
Figure 6. CIRIS Flight Trajectory

The CIRIS flight time is designated in seconds. It begins at time 26132 and ends at time 42000. Since the full ordered filter is computationaly intensive and because most of the high dynamic maneuvers occur early in the flight, only the first 2.25 hours of the flight are processed by the filter beginning at 26132 and ending at 34000. The T=34000 point is shown in Figure 6. This simulation required 17 hours of CPU time on a VAX 8650 computer. The latitude vs longitude and altitude vs longitude position trajectory plots, including transponder locations, for the abbreviated CIRIS flight profile are shown in Figure 7.

The data from transponder T-185 is selected for detailed residual and correlated error analysis. The characteristics of this transponder are considered representative of all the transponders. Transponder T-185 is designated T-185 and circled in Figure 7.

The full-ordered EKF is coded into the Multimode Simulation for Optimal Filter Evaluation (MSOFE) software package (2) to conduct the simulation. A FORTRAN program is used to transform the CIRIS flight tape data into data files used by MSOFE. The simulations are conducted on AFIT's VAX 8650 computer system.
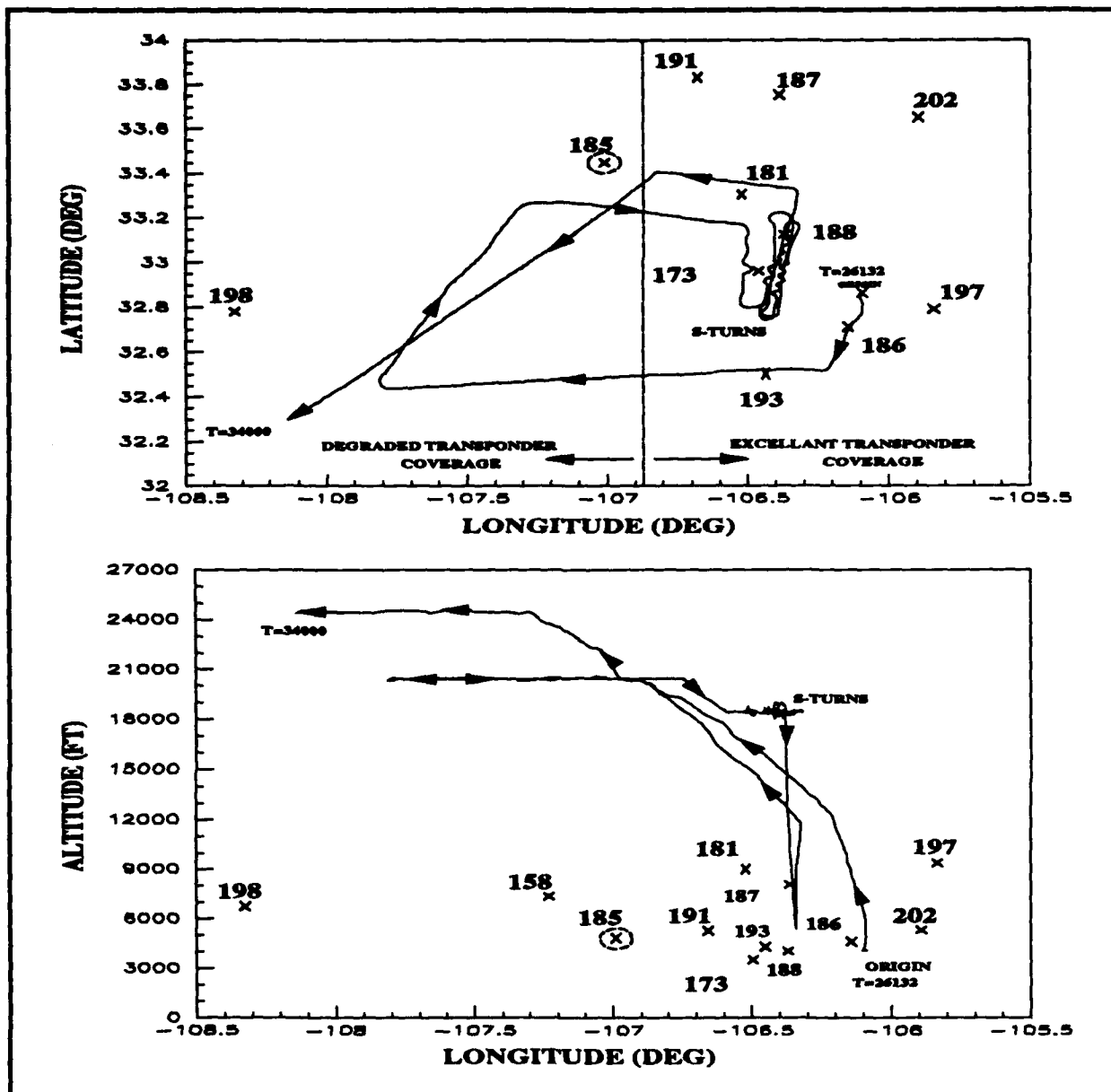
Figure 7. CIRIS Abbreviated Flight Profile

These data files are processed in MSOFE from takeoff at time 26132 to time 34000 (2.25 hours). The range and range rate measurements are updated from one transponder every second. A 7σ tolerance is used for residual rejection. Any measurement greater than 7 times the predicted residual 1σ is rejected for both range and range rate measurements. This residual monitoring technique rejected 14% of the 16,060 range and range rate measurements from all transponders. This number of rejected measurements is considered acceptable and does not effect the overall quality of the filter error estimation accuracy. Only the range residual and correlated errors for transponder T-185 are investigated in this paper, the complete analysis is found in Reference (8).

4.6.1 Range Residual for Transponder T-185

The range residuals are a direct indication of how well the Kalman filter model represents the physical world as explained in the "Current CIRIS" section. The full-ordered EKF range residual for transponder T-185 is shown in Figure 8. The 1σ designated curve is the filter prediction.
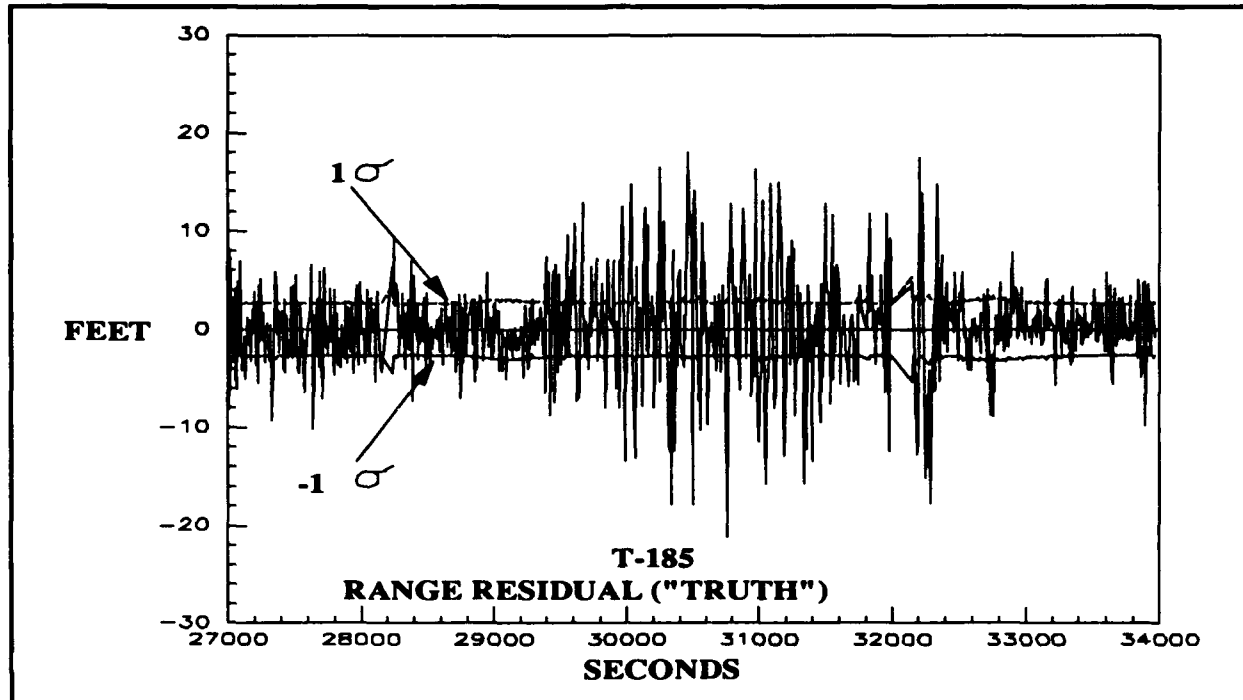
Figure 8. Full-Ordered Filter Range Residual

The predicted statistics of the range residual for this transponder are a mean of zero with a 1σ value of approximately 3 ft. The actual statistics are a mean of +0.28 ft with a 1σ value of 4.58 ft. This residual has a negligible bias and exhibits very few correlated error characteristics. The closer similarity to a "white" noise process is emphasized by a direct comparison of this range residual to the current CIRIS range residual shown in Figure 3. The improvement in the residual characteristics is attributed to using the EKF to estimate the transponder survey and atmospheric range measurement errors within the model accuracy.

The actual 1σ values for the full-ordered and current CIRIS filters are similar. This indicates that the magnitude of the random error in both filters is nearly the same. However, the full-ordered filter range residual characteristics are closer to the ideal (filter predicted) residual characteristics. Therefore, the position and velocity estimated errors predicted by the full-ordered filter based on the "truth" model are closer to the true errors than the current CIRIS filter error estimates.

4.6.2 Correlated Measurement Errors for Transponder T-185

Transponder T-185's error state means and 1σ values for the X' and Y' correlated measurement errors are shown in Figure 10. The aircraft trajectory with respect to this transponder is shown in Figure 8. The aircraft traverses the transponder vicinity to the South of its location. This geometric relationship is poor (resulting in poor observability of some error states) and the filter may have difficulty estimating these survey-errors in all 3 E-frame axes.

The final X' error attained a mean of -5 ft and a 1σ value of 2.6 ft. The Y' error attained a mean of -4 ft and a 1σ value of 4 ft. The two large transients apparent at times 29000 and 33000 are attributed to degraded observability due to poor geometry and large trajectory turns at these times. Initially the three elements of the survey-error are unobservable. However, as the aircraft-transponder line-of-sight geometry changes, three dimensional observability is accumulated in the EKF covariance matrix. The magnitude of these errors are reasonable for the survey-errors being estimated.

Transponder T-185's error state means and 1σ values for the Z' and atmospheric (ATM) correlated measurement errors are shown in Figure 9. The Z' error attained a mean of -13 ft and a 1σ value of 3.5 ft. The characteristics of this error are very similar to the X' and Y' errors shown in Figure 9. Again the magnitude of this error is reasonable indicating the filter is estimating the actual survey-error.

This data indicates the transponder survey-errors are observable and the filter's random bias shaping filter model is estimating the error magnitudes. The survey-error observability does not exist at any instant in time, however as the aircraft traverses through various relative positions to the transponder, the observability is accumulated in the Kalman filter covariance matrix. The geometric relationship of the line-of-sight vectors (aircraft to transponder) with transponder survey-error vector determines how well the error is estimated. Therefore, the ultimate accuracy of the survey-error estimates is directly related to the aircraft/transponder geometric relationship time history as described above. It is important to point out that the survey errors are being estimated with respect the WGS 84 geodetic model ECEF absolute reference. Since the recorded flight data tape does not include the CIRIS initialization, and the accurate initial conditions are not available to the filter. If the initialization were included, then the Kalman filter would have converged on the survey and other errors much more rapidly.

The atmospheric error shown in Figure 9. depicts the Kalman filter effort to estimate the line of sight error in the range measurement due to propagation delays caused by atmospheric conditions. This is a time varying error and is a function of weather conditions and aircraft distance to the transponder. This error is attributed to the changing atmospheric index of refraction (n) which causes a decrease in the electromagnetic wave propagation velocity, erroneously causing a increase in the measured range magnitudes. Therefore, the filter estimated atmospheric error is expected to be negative. However, the CIRIS computer makes an open loop correction to each range measurement before it is processed by the filter. This allows the atmospheric error to vary between negative and positive magnitudes. This characteristic is clearly observable in the atmospheric error time histories.

The atmospheric error state mean for transponder T-185 varies from -10 to +17 ft with an average 1σ value of 3.5 ft. The magnitudes and shapes of the error time-histories are reasonable for this type of error. This error is observable and the first-order Markov shaping filter allows the filter to accurately estimate this error.

Although these results were obtained using a single forward pass of the EKF, much improved estimation of the survey and atmospheric errors is expected when a backward pass is added in a smoother operation. This implementation is commonly referred to as an optimal smoother algorithm (6).
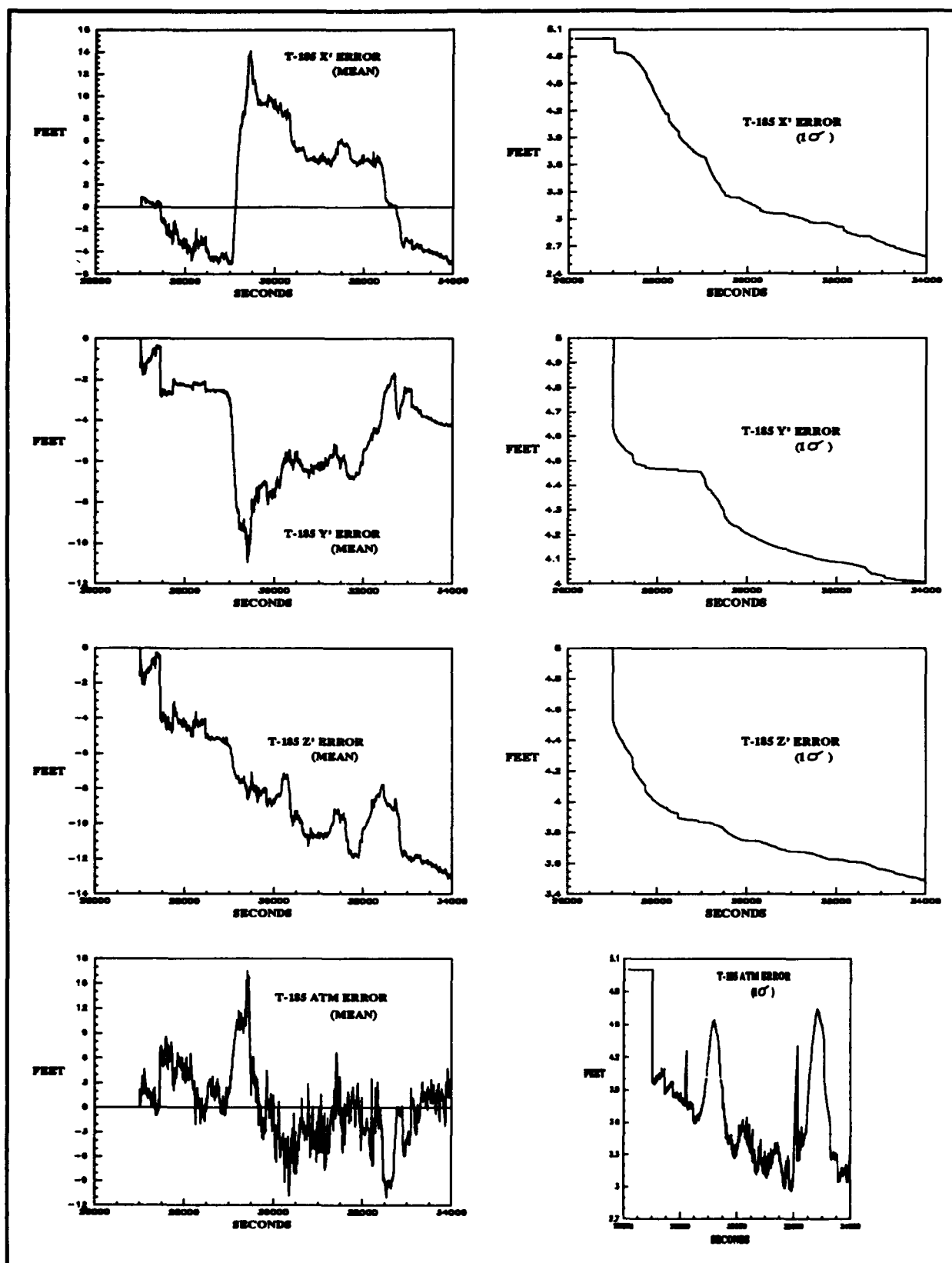
Figure 9. T-185 X', Y', Z' Position and Atmospheric Correlated Errors

5. GPS ERROR MODELING AND ANALYSIS

The next step in this research is the development of a Kalman filter that in addition to the transponder aiding of the INS, also uses pseudo-range measurements from the GPS system. The 70-state CIRIS II Kalman filter is the basis for this research. This 70-state "truth" model describes all the known error sources in the current CIRIS II system. The known error sources in the GPS system are modeled and augmented to the 70-state model. The resulting 98-state Kalman filter is used to process the empirical CIRIS flight data used in Reference (22). At this point it is only possible to conduct covariance analysis since GPS pseudo-range measurements are not yet available for the CIRIS flight. The correlated error state 1σ values for the GPS pseudo-range measurements are plotted and analyzed to determine observability. To further quantify the expected increase in performance with the 98-state filter, the position and velocity 1σ values are compared with the 70-state filter's 1σ values. The details of this filter structure are found in Reference (22). The GPS pseudo-range measurement error model must be augmented to this model to form the "truth" model for the GPS aided CIRIS system. These error models are developed in the following sections.

5.1 Brief Review of GPS Concept

The GPS system is expected to consist of a baseline constellation of 24 satellites operating in 12-hour orbits at an altitude of 10,898 nmi. It will provide a visibility of 6 to 11 satellites at 5 degrees or more above the horizon to users located anywhere in the world at anytime. Signals are transmitted at two L-band frequencies to permit corrections for ionospheric delays in signal propagation time. The signals are modulated with two codes: P, which provides for precision measurement of time and C/A, which provides for easy lock-on to the desired signal. Currently, only a small part of this constellation is in place and operational.

In its normal mode of operation, four satellites are required for navigation purposes; the four satellites offering the best geometry are automatically selected by the GPS user receiver. Ranges to the four satellites are determined by scaling the signal transit time by the speed of light. The transmitted message, from the satellite to the receiver, contains the satellite ephemeris and time of transmission. Using a least squares algorithm or Kalman filter, the user position (latitude, longitude, and altitude) and user clock error are determined. The four parameters calculated by the GPS algorithm, represent the four unknowns in the GPS navigation equations and therefore, four pseudo-range measurements from four satellites are required to solve the appropriate equations (18). Four satellites are not required when using GPS pseudo-range measurements to aid an INS if a highly precise user clock is available, or if other navigation aiding measurements are available. Certainly, more than four GPS satellite measurements can be used in aiding a navigation system, however the additional measurements are not expected to significantly increase the overall accuracy.

The GPS pseudo-range measurements have several sources of error. The largest error source is the user clock error. The user clock in the GPS receiver is of a lower quality than the GPS satellite clocks and therefore, less accurate. Errors also results from the narrow bandwidth of the GPS receiver phase-lock-loop, tropospheric atmospheric delays, and satellite orbit errors. These errors may be estimated by the Kalman filter used in aiding the INS (16).

In this mode of operation, the Kalman filter must be supplied with raw GPS pseudo-range and satellite ephemeris data. Some of the currently available GPS receivers do not provide raw pseudo-range and ephemeris data to the user. For example the Rockwell Collins, Phase III receiver does not provide the raw pseudo-range and delta range information on the MILSTD 1553 data bus, however this information is available through the instrumentation port.

5.2 GPS Correlated Measurement Error Models

The GPS pseudo-range measurement errors are similar to the measurement errors in the CIRIS transponder range measurement. In fact, the GPS satellites can be considered as an additional set of "transponders in the sky" and the errors associated with these measurements are similar to those of the Cubic transponders. The physical interpretation of these errors is depicted in Figure 10. There are 6 errors: the combination of the atmospheric and the residual uncorrected ionospheric delay error, phase-lock-loop error, user clock error, and the 3 E-Frame satellite orbit position errors.
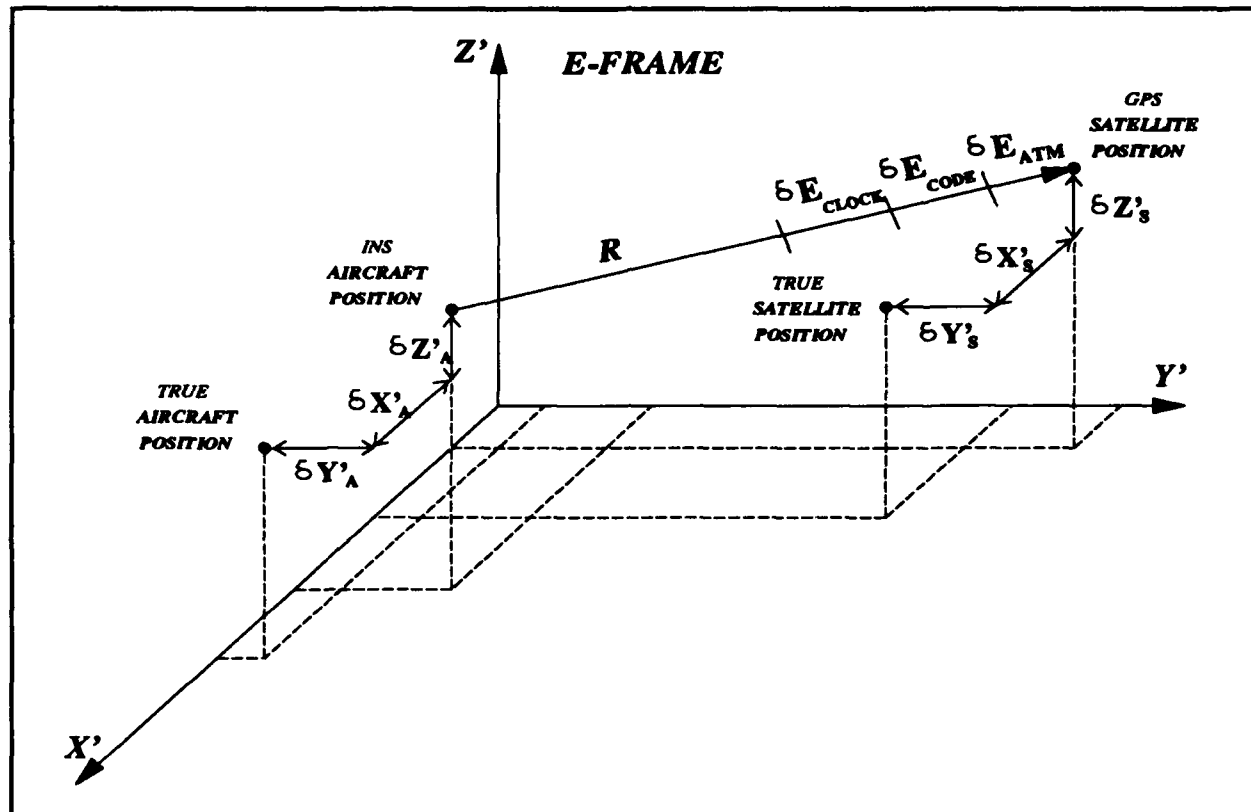
Figure 10. GPS Pseudo-range Error Sources

The INS position error shown in Figure 10. is already modeled in the 70-state filter model. The models for the six remaining errors are developed in this section.

5.2.1 User Clock Errors

The largest of these errors is the user clock error. The user clock is located in the aircraft GPS receiver and is not coherent with the GPS satellite clock. The user clock is also of a lower quality and is therefore less accurate. This error can be modeled with a bias and a drift component. This shaping filter model requires two states. The model is defined as:

$$\delta \dot{X}_B(t) \quad = \quad \delta X_D \tag{38}$$

$$\delta \dot{X}_D(t) \quad = \quad 0 \tag{39}$$

$$\delta \hat{X}_{CLOCK}(t_0) \quad = \quad \underline{0} \tag{40}$$

$$P_{\delta X_{CLOCK}}(t_0) \quad = \quad \begin{bmatrix} 9 x 10^{14} \, FT^2 & 0 \\ 0 & 9 x 10^{10} \, FT^2 \end{bmatrix} \tag{41}$$

The initial conditions chosen for the Kalman filter are taken directly from Reference (22). The large initial covariances represent the expected magnitude of the bias and drift errors. These error covariances are expected to drop significantly after several filter updates because the line-of-sight clock errors are observable. Also notice that there is not a "white" noise component in these models. Since these errors may not remain constant during the flight, a driving pseudo-noise component may be required to prevent the Kalman filter gains from going to zero. The pseudo-noise addition will not be considered in this study.

5.2.2 Code Loop Error

The GPS phase-lock-loop and the code loop each has a narrow bandwidth filter of approximately 1 Hz. Therefore the original broad-band noise entering this loop is highly correlated by the low bandwidth of this loop and can not be modeled as a "white" noise. A first order Markov shaping filter is used to approximate this error.

$$\delta \dot{E}_{CODE}(t) \quad = \quad -\frac{1}{1} \; \delta E_{CODE}(t) \; + \; W_{CODE} \tag{42}$$

$$\delta \hat{E}_{CODE}(t_0) \quad = \quad 0 \tag{43}$$

$$P_{\delta E_{CODE}}(t_0) \quad = \quad 0.25 \, FT^2 \tag{44}$$

$$E\{ W_{CODE}(t) \} \quad = \quad 0 \tag{45}$$

$$E\{ W_{CODE}(t) \, W_{CODE}(t + \tau) \} \quad = \quad 0.50 \frac{FT^2}{SEC} \; \delta(\tau) \tag{46}$$

The initial conditions for this model are taken from Reference (22). Note that a correlation time of 1 second is used with an initial covariance of 0.25 ft^2; these two quantities dictate a noise strength of .5 ft^2/sec.

5.2.3 Atmospheric Error

The GPS pseudo-range is already compensated for the ionospheric error by an open loop correction using dual frequencies L_1 and L_2. However, this correction is not perfect, and there is some residual ionospheric propagation error. Also there is an error introduced by the troposphere. A first order Markov shaping filter with a correlation time of 500 seconds is chosen for this combined error.

$$\dot{\delta E}_{ATM}(t) = -\frac{1}{500} \delta E_{ATM}(t) + W_{ATM} \tag{47}$$

$$\hat{\delta E}_{ATM}(t_0) = 0 \tag{48}$$

$$P_{\delta E_{ATM}}(t_0) = 1 \ FT^2 \tag{49}$$

$$E\{ W_{ATM}(t) \} = 0 \tag{50}$$

$$E\{ W_{ATM}(t) W_{ATM}(t+\tau) \} = 0.0040 \frac{FT^2}{SEC} \ \delta(\tau) \tag{51}$$

The initial conditions for this model are taken from Reference (22). This error is very similar to the transponder atmospheric error. However, for those aircraft trajectories that are at higher altitudes (30000 ft or higher), the GPS signal passes through only the upper 40000 ft of the troposphere (troposphere ends at 70000 ft point). For those flights the initial covariance can be decreased and the model's correlation time increased.

5.2.4 Satellite Orbit Position Errors

Each GPS satellite orbit is tracked on the ground and updated in the satellite computer. The typical error in satellite orbital position is considered to be 3-9 ft in the three axes of the E-Frame (22). The spectral characteristics of this error are modeled as a random bias. However, since this error may be slowly varying, a "white" pseudo-noise component may be required in this model to accurately portray the time varying nature of this error.

$$\dot{\delta \underline{P}}_s(t) = \underline{0} \tag{52}$$

$$\hat{\delta \underline{P}}_s(t_0) = \underline{0} \tag{53}$$

$$P_{\delta \underline{P}_s}(t_0) = \begin{bmatrix} 25 \ FT^2 & 0 & 0 \\ 0 & 25 \ FT^2 & 0 \\ 0 & 0 & 25 \ FT^2 \end{bmatrix} \tag{54}$$

The initial covariance for this model is chosen as 25 ft^2 to represent the midpoint of GPS orbital position accuracy. Again, pseudo-noise is not added to the model and the random bias model is considered adequate at this point of research. One state is required for each of the satellite E-Frame coordinates axes.

It is necessary to point out that the observability of the GPS satellite position errors is similar to that of the transponders, discussed in an earlier section, however there is also a difference. At any single instant of time, or during a brief period of time, in both the GPS and transponder case there is a lack of the three dimensional observability. The respective measurement contains position error information only along the single dimension of the line-of-sight between the aircraft and the transmitter (GPS or transponder). Recall from the earlier discussion that for the transponder case, when the aircraft trajectory created a time history of line-of-sight direction function, the Kalman filter retains this information about the three-dimensional probing of the three-dimensional survey error, and full observability is constructed. The key point is the ability to "fly around" the transponder and build up the observability.

In the GPS case, the situation is somewhat different. It is not possible for the aircraft to "fly around" a GPS satellite. However observability of the satellite position error can be generated, but this requires a longer time period. The satellite motion, combined with the aircraft motion, generates the variation of the line-of-sight direction. It is expected that this may be somewhat less effective in generating observability, compared to that of the transponder survey errors. Additionally three position error states may be insufficient to adequately model the time-varying character of the GPS satellite position errors. It may be necessary to use six states to completely model the full set of each space vehicle orbital parameter errors. In some cases, when the mission duration is short with respect to the magnitude of change in the apparent position error of the satellite, only that component of the position error projected onto (along) the line-of-sight need be modeled. In that case a single error state will suffice.

5.3 CIRIS/GPS Filter Model

The seven states defined in the previous section are unique to each satellite. The number of different satellites used during a CIRIS flight could be 4 or more. In order to reduce the computer requirements, the number of states kept as small as possible. The transponder window/switching concept defined earlier is used to achieve this. In the GPS scheme a four satellite window is considered adequate. This GPS model requires 28 states for the four satellite window. The CIRIS II INS/transponder/GPS "truth" model is defined as:

$$\delta \underline{\dot{X}}(t) \;=\; F(\underline{\hat{X}}, t)\, \delta \underline{X}(t) \;+\; \underline{W}(t) \tag{55}$$

$$\delta \underline{X} \;=\; \begin{bmatrix} \delta \underline{X'}_{INS} \\ \delta \underline{X}_{TRANS} \\ \delta \underline{X}_{GPS} \end{bmatrix} \qquad F \;=\; \begin{bmatrix} F'_{INS} & 0 & 0 \\ 0 & F_{TRANS} & 0 \\ 0 & 0 & F_{GPS} \end{bmatrix} \qquad \underline{W} \;=\; \begin{bmatrix} \underline{W'}_{INS} \\ \underline{W}_{TRANS} \\ \underline{W}_{GPS} \end{bmatrix} \tag{56}$$

$$\delta \underline{\hat{X}}(t_0) \;=\; [0], \qquad P_{\delta \underline{X}}(t_0) \;=\; \begin{bmatrix} P'_{INS} & 0 & 0 \\ 0 & P_{TRANS} & 0 \\ 0 & 0 & P_{GPS} \end{bmatrix} \tag{57}$$

$$E\{\underline{W}(t_0)\} \;=\; \underline{0} \tag{58}$$

$$E\{\underline{W}(t_0)\,\underline{W}(t_0 + \tau)\} \;=\; Q(t_0) \;=\; \begin{bmatrix} Q'_{INS} & 0 & 0 \\ 0 & Q_{TRANS} & 0 \\ 0 & 0 & Q_{GPS} \end{bmatrix} \tag{59}$$

The variable designated with "GPS" represents the 28 GPS measurement error state parameters. The complete model requires 98 states. This model already uses two measurements, transponder range and range-rate, and they have been defined previously. Third measurement equation is required for the GPS pseudo-range updates.

$$\delta Z_3 \;=\; \delta Z_{GPS} \;=\; R_C \;-\; R_M \;=$$

$$-\;\frac{X_s - X_A}{R}\,\delta X_A \;-\; \frac{Y_s - Y_A}{R}\,\delta Y_A \;-\; \frac{Z_s - Z_A}{R}\,\delta Z_A$$

$$+\;\frac{X_s - X_A}{R}\,\delta X_T \;+\; \frac{Y_s - Y_A}{R}\,\delta Y_T \;+\; \frac{Z_s - Z_A}{R}\,\delta Z_T$$

$$-\;\delta E_{CODE} \;-\; \delta E_{CLOCK} \;-\; \delta E_{ATM} \;+\; V_{GPS} \tag{60}$$

The X, Y, Z variables designated with subscripts A and S are the aircraft and satellite coordinates in the E-Frame, respectively. The quantities R and R_C represent the calculated range magnitude to the satellite which is the magnitude of the difference vector between the aircraft and satellite position vectors. The quantity R_M represents the raw GPS pseudo-range measurement. This equation in Kalman filter form is:

$$\delta Z_3(t_i) \;=\; \delta Z_{GPS}(t_i) \;=\; \left\{ [H_{GPS}(\hat{\underline{P}}_A, \hat{\underline{P}}_S, \hat{\underline{V}}_A, t_i)]^E\, C_C^E \right\} [\delta \underline{X}(t_i)]^C + V_{GPS}(t_i) \tag{61}$$

$$E\{\, V_{GPS}(t_i)\,\} \;=\; 0 \tag{62}$$

$$E\{\, V_{GPS}(t_i)\, V_{GPS}(t_j)\,\} \;=\; \begin{cases} 0.25\ \text{ft}^2 & t_i = t_j \\ 0 & t_i \neq t_j \end{cases} \tag{63}$$

The defined transformation is necessary because the INS states are in the computational frame while the H_{GPS} matrix is defined in the E-Frame. The quantity in brackets ({.}) is the Kalman filter H matrix for the GPS pseudo-range measurement update. This equation is added to the two transponder measurement equations. The Kalman filter updates with all three measurements each second. Since at this stage of research there are no GPS measurements available, the residual equations are not defined. The GPS aided CIRIS model is now complete.

5.4 CIRIS Flight Simulation

The same CIRIS flight trajectory, see Figure 6., is used for this simulation. The transponder locations are not depicted, but are defined in Reference (22).

The GPS satellite simulation is simplified by using four static satellites with positions as shown in Figure 11. The depicted geometry is for a representative Geometric Dilution of Precision (GDOP) of 5. The GDOP represents the precision in the GPS position estimates when the GPS system is used in its normal mode; the smaller the number, the higher the accuracy of the GPS position solution. In this case the GDOP is not really useful for selecting the best GPS satellites for CIRIS, but it is defined to indicate the good satellite geometry. In fact for CIRIS II with GPS, two satellites is most likely sufficient. However this analysis is performed with the four satellites. One satellite is chosen nearly overhead CIGTF, this simulates the best geometry possible for estimating the vertical position and velocity errors. This satellite position is chosen to determine the maximum increase in vertical channel accuracy using GPS pseudo-range measurements.

The entire 4.5 hour flight is processed in this GPS aided CIRIS simulation. The entire simulation (covariance analysis only) required 19 hours of CPU time on the AFIT's VAX 8650 computer. The results of this simulation are presented next.
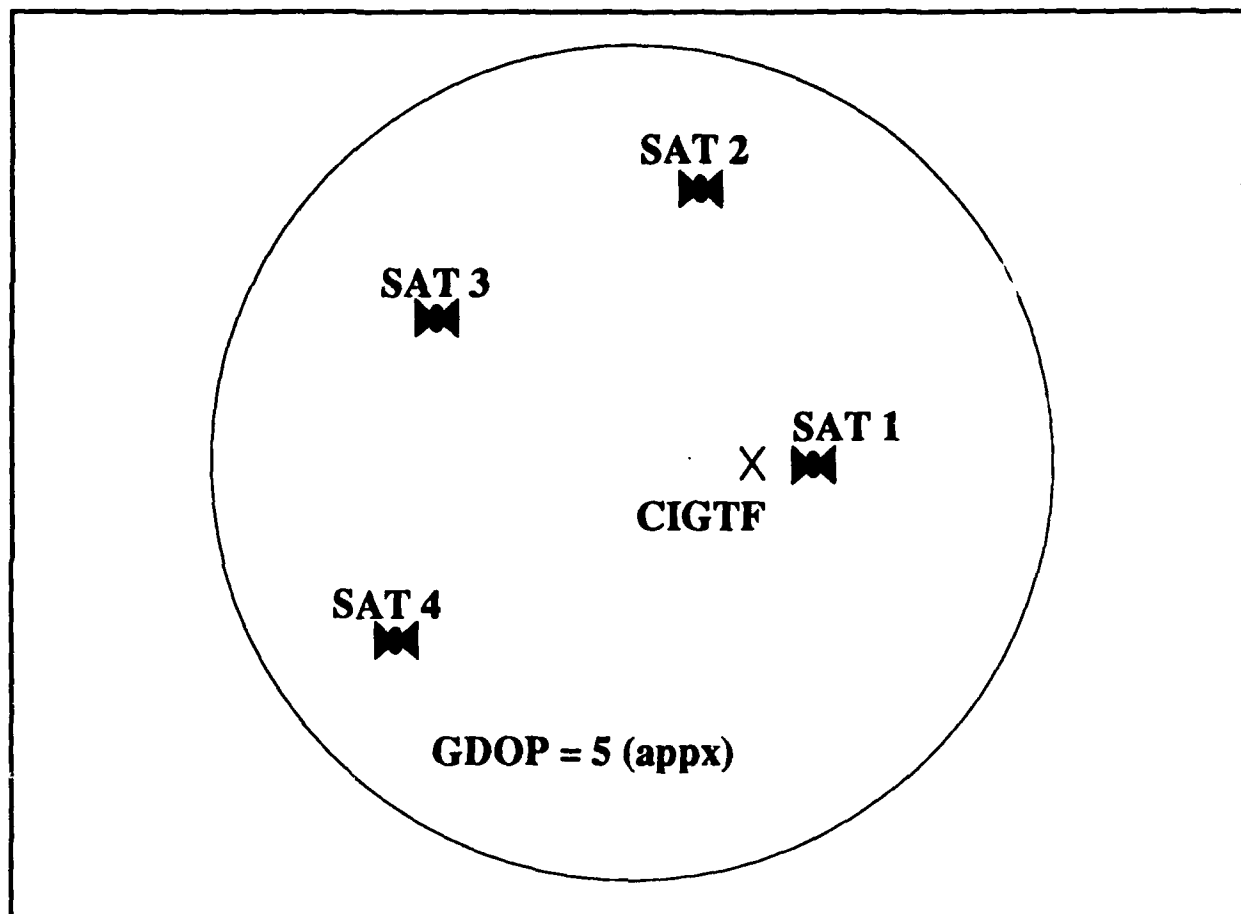
Figure 11. GPS Satellite Positions

5.4.1 User Clock Errors

The 1σ value time histories for the user clock bias and drift error states are presented first as shown in Figure 12. These time histories represent the filter predicted accuracies in estimating these errors.

As expected, after several propagation iterations, both time histories have dropped from the large initial covariance conditions to very small values. This indicates that these errors are observable and the filter can estimate them accurately. The user clock bias error time history indicates that the filter estimate is accurate to approximately 5 ft 1σ, which is reasonable. The user clock drift time history indicates that the magnitude of the user clock drift can be estimated to approximately 0.0005 ft/sec 1σ accuracy. However, since the 1σ is approaching zero, the Kalman filter gains may be approaching zero. This error is a candidate for pseudo-noise, but this idea is not pursued at this time.
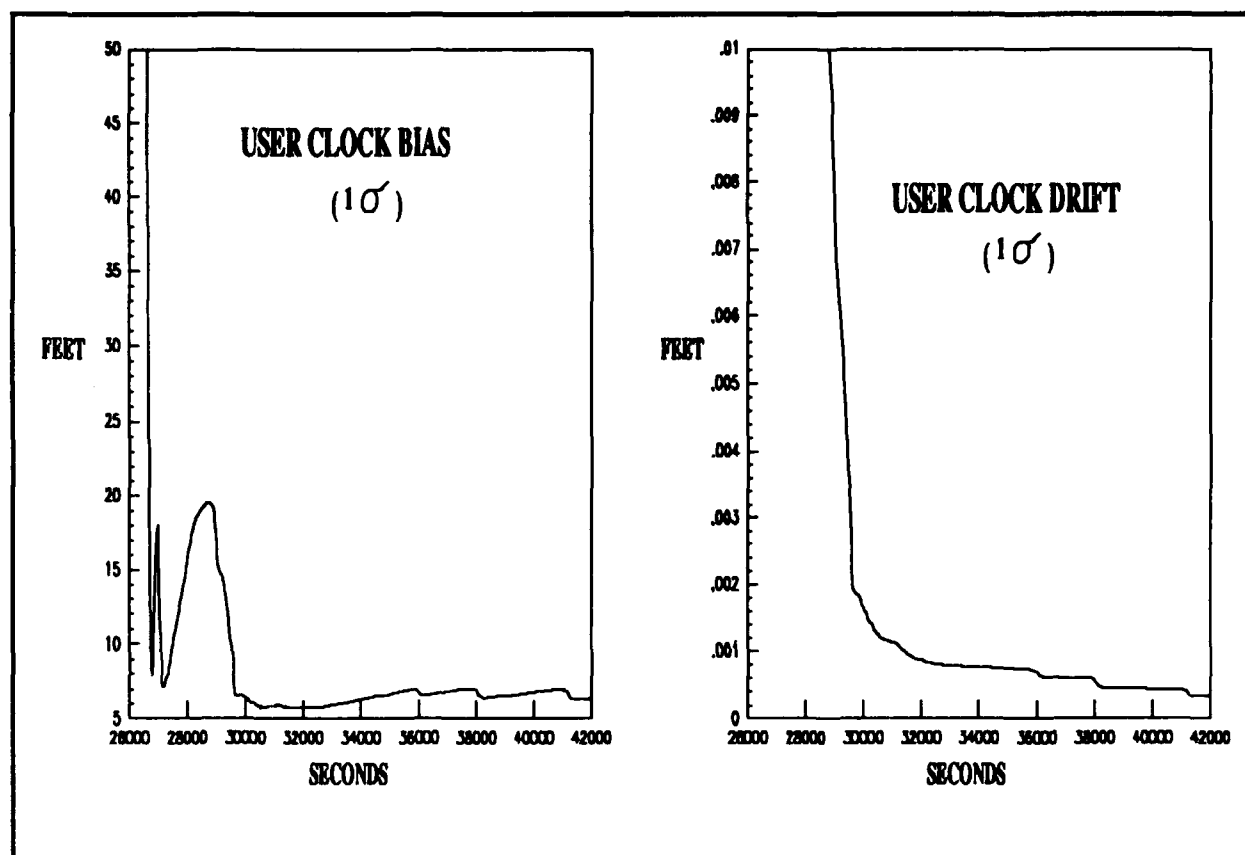
Figure 12. User Clock Bias and Drift Errors

5.4.2 Code Loop Error

The value time history of the GPS code-loop error (not shown) indicates the filter's predicted accuracy in estimating this error is not very good. The 1σ value changes only very slightly, 0.50 to 0.48 ft, during the entire 4.5 hour flight. However, the unobservability of this error is due to the static satellite positions. The code-loop error is summed with the tropospheric and satellite position errors. When the satellites are allowed to move, the 1σ value for this error is expected to continuously vary in time, in response to the satellite and aircraft trajectories and the code-loop error observability is expected to improve.

5.4.3 Atmospheric Error

The 1σ value time history for the tropospheric atmospheric error is shown in Figure 13. This time history reflects the predicted accuracy in estimating this error.

Once the filter begins observing the error, it varies between 0.92 and 0.82 ft which is a reasonable magnitude for this type of error. The time history indicates the error is observable and the filter can estimate its magnitude.

Figure 13. Atmospheric Error

5.4.4 Satellite Orbit Errors

The 1σ values for the three satellite orbit E-Frame errors are shown in Figure 14. This is the filter predicted accuracy in estimating these errors. The change in the 1σ values for all three errors is negligible. This indicates that these errors are unobservable. Again, this is due to the static satel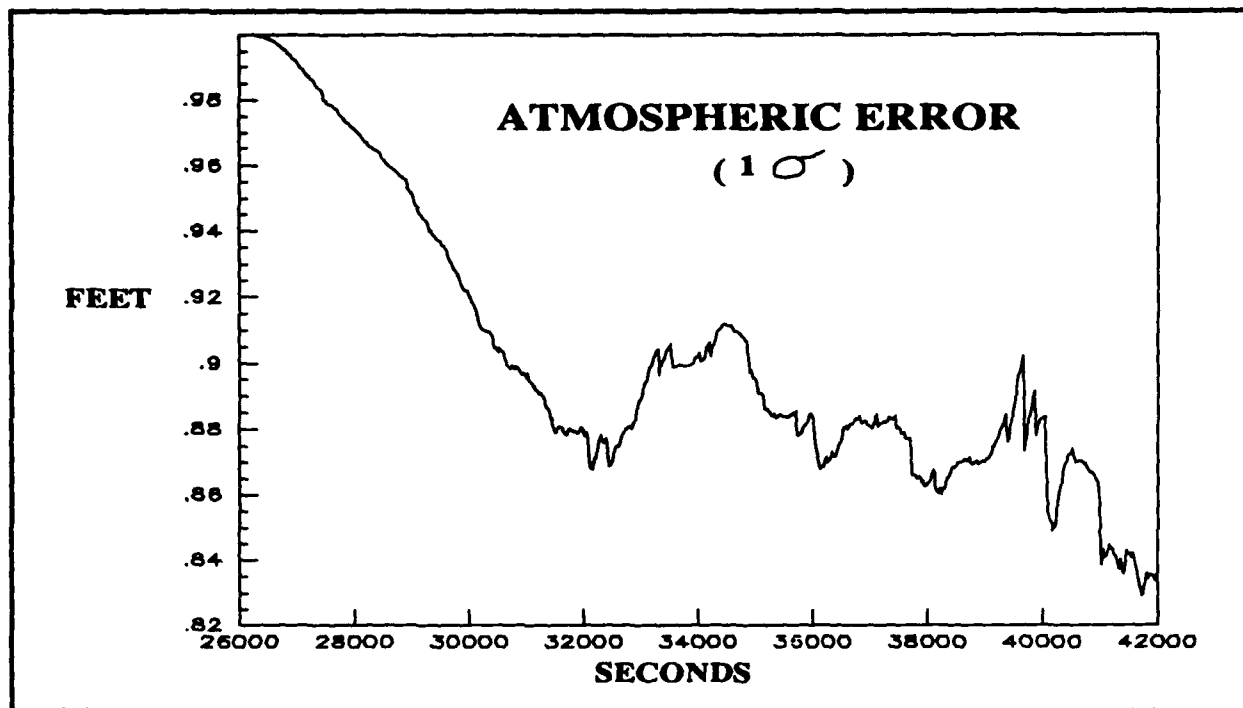lite positions. Once the simulation accounts for satellite motion these 1σ values are expected to decrease significantly. This is not explored and is left for future research.

5.4.5 Position/Velocity 1σ Value Comparison with Current CIRIS

The time histories of the 1σ values for the position and velocity error states for both the current CIRIS and GPS aided CIRIS are shown in Figure 15. The observability limitations, defined in the previous section, should be noted as these time histories are reviewed. Again, these limitations are due to the static satellite positions. Once the satellite motion is modeled the position/velocity accuracies should improve further.

The areas of current CIRIS degradation in estimation accuracies are due to poor transponder coverage (22). These areas are essentially eliminated by the GPS aided CIRIS filter. The increase in accuracy in all cases is significant. The altitude error reduction, less than 10 ft for entire flight, is the most dramatic. This characteristic is expected, however the increase in accuracy in the horizontal channels is also significant. The GPS aided CIRIS is outperforming the current CIRIS filter in all cases, indicating the significant potential accuracy gains by adding GPS pseudo-range measurements to the current CIRIS system.
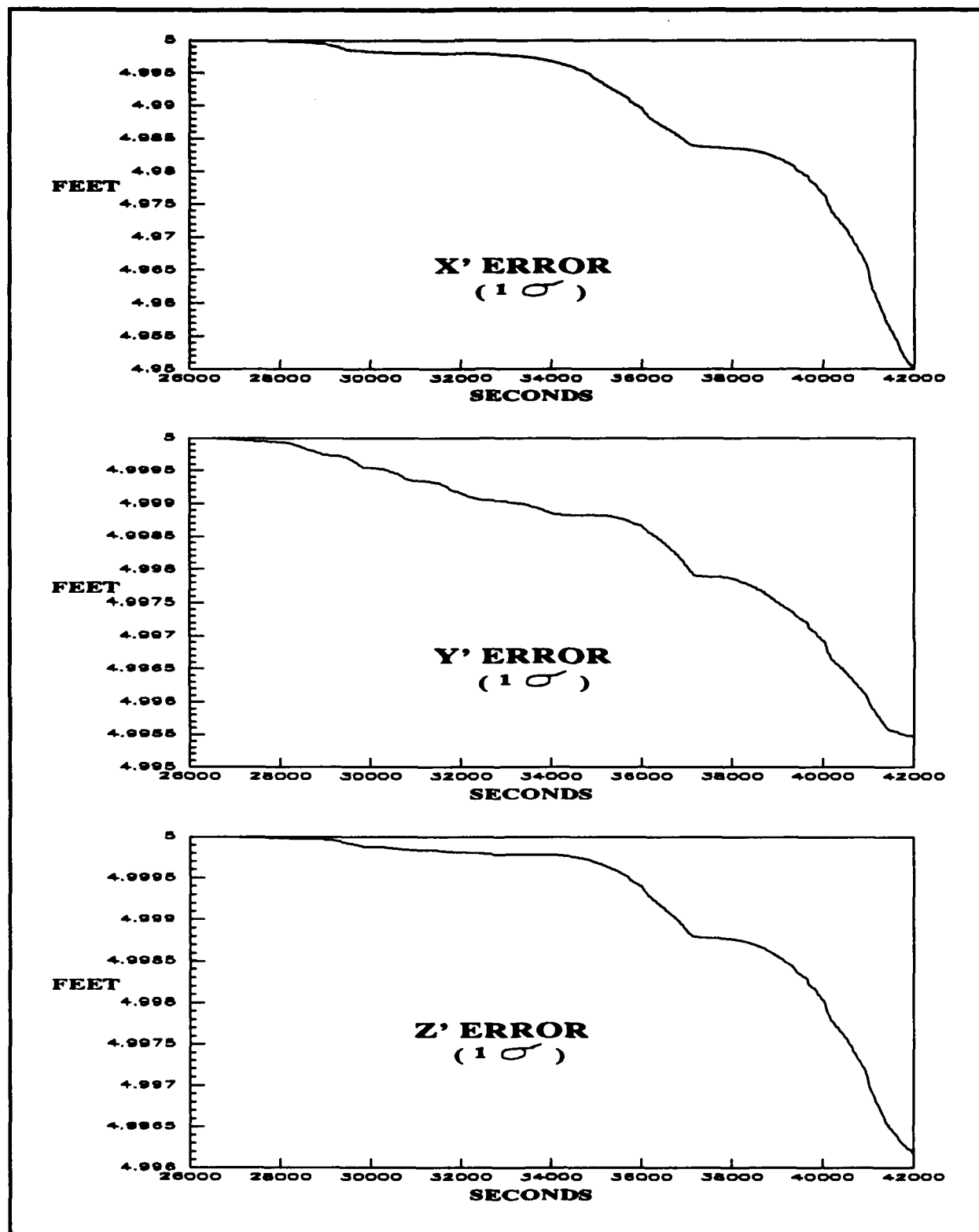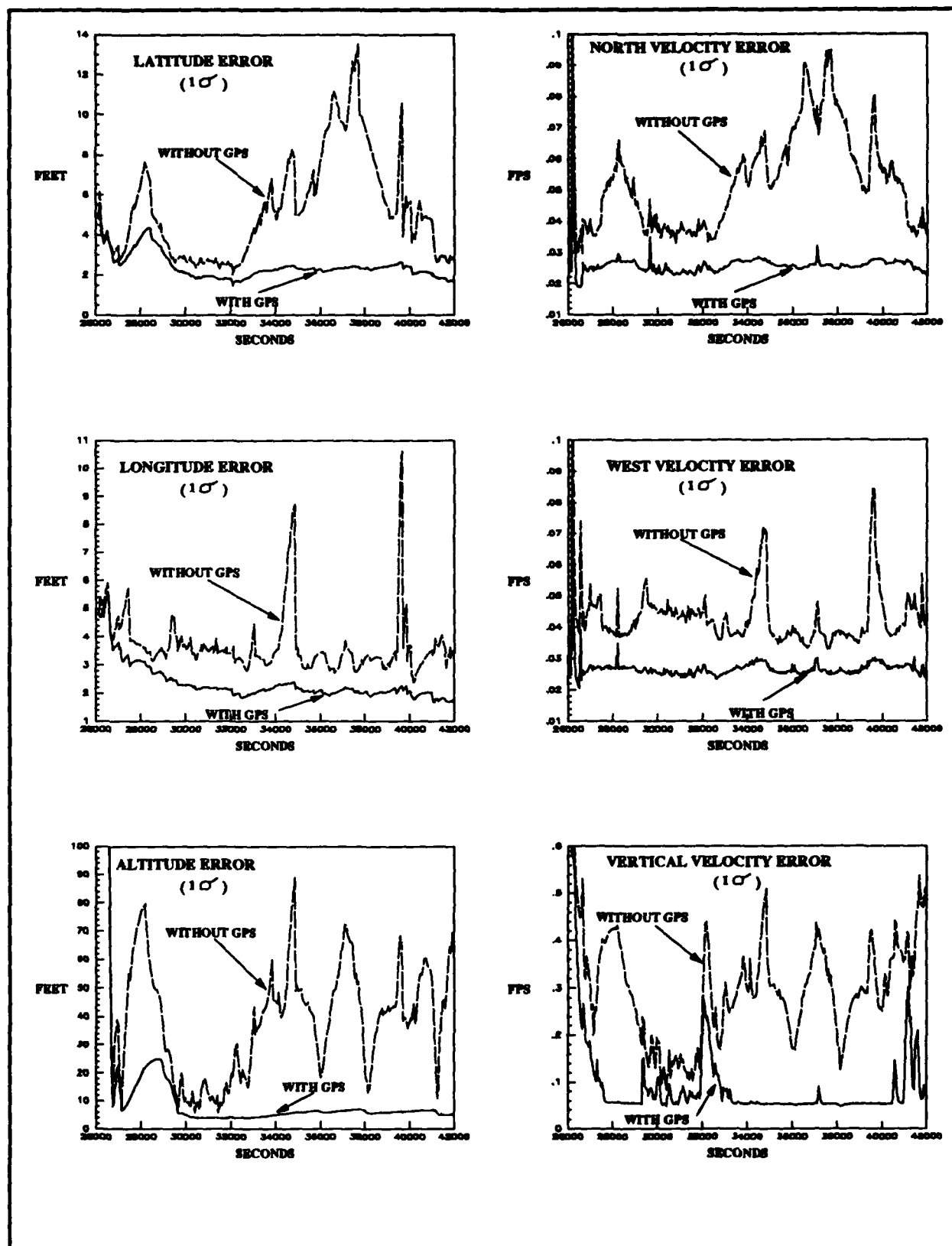
Figure 14. E-Frame Orbit Errors

Figure 15. Position/Velocity 1σ Value Comparison

6. CONCLUSIONS

6.1 INS/Transponder

Based on the residual and correlated error characteristics, the shaping filter models chosen for the transponder survey and atmospheric errors improve the Kalman filter performance. The time histories of these errors indicate that they are observable and the EKF is estimating their magnitudes. The absolute accuracy of these estimates can not be determined at this time. However, in an attempt to quantify the increase in performance of the full-ordered EKF filter, position estimates are differenced with the current CIRIS system. Results of this comparison are presented in Table 1.

Table 1
Position Error State Differences

Position Error States	Mean Difference		1σ Value Difference	
	Mean ft	1σ Value ft	Mean ft	1σ Value ft
Latitude	+3.37	7.98	+0.03	0.42
Longitude	+5.73	10.29	0.00	0.39
Altitude	+25.66	63.86	+6.82	5.04
Note: All differences are "Truth" - CIRIS				

The difference in the 1σ values are negligible. However, there are differences in the means of approximately 3 ft in latitude, 6 ft in longitude, and 26 ft in altitude. The range residual characteristics indicate a closer match between full-ordered filter model and the actual physical errors (compared to current CIRIS). This difference is interpreted as a step towards the correct model of the actual error dynamics and statistics as well as an increase in overall filter accuracy. The magnitude of the increase in accuracy is well within the current CIRIS accuracy tolerances and are reasonable for this full-ordered model.

6.2 INS/Transponder/GPS

The GPS aided CIRIS system promises significantly increased accuracy and eliminates accuracy degradation in the areas of poor transponder coverage. This system gives CIRIS the flexibility for a wider operational use, such as over water operations which are currently limited due to poor lack of transponder coverage.

The 98-state filter developed in this research can be applied immediately. As soon as GPS is installed and pseudo-range measurements become available, the fully integrated INS/transponder/GPS advanced CIRIS II can be implemented in a post-processing mode. When the analysis tools are modified to permit the optimal smoothing operation, this will become a more powerful tool. This CIRIS II "truth" model is the basis for additional development of a GPS aided CIRIS II system. This analysis indicates that a strong improvements in CIRIS are possible. The longer term goal is to augment these error models for further and substantial improvements in CIRIS performance where the transponder and GPS both are used in relative navigation mode. Furthermore, the interferometric GPS relative navigation, as has been demonstrated by several groups, promises unprecedented units of inch accuracies. However, rigorous modeling of all the dominant error sources will continue to be essential in reaching such goals.

7. BIBLIOGRAPHY

1. Air Force Avionics Laboratory. PROFGEN - A Computer Program for Generating Flight Profiles, Technical Report AFAL-TR-76-247, November 1976. AFWAL/AAAN-2, Wright-Patterson AFB, OH.

2. Breaux, Harold J. An Efficiency Study of Several Techniques for the Numerical Integration of the Equations of Motion for Missiles and Shell, Report No. 1358, Ballistic Research Laboratories, Aberdeen Proving Ground, Maryland, February 1967.

3. Britting, Kenneth R. Inertial Navigation System Analysis, New York: Wiley-Interscience, 1971.

4. Butler, R. R. And Rhue, G. T., "Kalman Filter Design for an Inertial Navigation System Aided by Non-Synchronous Navigation Satellite Constellations," Masters Thesis, Air Force Institute of Technology, Wright-Patterson AFB, Ohio, March, 1974.

5. Carlson, Neal A. And Stanton H. Musick. MSOFE User's Manual: Multimode Simulation for Optimal Filter Evaluation, October 1987. Contract F33615-86-C-1087, Subcontract 2013-S1, Avionics Lab, AFWAL/AAAN-2, Wright-Patterson AFB, Ohio.

6. Cox, D. B. "Integration of GPS with Inertial Navigation Systems," Global Positioning System, Papers Published in Navigation, Volume I, The Institute of Navigation, Washington, D.C., 1980.

7. Cubic Corporation. Range/Range-Rate Subsystem (RRS) for the Completely Integrated Reference Instrumentation System (CIRIS), AFSWC TR-7321, Cubic Corporation, 9233 Balboa Avenue, San Diego, Ca., August 1973.

8. Defense Mapping Agency. Department of Defense World Geodetic System 1984. Defense Mapping Agency Technical Report, No. DMA TR 8350.2. Washington, D.C., 30 September 1987.

9. Dyrd, D. Litton Design Engineer, Telephone Conversations, Litton Guidance and Control Systems, Woodland Hills, CA., Comm: 818-715-2991, April 1987.

10. Guidance and Control Division. LN-39 Standard Inertial Navigation System AN/ASN-141, Technical Description, Litton Systems INC., 5500 Canoga Avenue, Woodland Hills, Ca., September 1987.

11. Guidance Test Division. "CIRIS II Test Summary Report," In-House Report, CIGTF, 6585th Test Group, Holloman AFB, NM, May 1988.

12. Guidance Test Division. "The Completely Integrated Reference Instrumentation System (CIRIS)," Unpublished Contractor Informational Pamphlet, CIGTF, 6585th Test Group, Holloman AFB, NM.

13. Huddle, James R. "Inertial Navigation System Error Model Considerations in Kalman Filter Applications," Advances in the Techniques and Technology of the Application of Nonlinear Filters and Kalman Filters, AGARD-AG-256, Advisory Group for Aerospace Research and Development, 13-1:13-19 (March 1982).

14. Intermetrics Incorporated. Computer Program Detailed Technical Description CEI-II-72-B Post-Flight Processor for CIRIS, Volume III, Part II, Contract End Item Specification, Intermetrics Incorporated, Cambridge, MA, 7 May 1974.

15. Lewantowicz, Lt Col Zdzislaw H. Deputy Head, Department of Electrical and Computer Engineering, EENG635 and EENG735 Course Notes, Air Force Institute of Technology, Wright-Patterson AFB, Oh, 28 March thru 21 April 1988.

16. Maybeck, Peter S. Stochastic Models, Estimation, and Control, Volume I, New York: Academic Press, 1979.

17. Maybeck, Peter S. Stochastic Models, Estimation, and Control, Volume II, New York: Academic Press, 1982.

18. Milliken, R. J. And C. J. Zoller. "Principle of Operation of NAVSTAR and System Characteristics," Global Positioning System, Papers Published in Navigation, Volume I, The Institute of Navigation, 3-14 (1980).

19. Simkin, Gordon. CIRIS Post-Flight Performance Engineer, Personal Interviews, Central Inertial Guidance Test Facility, Holloman AFB, NM, 1-3 March 1989.

20. Smith, Carl O. Performance Characteristics of Integrated Inertial Navigation Systems, Masters Thesis, Air Force Institute of Technology, Wright-Patterson AFB, Oh, December, 1985.

21. Solomon, Joseph K. "CIRIS Special Study," Final Report, EENG 699, Air Force Institute of Technology, Wright-Patterson AFB, OH, March 1989.

22. Solomon, Joseph K. "Development of the Extended Kalman Filter for the Advanced Completely Integrated Reference Instrumentation System (CIRIS)," Maters Thesis, Air Force Institute of Technology, Wright-Patterson AFB, OH, March 1989.

23. Speiser, M. "Systems Engineering Analysis Report for the F-16 Standard Inertial Navigation Unit," Litton Guidance and Control Systems, Woodland Hills, CA.. Revision B, March 1985.

24. Walker, Robert, Charles Gregory, and Sunil Shah. "MATRIX$_x$: A Data Analysis, System Identification, Control Design, and Simulation Package," Control System Magazine, Volume 2, Number 4, 30-36 (December 1982).

THIS PAGE LEFT INTENTIONALLY BLANK

THIS PAGE LEFT INTENTIONALLY BLANK

THIS PAGE LEFT INTENTIONALLY BLANK

GENERAL DYNAMICS SERVICES COMPANY

P.O. Box 1488, Yuma, Arizona 85366-1488 - 602/328-2541

VERIFICATION OF A GPS TSPI SYSTEM

By
Darwin G. Abby
General Dynamics Services Company

VERIFICATION OF A GPS TSPI SYSTEM

Darwin G. Abby
General Dynamics Services Company

ABSTRACT

Tests were conducted at the US Army Yuma Proving Ground (USAYPG)to verify the accuracy of a Navstar Global Positioning System (GPS) Time Space Position Information (TSPI) system which uses a GPS Joint Program Office 5 channel 3A receiver in the test vehicle. The TSPI for a dynamic vehicle is produced using post-processing software available in the ground station used to collect the Differential GPS corrections. The YPG laser tracking system was used as truth to verify the position accuracy. Velocity accuracy was verified using data from a Draper Laboratories test conducted on a special laser range in the Northeast US. Position accuracies of less than 4 meters and velocity accuracies under 0.1 meters/second were demonstrated. A brief description of the GPS airborne system and the ground station is presented. The system was developed under contract to the GPS Joint Program Office to support test and evaluation of new navigation systems or other weapon systems requiring TSPI.

INTRODUCTION

Testing of todays advanced weapon systems which include sophisticated aircraft avionics packages, highly accurate navigation sensors, terrain matching devices, etc. has placed new requirements on test support activities. Developers require high accuracy truth reference systems over extended areas in operational environments where topography and ground cover are representative of targets and the test vehicle can maneuver under operational dynamics. The shear magnitude of items to be tested necessitated developing a TSPI system that removed the restrictions of operating on test ranges. The data collecting, processing and analysis has become more complex and time consuming.

One of the potential solutions for providing an accurate and autonomous positioning reference is Differential GPS. The use of this concept for test applications has been operational on a variety of projects for the Joint Program Office (JPO) since the early 1980's. The first Differential GPS test which was a real time system was performed at USA Yuma Proving Ground under JPO auspices in December 1979. The Range Applications Joint Program Office (RAJPO) is developing a complete family of Differential GPS equipment for test and training applications.

Differential GPS provides a position reference of $\pm$ 3-5 meters rms over a large geographic area in a passive mode (non real-time) with any GPS equipped vehicle or real time if a data link is added. A significant advantage of Differential GPS is it is extremely cost effective. One ground station which will support one user costs less than $200K. The operational costs consist of one operator and data processor to support a complete test program. The required ground station can be deployed to any location in the world to provide complete test support for a test project as long as an accurate survey marker is available.

This paper describes an operational system built in 1987 to support a test program and presents

data used to verify the system along with other data verification examples. The design concept was presented in a paper by J. Robbins at the Institute of Navigation, Satellite Division Technical Meeting, September 1987. This data processing is accomplished post-mission on the same Differential GPS ground station computer. If a program required real-time support, a data link could be added.

The use of Differential GPS requires a GPS receiver on the test platform. That receiver can either be installed specifically to support the test program or it can be the existing operational receiver on the platform. This offers the potential of minimizing modifications in support of test requirements and makes every GPS equipped vehicle a test platform. This approach will be demonstrated by investigating some F-16 data in this paper. This approach provides an alternate to that being taken by the Range Applications Joint Program Office (RAJPO) where specifically designed GPS equipment is being developed for test and training applications.

SYSTEM DESCRIPTION

The functional diagram of a complete system is shown in Figure 1. The two major subsystems are the test platform equipment and the ground station.

TEST VEHICLE EQUIPMENT

The two basic components are the GPS receiver and a data recording system. As stated earlier, many test vehicles will have GPS receivers on them and eventually they all will. The only item then which would require installation would be the data recording hardware. If the test platform has an Inertial Navigation System (INS) on board as most Air Force Aircraft do, the raw INS velocities can be used to aid the Differential

GPS TSPI. An aided solution will be described later.

GPS RECEIVER

The current software is programed to accept data from the Rockwell/Collins (R/C) Phase II and Phase III receivers and the Texas Instruments TI-4100 receiver. The raw pseudo-range and delta-range measurements required for processing are available via the instrumentation port on these receivers which is an RS-422 interface. The ground station front end software can be readily adapted to accept pseudo range and delta range measurements from other GPS receivers/sensors.

DATA RECORDING

Data can be recorded either directly off the RS-422 interface to a digital recording device or through a translator which puts the data on the 1553 bus where it can be pulled off for recording. On the systems currently deployed, the RS-422 output goes to a PC Buffer Box (286 or 386 PC) where it is recorded on hard disk or Bernoulli 5 1/4 inch removable disks. PC's used in the tests reported here included an IBM Industrial PC-XT upgraded with an 80386 processor, IBI industrial PC-AT and an Industrial PC-AT built by MILTOPE Corporation. On the F-16, data can be collected either via telemetry or sent to the 1553 bus via a translator and recorded on an analog tape. The B-52 GPS data was recorded on a 9 track Emerson Digital Tape Recorder.

GROUND STATION

HARDWARE

The ground station configuration is shown in Figure 2. It consists of four principle compo-

Figure 1
DIFFERENTIAL GPS SYSTEM

Figure 2
DATA ANALYSIS STATION
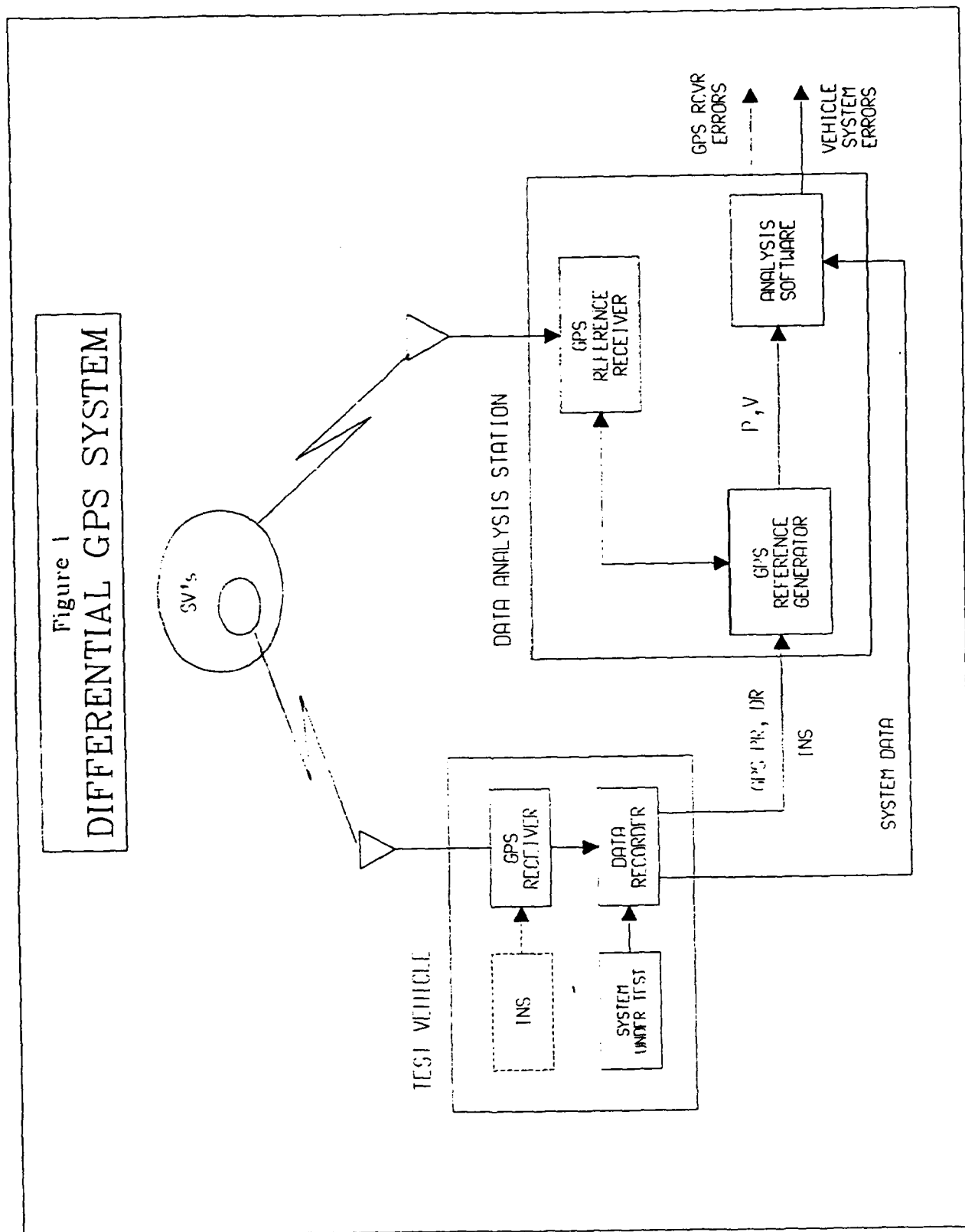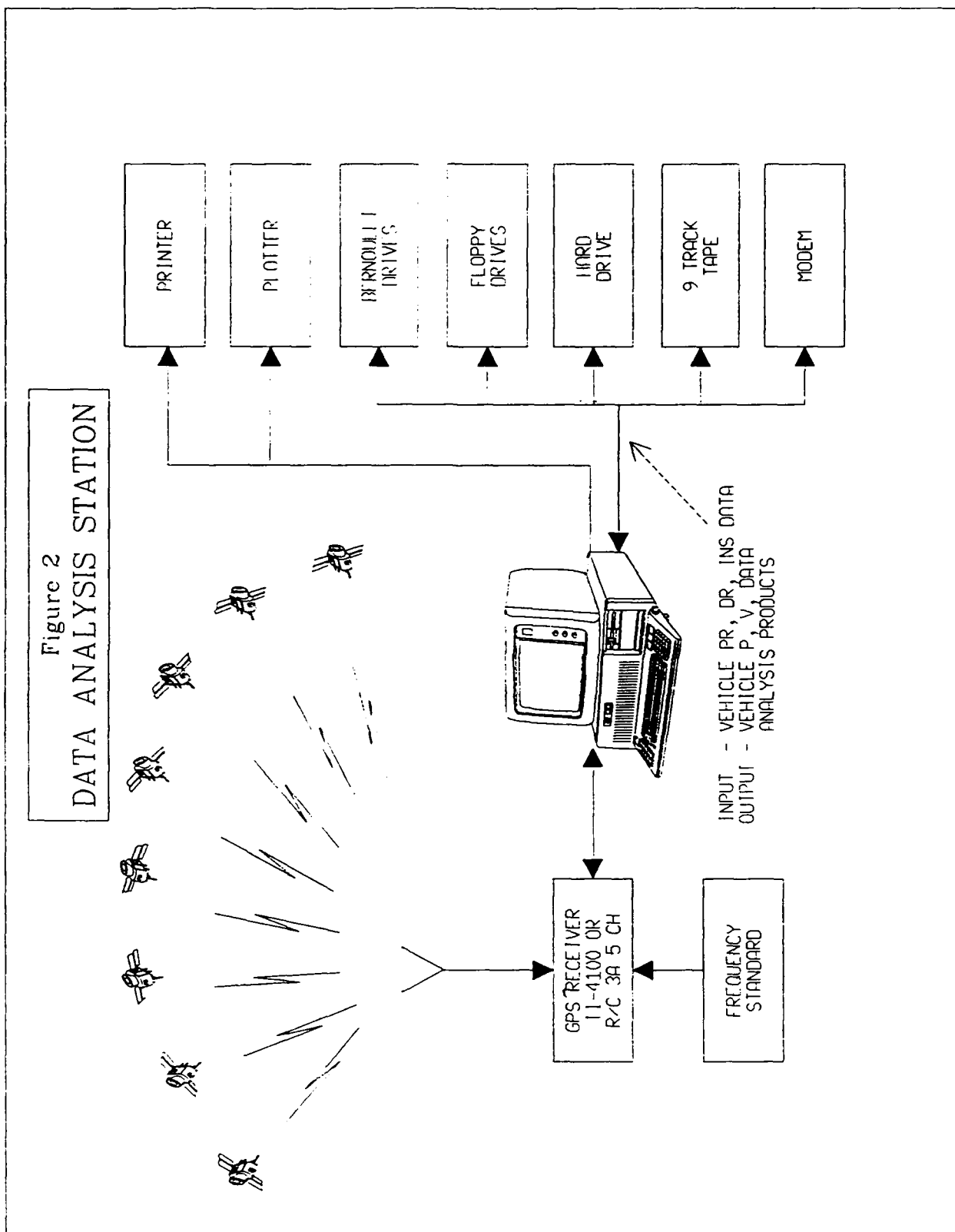
nents: GPS receiver, GPS antenna, computer and assorted input/output devices. The nomenclature associated with the ground station by the JPO is Data Analysis Station (DAS).

The GPS receiver is a TI 4100. It is a single-channel, two- frequency, digital multiplexing receiver with a navigation processor. The receiver is designed to track four satellites on both frequencies in a very rapid multiplexing mode such that it responds much like a four channel receiver. Since the ground station receiver must track all visible GPS satellites, external commands from the computer direct the receiver to step through a series of four different satellites at selected intervals. The raw pseudo-range and delta range measurements from up to 12 satellites are sent to the external computer for recording. The standard TI-4100 antenna is used and can be placed anywhere within 200 feet of the receiver where clear visibility to the satellites is available and objects which could cause multipath are eliminated.

The computer is a PC-AT which has been upgraded with a 80386 processor. Functions include control of the receiver, selection of satellites to be tracked, correction of measurements for propagation effects, computation of the position and velocity of the test platform in the desired coordinate system and communication with other systems and the operator through the input/output devices. In addition, the processor is used to process the TSPI data and the data from the system under test to produce data products for use in analysis and reporting.

The input/output devices include those items shown in Figure 2. The primary data recording system is the Bernoulli removable disk units either 8 or 5 1/4 inch size. The TSPI output for use by other agencies can be provided on either 9 track tape or Bernoulli disks. The plotter is used to generate data products, plots, etc. for analysis.

A task is currently underway to develop a new ground station which will replace the TI-4100 receiver with a Rockwell/Collins 3A receiver. The computer is being upgraded to a Compaq 386/25. This system is currently under test and four units will be delivered to the JPO in late July 1989.

SOFTWARE

The software includes three major programs: a tracking program, reference generator and an analysis program.

The tracking program controls the GPS receiver and processes measurements made at a known location to produce observed Range Errors (ORE) for each visible GPS satellite. The program includes receiver operations, space vehicle operations and autotrack. Receiver operations performs control of the TI-4100 receiver via the Control Display Unit (CDU) port and recovery of data via the instrumentation port. Space vehicle operations uses almanacs and operator inputs to create files for autotrack and general mission planning use. The autotrack function performs automatic tracking control and data processing in response to the tracking schedule generated by the space vehicle operations program.

The reference generator is a post-mission process which involves applying the ORE's to the pseudo-range and delta range measurements recorded by the GPS receiver in the test platform (the differential process) and then processing the corrected measurements in a navigation filter to generate position and velocity or Time Space Position Information (TSPI) of the test platform. A closed-form solution for determin-

ing position, an unaided Kalman filter solution and an inertially aided solution (if INS data is available) are generated. A check of the processing is performed by comparing the unaided position output with the deterministic solution and the aided Kalman is checked against the unaided Kalman states. For details on this implementation, see reference 1.

The analysis program accepts data from other test items on the test platform, such as the integrated system navigation solution output, INS or any other positioning system and processes it against the GPS derived TSPI. Error plots, statistics, listings, and other output are generated for analysis and subsequent report generation. Additional plots and analysis can be provided ad hoc to investigate anomalies.

TEST DESCRIPTIONS

The missions selected are directed at meeting the following objectives of this paper:

1. Verify the accuracy of GPS TSPI.
2. Evaluate the utility of GPS TSPI.
3. Demonstrate that GPS TSPI is independent of GPS aided navigation systems.

Data from six different test missions is included for the following purposes. First, the missions are conducted on a variety of test platforms with different conditions and dynamics. Second, much of the verification process has been accomplished piggy back on missions where primary objectives were not GPS TSPI verification therefore there was limited control of the scenarios and equipment configuration. And thirdly, as in all test programs, to get all systems up and running simultaneously is often not achieved. A summary of the missions is shown in Table 1.

The test data used to verify the operational readiness and accuracy of the TI-4100 DAS was collected on a B-52 mission flown over the YPG

Table 1

MISSION SUMMARY

TEST PLATFORM	DATE	GPS RECEIVER	MISSION DURATION	TSPI SOURCES
B-52	4 Nov 88	R/C 3A	2h 10min	Laser,GPS
M-35	8 Dec 88	R/C 3A	2h	Laser,GPS
Bus	5 May 89	R/C 3A	3h	Laser,GPS
F-16	29 Jun 89	R/C 3A	30min	Laser,GPS
RC-135	24 Feb 89	TI-4100	2h 30min	Laser,GPS
RC-135	8 Jun 89	TI-4100 & R/C Phase II	6h	GPS

range on 4 November 1988. This particular mission and platform were selected because the primary operational platform, the RC-135, was unavailable due to other priorities and the B-52 dynamics are similar to the dynamics of the operational program supported by the DAS. Verification of a 3 satellite/clock aided TSPI capability was performed on the 24 February 1989 RC-135 mission. The data presented here is only the 4 satellite data. The data from the other missions included demonstrate the applicability over a range of platforms.

Velocity verification has been difficult due to the lack of available truth reference systems accurate enough to verify GPS velocity which is specified to be 0.1 meter/sec. The YPG laser trackers velocity accuracy has been validated to an accuracy of approximately 0.2-0.3 meters/ sec. A piggy back data point was achieved in 1984 on a B-52 mission where GPS velocity was evaluated against the Spin-Geans INS velocity to be better than 0.1 meters/sec. A second data point was obtained by obtaining copies of raw data and a laser-inertial reference trajectory producded by Draper Laboratories on a test program in 1985. This data is described in the test results section.

B-52

The B-52 mission was a GPS weapon delivery mission with releases at 2,000 feet AGL. The aircraft flew a racetrack pattern at velocities up to 390 knots. The GPS raw data was obtained via the Receiver Instrumentation Port and recorded on a digital tape recorder. The YPG lasers tracked the aircraft continuously for the duration of the test.

M-35 AND BUS

The M-35 is an Army 2 1/2 ton truck which carries an instrumented shelter for test purposes. The Bus is an instrumented greyhound bus provided by CIGTF. Both of these vehicles operated on road courses at YPG and were tracked by a single laser as the truth reference. Maximum speeds achieved by the vehicles were 20 mph for the M-35 and 30 mph for the bus. R/C 3A receivers were mounted in the vehicles and raw GPS data was recorded on Bernoulli disks. The bus mission was a Selective Availability/Anti-Spoof (SA/A-S) test which included both authorized and unauthorized receivers on board. The data presented is from the unauthorized receiver an includes only the periods when SA was not on. The GPS reference station was located at YPG.

F-16

The F-16 mission on 29 June 1989 was a weapon delivery mission of 30 minutes duration. Six bombs were dropped individually straight and level at an altitude of 1,000 feet AGL with a high dynamic pullout after each release to 6,000 feet AGL.

RC-135

The primary purpose of the 24 February 1989 mission was to verify the TI-4100 3 SV/Clock aided performance. The RC-135 flew a racetrack pattern over the YPG range for 2 hours and 30 minutes with continuous laser track. The mission was flown during the 4 SV window therefore the 3 SV/Clock aided results were obtained by eliminating one of the measurements from the TI-4100 data in post-processing. TI-4100 4 SV data was available for processing as well which is what is shown here. This data provides results from another GPS receiver other than the Rockwell/Collins.

The 8 June 1989 RC-135 mission provides an opportunity to compare GPS TSPI solutions

from two separate GPS receivers simultaneously which in this case were the TI-4100 and a Rockwell/Collins Phase II receiver. Unfortunately, due to scheduling and equipment problems, there has not been an opportunity to collect data from both receivers on a YPG range mission. This mission was an operational mission of 6 hours duration flown with enroute navigation type dynamics within the western United States.

TEST RESULTS

For each of the six missions shown in Table 1,

GPS TSPI solutions were derived. All of the missions selected were flown over the YPG laser range except one and in that case, two GPS receivers were on board so the two GPS TSPI solutions were compared. The results of the position and velocity comparisons are shown in Tables 2 and 3 respectively. There are three sections in the position table. The first shows the comparison of GPS TSPI as derived from the R/C 3A receiver with the YPG laser Real Time Estimate (RTE). This data is also shown in Figure 3. The second section shows the comparison of GPS TSPI as derived from a Texas Instruments TI-4100 GPS receiver and the RTE

TABLE 2

POSITION COMPARISONS

		RMS POSITION DIFFERENCES				
TEST PLATFORM	DATE	HOR	VER	3D	LEP	CEP

1. R/C 3A GPS TSPI vs LASER

M-35	8 DEC 88	2.0m	2.7m	3.4m	1.8m	1.6m
BUS	5 MAY 89	1.5	2.9	3.3	1.8	1.2
B-52	4 NOV 88	2.6	4.0	5.0	2.6	2.7 *
F-16	29 JUN 89	2.0	3.8	4.3	2.0	1.6

2. TI-4100 GPS TSPI vs LASER

RC-135	24 FEB 89	3.3	3.9 \	5.1	2.6	2.8 **

3. TI-4100 GPS TSPI vs R/C PHASE II GPS TSPI

RC-135	8 JUN 89	2.0	3.3	3.9	2.3	1.7

Note: * Reference 3
    ** Reference 4

and the third section shows the comparison of GPS TSPI as derived from a TI-4100 and the R/C Phase II GPS receivers.

All the results are shown as RMS errors and probable errors for the position comparisons. At this point, it is not possible to address accuracy since the laser trajectory is only good to approximately 2-3 meters RMS. Other problems associated with the RTE are addressed later in this section. Dedicated tests are scheduled for the fall of 1989 to evaluate GPS TSPI against other systems such as cinetheodolites and the CIGTF Completely Integrated Reference and Instrumentation System (CIRIS).

The slightly better results from the Bus and M-35 shows the performance for a very low dynamic ground vehicle. The errors for the aircraft which have higher dynamics are slightly larger. It is dificult to isolate which system, laser or GPS TSPI, is most effected by the increased dynamics.

The F-16 data represents only the dynamics of a low-medium aircraft even though is was performing high dynamic maneuvers because of the following. At this time, the GPS TSPI is unaided and GPS measurements are only used when the receiver is tracking four satellites in state 5 on all four channels. Therefore, the GPS TSPI is only available during low to medium dynamics since in the case of the F-16 doing acrobatics, it will lose satellites for short periods. The next stage of development in the GPS TSPI is to include raw INS velocity measurements and generate an aided solution which should provide near 100% coverage.

The data shown in section 2 of Table 2 shows a comparison of TI-4100 GPS TSPI with the YPG laser RTE. The results are somewhat higher but

Figure 3

R/C 3A GPS TSPI vs LASER

RMS POSITION DIFFERENCES
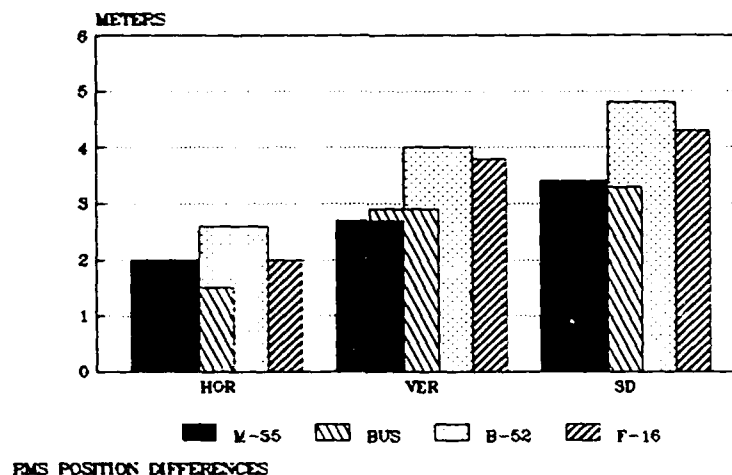
still comparable.

The third section of Table 2 shows a comparison of TI-4100 GPS TSPI with R/C Phase II GPS TSPI over a six hour operational mission. Figure 4 shows these results in comparison to the four R/C 3A GPS TSPI - laser comparisons. The difference between the two GPS systems is slightly better than the GPS vs laser comparisons.

Table 3 presents a summary of the velocity comparisons. The problem with these comparisons is that the laser RTE velocity accuracy is not as good as the specified GPS accuracy. The GPS velocity accuracy is specified at 0.1 meter/second while the laser velocity is estimated to be good to 0.2-0.3 meters/second and can be much higher in many cases.

Section 4 of Table 3 on the other hand shows the results of a comparison of GPS TSPI velocity with a highly precise velocity reference generated by Draper Laboratories on a special range on the East coast. This data was processed by J. Robbins and presented in reference 5. A R/C Phase II receiver was on board the aircraft and the raw measurements were recorded. This data was used to produce a GPS TSPI solution. The Draper velocity reference was generated from highly accurate INS velocity data and an airborne laser tracking system. The standard deviations of the velocity differences between GPS TSPI and the Draper reference were 0.03-0.05 meters/second in each axis.

The horizontal RMS velocity error between the two GPS TSPI solutions of 0.2 meters/second in section 3 of Table 3 is higher than expected and reflects a sampling problem between the two systems.

Samples of the data products produced by the analysis portion of the Data Analysis Station are shown in Figures 5 and 6. Figure 5 is the error
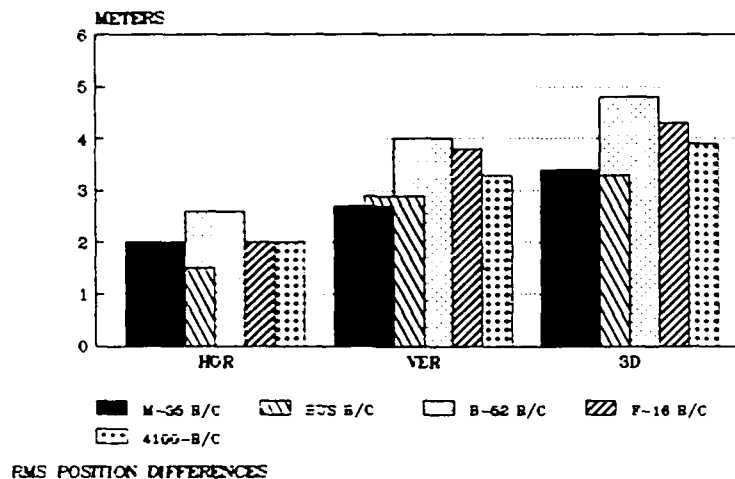
Figure 4
GPS TSPI EVALUATION

RMS POSITION DIFFERENCES

TABLE 3

VELOCITY COMPARISONS

	RMS VELOCITY DIFFERENCES			
TEST PLATFORM	DATE	HOR	VER	3D

1. R/C 3A GPS TSPI vs LASER

M-35	8 DEC 88	0.16m/s	0.08m/s	0.15m/s
BUS	5 MAY 89	0.20	0.15	0.25
B-52	4 NOV 88	0.39	0.49	0.63
F-16	29 JUN 89	0.47	0.50	0.67

2. TI-4100 GPS TSPI vs LASER

RC-135	24 FEB 89	0.41	0.43	0.60

3. TI-4100 GPS TSPI vs R/C PHASE II GPS TSPI

RC-135	8 JUN 89	0.20	0.16	0.26

4. DRAPER LABORATORY VELOCITY REFERENCE vs R/C GPS TSPI VELOCITY

RC-12	31 MAY 85	0.08	0.11	0.13 *

Note: * Reference 5

---

plot in delta x, delta y and delta z between the standard on board R/C 3A GPS navigation output and the laser Real Time Estimate (RTE). The Plots on the bottom are the horizontal and total position error differences. The statistics for three 10 minute periods are shown at the top. Figure 6 is the error plot in the same format between the R/C 3A GPS DAS TSPI and the RTE.

These samples were also selected to demonstrate the GPS TSPI ability to isolate problems with the laser tracking system. There is a significant amount of structured noise on both error plots. In order to isolate this structure, figure 7 shows Figure 6 with an overlay of laser switches (top) and retro switches as identified analytically in the YPG software (bottom).

The RTE is a single laser solution therefore as the aircraft moves around the range, the laser source changes based on distance from the laser and quality of the data. The top overlay shows those switches. There are two laser retroreflectors on the aircraft at a bottom and top location in order to provide continuous track during maneuvers. The distance between the top and bottom reflector is 4 meters.

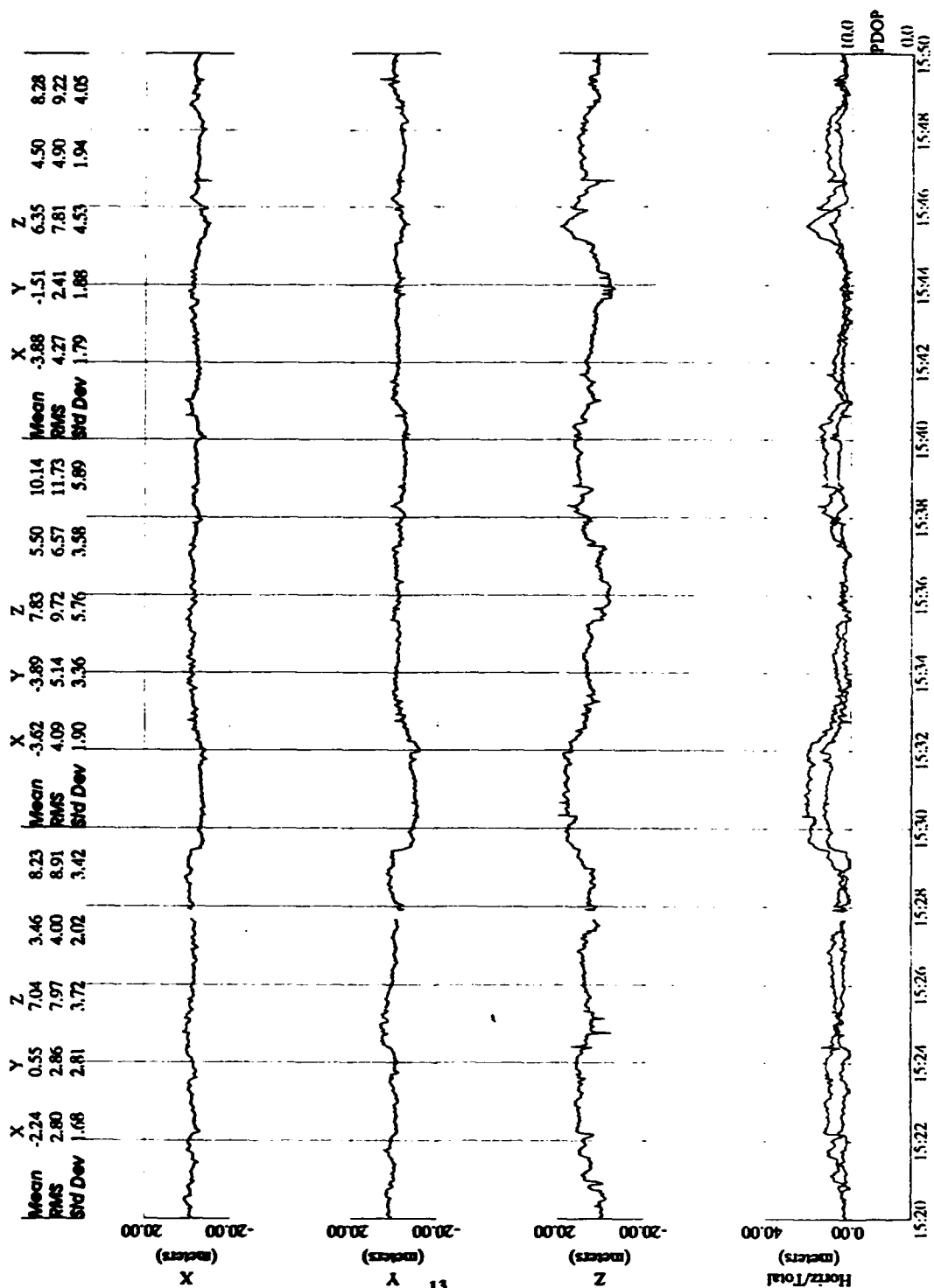FIGURE 5

11-4-88 GPS 8309RB5 B-52   GPS - RTE

FIGURE 6
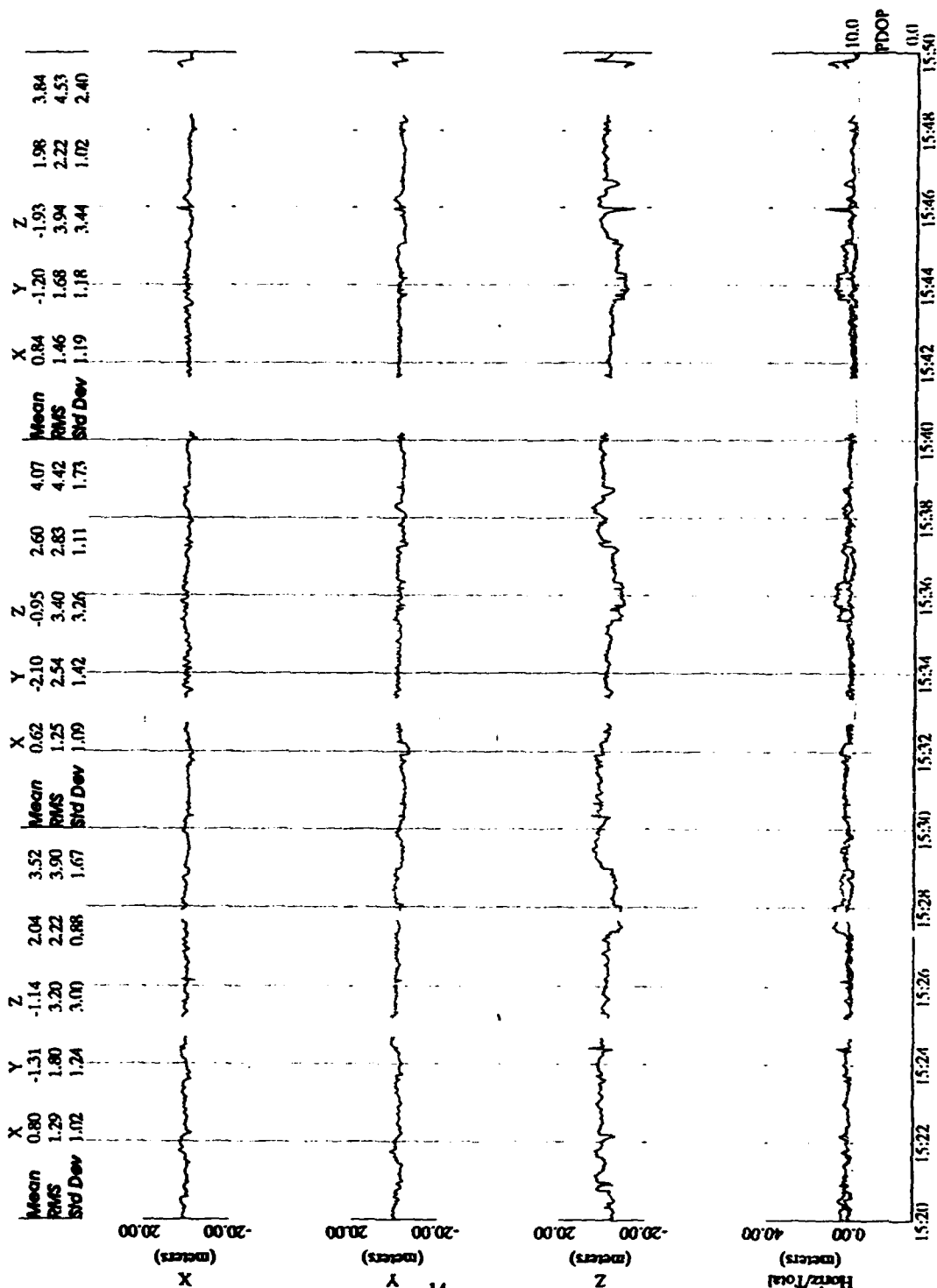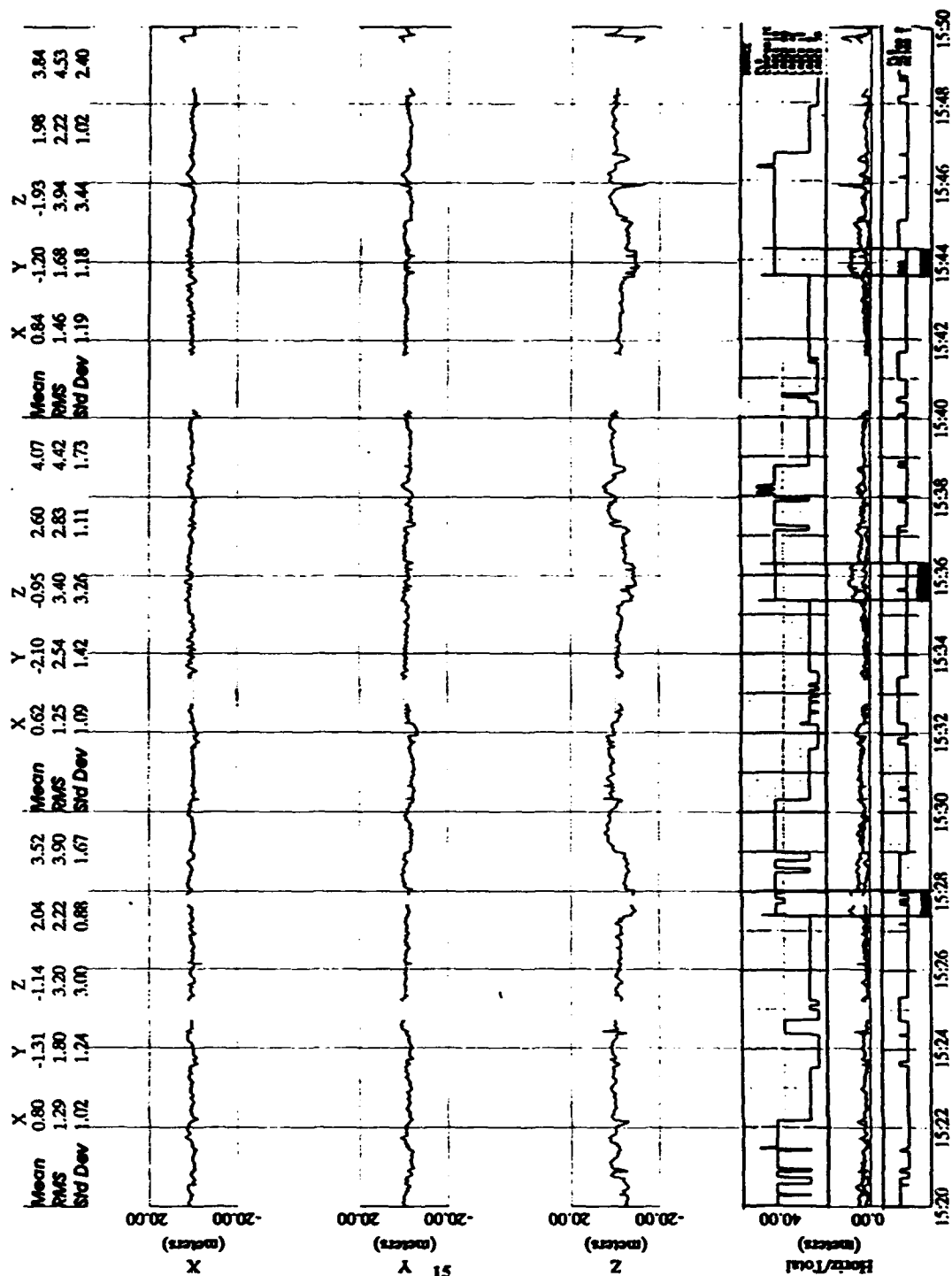
11-4-88 GPS 8309RB5 B-52 3A TSPI - RTE

FIGURE 7

11-4-88 GPS 8309RB5 B-52   3A TSPI - RTE

Much of the structure in the error plots can be associated with the laser and retro switches but there are three major problems which are identified in Figure 7. The B-52 was flying a racetrack profile and this 30 minute plot shows three trips around the racetrack. The events identified on the plots at times 1527, 1535 and 1543 all occurred at the same location in the racetrack profile. The structure in the plots at that time is in the form of a square wave. At the leading edge, there is always a switch from laser 9 to 18 and at the trailing edge, there is a retro switch from 1 to 2.

Even though the expected accuracy of the RTE is 2-3 meters RMS, there are operational anomalies which can affect the errors significantly and therefore hamper the ability to evaluate a system with comparable accuracy. In this case, there was a significant difference between the lasers 9 and 18 vertical solution adn the software model selected the wrong retro. The laser accuracy is much better than the specified GPS navigation accuracy of 16 meters SEP but the same structure can be seen in the GPS-RTE plots and obviously affects the evaluation of the on-board GPS as well.

CONCLUSIONS

A Differential GPS system which supports test project positioning requirements in a post-processing mode has been developed, verified and is operationally supporting a test program. The airborne receivers currently in operational use are the TI-4100, R/C Phase II and the R/C Phase III 3A. The current ground station which is called a Data Analysis Station (DAS) uses a TI-4100 GPS receiver, however a development is underway to replace the TI-4100 with a R/C 3A. This ground station is currently undergoing tests and four systems will be delivered to the government in late July 1989.

The GPS TSPI as compared with the YPG laser tracking range on five different test platforms of varying dynamics is good to 3-5 meters RMS in 3 dimensions. The vertical linear error probable is 2-2.5 meters and the circular error probable (CEP) is 1.5-3.0 meters. If one assumes the two positioning systems are of equal accuracy, then the GPS TSPI accuracy is on the order of a factor of one over the square root of 2 better or 2-4 meters RMS in 3 dimensions.

Additional dedicated tests are scheduled to be conducted this fall using other reference systems such as cinetheodolites and CIRIS as well as the laser trackers. At the same time, velocity verification tests will be performed by incorporating high precision INS velocity data in the reference system.

The operational platforms supported to date have been low to medium dynamic cargo type aircraft therefore the flight profile was very benign and GPS satellite tracking was continuous. To support the fighter type dynamics such as the F-16, development is being performed to include INS velocity data to aid the GPS TSPI solution. The data collected to date on the F-16 is very good but has gaps of a few seconds to 1-2 minutes where GPS measurements are not available.

The first two objectives of this paper were 1) verify the accuracy 2) evaluate the utility of GPS TSPI. The data has been presented to satisfy those objectives. The third objective was to demonstrate that GPS TSPI is independent of GPS aided navigation systems. If GPS TSPI is as good as the laser RTE which has been used to evaluate GPS aided systems, then one could conclude that the independence is proven. Although the GPS TSPI on the F-16 had gaps due to loss of GPS track, the comparisons of error plots between GPS TSPI and the F-16 Fire

Control Computer system navigation solution were identical with the laser RTE plots.

GPS TSPI provides a very cost-effective truth reference at an accuracy at least as good as 3-5 meters RMS in 3 dimensions over large operational areas anywhere there is GPS coverage. The ground station can be deployed to any location to support a test program and costs less than $200K. A test program could conduct tests anywhere in the southwestern US using the existing reference station at YPG. The capability is available for any GPS equipped aircraft whether it is the existing operational unit or a specially mounted one. The only additional requirement is a system for recording the GPS measurements. All test are currently supported in a post-processing mode however, if a project required real time support, a data link could easily be included.

ACKNOWLEDGMENTS

REFERENCES

1. Robbins, J.E., *Reference Trajectories From GPS Measurements*, NAVIGATION: Journal of The Institute of Navigation, Vol. 35, No. 1, Spring 1988.

2. *Computer System Operating Manual for the Global Positioning System Data Analysis Station*, General Dynamics Services Company.

3. *Acceptance Test for GPS Data Analysis Station*, General Dynamics Services Company, February 21, 1989.

4. *Acceptance Test Report for Three Satellite Navigation Post-processing Software Development*, General Dynamics Services Company, April 12, 1989.

5. Robbins, J.E., Briefing on *GPS TSPI Velocity Verification Results*, presented to the GPS Joint Program Office, March 1988.

THIS PAGE LEFT INTENTIONALLY BLANK

THE

AVIONICS RELIABILITY CENTER

A

RELIABILITY AND MAINTAINABILITY

TEST FACILITY

FOR

INERTIAL NAVIGATION SYSTEMS

AT THE

OKLAHOMA CITY AIR LOGISTIC CENTER

BY

MICHAEL A. FRIDAY
OC-ALC/MMIRN - ARC
TINKER AFB, OKLAHOMA 73145

PREPARED FOR THE

FOURTEENTH BIENNIAL GUIDANCE TEST SYMPOSIUM

3-4-5 OCTOBER 1989

HOLLOMAN AIR FORCE BASE, NEW MEXICO 88330-5000

ABSTRACT

This paper describes the Avionics Reliability Center, a unique inertial test facility at the Oklahoma City Air Logistics Center. This discussion includes the purpose of the facility, the test equipment being installed, the concept of operations, and the expected benefits of a reliability and maintainability oriented testing facility.

The Oklahoma City Air Logistics Center has logistic management responsibility for most of the Air Force Inertial Navigation Systems along with Flight Control Systems, compasses, and flight instruments. The Avionics Reliability Center provides the technical staff the capability to verify failure modes, isolate reliability problems, validate technical data, compare field and depot testing procedures, develop Environmental Stress Screening requirements, validate modifications or perform other special projects.

The Avionics Reliability Center occupies a section of the new wing to the Engineering Labratory on Tinker AFB in Oklahoma. The systems presently installed include the SPN/GEANS test set, a B-1B HAINS Test Station, the Optical Reference Set, Generic Test Set, the INS Reliability Analysis System, System Mock-ups, an Environmental Stress Screening Test Station Set and a Three-Axis table.

A reliability and maintainability initiative is identified by Material/Quality Deficiency Reports, high RTOKs, low MTBD, or a failure trend. Problems may be high failure rate components, hardware or software deficiencies, test procedures or equipment incompatibilities or Technical Order deficiencies. Investigations focus on problem areas and use the facility's capability to develop a course of action.

The ultimate goal of the Avionics Reliability Center is to reduce the Inertial Navigation and Flight Control System support costs. Goals of over $1 million per year per system can be accomplished through the combined effects of identifying and eliminating high failure rate components, reducing RTOKs, improving both field and depot diagnostic and repair capabilities, improving technical data and investigating Material Deficiency Reports to improve quality.

1.   BACKGROUND

The following paper describes the development, the resources and goals of the Avionics Reliability Center at Tinker Air Force Base. Until June 1988, OC-ALC/MMI did not have the technical facilities to support product improvement initiatives for Navigation and Flight Control Systems in the 6605, 6610, 6615 and 6620 stock classes. The ARC represents a $10M initial investment in the Air Force R&M 2000 initiative and Total Quality Management program.

2.   INTRODUCTION

        OC-ALC has total logistic responsibility for nearly every
Inertial Navigation System (INS) and Automatic Flight Control
System (AFCS) operated in USAF aircraft. Historically the
reliability and maintainability for these systems has been
characterized by low Mean Time Between Failure (MTBF) values,
high retest okay (RTOK) or Can Not Duplicate (CND) and high
installs/removals for field organizations. The result is high
support costs at both operational bases and depot repair
facilities. It is estimated that a 5% reduction in RTOK or a 5%
increase in MTBD can save $1M per system per year in support
cost. Further, many savings are recurring, and accrue exponen-
tially, making product improvement efforts very attractive. The
complexity of INS and AFCS require special facilities, test
equipment and a dedicated staff for organic implementation of R&M
2000 initiatives. The Avionics Reliability Center (ARC) was
conceived by the Item Management Division's Engineering and
Reliability Branch to isolate technical problems and work towards
their resolution. The ARC will focus on increasing reliability,
maintainability and reducing life cycle support costs. The
overall capabilities of the ARC include: diagnostic testing;
simulating operational environments; verification, validation and
development of Technical Orders; pre-emptive analysis; analysis
of test program sets; performance analysis and endurance testing.
The facility is currently testing Inertial Navigation Systems,
Attitude and Heading Reference Systems and the Digital Auto-
pilots. Preparation is underway for support of RLG/strapdown INS
technology, and avionic architecture which incorporates the
MIL-STD-1553 bus and MIL-STD-1750 microprocessors.


3.   CAPABILITY DESCRIPTION

3.1 FACILITY DESCRIPTION

        The Avionics Reliability Center is located at Tinker AFB,
OK. Approximately 4,500 square feet is devoted to the Center on
the main floor with the administration area located on the 2nd
floor. The Center area is arranged as shown in Figure 3.1-1.

        The ARC contains a sound isolated'room, approximately 12' x
25' within its area for housing the Environmental Stress
Screening (ESS) mechanical hardware. This equipment was
installed in a separate room because its dynamic operation is
inherently hazardous to personnel.

A 37854
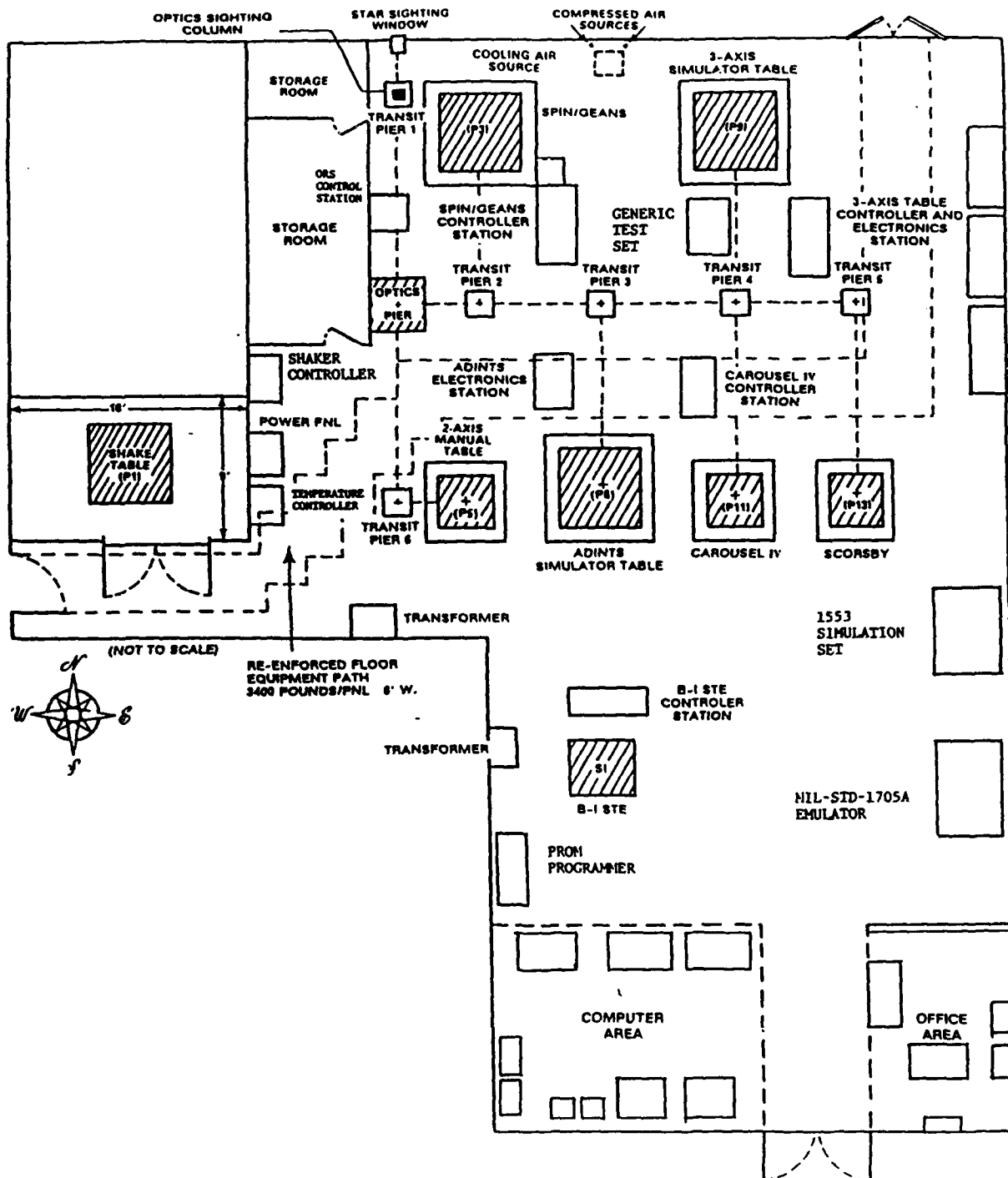
AVIONICS RELIABILITY CENTER FLOOR PLAN

FIGURE 3.1-1

The ARC was built with isolated test piers and a special optics pier as shown in Figure 3.1-1. The test piers are six foot cubed. The optics pier is six feet square, 25 feet deep and rests on a sandstone ledge. These piers provide a high degree of stability and vibration isolation. The piers are poured concrete flush with the subfloor. When required, granite blocks are used to raise the working surfaces to an appropriate level. Additionally there are transit piers which are isolated floor sections that provide a more stable and noise free surface for theodolites while performing optical transfers.

The facility is equipped with a raised computer floor. This promotes effective equipment cooling and provides a means for routing electricity, air, water and equipment interconnections. An equipment path is provided as a means for moving heavy equipment items.

Facility power which includes a variety of 60 HZ, 400 Hz, 28-Volts DC power and an emergency Uninterrupted Power System (UPS), is provided at each pier location via flexible conduit. A Halon fire suppression system, which is interconnected to facility power, activates in the event of fire alarm removing all power.

A compressed air source is also utilized for air bearing tables, equipment leveling/isolation, air drive tools and cleaning.

The ARC was designed to permit ease of configuration change due to addition of new systems or requirements. Within a few days new Peculiar Support Equipment can be put in operation.

The Optical Reference Set (ORS) (Figure 3.1-2) is an integrated system designed to provide 10 arcsecond alignments of test fixtures as referenced to true north. On the Optics Pier shown in Figure 3.1-1 is the Azimuth Standard which is calibrated and referenced to Polaris. The Sidereal Window is a motor driven portal that turns coincident with the nutation of Polaris. This configuration allows star sightings from within the building without distortion due to turbulence and refraction errors. The ORS Control Station consists of a Z-248 computer that collects data directly from the theodolite, WWV receiver, modem and marker. The Z-248 calculates true north from star sightings, corrected for time, nutation, and most' instrument/operator errors. The transit piers are used for transferring the true north reference to the test piers. The ORS represents the first automated system for Polaris observation. The system was designed to Air Force specifications, fabricated and installed by the Kearfott Navigation and Guidance Corporation in 1988.

OPTICAL REFERENCE SET
FIGURE 3.1-2

3.2 PECULIAR SUPPORT EQUIPMENT (PSE)

The facility contains both the Intermediate and Depot level diagnostic test systems for the B-52 SPN/GEANS Inertial Navigation System (INS) (Figure 3.2-1). This setup provides an ideal situation for validating Intermediate and Depot reported problems, maintaining tech data and resolving test discrepancies. The Depot test set also provides recertification. The capability exists to modify Test Program Sets (TPS) if determined necessary for special engineering investigations.
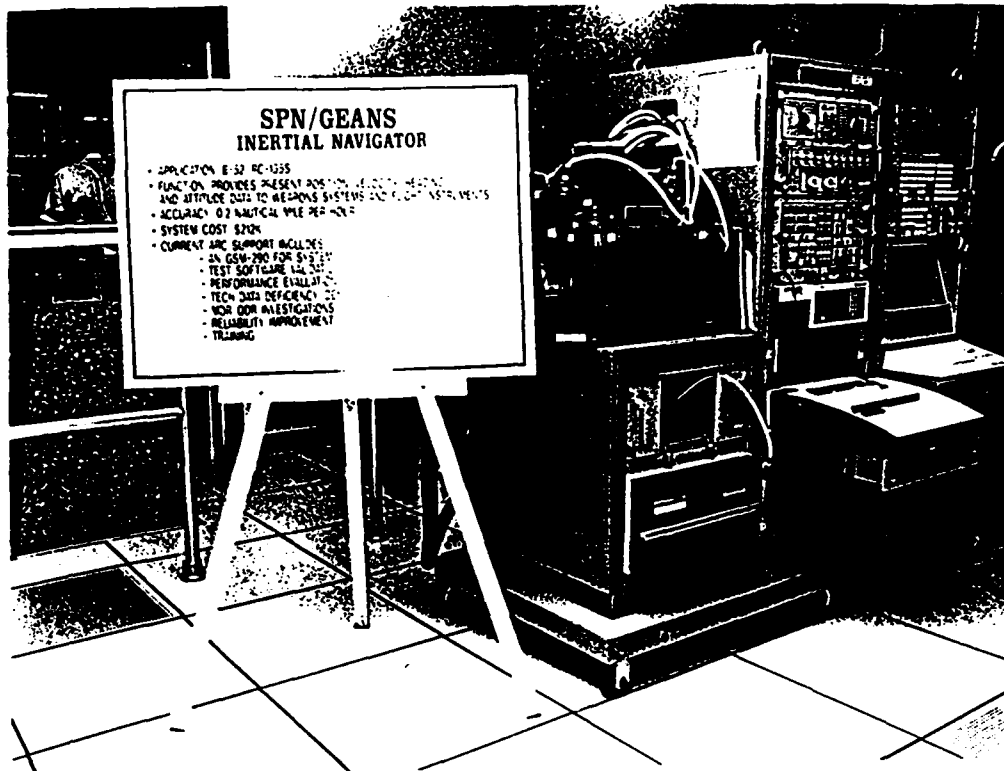
SPN/GEANS TEST STATION
FIGURE 3.2-1

The Automatic Depot Inertial Navigation Test Set (ADINTS)
consists of two-axis table, associated test station, test
adapters and TPSs. ADINTS is designed to test most of the Singer
inertial products (ARN101, KT-73, SKN 2400, HAINS). A Software
Development Station (SDS) is also being procured to enable
engineers to modify TPSs for special projects. Installation is
s. eduled for 1991.

Hot Mockup Benches are available for LN-12 (Figure 3.2-2),
LN-39 and Carousel (Figure 3.2-3) to provide a capability for LRU
fault isolation and operational ESS testing. These mockups,
which usually include flight instruments and indicators, provide
a very useful aid for training.
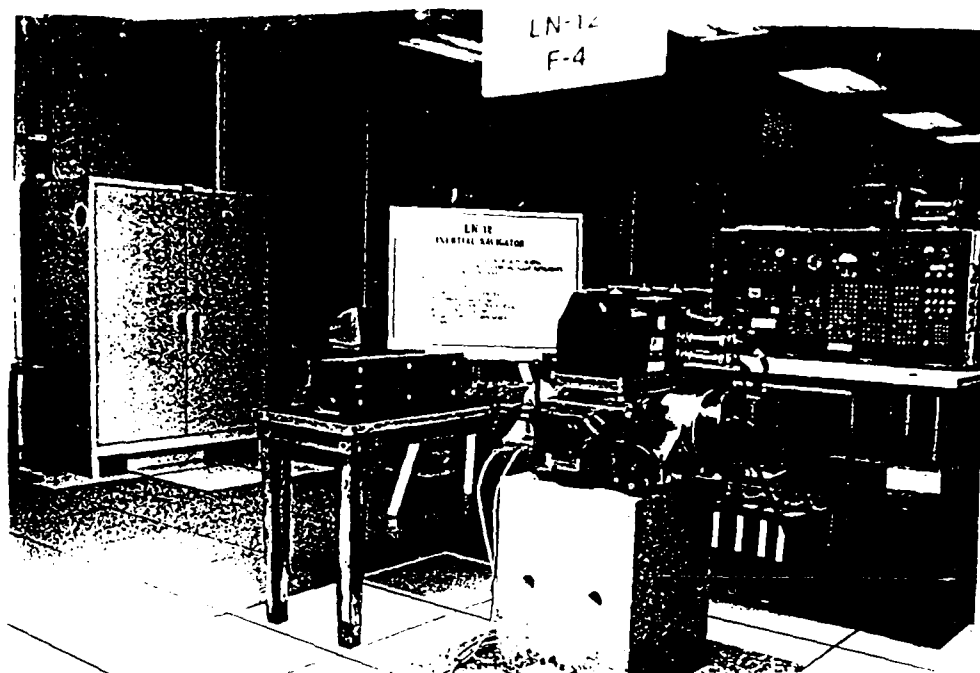
LN-12 HOT MOCKUP BENCH
FIGURE 3.2-2

The Singer B-1B STE (Figure 3.2-4) is a piece of Singer factory test equipment configured for diagnostic testing and certification of B-1B HAINS. This equipment was provided as part of the B-1B Avionics Integration Support Facility (AISF) also located within the building. Although ADINTS will be the Air Force Depot certification equipment for HAINS, the STE will be useful in resolving test deficiencies in the new depot test station.
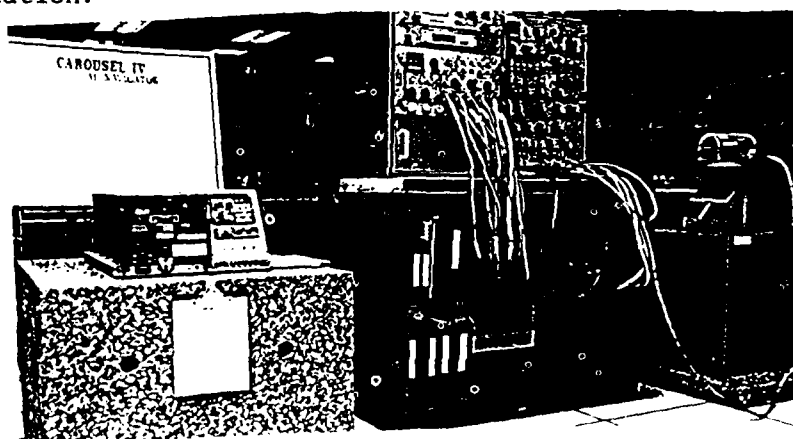
CAROUSEL HOT MOCKUP AND AHRS TEST SET
FIGURE 3.2-3
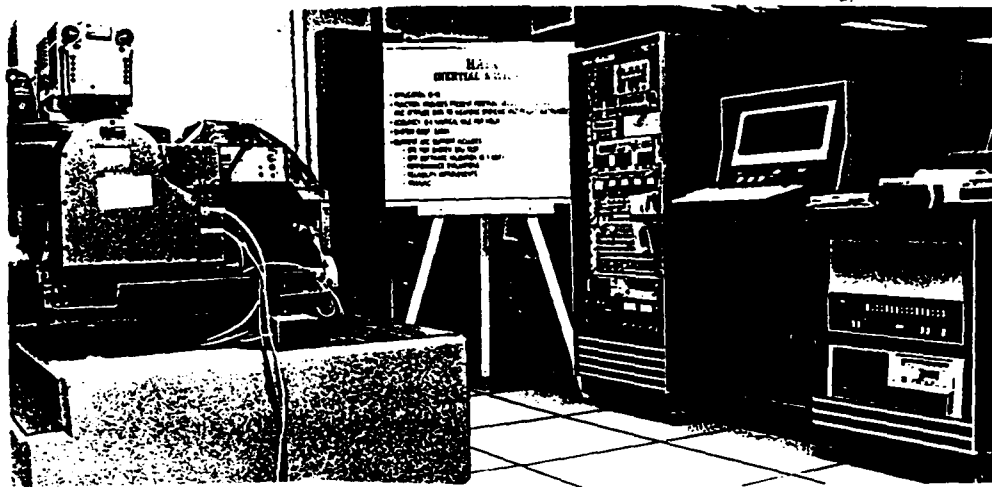
**B-1B HAINS SPECIAL TEST EQUIPMENT
FIGURE 3.2-4**

An AHRS Test Set provides a capability for Intermediate level system fault isolation of the A-10 AHARS. This set is adaptable for the entire LSI 6000 family of AHARS used on B-52, A-10 and C-141 aircraft. A Flight Control Test Set is in use for LRU testing of the new B-52 digital autopilot. This station is adaptive for the C-135 version with an additional cable set.

3.3 GENERIC TEST STATIONS (GTS)

The Generic Test Set (Figure 3.3-1 and 3.3-2) is a flexible multi-purpose test station with the capability to test multiple navigation systems. GTS is composed of a minicomputer, commercial test equipment, a signal conditioning unit (SCU) and an UUT specific personality module. The system is programmable in an enhanced Atlas derivative language called Common Test Language (CTL). The Generic Test Set concept has grown out of the need for a more flexible approach to Avionics testing. Currently, Peculiar Support Equipment (PSE) is used to test most systems. Each item of PSE is built specifically for a particular system. The tests that can be run on this equipment are usually fixed and not easily modified. In a test facility such as the ARC, a diversity of test equipment raises manpower, operating costs, training and support, as well as decreasing the overall effectiveness. The GTS concept may prove to be a cost effective alternative to PSE.

GENERIC TEST SET
FIGURE 3.3-1

3.4 ENVIRONMENTAL STRESS SCREENING (ESS)

The ARC provides the capability for in-depth R&M 2000 product improvement efforts through Environmental Stress Screening. The vibration test table and associated temperature chamber are located inside the isolation room. (See Figure 3.4-1). The associated controllers and amplifier are located adjacent to the room as shown in Figure 3.4-2. The Vibration Test Set provides for the empirical formulation of depot ESS screening requirements. This system can provide both temperature and vibration environments in a wide variety of combinations. UUTs with total weight of 100 pounds may be tested on the shaker and the temperature chamber will accommodate a package 30" x 30" x 30".
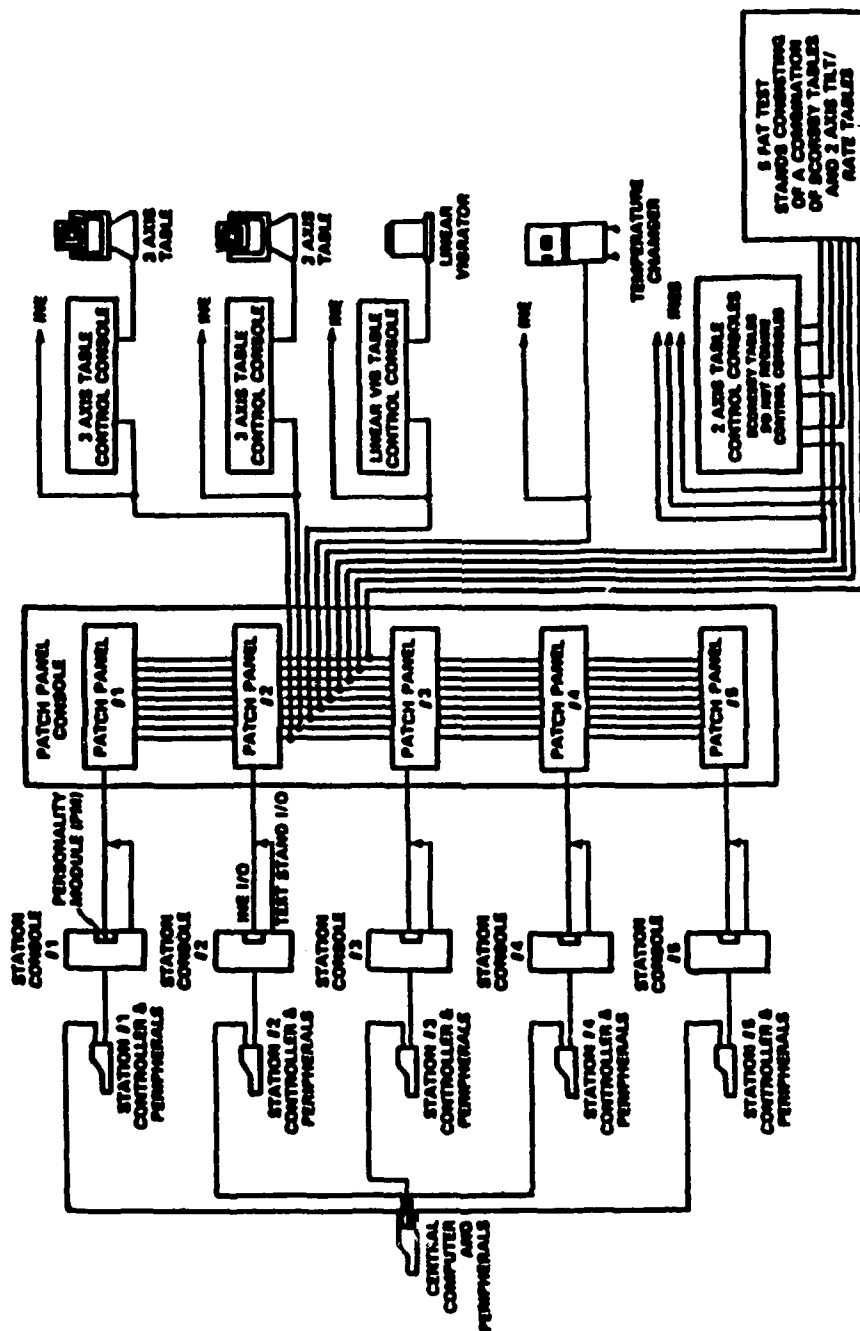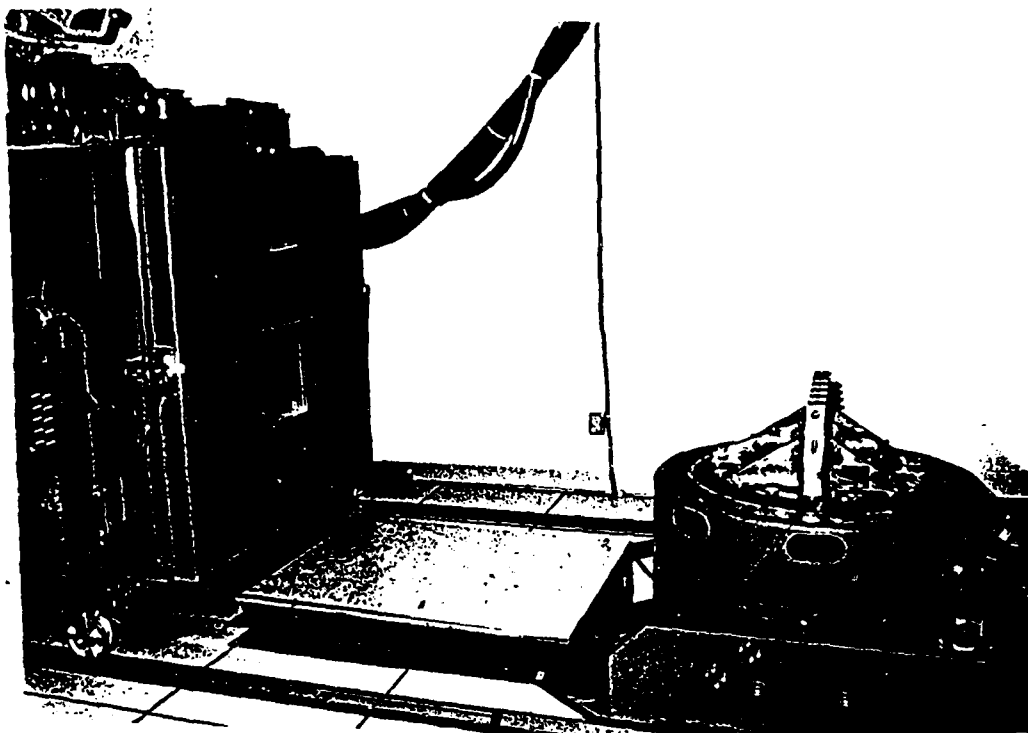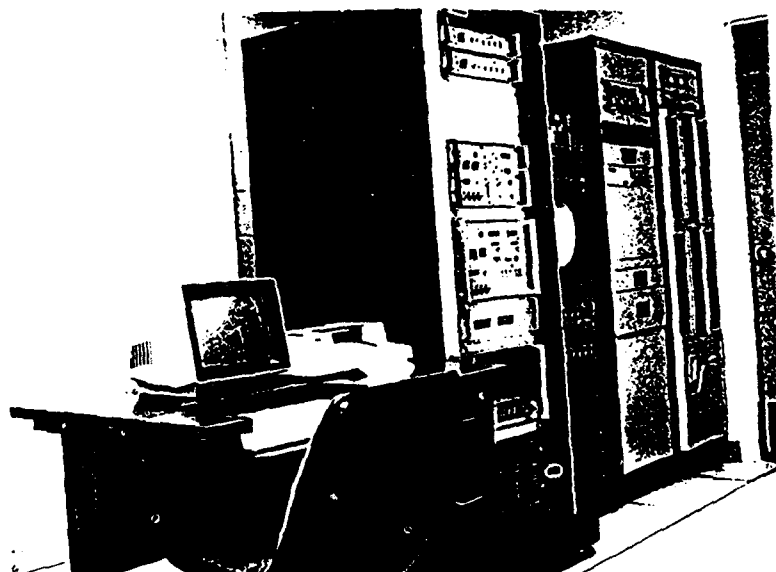
THE GENERIC TEST FACILITY CONCEPT

Figure 3.3-2

VIBRATION TEST SET
FIGURE 3.4-1

VIBRATION TEST SET CONTROL STATION
FIGURE 3.4-2

This resource can be utilized to isolate failure modes that are environment sensitive. Typically these failures result in a RTOK or CND when tested in a benign or quiescent environment.

Further, the Vibration Test Set will lend itself to accelerated life tests of a variety of avionics. This will provide valuable information on expected failure rates and subsequent logistics support requirements in the out years.

3.5 THREE AXIS MOTION SIMULATOR

A large three-Axis motion simulator equipped with an integral temperature chamber is shown on Figure 3.5-1. This unit is capable of producing simulated aircraft pitch, roll and yaw motions for dynamically testing of inertial navigation system and gyroscopic instruments. High rotation rates are possible using the simulator. A temperature chamber mounted on the inner gimball is capable of both hot and cold cycling operations and uses liquid nitrogen for cooling. UUTs of up to 100 pounds and package sizes up to 24" x 24" x 30" may be tested on this device.
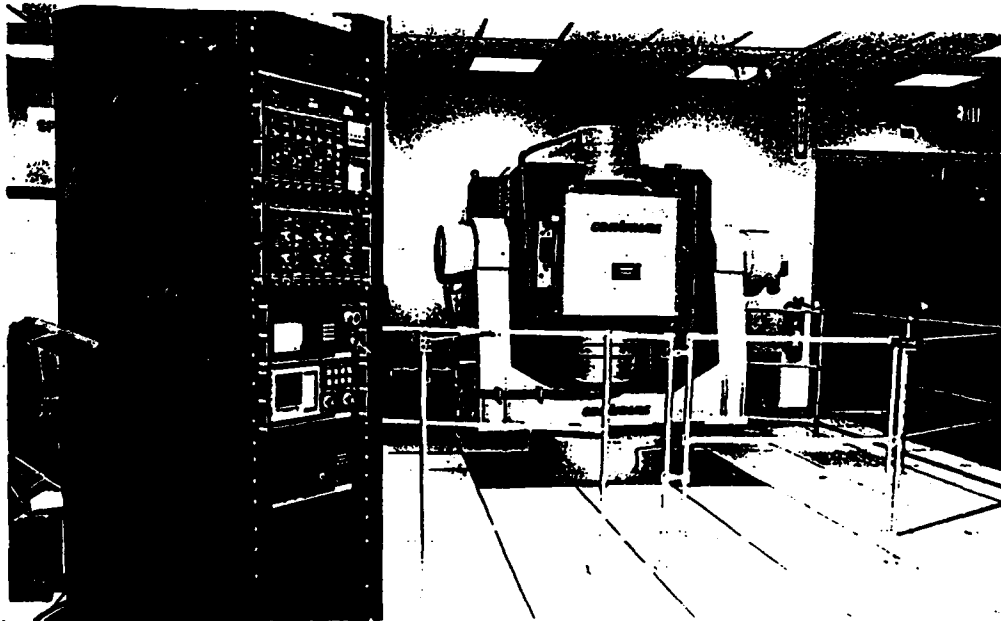
THREE-AXIS TABLE
FIGURE 3.5-1

3.6 GENERAL PURPOSE TEST EQUIPMENT

The ARC houses a wide variety of other test equipment. Among these other devices are a MIL-STD-1553B Bus Analyzer/Emulator, a MIL-STD-1750A Microprocessor Analyzer/Emulator, rate table, Scorsby tables and numerous pieces of general purpose test equipment such as spectrum analyzer, oscilloscopes, reflectro-meters, IC tester, curve tracer, etc.

3.7 OTHER PLANNED SUPPORT

The ARC will be expanded to include support for other managed systems. The alotted facility space will be our limiting factor. The following are known support items presently scheduled for installation within the next 24 months.

        Iron Man — SRU test station
        C141 Autopilot Integration Set
        Additional System Mockups
        LSI 2171 AHRS Test Set
        Standard Central Air Data Computer (SDADC) Test Set
        Flight Instrument Support Equipment
        Cruise Missile Guidance Test Station

3.8   SOFTWARE

3.8.1   INS Reliability Analysis System (IRAS)

A key part of the Facility capability is the IRAS system (Figure 3.8.1-1) which provides the means to analyze failure and repair data for trends, track reliability by configuration and record test synopsis. IRAS incorporates data from the following sources:

        G078C, Inertial Guidance and Configuration and
                Reliability Aircraft System (AGMC)
        D056E, Product Performance System
        AFTO Form 349, Maintenance Data Collection Record
        MDR, Material Deficiency Report
        QDR, Quality Deficiency Report
        WDTS, Warranty Data Tracking System
        Customized problem reporting forms
        Contractor delivered failure, repair and configuration
                data   ,
        Center Test Data

These data, although from a variety of sources have Serial number, Part Number, WUC, or National Stock Number as a means of relating the data. IRAS is menu driven analysis system can
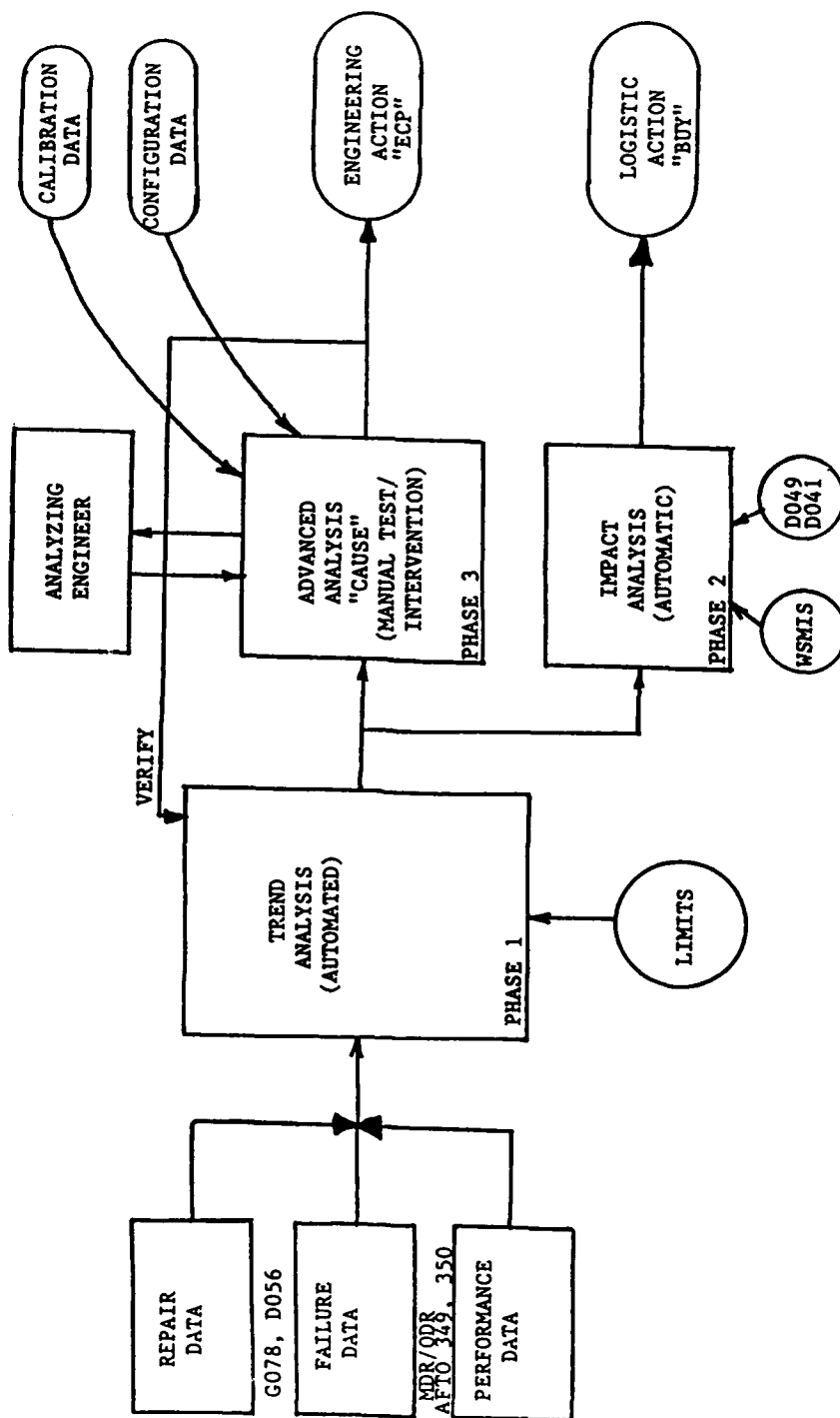
IRAS CONCEPT OF OPERATIONS

Figure 3.8.1-1

execute pre-programmed queries/reports, edit/validate any type
record, or management files. Typical outputs of the system are
as follows:

>   Management Summaries, tables or graphs that summarize
>   data into useful formats;
>
>   Rankings, reports which present data in descending order
>   based on a selected field
>
>   Detailed Listings, extensive listings of the actual data
>   that are formatted to accommodate user analysis
>   requirements
>
>   Historical Test Data
>
>   Queries, reports responding to questions about specific
>   data entities
>
>   Configuration

        IRAS is hosted on the HP 9000 and utilizes Oracle's SQL
query language. The use of IRAS to analyze the failure and
repair data permits the early identification of inertial system
reliability problems, so solutions can be implemented sooner.
The system has the ability to track all maintenance actions
performed on an individual LRU or SRU to the limit of available
data records.

3.8.2 SIMULATION

        A capability to simulate the performance of strapdown
Inertial technology has been developed to provide an evaluation
tool. The simulation programs are hosted on the HP 9000 and
allow the creation of simulated error effects that match the
system errors observed in testing. This will aid in predicting
the effects of RLG INS error sources on system performance under
simulated user environments.

        A strapdown INS trajectory generator is also available which
can provide mission tailored profile inputs to the simulation
program. This program provides inputs that simulate either
laboratory or airborne profiles to the RLG INS simulator to aid
in explaining anomalous behavior in actual INS operation. The
trajectory generator program will also be used to generate
laboratory and airborne inputs to the simulation program as a
personnel training tool for the understanding of RLG INS behavior
patterns.

A third component of the strapdown simulation capability is a generalized covariance simulation program. This program takes a user-defined error state model and a trajectory input profile and computes the state transition and propagated state process noise matrices, propagates the error state covariance matrix, and performs resets based on a user defined measurement model. This tool allows operator input of suboptimal Kalman gain options. Outputs include error sensitivity of each error state and error budgets defining the contribution of each error state initial value.

4.   FACILITY DEVELOPMENT

The facility development is proceeding in phases with the early phase characterized by the use of Peculiar Support Equipment (PSE). The development also includes transitioning to a Generic Test Station concept and maximizes the flexibility of the facility to perform testing of newer technology equipment. Initial efforts will include Material Deficiency Reports (MDR) and Quality Deficiency Report (QDR) investigations and will progress towards pre-emptive analysis. Studies will be performed on the effects of ESS on older systems and to develop screening profiles for depot implementation.

Phase I testing will be limited to diagnostic testing of those systems for which PSE can be obtained and will be con-strained to the test capabilities of that equipment. Phase I will also be characterized as an initial training period where engineers and technicians gain experience in systems, hardware, testing, analytical tools, and ESS in performing investigations of MDRs/QDRs, RTOK and Tech Order deficiencies.

Phase II will be a transitional period to Generic Test Stations (GTS). Growth of testing experience will permit a greater range of testing techniques and environmental conditions to be used in the isolation of problems. The IRAS will enable pre-emptive investigations by aiding the engineer in identifying failure trends. The facility will also be used in the qualification testing of new vendors and technology insertion efforts such as VHSIC.

5.   CONCEPT OF OPERATIONS

5.1   General System Test Concept

The function of the Avionics Reliability Center is to respond effectively to readiness problems experienced with deployed systems and to support the development of new technology systems. In order to correct design deficiencies or high-failure rate components, the Center will utilize pre-emptive analysis vis-a-vis IRAS, then determine which items are to be addressed based upon Life Cycle Cost Analysis (LCC). In addition, the facility will investigate apparent failures caused by testing incompatibilities (equipment, procedures, test conditions) of BITE, Intermediate level or depot level testing.

The ARC utilizes field and depot problem reports, operational and maintenance action data, and test data as key indicators. This combined data is analyzed, via statistical and graphical analysis techniques to detect trends that potentially impact the reliability of deployed systems. Based upon these indicators or other direction, the facility director initiates a project to investigate a potential problem. The first step is to validate the problem and then attempt to duplicate it in the Center by construction of a test scenario. Once the problem has been duplicated, the source must be identified and categorized (i.e., label the problem as hardware, software, test equipment or unknown). To expedite and assist with this process, IRAS can screen historical data in order to narrow the number of potential problem areas to a probable few.

A series of alternative failure and cause hypotheses are created and a set of test procedures and conditions are defined. The unit is subjected to these tests, and the test results are analyzed until the cause of the problem is isolated and a solution is identified. If the solution requires repair or modification of the unit, test equipment, or software, then it is corrected. If the solution requires an operational or procedural change, a recommendation for a Tech Order (T.O.) revision is prepared. In cases where a design change is recommended, or when the unit is still under contractor warranty, the Program Manager is advised so appropriate action is initiated.

The ARC will continuously monitor performance and reliability indicators of effected equipment to verify correction of the problem. Savings calculations will be summarized to determine the effectiveness of our actions. This information will be utilized for fine tuning our models and operation.

6.   SUMMARY

The Avionics Reliability Center represents a sizeable in-
vestment in the R&M 2000 product improvement program. The ARC
gives our technical staff the resources to organically perform
R&M initiatives without dependency on depot maintenance personnel
or prime contractors. As a result of the Center, the Air Force
anticipates an 8 to 1 return on capital investment through
logistics support cost savings from increased MTBD, lower
CND/RTOK, and improved quality.

These efforts not only provide savings to ourselves but also
to the test equipment managers, aircraft managers, development
programs, major commands and the OFP software support section.

We are currently working projects elementary in nature in
order to obtain experience and skill in order to tackle complex
issues in the future. As we progress, the Center will be
expanded to encompass support for other managed avionics and
lower levels of investigation. Our staff will be limited only by
our imaginations and determination.

THIS PAGE LEFT INTENTIONALLY BLANK

Modeling for ICBM Maintenance, Supportability and Replacement

by

Thomas E. Reed and Arnold J. Theisen

Charles Stark Draper Laboratory, Inc.

ABSTRACT

The ability to maintain an effective missile force long beyond its designated lifetime requires innovated planning and at times unconventional actions. The entire logistics of fleet maintainence is complicated by wide missile dispersement, supply schedules, security restrictions, transport delays, diagnostic uncertainties, decreasing MTBFs, long replacement procurements and an ever decreasing amount of spares. In spite of these problems, the present operational missile force is at a higher readiness level than the stated goals.

This complex operation has been kept stable, in the past, by the interaction of many dedicated men at the field sites, at the depots and at the procurement offices. As the problem becomes more complex there has become a need for a computerized model of the entire operation, not so much to learn how it works, but to allow future expectations and modifications to be tried out before the fact and see the long term effects.

The model to be shown was generated using a software package called STELLA™, which allows essentially any operation to be modelled using only three key elements. This paper will show how the logistic model operates and will also show how this type of modeling can be used for management, dynamic analysis and even financial planning.

Modeling for ICBM Maintenance, Supportability and Replacement

Preface

The technical world consists of four types: engineers, mathematicians, programmers and managers. Now most technical people prevail in one of these categories with some overlap into the others but in most projects there is more "underlap" than overlap. The engineers are there to interact with reality, be attuned to what's possible and translate the more complex problems into something that the mathematicians can handle.

The mathematicians, in turn, use matrices, or state theory, or whatever, to write out the mathematical procedure for solving the problem. They then give it to the programmer who completely seals it in an impenetrable array of GOTOs and IF statements and submits it to an even more impenetrable computer. If the project is lucky, the computer results are checked by the programmer for syntax error, by the mathematician for improper infinites and then by the engineer for believability. [Actually a good engineer knows the answer to within a few percent and is only using the rest of the team for fine tuning and because his manager, i.e. boss, doesn't have his confidence].

Now along comes a program called STELLA™ that for many problems, or projects, can short circuit this serial and inefficient method and allow the engineer to get confirmation with a method that even his boss, the manager, can understand.

Introduction

What this paper will do is to show how a logistics problem can be simulated skimpily in a manner that is visible and easily understood - even by managers. The method is not restricted to just logistic problems, it can be used to solve or simulate non-linear differential equations, thermal problems, logical problems or almost any definable situation. The software used is STELLA™[1] which is written for the Macintosh family of computers. To quote the STELLA™ literature: *"No matter what you are thinking about, STELLA™ can help to make your thoughts into a picture - an operational picture."*

Description

To obtain a full description of the STELLA™ software you should obtain the thick user's guide from High Performance Systems. What follows is just a quick and therefore incomplete definition of its capability. The intent here is to give enough information so you can fully understand the program to be presented.

STELLA™ consists of only four building blocks supported by three tools, see figure 1. The four building blocks can be picked up and moved to any location on your "playing field". They consist of:

    1. STOCK, a rectangular box that does only one thing, it accumulates. It increments all inputs and decrements all outputs from connected FLOWs.

---

2. FLOW arrow that goes into or out of a STOCK or flows from one STOCK to al ...er. If one end of the arrow does not connect to a STOCK, then it is terminated in a white cloud - indicating that you are extracting the value from thin air, or discarding it into thin air. The arrow has a circle hanging from it that dictates what flow is allowed.

3. CONVERTER, a circle which can be asked to do most everything. It can accept inputs and modify them, combine them or using them or self generated constants as arguments for most mathematical functions. If you don't like the functions, you can draw your own with a graph.

4. CONNECTOR. a skinny arrow that does nothing but connect the values contained in any of the above to other FLOWs or CONVERTERS. It must attach to one of the above at both ends.

Now that's all of the building blocks.

The tool kit consists of the following:

1. HAND, this hand has a finger which can reposition connectors on the edges of the building blocks to change their routes, which are straight lines or smooth arcs; select the names of the three active building blocks for changing; or moving any of the active building blocks without changing the connections.

2. GHOST, this ghost like figure can be used to select any active building block, clone it and move it to any other place. The name remains the same and its output is identical at all times to its"parent". This allows the diagram to be cleaned up by eliminating multiple and far reaching connectors.

3. DYNAMITE, this lit stick of dynamite is used to destroy any of the active building blocks. When either end of a connector is "blown-up" the connector also disappears.

All of the above are obtained by clicking and dragging the pictured items from the left side of the screen.

DEFINITION OF EXAMPLE

While the example chosen has a relatively crude model developed from the Minuteman II scenario, the parameters used are not intended to be those from the actual Minuteman, especially the amount of failures. It was developed to show an example of what this type of program could do in predicting a worse than worse case condition. It is intentionally kept small and simple to allow it to be presented within the 20 minutes or so allowed at the symposium.

The model shows the pipeline of missile guidance wafers starting from their failure in the field, through shipping to the repair depot, diagnostics and repair and then returning to the field as a spare. (See Figure 2)

Each of the FLOWs and CONVERTERS are given transfer functions, while the STOCKs are only given an initial value. The program then generates all the equations, see figures 3a & 3b. The STELLA™ simulation assumes a deployed force of 450 missiles with 130 spare wafers. The simulation uses time delays to represent the average times that each operation requires. These times are represented in the diagram by STOCKs (rectangles) and are listed below:

1. TITLE: "OPERATIONAL"
   DELAY: None
   OPERATION: This represents the number of operational missiles in silos ready for launch.

2. TITLE: "FIELD_OFFLINE"
   DELAY: 3 Days
   OPERATION: This is the time between a guidance system failure and the replacement, checkout and the restoration of full operation. Essentially this is the time that the silo is off-line.

3. TITLE: "PREPARATION"
   DELAY: 4 Days
   OPERATION: After the wafer is removed it is then sent back to the intermediate repair area where the battery is removed and the wafer is prepared for shipment to the depot.

4. TITLE: "SHIP_TO_AGMC"
   DELAY: 4 Days
   OPERATION: This represents the time required to transport the wafer from the field to AGMC.

5. TITLE: "DIAGNOSTICS"
   DELAY: 16 Days
   OPERATION: The wafer is attached to special diagnostic equipment to determine the cause of failure.

6. TITLE: "BACKLOG"
   DELAY: Flow rate dependent.
   OPERATION: This represents a holding area where wafers are waiting to be repaired. A limitation of 2.2 wafer repairs per day is the assumed throughput.

7. TITLE: "REPAIR"
   DELAY: 14 Days
   OPERATION: This represents the total time to repair.

   TITLE: "TEST"
   DELAY: 10 Days
   OPERATION: This is the average time required to perform acceptance testing.

8. TITLE: "SHIP_OUT_AGMC"
   DELAY: 3 Days
   OPERATION: This represents the time necessary to ship the wafer(s) back to the field site or OO-ALC

9. TITLE: "DISTRIBUTION"
   DELAY: None
   OPERATION: This is just a decision point. If the field spares have reached 36 then the repaired wafer(s) are sent to "DEPOT_SPARES", if not they are sent to "FIELD_SPARES". The stock only carries the residual of shipping as this is where the wafer flow is converted back to an integer form.

Note: All the above STOCKs contain integer numbers of wafers except "REPAIR", "TEST", "SHIP_OUT_AGMC" and "DISTRIBUTION".

The failure rate is computed every day. The MTBF used is one with an accelerated decline to show the effect of age on equipment. The model used is grossly unrealistic in order to show a very worst case condition. The MTBF starts off at 8000 hours. It is then decreased at a rate of 4 hours per day.

The actual failures per day are chosen randomly and are integers that have a range from zero to four per day with the average representing the current MTBF. This is accomplished by multiplying the computed failure rate by a random number whose range is uniformly distributed from zero to two. This number is then integerized with residuals retained.

Figure 4 shows the 30 day running average of the computed or ideal failures, i.e. lambda times the number of operational missiles, along with the actual failure rates.

The simulation is started by placing all 130 spares in "FIELD_SPARES" and all 450 missiles in "OPERATIONAL". The simulation is then allowed to reach a steady state over a period of 100 days. (This is accomplished by starting the simulation at -100 days with a constant MTBF of 8000 hours)

The useful simulation time, 0 to 1080 days, represents three years of operation (one year = 360 days).

Now any active building block can be either plotted or printed in a table. The parameters plotted are as follows:

Figure 5: 1. OPERATIONAL- The number of missiles that are operational. (Maximum 450)

Figure 6: 1. AGMC_TOTAL - The total number of wafers at AGMC.
2. DIAGNOSTICS - The number of wafers at AGMC that are being diagnosed.
3. REPAIR_AND_TEST - The number of wafers at AGMC that are being repaired or tested.
4. BACKLOG - The number of wafers at AGMC that are awaiting repair.

Figure 7: 1. FIELD_SPARES - The number of spare wafers at the field sites.
2. DEPOT_SPARES - The number of wafers at OO/ALC (i.e.Hill AFB).

The parameters printed for each day are as follows: (Figure 8)

1. TIME — Time in days

2. OPERATIONAL — The number of missiles that are operational.

3. FIELD_OFFLINE — The number of missiles that are not operational.

4. PREPARATION — The number of wafers being prepared for shipment at the field site.

5. SHIP_TO_AGMC — The number of wafers in route to AGMC.

6. DIAGNOSTICS — The number of wafers at AGMC that are being diagnosed.

7. BACKLOG — The number of wafers at AGMC that are awaiting repair.

8. REPAIR — The number of wafers at AGMC that are being repaired.

9. TEST	The number of wafers at AGMC that are being acceptance tested.
10. AGMC_TOTAL	The total number of wafers at AGMC.
11. DEPOT_SPARES	The number of wafers at OO/ALC (i.e. Hill AFB).
12. FIELD_SPARES	The number of spare wafers at the field sites.
13. LAMBDA	The failure rate per day per operational missile.
14. FAILURES	Failures each day.

CONCLUSION

The charts show that as the failure rate increases the amount of operational missiles decrease linearly until a critical point is reached which occurs when the failure rate exceeds the ability to repair. At this time AGMC saturates with 103 wafers in-house and the amount of operational missiles will decrease until the failure rate per day equals the AGMC throughput. For example if the MTBF stabilized at 3000 hours and the AGMC throughput was 2.2 per day then the average number of operational missiles will stabilize at 2.2x3000+24 or 275. This program is not needed to show this relationship, its worth lies in allowing changes to be made in the logistic flow and see the results immediately. For example, the number of "dead" missiles when spares are available is set entirely by the failure rate and by the field crews response time. This model could be expanded to model each crew and each wing and setting a limit on each crew's efficiency. It could include critical equipment failures and downtime due to weather and so forth.

The next step in the AGMC area would be to model the internal cycles of individual unit repair with each type of failure being modeled separately. This would allow AGMC management to try different solutions or work priorities prior to implementation. It could show where new personnel will be needed in time for proper training. It could simulate the loss of key personnel and its effect on the throughput.

This type of program can become a major management instrument in the complex world of military logistics.
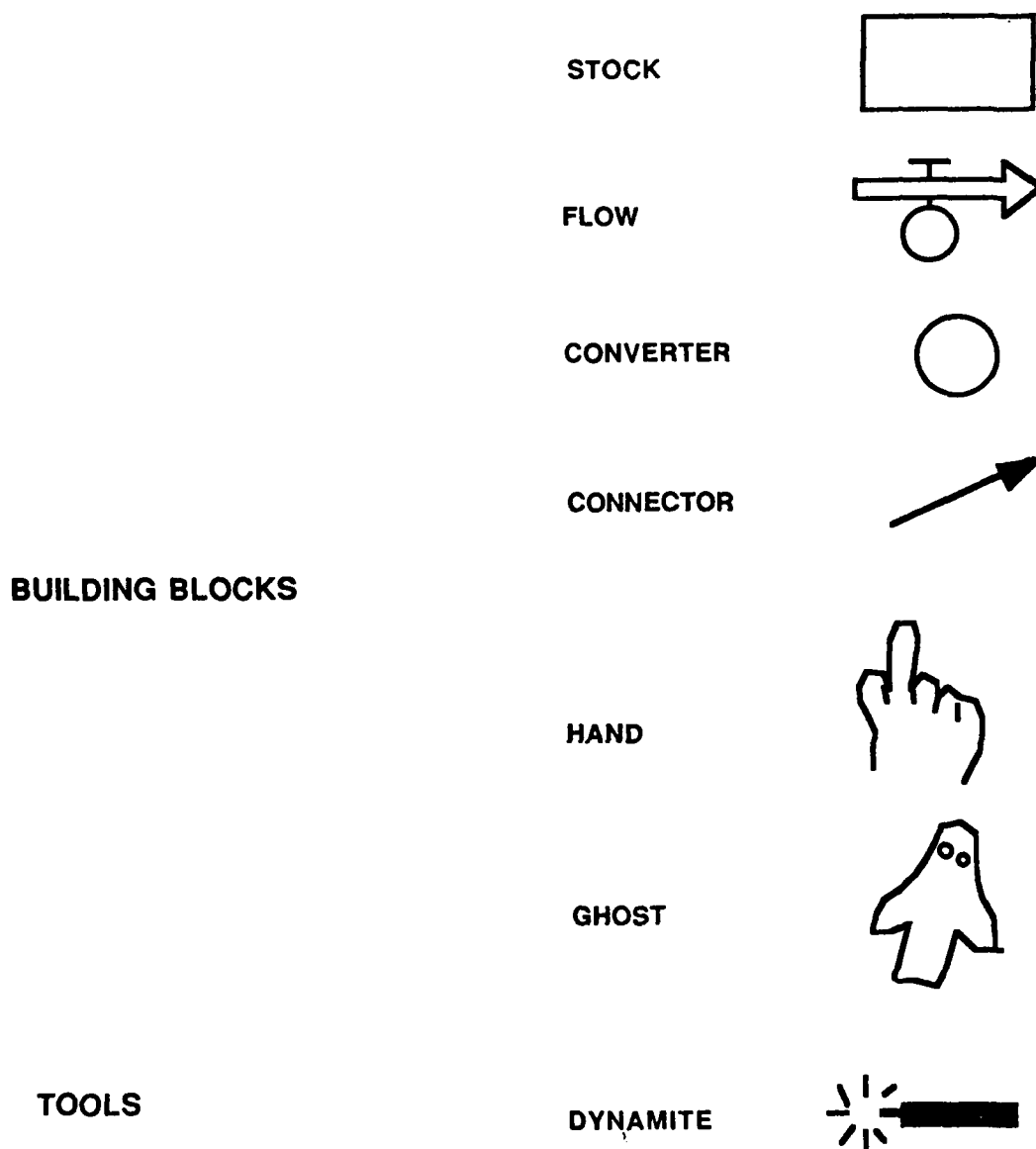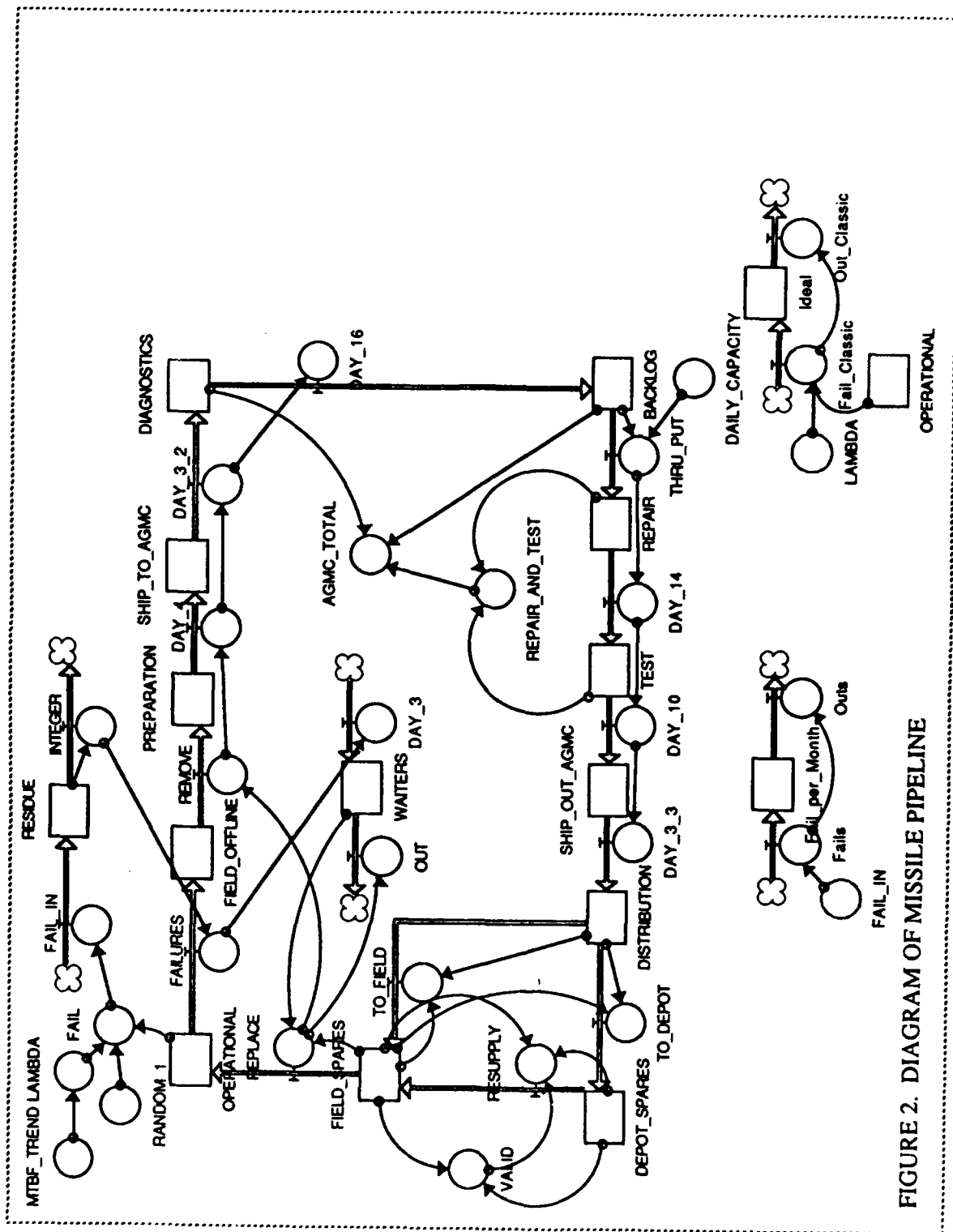
BUILDING BLOCKS

STOCK

FLOW

CONVERTER

CONNECTOR

HAND

GHOST

TOOLS

DYNAMITE

FIGURE 1. BUILDING BLOCKS AND TOOLS

FIGURE 2. DIAGRAM OF MISSILE PIPELINE

☐ BACKLOG = BACKLOG + dt * (DAY_16 - THRU_PUT)
INIT(BACKLOG) = 0
{This represents the number of wafers that are backlogged awaiting repair. This is set by the capacity of AGMC.}

☐ DEPOT_SPARES = DEPOT_SPARES + dt * (TO_DEPOT - RESUPPLY)
INIT(DEPOT_SPARES) = 0
{This is the amount of wafer spares that are located at OO-ALC.}

☐ DIAGNOSTICS = DIAGNOSTICS + dt * (DAY_3_2 - DAY_16)
INIT(DIAGNOSTICS) = 0
{This represents the number of wafers that are under going tests to determine the point of failure.}

☐ DISTRIBUTION = DISTRIBUTION + dt * (-TO_FIELD - TO_DEPOT + DAY_3_3)
INIT(DISTRIBUTION) = 0
{This is just a decision point to determine whether the wafer(s) are to be sent to a field site or to OO-ALC. It also stores the residual from the following integerizing.}

☐ Fail_per_Month = Fail_per_Month + dt * (Fails - Outs)
INIT(Fail_per_Month) = 0

☐ FIELD_OFFLINE = FIELD_OFFLINE + dt * (FAILURES - REMOVE)
INIT(FIELD_OFFLINE) = 0
{ This contains the number of fielded missiles that are non-operational - waiting for wafer replacement.}

☐ FIELD_SPARES = FIELD_SPARES + dt * (-REPLACE + TO_FIELD + RESUPPLY)
INIT(FIELD_SPARES) = 130
{This is the number of spare wafers in the field sites.}

☐ Ideal = Ideal + dt * (Fail_Classic - Out_Classic)
INIT(Ideal) = 0

☐ OPERATIONAL = OPERATIONAL + dt * (REPLACE - FAILURES)
INIT(OPERATIONAL) = 450
{This contains the number of operational missiles in the entire Minuteman II force.}

☐ PREPARATION = PREPARATION + dt * (REMOVE - DAY_4)
INIT(PREPARATION) = 0
{This represents the number of defective wafers being prepared for shipment - such operations as removing the flight battery, etc..}

☐ REPAIR = REPAIR + dt * (THRU_PUT - DAY_14)
INIT(REPAIR) = 0
{This represents the number of wafers that are in the repair area.}

☐ RESIDUE = RESIDUE + dt * (FAIL_IN - INTEGER)
INIT(RESIDUE) = 0
{This stock stores the residual when the daily failure rate is integerized assuring an accurate mean.}

☐ SHIP_OUT_AGMC = SHIP_OUT_AGMC + dt * (DAY_10 - DAY_3_3)
INIT(SHIP_OUT_AGMC) = 0
{This represents the number of wafers that are in transit from AGMC to the field site or OO-ALC.}

☐ SHIP_TO_AGMC = SHIP_TO_AGMC + dt * (DAY_4 - DAY_3_2)
INIT(SHIP_TO_AGMC) = 0
{This represents the number of wafers in transit from the field sites to AGMC}

☐ TEST = TEST + dt * (-DAY_10 + DAY_14)
INIT(TEST) = 0
{This represents the number of wafers that are being acceptance tested prior to approval for shipping.}

☐ WAITERS = WAITERS + dt * (DAY_3 - OUT)
INIT(WAITERS) = 0
{Missiles that have been non-operational for threedays or longer.}

○ AGMC_TOTAL = DIAGNOSTICS+BACKLOG+REPAIR_AND_TEST

○ DAILY_CAPACITY = 2.2
{This is variable that represents the estimated average daily capacity of AGMC.}

○ DAY_10 = DELAY(DAY_14,10,0)
{It is estimated to take an average of 10 days to complete testing.}

○ DAY_14 = DELAY (THRU_PUT, 14, 0)
{It is estimated that it takes an average of 14 days to repair a wafer.}

○ DAY_16 = DELAY(DAY_3_2 ,16 ,0)

FIGURE 3a. PIPELINE EQUATIONS

{It takes an average of 16 days to get through Diagnostics.}
O DAY_3 = DELAY(FAILURES,3,0)
{It takes three days, on the average, to repair a missile.}
O DAY_3_2 = DELAY(DAY_4,3,0)
{IT TAKES THREE DAYS TO GET THE WAFER TO THE DEPOT}
O DAY_3_3 = DELAY(DAY_10,3,0)
{It is estimated to take an average of 3 days to ship from AGMC to either the field site or OO-ALC.}
O DAY_4 = DELAY(REMOVE,4,0)
{IT TAKES FOUR DAYS TO PREPARE FOR SHIPMENT}
O FAIL = RANDOM_1*OPERATIONAL*LAMBDA
{This takes the failure rate per day and then multiplies it by the random number producing a random daily failure rate from zero to twice the computed one.}
O Fails = FAIL_IN
O FAILURES = INTEGER
{The daily integer number of failures is now used to transfer that number of operational missiles into non-operational ones.}
O Fail_Classic = LAMBDA*OPERATIONAL
O FAIL_IN = FAIL
O INTEGER = INT(RESIDUE)
{ This flow converts the daily failure rate and the last residual to the next lower integer and removes it from the stock.}
O LAMBDA = 24/MTBF_TREND
{Failures per Day per Unit}
O MTBF_TREND = If (TIME >0) Then (8000 - TIME*4) Else 8000
O OUT = REPLACE
{Missiles going back into operation.}
O Outs = DELAY(Fails,30,0)
O Out_Classic = DELAY(Fail_Classic,30,0)
O RANDOM_1 =2*RANDOM(31)
{This gives an equal distribution from zero to two with a mean of one, the 31 is a "seed" which allows exact repeats of each run}
O REMOVE = REPLACE
{Missiles going back in to operation.}
O REPAIR_AND_TEST =REPAIR+TEST
O REPLACE = IF (FIELD_SPARES≥WAITERS) THEN WAITERS ELSE FIELD_SPARES
{This represents the spare wafers going out to replace the failed wafers making the missiles operation again.}
O RESUPPLY = IF((DEPOT_SPARES+FIELD_SPARES)<37) THEN DEPOT_SPARES*VALID ELSE (VALID*(36-FIELD_SPARES))
{If the field spares drop below 24 then OO-ALC spares will be sent until field spares reach 36.}
O THRU_PUT = IF(BACKLOG≥DAILY_CAPACITY) THEN DAILY_CAPACITY ELSE BACKLOG
{This limits the flow of wafers to the daily capacity of AGMC.}
O TO_DEPOT = IF(FIELD_SPARES<36) THEN 0 ELSE INT(DISTRIBUTION)
{If the field spares are 36 are larger then the wafers go to OO-ALC.}
O TO_FIELD = IF(FIELD_SPARES<36) THEN INT(DISTRIBUTION) ELSE 0,
{If the field spares are less than 36 then the wafer(s) are sent to the field.}
O VALID = IF(FIELD_SPARES<24) AND (DEPOT_SPARES>0) THEN 1 ELSE 0
{See "RESUPPLY".}

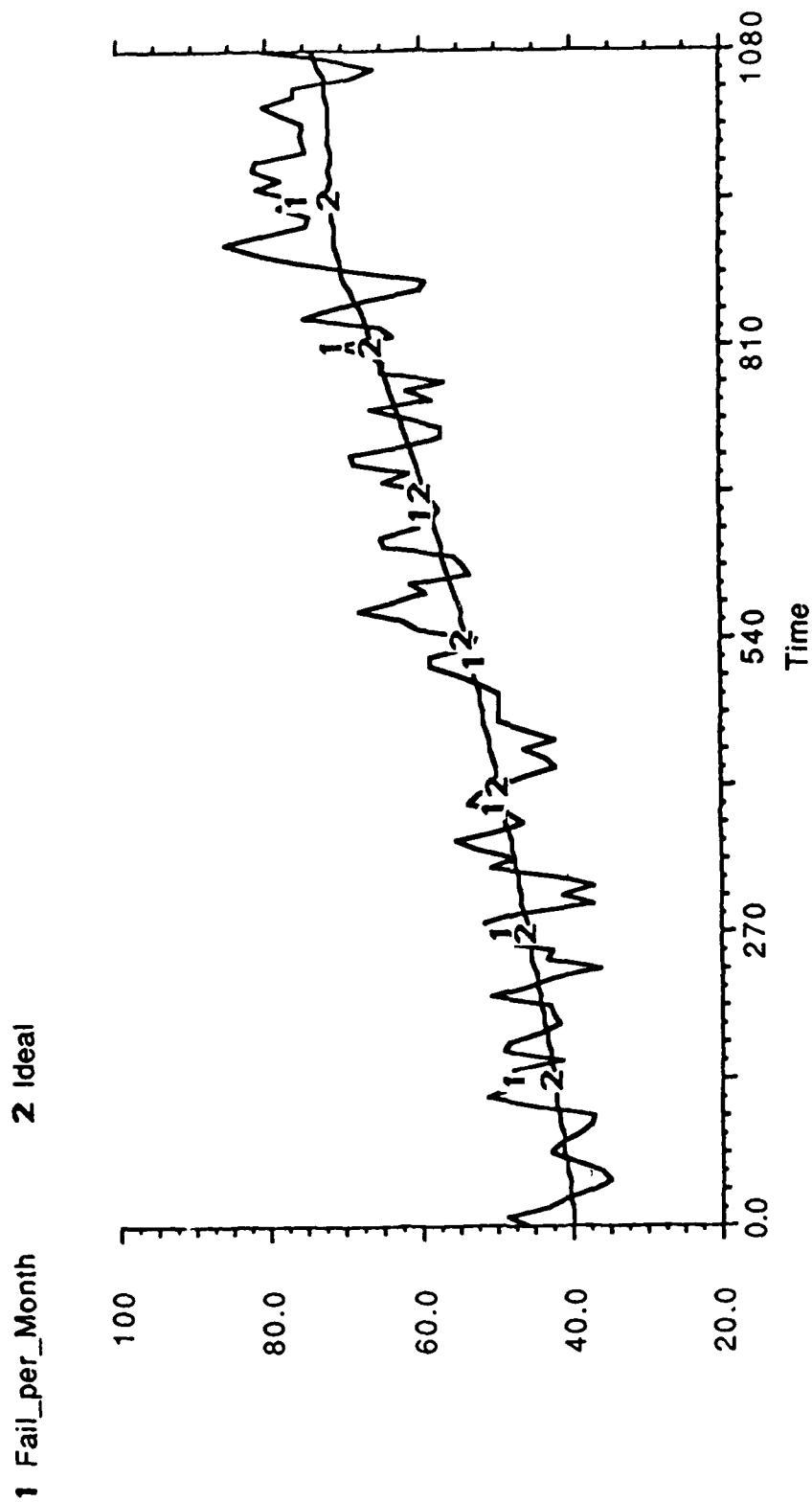## FIGURE 3b. PIPELINE EQUATIONS (CONTINUED)

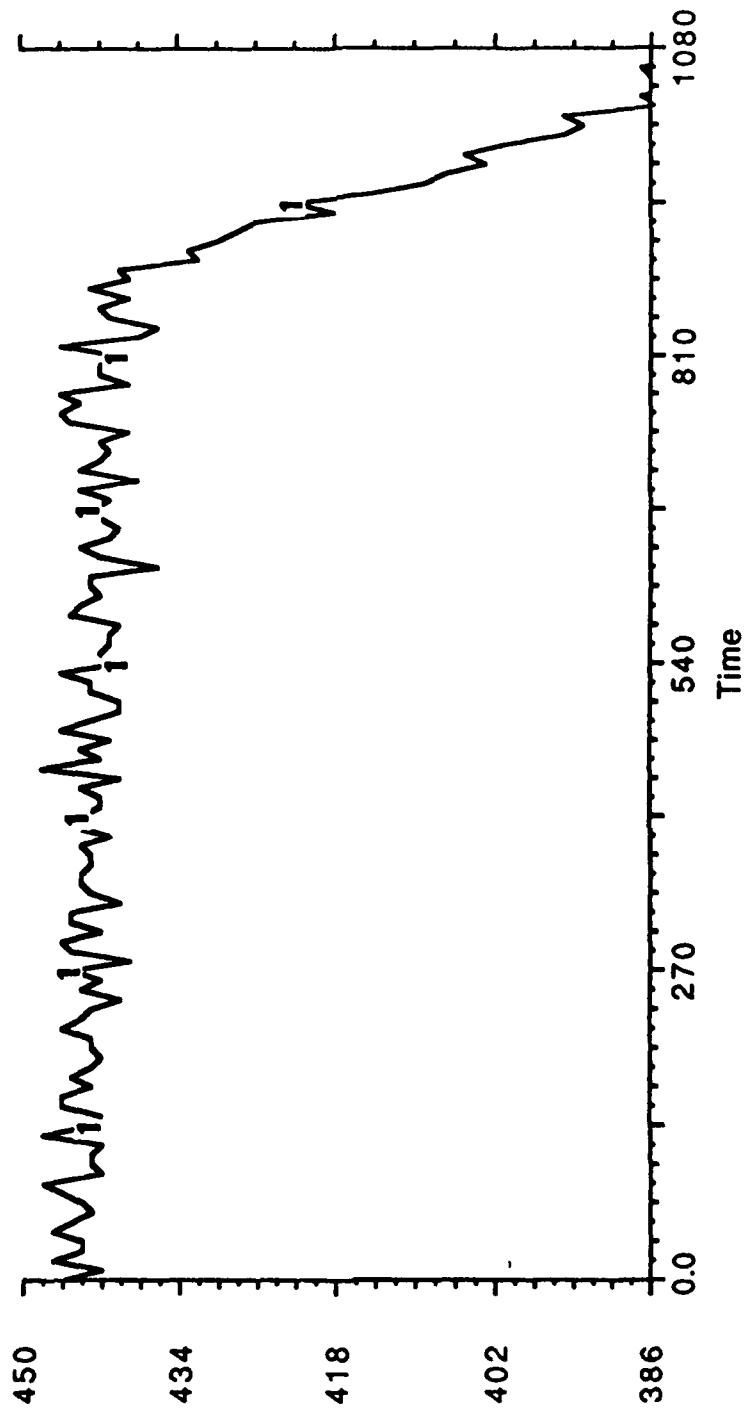FIGURE 4. 30 DAY RUNNING AVERAGE OF IDEAL AND ACTUAL FAILURES

FIGURE 5. OPERATIONAL MISSILES
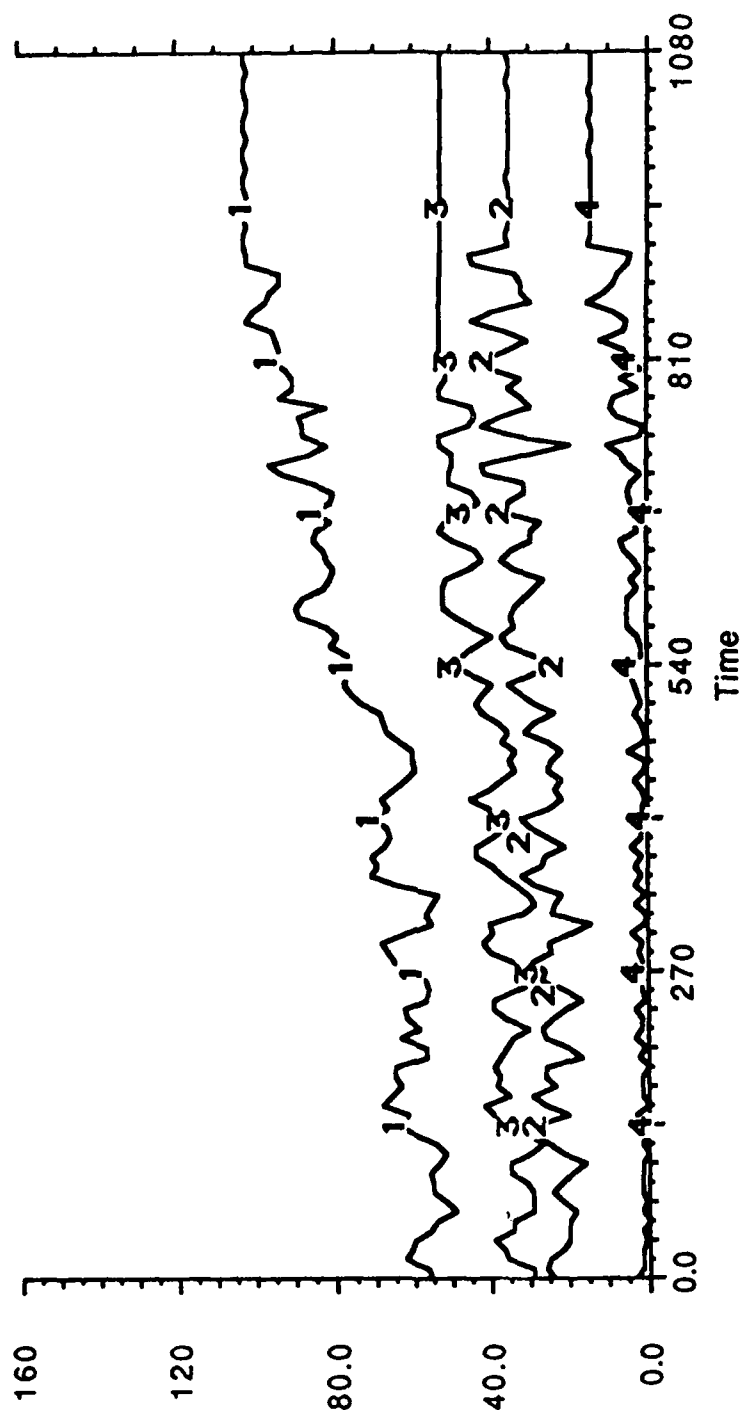
FIGURE 6. WAFERS AT AGMC
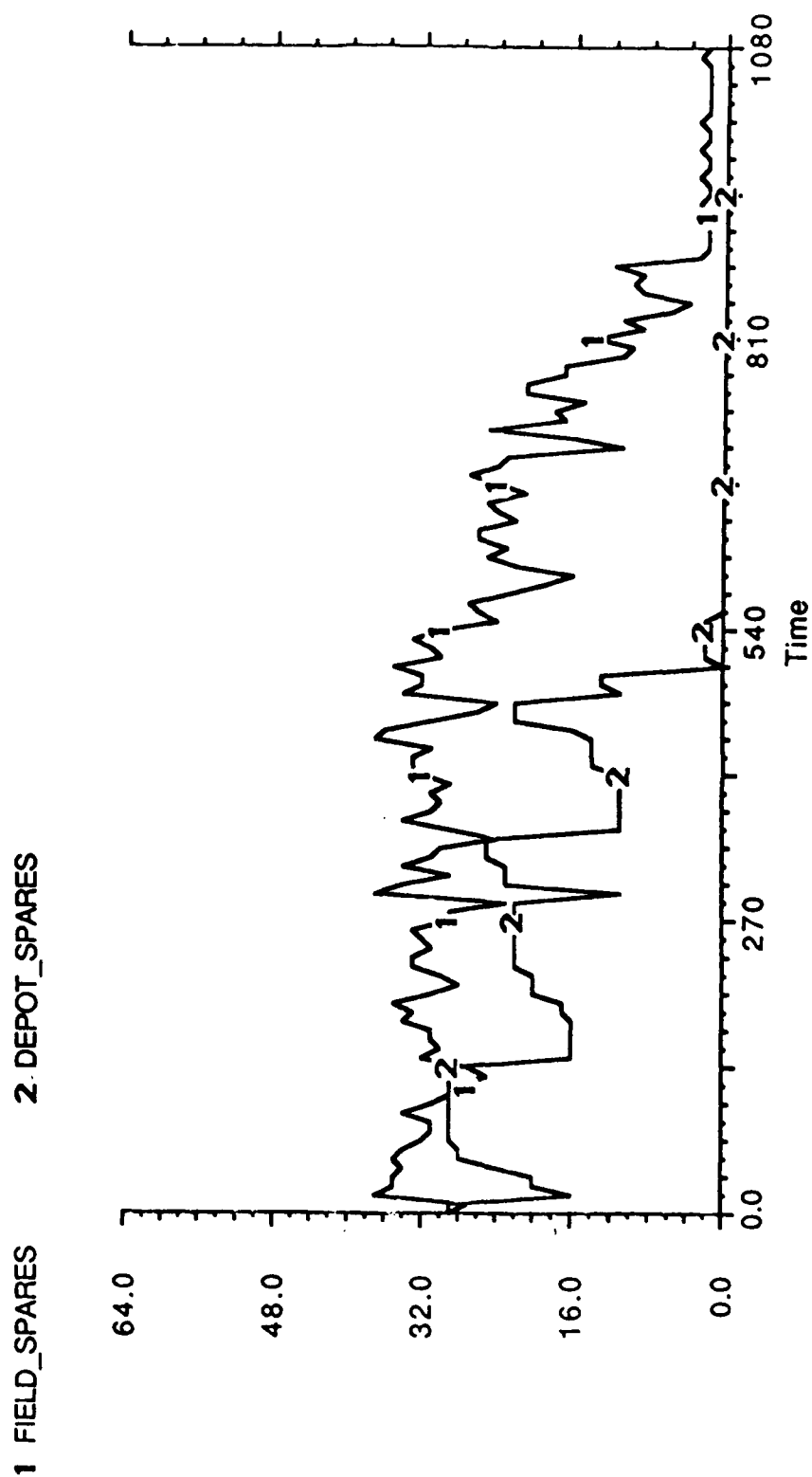
1 FIELD_SPARES   2. DEPOT_SPARES

FIGURE 7. WAFER SPARES, FIELD AND DEPOT (OO-ALC)

Time	OPERATIONAL	FIELD OFFLINE	PREPARATION	SHIP TO AGMC	DIAGNOSTICS	BACKLOG	REPAIR	TEST	AGMC TOTAL	DEPOT SPARES	FIELD SPARES	LAMBDA	FAILURES
0.0	446	4.00	7.00	4.00	24.0	3.00	17.0	12.0	56.0	29.0	29.0	0.00300	3.00
30.0	447	3.00	6.00	3.00	22.0	2.00	20.8	17.2	62.0	20.0	34.0	0.00305	3.00
60.0	445	5.00	6.00	3.00	19.0	1.00	17.8	11.0	48.8	28.0	34.0	0.00309	3.00
90.0	445	5.00	3.00	3.00	19.0	2.60	22.4	11.0	55.0	29.0	34.0	0.00314	2.00
120	442	8.00	7.00	5.00	26.0	2.00	18.0	12.0	56.0	29.0	28.0	0.00319	2.00
150	442	8.00	4.00	6.00	22.0	1.00	26.0	17.0	66.0	18.0	32.0	0.00324	1.00
180	446	4.00	4.00	3.00	30.0	0.0	21.4	15.8	67.0	17.0	35.0	0.00330	2.00
210	444	6.00	8.00	5.00	27.0	1.00	15.0	16.0	61.0	20.0	27.0	0.00335	2.00
240	446	4.00	7.00	2.00	18.0	1.20	24.8	17.0	61.0	22.0	31.0	0.00341	3.00
270	445	5.00	8.00	5.00	26.0	3.60	17.4	13.0	60.0	22.0	29.0	0.00347	0.0
300	446	4.00	3.00	4.00	26.0	0.0	23.0	15.4	64.0	16.0	37.0	0.00353	2.00
330	440	10.0	6.00	6.00	25.0	1.80	13.2	12.0	55.4	25.0	30.0	0.00359	3.00
360	444	6.00	6.00	8.00	28.0	1.00	26.0	17.0	67.0	11.0	31.0	0.00366	1.00
390	441	9.00	9.00	7.00	25.0	3.00	21.0	18.0	66.0	11.0	31.0	0.00373	2.00
420	444	6.00	6.00	5.00	21.0	1.00	28.0	13.0	68.0	14.0	32.0	0.00380	2.00
450	446	4.00	3.00	7.00	26.0	0.800	23.2	16.4	63.0	19.0	36.0	0.00387	2.00
480	445	5.00	5.00	6.00	29.0	2.80	19.6	14.6	66.0	11.0	34.0	0.00395	0.0
510	443	7.00	10.0	6.00	32.0	2.00	21.0	17.2	72.2	2.00	30.0	0.00403	3.00
540	440	10.0	8.00	3.00	23.0	5.20	29.2	19.8	77.2	2.00	30.0	0.00411	3.00
570	441	9.00	12.0	3.00	34.0	5.80	25.6	16.4	62.0	0.0	26.0	0.00420	2.00
600	444	6.00	8.00	3.00	31.0	6.00	29.6	22.0	88.6	0.0	22.0	0.00429	0.0
630	441	9.00	9.00	9.00	33.0	4.80	21.0	20.0	78.8	0.0	24.0	0.00438	0.0
660	439	11.0	8.00	4.00	30.0	2.00	30.6	22.0	84.6	0.0	23.0	0.00448	3.00
690	442	8.00	12.0	5.00	29.0	6.40	27.6	15.0	78.0	0.0	25.0	0.00458	1.00
720	444	6.00	8.00	2.00	37.0	5.00	29.8	19.4	91.2	0.0	19.0	0.00469	1.00
750	445	5.00	11.0	8.00	40.0	1.00	23.8	22.0	86.8	0.0	14.0	0.00480	1.00
780	441	9.00	4.00	9.00	35.0	3.40	30.8	22.0	91.2	0.0	16.0	0.00492	1.00
810	440	10.0	6.00	4.00	41.0	4.80	30.4	20.0	96.2	0.0	14.0	0.00504	3.00
840	442	8.00	10.0	10.0	38.0	5.80	30.8	22.0	98.6	0.0	3.00	0.00517	2.00
870	441	9.00	8.00	5.00	32.0	10.8	30.8	22.0	95.6	0.0	11.0	0.00531	1.00
900	431	19.0	9.00	6.00	45.0	4.80	30.8	22.0	103	0.0	2.00	0.00545	2.00
930	426	24.0	9.00	6.00	36.0	13.8	30.8	22.0	103	0.0	2.00	0.00561	4.00
960	410	40.0	9.00	6.00	36.0	13.8	30.8	22.0	103	0.0	2.00	0.00577	4.00
990	405	45.0	9.00	6.00	36.0	13.8	30.8	22.0	103	0.0	2.00	0.00594	4.00
1020	394	56.0	9.00	6.00	36.0	13.8	30.8	22.0	103	0.0	2.00	0.00612	1.00
1050	384	68.0	9.00	6.00	36.0	13.8	30.8	22.0	103	0.0	2.00	0.00632	1.00
1080	373	77.0	9.00	6.00	36.0	13.8	30.8	22.0	103	0.0	2.00	0.00652	5.00

FIGURE 8. PARAMETER PRINTOUT

Reliability Testing of Guidance Equipment

Herbert Hecht
SoHaR Incorporated

Tommy Dobson
6585th TG/GDL

INTRODUCTION

Formal reliability testing of guidance equipment has been carried out only infrequently in the past. The major reasons for this were (a) unavailability of the equipment for the lengthy test (typically about 6 months) and (b) the belief that equivalent information can be obtained by other means or, better yet, that the responsibility for attainment of reliability can be shifted to the manufacturer through reliability improvement warranties. The emphasis on reliability in Air Force Regulation 800-18 and recognition of some of the limitations of the RIW approach to reliability have prompted a re-examination of the role of reliability testing. A one year study on this subject conducted for the 6585th TG produced the following findings:

- When properly conducted in a combined environmental test facility, the results of reliability tests closely duplicated the long term service experience, both quantitatively and qualitatively. The MTBF estimates obtained in reliability tests were usually within 15% of those observed in service, and the ranking of the most significant causes of failure were the same.

- Reliability test results (based on early production equipment) can be made available up to two years before equivalent service data can be obtained. The reasons for this are low usage during the initial service period, restricted flight envelopes, and delays in compilation of field data. Reliability test results are more conclusive because of known environmental exposure and well documented maintenance.

- Until improvements under RIW become effective, the government bears the cost of grounded aircraft and logistic support, except for the comparatively small component of compensatory spares which is borne by the vendor. Avoidance of this cost typically amounts to over 5 times the cost of the reliability test.

Details on these findings are presented in the body of the paper. In addition, it has been found possible to modify the conduct of reliability tests so that they not only take less time but also yield data that are more useful for directing required improvements, and the final section of the paper includes an outline of an appropriate methodology.

THE VALUE OF RELIABILITY TESTING

Rreliability testing is of interest only if it yields results that are quantitatively (in terms of MTBF) and qualitatively (in terms of the failure modes identified) indicative of what can be expected in operational use of the equipment. The material presented in this section shows that these requirements were very well met in the only two comparisons of the results of reliability testing and operational reliability that could be identified during the last 12 years. The data described below come from two sources: the Air Force CERT facility that was operated by the Flight Dynamics Laboratory at Wright Patterson AFB, and from the Reliability Evaluation Division at the Navy Pacific Missile Test Center, Point Mugu, California. CERT was in operation approximately from 1975 to 1982; the Point Mugu test capability was established in 1974 and remains active to the present. The facilities and test results obtained by them are described below.

Results of the Air Force CERT Test Program

The Combined Environment Reliability Test (CERT) facility was established because it was realized that reliability testing conducted in accordance with the versions of MIL-STD-781 and MIL-STD-810 that existed in the early 1970's did not adequately simulate the environment of modern high performance aircraft, particularly in the area of combined vibration and temperature exposure, and in the rapid temperature cycling that were experienced by the equipment installed in these aircraft. The failure rate of typical electronic components was three to eight times that predicted [TREL77], and it was essential to identify design weaknesses.

The CERT facility simulated representative aircraft environments for vibration, temperature, and altitude. Reports on testing of four electronic units performed by CERT contain comparisons with field MTBF values. The results of "Full CERT" tests are compared with the field experience in Table 1.

Table 1 -- Comparison of CERT and Field MTBF

Equipment Nomenclature	Field MTBF hrs	CERT MTBF hrs	Reference
IFF Interrogator/Xmitter RT868A/APX-76	133	117	STAN77 Fig. 18
IFF Transponder RT1063B/APX-101	273	252	WARN81 Table 7
TACAN Set ARN84(V)9	170	159	WAGN81 Table 11
UHF Communication Set AN/ARC-109 (Rec/Xmt only)	95	85	THEI78 p. 7 & 38

The slight bias toward lower MTBF in the CERT tests may indicate (a) under reporting of failures in the field, (b) less severe environmental exposure in the field, such as fewer hours at high stress environments, or (c) a combination of the two factors.

A comparison of field and CERT failed parts from three of these components is presented in the following figures. A meaningful comparison of failed parts could not be conducted for the APX-101 because only two of the CERT failures were identified in the report.

These comparisons indicate that the failures induced by CERT were representative of those encountered in the field. The results are indeed remarkable when it is realized that the number of failures encountered in the CERT runs ranged from 10 to 18, making it unlikely that field failure modes that affected less than 10% of the population could be duplicated.

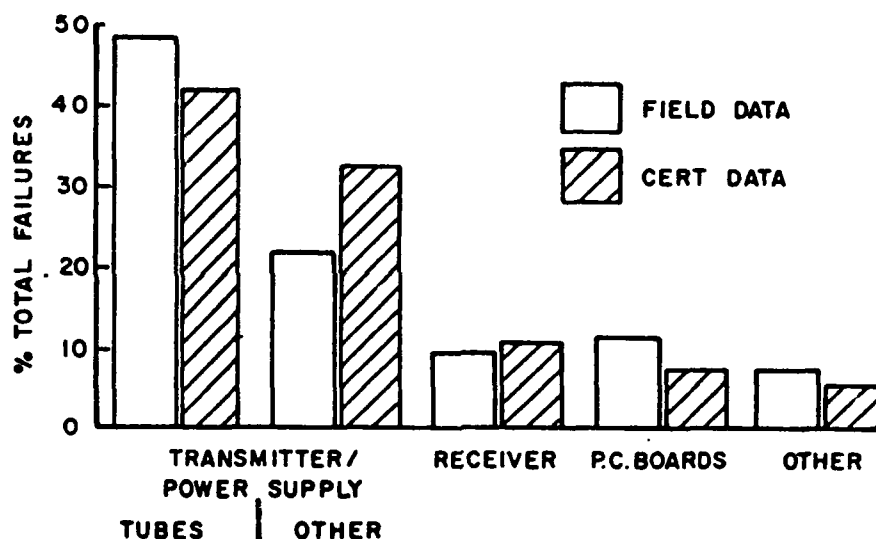## DATA FOR THE 5 LEADING CAUSES FROM AFFDL-TR-77-132

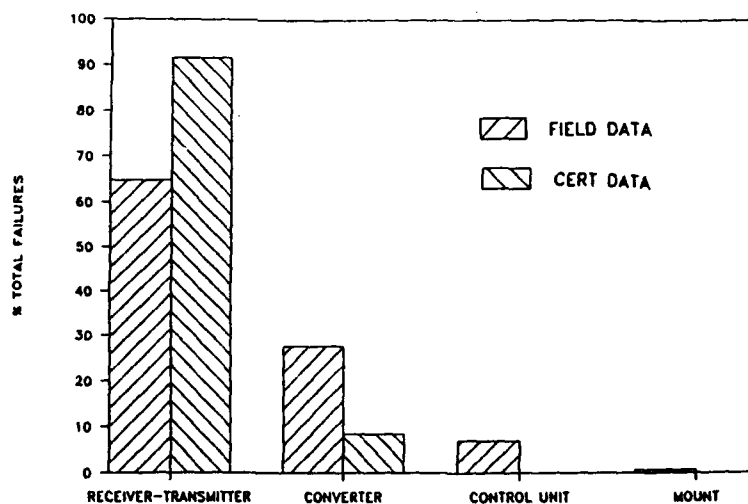Figure 1. Comparison of Field and CERT Failures for the APX-76

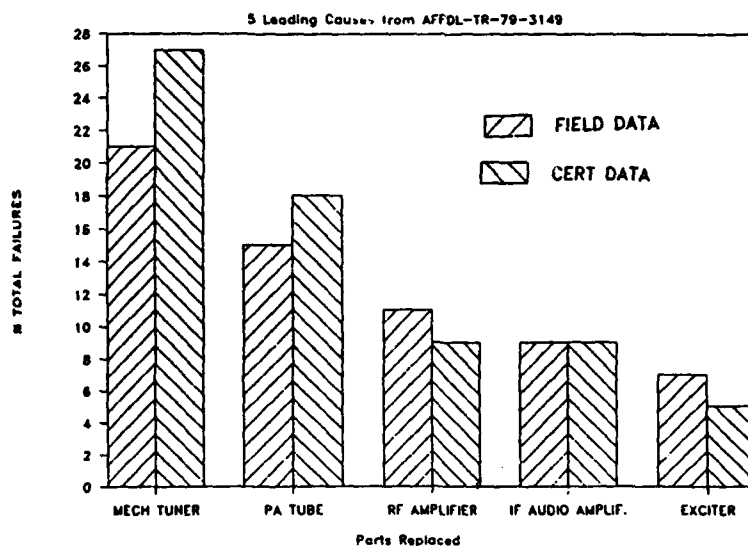**Figure 2. Comparison of Field and CERT Failures for the ARN84(V)9**

Figure 3. Comparison of Field and CERT Failures for the AN/ARC-109

The Navy Pacific Missile Test Center Program

Testing at PMTC is typically concerned with entire aircraft missiles, such as Phoenix, Sidewinder, Sparrow III, Harpoon and Shrike. In some cases the test concentrates on specific components, including guidance equipment. The test concept is called Production Acceptance Test and Evaluation (PATE) or Production Verification Test (PVT), the closest equivalent in MIL-STD-781D being the Production Reliability Acceptance Test (PRAT). Missiles are selected from designated production lots, are given a functional test, and are then installed in environmental test chambers and operated for a specified time that has been selected to yield a statistically meaningful estimate of the MTBF. The environment for a typical test includes temperature cycling and acoustic vibration. Low frequency vibration and humidity cycling are added for some items.

Most test chambers are large rooms (at least 12' x 12' x 10') that can accommodate four missiles at the same time. The thermal environment for each missile is controlled by an air shroud or a thermal blanket, with the latter procedure apparently becoming dominant. Chambers that permit both thermal cycling and mechanical (low frequency) vibration are here also referred to as CERT chambers.

The most widely used reliability measure at PMTC is mean-time-to-failure (MTTF). This differs from MTBF only when the time base for the latter includes repair time (which is not usually the case) and the more familiar MTBF is used in the following discussion. A comparison of MTBF measured in the reliability test (also referred to as Flight Test Simulation or FTS) and that estimated from flight data (referred to as Captive Flight) is shown in on the following page [PMTC81]. The center vertical bar in each rectangle represents the point estimate of MTBF, and the ends of each rectangle represent the 80% confidence limits. Particularly noteworthy in this example is the good agreement between test and flight MTBF over a very wide range of equipment reliability.

Typical results from a series of production verification tests run on different lots of a missile are shown in Figure 5 [TOM86]. The shaded rectangle designated as Sample 6 is the composite of five individual test results. Note that Sample 3 fell considerably below the specified reliability, but that the overall product reliability meets the requirement at this time. The pointed top of the Sample 2 bar indicates that the upper 80% confidence limit falls outside the vertical scale.

A comparison of test and field failure modes is not available for these tests. However, the fact that they have been carried out continuously for over ten years indicates that the Navy considers them valuable and cost-effective.
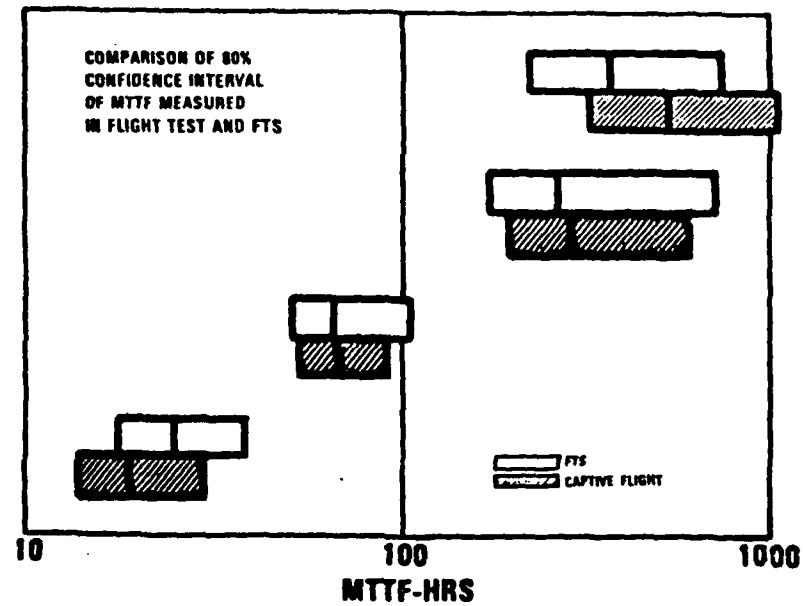
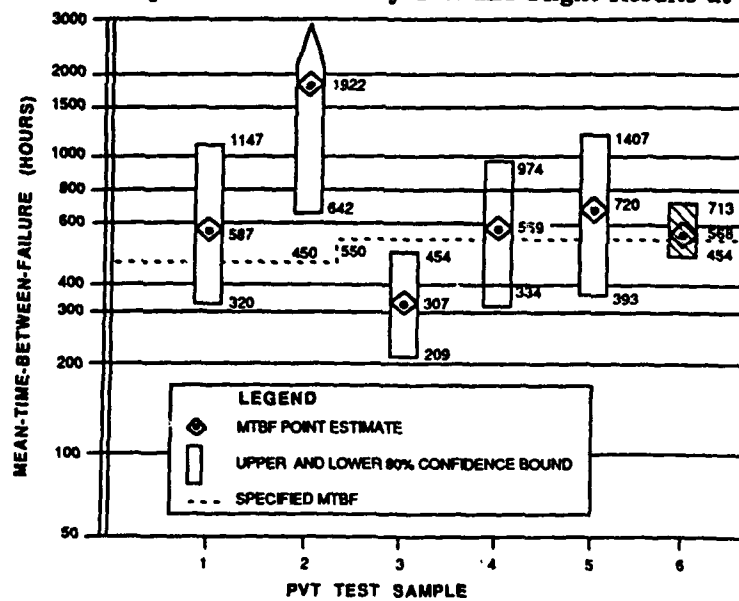**Figure 4. Comparison of Reliability Test and Flight Results at PMTC**

Figure 5. Typical Results of Reliability Testing at PMTC

ALTERNATIVES FOR ACHIEVING FIELD RELIABILITY

The following compares the economic consequences of reliability testing with several alternatives for achieving adequate in-service reliability. First several alternatives are ranked without detailed quantitative analysis, and then the two top candidates are compared in a quantitative manner.

Identification of Alternatives

The following alternatives to reliability testing were considered:

1.   No testing and no other provisions

2.   An intensive reliability surveillance program upon introduction to service (no testing)

3.   A reliability improvement warranty program (no testing)

4.   Testing at a government facility

5.   Testing at a contractor facility

The first alternative corresponds essentially to the conditions that prevailed prior to the R&M 2000 initiative: a high risk that newly acquired equipment does not meet the reliability requirements, and long delays before improved equipment can be introduced to the operational units. The effectiveness of new weapon systems is seriously impaired, and because much equipment has to be retrofitted high costs are incurred. This alternative is considered obviously inferior to alternative 2 and is not analyzed in detail.

In the second alternative the high cost of retrofit is recognized, and a reliability surveillance program is initiated immediately after introduction into service, or possibly at the operational test site. The surveillance achieves a modest reduction in the time required to identify reliability problems and to formulate corrective measures. It is only modestly effective because

- the weapon system is not operated in a typical fashion immediately upon introduction to service, and thus some operational modes are not utilized at all, and others are not subjected to full environmental stresses

- the causes of field failures are frequently difficult to analyze because the exact time and environment in which a failure occurred cannot be pinned down and because expert personnel may not be available at the site at which the failure occurred

- a considerable interval is required to negotiate the required changes with the vendor and to obtain approval for the contractual arrangements.

The next alternative, reliability improvement warranty, overcomes the last of these

drawbacks and shifts some of the cost and responsibility for the first two to the vendor (at a cost). It has generally been found to be superior to alternative 2 and is analyzed in detail in the following section.

Alternative number 4, reliability test at a government facility achieves reliability evaluation in a controlled environment before operational use of the equipment. Reliability difficulties are recognized early because the instrumentation provided as part of the test facility is much more sensitive than that available in operational units. Skilled personnel at the test facility can perform failure diagnosis, and test conditions can be exactly duplicated to verify the failure mechanism or its absence.

Alternative number 5, reliability testing at a contractor facility, shares the advantages enumerated above, but is inferior in that usually only the equipment from one vendor can be evaluated at a given facility (thus making comparative evaluations impossible or at least very difficult to verify), and in that contractual arrangements tend to be inflexible (changes in schedule or equipment allocation require renegotiation). This alternative was considered undesirable by the Air Force program offices contacted as part of this study and is therefore not evaluated in detail.

Evaluation Procedure

The two surviving alternatives are reliability improvement warranty and reliability testing at a government facility. These are evaluated below by comparing the cost for a reliability test against the cost of the delay in identifying failure modes that is typical of RIW approach. The analysis neglects (a) the cost of the RIW, and (b) the cost of diverting prototypes or early production units to the reliability test rather than having them available for operational evaluation or other uses. Neither one of these factors could be accurately determined within the limitations of this study. The omitted factors partially offset each other, and any remaining cost is believed to be small compared to the differential established in the analysis.

The LN-39 program is cited as an example in literature distributed by USAF/LE-RD [USAF88] and is therefore considered representative of costs and benefits of such programs. Figure 6 represents the graph of MTBF vs. time for the LN-39 RIW, but also shows hypothetical results from a reliability test program that is now described (broken line in the figure). It is emphasized that no reliability test program has been conducted, and that the probable results of such a program are a matter of judgment. However, the general approach taken here has been discussed with individuals within the Air Force and at the vendor without encountering major criticism.

The original graph (solid line) demonstrates the "soft environment" when equipment is introduced into service by the rising reliability line during the first six months which must be contrasted with the much lower reliability experienced subsequently, and it also shows the approximately one year delay between the manifestation of a serious reliability problem and evidence of a turn-around.

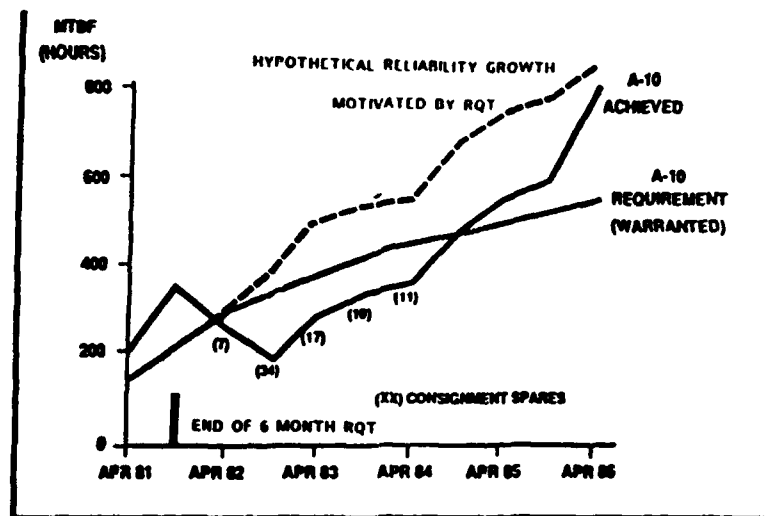## LN 39 Standard Navigation Unit Warranty

Figure 6. Comparison of Reliability Test and RIW

The benefit of the test program is that it surfaces the reliability problems earlier and therefore avoids the cost to the Air Force of the delayed introduction of the improvements. The dashed line has been constructed by paralleling the improvement (slope of the line) achieved under RIW but starting it 6 months after the end of the reliability test. This is justified by (a) earlier and more definitive identification of the failure mechanisms, and (b) the presence of fewer faulty units in the field.

A distinction must be made between RIW MTBF and the MTBF experienced in flight which is denoted by MFHBF (mean flight hours between failures). In all of the following it is assumed that MTBF = 2 * MFHBF. Thus, during the time when the MTBF hovered around 200 hours, (between April 81 and April 83), one failure was experienced on the average every 100 flight hours.

Cost of Reliability Testing

The cost of the reliability test consists of the following elements:

(a)   Cost of testing
       3 systems, 3 months (6,000 hours test exposure)   150,000

(b) Cost of refurbishing 3 systems after test   120,000

(c) Vendor support during test period   100,000

                        TOTAL   370,000

NOTES:

(a) Assumes 1 engineer for 9 months (which includes preparation and report writing time) at a cost of $90,000 and 3 technicians for 3 months at a cost of $60,000. No allowance for equipment and facility which are considered "sunk costs".

(b) Assumed at approximately 30% of the cost of new systems.

(c) Assumes one technician on site for four months, and one back-up engineer on call for three months.

Benefit of Reliability Testing

The benefit of the reliability test (compared to the RIW) consists of an average of 200 hr MTBF or 100 MFHBF improvement (difference between the dashed and solid lines in Figure 7) for a period of 3 years (October 82 - October 85). At the April 1984 midpoint of the improvement period, this equates to the difference between 200 MFHBF and 300 MFHBF. It is assumed that the fleet during this three year period averaged 500 aircraft, and that on the average 20 flight hours per month were accumulated on each aircraft, amounting to 10,000 flight hours per month.

At 200 MFHBF this will produce 50 failures per month, and at 300 MFHBF it will produce 33 failures per month, the difference being 17 failures. The cost of a failure to the Air Force under the RIW contract consists of

(1) A fraction of mission time due to degraded performance of the aircraft and/or return prior to completion of mission

(2) Technician time for failure diagnosis, removal and checkout of the equipment

(3) Downtime of the aircraft while awaiting installation of replacement equipment

(4) Technician time for reinstallation and verification of satisfactory operation.

(5) Logistic cost of exchange of equipment.

For the total of these items a cost of $5,000 per failure has been assumed. The reduction of 17 failures per month then produces a benefit of $85,000 per month or $3,060,000 for the 36 month period.

The cost of the reliability test is assumed to have been incurred in October 1981 and the center line for the benefit (increase in MFHBF) occurs in April 1984. Thus the cost was incurred 2.5 years before the mean benefit was achieved. In accordance with the requirements of AFR 178-1 a discount factor of 10% per year is assumed. The benefit then has to be discounted by

$$(1.1)^{2.5} = 1.27$$

The discounted benefit is 3,060,000/1.27 = $2,409,000

To obtain the net benefit, the $370,000 cost of reliability testing is subtracted, yielding

$2,039,000

Discussion of Results

The above analysis involves a number of assumptions and estimates which can be questioned. However, the benefits shown are so large, that the preference for reliability testing over RIW in this case is robust to any reasonable changes in these assumptions. As an example, the assumed $5,000 cost of a failure would have to change to less than $770 before there is a disbenefit to reliability testing.

In assessing the cost of reliability testing no allowance has been made for the cost of redesign and retest to achieve and verify the reliability improvement. These costs are also incurred in the RIW approach, and they are therefore not considered a cost differential between the alternatives.

The RIW alternative commits the government to contractor maintenance during the RIW period. Under reliability testing the maintenance may be performed by the contractor, the government (organic maintenance), or a third party. The benefits arising from these options have not been included in the analysis.

MAKING RELIABILITY TESTING EFFECTIVE

In spite of the existence of many known field reliability problems, reliability testing of guidance equipment is not widely practiced. Air Force Regulation 800-18 requires that reliability testing be employed where it is effective, and the lack of testing indicates that many organizations do not believe it to be effective. In meetings with program offices conducted as part of this study the following characteristics of reliability testing were considered obstacles to wider usage:

- it takes too long

- it ties up prototype or pre-production equipment that is urgently needed for other purposes

- results are frequently controversial or inconclusive

- reports tend to be late and therefore do not contribute to decisions.

These criticisms must be addressed if a viable reliability test program is to be established. The first two objections can be overcome if the test period can be reduced, and one step in that direction is the adoption of Probability Ratio Sequential Test (PRST) plans. These permit early termination of tests when few failures are encountered, and in the worst case extend the test time by only a modest amount. Additional possibilities for reduction of the test exposure are described below.

Test time can be reduced by increasing the discrimination ratio of a test or the risk, but these steps diminish the significance and usefulness of the test results. They should be reserved for early test sequences of equipment still under development where only a preliminary evaluation of reliability is required. The techniques explored in the following are aimed at a reduction of test time without reducing the statistical significance. This is achieved by detailed examination of the failure modes and providing analytical procedures and stresses specifically tailored to them.

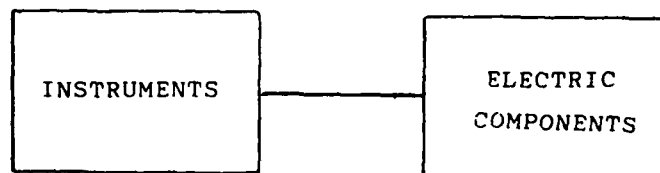The simple reliability model shown in Figure 7 is applicable to most guidance equipment

Figure 7. Reliability Model for Guidance Equipment

In over 7000 failure reports examined during this study at least 60% of the failures affected instruments but this may change to a more even distribution among the components of the model due to the increasing use of digital techniques. In the instrument part of the model, failures tend to manifest themselves in degraded performance while in the electrical/electronic part they are much more likely to cause gross errors or loss of functionality. Advanced test techniques can address each of these failure mechanisms separately:

- the tendency to degraded performance by measurements that capture the rate of degradation

- the electrical/electronic malfunctions by increasing the stresses known to precipitate these failures.

The tendency to degraded performance can be detected in several ways:

a. for an individual instrument there is a consistent shift in bias or scale factor or similar internal performance parameter, or an increase in the variability of bias and scale factor, over time.

b. for a given type of instrument (of which usually several are under test at the same time) there is a consistent shift or increase in variability over time.

c. a measure of system accuracy (such as attitude accuracy or CEP) shows degradation over time for an individual system

d. a measure of system accuracy shows degradation over time for the ensemble of systems under test.

In each of these cases it is assumed that the quantity being monitored is still within the specification limits but has changed from its pre-test value in a direction that will bring it outside the limits if the trend continues. The existence of such a trend then indicates with high probability that the instrument or system will fail at a future time, designated in the following as T. Assume that the test is terminated after t hours at which time n_i instrument failures have been observed and N failures are estimated by the trend analysis discussed above to lead to failure at time T. An estimate of the MTBF due to the instrument portion of the model, θ_i, is then

$$E[\theta_i] = T/(N + n_i T/t)$$

Assume that a test is terminated at 1,000 hours total test time with 3 observed failures and that trend analysis indicates that six failures are likely to be observed if the test were to be continued to 3,000 hours. The expected MTBF is then $3,000/(6 + 9) = 200$ hours. The reciprocal of the system MTBF, θ_s, can be approximated by

$$1/\theta_s \approx 1/\theta_e + 1/\theta_i$$

where the subscript e denotes the MTBF of the electronic portion of the system. .
An exact equation for the reliability of the system is

$$R_s(T) = e^{-T/\theta_s} = e^{-T/\theta_e} * e^{-T/\theta_i}$$

The prevalence of the degradation will determine whether this extrapolation should be
applied to the MTBF of a single instrument, single system, or to the ensemble of the items
under test.

If the degradation trend manifests itself in one-half the time required to exceed the
specification limit (a conservative assumption), the number of instrument failures will be
increased by 50% and the number of system failures increased by 30% due to this
technique. The test time to achieve a given test objective can be correspondingly reduced
because the risk associated with a given test plan is basically determined by the number
of failures that are expected to be observed.

To implement this technique it should be agreed to by all parties concerned, and criteria
for evaluating trends must be defined. Beyond that, the cost of more careful data
acquisition and analysis is quite small compared to the saving in test time and the ability
to furnish test results at an earlier date.

Now we turn to the electrical/electronic parts of the system where degradation mechanisms
are much more difficult to identify, and where therefore only manifest failures can be
observed. Here an increase in the stress levels may be used to increase the failure rate
and thereby reduce the test time. Semiconductor failure rates approximately double for
every 15 degrees C increase in ambient temperature. Failure rates of other elements of
the electronic parts of the system can be increased by high rates of temperature change.
Since there is usually some margin between the qualification limits of the system and the
envelope of the reliability test, a modest increase in the environmental stress may be
tolerated without damage to the equipment. The quantitative increase in failure probability
that can be achieved with this technique and the corresponding decrease in test time
depend on the ratio of semiconductor failure rates to other failure rates in the system, but
increasing the failure rate of the electronic portion by a factor of 1.5 should be possible
without too much difficulty.

Research in the area of failure inducing stresses is being carried out by the AVIP Project
at ASD/ENAS, and this work should permit structuring of failure accelerating environments
and estimation of the resulting acceleration factors. With the adoption of an environment
tailored to the AVIP recommendations, a test conducted in the RGQT format described
in the preceding section should meet all requirements of the ASD/EN and in addition
achieve a statistically meaningful estimate of the equipment reliability.

Together, the analysis of degradation trends for the instrument portion of the system and
the use of accelerated testing for the electronic components may permit a reduction in test

time by 25% - 40%. This is particularly significant when adverse conditions are encountered. The reduction in maximum test time from 7 months to 5 months may induce a program office that is doubtful about the effectiveness of reliability testing to give it a try.

The time to identify the cause is expected to be considerably shorter for failures observed in a reliability test than for those occurring in the field because of better instrumentation of the unit under test, control of the environmental conditions, and monotoring and recording of the test by skilled personnel (including representation by the manufacturer). And the old saying "Time is money" is very much applicable to the identification of failure mechanisms early in the equipment life. For these reasons efforts to improve reliability test techniques and to increase the use of reliability tests are expected to have a large payoff.

REFERENCES

PMTC81   Weapons System Test Department, Pacific Missile Test Center, "PATE" (brochure), August 1981

STAN77   Edmund A Stanczak, Jr., "An Evaluation of the Combined Environments Reliability Testing of the RT868A/APX-76 IFF Interrogator Receiver-Transmitter", Report #AFFDL-TR-77-132, December 1977

THEI78   E.C. Theiss, "An Evaluation of the Combined Environment Reliability Testing of the AN/ARC/-109 UHF Communication Set", Report #AFFDL-TR-79-3149, October 1978

TOM86   D.C. Tom and S.R. Palos, "Production Verification Test Report of Sparrow III, AIM/RIM-7M Production", Report # X1030-SP-11-004, General Dynamics Contract, Reliability Evaluation Division, October 1986

TREL77   Kenneth Trelewicz and John Herlihy, "Conceptual Designs for Combined Environments Reliability Test Facility", AFFDL-TR-77-3, Technical Report, June 1977

USAF88   HQ USAF, Office of the Special Assistant for R&M, "R&M 2000 Process", Washington DC, October 1988

WAGN81   John Wagner, 1Lt. USAF, "AN/ARN-84(V)9 Tacan Cert--A Guideline for Mission Profile Testing", Report AFWAL-TR-81-3033, August 1981

WARN81   John C. Warner, "An Evaluation of a Tailored Approach to Combined Environment Reliability Test (CERT) of the RT-1063B/AN/APX-101 IFF Transponder", Report AFWAL-TR-80-3108, April 1981

ACRONYMS

AFR	Air Force Regulation
AFWAL	Air Force Wright Aeronautical Laboratory
AVIP	Avionics Improvement Program
CEP	Circular Error Probable
CERT	Combined Environment Reliability Test
FTS	Flight Test Simulation
MFHBF	Mean Flight Hours Between Failures
MTBF	Mean Time Between Failures
MTTF	Mean-Time-To-Failure
PATE	Production Acceptance Test and Evaluation
PMTC	Pacific Missile Test Center
PRAT	Production Reliability Acceptance Test
PRST	Probability Ratio Sequential Test
PVT	Production Verification Test
R&M	Reliability & Maintainability
RGQT	Reliability Growth and Qualification Test
RIW	Reliability Improvement Warranty
UUT	Unit Under Test

THIS PAGE LEFT INTENTIONALLY BLANK

The Utilization of Time Domain

Parallel Processing Techniques

for Sensor Characterization

October 1989

Prepared by:

Robert Thede*
Applied Technology Associates, Inc.
1900 Randolph Road, SE
Albuquerque, NM 87106
505-247-8371
FAX 505-768-1378

Presented to:

Fourteenth Biennial Guidance Test Symposium
Department of the Air Force
Headquarters 6585th Test Group (AFSC)
Holloman Air Force Base, New Mexico 88330-5000

*Now with Litton Guidance and Control Systems Division
MS87, 5500 Canoga Avenue, Woodland Hills, CA 91367-6698
(818) 715-2625

Abstract

Techniques which require the testing of pairs of inertial sensors with their input axes parallel are frequently used to separate sensor characteristics from disturbing common inputs. Several fairly sophisticated procedures which operate in the frequency domain have been developed and used successfully to characterize sensor noise in the presence of relatively large disturbing inputs. In some areas of testing, procedures which operate in the time domain are preferred. For example, the determination of the variance or standard deviation of a set of data is almost universally performed to provide a basic measure of the dispersion of the data. Also, the characterization of the noise of laser gyros through the use of Allan variances has become an established practice. In these areas, parallel test analysis still typically consists of examining plots of the sensor outputs to qualitatively determine if they are correlated and differencing the outputs of the two sensors to remove common inputs. In this paper, time domain procedures which are analogous to the previously developed frequency domain procedures are developed. These procedures provide a quantitative determination of the amount of correlation between the outputs of pairs of sensors. Procedures are also presented which separate the individual sensor noise from common disturbing inputs. These procedures provide scalar quantities which complement the simple variance determinations as well as several functions which complement the commonly used "Green charts" for sensor noise characterization.

Introduction

The variance or standard deviation of a set of data is commonly used to provide an estimate of the dispersion of the data. Additional information concerning the characteristics of the noise are sometimes obtained by a method known as Allan Variances. This procedure determines the average variance or standard deviation of pairs of data points as a function of time between data points (Reference 1). This presentation of the standard deviation as a function of sample time is used extensively in characterizing the noise of laser gyros. The plots depicting the noise in this manner have come to be known as Green charts. As the performance of sensors improves, external inputs during the testing corrupt the estimates of the sensors noise. To overcome this problem, pairs of sensors are typically tested together with their input axes parallel. The outputs of the two instruments then are typically subtracted to remove the common input and the variance or Green chart is constructed from this differenced data. The assumption is then made that the noise from the two instruments is equal and it is divided accordingly. Procedures such as these have also been used in frequency domain noise characterizations; however, improved techniques which use the cross power and coherence function between the pairs of data sets are now being applied (Reference 2). These procedures give better estimates of the noise characteristics of the two instruments and also provide additional information concerning how well correlated the two data sets are. These procedures can also be applied to the time domain estimates of the variance.

Development of Procedure

The variance of a random variable is the expected value of the squared deviations about its mean, or its second central moment, i.e.,

$$\sigma_x^2 = E(X^2) - [E(X)]^2$$

where

$$\sigma_x^2 = \text{Variance of X}$$

$E(X)$ = Expected value of X

To simplify the computations the data are assumed to have had the mean removed so that $E(X)=0$.

A diagram of the parallel sensor test configuration is shown in Figure 1. The item of primary interest is the noise of the two sensors, m_1 and m_2, which is assumed to occur at the inputs to the sensors. X is the common input to the two sensors. The sensor scale factors are k_1 and k_2. The sensor outputs, Y_1 and Y_2, are given by

$$Y_1 = k_1\left(m_1 + X\right)$$

$$Y_2 = k_2\left(m_2 + X\right)$$
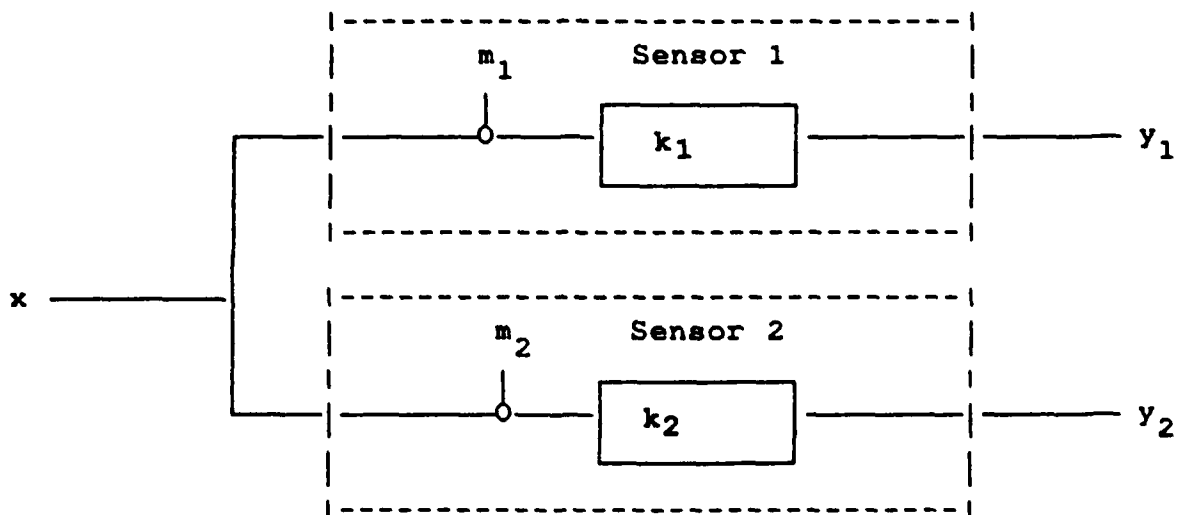
Figure 1. Parallel Equal Input Noise

Assuming the data are zero mean, the variances are given by the expected values of the squared outputs

$$\sigma_{y_1}^2 = k_1^2\, E\left(m_1 + X\right)^2$$

$$\sigma_{y_2}^2 = k_2^2\, E\left(m_2 + X\right)^2$$

or

$$\sigma_{y_1}^2 = k_1^2\left[E\left(m_1^2\right) + E\left(X^2\right) + E\left(m_1\,X\right)\right]$$

$$\sigma_{y_2}^2 = k_2^2\left[E\left(m_2^2\right) + E\left(X^2\right) + E\left(m_2\,X\right)\right]$$

It can usually be assumed that the sensor noise is uncorrelated with the common disturbances. Therefore

$$E(m_1 X) = E(m_2 X) = 0$$

and

$$\sigma_{y_1}^2 = k_1^2 \left[E(m_1^2) + E(X^2) \right]$$

In a similar manner the covariance between the two sensors can be determined.

$$\sigma_{y_1 y_2}^2 = k_1 k_2 \, E\left[(m_1 + X)(m_2 + X) \right]$$

or

$$\sigma_{y_1 y_2}^2 = k_1 k_2 \left[E(m_1 m_2) + E(X^2) \right]$$

It can usually be assumed that the noise of the two sensors is uncorrelated. Therefore

$$\sigma_{y_1 y_2}^2 = k_1 k_2 E(X^2)$$

The correlation coefficient between the two data sets is

$$\rho = \frac{\sigma_{y_1 y_2}^2}{\left[\sigma_{y_1}^2 \, \sigma_{y_2}^2 \right]^{1/2}}$$

The value of ρ will be between -1 and 1. A value close to -1 indicates the two data sets are highly correlated but in opposite directions. A value near zero indicates little correlation. Only the magnitude of the correlation function is of concern. Therefore

$$|\rho| = \frac{E(X^2)}{\left[\left[E(m_1^2) + E(X^2) \right] \left[E(m_2^2) + E(X^2) \right] \right]^{1/2}}$$

If the input noises of the two sensors are assumed to be equal, i.e., $E(m_1^2) = (m_2^2)$, this becomes

$$|\rho| = \frac{E(X^2)}{E(m^2) + E(X^2)}$$

From before

$$\sigma_{y_1}^2 = k_1^2 \left[E(m_1^2) + E(X^2) \right]$$

Therefore

$$k_1^2 E(X^2) = \sigma_{y_1}^2 - k_1^2 E(m^2)$$

Substituting this into the equation for the correlation coefficient gives

$$|\rho| = \frac{\sigma_{y_1}^2 - k_1^2 E(m^2)}{\sigma_{y_1}^2}$$

The sensor noise variance $k_1^2 \, E\,(m^2)$ therefore is

$$k_1^2 E(m^2) = \sigma_{y_1}^2 \, (1 - |\rho|)$$

Similarly for the other sensor

$$k_2^2 E(m^2) = \sigma_{y_2}^2 \, (1 - |\rho|)$$

These results are analogous to those obtained in the frequency domain using the equal input noise procedure (Reference 2).

In a similar manner it can be shown that if the noise occurs on the sensor outputs and is the same for the two sensors (Figure 2), the equal output variance is

$$E(n^2) = 0.5\left[\sigma_{y_1}^2 + \sigma_{y_2}^2 - \sqrt{\left(\sigma_{y_1}^2 - \sigma_{y_2}^2\right)^2 + 4\,|\sigma_{y_1 y_2}^2|^2}\right]$$

where n is the sensor output noise.
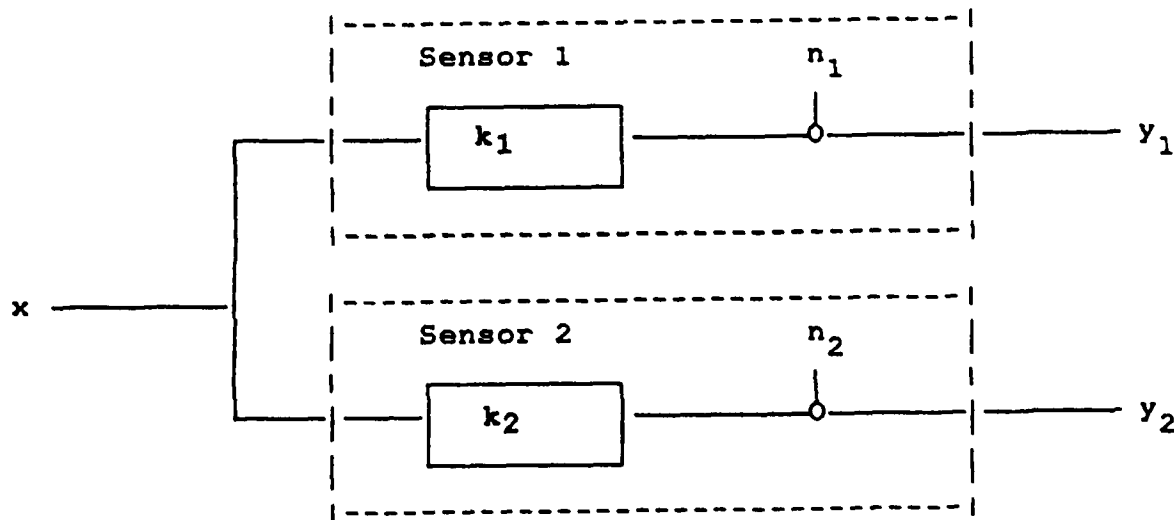
Figure 2. Parallel Equal Output Noise

Effects of Assumptions on Results

Certain assumptions were made in developing the procedures in the previous section. Certain assumptions are also made when sensor noise is determined by differencing the outputs of pairs of sensors. An investigation into the effects of these assumptions is therefore appropriate.

Noise Estimates without Assumptions

The procedure of determining sensor noise from the difference in the outputs of parallel sensors assumes three conditions: 1) the noise on the two sensors is the same; 2) the sensor scale factors are known exactly; and 3) the noise of the two sensors is uncorrelated. The estimated noise of either sensor, σ_δ^2, is given by

$$\sigma_\delta^2 = 0.5 \, E\left[\left[k_1(m_1 + X) - k_2(m_2 + X)\right]^2\right]$$

or

$$\sigma_\delta^2 = 0.5\left[k_1^2 \, E\left(m_1^2\right) + k_2^2 \, E\left(m_2^2\right) + (k_1 - k_2)^2 \, E\left(X^2\right) - 2k_1 k_2 \, E\left(m_1 \, m_2\right)\right.$$
$$\left. + k_1(k_1 - k_2) \, E(m_1 \, X) - k_2(k_1 - k_2) \, E(m_2 \, X)\right]$$

The equal input noise procedure assumes that the noises on the two sensors are equal and uncorrelated with each other and with the common input. The estimated noise for one of the sensors using this procedure is

$$\sigma_{EI1}^2 = \sigma_{y1}^2\left(1 - |\rho|\right)$$

$$\sigma_{EI1}^2 = k_1^2 \, E\left(m_1^2\right) + k_1^2 \, E\left(X^2\right)(1 - A) + k_1^2 \, E(m_1 \, X)(1 - A)$$
$$- k_1^2\left[E(m_1 \, m_2) + E(m_2 \, X)\right]A$$

where

$$A = \left[\frac{E\left(m_1^2\right) + E\left(X^2\right) + 2E\left(m_1 \, X\right)}{E\left(m_2^2\right) + E\left(X^2\right) + 2E\left(m_2 \, X\right)}\right]^{1/2}$$

The equal output procedure assumes there is equal noise on the outputs of both sensors and the sensor noises and common input noise are all uncorrelated. The estimated noise using this procedure is

$$\sigma_{EO}^2 = 0.5\left[\sigma_{y1}^2 + \sigma_{y2}^2 - \sqrt{\left(\sigma_{y1}^2 - \sigma_{y2}^2\right)^2 + 4\left|\sigma_{y1 y2}^2\right|^2}\right]$$

or

$$\sigma_{EO}^2 = 0.5\left[E\left(n_1^2\right) + E\left(n_2^2\right) + \left(k_1 + k_2\right) E\left(X^2\right) + E(n_1 \, X) + 2k_2 \, E(n_2 \, X)\right.$$
$$- \left[\left[E\left(n_1^2\right) - E\left(n_2^2\right) + \left(k_1^2 - k_2^2\right) E\left(X^2\right) + 2k_1 \, E(n_1 \, X) - 2k_2 \, E(n_2 \, X)\right]^2\right.$$
$$\left.\left. + 4\left|k_1 \, k_2 \, E\left(X^2\right) + E(n_1 \, n_2) + k_1(n_2 \, X) + k_2 \, E(n_1 \, X)\right|^2\right]^{1/2}\right]$$

Uncorrelated Noise Assumption - Equal Input Compared with Differencing

All three approaches assume that the sensor noises are uncorrelated with each other and with the common disturbances, i.e.,

$E(n_1 X) = 0$

$E(n_2 X) = 0$

$E(n_1 n_2) = 0$

$E(m_1 X) = 0$

$E(m_2 X) = 0$

$E(m_1 m_2) = 0$

If the sensor scale factors are approximately equal, the error caused by these assumptions in the differencing method is approximately $-k^2 E(m_1 m_2)$. For the equal input procedure if the sensor noises are approximately equal and the sensor noise plus the common noise are significantly larger than the covariance between the sensors and the common input, A will be approximately 1. Then the error caused by the correlations not being zero using this procedure will be approximately k_1^2 $[E(n_1 x) - E(m_2 x) - E(m_1 m_2)$. If the covariance between the sensor and the common noise is the same for the two sensors, the error will be the same as with the differencing procedure. In the equal output technique error terms such as $[E(n^2) E(nx)]^{1/2}$ will result. These could be significantly larger than the errors resulting from the uncorrelated assumptions for the other two methods.

Scaling and Equal Noise Assumptions - Equal Input Compared with Differencing

To evaluate the other assumptions the equations will be rewritten with the covariances equal to zero.

$$\sigma_D^2 = 0.5 \left[k_1^2 E(m_1^2) + k_2^2 E(m_2^2) + (k_1 - k_2)^2 E(X^2) \right]$$

$$\sigma_{EII}^2 = k_1^2 E(m_1^2) + k_1^2 E(X^2)(1 - A)$$

where

$$A = \left[\frac{E(m_1^2) + E(X^2)}{E(m_2^2) + E(X^2)} \right]^{1/2}$$

$$\sigma_{EO}^2 = 0.5 \left[E(n_1^2) + E(n_2^2) + (k_1 + k_2) E(X^2) \right.$$

$$\left. - \left[[E(n_1^2) - E(n_2^2) + (k_1^2 - k_2^2) E(X^2)]^2 + 4 k_1^2 k_2^2 E(X^2)^2 \right]^{1/2} \right]$$

The differencing procedure is highly dependent on the scaling of the two sensors being correct and the noise of the two sensors being the same. If the scaling is not correct, the common input will not be entirely eliminated. Scaling errors can be caused by errors in knowledge of the sensor scale factor and also by misalignments between the two sensors which result in one sensor sensing a proportionately larger or smaller common input than the other sensor. If scaling errors are not present, the differencing method will give the average variance of the two sensors. The equal input approach is not dependent on accurate scaling of the two sensors to cancel the inputs. All approaches assume the noise on the two sensors is the same. To evaluate the effect of this

assumption, it will be assumed that there are no scaling errors and no correlation between errors. The noise estimate from the differencing approach then becomes

$$\sigma_D^2 = 0.5 \left[K^2 E\left(m_1^2\right) + K^2 E\left(m_2^2\right) \right]$$

The estimate from the equal input approach is

$$\sigma_{EII}^2 = K^2 E\left(m_1^2\right) + K^2 E\left(X^2\right)(1 - A)$$

The error in each estimate then is

$$\Delta_{D1} = \frac{\sigma_D^2 - K^2 E\left(m_1^2\right)}{K^2 E\left(m_1^2\right)} = \frac{0.5}{E\left(m_1^2\right)} \left[E\left(m_2^2\right) - E\left(m_1^2\right) \right]$$

$$\Delta_{EII} = \frac{\sigma_{EII}^2 - K^2 E\left(m_1^2\right)}{K^2 E\left(m_1^2\right)} = \frac{E\left(X^2\right)}{E\left(m_1^2\right)} \left[1 - \left(\frac{E\left(m_1^2\right) + E\left(X^2\right)}{E\left(m_2^2\right) - E\left(X^2\right)} \right)^{1/2} \right]$$

To simplify this let

$$E\left(m_1^2\right) = P E\left(m_2^2\right)$$

$$E\left(X^2\right) = Q E\left(m_2^2\right)$$

then

$$\Delta_{D1} = \frac{0.5}{P} (1 - P)$$

$$\Delta_{EI} = \frac{Q}{P} \left[1 - \left(\frac{P + Q}{1 + Q} \right)^{1/2} \right]$$

When the errors on both sensors are the same, that is $P = 1$, both procedures give estimates with zero error. A direct comparison of the errors for $P \neq 1$ is not straightforward; however, it is sufficient to compare the rates of change of the errors in the estimates as P changes. That is

$$\Delta_{EI} \leq \Delta_{DI}$$

if

$$\frac{\delta}{\delta P} \Delta_{DI} \leq \frac{\delta}{\delta P} \Delta_{EI}$$

It is also sufficient to look at the rate of change of the absolute error rather than the percentage error.

$$\frac{\delta}{\delta P} Q \left[1 - \left(\frac{P + Q}{1 + Q} \right)^{1/2} \right] \leq \frac{\delta}{\delta P} \frac{1}{2} (1 - P)$$

or

$$\frac{Q^2}{Q^2 + Q + PQ + 1} \leq 1$$

Because P and Q must be greater than or equal to zero this is true for all allowable values of P and Q. Therefore the equal input procedure will provide an equal or better estimate of the individual sensor noises then is provided by the differencing procedure regardless of the magnitude of the common disturbance or the difference in magnitude of the noise of the two sensors. To provide a better comparison, plots of the error in estimate as a function of difference in noise of the two sensors for several different values of common noise are shown in Figure 3. These results show that in the presence of small common inputs, the estimate of the noise provided by the equal input approach is significantly better than that provided by the differencing techniques. For large common inputs the two techniques are comparable.
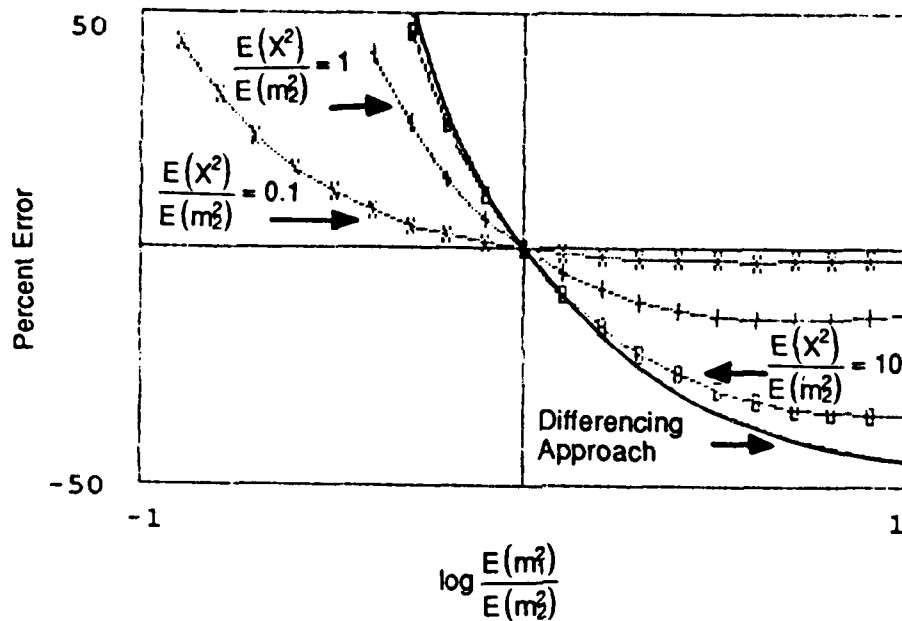
Figure 3. Errors in Equal Input Estimates

Errors from Equal Output Approach

If the scale factors are known exactly and are set to one, the estimated noise given by the equal output approach is

$$\sigma_{EO}^2 = 0.5 \left[E\left(n_1^2\right) + E\left(n_2^2\right) + 2E\left(X^2\right) \right.$$

$$\left. - \left[\left[E\left(n_1^2\right) - E\left(n_2^2\right) \right]^2 + 4E\left(X^2\right)^2 \right]^{1/2} \right]$$

The error in the estimate for sensor number 1 is

$$\Delta_{EOI} = \frac{\sigma_{EO}^2 - E\left(n_1^2\right)}{E\left(n_1^2\right)}$$

$$\Delta_{EOI} = \frac{0.5}{E(n_1^2)} \left[E(n_2^2) - E(n_1^2) + 2E(X^2) \right.$$

$$\left. - \left[\left[E(n_1^2) - E(n_2^2) \right]^2 + 4E(X^2)^2 \right]^{1/2} \right]$$

Comparing this with the error from the differencing approach it can be seen that the equal output error will be less than the differencing error if

$$\frac{0.5}{E(n_1^2)} \left[2E(X^2) - \left[\left[E(n_1^2) - E(n_2^2) \right]^2 + 4E(X^2)^2 \right]^{1/2} \right] < 0$$

or

$$4E(X^2)^2 < \left[E(n_1^2) - E(n_2^2) \right]^2 + 4E(X^2)^2$$

or

$$E(n_1^2) - E(n_2^2) > 0$$

Therefore, the equal output approach will always produce a better estimate than the differencing approach for the noisier sensor and a worse estimate for the quieter sensor.

A comparison of these two procedures is made in Figure 4 for several different values of *common noise*. A comparison of Figures 3 and 4 shows that the equal input approach will always give a more accurate estimate than the equal output approach.
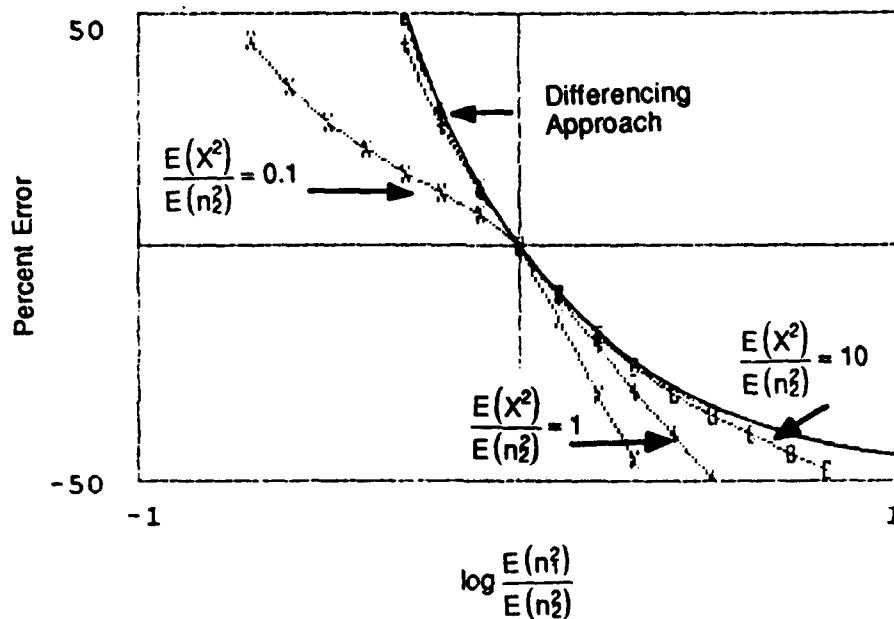
Figure 4. Errors in Equal Output Estimates

Three Sensor Testing

When three sensors are tested in parallel, estimates of the noise of the individual sensors can be obtained without assuming that noise on all of the sensors is equal. The assumption must still be made that the noise on all sensors is uncorrelated with each other and with the common input. The variance of the noise as measured by sensor number 1 is

$$\sigma_{y_1}^2 = K_1^2 \left[E(m_1^2) + E(X^2) \right]$$

The correlation coefficients between each of the sensors is

$$|\rho_{12}| = \frac{E(X^2)}{\left[E(m_1^2) + E(X^2) \right]^{1/2} \left[E(m_2^2) + E(X^2) \right]^{1/2}}$$

$$|\rho_{13}| = \frac{E(X^2)}{\left[E(m_1^2) + E(X^2) \right]^{1/2} \left[E(m_3^2) + E(X^2) \right]^{1/2}}$$

$$|\rho_{23}| = \frac{E(X^2)}{\left[E(m_2^2) + E(X^2) \right]^{1/2} \left[E(m_3^2) + E(X^2) \right]^{1/2}}$$

Combining these equations gives

$$K_1^2 E(m_1^2) = \sigma_{y_1}^2 \left[1 - \left| \frac{\rho_{12} \, \rho_{13}}{\rho_{23}} \right| \right]$$

Similar results are obtained for the other two sensors.

$$K_2^2 E(m_2^2) = \sigma_{y_2}^2 \left[1 - \left| \frac{\rho_{12} \, \rho_{23}}{\rho_{13}} \right| \right]$$

$$K_3^2 E(m_3^2) = \sigma_{y_3}^2 \left[1 - \left| \frac{\rho_{13} \, \rho_{23}}{\rho_{12}} \right| \right]$$

Areas of Application

The variance of the output of a sensor provides an estimate of the noise on the sensor. A qualitative assessment of the amount of cultural noise present during the test is often obtained simply by comparing plots of the two sensors. A much better quantitative assessment can be obtained by computing the correlation coefficient. If significant correlation exists, the equal input procedure can be used to obtain estimates of the noise on each sensor. For the typical drift test where the sample rate is very slow, these computations can be made in real time and displayed continuously during the test. If unexpected high correlation occurs because of problems with the test equipment, early detection will be possible and adjustments can be made without significant delays to the test program.

Another area where these techniques can be employed is in the determination of noise on laser gyros through the use of Allan variances. The Allan variance is defined as

$$\sigma_\omega(\tau, m) = \frac{1}{2(m-1)} \sum_{k=1}^{m-1} \left(\overline{\omega}_{k+1} - \overline{\omega}_k \right)^2$$

where

$$\overline{\omega}_k = \frac{1}{\tau} \int_{t_k}^{t_k + \tau} \omega(t) \, dt$$

This is the average variance of pairs of successive data points where the data points are sensor outputs averaged over time. With these definitions it is now possible to define a cross Allan variance and an Allan correlation function. Both of these will be functions of the averaging time.

$$\sigma_{\omega z}^2 (\tau, m) = \frac{1}{2(m-1)} \sum_{k=1}^{m-1} (\overline{\omega}_{k+1} - \overline{\omega}_k)(\overline{Z}_{k+1} - \overline{Z}_k)$$

$$\rho_{\omega z}(\tau, m) = \frac{\sigma_{\omega z}^2}{(\sigma_\omega^2 \sigma_z^2)^{1/2}}$$

The computation of the Allan correlation coefficient will permit the determination of the influence of common inputs as a function of averaging time. If there are significant common inputs, the equal input procedures can be applied to the Allan variances to characterize the individual sensors.

Conclusions

Procedures for determining the variance of signals contaminated by common disturbances to pairs of sensor tested in parallel have been developed. These procedures give a better estimate of the noise of individual sensors than is obtainable by simply subtracting the outputs of the two sensors. The procedures required the computation of the correlation coefficient which provides a good measure of the amount of common noise present to the two sensors. These procedures are also applicable to noise characterizations in the form of Allan variances and Green charts. Allan correlation functions can be computed which will show the amount of correlation present between the outputs of pairs of sensors as a function of observation time.

The procedures developed have also been extended to the testing of three instruments in parallel. In this case assumptions concerning the equality of the noise on the sensors is no longer required.

Application of the procedures developed can be implemented on a real-time basis to provide quick-look information concerning test quality. Their application to the testing of precision instruments in the presence of disturbing influences will lead to a more accurate evaluation of those instruments.

References

1. Kochakian, Charles R., *Time-Domain Uncertainty Charts (Green Charts) A Tool for Validating the Design of IMU/Instrument Interfaces*, The Charles Stark Draper Laboratory, Inc., Cambridge, MA, P-1154, July 1980.

2. Morgan, Felix E. and Goucher, Randall O., *Alternative Techniques for Determining Sensor Noise in High Signal-to-Noise Parallel Tests*, Applied Technology Associates, Inc., Albuquerque, NM.

THIS PAGE LEFT INTENTIONALLY BLANK

REVERSE VELOCITY SLED TEST SIMULATIONS TO DETERMINE UNCERTAINTIES IN ACCELEROMETER MODEL COEFFICIENTS

BY
CAPT ROBERT L. NIELSEN
BARBARA A. COSENTINO
ROBERT S. LAWRENCE
SEAN M. DOYLE

PREPARED BY
CENTRAL INERTIAL GUIDANCE TEST FACILITY
GUIDANCE TEST DIVISION

6585TH TEST GROUP
HOLLOMAN AFB, NEW MEXICO 88330-5000

3, 4, & 5 OCTOBER 1989
GUIDANCE TEST SYMPOSIUM

THIS PAGE LEFT INTENTIONALLY BLANK

REVERSE VELOCITY
SLED TEST SIMULATIONS TO
DETERMINE UNCERTAINTIES IN
ACCELEROMETER MODEL
COEFFICIENTS

TABLE OF CONTENTS

THIS PAGE LEFT INTENTIONALLY BLANK

LIST OF FIGURES

LIST OF TABLES

THIS PAGE LEFT INTENTIONALLY BLANK

REVERSE VELOCITY
SLED TEST SIMULATIONS TO
DETERMINE UNCERTAINTIES IN
ACCELEROMETER MODEL
COEFFICIENTS

1. INTRODUCTION

Increased accuracy specifications state-of-the-art inertial guidance systems require more precise error compensation models and more precise error determination. These in turn require improved testing and analysis techniques to identify and quantify specific errors of a given system. This simulation study was conducted as a first, preliminary, attempt to quantify the results attainable via reverse velocity testing as compared to high-G positive-velocity monorail testing.

1.1 Basic Concepts. Testing in a 1 g environment permits determination of many errors but does not solve the difficult, sometimes impossible, task of analytically separating lumped parameters and highly correlated error functions. High-G dynamic testing, such as rocket sled testing on the Holloman test track, permits better error determination, but some error functions still defy quantification.

This led to the development of the reverse velocity sled test concept which adds a period of high negative acceleration in addition to the usual low deceleration of water brake. This greatly improves analytical error separation out of the noise and from one another. Figure 1 shows an artist's sketch of a monorail sled and towing outrigger sled as required for reverse velocity sled runs. In several test runs, the monorail sled was towed northward downtrack by the outrigger sled and while still moving, the sleds decoupled and the monorail sled accelerated southward back down the track past the start point.

The basic idea was to optimize the acceleration profile for separation of higher order, highly correlated terms, such as K_2 (G_2 non-linear scale factor) and K_3 (G_3 non-linear scale factor). The optimum ratio for positive to negative accelerations is about 1 to -3. Sample acceleration profiles and the corresponding relationship of K_2 to K_3 error functions are depicted in Figure 2. The reverse velocity concept is apparent in Figure 2 in that the optimum ratio of accelerations result in a negative velocity. This optimized acceleration profile enhances error determination because of the unique error function signatures it creates. Notice in Figure 2 that even-powered terms step up at reverse boost while odd-powered terms step down. This enhances separation of even and odd powered terms.

Additionally, the negative velocity results in a sled and test guidance system traveling at high velocity in two different directions over the same portion of the test track. This presents the highly desirable, unique situation of having two sets of test data which are exactly correlated in distance but dynamically different in both velocity and acceleration. In effect, this provides simultaneous equations for every location on the track during the test. This permits elimination of track reference anomalies because it becomes possible to match exact locations from the first half of the sled run with the data from the second half (Figure 3).

1.2 Objectives. The objectives of this simulation were: (1) to determine the error model coefficient uncertainty due to noise and high correlation of terms and (2) to determine the separability of error terms as related to run profiles, specifically: (a) low-G and (b) high-G reverse velocity runs and (c) a high-G positive velocity (monorail) run.

2. DATA GENERATION AND PROCESSING

The simulation data was generated to be as close to actual sled test data as possible without making the data simulation too complex.

2.1 Normal Data Processing. For an abbreviated flowchart showing the normal reference position vector processing and data analysis flow see Figure 4.

2.1.1 Normal Reference Position Vector Processing. The sled test space time system consists of a series of interrupter blades placed nominally 4.33 feet apart along the east rail of the te. ⁺ track and a space-time head attached to the sled. The space-time head, consisting of a light source and sensor, generates a signal when the light beam is interrupted by an interrupter blade. This signal is time correlated in real time on board the sled and then this time series is correlated with the surveyed position of the interrupter blades during post-run data processing. Survey measurement accuracies are shown in Table 1.

Next incorporated is the data from the linear variable displacement transducers (LVDT), which measure relative motion between the sled forebody (hard-side pallet) and the vibration isolated soft-side pallet where the system is mounted. Incorporating the LVDT data into the reference data produces a reference position vector without gravity or coriolis.

Finally, before comparing reference and system data, the reference position vector is normally compensated for gravity and coriolis effects. This correlates the reference position vector frame with the inertial system sensing frame.

The coordinate system usually used for sled test analysis is commonly referred to as the Launch Centered Earth Fixed frame (LCEF). The LCEF has an X axis collinear with the average track azimuth in the downtrack (northerly) direction, a Z axis collinear upward with the launch point gravity vector, and a Y axis nominally westward completing the orthogonal triad of axes.

Thus, the reference position vector basically correlates reference time, surveyed interrupter locations, LVDT data, and gravity and coriolis effects. This reference position vector can then be directly compared to system data for analysis.

2.1.2 Normal System Data Processing. In an actual sled test, the system data is collected and time correlated to tape real time during the sled run. Then, during post processing, the system data is compensated for known errors and the data is integrated from the acceleration (A) or velocity (V) domain to the distance (S) domain. The reference position vector is subtracted from the system data creating a delta-S in the LCEF frame. Then, an average derivative of the delta-S generates a delta-V.

2.1.3 Normal Data Analysis. Finally, in the analysis phase of actual sled testing, component and system errors are identified and the compensation model is verified via regression analysis in both the delta-S and delta-V domains. Specific errors are represented by calculated error functions generated from the mission's actual acceleration profile and used as fit functions in regression analysis. The determined coefficients can be iteratively applied in the compensation model for verification.

2.2 Simulation Data Generation. An abbreviated overview of the simulation method can be seen in Table 2.

2.2.1 Simulation Reference Position Vector Processing. The differences from normal reference position vector generation for this simulation were; the simulated time series, no LVDT data, no gravity or coriolis effects, and a nonstandard coordinate system.

The time series (T_s) corresponding to times normally generated by the space-time head was generated using basic equations, with the entire sled test profile broken into phases. For reverse velocity, the five phases were:

      (1). Forward Boost
      (2). Forward Coast
      (3). Reverse Boost (Positive Velocity)
      (4). Reverse Boost (Negative Velocity)
      (5). Reverse Coast

For each phase, three quantities of acceleration were calculated and summed to determine the total acceleration over that phase of the profile. The equations and the constants used can be found in Tables 3 and 4. These three quantities were:

      (1). Acceleration due to boost
      (2). Acceleration due to friction
      (3). Acceleration due to air resistance

The same methods were also employed for the monorail simulation, but the phases were:

      (1). Forward Boost
      (2). Forward Coast
      (3). Water Brake (Deceleration)
      (4). Forward Coast

The actual surveyed downtrack distances between interrupter blades were then used to calculate the time series corresponding to the specific sled test profile. This time series was used to generate a reference position vector just as if the time series had been generated by the space-time heads as a sled moved down the track.

As previously mentioned, no LVDT data was generated or used for the simulated reference position vectors. But, the actual survey data was used so actual survey anomalies were incorporated in the simulation. Additionally, gravity and coriolis effects were not used since they cancel out when system and reference data are differenced.

The reference position vector simulation method was verified in S, V, and A domains by comparing the profiles with an actual reverse velocity sled run. Profile plots of this simulation and the actual run with similar acceleration characteristics can be seen in Figure 5.

The coordinate system chosen for simulation analysis was the Curvilinear Rail Earth Fixed (CREF). The major difference between LCEF and CREF is that CREF is uniquely defined at every interrupter blade location. The X axis was still downtrack along the average track azimuth, and the Y axis was still directed west and was orthogonal to the X and Z axes, but the Z axis was upward and collinear with the gravity vector at each interrupter location, i.e., not just with the gravity vector at the launch point.

2.2.2 Simulation System. For these simulations, a triad of accelerometers comprised the "system" under test. These accelerometers were considered to nominally have their output axes along the axes of the CREF coordinate system.

2.2.2.1 Simulation System Errors. There were four error models used for the simulations, but only data and results from the Model # 4, the most complex, are presented in this paper. These four models only use six error functions. Figures 6 - 15 show plots of these six individual error functions for all three profiles. Total error Model # 4 is shown in Figures 16 - 18 for the three profiles. The equations for the four models in the acceleration domain are:

(1). $E_A = K_2 A^2 + A_3 A^3$

(2). $E_A = K_1 A + K_2 A^2 + K_3 A^3$

(3). $E_A = K_1 A + K_2 A^2 + K_3 A^3 + \tau \, dA/dt$

(4). $E_A = K_1 A + K_2 A^2 + K_3 A^3 + \tau \, dA/dt + K_4 A^4 + K_1' \, |A|$

Where the corresponding error functions are:

$K_1 A$ – Scale Factor, G Sensitive

$K_2 A^2$ – Scale Factor, G^2 Sensitive

$K_3 A^3$ – Scale Factor, G^3 Sensitive

$\tau \, dA/dt$ – Timing Error

$K_4 A^4$ – Scale Factor, G^4 Sensitive

$K_1' \, |A|$ – Asymmetric Scale Factor

2.2.2.2 Simulation Coefficients and Error Functions. Table 5 shows the actual coefficients and corresponding error magnitudes used in the simulation error models.

2.2.2.3 Simulation System Data Generation. The simulated reference position vector (S_R) was used to generate the fit functions (c_F) as usual. Specific fit functions were then scaled to approximate error functions $(c_{Si}, i = 1, 2, 3 \ldots)$ corresponding to approximate error budget values. Intentionally, these errors do not precisely represent errors from any specific error budget, but they were scaled to create a total error (Σc_{Si}) composed of highly correlated individual errors. With normal single direction sled runs these would be extremely difficult, if not impossible to separate from each other, as well as being difficult to extract out of the "noise."

The "noise" in the distance domain (NS) was generated from real sled test data. The final residual error from a well characterized system was used as the source for this "noise." This final residual was composed mainly of reference anomalies. Plots of the noise for each simulation profile can be seen on Figures 19 - 23. It should be noted however that the noise plotted for the del-delta domains is the noise used in one direction only since the del-delta noise would have canceled.

The simulated system (S_S) data in the distance domain was finally created by summing the noise, the total error, and the simulated reference position vector. These were summed after being matched according to interrupter location.

2.2.2.4 Simulation Profiles. Three sled run profiles were simulated; one monorail (positive velocity only) and two reverse velocity (positive and negative velocity):

TYPE PROFILE	RUN NO.	ACCELERATION	
		POSITIVE	NEGATIVE
REVERSE VELOCITY	R1	17 G	– 47 G
REVERSE VELOCITY	R2	46 G	–116 G
MONORAIL	R3	120 G	– 60 G

2.3 Simulation Data Processing and Analysis.

2.3.1 Simulation Data Processing. The delta-S was made by simply subtracting the reference position vector from the system data. Taking a first derivative of the delta-S yielded the delta-V.

The reverse velocity profile permits the use of two additional new domains which are unavailable on single direction runs, the del–delta–S and the del–delta–V. The del–delta–S was made by subtracting the delta–S for the segment of the mission where the sled traveled north from the segment of the mission where the sled traveled south (See Figure 3). Further, the del–delta–V could not be generated from the del–delta–S but was generated from the delta–V data instead. This procedure could only be accomplished using specially adjusted space–time and survey data and of course only with reverse velocity data. The special adjustment to the data relates to the difference between north edge and south edge of the interrupters. As the sled travels northward, the space–time head senses the south edge of the interrupters. However, as the sled travels southward, the head senses the north edge of the interrupters. Therefore, in generating the del–delta–S, the reference position vector was created using adjusted times and survey data for the southward segment of the run. The time series was adjusted to reflect the south edge of the interrupters and survey data for the south edge was used.

2.3.2 Simulation Data Analysis. The delta–S and delta–V analysis was conducted normally as described above in 2.13 with one unique difference. For the simulation analysis, the individual error functions were known and only the correct functions were used in regression analysis. This eliminated the phase of analysis which requires error function determination, simplifying analysis to only determining the contribution of the known error functions. This was entirely justified for the purposes of this simulation.

An advantage to reverse velocity lies in the high positive and negative accelerations and velocities. An important advantage to performing analysis in the del–delta domains lies in the cancellation of reference anomalies. This cancellation also lowers the "noise" level from the reference in the del–delta domains.

Analysis in the simulated del–delta–S and del–delta–V domains also had the advantage of a-priori identification of error functions. Additionally, the fit functions used for this regression analysis and for

total error generation were formed using adjusted reference position vector and in a manner similar to the del-delta's themselves in that they too involved differencing of the positive and negative parts of the run. Similarly to del-delta-V generation, the fit functions for the del-delta-V domain were formed from the velocity domain fit functions, not from the del-delta-S fit functions.

3. SIMULATION ANALYSIS RESULTS

Results of these simulations are presented in two basic formats, tabular and graphical, in an attempt to clarify the results. Because the assumption was made that the model should be complex and the terms should be highly correlated, only analysis results for Model # 4 are presented.

Tabular results are presented in Tables 6 - 7 for delta-S and delta-V and in Tables 8 - 9 for del-delta-S and del-delta-V. These Tables present the quantitative results. First, each known coefficient (TRUE COEFF) used to make the simulated system error is presented. For numerical comparison, the coefficient determined (COEFF) by analysis for each profile is presented. That is followed by one-sigma (SE, or Standard Error) of each individual coefficient. Also given is the percent error (% DIFF) of the determined coefficient from the TRUE COEFF. Finally, the last quantitative value, the sigma of the residual (σ_{RES}) for each profile is shown. Lastly, a " * " indicates that the COEFF was within 1 σ of the TRUE COEFF. Cumulative comparison of accuracy is given in Table 10 which presents the percentile error for all coefficients determined.

The following relationships were used in these tables:

(1). % DIFF $= \dfrac{(COEFF - TRUE\ COEFF) * 100}{(TRUE\ COEFF)}$
(ie. % error)
(indicates accuracy of coefficient found)

(2). " * " means the COEFF is within 1 σ of the TRUE COEFF
(indicates certainty of individual coefficient)

(4). σ_{RES} = sigma of the Residual of the fit
(indicates uncertainty of entire fit)

Table 10 presents a quantitative and qualitative overview of the results for all profiles and domains by indicating:

(1). % ERROR (% DIFF)

(2). Number of Coefficients with
< .10 % Error (ie. < 1000 ppm Error)
< .01 % Error (ie. < 100 ppm Error)
(indicates coefficient separability vs profile and coefficient separability vs domain)

The graphical results are presented for delta-S and for del-delta-S domains in Figures 19 - 23. Each Figure shows the difference between system and reference position vector at the top, followed by a plot of total error (dni), a plot of the "noise" and finally the bottom plot shows the residual after the determined errors were removed. Of special importance in reading this graphical simulation data is in the independent variable used for the plots. For the monorail runs, the horizontal axis can be time

or nominal station distance, which corresponds to the nominal downtrack distance. Likewise, for the reverse velocity runs, the horizontal axis can be time or nominal station distance but the plots appear quite different, with two values for most of the downtrack distances. However, for the del-delta-S and del-delta-V, the horizontal axis must be nominal downtrack distance. Figures 24-26 show the total error model remaining (without noise) for each profile and in each domain after removing the determined error model from the true error model (i.e. true simulated error model without noise minus the error model as determined by analisis). The noise remains only in R1 for delta-V and del-delta-V (Figure 24). Time is used for Figures 2, 5 - 11 and 19 - 21 but nominal station distance is used for Figures 12 - 18 and 22 - 26.

3.1 Discussion of Results.

3.1.1 Discussion of Graphical Results. It is apparent from Figures 19 - 21 that most of the simulated error model was determined and removed for the reverse velocity profiles. For the case of both reverse velocity profiles (Figures 18, 20, 24, & 25), the residual appears to be almost identical to the noise. However, for the monorail profile (Figures 21 & 26), the error model was not nearly as well determined as the residual still contained errors other than just the noise.

The residuals in the del-delta plots (Figures 22 & 23) appear to consist of nearly zero-mean noise which indicates excellent results in determining and removing the known error model. Therefore, the graphical results indicate the best analysis results were obtained for the reverse velocity profiles in the del-delta domains.

This was, of course, predictable by comparing the plots of the specific error functions used in the simulation (Figures 6 - 15). Comparing the six functions in the velocity domain (Figures 9 - 11) makes it apparent that the highly correlated errors would be easier to separate in data from a reverse velocity profile (R1 & R2) than from a monorail profile (R3). The value of the del-delta domains is not so readily apparent from Figures 12 - 15.

3.2 Discussion of Tabular Results. Tabular results as discussed above in 3.0 and presented in Tables 6 - 10 also indicate reverse velocity results are better than monorail. Comparison of the % ERROR for each coefficient determined (Table 10) makes it apparent that the coefficients were most accurately determined with the high-G reverse velocity profile (R2) in the del-delta-S domain. All of those coefficients except K1 were determined with less than +/-0.2 % error. The delta-S domain for R2 yielded the next best results.

4. CONCLUSIONS

This simulation was conducted using data as realistic as possible to include: software, survey data, noise, and reference anomalies. The error model functions used for the simulated system were chosen to make error function separation extremely difficult, if not impossible.

The six highly correlated error model terms used could not be determined with any degree of certainty for the high-G monorail simulation in either the delta-S or delta-V domains. The same six highly correlated error model terms were better determined for the reverse velocity profiles in the del-delta-S domain. However, analysis in the del-delta-S domain for the high-G reverse velocity profile yielded by far the best results.

Table 1. Track Survey Accuracies.

MEASUREMENTS	ACCURACY
BENCHMARK GRAVITY	+/- 0.1 MGALS
DOWNTRACK IC DISTANCE	+/- 0.5 MM
DOWNTRACK BM DISTANCE	+/- 0.02 FT
DISTANCE FROM BENCHMARK TO IC AZIMUTH	+/- 0.5 MM
PRIME VERTICAL COMPONENT OF DEFLECTION OF THE VERTICAL	+/- 0.25 ARCSEC
MERIDIAN COMPONENT OF DEFLECTION OF THE VERTICAL	+/- 0.1 ARCSEC
LATITUDE	+/- 1 PPM
LONGITUDE	+/- 1 PPM
GEOID HEIGHT ABOVE THE ELLIPSOID	+/- 0.01 M
INTERRUPTER BLADE DISTANCES	.0001 FT PER 4.33 FT
BENCHMARK ELEVATION	+/- 1/32 IN
BENCHMARK CROSSTRACK	+/1 1/32 IN
IC CROSSTRACK	+/- 1/32 IN

Table 2. Simulation Method.

1. GENERATE SPACE/TIME DATA $\qquad$ T_S

2. BUILD POSITION VECTOR WITH
   REAL SURVEY DATA $\qquad$ S_R

3. BUILD ERROR FUNCTIONS
   FROM S_R $\qquad$ $\mathcal{E}_F$

4. BUILD ERROR MODELS BY
   SCALING $\mathcal{E}_F$ $\qquad$ $\mathcal{E}_{Si}$;i = 1 , 2 , 3 , 4

5. GENERATE NOISE FROM REAL RUN
   RESIDUAL $\qquad$ N_S

6. GENERATE SYSTEM DATA $\qquad$ $S_S = S_R + N_S + \sum \mathcal{E}_{Si}$

7. MAKE $\triangle S$ AND $\triangle V$ $\qquad$ $\triangle S_i = S_S - S_R = N_S + \mathcal{E}_{Si}$

   $\triangle V_i = V_S - V_R = N_V + \mathcal{E}_{Vi}$

8. GENERATE $\triangle\triangle S_i$ AND
   $\triangle\triangle V_i$ MATCHED BY
   INTERRUPTER (REVERSE $\qquad$ $\triangle\triangle S_i = \triangle S_{i2} - \triangle S_{i1}$
   VELOCITY ONLY) $\qquad$ $\triangle\triangle V_i = \triangle V_{i2} - \triangle V_{i1}$
   (2nd BOOST – 1st BOOST)

9. FIT: $\mathcal{E}_{SF}$ AND $\mathcal{E}_{VF}$
   TO $\triangle S_i$ AND $\triangle V_i$
   $\triangle\mathcal{E}_{SF}$ AND $\triangle\mathcal{E}_{VF}$
   TO $\triangle\triangle S_i$ $\triangle\triangle V_i$
   (USING REGRESSION ANALYSIS)

Table 3. Equations.

THESE ARE THE EQUATIONS THAT ARE USED FOR EACH PHASE OF THE REVERSE VELOCITY SIMULATION:

ACCELERATION DUE TO BOOST:

$A_b = (ALPHA*V_o)/(M_o - ALPHA*T)$ WHERE

A_b = BOOST ACCELERATION

ALPHA = CHANGE IN MASS OF SLED OVER TIME

M_o = INITIAL MASS OF SLED

V_o = EXHAUST VELOCITY OF ENGINES

T = TIME

ACCELERATION DUE TO FRICTION:

$A_f = C_f*Mg/M = C_f*g$ WHERE

A_f = ACCELERATION DUE TO FRICTION

C_f = COEFFICIENT OF FRICTION

M = MASS OF SLED

g = ACCELERATION DO TO GRAVITY

ACCELERATION DUE TO AIR RESISTANCE:

$A_d = C_d*S*(.5*Rho*V^2)/M$ WHERE

A_d = ACCELERATION DUE TO AIR RESISTANCE

C_d = COEFFICIENT OF DRAG

$.5*Rho*V^2$ = DYNAMIC PRESSURE

V = VELOCITY

M = MASS OF SLED

S = SURFACE

Table 4. Parameters Used in Reverse Velocity Simulation.

MASS OF OUTRIGGER AND MONORAIL	196.70081 SLUGS
MASS OF MONORAIL	24.8447 SLUGS
RATE OF PROPELLANT USAGE (IHJ)	17.3913 SLUG/SEC
RATE OF PROPELLANT USAGE FOR MONORAIL (5 ZUNIS)	4.4558 SLUG/SEC
FRONTAL SURFACE AREA OF OUTRIGGER AND MONORAIL	11.000 FT^2
FRONTAL SURFACE AREA OF MONORAIL	1.6000 FT^2
EXHAUST VELOCITY (IHJ)	6700.0000 FT/SEC
EXHAUST VELOCITY FOR MONORAIL	7200.0000 FT/SEC
COEFFICIENT OF FRICTION FOR OUTRIGGER AND MONORAIL	0.4800
COEFFICIENT OF FRICTION FOR MONORAIL	0.4500
COEFFICIENT OF DRAG FRO OUTRIGGER AND MONORAIL	*
COEFFICIENT OF DRAG FOR MONORAIL	*
SPEED OF SOUND	1097.0000 FT/SEC
AIR DENSITY	$.00205 \text{ SLUG/FT}^3$

*THESE VALUES DIFFER AT DIFFERENT MACH NUMBERS AND DIFFERENT
PHASES OF THE SLED RUN. SEE THE FINAL REPORT "REVERSE
VELDOCITY/MONORAIL SLED TEST PROGRAM" (TEST TRACK DIVISION,
APRIL 1983, PP 74-76)

Table 5. Simulation Error Coefficients and Magnitudes (Acceleration Domain).

COEFF	FUNCTION	COEFF VALUE	COEFF UNITS	COEFF VALUE	UNITS
K_1	A	1.E−4	RAD	100	$\mu g/g$
K_2	A^2	.311E−7	$\dfrac{RAD}{(ft/s^2)}$	.9991	$\mu g/g^2$
K_3	A^3	.193E−10	$\dfrac{RAD}{(ft^2/s^4)}$	.01992	$\mu g/g^3$
τ	dA_1/dt	.111E−3	SEC	111	μsec
K_4	A^4	.187E−11	$\dfrac{RAD}{(ft^3/s^6)}$	.06199	$\mu g/g^4$
$K_1{}^\cdot$	$|A|$	1.E−5	RAD	10	$\mu g/g$

Table 6. Uncertainties from Accelerometer Error Model #4 (Delta-S).

	TRUE COEFF	12.0g/−60g			17g/−47g			46g/−116g		
		COEFF	SE	% DIFF	COEFF	SE	% DIFF	COEFF	SE	% DIFF
K_1	1.0−4	−0.2687−4	0.4860−5	126.878	0.9948−4	0.2250−7	−0.52	0.9932−4	0.2233−7	−0.6761
K_2	3.11−2	.01016	0.1853−2	−67.333	.01889	0.6098−3	−99.3926	.03020	0.6402−4	−2.8932
K_3	1.93−2	−0.1887−2	0.1344−2	−109.776	.02961	0.4897−3	53.4196	.01961	0.3210−4	2.6660
Tau	1.11−4	0.8861−4	0.5560−6	−20.1725	0.1081−3	0.2409−6	−2.6126	0.1112−3	0.9751−7	0.2250
K_4	1.87	1.8808	0.3433−3	0.5799	1.8824	0.5970−3	0.6631	1.8702	0.1235−4	0.1032
K_1'	1.0−2	0.9872−2	0.4977−5	−1.2738	.01000	0.3601−7	0	.01000	0.2542−7	0.2105
σ_{RES}		5.3679−3			7.0535−3			6.6125−3		

*COEFFICIENT +/− STANDARD ERROR INCLUDES TRUE COEFFICIENT

Table 7. Uncertainties from Accelerometer Error Model #4 (Delta-V).

	TRUE COEFF	120g/-60g			17g/-47g			46g/-116g		
		COEFF	SE	% DIFF	COEFF	SE	% DIFF	COEFF	SE	% DIFF
K_1	1.0-4	0.114	0.1382-2	111288.89	0.2142-3	0.1827-5	114.2481	0.1582-2	0.2761-4	1482.1578
K_2	3.11-2	-27.8213	0.5268	-89557.65	3.6522	0.02981	11643.308	1.8399	0.04841	5816.2287
K_3	1.93-2	-26.7511	0.4129	-138706.7	-3.3627	0.02898	-17523.05	-1.0166	0.02337	-5367.129
Tau	1.11-4	0.1630-2	0.8311-4	1368.4506	0.2026-3	0.3302-5	82.5485	0.1564-2	0.2554-4	1309.0768
K_4	1.87	6.9518	0.1076	271.7518	-1.7835	0.03336	-195.3758	2.1773	0.9057-2	13.2236
K_1'	1.0-2	0.1225	0.1400-2	1125.3536	0.9844-2	0.2824-5	-1.5556	0.9714-2	0.3288-4	-2.8623
σ_{RES}		1.4245			6.5546-2			1.5213		

*COEFFICIENT +/- STANDARD ERROR INCLUDES TRUE COEFFICIENT

Table 8. Uncertainties from Accelerometer Error Model #4 (Del-Delta-S).

	TRUE COEFF	120g/-60g			17g/-47g			46g/-116g		
		COEFF	SE	% DIFF	COEFF	SE	% DIFF	COEFF	SE	% DIFF
K_1	1.0-4				0.1951-3	0.5786-3	* 95.1146	0.9832-4	0.3483-4	* -1.6774
K_2	3.11-2				.03065	0.3370-2	* -1.4463	.03106	0.1272-3	* -0.1184
K_3	1.93-2				.02010	0.5331-2	* 4.1827	.01933	0.1386-3	* 0.1615
Tau	1.11-4				0.1110-3	0.3406-6	* .02923	0.1109-3	0.1325-6	* -0.8495-3
K_4	1.87				1.8706	0.4351-2	* .03276	1.8700	0.4645-4	* 0.6020-3
K_i'	1.0-2				0.999-2	0.1134-6	* -0.1813-3	0.9999-2	0.6512-7	* -0.7240-4
σ_{RES}					2.3586-3			2.3082-3		

*COEFFICIENT +/- STANDARD ERROR INCLUDES TRUE COEFFICIENT

Table 9. Uncertainties from Accelerometer Error Model #4 (Del-Delta-V).

	TRUE COEFF	120g/-60g			17g/-47g			46g/-116g		
		COEFF	SE	% DIFF	COEFF	SE	% DIFF	COEFF	SE	% DIFF
K_1	1.0-4				0.6756-3	0.1196-4	575.5552	0.5262-2	0.9868-4	5162.1699
K_2	3.11-2				5.0368	0.05086	16095.573	1.9199	0.06769	6073.5009
K_3	1.93-2				-6.0957	0.07667	-31683.91	-3.3664	0.06377	-17542.702
Tau	1.11-4				0.1959-3	0.4745-5	76.52721	0.1803-2	0.3963-4	1524.3158
K_4	1.87				-4.1924	0.07245	-324.1936	1.4880	0.01966	-20.4270
K_1'	1.0-2				0.9811-2	0.3939-5	-1.892484	0.01046	0.3972-4	4.5643
σ_{RES}					8.0538-2			1.9681		

*COEFFICIENT +/- STANDARD ERROR INCLUDES TRUE COEFFICIENT

Table 10. Uncertainties from Accelerometer Error Model #4 (% Error).

	120g/-60g		17g/-47g				46g/-116g			
	dv	ds	dv	ddv	ds	dds	dv	ddv	ds	dds
K₁	111288.89	126.878	114.2481	575.5552	-0.52	95.1146	1482.1578	5162.1699	-0.6761	-1.6774
K₂	-89557.65	-67.333	11643.308	16095.573	-99.3926	-1.4463	5816.2287	6073.5009	-2.8932	-0.1184
K₃	-138706.7	-109.776	-17523.05	-31683.91	53.4196	4.1827	-5367.129	-17542.702	2.6660	0.1615
Tau	1368.4506	-20.1725	82.5485	76.52721	-2.6126	.02923 *	1309.0768	1524.3158	0.2250	-0.8495-3 **
K₄	271.7518	0.5799	-195.3758	-324.1936	0.6631	.03276 *	13.2236	-20.4270	0.1032	0.6020-3 **
Kᵢ	1125.3536	-1.2738	-1.5556	-1.892484	0 **	-0.1813-3 **	-2.8623	4.5643	0.2105	-0.7240-4 **

** = <.01% or <100 ppm

* = <.1% or <1000 ppm
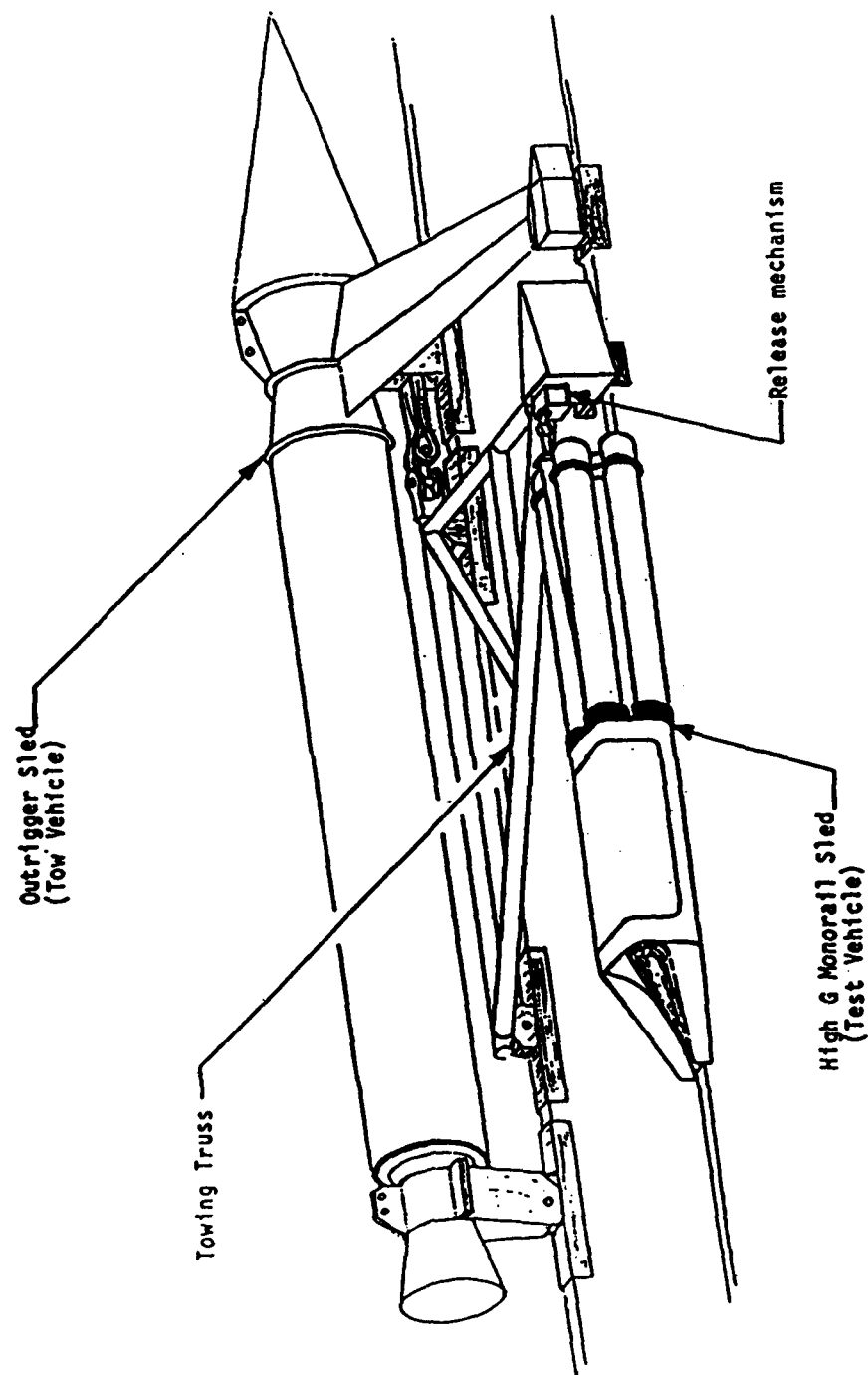
Figure 1. Reverse Velocity Sled Configuration.
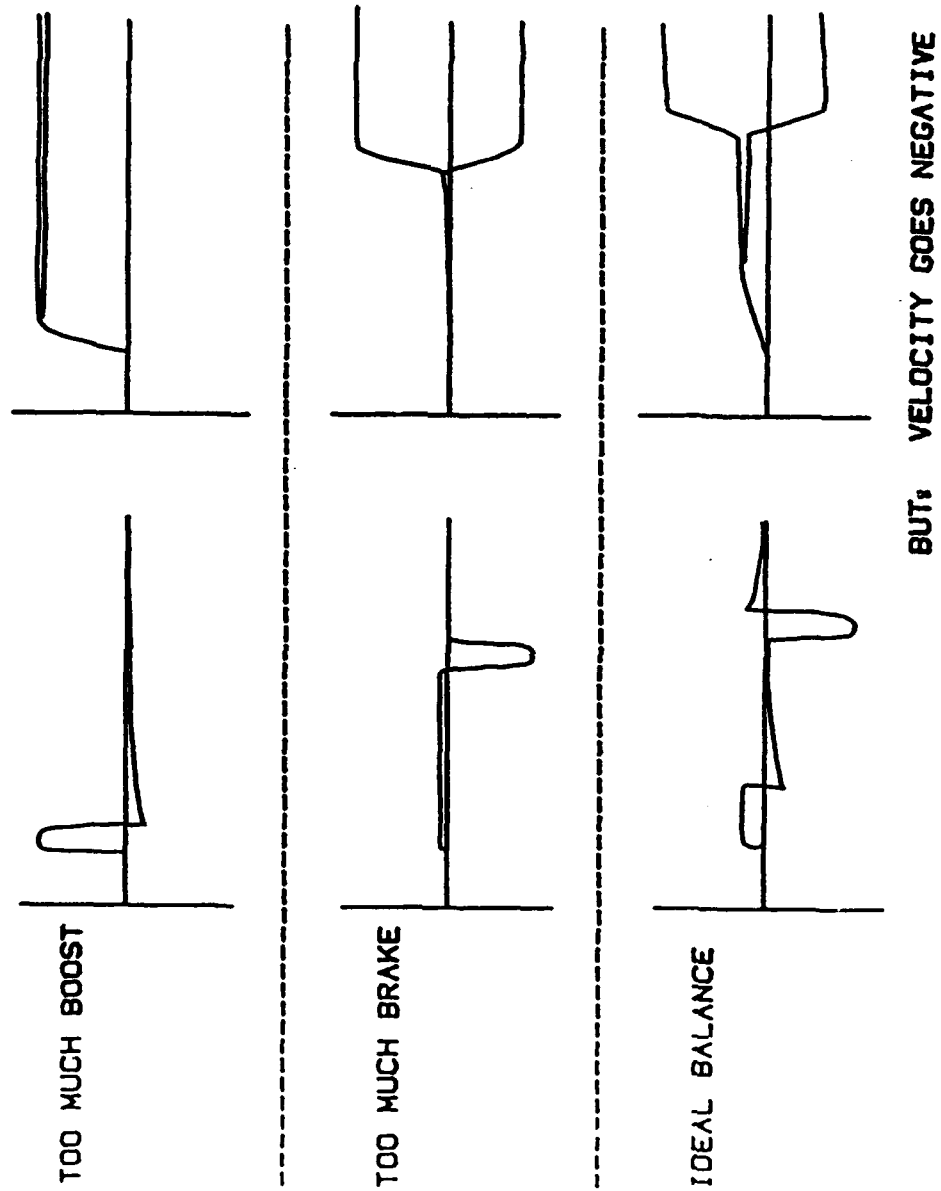
Figure 2. Optimized Acceleration.
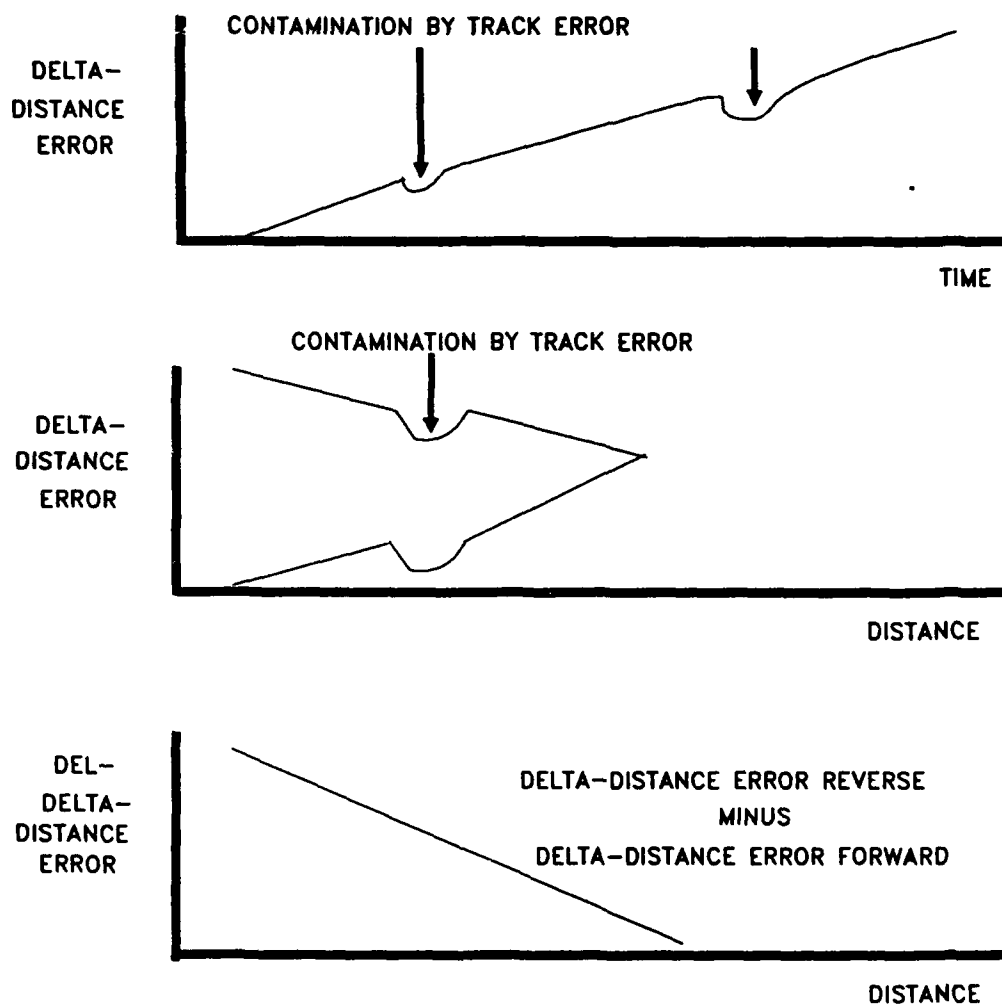
Figure 3. Contamination by Track Error – Reverse Velocity.
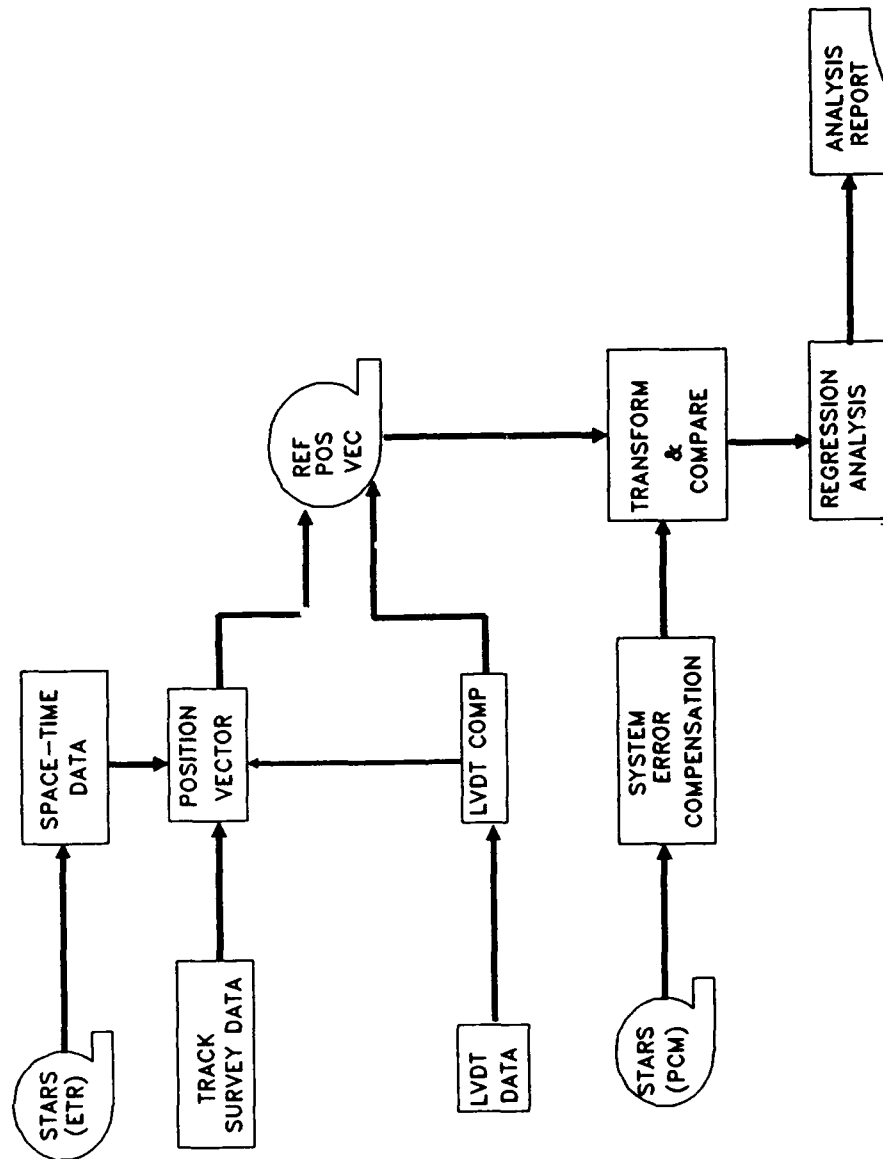
Figure 4. Position Vector Data and Analysis Flow Diagram.
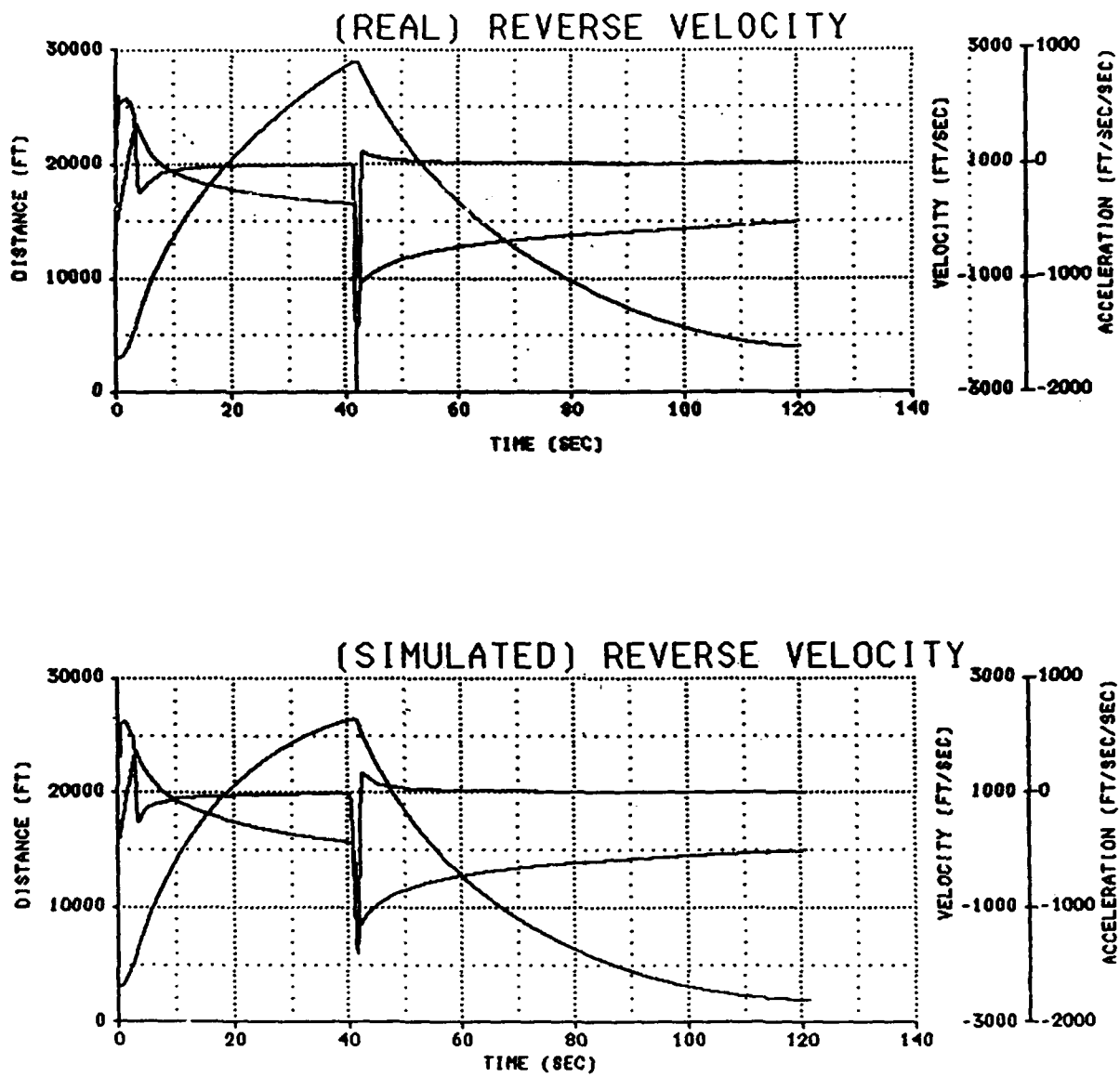
Figure 5. VMS Forward Head.
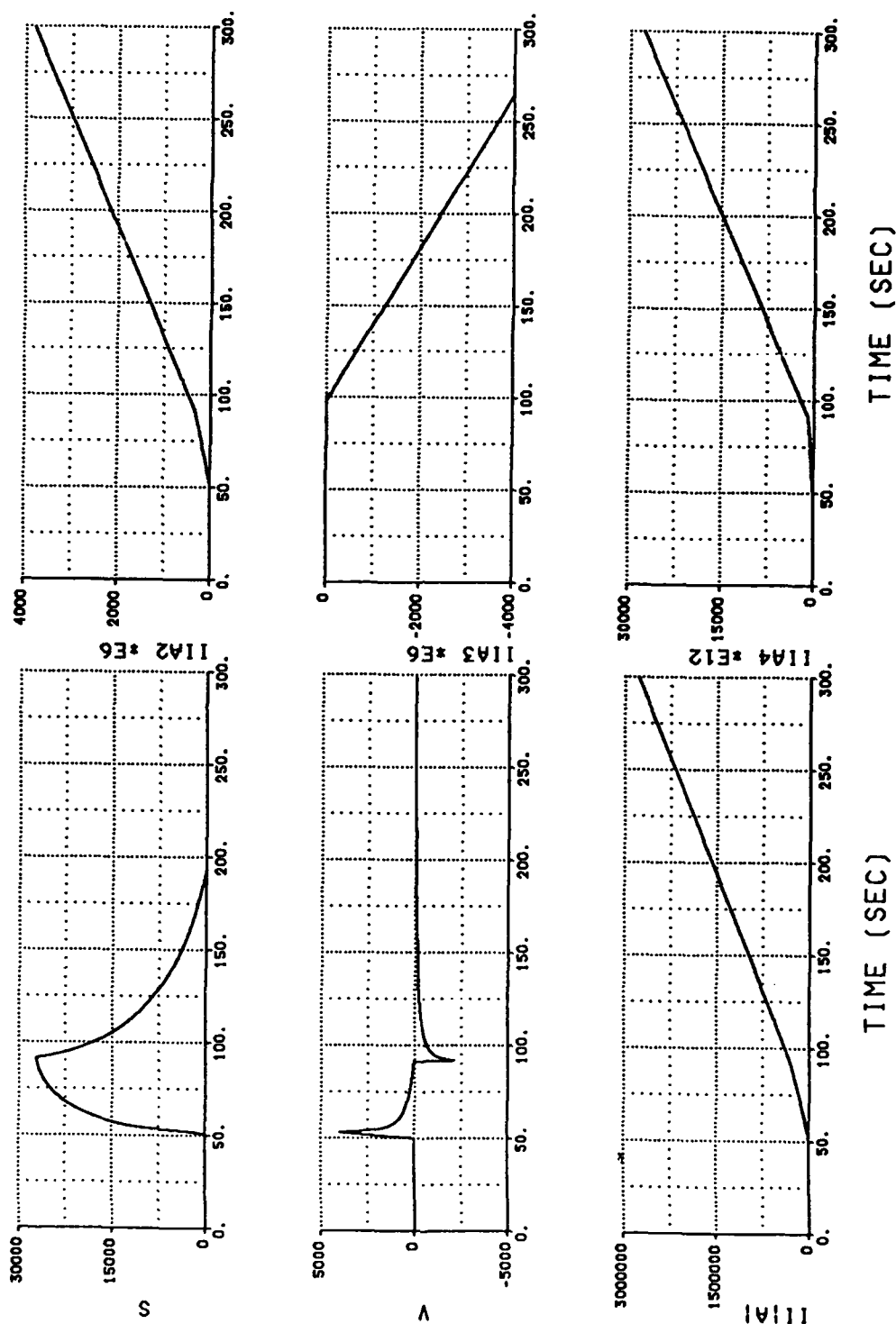
Figure 6. Fit Functions, R1 Delta-S Domain.
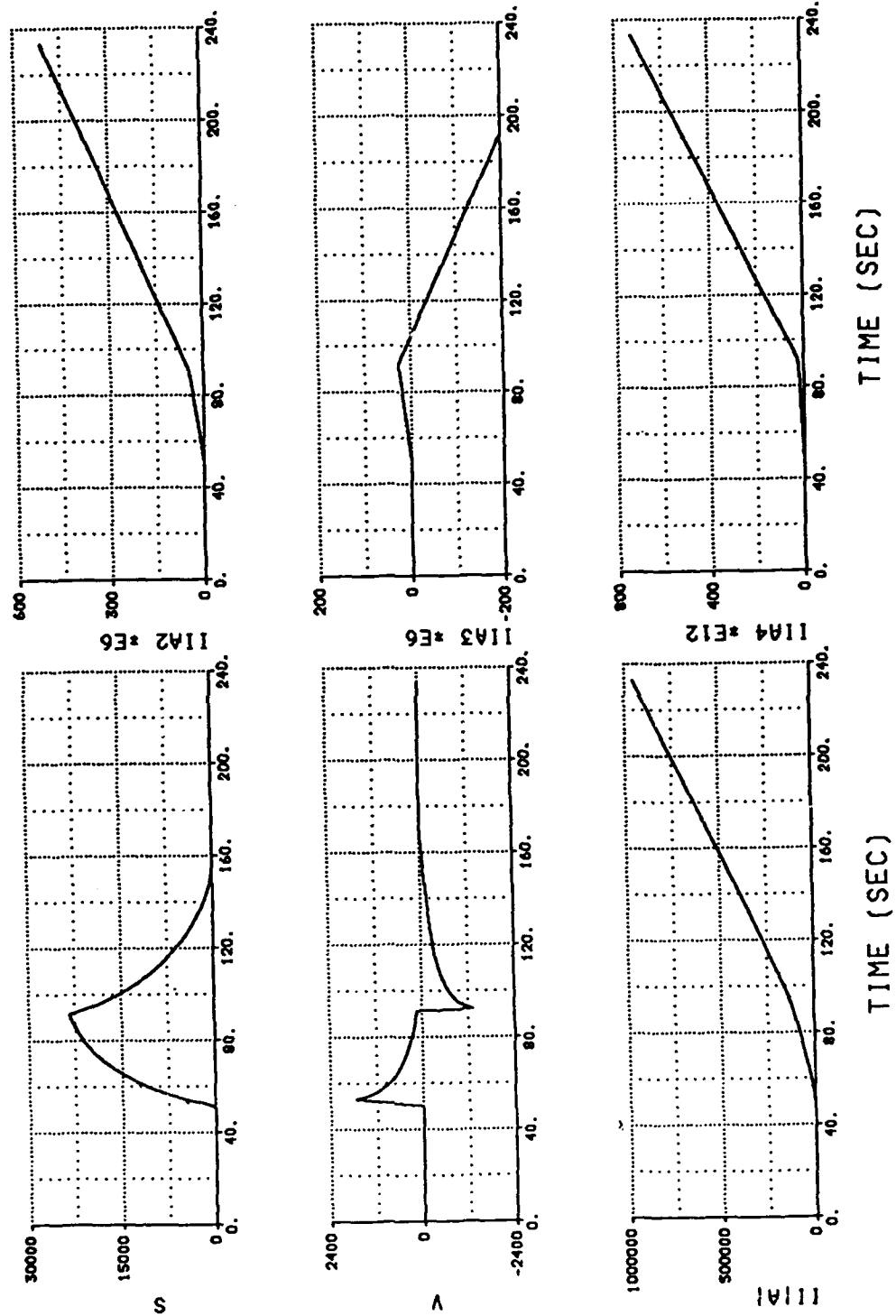
Figure 7. Fit Functions, R2 Delta-S Domain.
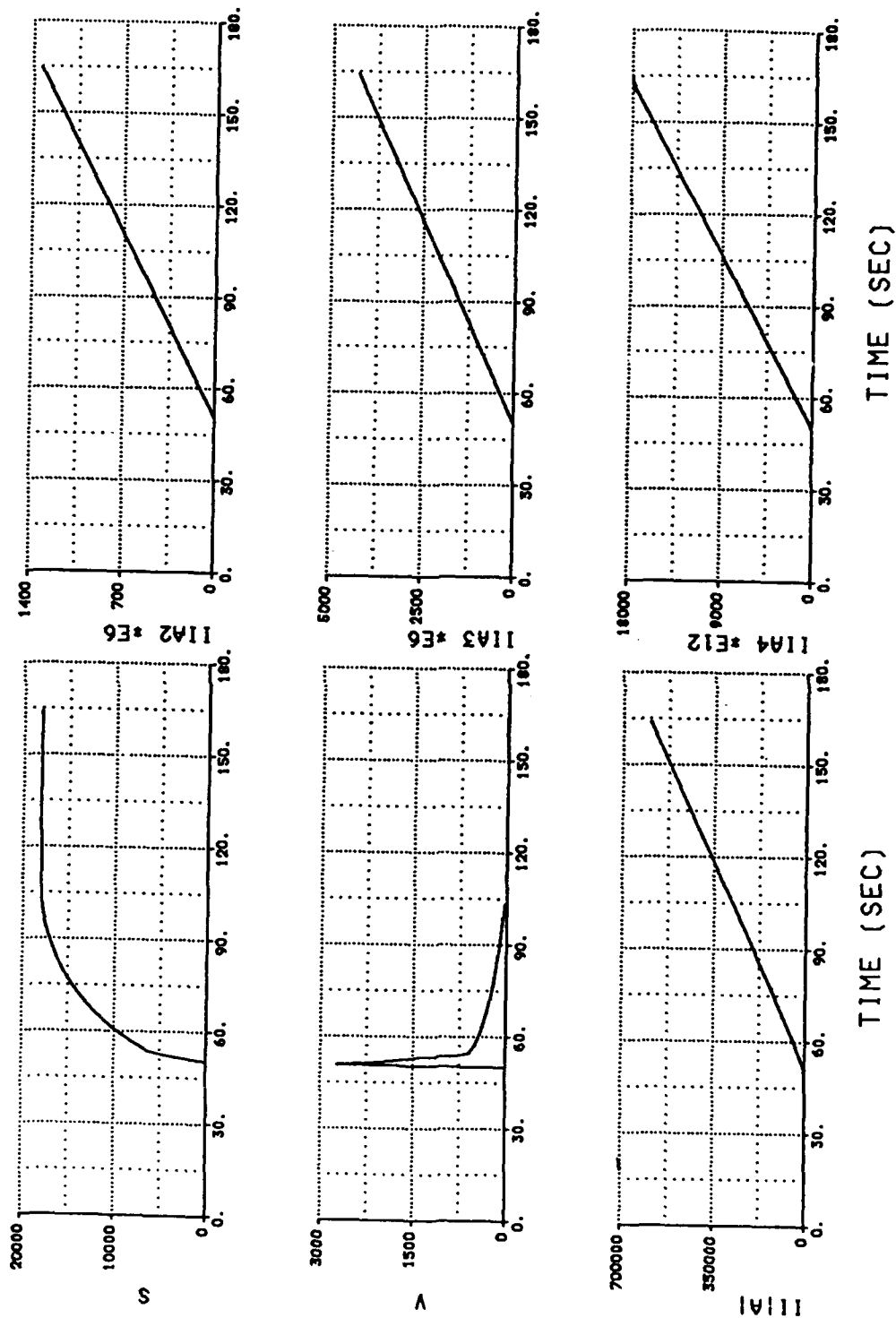
Figure 8. Fit Functions, R3 Delta-S Domain.
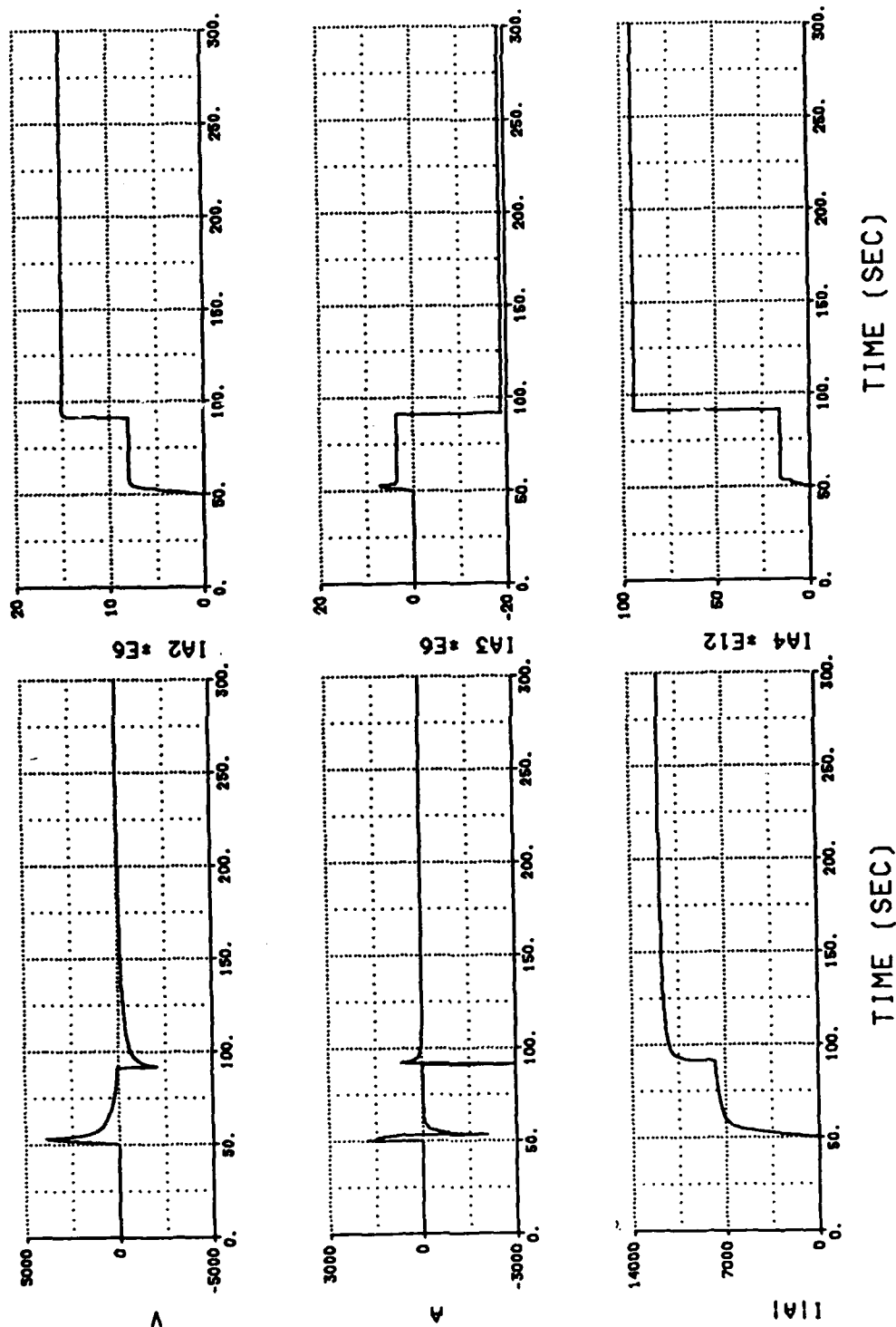
Figure 9. Fit Functions, R1 Delta-V Domain.
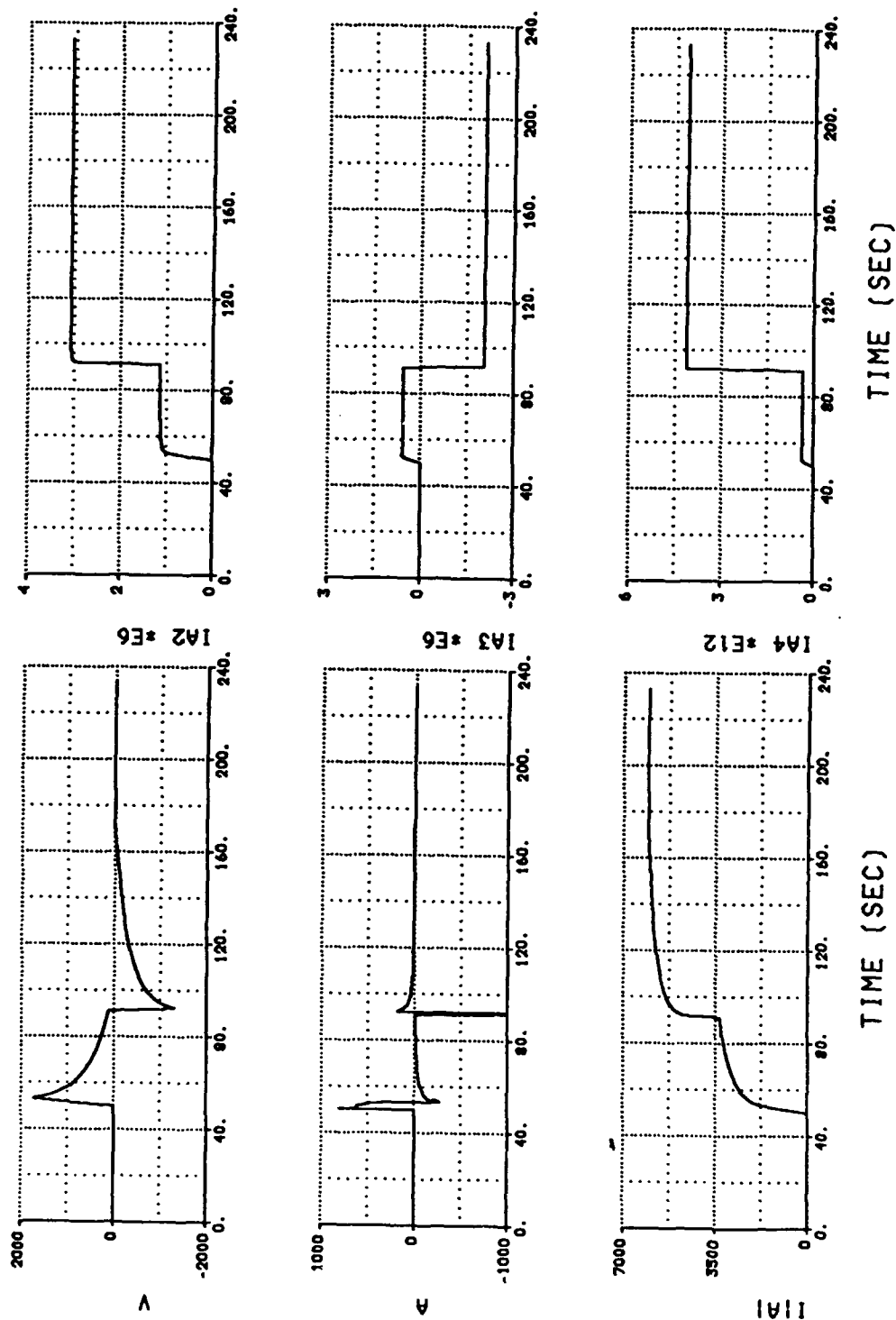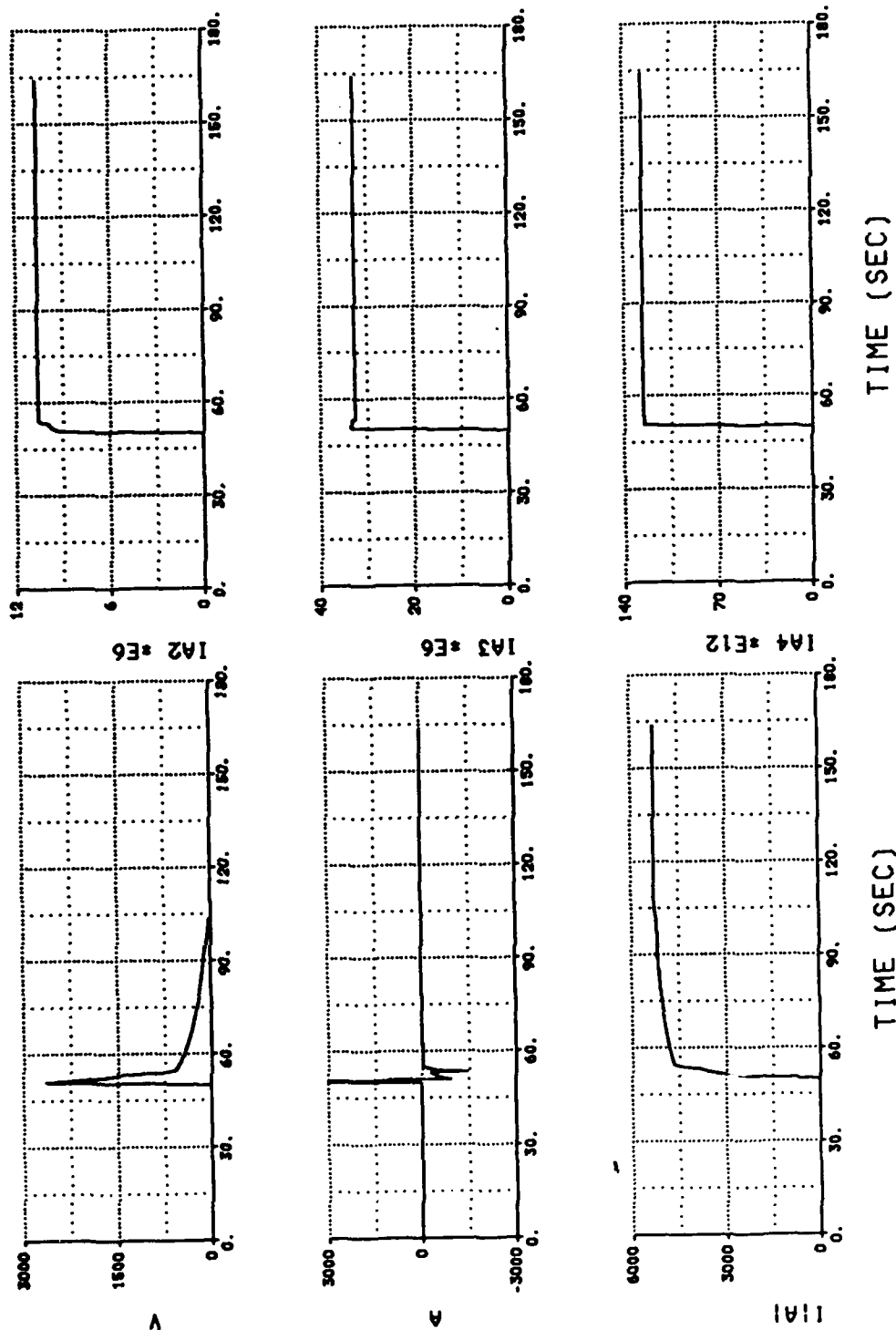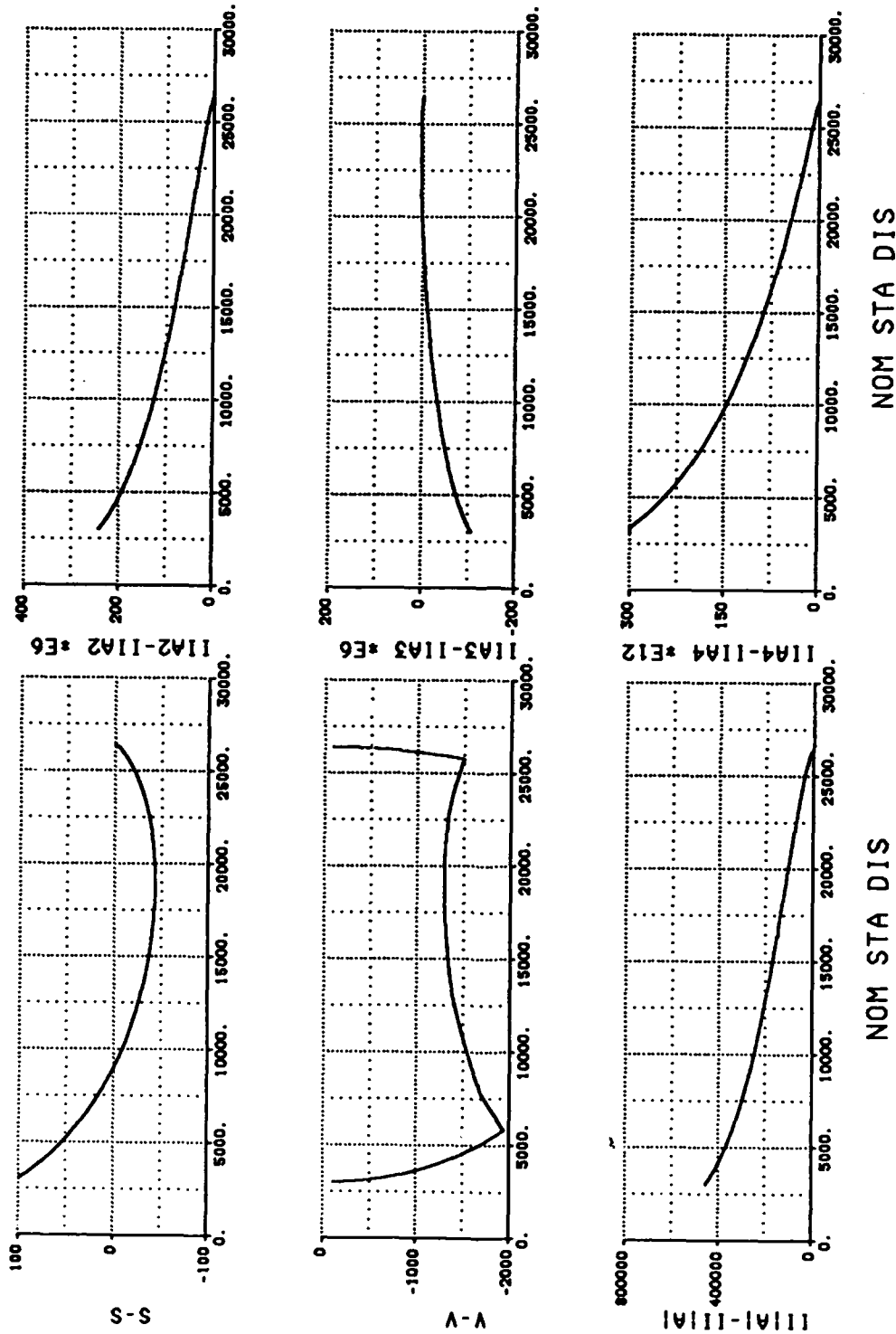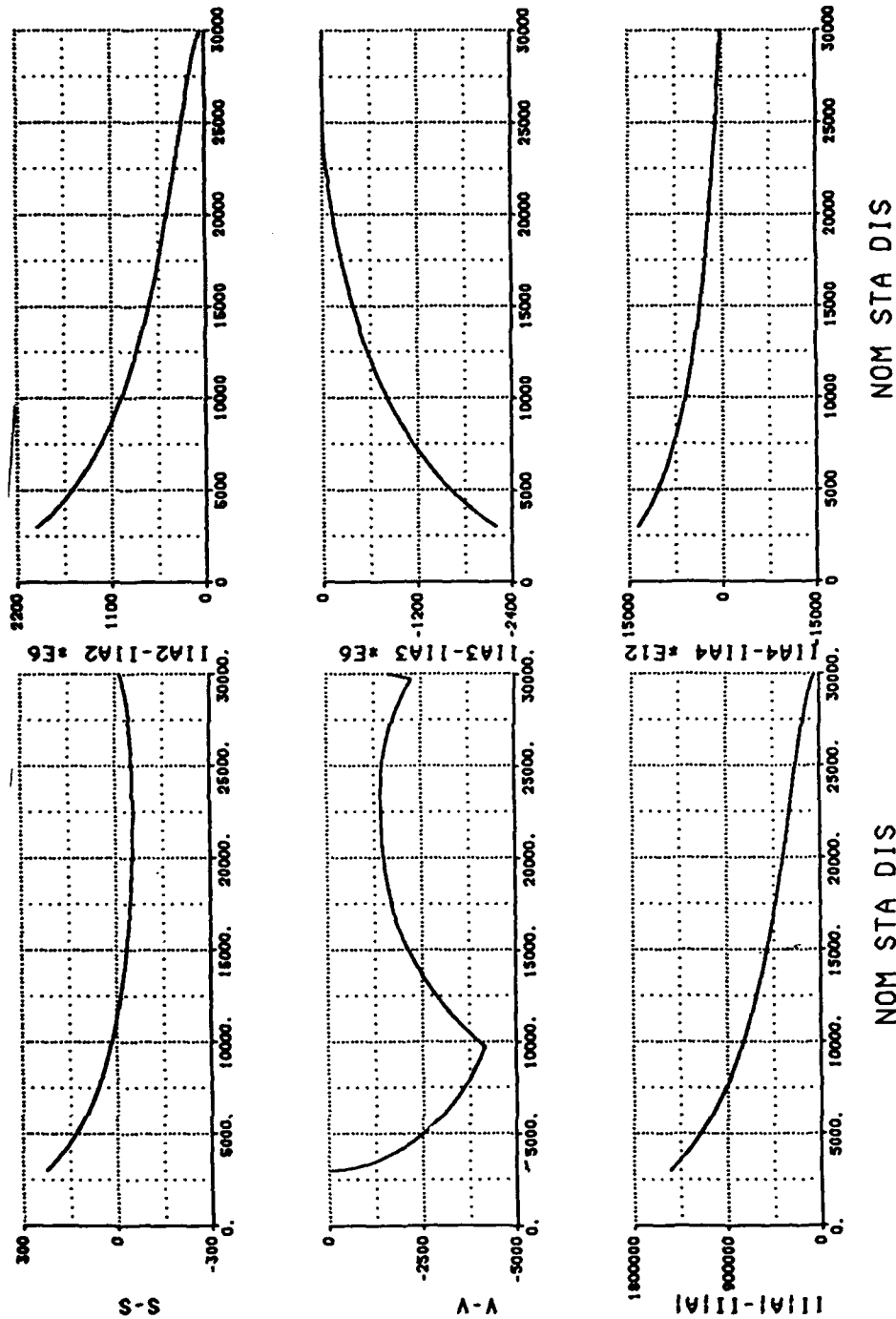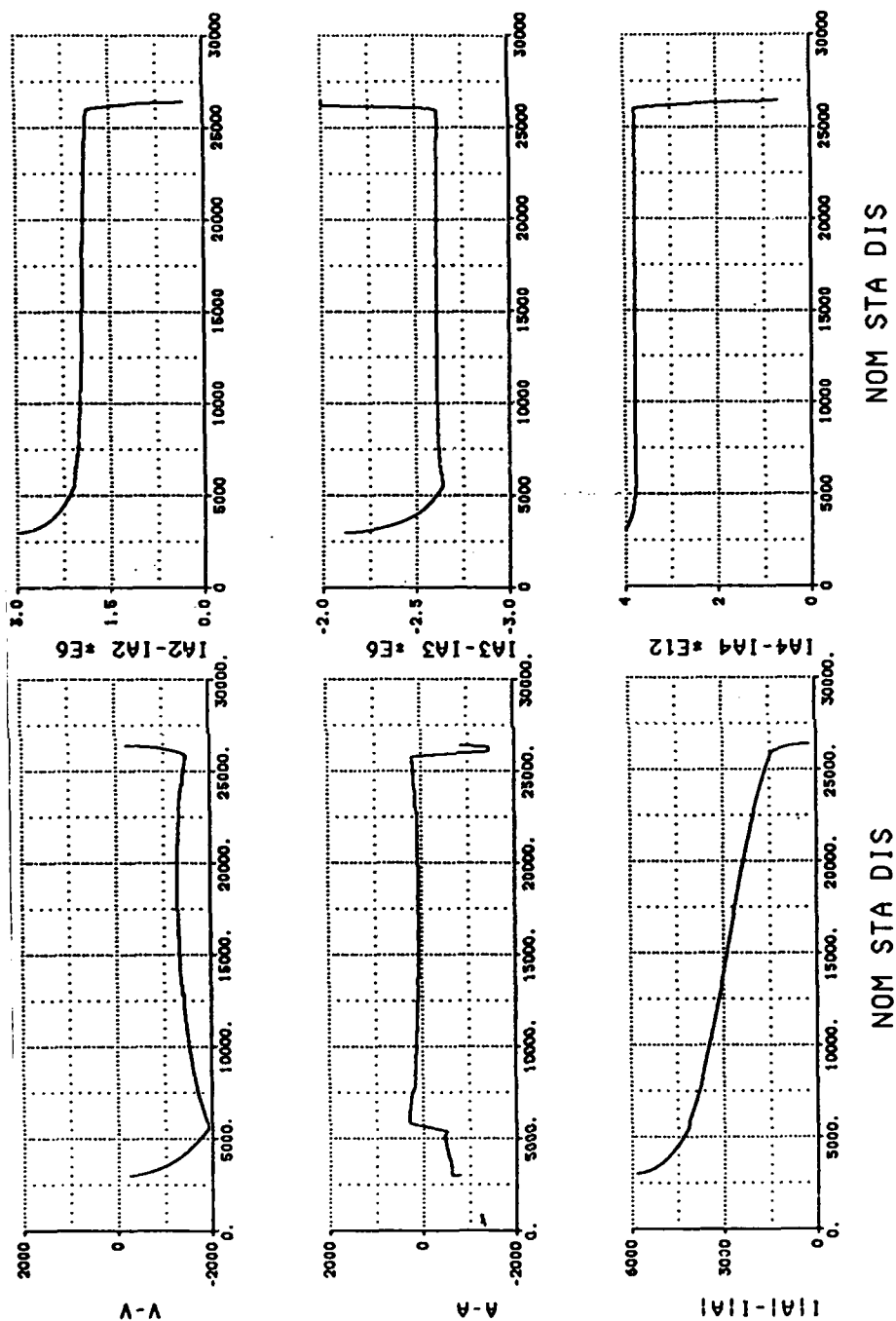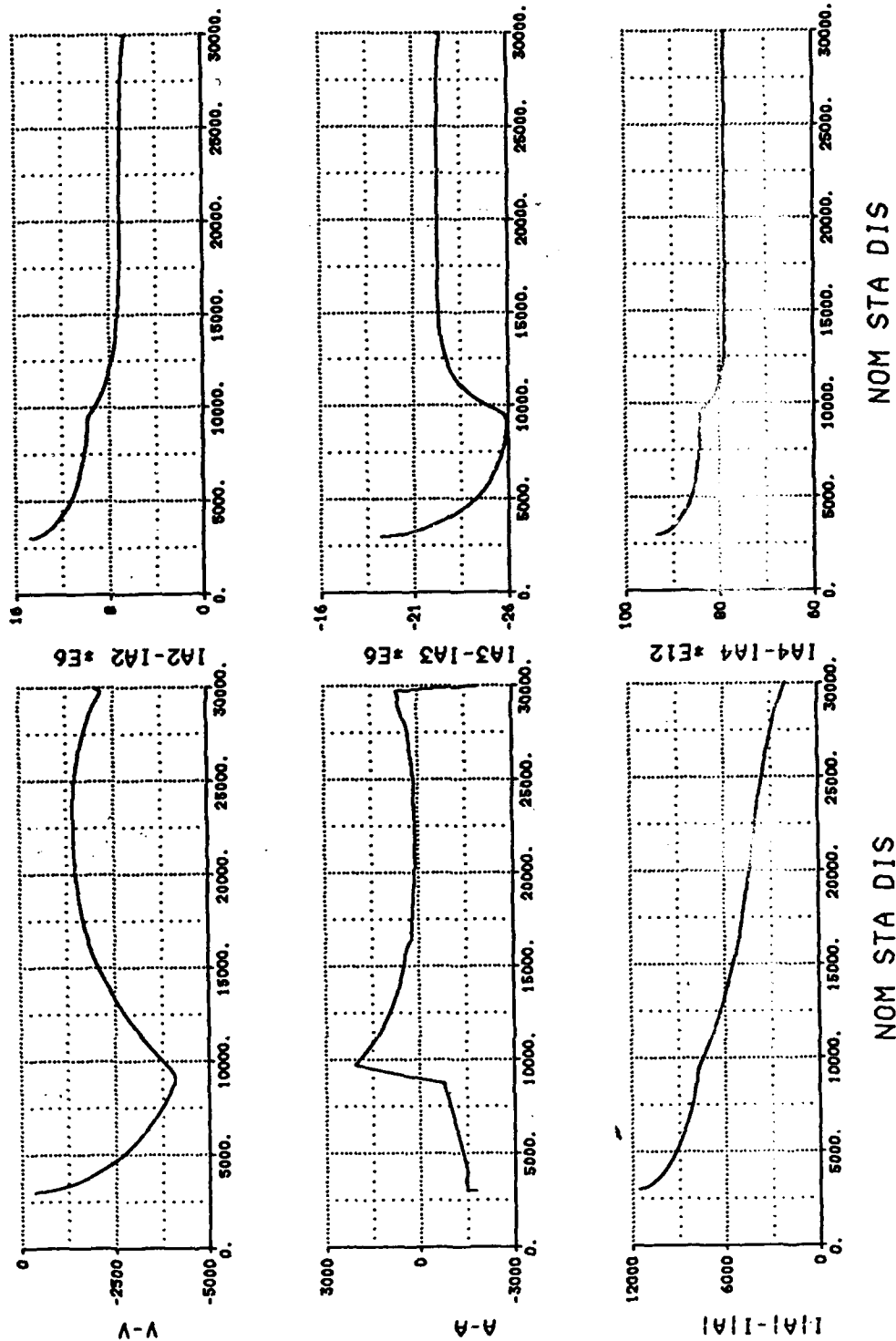
Figure 10. Fit Functions, R2 Delta-V Domain.

Figure 11. Fit Functions, R3 Delta-V Domain.
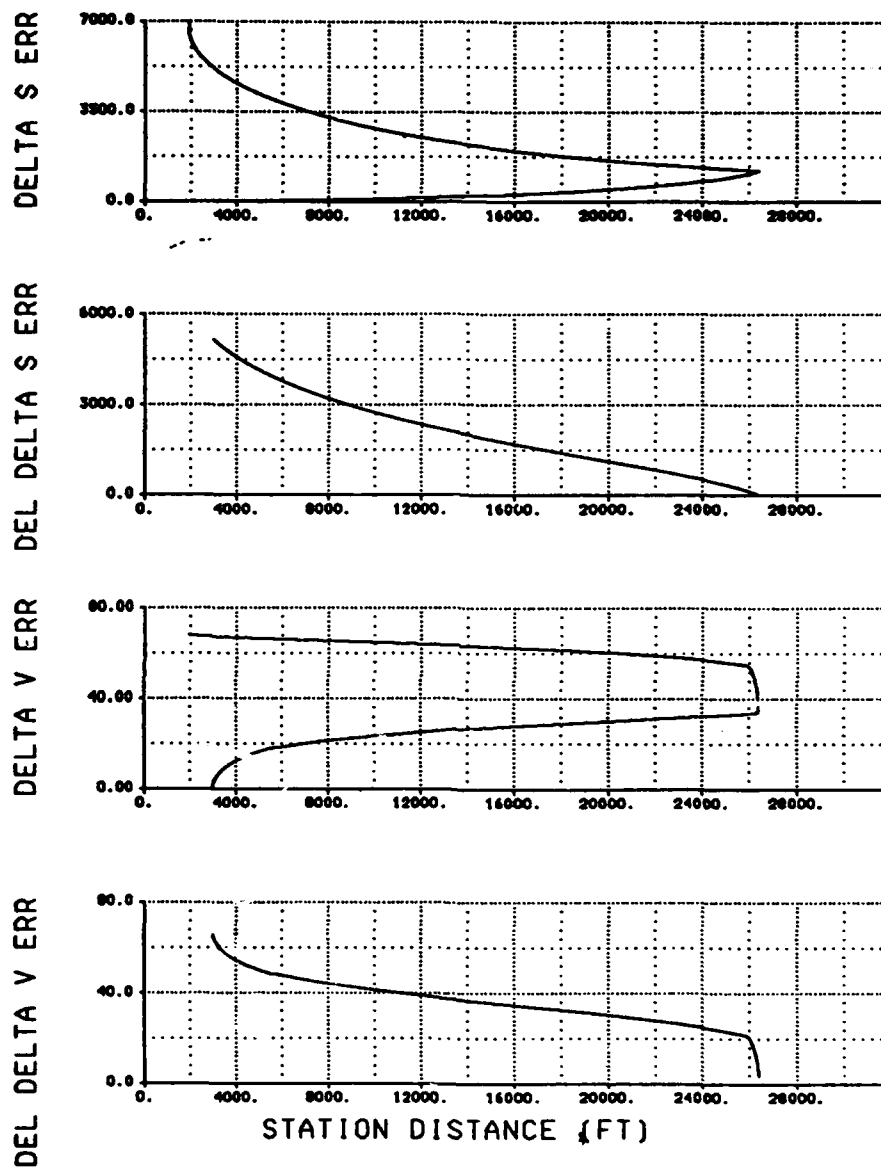
Figure 12. Fit Functions, R1 Del-Delta-S Domain.

Figure 13. Fit Functions, R2 Del-Delta-S Domain.

Figure 14. Fit Functions, R1 Del-Delta-V Domain.

Figure 15. Fit Functions, R2 Del-Delta-V Domain.

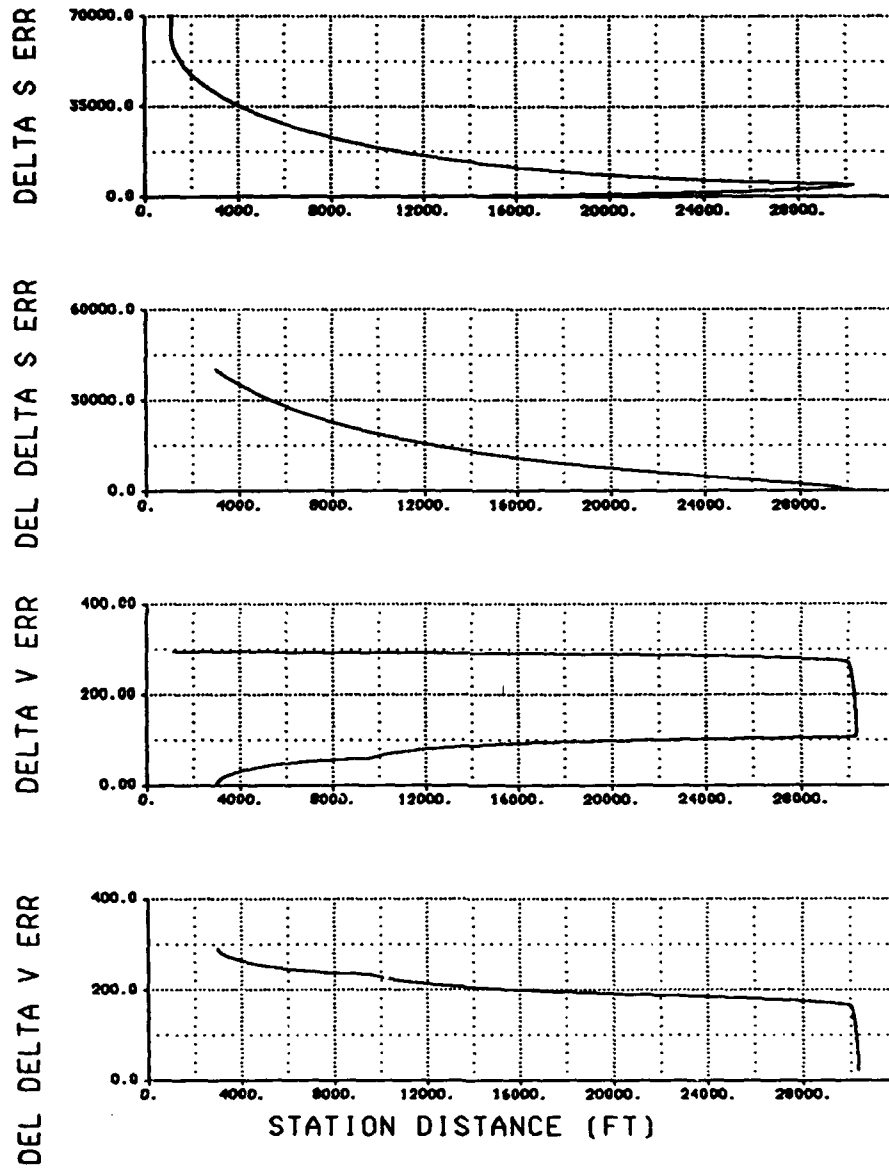**Figure 16. Reverse Velocity Simulations, R1 Error Model #4.**

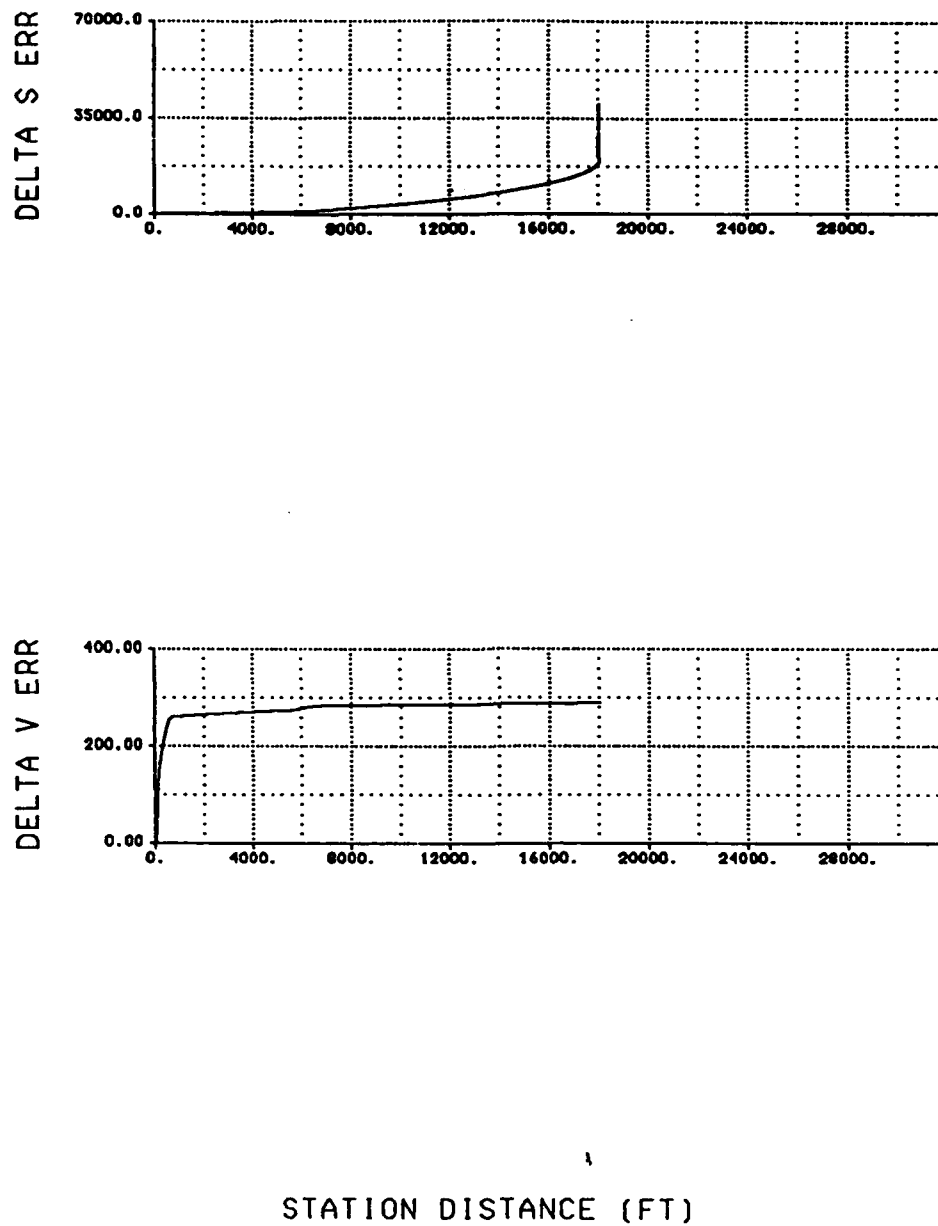**Figure 17. Reverse Velocity Simulations, R2 Error Model #4.**

STATION DISTANCE (FT)

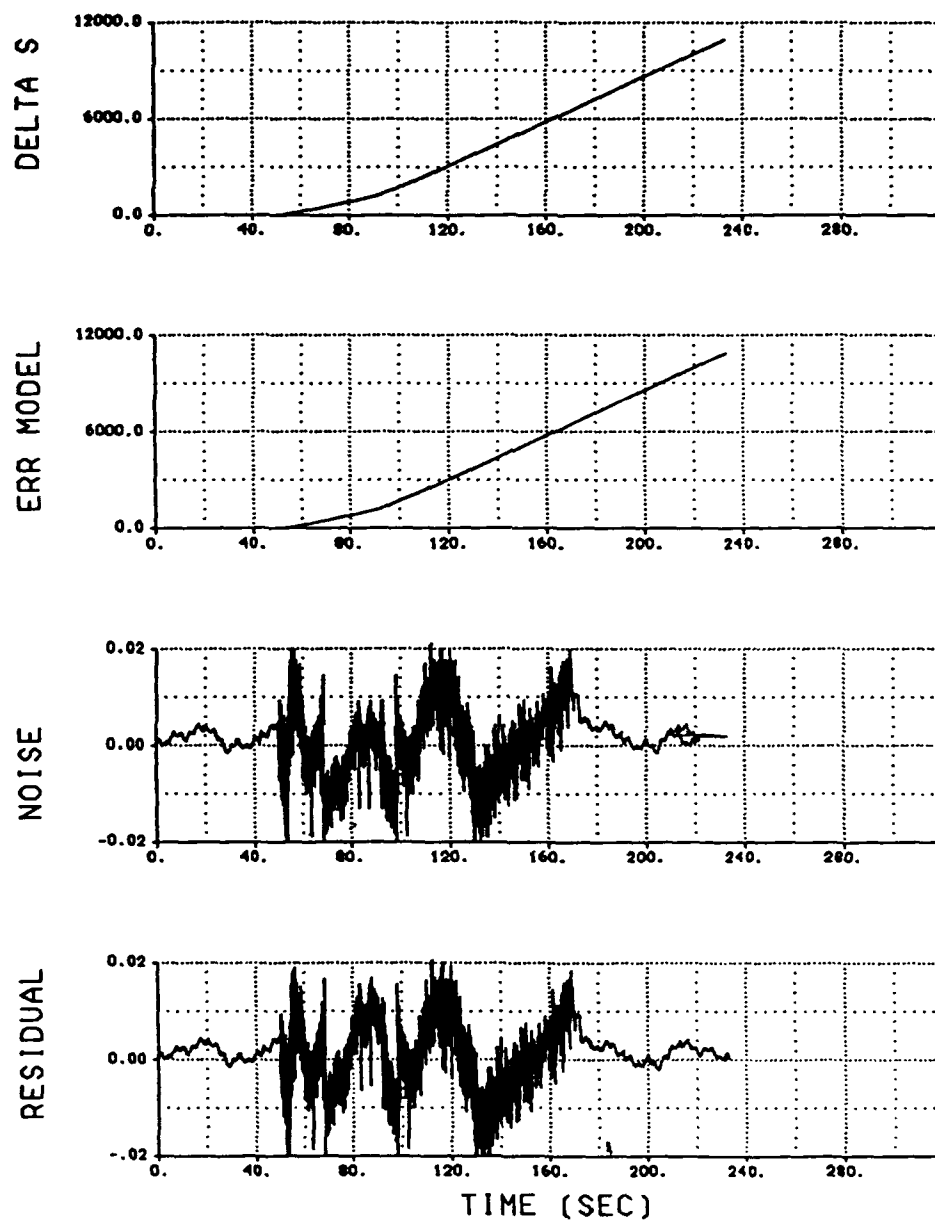Figure 18. Reverse Velocity Simulations, R3 Error Model #4.

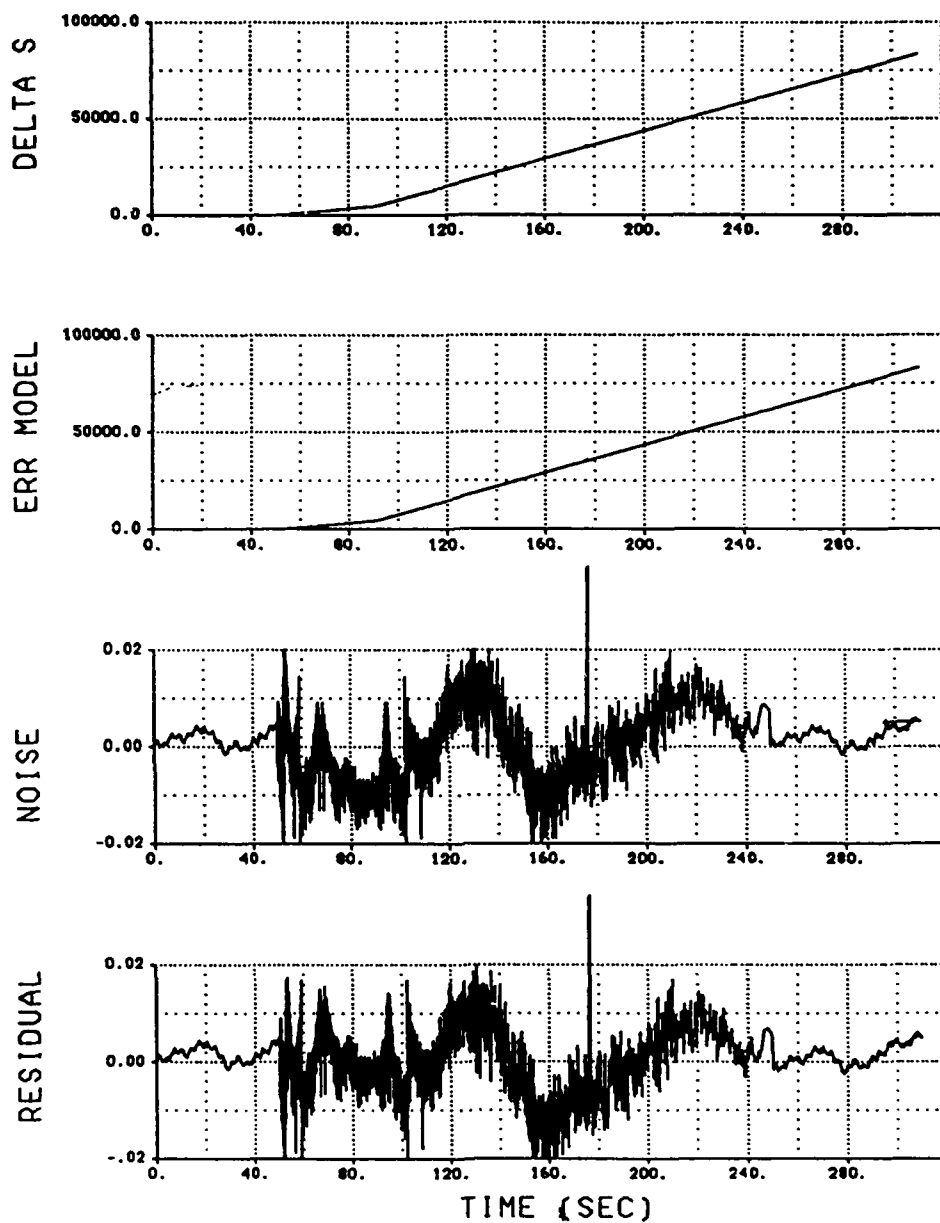Figure 19. Reverse Velocity Simulations, R1 Error Model #4.

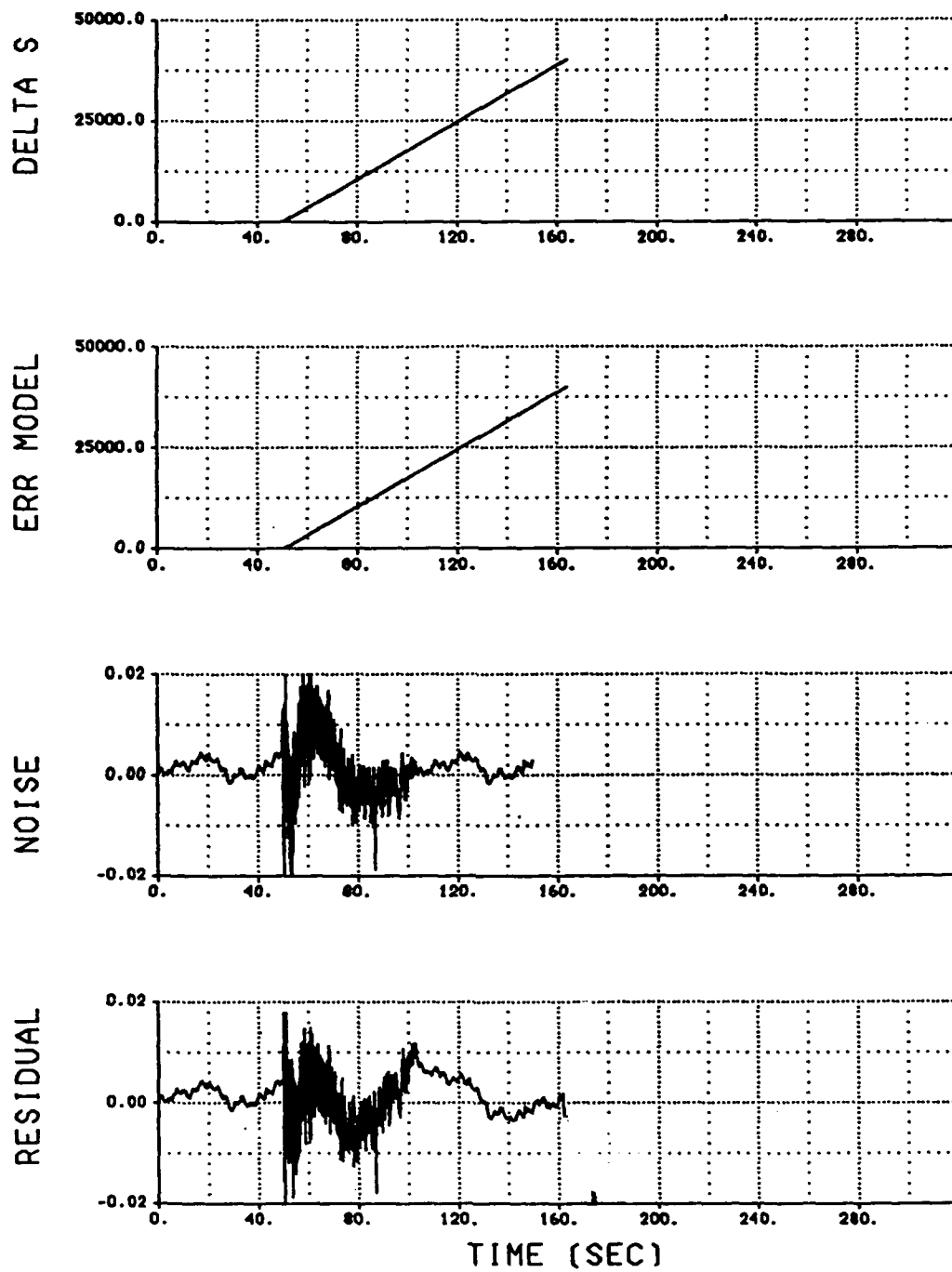Figure 20. Reverse Velocity Simulations, R2 Error Model #4).

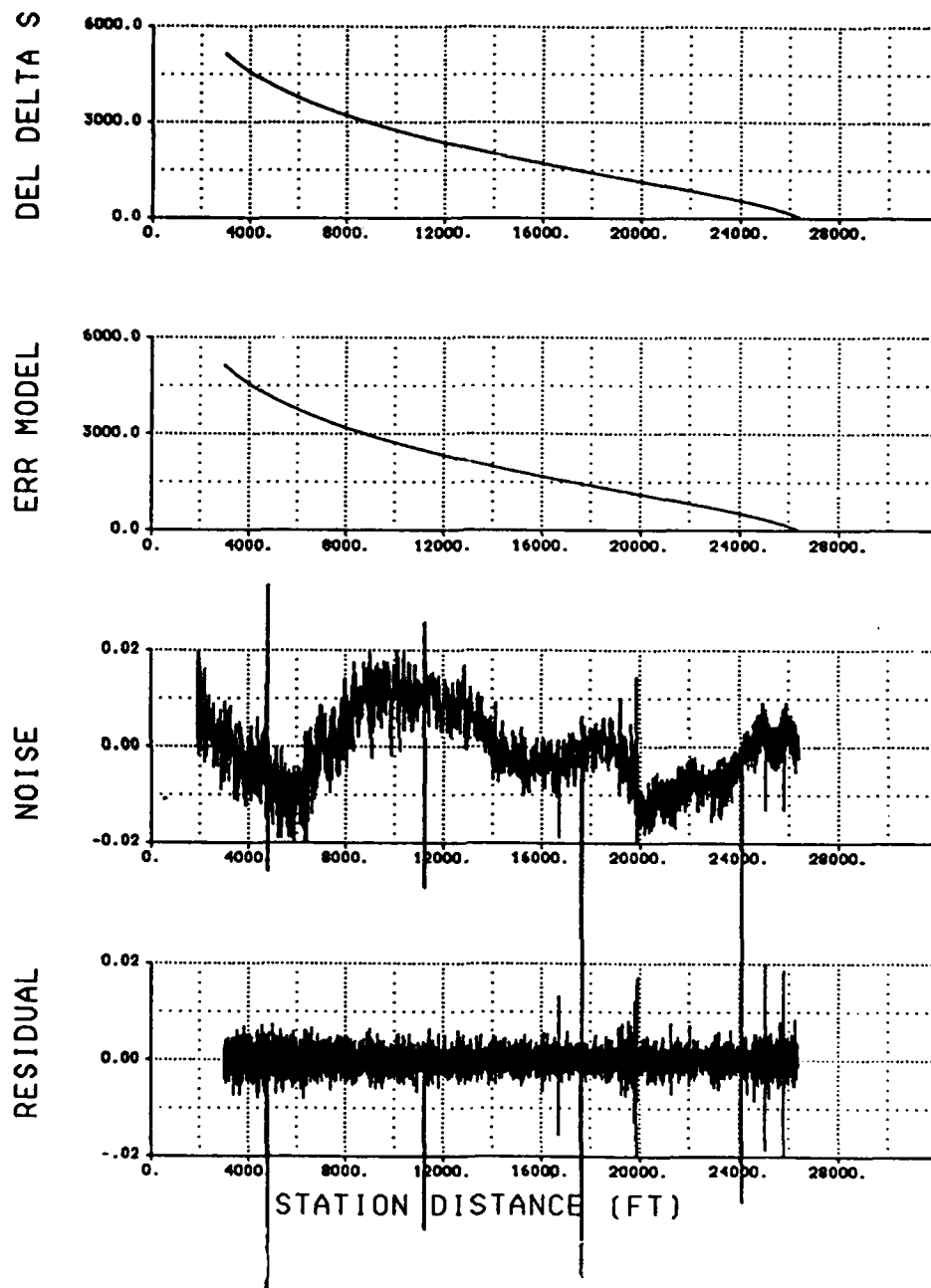**Figure 21. Reverse Velocity Simulations, R3 Error Model #4.**

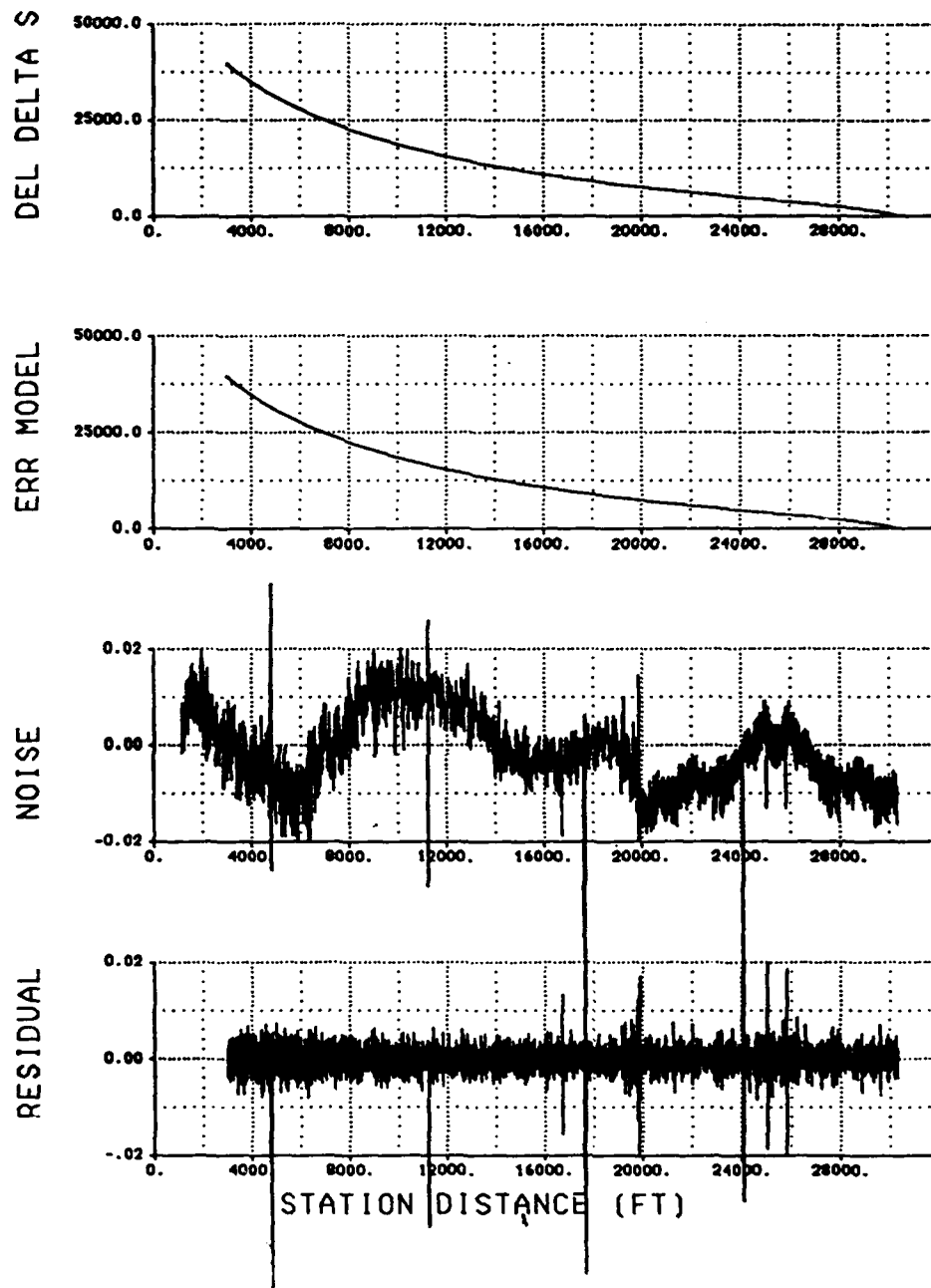**Figure 22. Reverse Velocity Simulations, R1 Error Model #4.**

Figure 23. Reverse Velocity Simulations, R2 Error Model #4.
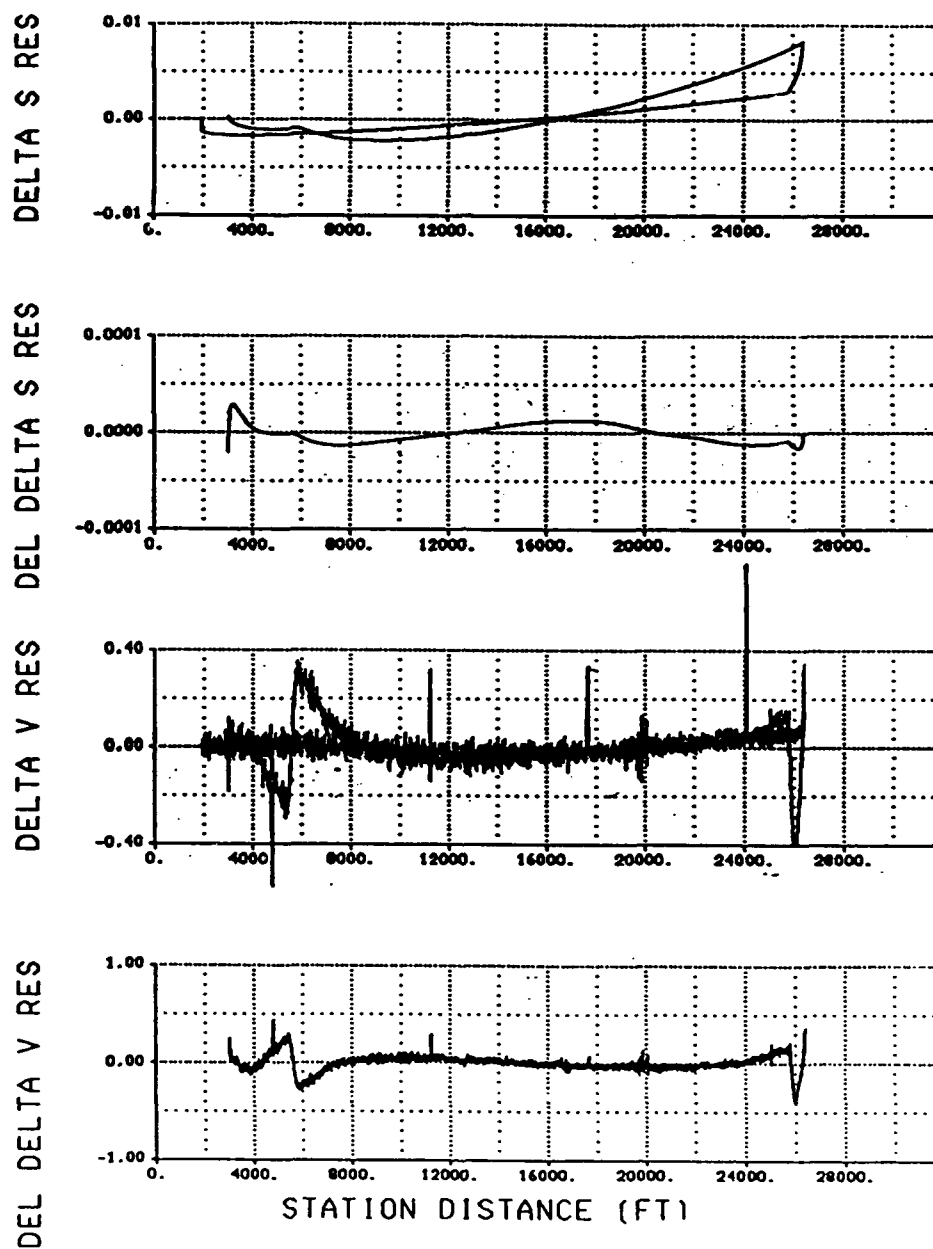
Figure 24. Reverse Velocity Simulations, R1 Error Model #4.
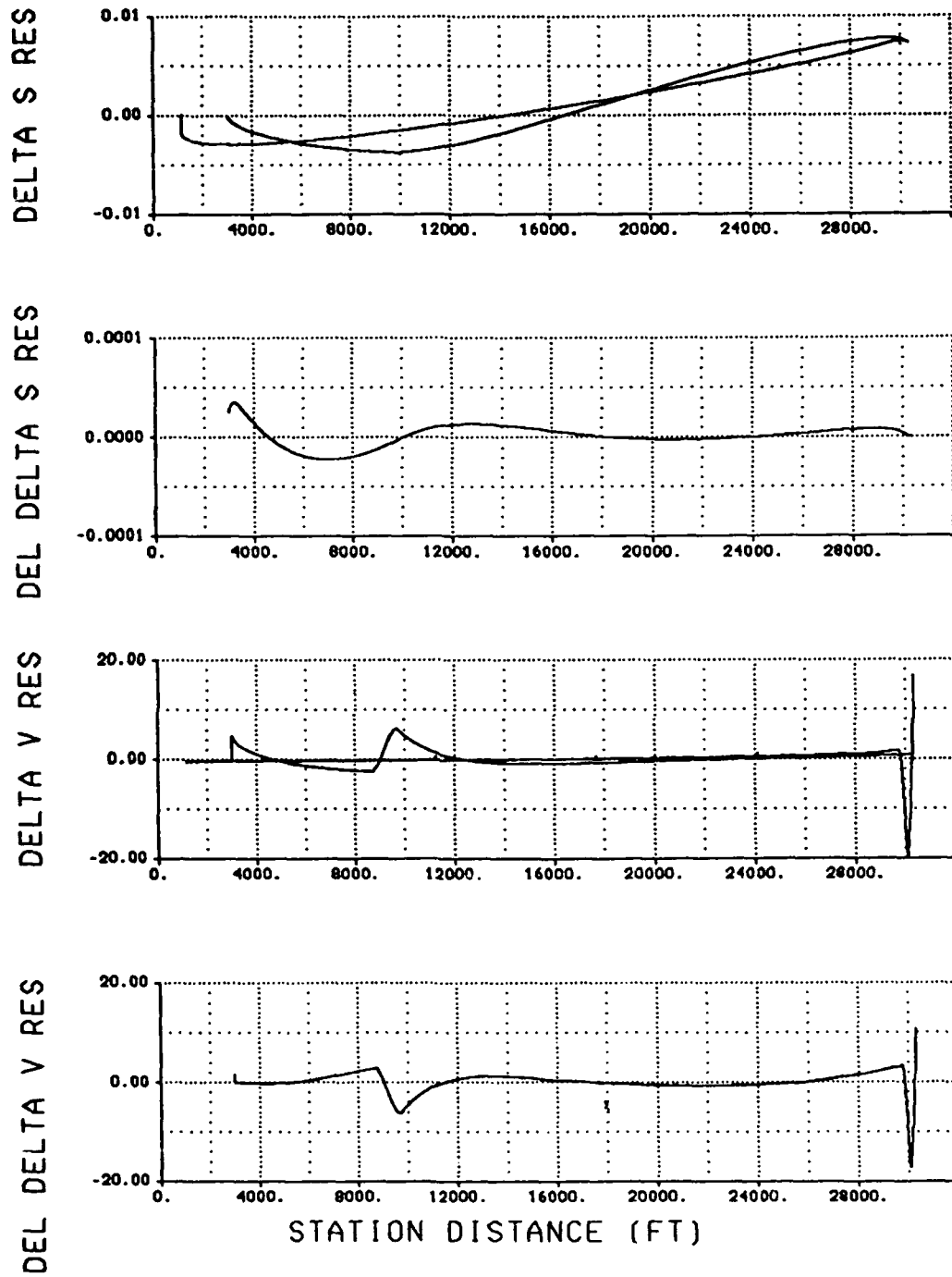
Figure 25. Reverse Velocity Simulations, R2 Error Model #4.
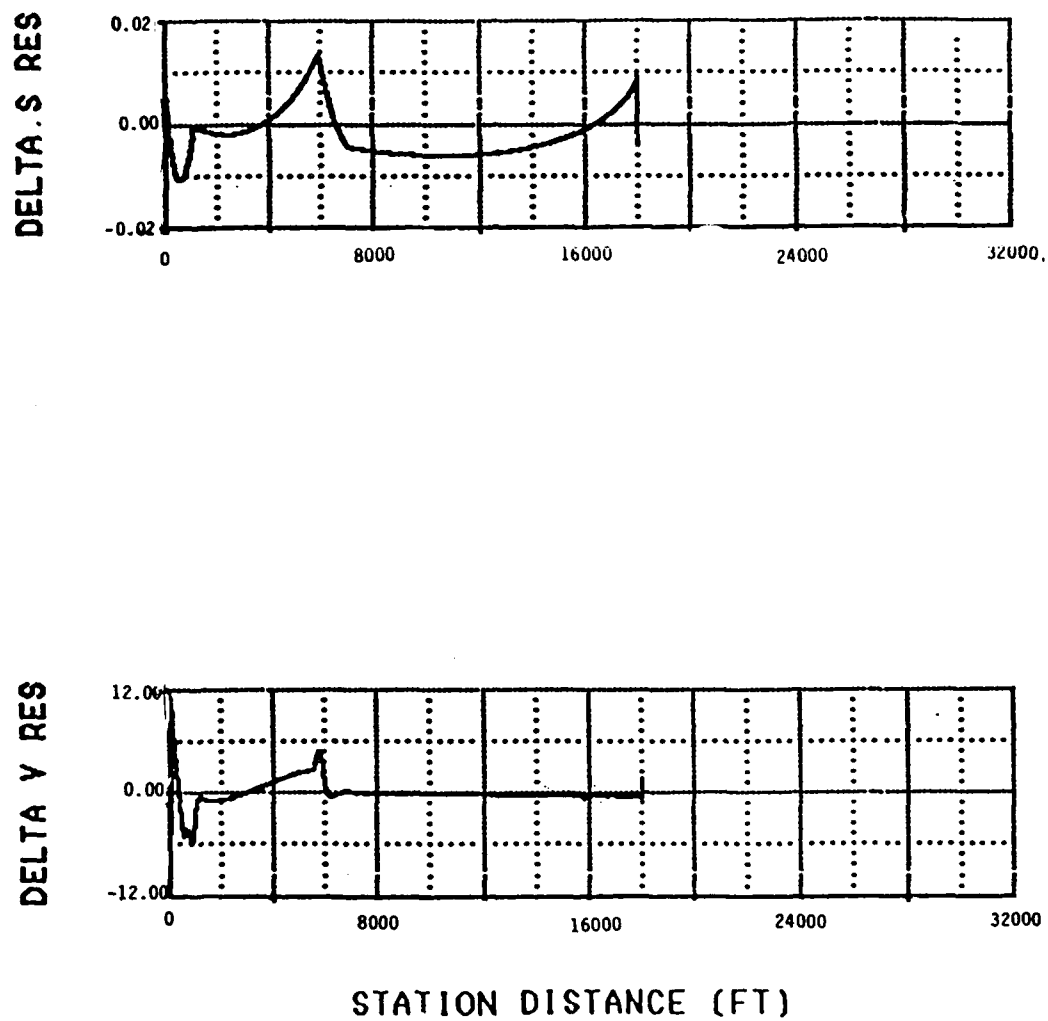
Figure 26. Reverse Velocity Simulations, R3 Error Model #4.

THIS PAGE LEFT INTENTIONALLY BLANK

STANDARD RING LASER GYRO (RLG)

INERTIAL NAVIGATION UNIT (INU)

MULTIPLE USER INTEGRATION — LESSONS LEARNED

By

C. Robert Blizzard
Senior Project Staff Engineer
Telephone Number: 813/579-6611

HONEYWELL, INC.
Military Avionics Division, M.S. 524-M
13350 U.S. Highway 19 South
Clearwater, Florida 34624-7290

The U.S. Air Force is sponsoring the production of common RLG INUs for deployment in multiple applications for a wide variety of users. That sponsorship requires a common hardware and software interface, while meeting a standard set of performance requirements per the USAF SNU 84-1 Specification. This paper provides a historical summary of the evolution of the Standard INU program, a discussion of the multiple applications to date with the successes and problems encountered, an examination of lessons learned, and recommendations for future standard avionics programs.

The RLG-based Standard INU program resulted in contract awards to two of three competing contractors (Honeywell and Litton) in 1985. These contractors had developed, at private expense, two somewhat different internal implementations to meet the requirements of the evolving USAF SNU 84-1 Specification. User Interface Control Working Group meetings were used to update/control the SNU 84-1 Specification. This proved to be an arduous and time consuming, though necessary, process.

The initial applications (C-130 SCNS, MH-53J ENS, 4950th Test Wing) were required to be dual contractor integrations. These were followed shortly by additional integration programs (F-4 NWDS, F-111 AMP, AC-130U, Army OV-'D MSIP, and A-7 RIMS), each having its unique use of the Standard INU. The initial applications quickly evolved into a leader/follower integration mode. INU transparency became a program issue, requiring extensive INU contractor engineering support. The successes and major problems of this effort are highlighted in this paper.

The process of providing mature, interchangeable (i.e., transparent) Standard INUs for multiple users is also examined in the paper. Possible and probably mandatory improvements in the process of procuring/accepting INUs are discussed, including use of common USAF controlled/approved Acceptance Test Procedures (ATPs), Operational Flight Program (OFP) validation/verification procedures, INU physical configuration drawings, and last, but not least, INU mount configuration drawings.

The paper concludes with an assessment of the benefits versus the problems encountered and offers suggestions on improving the standard avionics procurement process for future programs and applications.

1. HISTORY

The Standard Inertial Navigation Unit (INU) Program (often called F^3 for Form, Fit, Function) was initiated by the USAF to provide a common INU usable by multiple applications, developed at private expense and manufactured by multiple vendors, with lower acquisition cost resulting from higher volume production, lower organic maintenance costs by use of Reliability Improvement Warranties (RIW), and common support equipment.

The early F-16A/B aircraft INU was the technical baseline for the initial Standard INU program. The Kearfott/General Dynamics Fort Worth Division Interface documents/specifications defined the electrical, physical, and functional interface. General Dynamics Specification 16ZE013 was the primary document for the INS. It was at this time that the current INU P131 and P132 connector interface was defined with little emphasis on preventing the interchanging of the power and signal connector interfaces. This interface is now used in over 4000 installations. This configuration utilizes the Unique Control/Display Unit (UCDU) interface of the F-16A/B aircraft. The UCDU is more commonly called the Fire Control/Navigation Panel by the F-16 user community.

When the USAF A-10 aircraft was in development in the early 1970s, the original Standard INU program was initiated with the A-10 as the aircraft platform. The USAF ENAC 77-1 Technical Requirement was generated using the F-16A/B INU interface as the technical baseline. At this time, the requirement for the Generalized Control/Display Unit (GCDU) interface, as defined by the USAF ENAC 79-1 Technical Requirement, was added. Subsequently, the FB-111 AMP and F-16C/D aircraft were specified to utilize the newly defined Standard INU.

Three INU vendors, Kearfott (SKN-2416 modified), Litton (LN-39), and Rockwell Autonetics (N73 MICRON) developed prototype INUs and competed for the five year production contract award. The Kearfott and Litton INUs used Dry Tuned Rotor (DTR) gyros and Rockwell used Electrically Suspended Gyros (ESGs) for its entry in the competition. Honeywell, using the emerging Ring Laser Gyro technology, monitored the ENAC 77-1 procurement and initiated studies leading toward development of a RLG based Standard INU, but did not compete in the initial Standard INU program. Litton won this competition with its LN-39, DTR technology based, Standard INU.

In the early 1980s, the USAF initiated effort toward competing the next five year procurement of Standard INUs. Honeywell, continuing development of its MIL-LINS entry in the Standard F^3 INU, entered the competition. Honeywell concurrently won the F-5G/F-20, F-15E, and SAAB JAS-39 INU competitive procurements using RLG technology that provided faster reaction times and much improved reliability. Honeywell's H-423 Block 1 LINS was compliant with ENAC 77-1 Technical Requirement and entered prototype production in 1984.

The USAF initially planned on updating the ENAC 77-1 Technical Requirement to include the benefits of RLG technology, MIL-STD-1750 processors, and other leading edge technologies, yet retain the mature DTR based Standard INUs in the next Standard INU competition. The desire to add other requirements led to the creation of the USAF SNU 84-1 Specification for medium accuracy Standard INUs and SNU 84-3 Specification for Standard Precision Accuracy (SPA) INUs. The SNU 84-1 quickly evolved into an RLG INU specification only with Honeywell H-423, Kearfott SKN-4016, and Litton LN-93 Standard RLG INUs competing for the production award. The size of the procurement was sufficient to justify two INU contractors. Honeywell and Litton won this competition.

The SNU 84-3 Specification was based on DTR technology with Kearfott SKN-2443 and Litton LN-39H competing for the production award. Kearfott won the production award.

Concurrent with the development of RLG based Standard INUs by domestic INU contractors, two British firms have also developed Standard RLG INUs based on the SNU 84-1 Specification. These are British Aerospace with its LINS 300 INU and Ferranti with its Model 3020. The LINS 300 has entered prototype production.

2. MULTIPLE APPLICATIONS/INTEGRATION SUPPORT

Multiple applications and successful integrations make a form, fit, function standard avionic equipment procurement/deployment successful. Failure to achieve successful integration destroys the premise on which common or standard avionics are based. Successful dual INU contractor integrations are harder to achieve and require the total support of all participants (i.e., USAF ASD/AE, ALCs, Integrators and INU contractors).

The scope of each individual integration support task includes, as a minimum, the following elements:

- Providing INU technical expertise for rapid evaluation, analysis, problem resolution, and recommendations relating to subsystem integration.

- Expedited workarounds/corrections of INU hardware and/or software deficiencies and/or failures.

- Providing INU technical support for the integration site on an "as needed" basis no later than two working days after being notified in writing (e.g., FAX or TELEX) by the aircraft or avionics integrator.

- Generation, publication, and distribution of telecon records, technical correspondence (e.g., Customer Engineering Letters (CELs), Interface Memorandums (IFMs), Interface Control Documents (ICDs), etc.), and internal status reports.

- Maintenance/Publication/Distribution of the INU verified Problem Log. In addition, the historical log of all reported integration problems, including those verified and unverified, must be maintained.

- Conduct, where possible, verification testing at the INU contractor of all reported integration problems.

- Support all scheduled Interface Control Working Group (ICWG) meetings and INU contractor/Aircraft Integrator Technical Coordination Meetings (TCMs). Includes generation of meeting minutes in contractor format where the INU contractor is host and trip reports where the INU contractor is a participant.

- Technical support to the transition from one SNU 84-1 configuration to the next configuration (where applicable). Example: Revision 3, Amendment 1 to Amendment 2.

The required level of support is directly related to the complexity of the integration effort and, to a lesser degree, the skill and experience of the integrator. It is also related to the number of integration sites and organizations for each INU application.

A low complexity INU integration is characterized by the following:

- Mechanical boresighting

- Default orientation

- Stored Heading (SH) and Gyrocompass (GC) Align Modes

- Inertial Navigation Mode.

Our low complexity INU applications have included 4950th Test Wing, FAA, Naval Coastal Systems Center, etc.

A medium complexity INU integration is characterized by the following:

- Mechanical boresighting

- Orient Mode

- SH and GC Align Modes

- Inertial Navigation Mode

- Update Modes

- Grid Mode.

Medium complexity INU applications include 4950th Test Wing Special Applications, A-10, A-7 RIMS, NC-135, etc.

A high complexity INU integration is characterized by the following:

- Software Boresighting
- Orient Mode
- SH & GC Align Modes
- Inertial Navigation Mode
- Doppler/Inertial Aided Navigation
- GPS/Inertial Aided Navigation
- Vertical/Baro Loop Aiding
- Update Modes
- Grid Mode
- Cold Start Air Align Modes

     Doppler/Compass

     GPS

- 200 Hz Message Operation

     Radar Stabilization

     LANTIRN, etc.

- INU/AFCS Integration.

High complexity INU applications include C-130 SCNS, MH-53J ENS, F-4 NWDS, OV-1D Block Improvement, F-16A/B, F-16C/D Post Blk 50, T-39 GPS Test Bed, EF/F-111A/E AMP, F-111D/F Pacer Strike, AC-130 Gunship, etc.

The number of integration sites and integrator organizations participating on each aircraft INU application program can affect the complexity and support requirements for the integration effort.

Current/past examples of programs, organizations, and locations include:

- C-130 Self Contained Navigation System (SCNS) Program

     Smith Ind., SLI Avionics Systems Corp. — Grand Rapids, MI

     Pope AFB, NC

     WR-ALC, Robins AFB, GA

     CIGTF, Holloman AFB, NM

- A-7 Replacement Inertial Measurement System (RIMS) Program

     SM-ALC, McClellan AFB, CA

Rockwell Collins Government Avionics Division — Cedar Rapids, IA

LTV Aircraft Products Group — Dallas, TX

162nd Tactical Fighter Group (TF)/MMECZA, Tucson, AZ

- F-16A/B

  General Dynamics/Fort Worth Division — Ft. Worth, TX

  OO-ALC, Hill AFB, UT

- F-16C/D Post Blk 50 Program

  General Dynamics/Fort Worth Division — Ft. Worth, TX

  F-16 SPO, Wright-Patterson AFB, OH

- MH-53J Enhanced Navigation System (ENS) Program

  Systems Research Labs, Inc., Defense Electronics Division — Dayton, OH

  Systems Research Labs, Inc., Pensacola Division — Pensacola Naval Air Station, FL

  Canadian Marconi Avionics Division — Kanata, Ont.

  IBM Federal Systems Division — Owego, NY

  MH-53J SPO, Robins AFB, GA

- F-4 Navigation Weapons Delivery System (NWDS) Program

  Boeing Military Airplane — Wichita, KS

  Eglin AFB, FL

  OO-ALC, Hill AFB, UT

- MC-130 Combat Talon Program

  Lockheed Air Services — Ontario, CA

  Eglin AFB, FL

- AC-130U Gunship Program

  AC-130U SPO — Wright-Patterson AFB, OH

  Rockwell North American Aircraft Operations — Lakewood, CA

- 4950th Test Wing, Wright-Patterson AFB, OH

  Special Applications

  Radar Test Bed

  MILSTAR

  etc.

- Federal Aviation Agency (FAA)

  Research Center — Atlantic City, NJ

- T-39 GPS Testbed

    JPO, Los Angeles, CA

- Naval Coastal Systems Center (NCSC)

    Ft. Walton Beach, FL

- MH-60G

    Systems Research Labs, Inc., Defense Electronics Division — Dayton, OH

    Canadian Marconi Avionics Division — Kanata, Ont.

    MH-60G SPO, Robins AFB, GA

    TCS, INC. — Robins AFB, GA

3. INTERFACE CONTROL

A key to the successful Standard INU program is aggressive control and maintenance of the SNU 84-1 Specification. Because of the evolving needs of the user, the baseline documentation must also evolve. SNU 84-1 has evolved from Revision 1 to Revision 2 to Revision 3, no amendment, to the current Revision 3, Amendment 1 configuration. Revision 3, Amendment 2, was initiated in the fourth quarter of 1987 and is still in process. It is expected that SNU 84-1 R3A2 compliant INUs will be available in 1990.

The evolution of the specification is conducted by means of scheduled "Open Forums" or User Interface Control Working Group (ICWG) meetings in which users, INU contractors, and prime avionics integrators are invited. The meetings are often preceded by INU contractor/USAF Engineering meetings, in which proposed changes/enhancements are discussed and agreed upon for presentation at the User ICWG meeting. The output of these meetings results in a final draft SNU 84-1 Specification, which then becomes the baseline for Engineering Change Proposals (ECPs) by the INU contractors for INU changes and the integrators for INU interface changes affecting their INU implementation. The success of the above process is directly proportional to participation of the users. Funding for participation by all concerned parties must be well planned and consistent. Funding of the subsequent ECPs must be just as consistent and timely.

The next most important element in successful integration of the Standard INU on a given application is the establishment of strong technical communication between the INU contractors and the prime avionics integrator. This should be accomplished by the use of Associate Contractor Agreements, formalized communications, execution of Interface Control Documents, and frequent Technical Coordination Meetings. This usually tends to not be the case as neither the integrator nor the INU contractor has been funded for this task. The assumption has been that the integrator can integrate to the SNU 84-1 Specification. In practice, this has not been a good assumption. The evolution and maturing process of the SNU 84-1 Specification illustrates that the process is not perfect. In addition, each new integrator finds a new way to try and use the INU that was not anticipated by the SNU 84-1 Specification writers. This should not be unexpected when versatile equipment, such as the current RLG-based INUs, are involved.

4. RECOMMENDATIONS/LESSONS LEARNED

Based on the author's experience on the Standard INU program since 1984, the following recommendations are provided for consideration:

- In the area of Interface Control and Specification Control/Maintenance, it's important to provide engineering staffing continuity. There have been multiple changes in responsible individuals since 1984. Each individual change results in a break in continuity, loss of prior experience, and the coming up to speed of a new individual. The continuity for the SNU 84-1 interface should not be allowed to reside only with the INU contractors, without similar continuity on the government side.

- The *USAF Standard INU Program Management*, for both contractor control and integration support, has involved many different individuals. With the substantial number of users involved, strong, experienced, knowledgeable management is very important.

- To ensure transparency between INU contractors at the interface level, a common Acceptance Test Procedure and common OFP Demonstration Procedure needs to be written and controlled by the Air Force. Common ATP and OFP Demonstration Procedures should be used by all SNU 84-1 compliant INU contractors.

  An alternative is for the Air Force to conduct ATP and OFP Demonstration Tests on each INU contractor's equipment using the other contractor's procedures and test equipment. If the INUs are truly transparent, the tests should be successful. This applies to the F-15/FNU 85-1 compliant INUs also.

- The INU physical configuration, as defined by SNU 84-1, needs to be better documented using applicable DoD Standards.

- The INU mount configuration must be controlled. Currently there exist five different INU mount implementations, which are contractor specific.

- INU Integration Support must be planned for and funded. This includes the INU contractors, Avionics subsystem integrators, USAF Aircraft SPOs and/or ALCs, and the Standards SPO. Otherwise, there may be a return to many application unique INUs funded by individual users.